nature

www.nature.com/nature

Vol 464 | Issue no. 7291 | 15 April 2010

Testing time for gene patents

A surprising US court decision highlights the need to modernize gene-patenting practices if patients are to benefit from advances in genetic research.

The idea of awarding patents for specific gene sequences has been a contentious subject since at least the early 1990s, when it first became technologically possible to generate such sequences in large numbers. But US courts have consistently upheld these patents. Even in Europe, where the practice is particularly controversial, gene patenting has been codified into law since 1998. For better or worse, gene patents had seemed destined to be a settled part of the intellectual-property landscape.

Until 29 March, that is, when the US District Court for the Southern District of New York shocked the biotech community by invalidating patents covering mutations in the *BRCA1* and *BRCA2* genes that are used to assess the risk of breast and ovarian cancer. Myriad Genetics, a company based in Salt Lake City, Utah, holds exclusive licences on these patents and has aggressively defended them. In 2009, a group of patients, researchers and clinicians sued Myriad, asserting, among other complaints, that the patents hamper medical research. And District Court judge Robert Sweet largely agreed.

"As the biotech industry inches closer to the long-anticipated era of personalized medicine, genetic tests promise to exert increasing influence in the clinic."

Beyond the ruling's power to make headlines, industry observers and legal experts see little chance that it will pose a real threat to gene patents. Not only are US courts outside the boundaries of New York's southern district not compelled to follow Sweet's precedent, but Myriad Genetics has pledged to appeal. The case will next be heard in the Court of Appeals for the Federal Circuit in Washington DC, which many observers feel favours patent holders.

Nevertheless, the decision does reflect growing concern about the impacts of gene patents on genetic testing. As the biotech industry inches closer to the long-anticipated era of personalized medicine, genetic tests promise to exert increasing influence in the clinic. But fully realizing that promise will require a view of gene patenting that is considerably more sophisticated than the one-size-fits-all standard that now prevails.

Genetic testing is undergoing a revolution. Classic tests relying on mutations in one or two genes, such as the *BRCA1* and *BRCA2* tests, are giving way to complex analyses involving many genetic signatures. Tests for a genetic heart condition called long QT, for example, now assay a dozen genes. Eventually, moreover, these complex analyses will themselves give way to whole-genome sequencing. Strict enforcement of single-gene patents in this landscape could ensnare genetic tests in a patent thicket — a tangled web of patents that would have to be negotiated before a given test could be performed. Such a situation threatens to hinder innovation.

There are also legitimate concerns that gene patents can limit patient and researcher access to genetic tests. This need not always be the case: tests for mutations associated with cystic fibrosis are patented, and the patents licensed to many companies. Those companies seem to have managed to turn a profit on the tests without creating a monopoly.

But in light of these concerns, an advisory committee to the US Department of Health and Human Services recently embarked on an analysis of the impact of gene patents on genetic testing. Its report, finalized in February, distinguishes between the use of a gene patent to cover a genetic test — in which the tester simply observes the sequence of a gene — and the use of that patent to protect investment in developing biotherapeutics, when patent holders use genetic information as a platform for invention. Given this distinction and the importance of preserving access to gene tests in the clinic, the committee recommended that gene-patent rights should not be enforced when they are violated in the course of research or genetic testing.

This proposal leaves many details still to be hammered out — and in any case it faces an uncertain future. Health-department secretary Kathleen Sebelius has yet to decide whether to recommend that Congress adopts the changes — and no bill has yet been introduced. But the proposal has already prompted a sharp outcry from biotechnology lobbyists and some members of Congress, who fear that it could hurt the nascent genetic-testing industry. Nevertheless, the advisory committee has provided one way forward. But whichever way they choose, Sebelius, Congress and the biotechnology industry should act without delay, implementing the basic principle of access to valuable genetic information for patients and researchers alike. ■

Winners take all

Scientific competition is lacking in Japan, and efforts to increase it are not always best focused.

In a country such as Japan, where personal loyalties are strong and university pedigrees are often akin to a family bond, objective evaluation of grants can be a challenge.

That is perhaps one reason why Japan has historically distributed comparatively little of its science funding through competitive grants, preferring instead to spread it more evenly by funnelling the money into the basic operating budgets of universities and research institutions. In 2009, only 13.8% of the country's reseach funding was allocated through competitive grant schemes — up from just 8.9% in 2002 — a considerably lower proportion than in the United States.

Although this approach might seem democratic and fair, Japanese

officials have increasingly come to realize that it often fails in the larger test of picking the best science. During the past decade, as Japan has struggled with a stagnant economy, international patent disputes and competition from an emergent China, officials have repeatedly sought to make Japanese researchers stronger on the international scene by upping the competition at the domestic level.

Those efforts have not always paid off — for example, plans to double competitive funding between 2001 and 2005 fell short because the economy couldn't keep up and the science budget plateaued. But change may now be afoot with the massive ¥100-billion (US$1.1 billion) Funding Program for World-Leading Innovative R&D on Science and Technology (FIRST) — a plan that was slashed by the new government last year, but that is nevertheless handing out some of the biggest competitive grants Japanese researchers have ever seen (see page 966). The 30 winning scientists will now have four years to spend an average of ¥3.3 billion each, and will enjoy much greater autonomy under this 'researcher-focused' plan than that offered by previous grant programmes.

FIRST represents an ambitious and worthwhile step for Japan. However, the programme could have been better planned. Consider, for example, that most of the 30 FIRST winners are already world-leading innovators — they include a Nobel laureate and some of the top-cited scientists in their fields. The majority of them were already the recipients of significant grants, and four have been leaders or co-leaders at one of the five World Premier International Research Centers — a 2007 initiative intended to attract top-quality scientists from around the world to work with their Japanese counterparts. These outstanding researchers have accomplished much, and will undoubtedly accomplish more. But it would have been encouraging to see some new faces. Because Japan's strategy for world-class innovation rewards researchers solely on the basis of their past success, it runs the risk of missing some excellent ideas from younger, less-established researchers.

"The government should make sure that the country's basic foundations for science are in good repair — and that it is seeking out the most creative projects."

It is also worth asking whether all of these projects require such huge investment. Some clearly do — one example being the Hitachi corporation's effort to develop a holographic electron microscope. This could open a new window onto atomic structures, thereby benefiting hundreds of researchers in various fields. But it is less clear whether all of the FIRST projects will be able to make such productive use of their massive budgets.

A proportion of the FIRST money might arguably have been better spent on increasing the pot of money available through the already-existing mechanism for doling out small competitive grants: the 'Grants-in-Aid' programme administered by one of the country's leading research funding agencies, the Japan Society for the Promotion of Science. Such funding is crucial for small groups hoping to look into risky but potentially groundbreaking ideas — the way that many of the FIRST project leaders made the major discoveries that led them to fame. Moreover, the Grants-in-Aid programme has been forced to cut the average size of its awards in recent years, from ¥3.34 million in 2003 to ¥2.89 million in 2008, because Japan's overall research budgets have remained flat even as the country tries to support an increasing number of researchers. That surge was created, in part, by a programme launched in 1995 that successfully produced thousands of new postdocs but didn't find them jobs (see *Nature* **449,** 1084–1085; 2007).

These concerns aside, however, Japan's government and research community must now follow through on FIRST, giving these projects the support and participation they need to realize their full value. But the next time the government invests large sums in competitive funding, it should first make sure that the country's basic foundations for science are in good repair — and that it is truly seeking out the most creative projects. They are not always in the obvious places. ■

Welcome *Nature Communications*

Since the launch of *Nature Genetics* in 1992, the number of Nature research journals has grown to 16 — the most recent, *Nature Chemistry*, was launched a year ago. This month sees the launch of the seventeenth: *Nature Communications*.

All of the previous Nature research journals have focused on a particular discipline or community of research interests. Their aim is to publish the most original and scientifically impact-making research appropriate to those particular audiences. Their high ranking in the citation league tables would suggest that this goal is generally being fulfilled.

Nature Communications differs in being multidisciplinary. It aims not to compete with the established Nature journals, but to publish rigorous and comprehensive papers that represent advances of significance to specialists within each field. In addition, it welcomes submissions in fields that are not represented by a dedicated Nature research journal — for example, developmental biology, plant science, microbiology, ecology and evolution, palaeontology, astronomy and high-energy physics (see go.nature.com/xJzuY5). Readers will find in the launch issue papers on topics including classical and quantum correlations under decoherence; a candidate gene for mechanoreception in *Drosophila* sensory cilia; a strategy to obtain sequence-regulated vinyl copolymers using metal-catalysed step-growth radical polymerization; how a ritualized vibratory signal evolved from locomotion in territorial caterpillars; and more besides.

Like all Nature journals, it is editorially independent. It is also the first Nature research journal to be funded in hybrid fashion: by both subscriptions and optional authors' fees that allow instant free access to their published papers. (It is our publishers' policy to keep subscription rates of hybrid journals under review to reflect the volume of content that is behind the subscription firewall.) Furthermore, it is the first Nature journal to be launched entirely without a print edition: its content is available only online.

Nature welcomes this distinctive new sibling publication — this time, serving the whole research community. ■

RESEARCH HIGHLIGHTS

Behind enemy lines

Nature Commun. doi:10.1038/ncomms1002 (2010)
Animal displays are thought to evolve from ancestral behaviours that turn, over time, into ritual communication signals.

The masked-birch caterpillar (*Drepana arcuata* Walker, pictured) conveys ownership of its territory with vibrations, including the dragging of its anal segment across a leaf to make a scratching noise. The behaviour typically staves off intruder caterpillars. Jayne Yack of Carleton University in Ottawa, Canada, and her colleagues have found that the anal scraping seems to be a modified component of a typical territorial behaviour observed in a number of related, ancestral species — an aggressive crawl towards intruders.

Body movements previously associated with fighting can become ritualized, the authors suggest, permitting conflict resolution without physical altercation.

J. YACK

PATHOLOGY

Bent out of shape

Biophys. J. **98,** 1302–1311 (2010)
Researchers in Belgium have spied on the earliest steps in a process that leads to Parkinson's disease: the formation of protein clumps in the brain.

Yves Engelborghs and his colleagues at the University of Leuven used a technique called fluorescence correlation spectroscopy, which tracks the size of molecules by measuring their diffusion rates. The team watched individually labelled α-synuclein proteins *in vitro* as they bunched together.

These clumps are found in larger structures called Lewy bodies in the neurons of people with Parkinson's disease. The team found that the early protein clumps formed in regions in which α-synuclein proteins were highly concentrated. The proteins in these clumps adopted a shape intermediate between those of the individual proteins and those of proteins in the final, toxic aggregates found in Lewy bodies.

NANOTECHNOLOGY

Down the tube

Phys. Rev. Lett. **104,** 133002 (2010)
Super-sensitive single-atom detectors are the latest brainchild of researchers working with single-walled carbon nanotubes.

Anne Goodsell and her co-workers at Harvard University in Cambridge, Massachusetts, harnessed one of the tubes' many unusual properties: their ability to create a powerful electric field when charged. The researchers suspended a 10-micrometre-long nanotube between two electrodes and charged it to hundreds of volts. They then fired a beam of cold rubidium atoms at the tube. Atoms spiralled quickly around the tube until an electron jumped from a neutral atom to the positively charged tube. Once ionized, the atom was repelled by the tube, and shot out at high speed into a nearby detector.

The team believes that the technique could be useful as an atom 'sniffer' or counter.

PLANETARY SCIENCE

Venus vents

Science doi:10.1126/science.1186785 (2010)
Volcanoes on Venus spewed lava as recently as three centuries ago, say Suzanne Smrekar of the Jet Propulsion Laboratory in Pasadena, California, and her colleagues. The evidence points to a geologically active planet.

Using data from the European Space Agency's Venus Express orbiter, the researchers looked at the surface composition of three hotspots — locations analogous to Hawaii — where plumes from the hot mantle pierce the crust (pictured below). The surfaces were extraordinarily fresh, leading to an age estimate for the lava flows of between 2.5 million and 250 years.

This suggests that Venus vents its internal heat in regular small eruptions, resurfacing itself piecemeal. This contrasts with the long-held view that Venus undergoes catastrophic episodes in which the crust founders and the entire planet is bathed in molten rock.

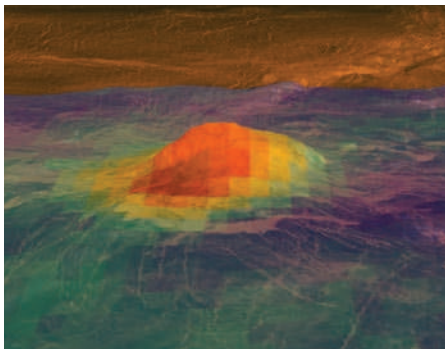

R. OLLERENSHAW/E. DEJONG/SOLAR SYSTEM VISUALIZATION GROUP/NASA/JPL CALTECH/ESA

NEUROSCIENCE

Stressing memory

J. Neurosci. **30,** 5037–5046 (2010)
The emotional arousal associated with a class of stress hormones may be required to form long-term memories, say Benno Roozendaal at the University of Groningen in the Netherlands, Marcelo Wood at the University of California, Irvine, and their colleagues.

The authors gave glucocorticoid hormones to rats and mice and tested how well the animals remembered objects and their locations. They found that the hormones improved memory by boosting acetylation, the addition of acetyl groups to nuclear targets.

This modification appears to facilitate some of the gene transcription required to consolidate memories. But promoting acetylation in the absence of the hormone didn't improve memory. The hormone had to first activate receptors on the cell membrane in order to trigger a cascade of events involved in laying down memories.

PHYSICS

Monopoles on demand

Nature Phys. doi:10.1038/nphys1628 (2010)
Elusive magnetic monopoles — regions of lone north or south magnetic charge — have recently been detected in very cold 'spin ices', a class of tetrahedral crystals. Now Will Branford and his colleagues at Imperial College London have created monopoles at

room temperature, and imaged them directly.

The team arranged cobalt nanorods into a honeycomb lattice on silicon to form a two-dimensional analogue of the spin-ice structure. By applying magnetic fields they disrupted the bars' magnetic alignments, so that regions of north or south magnetic charge were trapped at points where three bars met.

OCEANOGRAPHY

Early bloomers

Ecology doi:10.1890/09-1207.1 (2010)

An analysis of satellite data suggests that the vast phytoplankton blooms that grace oceans around the globe in springtime actually start to develop in the depths of winter, challenging long-held theories about what drives them.

With almost 10 years' worth of data from NASA's SeaStar spacecraft, Michael Behrenfeld of Oregon State University in Corvallis found that phytoplankton populations begin to increase during winter, when deeper, nutrient-rich waters mix with the ocean surface layer and disperse zooplankton grazers that keep phytoplankton in check.

J. SCHMALTZ/MODIS RAPID RESPONSE TEAM/NASA GSFC

The visible bloom (pictured right) occurs in spring, months after the active surface layer stops deepening. Phytoplankton, multiplying quickly, are concentrated in the layer and nourished by spring sunshine — previously believed to be a major factor in initiating the bloom.

The bloom ends when grazing zooplankton or dwindling surface nutrients bring the phytoplankton population back under control.

BEHAVIOURAL GENETICS

South bee-ch diet

PLoS Genet. **6,** e1000896 (2010)

Foraging behaviour in the honeybee *Apis mellifera* can be altered by tweaking the expression of a gene in abdominal fat cells.

Gro Amdam and her colleagues at Arizona State University in Tempe watched bee strains that had been selected for their foraging preference — for either pollen or nectar. After lowering the expression of a gene related to insulin signalling in the insects' fat cells, bees of both strains cut down on their collection of sugary nectar in favour of protein-containing pollen. However, the treatment had no effect on the bees' sensory response to sugar.

The results suggest that systems other than the nervous system can affect behaviour, although the subtleties in the shift indicate that multiple genes are involved.

SEISMOLOGY

On shaky ground

Geophys. Res. Lett. doi:10.1029/2009GL042352 (2010)

The earthquake that struck the Italian city of L'Aquila on 6 April 2009 killed about 300 people. It was preceded by many foreshocks, but the authorities did not evacuate buildings and were heavily criticized after the event.

However, Thomas van Stiphout of the Swiss Seismological Service in Zurich and his colleagues show that, given the uncertainties of earthquake forecasting, evacuations are rarely cost-effective. Combining a seismic-hazard model with an analysis of the costs and benefits of evacuation, they found that an expensive, general evacuation was not justified in the weeks and hours leading up to the L'Aquila quake.

The model also showed that weak buildings and loose soil conditions contributed most to overall risk. The authors say that future mitigation strategies should focus on these factors for targeted evacuations or the placement of civil first-aid groups.

ASTROPHYSICS

The odd couple

Astrophys. J. **714,** L84–L88 (2010)

Astronomers have found a planet that may have formed like a star — through gravitational collapse. Kamen Todorov of Pennsylvania State University in University Park and his colleagues spotted a planet 5–10 times the mass of Jupiter orbiting a brown dwarf — a star too small to ignite by fusion.

The brown dwarf is only about one million years old, so its companion is too young to have slowly accreted from the dwarf's disk of dust and gas. Yet the planet is much too big to have quickly collapsed from a large lump in a dwarf's modest disk.

The authors suggest that the dwarf and its planet formed unusually, in the same way that binary star systems do — with a vast, primordial gas cloud fragmenting and collapsing gravitationally into two objects.

JOURNAL CLUB

Xing Xu
Chinese Academy of Sciences, Beijing

A palaeontologist considers the evolution of birds' mechanism of breathing.

During both inhalation and exhalation, the air in birds' lungs moves in just one direction, through small tubes. This is unusual: most animals move air tidally, in and out of dead-end gas-exchange structures. The question of when and how the avian breathing mechanism evolved is interesting to palaeontologists like me who study these unusual features.

Traditionally, the avian pattern of one-way breathing has been thought to depend on special accessory air sacs that work similarly to bellows. Largely because they don't have these air sacs, alligators have always been presumed to be tidal breathers. However, this has now been questioned by Colleen Farmer and Kent Sanders at the University of Utah in Salt Lake City, who suggest that alligators actually breathe like birds (C. G. Farmer & K. Sanders *Science* **327,** 338–340; 2010).

By measuring air and water flows in the lungs of anaesthetized and dead alligators, respectively, the authors demonstrate unidirectional flow. They draw the reasonable inference that this bird-like breathing is characteristic of the archosaurs, a broad group that includes both alligators and birds.

The finding is leading to changes in the direction of palaeontological research. Farmer and Sanders' results imply that air sacs are not essential for unidirectional breathing. The function of these sacs in extinct ancestors of birds — dinosaurs such as theropods — should thus be reconsidered.

Unidirectional breathing probably appeared among ancestral archosaurs during the Early Triassic period, some 250 million years ago, a time of low oxygen levels that might have encouraged evolutionary experimentation with improved ventilation. This raises the question of whether the drastic conditions led to other notable changes in Triassic animals.

Discuss this paper at **http://blogs.nature.com/nature/journalclub**

NEWS BRIEFING

RESEARCH

Ice satellite launched: Four and a half years after a launch failure saw its first incarnation splash into the Arctic Ocean, the European Space Agency's ice-measuring CryoSat-2 has successfully made it into orbit. Launched from the Baikonur Cosmodrome in Kazakhstan on 8 April, the space probe will monitor variations in the extent and thickness of polar ice. The information it provides about the behaviour of coastal glaciers that drain thinning ice sheets will be key to better predictions of future sea-level rise (see also *Nature* **464,** 658; 2010).

Gulf War diagnosis: After examining some 400 studies published since 2005, the US Institute of Medicine said in a report released on 9 April that a complex of symptoms including joint pain and fatigue, popularly known as Gulf War syndrome, is associated (but not necessarily causally) with service in the Gulf War. The 12 authors called for further research refining the diagnosis and developing treatments for Gulf War syndrome — which it dubs "multisymptom illness". Of nearly 700,000 US personnel who were deployed to the Gulf region, more than 250,000 suffer from persistent, unexplained symptoms.

Deepest vents: The deepest underwater hydrothermal vents ever found have been spotted by a robot exploring waters off the Cayman Islands in the Caribbean. The black smokers are 5 kilometres down in the Cayman Trough, more than 900 metres deeper than previously known. The vents consist of spires of copper and iron ores erupting superheated water from the sea floor, at temperatures hot enough to melt lead. Scientists from the University of Southampton, UK, who are leading the Cayman expedition on the research ship RRS *James Cook,* announced the find on 11 April.

R. BECK/AFP/GETTY

RESEARCHERS RALLY

A rally in defence of scientists who use animals in research drew between 300 and 400 supporters at the campus of the University of California, Los Angeles (UCLA) on 8 April. Organized by the group Pro-Test for Science — founded by UCLA neuroscientist David Jentsch — it follows a similar rally in 2009. Since Pro-Test has begun confronting anti-research protesters on campus and organizing dialogue with peaceful groups who oppose animal research, animal-rights activists have stepped down attacks on UCLA researchers, Jentsch says. "They still come to my house and scream obscenities at me. But the most important objective has been achieved, which is that nothing has been burned or blown up." See go.nature.com/54MVKO for more.

Element 117: A new superheavy element with atomic number 117 has been synthesized at Russia's Joint Institute for Nuclear Research in Dubna, an international team of researchers announced on 6 April (Y. T. Oganessian *et al. Phys. Rev. Lett.* **104,** 142502; 2010). Six atoms of 'ununseptium' (the element's temporary name) were made by smashing calcium-48 into a berkelium-249 target that was made at Oak Ridge National Laboratory, Tennessee.

BUSINESS

Wind energy: The US wind-energy industry installed more than 10 gigawatts (GW) of new wind-power-generating capacity in 2009, bringing the total capacity (all onshore) to some 35 GW — about 1.8% of the country's electricity generation.

Texas has installed the largest capacity (9.4 GW), whereas Iowa is the state most reliant on wind energy: its 3.7 GW generated 14.2% of its electricity last year.

The figures come from a report released on 8 April by the American Wind Energy Association, an industry group based in Washington DC. An inadequate transmission grid threatens further expansion of the industry, the report said.

Software merger: Two large producers of scientific software, Accelrys and Symyx Technologies, will merge, the firms announced on 5 April. Symyx, headquartered in Santa Clara, California, produces electronic laboratory notebooks and chemical informatics software. Accelrys, headquartered in San Diego, California, offers modelling and simulation software. The combined firm will be based in San Diego.

SOUND BITES

"Both are correct heights. No measurement is absolute. This is a problem of scientific research."

Raja Ram Chhatkuli, director general of Nepal's survey department, confirms that China and Nepal have agreed to disagree over Mount Everest's exact height.

Source: Reuters

POLICY

Royal Institution coup: The council of the UK's Royal Institution successfully fought off a coup attempt this week.

Members of the UK's oldest scientific research organization, founded in 1799, overwhelmingly rejected proposals put to a special general meeting that the entire governing council, bar the president, be removed.

The move was sparked by a group of members lamenting the removal in January of former director Susan Greenfield, a high-profile neuroscientist at the University of Oxford, and the multimillion pound funding shortfall that prompted the redundancy.

Nuclear review: Nuclear-weapons research could benefit from the US Nuclear Posture Review. The policy, unveiled on 6 April ahead of both an agreement signed with Russia on 8 April to reduce nuclear stockpiles and a nuclear-security summit in Washington DC this week, tempers the threat of nuclear attacks against other countries and repeats that no new nuclear weapons will be built. But it may also boost basic research at national-security laboratories. See page 965 for more.

Climate deadlock: At the latest round of United Nations climate talks last week in Bonn, Germany, delegates from 175 nations failed to break the impasse in international climate diplomacy. Delegates agreed to hold two additional meetings before the next UN climate summit in late autumn in Cancun, Mexico. Even so, prospects are "slim" that a new climate agreement can be reached by the end of the year, Yvo de Boer, head of the UN's Framework Convention on Climate Change, told the meeting on 11 April.

NUMBER CRUNCH

1.2%

The average salary gain for a full-time US faculty member in 2009–10, over 2008–09; a 1.5% decrease when adjusted for inflation.

Source: American Association of University Professors survey, 12 April

Ethiopian science academy: The Ethiopian Academy of Sciences (EAS) was launched on 10 April in Addis Ababa. A growing number of African countries — most recently, Zambia, Mauritius and Mozambique — are establishing such organizations to promote research quality and offer scientific advice. The EAS starts with 50 fellows from both the natural and social sciences; its elected president is Demissie Habte (pictured below), former dean of medical research at Addis Ababa University. Its funding structure is not yet clear, but the founders hope the government will support the body. See go.nature.com/K6tBzV for more.

Food failures: A US government report has found "significant weaknesses" in the inspection of domestic food facilities by the Food and Drug Administration (FDA). The agency has also failed to take adequate regulatory action against some facilities, said the report, released on 6 April by the Office of Inspector General for the Department of Health and Human Services, the FDA's parent agency. Legislation that would boost the FDA's food-safety inspection powers has stalled in the Senate. The FDA says it had already addressed many of the issues in the report, which covered 2004–07.

THE WEEK AHEAD

17–21 APRIL
Studying the genomes of individual cancer types is a hot topic at the American Association for Cancer Research's 101st annual meeting, in Washington DC.
go.nature.com/IDRmCV

19–22 APRIL
The World People's Conference on Climate Change and the Rights of Mother Earth is held in Cochabamba, Bolivia. The country's president, Evo Morales, announced the summit, which expects thousands of attendees, after the failure of talks in Copenhagen.
http://pwccc.wordpress.com

19–20 APRIL
New ways of measuring biological diversity — and of conserving it — will be discussed at the Royal Society in London.
go.nature.com/eqb5BD

20–23 APRIL
Barcelona, Spain, hosts the first ever European Energy Conference — an interdisciplinary meeting focused on energy technology research.
www.e2c-2010.org

FUNDING WATCH

A call for more research funding for the US National Institutes of Health (NIH) in Bethesda, Maryland, shows how much the agency has relied on the national stimulus package to boost its spending power. The Federation of American Societies for Experimental Biology (FASEB) — an advocacy group based in Bethesda that represents 23 biomedical societies — has published trends summarizing how the NIH's budget has been falling in real terms since 2004, taking into account the rate of inflation for biomedical-research costs (see chart).

The stimulus bonanza brought the NIH's budget up to US$36.4 billion in 2010 (above that of 2004, in real terms). US President Barack Obama's 2011 budget request (see *Nature* **463,** 594–595; 2010) boosted the agency's basic budget by $1 billion to about $32 billion — an increase of 3.2%. But with no stimulus, that represents a 14.3% decrease from the 2010 purchasing power of the NIH. FASEB calculates that the total number of research-project grants that the NIH will be able to support may drop from 39,579 in 2010 to 35,202 next year. The federation also expressed concern that the NIH's assumption used for that calculation — a 1.4% rise in average research-grant costs — is too low. Fearing the looming cliff of the post-stimulus sag, the group recommends that Congress appropriate $37 billion for the agency in 2011.

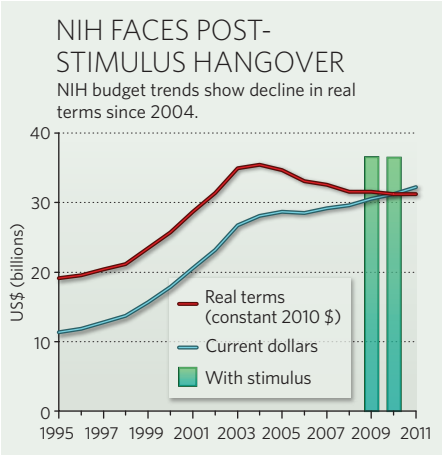

SOURCE: FASEB

NEWS

Lab-animal battle reaches truce

Biomedical scientists say revised European directive on animal welfare averts feared disaster for research.

After more than a decade of pitched battles between research advocates and animal-rights campaigners, European Union (EU) legislators have finally agreed on a new legal framework to regulate the use of animals in research.

A closed-door meeting between representatives of the European Commission, the European Parliament and the European Council (respectively, the EU's executive and two legislative bodies) reached a compromise on a directive covering the protection of animals used for scientific purposes (86/609/EEC) on 7 April. The directive must still be ratified by the parliament and council, but this is likely to happen without further debate by July.

Previous drafts of the directive had seemed set to severely hamper European biomedical research, by placing significant restrictions on invasive studies using primates, for example (see *Nature* **456,** 281–282; 2008). But the final directive has largely diffused scientists' concerns. Basic research using primates will now be allowed, for example, and animals will not have to be destroyed immediately after research procedures that cause "moderate" discomfort, as previous forms of the directive had decreed. Instead, the animals can be used in other procedures. At the same time, the draft addresses concerns about animal welfare by introducing minimum cage sizes and other measures.

"It is a political document, a compromise text," says Stefan Treue, director of the German Primate Centre in Göttingen. "But it could have been worse and we can live with it."

"The compromise that has been reached is something we can live with," agrees Kirsty Reid of the Brussels-based animal-welfare lobby group Eurogroup for Animals, adding that she still regrets the many exemptions to bans on several types of research.

The legislation was designed to update 1986 rules for protecting research animals and to harmonize regulations across the EU. Political discussions began in 1998, and in 2002 the European Parliament mandated the commission to write a draft also taking into account the EU's new commitment to the reduction, replacement and refinement of animal tests.

The commission draft that eventually emerged in November 2008 alarmed both academic researchers and the pharmaceutical industry by proposing extreme restrictions on research and increasing bureaucratic demands on researchers. For example, it banned research on non-human primates unless it was directly applicable to the treatment of "life-threatening or debilitating human conditions", thus blocking basic research, particularly on the brain.

A minimum cage size for research animals is one factor addressed in proposed EU legislation.

G. ROBERTSON/EYEVINE

"The compromise that has been reached is something we can live with."

Its scope was so broad that it forbade the scientific use of hens' eggs, essential for vaccine production. And in insisting that animals be destroyed after an experiment causing mild discomfort, it would have dramatically increased the number of animals used in research.

"That draft was a big wake-up call to the scientific community, which didn't lobby enough at the right time," says Simon Festing, chief executive of the London-based research lobby group Understanding Animal Research. Instead, he claims, the commission was exposed to the emotionally powerful influence of the well-organized animal-welfare and anti-vivisection lobby.

But in 2009, research organizations swung into action to persuade parliament to be more sympathetic to their point of view. In its first parliamentary reading in May 2009, most of the controversial restrictions in the draft directive had been removed (see *Nature* **459,** 139; 2009). But the new parliament added a clause of its own, requiring sharing of data generated on animals. Drug-development companies pointed out that this would be difficult for them to comply with, given that much of this information is proprietary intellectual property.

The battle continued through 2009 as the amended draft was discussed by the European Council, which comprises representatives of the EU's 27 member states, many of which considered it too liberal towards researchers. After a new parliament was elected last June, the animal-welfare lobby pounced on new members, convincing many to argue for further restrictions, says Julian Böcker, parliamentary assistant to directive rapporteur Elisabeth Jeggle. "I'd like to be able to convey just how hard we had to fight to maintain research-friendliness in the directive," says Böcker.

Endangered experiments

The outcome is less than perfect, but at least animal research will be possible, says an administrator at the DFG, Germany's largest grant-giving agency. The directive does ban some forms of research — those involving great apes or causing extreme and prolonged pain. But researchers can appeal for an exemption, on grounds of clinical urgency, through a special committee to be set up in Brussels.

The final draft of the directive also allows experiments on endangered species, such as the barn owl (*Tyto alba*), which is bred in captivity specifically for auditory research. Procedures for project applications and evaluations are more streamlined than in earlier drafts, and the bureaucratic burden should not increase for researchers from countries in which rules are already strict, such as Britain, Germany and France. Mandatory sharing of animal-research data has also been dropped.

But some scientists are still worried that problems could arise when the loosely worded directive is translated into more tightly worded national laws, which will have to specify, for example, which types of experiment are considered to cause "long-lasting, severe pain". Others maintain that an outright ban on some types of studies clashes with Europe's constitutional duty to carry out research, as enshrined in the Lisbon Treaty, adopted in December 2009.

And physiologist Rainer Nobiling of the University of Heidelberg in Germany worries that restrictions on the use of non-human primates might encourage more testing of experimental therapies in humans, against the Nuremberg code of research ethics. ■

Alison Abbott

S. MORRISON/EPA/CORBIS

SWIRLING DUST SHOCKS PHYSICISTS
Swarms of self-charging particles defy expectations.
www.nature.com/news

US nuclear policy could boost basic research

US President Barack Obama's nuclear-weapons policy represents a delicate compromise that could limit research on new warheads but bolster the workforce of scientists at the national security laboratories. The balancing act came into sharp focus in the 2010 Nuclear Posture Review (NPR), publicly released last week.

The policy downplays the role of nuclear weapons in US foreign policy and formally abandons efforts to build new warheads. But the language contains loopholes that could allow most nuclear-weapons design work at the laboratories, Los Alamos and Sandia in New Mexico, and Lawrence Livermore in California, to continue unfettered.

The NPR also emphasizes the need to modernize nuclear infrastructure (see 'Laser-fusion showdown') and maintain and expand scientific expertise at the weapons labs. The National Nuclear Security Administration, which manages the nuclear-weapons programme, employs thousands of scientists and engineers at these labs and draws recruits from fields such as astrophysics. The document follows up the president's fiscal 2011 budget, which would boost weapons and non-proliferation spending by more than 13%, to US$11.2 billion. Many experts see the administration's moves as an effort to please the leadership at the weapons labs.

"The administration needs to work with the lab directors very closely to make sure they are happy," says Stephen Young, a nuclear expert with the Union of Concerned Scientists in Washington DC. Obama will need their support as he tries to finally win Senate approval of the 1996 Comprehensive Nuclear-Test-Ban Treaty outlawing all nuclear testing. "The large budget increases for the labs are a principal demonstration of that fact," says Young.

Obama unveiled his international agenda on nuclear security and non-proliferation a year ago in Prague, recommitting the United States "to seek the peace and security of a world without nuclear weapons". On 8 April, two days after releasing the NPR, Obama signed a new arms-reduction treaty with Russia, reducing the cap on deployed weapons from 2,200 to 1,550 per country over the next seven years. He followed that up earlier this week by hosting a two-day summit in Washington DC to discuss broader nuclear-security issues.

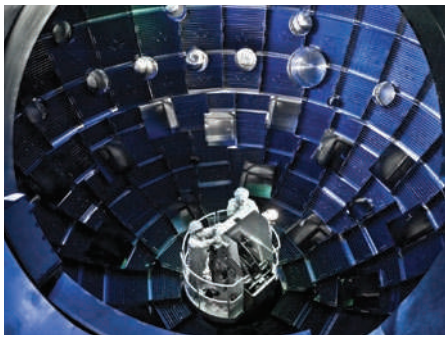

LLNL

The National Ignition Facility is part of the US push to modernize its nuclear infrastructure.

William Press, a physicist who is on the president's science advisory board and who formerly served as deputy director for science and technology at the Los Alamos lab, supports the general thrust of the new weapons policy but regrets that the NPR doesn't make clear what kind of work will be allowed at the labs. For example, although modifying nuclear components in a weapon would require authorization from the president and Congress, Press says that one loophole would allow the labs to build weapons that are in many respects 'new' by mixing and matching components that have been tested in the past. Although this may satisfy lab directors who are concerned about maintaining the skills of weapons designers, Press is worried about these loopholes and says that they deserve broader discussion.

Nonetheless, Press supports the additional funding for nuclear-weapons research. "The labs have been starved in a way that is not healthy," he says.

The extra money, he adds, will benefit the full suite of US scientific work — from climate and materials sciences to all manner of computational and simulation expertise — that underpins the nuclear programme and provides it with new talent.

William Rees, who manages non-proliferation programmes as principal associate director for Global Security at Los Alamos National Laboratory, says that the lab needs to ensure a broad scientific base as an entry point for new recruits. Initially, these researchers might start work at the lab in its non-weapons programmes, such as projects in studying greenhouse-gas emissions and seismology. Some of those may then move into the weapons programme.

Rees says there are no guarantees that Congress will agree to the budget boost or that those numbers will be sustained in future years. He adds, however, that "we are cautiously optimistic". ■

Jeff Tollefson

Laser-fusion showdown

A watchdog office of the US government criticized the Department of Energy's showcase laser-fusion facility last week, warning that management problems there could hamper the ability of scientists to use it to ensure the reliability of the US nuclear arsenal.

Construction of the US$3.5-billion National Ignition Facility (NIF) began at Lawrence Livermore National Laboratory in California in 1997 and was completed in 2009. NIF's 192 lasers are designed to blast a target smaller than a dime with 1.8 megajoules of energy, igniting the fusion reaction that occurs in hydrogen bombs.

The most powerful laser facility in the world, NIF was billed as a tool that would allow scientists within the energy department's National Nuclear Security Administration (NNSA) to ignite tiny fusion explosions, gleaning data needed to maintain nuclear weapons in the absence of actual underground tests, which ended in 1992. But the new report, from the Government Accountability Office (GAO), says that NIF is 25% above its original $1.6-billion budget for 2006–12 and may not achieve 'ignition' within that time frame.

"Any long-term failure to achieve ignition and produce significant energy gains could erode NNSA's confidence in its ability to certify the safety and reliability of the nuclear weapons stockpile," the GAO warned.

The report says that the NNSA has not resolved problems with the laser optics as well as with key scientific challenges. JASON, an independent committee of eminent scientists, recommended in 2005 that the NNSA appoint a separate science panel to advise on the project, but the agency waited four years before doing so. Even then, the NNSA failed to give that panel the needed authority, scope and representation, the GAO said.

In its response to the GAO, the NNSA said the report is generally "fair and properly reflects the significant progress NIF has made". **J.T.**

Japan rolls out elite science funds

FIRST scheme targets large grants to world-leading researchers.

Physicist Akira Tonomura struggled for seven years to raise funding for his dream project: developing a microscope able to image three-dimensional arrays of atoms in unprecedented detail. Last March, with little hope of finding this financial support, he even considered retiring from his research fellowship at the Hitachi Advanced Research Laboratory in Hatoyama, Japan.

Then, last month, the Japanese government awarded him ¥5 billion (US$53.6 million) — the biggest grant for an individual research project in the country's history. Tonomura has already set to work on creating his ultra-high-voltage holographic electron microscope, which will measure the phase of electrons scattering off a sample, rather than their intensity, as in conventional electron microscopes. These phase measurements can produce an image with much higher resolution.

Tonomura was one of 30 scientists to win a grant from the ¥100-billion Funding Program for World-Leading Innovative R&D on Science and Technology (FIRST). The awards, announced on 9 March after a roller-coaster six months that saw the programme cut drastically, mark a major shift in the landscape of Japanese science funding.

Akira Tonomura has received ¥5 billion to build his dream microscope.

D. CYRANOSKI

At between ¥1.8 billion and 5 billion per project, many of the grants are more than double the size of the largest from the Japan Science and Technology Agency, which until now offered the country's most prestigious and generous funding awards. And unlike conventional grants in Japan, FIRST awards give researchers the freedom to spend their grant money at any time during the grant's four-year period.

Funding shift

In general, FIRST's 30 grants are targeted towards areas in which Japan is already a world leader, such as microscopy, stem-cell research and electronics. Tonomura, one of only two scientists to receive the largest possible FIRST grant of ¥5 billion, pioneered electron holography in the 1960s. The other big winnner is Kyoto University's Shinya Yamanaka, who wowed the world of stem-cell research in 2006 with his group's creation of induced pluripotent stem cells.

The awards also mark the latest chapter in Japan's effort to spend a greater proportion of its overall research budget on competitive grants (see 'Getting competitive'), a process that seems to be putting bigger chunks of money into the hands of fewer scientists. It is not yet clear how this shift is affecting the scientific community, says Atsushi Sunami, a science-policy expert at the National Graduate Institute for Policy Studies in Tokyo. However, many scientists in Japan have been privately critical of the heavy concentration of funds, which they believe could be better spent on a larger number of smaller, focused research projects.

"I want to create a history-making instrument."

Part of the motivation for the shift in funding was the perception that other countries were benefiting from greater investment in competitive grants. Earlier efforts to direct funding into large competitive grants included a centres of excellence programme rolled out in 2002 (see *Nature* **419,** 547; 2002) and the World Premier International Research Centers that were created in 2007 (see *Nature* 4**47,** 362–363; 2007).

At the same time, organizational reforms in 2004 saw basic operating budgets for universities and research institutes pared down by 1% per year. At the University of Tokyo, for example, these operating budgets accounted for 46% of total income in 2004; this shrank to 40% by 2009. However, that decrease was balanced by a growth in competitive funding over the same period, upping its contribution to the university's income from 30% to 35%. That proportion is sure to grow: the university has won funding for five FIRST projects, bringing in an extra ¥17.6 billion.

Scientists at the university are wasting no time. Although his FIRST funding cheque had yet to arrive, Yoshinori Tokura held a retreat on 30 March for core members of his ¥3.1-billion study on correlated electrons. The group hopes that controlling the interactions between electrons — based on characteristics such as charge and spin — could help to develop materials useful for energy-efficient electronics, high-temperature superconductors and new types of battery.

Meanwhile, Shizuo Akira of Osaka University has already started spending his ¥2.5-billion FIRST grant, which he says will give him the freedom to "do some gambling" at the frontiers of immunology. Akira — the most cited scientist in the world in 2005–06 and 2006–07, according to academic data-provider Thomson Scientific — hopes to create a comprehensive picture of

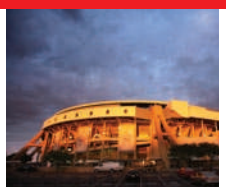

T. FOX/DALLAS MORNING NEWS/CORBIS

STADIUM DEMOLITION A BOON TO SCIENCE
American football's loss may be seismologists' gain.
www.nature.com/news

GETTING COMPETITIVE

Japan is awarding a growing amount of research funding through competitive grants, despite the overall science and technology budget remaining flat over the past few years.

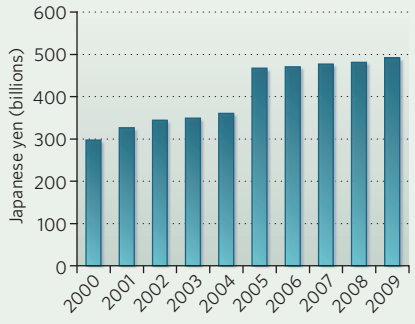

Source: Council for Science and Technology Policy

the immunological mechanisms involved in eliminating pathogens and cancer cells, and to then try to control those mechanisms. He has already hired postdocs and technicians, and has ordered a two-photon microscope, an electron microscope, mass-spectrometry equipment and DNA-sequencing machines.

Not so bold

Despite the air of excitement that the awards have generated, some scientists point out that the FIRST grants were supposed to be bigger, and the projects bolder. In June 2009, the Council for Science and Technology Policy under the then-ruling Liberal Democratic Party announced that FIRST would distribute ¥270 billion. Council members had already selected the 30 recipients before the Democratic Party of Japan came to power.

The new government promised to re-evaluate all large spending programmes (see *Nature* **461,** 854–855; 2009), eventually slashing the budget and capping the largest projects at ¥5 billion. Some scientists had hoped to get considerably more: Yamanaka, for example, originally applied for ¥15 billion.

All of the grantees then had to reapply for their funding with scaled-back projects. "Every strategic research plan was shrunk and every brave enterprise was cut," says Tokura. Yamanaka, for example, has dropped plans to carry out preclinical trials with induced pluripotent stem cells for diabetes and other diseases. Tonomura, meanwhile, says that his FIRST grant will still leave him ¥2 billion short of what his project requires, an amount he hopes to persuade Hitachi to chip in.

But with the money he already has in hand, he has no immediate plans to retire: "I want to create a history-making instrument," he says. ■

David Cyranoski

See Editorial, page 957.

Stem-cell funding in sight

Two of the most widely used embryonic stem (ES) cell lines could be just weeks away from being eligible for US federal funding. The lines, which were approved under the administration of former president George W. Bush, have spent months in limbo pending the go-ahead from the current administration of President Barack Obama. Researchers' frustrations are boiling over at the amount of time lost because of the delays. "The stem-cell community has really been jerked around," says Julie Baker, an associate professor of genetics at Stanford University, California.

The two key cell lines — known as H9 and H7 — that Baker and others are desperate to see approved were derived more than a decade ago and are owned by the WiCell Research Institute in Madison, Wisconsin. According to a stem-cell registry maintained by the University of Massachusetts Medical School in Worcester, H9 has led to 551 publications, and H7 has been used in 133 reports — an order of magnitude more than any of the other 19 Bush-era lines, with the exception of another heavily used WiCell line called H1, which was approved for federal funding in January.

Under guidelines announced in July 2009 by the US National Institutes of Health (NIH) in Bethesda, Maryland, ES cell lines must meet extensive informed-consent conditions before research using the cells can be funded. Whereas the NIH has approved 51 ES cell lines for federal funding since December 2009, H1 is the only Bush-era line to win the agency's approval so far.

"The H7 [and] H9 submission is still in draft and has not been submitted to the NIH," says NIH spokesman John Burklow, adding that the agency has contacted all of the Bush-era line holders and offered technical assistance in preparing their submissions. "The NIH does recognize that these lines are important to many NIH-funded researchers now and in the future."

Erik Forsberg, executive director of WiCell, says that he expects approval "in the next month or so" for four outstanding WiCell lines, including H7 and H9. "We are extraordinarily close to getting all the documents that we anticipate are needed for approval," he says. But scientists are still concerned that there could be further hitches. "With the Obama administration, we thought things were going to get better, and this is almost worse," says Baker. "If they don't approve these lines, we have to go backwards."

It's crucial that the lines held by WiCell are approved, adds Joseph Itskovitz-Eldor, a stem-cell expert at the Technion-Israel Institute of Technology in Haifa, who helped to derive the four H-lines held by WiCell using donated Israeli embryos. "They are being used so widely. To switch to other cell lines is going to be time-consuming and costly."

Gathering the paperwork needed for the NIH application has been slowed by translation requirements (the original documents are in Hebrew) and other problems. One donating couple had not been informed that the lines could be used commercially and that they would not benefit financially — requirements that are spelled out in the NIH guidelines. Itskovitz-Eldor e-mailed patient re-consent forms, and institutional review board approvals for them, to WiCell on 8 April. "At this point, we have completed our part. But I am sure that more documents will be needed. The whole process may take some weeks or maybe more," he says.

The hoped-for approval can't come soon enough for Baker, who almost exclusively uses H9 in her lab. "The one that's really easy to produce in the lab, which grows well, is H9. That's why all the publications use it," she says. In early March, Baker submitted an NIH grant application to use H9 to examine how ES cells use cell signalling to form endoderm, which gives rise to many internal tissues. If H9 is not approved soon, she plans to write to reviewers and suggest that she switch to using H1. But that would require extra work to extrapolate data she has already generated in "extremely expensive" H9 experiments to H1.

Even if the four outstanding WiCell lines are approved, that still leaves 16 Bush-era lines unapproved. "Obama made his announcement over a year ago and right now there is only one of the [formerly approved] lines on the federal registry," says Tim Kamp, the director of the Stem Cell and Regenerative Medicine Center at the University of Wisconsin–Madison. "Is it going to take another two months? Another year? We just don't know." ■

Meredith Wadman

L. BERGER/UNIV. WITWATERSRAND

'HUMAN ANCESTOR' SPARKS FURORE
Does fossil represent a new hominin species?
www.nature.com/news

Q&A: What it will take to feed the world

Marion Guillou is the chief executive of France's National Institute for Agricultural Research, Europe's largest agricultural-research agency. She talks to **Declan Butler** about how researchers are trying to meet the challenge of feeding a world population that is estimated to grow to 9 billion people by 2050.

Agricultural researchers held the first ever Global Conference on Agricultural Research for Development last week in Montpellier. What came out of that?
The conference showed that agricultural researchers are mobilized and recognize themselves as a global community. At the same time, there is strong tension between the CGIAR [Consultative Group on International Agricultural Research] international research centres and the global agricultural research community. The centres tend to be too closed to those outside, and there is pressure to open them up to national and other agricultural research bodies.

Developing countries at the conference also sent a strong message about the return in strength of family farms; that making these more productive is key to both alleviating poverty and meeting local and global food demand. It's a new political message: count on and help small farms. The international focus has long been on large-scale industrial farming, so this changes quite a few things. The themes of research for smallholdings are very different from those of large-scale farming, involving, for example, concepts such as crop rotation, complements of animals and plants, and the use of animal waste as fertilizer, so the research questions are not the same.

What are the most promising routes to feeding 9 billion people?
The first priority is to fight loss and waste. We lose as much as 30 to 35% of the world's food output. That gives us a large margin of manoeuvre to increase the food available. We are doing research with food processors and distributors to explore solutions. We certainly won't be able solve the problem, but we can improve it.

Diet will also be a major determinant in our capacity to nourish the world [animal products require considerably more energy and land than plants]. We need to ensure food availability of 3,000 kilocalories a day per person, of which only 500 kilocalories is from animal products — we are not trying to transform everyone into vegetarians. This provides a healthy and satisfying diet, but is far from a typical Western diet. If we continue

HAMILTON/REA

the current dietary regime typical of OECD [Organisation for Economic Co-operation and Development] countries, and if many other countries follow us on this trajectory, we will not have the same results in terms of food availability as we would with a more moderate diet worldwide.

What's the role of food prices?
One really big research area is studying the volatility of prices. It is the main problem. Remember the food riots in several countries in 2008? We are still trying to understand what happened, but much of it was because of financial speculation. We already have enough food to feed everyone on the planet at 3,000 kilocalories per day, but it is a question of price. We need research to find out which economic tools are available to stabilize prices at the international level, and to ensure, for example, adequate available reserves of cereal. We need to propose economic solutions, and regulation of markets of agricultural foodstuffs to avoid the yo-yo whereby prices can go so high that people do not have access to food. We also have to guarantee minimum prices if farming is to remain viable.

Much media coverage on developing-world agriculture has focused on genetically modified organisms (GMOs). Are these the silver bullets they are often made out to be?
It's clear that genetic progress in the past in France and other rich countries accounted for much of the increase in production, so genetics is far from passé; it's still the number-one technique for increasing yields, for example. For Africa to improve its yields, we clearly need new genetically selected varieties, engineered by either genetic modification or classic breeding techniques. For me, GMOs are not a magic bullet, but we should not refuse them a priori. It's critical to look at GMOs on a case-by-case basis. The first generation of genetically modified organisms on the market is not the one that will solve Africa's problems, although one crop, a Chinese GMO cotton that is resistant to bollworm, has proved extremely useful to the population, because it avoids the spraying of dangerous pesticides — the risk–benefit equation is clearly in favour of its use.

We are now at a stage where we have years of extensive research results on the ecological, economic and health aspects of many GMOs. There are GMOs for which the assessment is undisputedly positive, but there are others — in particular some crops engineered to be resistant to this or that herbicide — for which this is not so. For example, some GMOs result in increased use of herbicides, which can lead to concentration of these chemicals in the environment and negative effects. The results are mixed — that's why it is important not to speak of GMOs in general, but case-by-case. Pest resistance is a really promising and important application for genetic selection because there are a lot of health problems in developing countries that have been linked to the spraying of pesticides.

Public funding of agricultural research in rich countries has declined, and is increasingly shifting to the private sector, which has less interest in the needs of poorer countries. What's the overall funding outlook?
We need to continue to innovate and reinvest, in particular to increase yields. This isn't happening in rich countries, but worldwide budgets are on the increase — largely in emerging economies such as China, India and Brazil. China is heavily involved in training and technology transfer to Africa, and in Europe we should be trying to offer Africans an alternative; we have the scientific capacity. It would be a pity if we were to leave all collaborations in the hands of the Chinese.
This is a translated and edited version of an interview conducted in French.

Pentagon turns to 'softer' sciences

US defence research to focus more on biology, cybersecurity and social sciences to help win conflicts.

By highlighting the limits of traditional military technology, the drawn-out conflicts in Iraq and Afghanistan have spurred the US defence department to shake up its US$12-billion science and technology research programme. The defence research and engineering office, headquartered at the Pentagon in Washington DC, is overseeing a budget shift away from applied research that supports weapons and into areas such as biology, computer science and the social sciences. All of these have "a potential for being game-changers" on the battlefield, says Zachary Lemnios, the defence department's chief technology officer and director of defence research and engineering.

Lemnios, who is nearing the end of his first year as research director, recently testified before Congress for the first time since he was confirmed for his position, and answered questions from *Nature* about his scientific priorities. He says that the new emphasis will have reverberations outside the Pentagon, noting that US universities will receive more than half of the $1.8 billion that the defence department will spend on basic research in the current fiscal year. "Basic research funding not only leads to the next generation of technology but, just as importantly, supports a pipeline of researchers and graduate students," he says.

M. A. BURGESS, US NAVY

Zachary Lemnios is overseeing the research shake-up.

Among the areas that are fast becoming a priority for the Pentagon is synthetic biology, which seeks to build new organisms or re-engineer existing ones to perform specific functions. Lemnios says that the Pentagon is interested in understanding "how organisms sense and respond to stimuli — such as chemicals, ions and metals, or electrical, magnetic, optical and mechanical impulses — at a genetic level". That knowledge, he says, could help researchers to design "living sentinels" that can monitor the presence of explosives or chemical pollutants. "We can also develop tools that will allow us to detect adversarial uses of synthetic biology," he says.

According to Lemnios, the Office of Naval Research in Arlington, Virginia, is looking at how to biosynthesize targeted antibiotics that work by sensing and attacking specific pathogens. President Barack Obama's proposed budget for next year would also provide $20 million to the Defense Advanced Research Projects Agency (DARPA), another research arm of the Pentagon, to fund work in synthetic biology.

As potential adversaries of the United States strengthen their abilities to attack computer networks, cybersecurity is another growing priority in the defence department's research portfolio, says Lemnios. He and the director of the Intelligence Advanced Research Projects Activity, Lisa Porter, last summer launched a joint study to look at where cybersecurity research dollars could be best spent. The results are feeding into a proposal to Congress for a new $200-million research and technology programme in cybersecurity. As part of that programme, Lemnios told a House of Representatives panel on 23 March, his office will sponsor research to "harden key network components; increase the military's ability to fight and survive during cyber attacks; disrupt nation-state level attack planning and execution; measure the state of cybersecurity; and explore and exploit new ideals in cyberwarfare".

> **"New funding programmes like this are out there, while money for basic social science has gone away."**

The unconventional wars now being fought by the US military have also bolstered interest in the social sciences. With the military trying to stave off a growing insurgency in Afghanistan, the Pentagon now believes that understanding cultural dynamics is at least as important as weapons. Consequently, Lemnios is ramping up funding in social-science projects, including a model developed by Los Alamos National Laboratory in New Mexico to simulate the opium trade in Afghanistan and analyse the effectiveness of efforts to combat it. The office is also supporting a project at the University of Chicago, Illinois, to model and predict potential conflicts.

Not all social scientists welcome the Pentagon's support, particularly if they are not happy with the direction that the military pushes the research. "There's something that happens when social science enters into this militarized model; all the rough edges, no matter how complicated, are smoothed, and the models themselves become pretty simplistic," says David Price, a cultural anthropologist at Saint Martin's University in Lacey, Washington state. "I worry in general what's happening to social science; new funding programmes like this are out there, while money for basic social science has gone away."

In the 1960s and 1970s, the office now headed by Lemnios held immense power in the Pentagon, but in recent decades it has had more of an advisory role. "They controlled no budget; that was my experience with them," says Subrata Ghoshroy, a research associate in the Program in Science, Technology, and Society at the Massachusetts Institute of Technology in Cambridge, Massachusetts, and a former congressional staff member. "It was an organization without any teeth."

But the office has gained renewed stature in recent years, and Lemnios now has a role in evaluating the Pentagon's weapons. That means ensuring that the technology in new weapons is mature enough for combat, and speeding the development of new technologies, notes Guy Ben-Ari, a fellow at the Washington-based Center for Strategic and International Studies.

For a country that has troops fighting in Afghanistan and Iraq, focusing on moving science from the lab to the battlefield quickly is critical, says Ben-Ari. "They're getting shot at today." ■

Sharon Weinberger

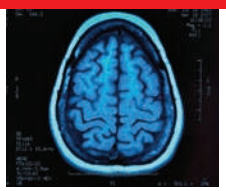

HERREID14/ISTOCKPHOTO

CHILDREN WITHOUT RACIAL STEREOTYPES
Brain disorder eradicates ethnic but not gender bias.
www.nature.com/news

Panel to take broad view of bioethics

US President Barack Obama last week announced the full membership of his bioethics advisory council, unveiling a more diverse body and one that is likely to have a greater impact on policy than its predecessor.

In the past decade, ethical questions in science have made headlines on issues such as the patenting of human genes, financial conflicts of interest in biomedical research and risk assessments related to environmental exposure to chemicals.

These issues were largely ignored by the bioethics commission established by former president George W. Bush, which maintained a relatively narrow focus on stem cells, cloning and abortion. But all fall within the remit of the new Presidential Commission for the Study of Bioethical Issues, as outlined by the executive order which established it in November 2009.

Obama had already broken with the past by not appointing a bioethicist to chair the commission, instead selecting Amy Gutmann, a political scientist at the University of Pennsylvania in Philadelphia (see *Nature* 462, 553; 2009).

The 12-person panel unveiled on 7 April includes six scientists and two lawyers and has a wide range of expertise and viewpoints. Unlike the previous 18-member commission, Obama's panel features only two bioethicists. The diversity and qualifications of the new panellists means that "this group has tremendous power and potential," says Patrick Taylor, chief counsel for Research Affairs at Children's Hospital Boston in Massachusetts, adding that the committee's diversity makes it hard to predict how much influence the views of individual members will have on its reports.

Obama's panel reports to the Secretary of Health and Human Services and includes three members from government agencies, who would have been ineligible for previous panels. In February 1998, bioethicist Ezekiel Emanuel had to leave former president Bill Clinton's bioethics panel on his appointment as chair of the bioethics department at the National Institutes of Health (NIH) in Bethesda, Maryland. The current commission, however, includes Christine Grady, an expert in human subjects research who is currently the acting bioethics chief at the NIH.

George Annas, a bioethicist at Boston University in Massachusetts, fears that the government employees could wield "effective veto power". But bioethicist Thomas Murray of the Hastings Center in Garrison, New York, who served on the commission with Emanuel in the 1990s, thinks that the links may empower the committee: "Individuals placed in government could be in a better position to ensure that the commission's reports get some traction." ■

Brendan Borrell

NATURE|Vol 464|15 April 2010

The CANCER GENOME challenge

Databases could soon be flooded with genome sequences from 25,000 tumours. Heidi Ledford looks at the obstacles researchers face as they search for meaning in the data.

When it was first discovered, in 2006, in a study of 35 colorectal cancers[1], the mutation in the gene *IDH1* seemed to have little consequence. It appeared in only one of the tumours sampled, and later analyses of some 300 more have revealed no additional mutations in the gene. The mutation changed only one letter of *IDH1*, which encodes isocitrate dehydrogenase, a lowly housekeeping enzyme involved in metabolism. And there were plenty of other mutations to study in the 13,000 genes sequenced from each sample. "Nobody would have expected *IDH1* to be important in cancer," says Victor Velculescu, a researcher at the Sidney Kimmel Comprehensive Cancer Center at Johns Hopkins University in Baltimore, Maryland, who had contributed to the study.

But as efforts to sequence tumour DNA expanded, the *IDH1* mutation surfaced again: in 12% of samples of a type of brain cancer called glioblastoma multiforme[2], then in 8% of acute myeloid leukaemia samples[3]. Structural studies showed that the mutation changed the activity of isocitrate dehydrogenase, causing a cancer-promoting metabolite to accumulate in cells[4]. And at least one pharmaceutical company — Agios Pharmaceuticals in Cambridge, Massachusetts — is already hunting for a drug to stop the process.

Four years after the initial discovery, ask a researcher in the field why cancer genome projects are worthwhile, and many will probably bring up the *IDH1* mutation, the inconspicuous needle pulled from a veritable haystack of cancer-associated mutations thanks to high-powered genome sequencing. In the past two years, labs around the world have teamed up to sequence the DNA from thousands of tumours along with healthy cells from the same individuals. Roughly 75 cancer genomes have been sequenced to some extent and published; researchers expect to have several hundred completed sequences by the end of the year.

The efforts are certainly creating bigger haystacks. Comparing the gene sequence of any tumour to that of a normal cell reveals dozens of single-letter changes, or point mutations, along with repeated, deleted, swapped or inverted sequences (see 'Genomes at a glance'). "The difficulty," says Bert Vogelstein, a cancer researcher at the Ludwig Center for Cancer Genetics and Therapeutics at Johns Hopkins, "is going to be figuring out how to use the information to help people rather than to just catalogue lots and lots of mutations". No matter how similar they might look clinically, most tumours seem to differ genetically. This stymies efforts to distinguish the mutations that cause and accelerate cancers — the drivers — from the accidental by-products of a cancer's growth and thwarted DNA-repair mechanisms — the passengers. Researchers can look for mutations that pop up again and again, or they can identify key pathways that are mutated at different points. But the projects are providing more questions than answers. "Once you take the few obvious mutations at the top of the list, how do you make

GENOMES AT A GLANCE

Circos plots can give a snapshot of the mutations within a genome. The outer ring represents the chromosomes and the inner rings each detail the location of different types of mutations.

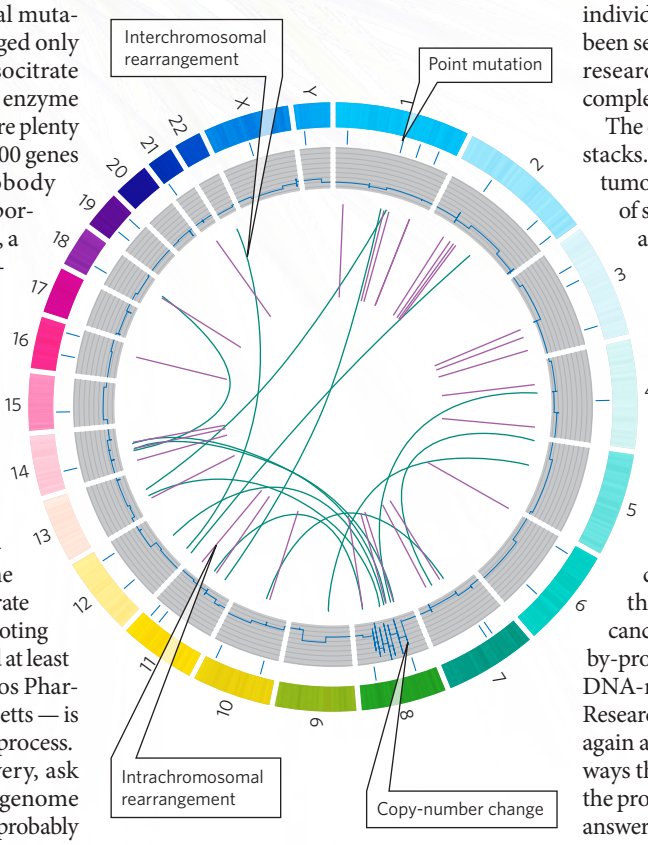

ADAPTED FROM M. R. STRATTON, P. J. CAMPBELL & P. A. FUTREAL *NATURE* **458**, 719–724 (2009).

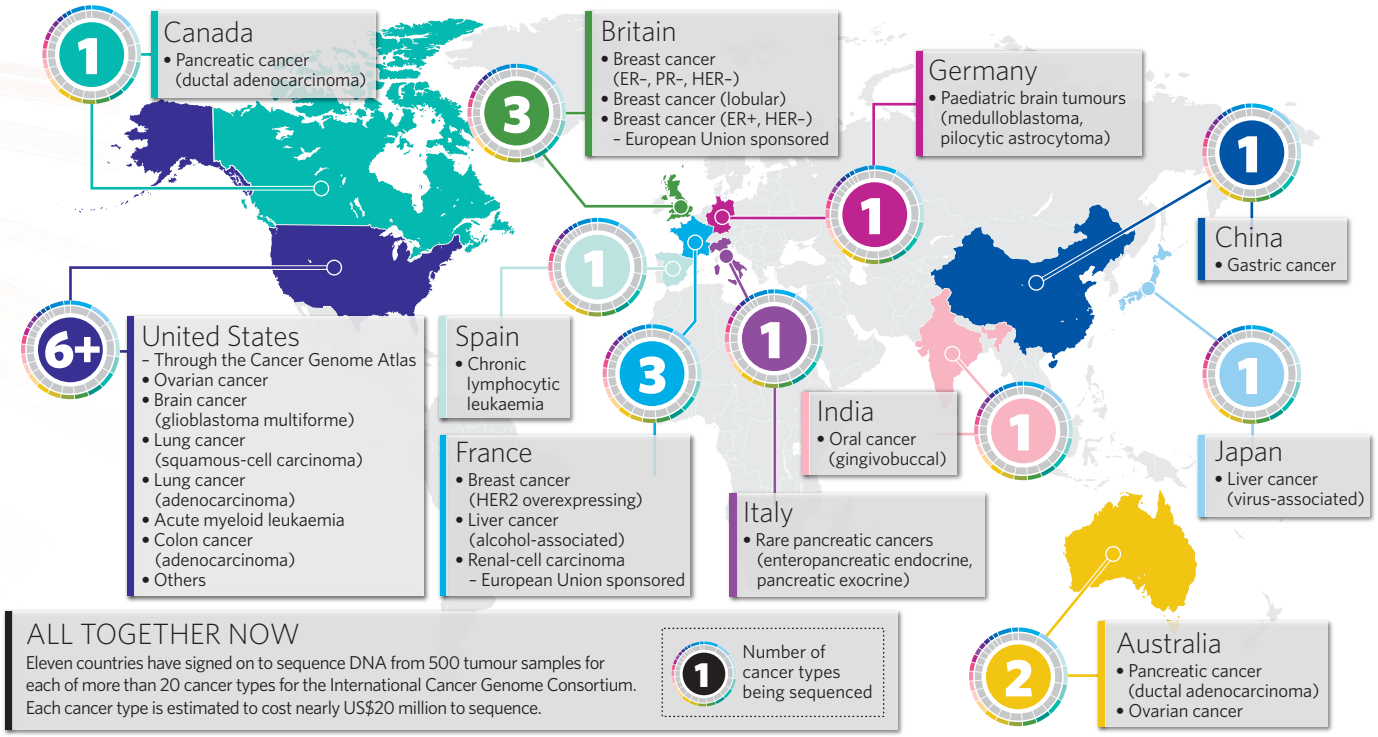

sense of the rest of them?" asks Will Parsons, a paediatric oncologist at Baylor College of Medicine in Houston, Texas. "How do you decide which are worthy of follow up and functional analysis? That's going to be the hard part."

Drivers wanted

Because cancer is a disease so intimately associated with genetic mutation, many thought it would be amenable to genomic exploration through initiatives based on the collaborative model of the Human Genome Project. The International Cancer Genome Consortium (ICGC), formed in 2008, is coordinating efforts to sequence 500 tumours from each of 50 cancers. Together, these projects will cost in the order of US$1 billion. Eleven countries have already signed on to cover more than 20 cancers (see map). The ICGC includes two older, large-scale projects: the Cancer Genome Project, at the Wellcome Trust Sanger Institute near Cambridge, UK, and the US National Institutes of Health's Cancer Genome Atlas (TCGA). The Cancer Genome Project has churned out more than 100 partial genomes and roughly 15 whole genomes in various stages of completion, and intends to tackle 2,000–3,000 more over the next 5–7 years. TCGA, meanwhile, wrapped up a three-year, three-cancer pilot project last year, then launched a full-scale endeavour to sequence up to 500 tumours from each of more than 20 cancers over the next five years.

Although the groups collaborate, TCGA has not yet been able to fully join the ICGC owing to differences in privacy regulations governing access to genome data. For now, members of both consortia are sequencing a subset of tumour samples from each cancer type — around 100 — and will follow this by sequencing promising areas in the remaining 400. That's useful, says Joe Gray, a cancer researcher at Lawrence Berkeley National Laboratory in California, but it's just a start. "In the early days, I thought that doing a few hundred tumours would probably be sufficient," he says. "Even at the level of 1,000 samples, I think we're probably not going to have the statistics we want."

What bigger numbers could provide is more driver mutations like the one in *IDH1*. These could, researchers argue, provide the clearest route to developing new cancer therapies. Many scientists have looked for mutations that occur repeatedly in a given type of tumour. "If there are lots and lots of abnormalities of a particular gene, the most likely explanation is often that those mutations have been selected for by the cancers and therefore they are cancer-causing," says Michael Stratton, who co-directs the Cancer Genome Project. This approach has worked well in some cancers. For example, with a frequency of 12%, it is clear that the *IDH1* mutation is a driver in glioblastoma. Such searches should be fruitful for cancers that have fewer mutations overall. The full genome sequence of acute myeloid leukaemia cells yielded just ten mutations in protein-coding genes, eight of which had not previously been linked with cancer[5].

"It's going to take good old-fashioned biology to really determine what these mutations are doing."

Other cancers have proved more challenging. *IDH1* was overlooked at first, on the basis of the colorectal cancer data alone. It was not until the search was expanded to other cancers that its importance was revealed. Moreover, some mutations shown to be drivers haven't turned up as often as expected. "It's very clear, now that all the genes have been sequenced in this many tumours, you have drivers that are mutated at very low frequency, in less than 1% of the cancers," says Vogelstein. To find these low-frequency drivers, researchers are sampling heavily — sequencing 500 samples per cancer should reveal mutations that are present in as few as 3% of the tumours. Although they may not contribute to the majority of tumours, they may still have important biological lessons, says Stratton. "We need to know about these to understand the overall genomic landscape of cancer."

Another popular approach has been to look for mutations that cluster in a pathway, a group of genes that work together to carry out a specific process, even if the mutations strike it at different points. In an analysis of 24 pancreatic cancers[6], for instance, Vogelstein and his colleagues identified 12 signalling pathways that had been altered. Nevertheless, Vogelstein cautions that this approach is not easy to pursue. Many pathways overlap, and their boundaries are unclear. And because many have been defined using data from different animals or cell types, they do not always match what's found in a specific human tissue. "When you layer on top of that the fact that the cancer cell is not wired the same as a normal cell, that raises even further difficulties," says Vogelstein.

How much is enough?

Separating drivers from passengers will become even more difficult as researchers move towards sequencing entire tumour genomes. To date, only a fraction of the existing cancer genomes are complete sequences. To keep costs low, most have covered only the exome, the 1.5% of the genome that directly codes for protein and is therefore the easiest

NATURE|Vol 464|15 April 2010

CANCER GENOMES COMING FAST

A few examples of fully and partially sequenced cancer genomes and their defining characteristics.

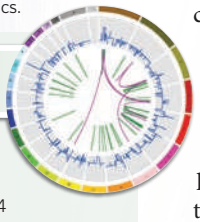

LUNG CANCER
Cancer: small-cell lung carcinoma

- Sequenced: full genome
- Source: NCI-H209 cell line
- Point mutations: 22,910
- Point mutations in gene regions: 134
- Genomic rearrangements: 58
- Copy-number changes: 334

Highlights:
Duplication of the *CHD7* gene confirmed in two other small-cell lung carcinoma cell lines.

Source: E. D. Pleasance *et al. Nature* **463,** 184–190 (2010).

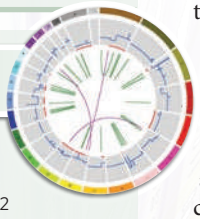

SKIN CANCER
Cancer: metastatic melanoma

- Sequenced: full genome
- Source: COLO-829 cell line
- Point mutations: 33,345
- Point mutations in gene regions: 292
- Genomic rearrangements: 51
- Copy-number changes: 41

Highlights:
Patterns of mutation reflect damage by ultraviolet light.

Source: E. D. Pleasance *et al. Nature* **463,** 191–196 (2010).

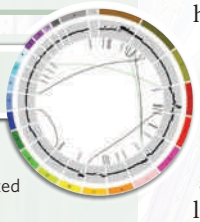

BREAST CANCER
Cancer: basal-like breast cancer

- Sequenced: full genome
- Source: primary tumour, brain metastasis, and tumours transplanted into mice
- Point mutations: 27,173 in primary, 51,710 in metastasis and 109,078 in transplant
- Point mutations in gene regions: 200 in primary, 225 in metastasis, 328 in transplant
- Genomic rearrangements: 34
- Copy-number changes: 155 in primary, 101 in metastasis, 97 in transplant

Highlights:
The *CTNNA1* gene encodes a putative suppressor of metastasis that is deleted in all tumour samples.

Source: L. Ding *et al. Nature* **464,** 999–1005 (2010).

BRAIN CANCER
Cancer: glioblastoma multiforme

- Sequenced: exome (no complete Circos plot)
- Source: 7 patient tumours, 15 tumours transplanted into mice (follow-up sequencing on 21 genes for 83 additional samples)
- Genes containing at least one protein-altering mutation: 685
- Genes containing at least one protein-altering point mutation: 644
- Copy-number changes: 281

Highlights:
Mutations in the active site of *IDH1* have been found in 12% of patients.

Source: E. R. Mardis *et al. N. Engl. J. Med.* **361,** 1058–1066 (2009).

to interpret. Assigning importance to a mutation found in the murky non-protein-coding depths of the genome will be more challenging, especially given that scientists don't yet know what function — if any — most of these regions usually serve. The vast majority of mutations fall here. The full genome sequence of a lung cancer cell line, for example, yielded 22,910 point mutations, only 134 of which were in protein-coding regions (see graphic, left)[7]. Nevertheless, finding them is worth the cost and effort, argues Stratton. "It could be that none of those mutations pertain to the causation of cancer," he says. "But it equally could be that some do. We'll never find out unless we systematically investigate."

"Even at the level of 1,000 samples, I think we're probably not going to have the statistics we want."

Not everyone agrees. Some researchers argue that the costs of cancer-genome projects currently outweigh the benefits. Prices are poised to drop dramatically in the next few years as a new generation of sequencing machines comes online, says Ari Melnick, a cancer researcher at Weill Cornell Medical College in New York. "Why not wait for that?" he asks. In the meantime there are lower-hanging fruit to pick, says Stephen Elledge, a geneticist at Harvard Medical School in Boston, Massachusetts. Mutations that affect how many copies of a gene are found in a genome, he argues, are cheaper to assess and provide a more intuitive insight into biological processes. "If you delete something, you can turn a pathway off very efficiently," he says. "And if you amplify something, you can increase flow through the pathway. Making point mutations in genes to activate them is a little dicier."

Changes in gene copy number can be detected using fast, relatively inexpensive array-based technologies, but sequencing can provide a higher-resolution snapshot of these regions, says Elaine Mardis, a sequencing specialist at Washington University in St Louis, Missouri. Sequencing can enable researchers to map the boundaries of insertions and duplications with more precision and to catch tiny duplications or deletions that might have gone undetected by an array. Mardis, along with her colleague Richard Wilson and others, used sequencing to detect overlapping deletions in a breast cancer that had spread to other parts of the body (see page 999)[8]. The deletions spanned the region containing *CTNNA1*, a gene thought to suppress the spread, or metastasis, of cancer.

Meanwhile, cancer genomics is spreading out from under the large, centralized projects. For example, a $65-million, three-year paediatric-cancer genome project headed by researchers at St Jude Children's Research Hospital in Memphis, Tennessee, and Washington University aims to sequence 600 tumours. And more small projects seem poised to pop up. "Pretty much any cancer centre with any interest in the genomics of cancer is now buying these sequencers and using them," says Sam Aparicio, a cancer researcher at the University of British Columbia in Vancouver, Canada.

Part of the reason that cancer-genome proponents don't want to wait for sequencing costs to drop is that the real work starts after the sequencing is over. As Velculescu puts it, "Ultimately it's going to take good old-fashioned biology and experimental analyses to really determine what these mutations are doing." With this in mind, the US National Cancer Institute established two 2-year projects in September last year to develop high-throughput methods to test how the mutations identified by the TCGA pilot project affect cell function. The two centres — one at the Dana-Farber Cancer Center in Boston, and another at Cold Spring Harbor Laboratory in New York — aim to systematize the way that researchers pull other needles like the *IDH1* mutation from the cancer-genomes haystack and make sense of them. The Boston team will systematically amplify and reduce the expression of genes of interest in cell cultures, and the Cold Spring Harbor centre will study cancer-associated mutations using tumours transplanted into mice.

In addition, large-scale projects are being run in parallel with the cancer-sequencing consortia to assess the effects of deleting each gene in the mouse genome, enabling researchers to learn more about the normal function of genes that are mutated in cancer. Sequencing is all very well, researchers have realized, but it won't be enough. "Some people say statistics should get us all the drivers that are worthwhile," says Lynda Chin, an investigator with TCGA at Harvard Medical School. "I don't agree with that. At the end of the day, we need these functional studies to prioritize the list of potential cancer-relevant candidates." ■

Heidi Ledford is a reporter for *Nature* in Cambridge, Massachusetts.

1. Sjöblom, T. *et al. Science* **314,** 268–274 (2006).
2. Parsons, D. W. *et al. Science* **321,** 1807–1812 (2008).
3. Mardis, E. R. *et al. N. Engl. J. Med.* **361,** 1058–1066 (2009).
4. Dang, L. *et al. Nature* **462,** 739–744 (2009).
5. Ley, T. J. *et al. Nature* **456,** 66–72 (2008).
6. Jones, S. *et al. Science* **321,** 1801–1806 (2008).
7. Pleasance, E. D. *et al. Nature* **463,** 184–190 (2010).
8. Ding, L. *et al. Nature* **464,** 999–1005 (2010).

See also News and Views, page 989.

Moment of reckoning

Tough choices lie ahead in UK research policy, and they need to be debated openly in the general election campaign, says **Colin Macilwain**.

Science issues are set to receive a wider airing than usual in the British general election campaign, which, after running on slow-burn all winter, officially kicked off last week. With the country facing an estimated £166-billion (US$250-billion) fiscal deficit this year and its biggest sector — financial services — in intensive care, politicians are looking to science, technology and innovation as a possible path to an export-led economic recovery.

But rhetorical differences aside, the laissez-faire approach of the three main parties is basically the same: spend on science and engineering in the universities, leave industry well alone and hope that innovation will flourish. No one has had the time or inclination to formulate anything more radical, despite nagging suspicions that this approach is not equal to Britain's daunting competitiveness challenges.

This is unfortunate in a country that, whatever its other woes, remains a major power in many scientific disciplines. Voters need to know what the parties' real research priorities will be when, as many economists forecast, public spending falls by 10% or more over the next four years. The electorate — especially that portion of it about to be thrown out of work by these spending cuts — should be asking how well research spending will serve its needs. Most of all, the parties need to explain how, after 30 years of spurning the kind of industrial policies pursued by France and Germany, Britain can achieve export-led growth.

Record to defend

Encouraged by the example set by Barack Obama in his campaign for the US presidency, the ruling Labour Party is portraying the opposition Conservative Party as anti-science, alleging with some justification that they are likely to make large cuts to science and university funding. But Labour will struggle to put this argument across. They are cutting science too — £600 million in 'efficiency savings' have already been requested from the universities — and it is they, not the Conservatives, who have a 13-year record to defend.

Part of this record is outstanding. In a move personally orchestrated by Prime Minister Gordon Brown when he was chancellor of the exchequer, the Labour government has doubled the annual university research budget to £6 billion over the past decade. Other aspects

of Labour's record are less impressive. Industrial research spending has stagnated, and government laboratories, in everything from agriculture to defence, have been scaled back or closed.

Labour has also done little to shift research priorities towards meeting social goals — in housing, health and transport, for example — as opposed to commercial ones. It has consulted endlessly with business interests, but seldom stooped to listen to its main groups of supporters, the liberal-minded middle classes and the shrunken industrial working class, who might benefit from a different set of research priorities. And it largely missed the opportunities that arose after the bovine spongiform encephalopathy (BSE) outbreaks and the public's rejection of genetically modified food to develop more advanced approaches to public consultation.

"British scientists have never had it so good, and they know it."

Paul Drayson, the biotechnology entrepreneur who has served as Labour's science minister since 2008, says that he has sought to break down elitism in science and to welcome a broad range of voices, on issues such as stem cells and nanotechnology. He even says, in response to the charge that Labour only heeds the Confederation of British Industry (CBI), that Labour is listening to the trade unions.

However, only last month, the government began a crucial, early consultation on future research priorities that will include the Royal Society and the CBI, yet exclude the unions, local authorities, and environmental groups.

The Conservative Party, which, according to the bookmakers, remains likely to form the next government, is doing its best to avoid firm commitments that might limit its future room for manoeuvre. Its clearest position is that more attention should be paid to teaching at universities.

Party leader David Cameron — perhaps fearing unfavourable comparisons with Brown's impressive Oxford lecture on science (see go.nature.com/6rNuES) — dropped plans to devote a speech to the topic last summer. Cameron instead commissioned a report on innovation from James Dyson, the inventor of stylized vacuum cleaners. Last month, Cameron welcomed its findings — without promising to implement them. These included more focused research-and-development tax credits and more sponsorships for science and engineering students.

Deciding vote

The most progressive noises in the campaign so far have come from the Liberal Democrats, led by Nick Clegg, whose ambition is to hold the balance of power after the election. Their science spokesman, Evan Harris, has called for the government to adopt the Royal Society's recommendations on the treatment of independent scientific advice. He also wants reform of the libel laws to protect free scientific discussion in light of the case of Simon Singh, a science writer whose legal battle with chiropractors has become a cause célèbre for liberals and rationalists.

The Royal Society sought to lay the ground for the consideration of science issues ahead of the 6 May election by publishing a report, *The Scientific Century*, on 9 March. The authors hoped that it might replicate the influence of *Rising Above the Gathering Storm*, a similar report published by the US National Academy of Sciences in 2007, which presaged $21 billion of additional science spending by the US Congress. Britain won't have the money for that kind of thing — science instead faces a severe funding crunch.

A series of three live, televised debates will now take place between the three party leaders for the first time and will, at the media's insistence, come to dominate the campaign. The embattled prime minister should use these to advertise some of his under-exposed knowledge of and compassion for science, and challenge anticipated Conservative spending cuts.

Until the September 2008 financial crisis, Brown's campaign message to Britain would have echoed that of Conservative prime minister and one-time publisher of this journal, Harold Macmillan in 1957: "You've never had it so good." Scientists haven't, and they know it. But no government can now save them from the austerity ahead. ■

Colin Macilwain is based in the United Kingdom.
e-mail: cfmworldview@gmail.com

See go.nature.com/ILx8PC for more columns.

CORRESPONDENCE

Questioning how different societies respond to crises

In his Review of our book *Questioning Collapse* (*Nature* **463,** 880–881; 2010), Jared Diamond alleges that it contains factual errors, which he uses to justify his devaluation of our emphasis on human resilience. In doing so, he shores up what we contend are his simplistic theses regarding societal 'collapse'. Given that our book critically examines two of Diamond's works — *Guns, Germs, and Steel* and *Collapse: How Societies Choose to Fail or Succeed* — we are surprised that *Nature* published this review without printing a fuller disclosure of the author's position in relation to our book.

We consider that there are errors in Diamond's review to which we wish to respond briefly. First, Niels Lynnerup, author of *The Greenland Norse: A Biological-Anthropological Study* (Meddelelser om Grønland, Man and Society, 1998), reiterated in a recent phone conversation with us that he knows of no evidence of starvation of the Greenland Norse. Second, as Chaco Canyon in New Mexico has never been sited in lush coniferous forest but in dry, scrub vegetation, wood for buildings was always imported from increasingly further away as nearby forests became exhausted. The search for wood was not the reason for Chaco's abandonment. Third, David Cahill's chapter shows that when Spaniards came to Peru, the Inka were engaged in a civil war as well as imperial expansion. Consequently, the Inka had many local enemies, some of whom allied with the Spaniards against the Inka. Fourth, Christopher Taylor's description of the culture and history of the Rwandan genocide refutes Diamond's 'Malthusian explanation' for this tragedy. And finally, we believe, based on considerable evidence, that the man named Yali whom Diamond declares to have met in Papua New Guinea and the Yali discussed by Deborah Gewertz and Frederick Errington are the same person. Neither Diamond nor anyone else has produced evidence that would lead us to question this.

The point of *Questioning Collapse* is that everyone didn't "end up dead" in cases of 'collapse', but that many survived and some flourished under changed political and cultural circumstances. The conflation of profound societal change with the notion of biological extinction is a persistent error that runs through much 'collapse' scholarship. We believe that our book presents ample archaeological and historical data that contextualize how societies moved through periods of crisis. Our book is more than a critical evaluation of Diamond's views: it is about how we understand change in the past, how we grapple with the legacy of colonialism and with inequalities in the present, and how we can move forward productively and resiliently into the future.

Patricia A. McAnany Department of Anthropology, University of North Carolina, Chapel Hill, North Carolina 27599, USA
e-mail: mcanany@email.unc.edu
Norman Yoffee Department of Near Eastern Studies and Department of Anthropology, University of Michigan, Ann Arbor, Michigan 48104, USA.
The full list of 10 additional signatories is available online at http://dx.doi.org/10.038/464977a

Students caught up in legal impasse at Mexican institute

As graduate students from the nanoscience and nanotechnology group of the Institute for Scientific and Technological Research of San Luis Potosí (IPICYT), we wish to update you on events affecting us since the departure of Humberto and Mauricio Terrones (*Nature* **464,** 148–149; 2010).

We have no wish to discredit the authorities of our institute, but we are concerned about the way in which they are handling our situation. It is evident that political and legal problems are interrupting our academic development.

The academic authorities at IPICYT have assured us that we would receive their complete support, so that we could continue with our thesis projects and dissertations. Most of our laboratory requirements have been met, and the authorities have agreed that we could choose our own advisers, whether from inside the institute or outside — including the Terrones professors.

However, the current legal situation means that, if we did choose Humberto or Mauricio Terrones, they would be unable to supervise or examine us on IPICYT premises. And it is not clear whether the IPICYT authorities would actually recognize academic connections between students and the Terrones professors.

In that case, we would need either to remain at the institute and terminate academic relations with the Terrones, or to continue our research and academic studies elsewhere. Neither option, however, would enable us to complete our thesis projects satisfactorily.

Aarón Morelos Gómez, Eduardo Gracia Espino, Juan Carlos García Gallegos and students of the Nanoscience and Nanotechnology Group, IPICYT, Camino a la Presa San José 2055, Col. Lomas 4a. Secc. SLP, CP78216, México
e-mail: estudiantesnyn@gmail.com
The full list of additional signatories is available online at http://dx.doi.org/10.038/464977b

Weighing up the case for telescope site on La Palma

The European Southern Observatory (ESO) Council will soon decide where to install the European Extremely Large Telescope (E-ELT). The currently recommended site is Armazones, a sierra near Paranal in Chile (*Nature* **464,** 146; 2010). But there is also a strong case for considering the Roque de los Muchachos Observatory (ORM) on the Canary Island of La Palma.

This European site has the support of the European parliament and meets the astronomical requirements and logistical services necessary to make the operation cost-effective. For example, the E-ELT will need to use adaptive optics, which require a high-quality atmosphere in which the turbulent layers are as near to the telescope entrance as possible: the ORM's stable and predictable atmosphere makes it the best-quality site under consideration, as well as the most well studied.

Spain has offered the €300 million (US$400 million) needed to implement the project. Siting the telescope in this European ultra-peripheral region would make it eligible for additional funding for its construction and operation.

At the meeting of the European Conference on Research Infrastructures held last month in Barcelona, it was stressed that all European research-infrastructure projects must minimize and optimize their construction and operational costs. These stipulations could be fulfilled by choosing the ORM option.

Another factor is the high seismicity of the Armazones region, which could affect the E-ELT's huge structure, multiple mirrors, complex instrumentation and adaptive optics. Additional security provisions could double the estimated costs.

European astronomy should not put all its eggs into one shaky basket, when there is an alternative secure site nearer home that offers equally good astronomical conditions.

Francisco Sanchez Instituto de Astrofísica de Canarias, Via Lactea s/n, La Laguna, Tenerife 38200, Canary Islands, Spain

Contributions may be submitted to correspondence@nature.com.

OPINION

Let parents decide

Twenty years on from the first pregnancies after preimplantation genetic diagnosis, **Alan Handyside** argues that informed prospective parents are largely good guides to the use of the thriving technology.

Twenty years ago this month, my colleagues and I published a paper in *Nature* describing how our small team at Hammersmith Hospital in London helped to bring about the first pregnancies following preimplantation genetic diagnosis (PGD). We used the technique in several couples. They risked having children with serious inherited diseases linked to the X chromosome that typically affect boys, such as Duchenne muscular dystrophy. After fertilizing the eggs *in vitro* and testing to identify gender, we implanted only unaffected female embryos.

A few days later, the House of Commons passed the Human Fertilisation and Embryology Bill. As well as regulating fertility treatment, the act sanctioned research on early human embryos, which, as our Nature study demonstrated (A. H. Handyside *et al. Nature* **344,** 768–770; 1990), could have profound clinical benefits. Since then, the act has been updated several times by court judgments, and was amended completely in 2008, to keep pace with changing social attitudes and with rapid developments in fertility treatment and embryo research. Among other things, the 2008 act allows the creation of animal–human hybrid embryos, approves the use of PGD to create 'saviour siblings' and bans the use of gender selection for non-medical reasons.

Over the next decade, the field is likely to progress even more rapidly. As genome-wide analysis becomes easier and cheaper, clinicians will be able to test embryos for many more chromosomal or single-gene defects. Increasingly, they will also be able to provide information about physical characteristics and predisposition to common diseases. These new possibilities will come with ethical and social challenges. They are bound to increase demands for PGD from prospective parents who want to know — or control — how their child will turn out. Future regulation should focus not on the seriousness of an inherited condition — currently the main determinant of whether selection is allowed — but on what information about their embryos parents should have access to and what they may do with it.

It is important to acknowledge the limitations of PGD. Many people are concerned about 'designer babies', but the scope for selecting embryos with desirable traits beyond common characteristics such as gender, hair or eye colour is constrained by several factors. The first is that the genetic elements underlying a trait must be present in one or both parents. The second is that since a typical *in vitro* fertilization (IVF) cycle results in only a handful of fertilized embryos for biopsy and testing, the chances of one embryo inheriting the right combination of genetic elements to give the desired characteristic may be too low to make the procedure worth trying, particularly as only a fraction of embryos implant successfully even in fertile couples. Finally, although complex traits such as intelligence are known to have a strong genetic component, many other variables would make it impossible to identify individual embryos with desired traits.

That said, improved sequencing technologies and progress in identifying genetic variants that contribute to trait heritability will lead to increasingly accurate predictions. These could include an embryo's future risk of diabetes, cancer, schizophrenia and other common diseases, and of abnormalities such as congenital malformations, mental retardation and autism. Even greater opportunities will emerge when falling costs enable the sequencing of the whole genomes of early embryos, possibly within the next five years. This will allow the detection of inherited genetic defects and those arising during the formation of the gametes or during early embryonic development. This is still some years off because whole-genome amplification from single cells remains prone to errors.

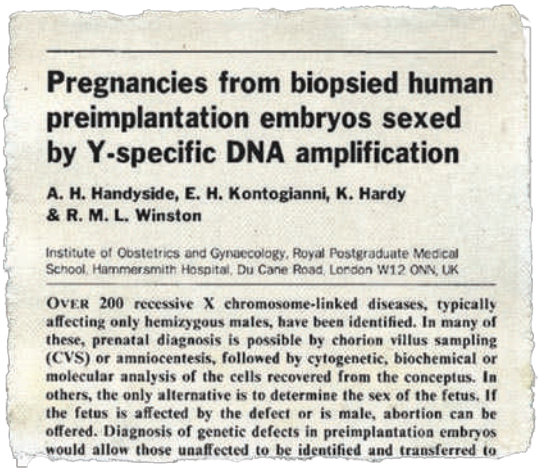

Pregnancies from biopsied human preimplantation embryos sexed by Y-specific DNA amplification

A. H. Handyside, E. H. Kontogianni, K. Hardy & R. M. L. Winston

Institute of Obstetrics and Gynaecology, Royal Postgraduate Medical School, Hammersmith Hospital, Du Cane Road, London W12 ONN, UK

OVER 200 recessive X chromosome-linked diseases, typically affecting only hemizygous males, have been identified. In many of these, prenatal diagnosis is possible by chorion villus sampling (CVS) or amniocentesis, followed by cytogenetic, biochemical or molecular analysis of the cells recovered from the conceptus. In others, the only alternative is to determine the sex of the fetus. If the fetus is affected by the defect or is male, abortion can be offered. Diagnosis of genetic defects in preimplantation embryos would allow those unaffected to be identified and transferred to

A. H. HANDYSIDE *ET AL. NATURE* **344,** 768–770 (1990)

Regulation needs to change to accommodate new technologies. In many countries, including the United States, Spain and Belgium, PGD is either regulated liberally or not at all. In the United States, there are no federal restrictions on what couples may use PGD for — the practice is generally policed on a case-by-case basis by doctors. Even non-medical applications such as gender selection are widely permitted. At the other extreme, in Germany and Switzerland all research and interventions on embryos, including PGD, is outlawed. Amid this patchwork of approaches, it is worth examining the United Kingdom, which is something of a trailblazer, as it was the first country to establish a regulatory body to oversee fertility treatment and research.

Best practice?

The UK Human Fertilisation and Embryology Authority (HFEA), set up in 1990, makes decisions about PGD on a case-by-case basis. It allows embryo selection for inherited conditions deemed to be clinically 'serious', in terms of the disability or suffering they cause. So far it has licensed around 130 conditions, such as sickle-cell anaemia, cystic fibrosis and Huntington's disease. This approach is flawed: in many cases it is impossible to categorize inherited conditions as mild or serious because severity can vary between families. Moreover, judging whether a condition is serious or not can be highly subjective, and it is important to take the views of patients into account. The only application the HFEA has turned down in the past five years was to selectively transfer female embryos to avoid a Y-chromosome deletion causing almost complete infertility. The authority argued that even though the infertility was bound to be passed from father to son, it was not a serious enough condition because it was treatable by surgically extracting sperm and micro-injecting it into an egg — a seemingly perverse position for a fertility regulator.

A more sensible approach, given the opportunities afforded by the developing technology, would be to let couples decide for themselves whether a condition warrants PGD. As with prenatal diagnosis, they should be permitted to make this decision in private, guided by clinical geneticists. This could change PGD from a 'special case' technology

M. ROBERTS/REUTERS/CORBIS

Happy family: British parents Shanana (left) and Raj Hashmi were given permission in 2003 to select an embryo with tissue that matched that of their son Zain, terminally ill with β thalassaemia.

to one that clinicians actively promote.

The real challenge for regulators is to decide whether prospective parents should have access to other information provided by genome-wide analysis about the health of the embryo. It would seem sensible to tell them about any chromosomal abnormalities or copy-number variations affecting the viability and normal development of the embryo. Admittedly this could lead to a demand to select embryos to avoid a wide range of common, non-fatal conditions such as diabetes, Alzheimer's disease or even asthma, which some oppose because it would involve discarding otherwise healthy embryos.

Beyond that, we will need to decide whether parents should be allowed data about other characteristics such as gender or hair, skin and eye colour. Here it may be necessary to regulate to reassure the public that PGD is being used for the benefit of the child rather than to fulfil the wishes of the parents. Attempting to select an embryo for traits such as body shape (or, for that matter, temperament or intelligence) is unlikely to be popular because it would be so prone to error. Such traits generally involve a complex interaction of genetic and non-genetic variables that make it impossible to identify an individual embryo with the desired trait. Indeed, the genetic information obtained may not add much to what can already be predicted from family history.

In the main, I believe that there is no need to resort to new legislation unless there is a serious risk to people's health or to society — as with reproductive cloning or genetic manipulation, for example. Legislation is inflexible, whereas regulating within the current law allows authorities to reflect societal changes and swings in public preferences. For example, although gender selection is available in several European countries and in the United States, it has been regulated against in Britain since the early 1990s. This worked well, yet in 2008 the government decided to legislate against gender selection, effectively making it a criminal offence. This seemed unnecessary, and it will make it difficult to change the rules if, for example, public pressure to allow family balancing becomes overwhelming.

> "Legislation is inflexible, whereas regulating within the current law allows authorities to reflect societal changes."

Crucial decade

The next decade will be a crucial one for the study of the genetics of fertility, in particular how genetic defects arise during early development. Humans have an exceptionally high rate of pregnancy failure and loss, much of which derives from the inheritance of abnormal numbers of chromosomes in the gametes. Human eggs, which are formed before birth but do not mature until decades later, are five times more likely than sperm to develop an abnormality. This likelihood increases exponentially as a woman in her late-thirties and mid-forties approaches the menopause. Because these abnormalities arise when chromosomes behave irregularly during cell division before fertilization, genome-wide analysis could elucidate the differences between eggs that navigate this developmental stage successfully and those that don't. It could also reveal whether ovarian stimulation during IVF treatment causes some abnormalities, as many clinicians suspect.

Already genome-wide association studies have had some success in identifying genetic regions implicated in fertility problems. For example, a single-nucleotide polymorphism — a one-letter variation in the DNA sequence — turns out to cause ovarian follicles to respond poorly to stimulation during IVF. As more people receive genome-wide analysis, researchers should be able to identify variants that underlie particular causes of infertility, such as premature menopause. This could lead, for example, to young women being tested for these variants, giving them the option of freezing eggs while they are still fertile.

DNA technologies are set to revolutionize fertility science in ways that were barely imaginable 20 years ago. Societies may take time to adjust, but it is important that authorities don't prejudge by legislating against the possibilities that will emerge. ■

Alan Handyside is at the London Bridge Fertility, Gynaecology and Genetics Centre, London SE1 9RY, UK.
e-mail: ahandyside@thebridgecentre.co.uk

The author declares a conflict of interest that is available online at go.nature.com/mzECuU.

BOOKS & ARTS

Beyond the image of the tragic genius

Our stereotypical view of mathematicians shifted during the Romantic era from worldly scholar to tortured soul, explains **Jascha Hoffman**.

Duel at Dawn: Heroes, Martyrs, and the Rise of Modern Mathematics
by Amir Alexander
Harvard University Press: 2010. 320 pp.
$28.95, £21.95

A lonely man flirts with madness in search of truth, but dies alone and misunderstood. Similar stories have played out in films about mathematicians from *Pi* to *Proof*. Where did the figure of the tragic mathematician originate?

According to historian Amir Alexander, author of *Duel at Dawn*, this characterization is inherited from the Romantic era, when "eccentricity, mental illness, and even solitary death" were regarded as virtues when applied to the likes of John Keats, Frédéric Chopin and Vincent Van Gogh. If mathematics must ultimately be justified as art, as British mathematician G. H. Hardy famously claimed, then it stands to reason that mathematicians should also be driven to the brink by their pursuit of the truth.

It was not always this way. In his previous book *Geometrical Landscapes* (Stanford University Press, 2002), Alexander maintained that seventeenth-century mathematicians, such as Isaac Newton and Gottfried Leibniz, were seen by their contemporaries as brave explorers on the seas of geometry. In *Duel at Dawn*, he takes up this thread at the turn of the nineteenth century, when the Enlightenment view of maths as a worldly pursuit yielded to the Romantic myth of tragic genius.

Alexander pierces the haze that has gathered around some great mathematical lives. He shows how the eighteenth-century French mathematician Jean le Rond D'Alembert — who collaborated with French philosopher Denis Diderot on the prime Enlightenment text, the *Encyclopédie* — acquired a reputation as a man who rose from orphanhood to pursue a pure and harmonious life in maths. Then the author reveals that D'Alembert was, in fact, an ambitious man whose "prolonged and bitter disputes … managed to alienate all of his most prominent colleagues".

Moving to the Romantic era, Alexander exposes the complex lives of a trio of martyred heroes. He shows how Norwegian mathematician Niels Henrik Abel and Hungarian geometer János Bolyai — despite their later reputations as prodigies spurned by the establishment — were well respected by their colleagues. The prime figure in the pantheon of mathematical martyrs, however, is the young and fiery Frenchman Evariste Galois. A teenage genius shunned by the great men of his age, Galois turned to radical politics and penned the founding document of modern group theory just hours before he was fatally shot in a duel at the tender age of 20. Or so the story goes.

In his painstaking debunking of this tale, Alexander demonstrates that although some of the legend is true — Galois was killed in a duel, and he did lay the foundations for group theory — he was not an innocent martyr to truth, as he has been depicted by generations of fawning biographers. Galois was a prickly rebel whose self-serving delusions and "paranoid and provocative behavior" lead Alexander to suggest that his early death was inevitable and, in a sense, self-inflicted.

Not satisfied with dispelling myths, Alexander argues that such folklore arose in tandem with substantial changes in maths at the beginning of the nineteenth century. As the ideal of the mathematician shifted from worldly scholar to tortured soul, so did the pursuit of maths itself, from an Enlightenment effort to model the Universe to a Romantic quest for a hidden truth.

On the question of how much the stories have affected the history of this field, Alexander is cautious, saying that the myths and maths "went hand in hand". He sometimes ventures further, arguing that the "new story of genius and martyrdom … legitimized and allowed for a new type of mathematical knowledge".

It is strange that the Romantic archetype has endured, through twentieth-century mathematicians such as Kurt Gödel, Srinivasa Ramanujan, John Forbes Nash and, recently, Grigory Perelman, who solved the Poincaré conjecture in 2003 only to withdraw from maths and public life. Yet Alexander speculates that, in this era of computer-assisted proofs, the vision of the mathematical martyr might fade away to be replaced by a different stereotype — the power-hungry nerd.

Duel at Dawn suggests how preconceptions about the trappings of genius have radiated from art to maths. But its greater value lies in peeling back the layers of hagiography from figures such as Galois to reveal gloriously complicated men. ■

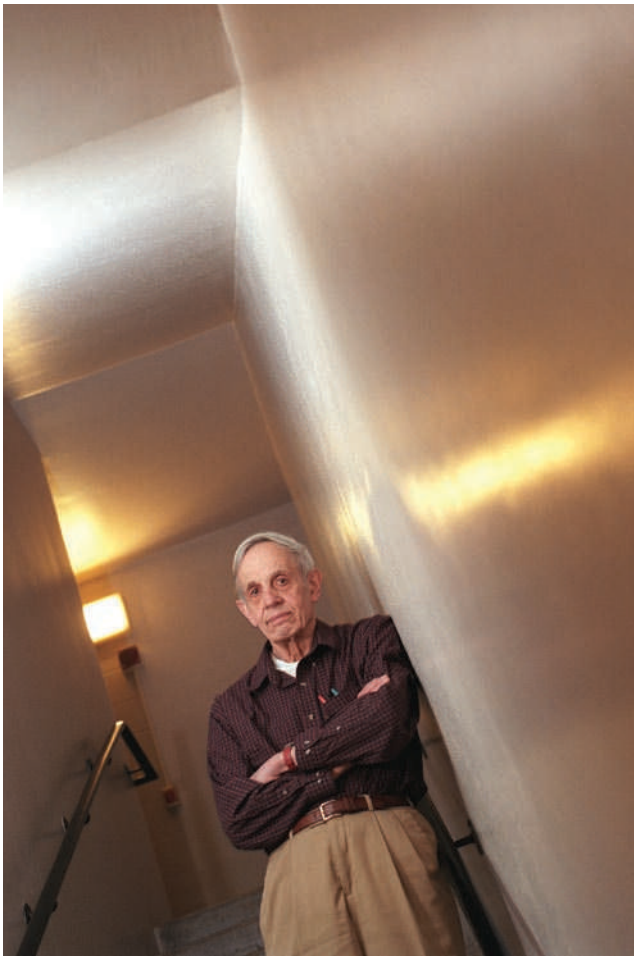

REDUX/EYEVINE

John Forbes Nash's intellectual and personal struggles with mental illness were charted in Sylvia Nasar's 1998 book *A Beautiful Mind*.

Jascha Hoffman is a writer based in San Francisco, California.
e-mail: jascha@jaschahoffman.com

Calibrating the scales of suffering

Do Fish Feel Pain?
by Victoria Braithwaite
Oxford University Press: 2010. 256 pp.
$29.95, £14.99

B. CHAN

Fish have nerve endings that detect harmful stimuli, but it is difficult to prove that they feel pain.

Biologist Victoria Braithwaite found herself in the media spotlight in 2003 after publishing research findings suggesting that fish feel pain. After injecting the faces of trout with bee venom and vinegar, anatomical and physiological studies revealed nerve endings called nociceptors, which respond to noxious stimulation. These interventions caused the fish to show increased breathing rates and decreased feeding behaviours that persisted for more than an hour. Fish subjected to noxious stimuli also became less fearful of a novel object in their tank, which Braithwaite suggests could be because their pain made them less attentive to unfamiliar objects.

In *Do Fish Feel Pain?*, Braithwaite recounts these experiments and discusses their implications, integrating a range of studies on the behaviour and cognition of fish. She is careful to point out that behavioural responses and the presence of nociceptors are necessary but insufficient criteria to demonstrate that fish experience pain. She structures her argument simply: to feel pain, fish need nociceptors to detect potentially damaging stimulation; they need to show awareness of this stimulation through a behavioural reaction that goes beyond a simple reflex; and they must indicate that they are conscious by succeeding in a complex task that requires mental representations for its solution. In showing all of these steps through varied experiments, she argues, fish feel pain.

However, the issues surrounding consciousness and pain are more complex than Braithwaite's simple syllogism implies. Fully conscious humans do not always experience pain on being exposed to noxious stimuli. For example, in the heat of battle, soldiers with terrible wounds might not report pain. By contrast, one may feel pain when no stimulus is applied; for instance, a person can report pain in an amputated limb that he or she no longer possesses. Complex tasks can also be completed without conscious awareness. People often have no insight into how they solve complex reasoning problems, such as deducing how to connect a pattern of dots with a minimal number of lines. Thus, the solution of complex tasks, nociception and pain experience are not strongly linked.

"Consciousness and pain are more complex than Braithwaite's simple syllogism implies."

The task that Braithwaite appeals to as evidence that fish form conscious mental representations is called transitive inference. It is a form of reasoning in which an individual is given partial information — such as 'A is greater than B' and 'B is greater than C' — and then tested to see if they have deduced the valid inference: that A is greater than C. Ingenious experiments by then-undergraduate Logan Grosenick and his colleagues at Stanford University in Palo Alto, California, demonstrated that male African cichlids — aggressive freshwater fish — could make these judgements.

Permitted to watch contests between other fish, the cichlids observed how fish A could beat fish B in combat, and fish B could defeat fish C. To test the observer's powers of deduction, he was placed in a glass container between fishes A and C. It is known that a male cichlid who finds himself in a three-way fight will always first attack the fish he perceives to be the weakest. Thus, the observer cichlid should choose to attack fish C if he can solve transitive inference, as he did in these experiments.

Impressive as this demonstration is, the cichlids' behaviour does not prove that fish are conscious. There are many competing explanations for how humans and other species may solve this task, including one that relies simply on associative learning. Even if one assumes that fish solve the transitive inference problem consciously, it is a further leap to conclude from this that fish consciously experience pain.

Humans can be consciously aware of many things, from the most exquisite ecstasy to the most diabolical agonies. Yet even in a waking state, the same stimuli may pass us by without evoking any conscious awareness. It is therefore unlikely that clear answers to the question of whether animals feel pain will be obtained simply from behavioural responses.

Braithwaite is careful to weigh up the ethical implications of her conclusions. Although she thinks that fish feel pain when caught by anglers, she recognizes that the hobby of angling has positive effects, including increasing public awareness of the importance of preserving fish habitats. If angling were banned, the quality of waterways might decline, and the net outcome for fish could be negative. This recognition of the complexities of ethical decisions — and the need for nuance rather than stridency in finding the best way forward for humans and other species — redeems the book. *Do Fish Feel Pain?* is a fascinating excursion through the recent studies of the surprisingly complex behaviour of fish. ■

Clive Wynne is associate professor of psychology in the Department of Psychology, University of Florida, Gainesville, Florida 32611, USA.
e-mail: wynne@ufl.edu

BOOKS IN BRIEF

To what extent are we in control of our actions? Not as much as we think, says neuroscientist Eliezer Sternberg in *My Brain Made Me Do It* (Prometheus Books, 2010). Exploring thorny issues of moral responsibility in the light of recent developments in neuroscience, Sternberg asks how the brain operates when we exercise our will, whether future criminals might be spotted from their brain chemistry and how consciousness might have evolved.

The Little Book of String Theory (Princeton Univ. Press, 2010) by theoretical physicist Steven Gubser puts into words the abstract maths of some of the most challenging areas of physics, from energy and quantum mechanics to branes, supersymmetry and multiple dimensions. Describing the field as "promising" rather than esoteric, Gubser emphasizes string theory's links to other areas of physics and anticipates forthcoming results from the Large Hadron Collider at CERN, Europe's particle-physics laboratory near Geneva, Switzerland, that will test the theory.

In *Elegance in Science* (Oxford Univ. Press, 2010), physiologist Ian Glynn examines why we find a good experiment or theory so satisfying. Detailing a range of beautiful and imaginative discoveries across the history of science, from Johannes Kepler's determination of the laws of planetary orbits to elucidation of the structure of DNA, Glynn concludes that economy and creativity are the qualities that bring us most aesthetic pleasure.

Creating wetlands around Manhattan could protect the city from rising waters.

ARCHITECTURE RESEARCH OFFICE/DLANDSTUDIO

Artificial reefs to buffer New York

Rising Currents: Projects for New York's Waterfront
Museum of Modern Art, New York
Until 11 October 2010

Within the next 40 years, projected sea-level rises of up to a third of a metre threaten coastal cities, including New York. By 2100, rising sea levels could inundate 21% of Lower Manhattan at high tide and warmer ocean temperatures could bring more frequent hurricanes, accompanied by storm surges 7 metres high.

On show until October at New York's Museum of Modern Art (MoMA) are five proposals for shielding low-lying areas of the city from encroaching waters. Each addresses a different zone, from Lower Manhattan to the New Jersey coast, using principles that have global applications. Rather than relying on defensive barriers, such as levees and sea walls, the local design teams participating in *Rising Currents* suggest using wetlands, artificial islands and living reefs to absorb water and attenuate waves.

In the project Oyster-Tecture, Kate Orff and her team from the urban design studio SCAPE/Landscape Architecture plan to seed oysters in the waters of the Bay Ridge Flats off Brooklyn to recreate a long-lost natural oyster reef. The SCAPE project also encompasses the Gowanus Canal, a former industrial waterway polluted by pesticides and heavy metals. Oyster beds act as a natural filtration system, and could clean millions of litres of harbour water each day — a single oyster can filter 3 litres of water an hour.

"The project doesn't require a billion-dollar investment, just biology in the form of the oyster," says Orff. A model of Oyster-Tecture, a rope and timber "mosaic landscape for marine life and people" populated by wooden birds, turtles, fish and human figures, has been hand-knitted by the Brooklyn-based Bergen Street Knitters.

A dredged-up oyster shell sits beside Matthew Baird Architects' model of 'Working Waterline', a scheme for the low-lying lands of Bayonne, New Jersey, and the Kill van Kull, the tidal strait that separates them from Staten Island. The company proposes creating an artificial reef and breakwater by sinking thousands of 75-centimetre-high recycled-glass 'jacks' (shaped as in the game) into the sea bed. Accumulated sediment, explains ecologist and artist Nim Lee, would host algae and create habitats for marsh grasses and marine life.

Local warehouses and piers could be converted to recycle the necessary materials: New Yorkers discard nearly 3,000 tonnes of glass each week, of which only around half is recycled. Bayonne's 'tank farm' of industrial containers — used in an infamous 1960s 'salad-oil swindle', in which a commodities trader conned banks out of US$150 million by pretending the mostly water-filled tanks were full of soybean oil — could be turned into a sewage-fertilized algae farm producing algal oils for biodiesel as a project by-product.

Water overflow is a persistent problem in New York: thanks to outmoded sewers, more than 100 billion litres of raw sewage and polluted storm water are discharged into the harbour each year. In their project 'A New Urban Ground', Architecture Research Office (ARO) and designers dlandstudio suggest filling the streets of Lower Manhattan with 'greenways' — freshwater wetlands and saltwater marshes that act as sponges. "We didn't envision it to be an apocalyptic scene of nature overtaking the city," says Adam Yarinsky of ARO. "It's very much about the city perpetuating, not diminishing."

Population growth is another factor to take into account: New York City is projected to grow by 800,000 people by 2030. Extending the

city into the water is the goal of 'New Aqueous City', which covers Sunset Park, Bay Ridge and Staten Island. Designers nArchitects' solution is to build an archipelago of concrete islands connected by inflatable storm barriers that accumulate silt and provide resilience against storm surges. In 'Water Proving Ground', LTL Architects propose a series of landscaped finger-shaped piers for the zone that includes Liberty State Park and the Statue of Liberty.

Curator Barry Bergdoll of MoMA hopes that the projects will be realized: "I don't want them to become like [French architect Etienne-Louis] Boullée's late-eighteenth-century paintings in which a seemingly impossible future is projected. We want them to percolate into real projects or into public policy." ■

Josie Glausiusz is a journalist based in New York.

Q&A: John Sims on mathematical art

While pursuing his doctorate in dynamical systems, John Sims was drawn to explore the connections between mathematics and art. Now curating a year-long series of maths–art shows at the Bowery Poetry Club in New York City, the conceptual artist explains the cultural significance of maths.

What is mathematical art?

It is art that embraces the spirit, language and process of mathematics. Both maths and art are concerned with truth, but they differ in their ways of searching for it. Maths uses analysis and proof; art uses the senses and emotions. But maths can harness the spirit of creativity and art can be analytical. Together they form a great alliance for understanding the world around us.

How did you come to straddle both worlds?

I grew up in Detroit, Michigan, and became interested in maths through a high-school science-fair project on Pythagorean triples. It was in graduate school that I started to connect maths and art. I taught a calculus course where I allowed the students to make a 'cheat sheet' of notes and formulae to take into the exam. One was visually stimulating, so I bought it. Later, I met mathematician John Horton Conway and sculptor Brent Collins who got me excited about visual maths and art. Soon after, I went to Ringling College of Art and Design in Sarasota, Florida, to develop a maths curriculum for art students.

Why run a series of maths–art shows this year in New York City?

The aim of the Rhythm of Structure series is to create an opportunity for call-and-response across maths, art and poetry — where mind meets hand meets heart. The hope is to balance the emptiness of pop culture with work that encourages deeper thinking. Nine exhibitions deal with the geometric, conceptual and social aspects of mathematical art. The geometry series included works by mathematicians Mike Field, Davide Cervone and Carlo Séquin. Another show examined how statistics can be used to distort the truth. The current exhibition includes a large geometric drawing by the late artist Sol LeWitt and a response to it by artist Adrian Piper, in the form of a 2-metre-square 'wall deletion'

D. DEAMORIM

that exposes beam and brick. Mark Strand, the former US Poet Laureate, responded to the pairing in verse.

Can art be useful in teaching maths?

Sometimes. However, I think maths education is failing marginalized groups such as artists. It would be better if maths was presented less as a slave to science and more as a partner to art. Our next set of shows engages students and teachers. A class at the Brooklyn Academy of Science and the Environment is preparing a giant tessellation, inspired by M. C. Escher, that will cover a wall. Later, we will open that wall to mathematicians and maths educators, who will use the language of maths to create graffiti that will let them see their own formal symbols as objects of art, challenging the distinction between the two fields.

Do views of maths differ across cultures?

Ethnomathematics is the study of how maths is embedded in culture. One can ask how the prevailing ideas of a culture have shaped its maths. Or one can search for maths in cultural artefacts, such as the patterns in Native American basket weaving or the fractals that are said to be found in Jackson Pollock's paintings. Paulus Gerdes, an educator and mathematician from Mozambique, has written extensively on how native mathematical thinking can inspire contemporary work. I have translated a knot diagram that Gerdes designed — inspired by African and Celtic sources — into a rope sculpture. For the last show of the series, we will create a wall of mathematical quilts from all over the world.

What will you work on next?

I am finishing a project featuring 13 quilts based on visualizations of pi and Pythagorean triples, in collaboration with Amish quilters from Sarasota. After that, I am developing an online virtual Museum of Mathematical Art.

Who has influenced you?

I am inspired by Pythagoras, who saw maths sitting at the centre of art, life and nature. I admire the work of the sixteenth-century painter Albrecht Dürer, particularly his use of magic squares [number grids in which every row, every column and the diagonals sum to the same constant]. I like the way that M. C. Escher was able to draw on the tradition of Islamic geometric art in a representational context, and I like his lithograph of an impossible waterfall inspired by the work of British mathematician Roger Penrose. In the conceptual realm, I like the surrealist artist Marcel Duchamp for his subversive audacity. However, my greatest influence is the unfolding system of structures, patterns and cycles of nature itself. ■

Interview by **Jascha Hoffman**, a writer based in San Francisco, California.
e-mail: jascha@jaschahoffman.com

Rhythm of Structure: Mathematics, Art, and Poetic Reflection
Bowery Poetry Club, New York City
Until 30 August 2010.
See go.nature.com/ZCUbdS for details.

NEWS & VIEWS

COMPLEX NETWORKS

The fragility of interdependency

Alessandro Vespignani

A study of failures in interconnected networks highlights the vulnerability of tightly coupled infrastructures and shows the need to consider mutually dependent network properties in designing resilient systems.

Life as we know it in the modern world is more and more dependent on the intricate web of critical infrastructure systems. The failure or damage of electric power, telecommunications, transportation and water-supply systems would cause huge social disruption, probably out of all proportion to the actual physical damage. Although urban societies rely on each individual infrastructure, recent disasters ranging from hurricanes to large-scale power outages and terrorist attacks have shown that the most dangerous vulnerability is hiding in the many interdependencies across different infrastructures[1,2]. Relatively localized damage in one system may lead to failure in another, triggering a disruptive avalanche of cascading and escalating failures.

Understanding the fragility induced by multiple interdependencies is one of the major challenges in the design of resilient infrastructures[1,2]. On page 1025 of this issue, Buldyrev and co-workers[3] lay out the framework for the analysis of catastrophic failures in interdependent networks. Their work, building on the 'percolation analysis' of two mutually dependent networks, highlights the subtleties of this problem and clearly shows that systems made of interdependent networks, such as transport networks (Fig. 1), can be intrinsically more fragile than each network in isolation.

Over the past two decades it has become obvious that the analysis and understanding of large-scale infrastructures transcend engineering and design issues. Although generally subject to local design, engineering and optimization, infrastructures evolve globally through unplanned aggregation of isolated parts, adaptation to anticipated and unanticipated demands, and the transformation of services according to evolving social needs. A classic example is the physical Internet made of computers and their physical connections, which, as the result of an unsupervised and exponential growth, has become one of the first human artefacts that we study as a natural phenomenon by devising experiments aimed at tracing its network structure and geographical distribution[4,5].

Viewed from this perspective, critical infrastructures are complex systems for which it is generally impossible to abstract the global behaviour from the analysis of single components, especially under conditions such as failures and disasters. Work on the mechanics and performance of components, new materials and innovative engineering principles are crucial in the design of resilient infrastructures, but there is also a need to understand the general principles leading to the complex global architecture of these systems and their ability to withstand failures, natural hazards and man-made disasters. In this context, a large body of research has shown that most real-world infrastructure networks present globally dynamic self-organization and a high level of heterogeneity characterized by statistical distributions that vary over several orders of magnitude[6,7]. In principle, these global and heterogeneous properties may have a strong impact on the vulnerability of large-scale systems as well as on the strategies that might be used to contain the spreading of failures in them. Such an impact has recently been studied in a global-behaviour perspective using the framework of complex networks[8–10].

B. GONÇALVES *ET AL.*, INDIANA UNIV.

Figure 1 | Interconnected networks of human mobility in North America. The blue network represents short-range commuting flows by car, train and other means of transportation and transport infrastructures. Yellow-to-red lines denote airline flows for a few selected cities; red corresponds to greater traffic intensity. Population density is identified on the grey/white colour scale, with white corresponding to areas of higher density. All features in this map were obtained from real data[10].

Although investigations of the resilience of complex networks have triggered enormous interest and debate, most studies have focused on single, isolated networks. Such a situation is more the exception than the norm, however. Infrastructures show a large number of interdependencies of differing types: physical interdependency when energy, material or people flow from one infrastructure to another; cyber interdependency when information is transmitted or exchanged; geographical interdependency such as the close spatial proximity of the elements of the infrastructure; logical interdependency such as financial dependence, political coordination and so on. All of these interdependencies are the nexus allowing failures in one infrastructure to propagate to other infrastructures, and are often the cause of widespread disruption, as in the 2003 blackout in the northeastern United States and southeastern Canada, and the disaster following Hurricane Katrina in 2005[1,2,11].

In their study, Buldyrev *et al.*[3] define a general

theoretical framework for analysing the effect of system-wide interdependencies by studying the resilience of a system composed of two networks whose nodes are mutually dependent. To probe the functional integrity of the composite network, they use the number of nodes (size) of the 'giant component' of the system, the largest connected set of nodes. They study this quantity both analytically and numerically as a function of the progressive removal of network nodes, with each node removal simulating the failure of a specific network element. To do this they used the elegant framework of percolation theory, which concerns the connectivity properties of networks. In isolation, standard networks exhibit a critical threshold value for the fraction of nodes that can be removed above which the network becomes totally fragmented. On approaching this threshold the integrity of an individual network progressively decreases, and the giant component shrinks to zero at the critical threshold. In the case of interdependent networks, however, the authors find striking differences to this behaviour (Fig. 2).

In their model[3], the failure of nodes in one network can lead to the failure of nodes in a second network that in turn can cause the escalation of failures in the first network, ultimately leading to the disruption of the system. As a result, the value of the critical threshold is smaller than in an isolated network, indicating that a complete breakdown of the system will occur at a smaller level of sustained damage. More important, however, is the nature of the breakdown transition. In interdependent networks the fragmentation occurs with an abrupt 'first-order' transition, with the size of the giant component suddenly jumping from a finite value to zero at the transition point (Fig. 2). This makes complete system breakdown even more difficult to anticipate or control than in an isolated network.

Even more striking is the case of mutually dependent heterogeneous networks, where the degree distribution — the probability that each node in the system is connected to n neighbouring nodes — is 'heavy-tailed'. Buldyrev and co-workers[3] model this situation with two tightly coupled networks, each with power-law degree distributions, and find the reverse of the now-classic result that sees isolated heterogeneous networks as extremely resilient, with total fragmentation of the network occurring only when all the nodes of the network are damaged. By contrast, in interdependent networks total fragmentation is found above a finite and small fraction of failing nodes, and the more heterogeneous the networks the smaller the damage that can be sustained before functional integrity is totally compromised.

On the one hand, the results of Buldyrev *et al.*[3] offer a clear example of the complexities of and fragilities induced by network interdependencies. On the other hand, the percolation model is a very stylized model of networks' reactions to local damage, and therefore lacks the realism needed to capture many of the features that contribute to the resilience and robustness of real-world networks. After all, most physical and cyber interdependencies are defined by the flow of a physical quantity across the networks; the failure event and the network integrity are not just a connectivity problem. Nevertheless, Buldyrev and colleagues have set the scene for future research that will capitalize on these simple models by introducing higher levels of realism, and by simultaneously tackling engineering issues and globally emerging features in the analysis of infrastructure resilience. ■

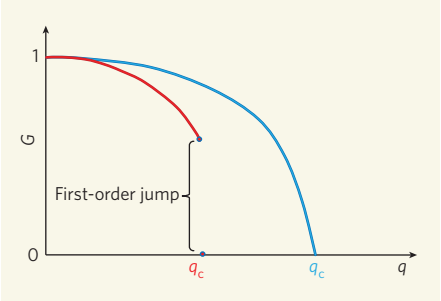

Figure 2 | Breakdown of isolated and interconnected networks. The quantity G is the largest number of connected nodes in a network, and is expressed as a fraction of the total number of network nodes; q is the fraction of nodes removed from a network and q_c is the critical fraction of nodes that on removal lead to a complete fragmentation of the network ($G = 0$). In isolated networks (blue curve), complete network fragmentation is approached continuously. Buldyrev and colleagues[3] show that in interdependent networks (red curve) it occurs abruptly ('first-order' transition) at a smaller value of q_c than in isolated networks.

Alessandro Vespignani is in the Center for Complex Networks and Systems Research (CNetS), School of Informatics and Computing, and the Pervasive Technology Institute, Indiana University, Bloomington, Indiana 47406, USA, and in the ISI Foundation, Turin, Italy.
e-mail: alexv@indiana.edu

1. Chang, S. E. *The Bridge* **39,** 36–41 (2009).
2. Rinaldi, S. M., Peerenboom, J. P. & Kelley, T. K. *IEEE Control Syst. Mag.* **21,** 11–25 (2001).
3. Buldyrev, S. V., Parshani, R., Paul, G., Stanley, H. E. & Havlin, S. *Nature* **464,** 1025–1028 (2010).
4. Krioukov, D. *et al. SIGCOMM Comput. Commun. Rev.* **37,** 69–73 (2007).
5. Pastor-Satorras, R. & Vespignani, A. *Evolution and Structure of the Internet* (Cambridge Univ. Press, 2004).
6. Barabási, A.-L. & Albert, R. *Science* **286,** 509–512 (1999).
7. Barrat, A., Barthelemy, M. & Vespignani, A. *Dynamical Processes on Complex Networks* (Cambridge Univ. Press, 2008).
8. Albert, R., Jeong, H. & Barabási, A.-L. *Nature* **406,** 378–482 (2000).
9. Cohen, R., Erez, K., ben-Avraham, D. & Havlin, S. *Phys. Rev. Lett.* **85,** 4626–4628 (2000).
10. Balcan, D. *et al. Proc. Natl Acad. Sci. USA* **106,** 21484–21489 (2009).
11. Leavitt, W. M. & Kiefer, J. J. *Publ. Works Mgmt Pol.* **10,** 306–314 (2006).

GENOMICS

Lessons in complexity from yeast

David B. Goldstein and Mohamed A. F. Noor

A challenge in biology is to understand complex traits, which are influenced by many genetic variants. Studies in yeast provide the prospect of analysing such genetic variation in detail in other organisms, including humans.

Ever since the modern understanding of evolution and genetics in terms of natural selection and Mendelian inheritance was formulated, generations of scientists have struggled to explain the genetic bases and evolutionary significance of the remarkable variation among individuals, which is observed in many species. Despite considerable progress in finding the main genes that determine genetically simple traits, genetic variants of individually small effect that influence the so-called complex traits — which include height, weight and disorders such as neuropsychiatric diseases and cancers — have proved elusive. On page 1039 of this issue, Ehrenreich *et al.*[1] report a method in yeast that offers great statistical power for identifying multiple genomic regions that contribute to complex traits. Their work affords significant hope that similar genomic studies will be possible in many other species.

Over the past 20 years, various analytical and empirical approaches have been developed to find gene variants that influence complex traits[2,3]. One experimental technique, called bulk segregant analysis[4], examines progeny from crossing two different yeast strains and can potentially pinpoint multiple genes contributing to trait differences, especially when coupled with high-throughput analysis of the progeny's genotype[5]. More recently, these techniques have been merged with ways to select for progeny with extreme traits[6], thus allowing greater mapping precision and power. Ehrenreich and colleagues' paper now hints that we are finally poised for what may be a step change in our understanding of the genetic basis of organismal diversity.

The authors[1] report genetic variations in yeast that mediate 17 complex traits related to resisting chemicals. The main innovation here is to couple the generation of very large populations of progeny from an inter-strain cross

NATURE|Vol 464|15 April 2010

50 & 100 YEARS AGO

50 YEARS AGO

In form, texture and structure chondrules are not like any spheroidal bodies observed in terrestrial rocks, and their origin has been argued by investigators for more than a century ... These hypotheses are often linked with the generally accepted belief that these meteorites are fragments of a disrupted body of asteroidal or planetary dimensions. I would suggest an alternative hypothesis, that the structure of chondritic meteorites is the result of reaction and recrystallization of pre-existing material essentially in the solid state, and that many ... have always been independent and individual objects ... The texture and structure of the chondritic meteorites is quite remarkable if they have originated in any body with a considerable gravitational field. Many of them are very porous and friable, so much so that they can be crumbled in the hand, indicating that they were not consolidated under pressure. **Brian Mason**

From *Nature* 16 April 1960.

100 YEARS AGO

Some time ago an ordinary all-black cat was accidentally shut up in a refrigerating chamber on one of the Orient Line mail steamers when the vessel was in Sydney Harbour. The chamber was not opened until the ship was off Aden, which is about thirty-two days out. When the cat was brought out it was scarcely recognisable. Its coat had become long and thick, and the fur on its back was nearly white. It had lost one ear through frost-bite. The change in the cat's environment from the intense frost of a refrigerating chamber to the intense heat of the Red Sea was accompanied by a rapid change in the cat's appearance. The heavy white coat rapidly fell out, and by the time the ship reached London the cat had practically regained its normal appearance. I did not see the cat, but have inquired carefully into the statements, and have had their truth vouched for by one of the directors of the Orient Company. **A. Campbell Geddes**

From *Nature* 14 April 1910.

with the selection of extremes of a trait from the population. Ehrenreich *et al.* then compare the frequencies of marker alleles (gene variants that are not thought to influence the trait but that flag up particular genomic regions) in the selected and unselected populations and test for significant deviation. When allele frequencies differ significantly between the two populations, the authors infer the presence in that region of a genetic variant influencing the trait. Because this method uses a large base population, and compares the extremes of a trait distribution, it can detect variants that make only modest contributions to the variation of the trait, which in principle allows comprehensive genetic dissection. As a key proof of concept, the authors evaluate the contribution of the variants they identified for one trait: resistance to the DNA-damaging agent 4-nitroquinoline. They find that differences in the genomic regions pinpointed by these variants can explain 54% of the variation among all the progeny of the same cross — an unusually high proportion in comparison with most traits studied in most species so far.

The genetic architectures of the 17 chemosensitivity traits studied by Ehrenreich *et al.* show remarkable diversity — ranging from ones influenced mostly by a single gene to others affected by up to 20 genes in different genomic regions. Thus, even in a single species, and for apparently similar traits, the underlying genetic architectures can be remarkably variable. Early indications from other studies suggest that such diversity of genetic architecture is to be broadly expected across many species. In humans, for example, comprehensive study of common gene variants has explained virtually none of the risk associated with most neuropsychiatric disorders[7], but the yield for many autoimmune diseases has been much better: in Crohn's disease, for instance, up to 20% of the genetic component of risk has been explained[2]. One of the more interesting areas of study for the future will be the underlying evolutionary and developmental reasons behind such broad variation in the genetic architectures of different types of complex trait.

It is worth emphasizing that many of the key elements critical to the authors' success with yeast[1] are applicable to other organisms (including humans), for example through selection of the extremes from a large base population and rapid assessment of gene-variant frequencies. For humans, selection of extremes happens routinely as part of clinical care. Individuals who are formally diagnosed with epilepsy or schizophrenia, for instance, represent just 1% or so of the general population. Other traits of immediate medical interest represent even greater extremes; these include drug-induced liver injuries and heart arrhythmias, two frequent reasons that potential therapeutic agents are halted in mid-development and prescription drugs are pulled from the market. Such extremes identified as 'cases' in the clinic can be compared with the general population or, in other settings, the extremes of a given distribution (for example, weight, height, birth weight and blood pressure) can be compared to identify the underlying genetic variations influencing the trait. Next-generation sequencing now makes comprehensive identification of virtually all gene variants present in large samples logistically possible.

For model organisms other than yeast, mapping with large sample sizes and selection of extreme traits have already been applied to the nematode *Caenorhabditis*, the fruitfly *Drosophila* and the plant *Arabidopsis* to analyse traits such as nutrient uptake, starvation resistance and heavy-metal tolerance. The advantage of yeast, however, is its very high meiotic recombination (crossover) rate — orders of magnitude higher than the average rates observed in these other species — which enables the effects of individual genes to be localized with greater precision. Nonetheless, Ehrenreich and colleagues' automated selection approach[1] can be adapted for other model systems to localize modest-effect variants contributing to ecological and behavioural traits.

That said, we do not wish to trivialize the amount of work ahead, nor the complications inherent in studies of organisms other than yeast. Despite startling advances in sequencing technology, it remains difficult, for instance, to identify accurately many classes of genetic variation — in particular, structural variants and any variants in 'difficult-to-sequence' genome regions. Accurate measurement of trait features also remains a challenge, especially for behavioural traits and, in humans, for most mental illnesses. Even when causal variants for a given trait are identified, we face the still more difficult task of determining the functional effects associated with each of the variants and how to piece them together.

Nevertheless, a field of study sometimes suddenly enters a golden age when the necessary conceptual and technological ingredients combine to permit discovery at a rate that would have been difficult to imagine, let alone achieve, at any previous time. The study of the genetic basis of organismal diversity seems set at last to enter its own golden age, where even genetically complex traits will yield many of their long-held secrets. ■

David B. Goldstein and Mohamed A. F. Noor are in the Center for Human Genome Variation and Department of Biology, respectively, Duke University, Durham, North Carolina 27708, USA.
e-mail: d.goldstein@duke.edu

1. Ehrenreich, I. M. *et al. Nature* **464,** 1039–1042 (2010).
2. McCarthy, M. I. *et al. Nature Rev. Genet.* **9,** 356–369 (2008).
3. Kao, C. H., Zeng, Z. B. & Teasdale, R. D. *Genetics* **152,** 1203–1216 (1999).
4. Michelmore, R. W., Paran, I. & Kesseli, R. V. *Proc. Natl Acad. Sci. USA* **88,** 9828–9832 (1991).
5. Borevitz, J. O. *et al. Genome Res.* **13,** 513–523 (2003).
6. Nuzhdin, S. V., Harshman, L. G., Zhou, M. & Harmon, K. *Heredity* **99,** 313–321 (2007).
7. Need, A. C. & Goldstein, D. B. *Dialogues Clin. Neurosci.* (in the press).

SINGLE-MOLECULE ANALYSIS

A ribosome in action

Susanne Brakmann

The manufacture of proteins by ribosomes involves complex interactions of diverse nucleic-acid and protein ligands. Single-molecule studies allow us, for the first time, to follow the synthesis of full-length proteins in real time.

Protein synthesis involves a complex interplay of various cellular components. Ribosomes are the cell's protein-production factories, and interact with messenger RNA (the template), amino-acylated transfer RNAs (which act as adaptors between mRNA and amino-acid residues) and diverse co-factors (for the initiation of synthesis, elongation of the nascent chain and release of the mature polypeptide). In this issue, Uemura *et al.*[1] report the use of an extremely sensitive single-molecule detection technique to observe this process at unprecedented resolution: the stepwise synthesis of a single protein (page 1012).

Ribosomes are evolutionarily conserved molecular nanomachines with a diameter of about 25 nanometres and a molecular weight of around 2.5 megadaltons. In functional terms, they are amino-acid polymerase enzymes with an RNA 'heart'. They accelerate the rate of protein synthesis by at least one millionfold, owing exclusively to entropic effects that involve the positioning of aminoacyl-tRNAs, the shielding of the reaction from bulk solvent and the organization of their own active site[2,3]. Ribosomes also check the quality of their polypeptide products — inaccurate amino-acid sequences could result in an altered three-dimensional protein structure and even cellular toxicity.

Structural analyses of functional ribosome complexes have formed the basis of a consistent biochemical model for the mechanism of protein synthesis[4], suggesting that this process depends on large-scale conformational changes in the ribosome. But the nature, timescale and magnitude of these dynamic changes have remained undefined.

Traditional biophysical investigations of dynamic molecular processes yield ensemble-averaged data. These may hide crucial information owing to the presence of asynchronous conformational states and varying stages of the enzymatic reaction. By contrast, single-molecule studies circumvent the need for synchronous molecular behaviour and the use of uniform samples, thus allowing the identification and direct characterization of transient, rare and so physiologically relevant events. With the use of sensitive fluorophores, single-molecule spectroscopy and force-based techniques, researchers can observe changes in distance on the subnanometre scale with a temporal resolution in the millisecond range.

To study the details of translation, for example, fluorophores can be chemically coupled to tRNA molecules. Consequently, after binding to the ribosome, the fluorescently labelled tRNAs 'report' with high sensitivity on how they are selected by the ribosome, their motion within the ribosome and even conformational changes in the ribosome.

Indeed, single-molecule analyses of fluorescently labelled tRNAs have allowed the monitoring of tRNA selection and (single) peptide-bond formation in real time, as well as studies of tRNA dynamics on the ribosome during elongation, and single-molecule force measurements have helped to determine the strength of ribosome–mRNA interactions[5]. Although such studies have revealed previously unknown details of tRNA selection and catalytically important ribosomal states, the findings were limited to the initial stages of translation. A desirable extension of this is the investigation of several rounds of peptide-bond formation — for instance, study of the continuity of synthesis (processivity) or its accuracy (translational fidelity).

The first study to attempt this[6] used specifically designed, single hairpin-shaped mRNA sequences tethered by their ends to optical tweezers, and determined their translocation along the ribosome. The translocation measured three mRNA bases (one codon) and occurred as a series of movement–pause–movement events, with pause durations ranging from a fraction of a second to several seconds. The 'dwell' time at each codon was the time taken for tRNA selection and peptide-bond formation, which can be correlated to the sequence context.

Uemura and colleagues[1] now take these methods even further. Their approach is based on a set of tRNAs labelled with distinct fluorophores, allowing their immediate identification after ribosomal binding and so real-time 'reading' of the underlying mRNA sequence. By watching tRNA substrates instead of the template mRNA, the authors were able to follow tRNA binding and transit on individual translating ribosomes during multiple rounds of chain elongation in the synthesis of short peptides (4–13 amino acids long). Moreover, they showed that only two tRNA molecules simultaneously bind to the ribosome, allowing them to explore the mechanism of tRNA transit in relation to other reactants (Fig. 1).

What is of utmost importance is that Uemura *et al.* were able to study translation at physiologically relevant (micromolar) concentrations of tRNA and other factors using extremely small reaction vessels known as zero-mode waveguides, which were generated from nanophotonic metal films and illuminated from below by a laser. The resulting observation volumes of 10^{-21} litres were therefore occupied by, on average, not more than one molecule (Fig. 1). Because the duration of binding of the correct fluorescently labelled tRNA to the ribosome was much longer than the timescales associated with the freely

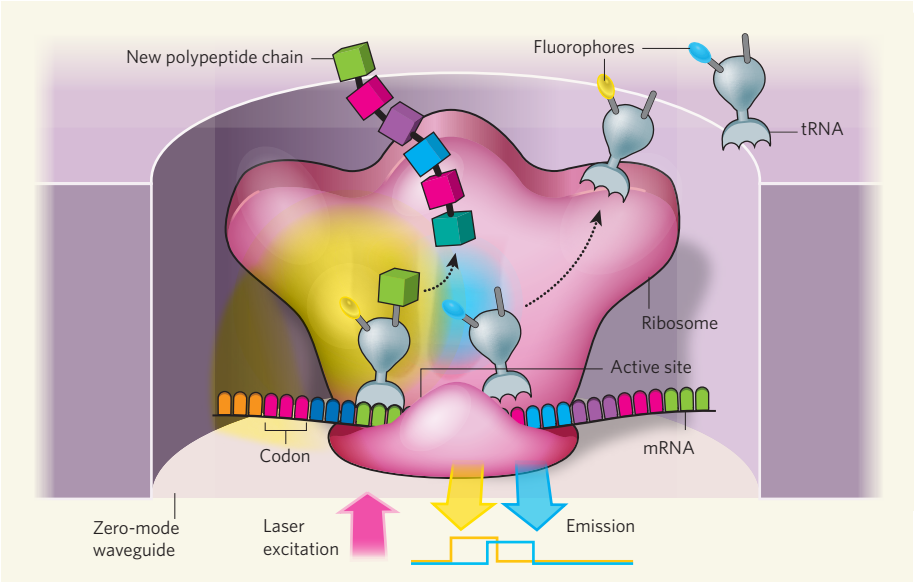

Figure 1 | Close-up view of a zero-mode waveguide vessel. Uemura and colleagues' set-up[1] consisted of a nanostructured metal film called a zero-mode waveguide, containing circular holes of diameter 50–200 nanometres. Using this, they analysed sample volumes as small as 10^{-21} litres to detect individual fluorescent tRNA molecules against the background signal from freely diffusing tRNA molecules. The binding of fluorescently labelled, cognate tRNA molecules — each labelled with a different fluorophore — within the ribosomal active site causes an elevation in fluorescent emission on the corresponding colour channel.

diffusing tRNA molecules, genuine signals were reliably distinguished from low and constant background.

The real-time monitoring of single translating ribosomes is truly a breakthrough for studying the process of translation, how its accuracy is controlled and the conformational changes that it involves in ribosomes. It should now be only a small step to elucidating the correlation between tRNA binding and changes in ribosomal conformation, to probing the dynamics of translational control, and to studying the synthesis and folding of full-length proteins in real time. Beyond that, Uemura and colleagues' impressive demonstration[1] of how their powerful technique (originally developed for 'next-generation' DNA sequencing[7]) can be used to answer biological questions will play a decisive part in studying other processes, including RNA sequencing, the sequencing of genomic sites modified by methyl groups, and various time-dependent regulatory processes. ■

Susanne Brakmann is in the Department of Chemical Biology, Technische Universität Dortmund, D-44227 Dortmund, Germany.
e-mail: susanne.brakmann@tu-dortmund.de

1. Uemura, S. *et al. Nature* **464,** 1012–1017 (2010).
2. Bieling, P., Beringer, M., Adio, S. & Rodnina, M. V. *Nature Struct. Mol. Biol.* **13,** 423–428 (2006).
3. Schmeing, T. M. & Ramakrishnan, V. *Nature* **461,** 1234–1242 (2009).
4. Ehrenberg, M. http://nobelprize.org/nobel_prizes/chemistry/laureates/2009/cheadv09.pdf (2009).
5. Marshall, R. A., Echeverría Aitken, C., Dorywalska, M. & Puglisi, J. D. *Annu. Rev. Biochem.* **77,** 177–203 (2008).
6. Wen, J.-D. *et al. Nature* **452,** 598–603 (2008).
7. Eid, J. *et al. Science* **323,** 133–138 (2009).

INFORMATION SCIENCE

Guaranteed randomness

Valerio Scarani

You have received a device that is claimed to produce random numbers, but you don't trust it. Can you check it without opening it? In some cases, you can, thanks to the bizarre nature of quantum physics.

From the stock market to the weather, we are surrounded by processes that are best described by unpredictable, random elements. But randomness is a notoriously difficult property to test. Worse still, when it is used to protect personal details, the random elements must be private. On page 1021 of this issue, Pironio and co-workers[1] describe a method for obtaining numbers that are guaranteed to be random and private from an unknown process, provided that the numbers are certified as being derived from measurements on quantum systems. Some may surmise that this claim is trivial, because quantum physics has long been known to produce randomness. Some may even surmise that this claim is wrong, on the basis of the idea illustrated by the Dilbert comic strip 'Tour of Accounting' reproduced here. But the result is both new and correct.

Starting with the comic strip, Dilbert's guide is uttering a scientific truth: the list 9, 9, 9, 9, 9, 9 is as valid an output of a generator of random numbers as is 1, 2, 3, 4, 5, 6 or 4, 6, 7, 1, 3, 8. In fact, in a long enough sequence of lists, any list of numbers should appear with the same frequency. Classic, 'black-box', tests of randomness exploit this idea: they check for the relative frequencies of lists. But, in practice, no such test can distinguish a sequence generated by a truly random process from one generated by a suitable deterministic algorithm that repeats itself after, for example, 10^{23} numbers. Moreover, in this way, whether the numbers are private cannot be checked: even if the sequence had initially been generated by a truly random process, it could have been copied several times, and the random generator may just be reading from a record.

It seems therefore that only a careful characterization of the process — that is, an 'open-box' test — can guarantee randomness, especially of the private kind. But nature sometimes dares to go where abstract thinking alone cannot. Pironio and colleagues[1] take an alternative route for generating guaranteed, private randomness in their study, using one of the most remarkable phenomena of quantum physics: the violation of the 'Bell inequalities'[2], which has been observed in numerous different experiments in the past three decades[3].

To understand what Bell inequalities are, first consider two quantum systems, for example two photons emitted by the same source and propagating away from one another. Consider further that a measurement is made of each of the photons, which are now spatially distant. For example, the polarization of each photon can be measured, assigning the value 0 if a photon is transmitted through a polarizer and the value 1 if it is reflected. For certain specific sources, the outcomes of the two measurements are not independent. For instance, when the two polarizers are set in the same direction, only the pairs of outcomes (0, 1) and (1, 0) are observed: the photons are never both transmitted or both reflected. Such correlations between distant events are striking, raising the question of where the connection is. There is surely no communication between the two photons, because the signal would need to propagate faster than light. The only plausible hypothesis therefore is that the photons leave the source with a common 'list of instructions', which dictates the outcomes of each possible measurement.

Bell inequalities are criteria that, when applied, allow this latter hypothesis to be proved false. If the statistics of the measurement outcomes violate the inequalities, then the observed correlations cannot arise from a pre-established common list. Quantum correlations violate Bell inequalities and thus cannot come from a pre-established list either, and there is no classical mechanism that explains those correlations.

So how can random numbers be obtained using Bell inequalities? Following on from the example above, many pairs of photons are taken, and the measurement procedure is repeated: two sequences of 0s and 1s are produced, one at each measurement location. If these sequences violate Bell inequalities, they are guaranteed to be private random numbers: random, because there was no information about them before their generation; and private, because, given that the information did not exist, nobody else could have had access to it.

This line of qualitative reasoning has been known for many years. However, only recently have physicists been realizing and using its full power by stressing that Bell inequalities depend solely on the statistics of the observed outcomes and not on the description of the physical system or on the measurements that are carried out on it. In other

words, Bell inequalities define a black-box test. The only caveat is that the statistics that are computed are conditional on some choices by the users: the box must allow input. A box that produces numbers without any input from the external world, like the troll in the comic strip, cannot be checked by this method.

Before the study by Pironio and colleagues[1], the idea of exploiting Bell inequalities had proved fruitful in quantum cryptography[4] and in assessing the quality of a source for producing 'quantum entanglement'[5]; another investigation[6] had also addressed the issue of randomness. In their study, Pironio *et al.* meet three previously unmet challenges.

First, they obtain a quantitative estimate of how many random numbers can be extracted in a real experiment, in which the measurement outcome correlations are not necessarily the ideal ones and the sequences are not infinitely long.

Second, the 'boxes' require that the user makes 'choices', so the users must supply some of the initial randomness. But, in the authors' study, the initial randomness is cheap (it can come from the user's brain), and the protocol can generate many more random numbers than were initially supplied.

Third, such random numbers are actually produced by an experiment[1] involving two atoms. Experimental results that violate Bell inequalities are not new, but an additional constraint must be met for black-box assessments: the detection process needs to be very efficient. For two photons, as in the example, this is not possible at present. But it is possible for two atoms, hence the choice of these as quantum systems by Pironio and colleagues[1]. Admittedly, the experiment is not a fully black-box experiment: we need to trust that atoms are indeed being measured and that atoms in different metallic boxes do not 'talk' to each other. But these are the only features that need to be trusted: there is no need to know which properties are measured or how they are measured.

A final point to consider is that Bell inequalities are independent of quantum physics. Their violation falsifies the existence of a common list of instructions, and a falsification is a fact that will remain true regardless of the nature of the physics, whether quantum physics or an as-yet-unveiled form of physics. With their study, Pironio and colleagues[1] demonstrate a method for generating guaranteed, private randomness that will be useful for the ages to come. ■

Valerio Scarani is at the Centre for Quantum Technologies and the Department of Physics, National University of Singapore, 117543 Singapore.
e-mail: physv@nus.edu.sg

1. Pironio, S. *et al. Nature* **464,** 1021–1024 (2010).
2. Bell, J. S. *Physics* **1,** 195–200 (1964).
3. Scarani, V. *Quantum Physics: A First Encounter* (Oxford Univ. Press, 2006).
4. Acín, A. *et al. Phys. Rev. Lett.* **98,** 230501 (2007).
5. Bardyn, C.-E. *et al. Phys. Rev. A* **80,** 062327 (2009).
6. Colbeck, R. PhD thesis, Univ. Cambridge (2007); available at http://arxiv.org/abs/0911.3814 (2009).

CANCER

Genomics of metastasis

Joe Gray

Cancer cells that invade other parts of the body do so by accumulating genomic aberrations. Analysis of the genomic differences between primary and metastatic tumours should aid the understanding of this process.

The massively parallel sequencing technologies now available are sufficiently powerful and cost-effective to allow high-resolution analysis of changes that occur in the genome of patients with cancer. These include variations in the number of copies of specific genomic regions, changes in DNA sequence, and structural aberrations[1–3]. On page 999 of this issue, Ding *et al.*[4] report their application of this technology to analyse the genomic features of primary and metastatic tumour samples from a 44-year-old African-American patient with basal-like breast cancer. Their results provide insight into how cancer genomes evolve as the disease progresses.

The way in which tumour cells escape their primary site and colonize other locations in the body — often with lethal results — is becoming increasingly clear[5–8]. Underlying biological changes include variations in cell differentiation, in the ability to sense cell-death signals, in cell-cycle regulation and in genome stability. Other hallmarks of tumour-cell metastasis are increased cell motility and invasion, new blood-vessel formation and inflammation.

Although the biology of many aspects of metastasis is understood, information about the underlying genomic and epigenomic aberrations is emerging more slowly. In their paper, Ding *et al.* not only search for the genomic changes that occur as a primary tumour gives rise to a distant metastasis, but also use massively parallel technologies to study the DNA-sequence differences among all samples analysed.

To investigate the genomic changes that develop in basal-like breast cancer (which is characterized by absence of the ERBB2 protein and of oestrogen and progesterone receptors), the authors[4] took a biopsy from the patient's breast tumour — and a blood sample as a normal control — at the time of initial surgery (Fig. 1). They also introduced cells from this biopsy into an immunodeficient mouse to produce a xenograft tumour. Eight months later, despite chemotherapy, the cancer had spread to the patient's brain, from which the authors also obtained a sample. They then performed whole-genome sequencing on all four samples — the patient's primary and secondary tumours, the mouse xenograft tumour and the patient's blood sample — to search for structural rearrangements in the genomes, abnormalities in the copy number of genomic regions, and mutations.

The authors' data show that the spectrum of structural aberrations was similar in all three tumours. Also, most of the copy-number abnormalities in the primary tumour were present in the xenograft and metastatic tumours, although the extent of many of the copy-number abnormalities had expanded in the xenograft and metastatic tumours and some new aberrations had also surfaced. As for mutations, most were also common to all three tumours. But a particularly notable result came from assessment of the prevalence of mutant sequences.

Because the sequencing technologies used measure mutations in individual strands of DNA, the authors were able to calculate the prevalence of mutations as a fraction of the sequences at each genomic region carrying a mutation. They found that the prevalence of

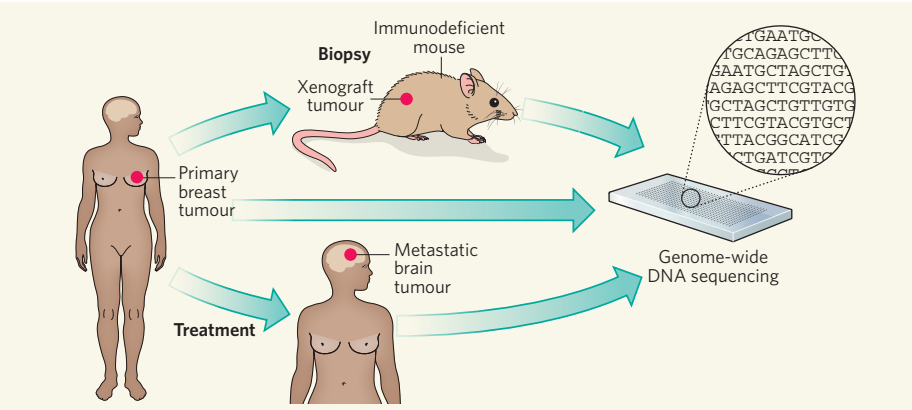

Figure 1 | Covering all the bases in metastatic assessment. Ding *et al.*[4] performed genome-wide analysis on three tumour samples: a patient's primary breast tumour; her metastatic brain tumour, which formed despite therapy; and a xenograft tumour in a mouse, originating from the patient's breast tumour. They find that the primary tumour differs from the metastatic and xenograft tumours mainly in the prevalence of genomic mutations.

VISION

Fisheye views

Archerfish eyes must cope with the light spectrum of two very different media. These fish live among mangroves and in rivers, and are renowned for their ability to bring down an insect target from overhanging foliage by spitting a stream of water at their prey, as pictured here. Shelby Temple and colleagues have investigated the visual pigments and spatial resolving power of archerfish eyes, and present the results in the context of the requirements for vision at the water–air interface (S. Temple *et al. Proc. R. Soc. Lond. B* doi:10.1098/rspb.2010.0345; 2010).

Using microspectrophotometry, the authors find that — as is known in other species — the pigments and spectral tuning vary between different parts of the retina (in this case, subdivided into dorsal, ventro-nasal and ventro-temporal regions). They interpret these variations in terms of the tasks the eye has to perform when operating along three visual axes; that is, three directions in which the eye might look.

A simplified description of their conclusions is that the dorsal retina has maximum spectral sensitivity at 454 and 570 nanometres, a combination that Temple *et al.* consider is well suited for discriminating between shades of brown, and for identifying objects

S. TEMPLE

beneath them. The values for the ventro-nasal retina (visual axis up and behind) are 502 nm and 620 nm. The 502-nm peak is tuned, the authors suggest, for detecting dark images against a background of bright sky, such as the silhouette of an aerial predator.

The ventro-temporal retina presents peak sensitivities at 453 nm, 535 nm and 565 nm. This combination is possibly used for colour vision along the visual axis appropriate for sighting prey against a background of foliage. From video recordings, Temple *et al.* conclude that this part of the retina aligns with spitting angles, and they estimate that the visual resolution allows an archerfish to tell the difference between two objects 2 mm apart at a range of 550 mm.

Archerfish can be trained to spit at coloured targets. That, say Temple *et al.*, makes them excellent subjects for investigating further aspects of the function of intra-retinal differences. **Tim Lincoln**

20 of the mutations was comparable for all three tumours, that 26 showed increased prevalence in the xenograft and/or the metastatic tissue, and that the prevalence of 2 was significantly decreased relative to the primary tumour. This suggests that at least three cell clones from the primary tumour carried over into the metastatic and xenograft tumours: one carried mutations that decreased in prevalence, one had mutations that increased in prevalence, and one carried mutations whose prevalence did not change compared with the primary tumour. This metastasis therefore does not seem to have formed from a single cell, but rather from a cell population that, in this case, contained at least these three clones.

Another remarkable result was that 16 of the 20 mutations present at increased prevalence in the metastatic tumour were also present with higher prevalence in the xenograft. This pattern of concordant selection of one or more clones carrying common mutations during progression to metastasis and establishment of a xenograft suggests that similar evolutionary pressures are at work on these cells in both environments. This may provide some indication of the aspects of the metastatic process that are influenced by the aberrations carried in the selected clone, because some processes needed for metastasis, such as invasion and barrier penetration, may not be important selective forces in the xenograft environment. These aspects of metastasis therefore may not be influenced by aberrations that are selected in both xenograft and metastasis.

Of course, Ding *et al.*[4] assessed the evolution of only one tumour. But if their results can be reproduced in larger studies, comparative investigations of primary-tumour/xenograft/metastasis triplets might facilitate identification of genomic aberrations that play a significant part in the pathophysiology of the tumour and metastasis, and provide clues about the biological roles of these genomic regions. They could also provide information about clonal diversity in metastatic lesions, which may help to identify subpopulations of cellular molecules, and thus influence cancer therapy.

Ding and colleagues' data therefore hint that future sequencing of some metastatic-cancer genomes should be considerably deeper than contemplated at present to allow statistically robust estimates of mutation prevalences to be obtained. Moreover, functional assessments of the affected genomic regions will be needed to determine which genes in the selected clones are drivers and which mere passengers. Concordant selection of mutations in the metastatic and xenograft tumours could provide initial clues to the most useful candidates for functional assessment. ■

Joe Gray is in the Lawrence Berkeley National Laboratory, Life Sciences Division, Berkeley, California 94720, USA.
e-mail: jwgray@lbl.gov

1. Mardis, E. R. & Wilson, R. K. *Hum. Mol. Genet.* **18,** R163–R168 (2009).
2. Metzker, M. L. *Nature Rev. Genet.* **11,** 31–46 (2010).
3. Morozova, O., Hirst, M. & Marra, M. A. *Annu. Rev. Genomics Hum. Genet.* **10,** 135–151 (2009).
4. Ding, L. *et al. Nature* **464,** 999–1005 (2010).
5. Nguyen, D. X., Bos, P. D. & Massagué, J. *Nature Rev. Cancer* **9,** 274–284 (2009).
6. Gupta, G. P. & Massagué, J. *Cell* **127,** 679–695 (2006).
7. DeNardo, D. G., Johansson, M. & Coussens, L. M. *Cancer Metastasis Rev.* **27,** 11–18 (2008).
8. Langley, R. R. & Fidler, I. J. *Endocr. Rev.* **28,** 297–321 (2007).

See also News Feature, page 972.

BEHAVIOURAL ECOLOGY

Ways to raise tadpoles

Hanna Kokko and Michael Jennions

To reduce parental care, just add water — that's the conclusion of an intriguing investigation into the extent of the motherly and fatherly devotion that different species of frog extend to their offspring.

Nature documentaries frequently invite their viewers to contemplate that only a tiny minority of the perfectly formed larvae floating in the sea, or crawling on land, can ever hope to make it to the adult stage. Parents of many species seem surprisingly unconcerned, leaving their progeny to fend for themselves. In some species, however, parents provide their offspring with costly, time-consuming services, ranging from protecting them against predators and environmental stresses to giving them shelter or food.

Why does this diversity of solutions exist? Theoreticians state that parents may reduce care to increase the number of young produced and/or to improve the parents' own survival. Both trade-offs reduce the lifetime fecundity of parents, so parents are likely to provide care

only if it substantially improves the survival of the offspring they do produce[1]. A study of frogs by Brown *et al.*[2], just published in *The American Naturalist*, shows that a species' breeding habitat can influence offspring survival in a surprisingly deterministic way: tadpoles have a chance of surviving on their own only if they live in relatively large pools of water.

It has proved difficult to identify specific ecological factors that affect whether parental care will evolve, yet the answer provided by Brown and colleagues[2] is simple and elegant. To start with, they built a phylogeny depicting the evolutionary relationships among 404 frog species that are distributed across the order Anura and that have been investigated for whether and how they provide parental care.

Frog species differ enormously in whether they care for their young and in the type of care given: parents may protect eggs by laying them in terrestrial burrows, or brood the young in pockets of tissue on their back or in the mother's stomach[3]. Although Brown *et al.* did not consider all frog species (of which there are more than 5,300), their phylogeny uncovered compelling ecological generalities. Species that deposit eggs and tadpoles into phytotelmata (small pools of water found in hollows in plants) are more likely to provide parental care than those breeding in terrestrial waters such as streams, ponds and rivers. The estimated rate of evolutionary transitions from providing no care to providing care was nine times higher in species that breed in these tiny pools than in those that use terrestrial waters.

Why does a limited water source turn frogs into devoted parents? One possible answer is that the food supply that a small body of water offers is so meagre that parents using these as breeding grounds have been strongly selected to improve the survival of their offspring. To test this idea, Brown *et al.* investigated one of the evolutionary contrasts in their data set in detail, reporting fascinating differences between two species of poison frog that live in the same habitat in Peru.

Individuals of the variable poison frog species (*Ranitomeya variabilis*) have large home ranges, and both sexes frequently switch mating partners. Eggs are laid above a suitable phytotelma, and either the tadpoles fall into the water or, more commonly, the male parent returns and helps the tadpoles to rupture the egg membrane. He then transports the tadpoles on his back (Fig. 1) to another hollow. In this species, males place tadpoles in water volumes averaging about half a cup (112 millilitres). In the closely related, similarly sized mimic poison frog (*Ranitomeya imitator*), mating pairs are often monogamous. Their home ranges are small, and males carry the tadpoles to a tiny phytotelma which is, on average, the volume of half a shot glass (24 ml). The male parent thereafter returns periodically to monitor whether it is time to feed the tadpoles. If he calls incessantly, the female makes her way to the pool and lays a specialized 'trophic' egg, which is promptly eaten by the tadpoles.

JASON L. BROWN

Figure 1 | Tadpole transport. After tadpoles have emerged from eggs, males of both the variable poison frog (*Ranitomeya variabilis*; top) and the mimic poison frog (*Ranitomeya imitator*; bottom) carry these offspring on their back from the place of birth in a phytotelma (a water-filled hollow in a plant) to another phytotelma. Brown *et al.*[2] find that these frogs otherwise differ considerably in the amount of care provided by the parents. The smaller phytotelmata favoured by *R. imitator* are associated with a greater degree of parental attention being paid to the tadpoles.

Tadpoles of both species are thus cared for, but tadpoles of the variable poison frog develop without being fed and receive care from only one sex (males). Is it a coincidence that variable poison frogs use larger breeding pools than mimic poison frogs, or did feeding evolve in mimic poison frogs specifically to combat a low food supply in tiny pools?

To shed light on this question, Brown *et al.*[2] carried out a translocation experiment. They show that tadpoles of both species grow and survive poorly in small pools when they are denied parental attention, whereas such problems do not arise in larger pools. The fact that tadpoles of both species suffered similar fates is crucial to the interpretation of the experiment. It allowed Brown *et al.* to circumvent the chicken-and-egg problem that species in which care is routinely given might have evolved tadpoles that obligately rely on parental care, which could have led to an overestimation of the value of parental care in small pools.

The phylogeny constructed by Brown *et al.* also reveals that the production of trophic eggs is generally associated with breeding in phytotelmata. However, trophic egg production by frogs is rare, so factors other than the need to feed offspring are probably required to explain the patterns of parental care in frogs more fully. For example, breeding in a small body of water could decrease the likelihood of brood parasitism (in cases in which more than one pair are using a breeding pool), because later-hatching tadpoles are often cannibalized by those that hatched earlier[4]. In addition, the use of a small breeding ground increases the certainty of genetic parentage, making it more likely that parental care will evolve. It also influences which sex provides care — males, females or both parents[5] — but evolutionary transitions do not occur as easily in all directions[6]. It might not be a coincidence that the poison frog species that engages in biparental care is also the one that is genetically more monogamous.

Even so, caution should be exercised in using the argument that monogamy is conducive to biparental care and therefore concluding that circumstances that make offspring needy also favour monogamy. The co-evolution of traits tends to occur with a delay. Thus, the first monogamous parents of a hypothetical species might not reap any benefits from their behaviour as they will not yet have responded to the novel conditions of reliable parentage by switching to a more intensive form of care. It may be, however, that home-range size or other ecological factors make monogamy more likely in some species and that this later selects for care by both parents.

Regardless of the details of the final story, there is little doubt that frogs, with the diverse ways in which they care for their offspring and an increasingly well-resolved phylogeny, are becoming an important group in helping to explain why there is so much variation in parental care among animals[7]. Unfortunately though, this diversity continues to be lost. For instance, the details of the ecology of the only two species of gastric-brooding frog will never be known, as both became extinct in the mid-1980s. ■

Hanna Kokko is in the Department of Biological and Environmental Science, PO Box 65, University of Helsinki, Helsinki 00014, Finland. Michael Jennions is in the Ecology, Evolution and Genetics Division, Research School of Biology, Australian National University, Canberra, ACT 0200, Australia, where H.K. is currently a visiting fellow.
e-mails: hanna.kokko@helsinki.fi; michael.jennions@anu.edu.au

1. Klug, H. & Bonsall, M. B. *Evolution* **64,** 823–835 (2010).
2. Brown, J. L., Morales, V. & Summers, K. *Am. Nat.* **175,** 436–446 (2010).
3. Wells, K. D. *The Ecology and Behavior of Amphibians* (Univ. Chicago Press, 2007).
4. Brown, J. L., Morales, V. & Summers, K. *Biol. Lett.* **5,** 148–151 (2009).
5. Kokko, H. & Jennions, M. D. *J. Evol. Biol.* **21,** 919–948 (2008).
6. Kokko, H. *Ecol. Lett.* **2,** 247–255 (1999).
7. Summers, K., McKeon, C. S. & Heying, H. *Proc. R. Soc. Lond. B* **273,** 687–692 (2006).

OBITUARY

Leena Peltonen-Palotie (1952–2010)

A visionary in medical genetics.

On 11 March, science lost an inspiring leader with the death of Leena Peltonen-Palotie, at the age of 57, following a two-year battle with bone cancer.

Known to those in the field as Leena Peltonen (she was married to her close collaborator Aarno Palotie), she was a key player in human molecular genetics. This was true both in the early days of identifying the genes and mechanisms underlying rare diseases, and more recently in trying to track the causes of common inherited disorders. Peltonen left an invaluable legacy to medical genetics by authoring more than 600 papers and mentoring some 70 PhD students. But perhaps her most enduring contribution was to show how understanding the causes of genetic diseases in isolated populations can offer clues for large-scale studies that probe the risk factors linked to common diseases such as diabetes, obesity and heart disease.

Peltonen completed her PhD at the University of Oulu in Finland in 1978. After postdoctoral work at Rutgers University in New Jersey, she returned to the National Public Health Institute in Helsinki, becoming a professor in 1991.

In the first half of her career, Peltonen's main focus was the diseases that comprise the Finnish Disease Heritage. This is a group of about 40 rare recessive diseases — including metabolic, skin and eye disorders — that are more prevalent in Finland than anywhere else in the world. This prevalence is due to Finland's unusual demographic history: 2,000 years ago, "the edge of the inhabitable world", as Peltonen put it, was populated by relatively small groups of settlers who carried a limited set of mutations.

Peltonen identified the genes and mechanisms responsible for two dozen of these diseases, and helped find the factors underlying the rest. Her work has allowed physicians around the world to screen and counsel individuals — although ironically, and to her disappointment, Finland itself still lacks a screening programme.

Peltonen's vision and flamboyance, and her ability to raise and employ public awareness about the Finnish Disease Heritage, has helped to transform Finland into one of the most advanced places in the world for human medical genetics. In recognition of this, she was appointed Finnish Academy professor in 2003 and awarded the title Academician of Science in 2009.

During the 1990s, the advent of powerful tools in molecular genetics enabled researchers to home in on the genetics of common diseases that cluster in families. Peltonen's team was

RAGNHILD ARTIMO

at the forefront of this fresh wave of research, identifying an osteoarthritis gene in 1989. But as the hunt for risk factors ramped up, geneticists became engaged in a fierce debate over whether isolated inbred populations held clues to the factors responsible for common diseases. Although she was convinced that they did, Peltonen hedged her bets and stepped up her involvement in worldwide biobank studies in outbred populations, while continuing to pursue her work on isolated populations. In 2002, she united the registries for data on twins in eight European countries to form the GenomEUtwin project. This was the first integrated project to be funded by the European Union (EU), kick-starting European involvement in large-scale genetics. Her push for integration went further in 2003 when the backers of GenomEUtwin, the Canadian CARTaGENE biobank and the Estonian biobank founded P^3G, the Public Population Project in Genomics, which unites the data of more than a dozen large biobanks worldwide.

In 2007, Peltonen initiated the unification of most of the European biobanks within the overarching Biobanking and Biomolecular Resources Research Infrastructure (BBMRI). This has been a great success, and now has 52 participants and 150 associated members. Finally, based on the achievements of genome-wide association studies — which involve scanning markers in the genomes of many people to find variations associated with specific diseases — Peltonen, along with Mark McCarthy of the Wellcome Trust Centre for Human Genetics in Oxford, UK, started an EU consortium called ENGAGE in 2007. This collated genome-wide data from 100,000 individuals. As a way of connecting researchers with existing data it was hugely successful, yielding many high-profile papers in just a few months.

Ultimately, Peltonen's parallel pursuit of genetic studies in isolated populations proved prescient. The enrichment of a limited set of mutations yields a simpler picture than that obtained from the larger-scale hunts for the factors underlying complex diseases. Yet some of the components unearthed from the smaller studies, such as the disrupted gene underlying osteoarthritis, have been found to be involved in complex forms of the same disorders.

Peltonen's interest in complex genetics always went beyond merely mapping genes. In 2002, her team unravelled the mechanism of lactose intolerance. Then in 2004 and 2005, her group found the link between a variant of a gene called *USF1*, which causes a lipid disorder that clusters in families, and insulin resistance. She was particularly proud of these findings, as in both cases the variant genes altered regulatory functions. This suggested a fundamental mechanistic difference between the basic genetic defects typical of Mendelian disease and the more subtle regulatory alterations underlying complex disease.

An outspoken voice on European science policy in Brussels and elsewhere, and a member of the European Research Council, Peltonen was also a world citizen. She received prominent international honours and alternated her career in Finland with missions abroad. She founded and led the Department of Human Genetics at the University of California, Los Angeles, during 1998–2002, was a visiting professor at the Broad Institute in Cambridge, Massachusetts, from 2005 and became head of human genetics at the Wellcome Trust Sanger Institute in Cambridge, UK, in 2007.

Leena Peltonen's drive, radiance and inimitable style were as impressive as her achievements. Few will forget how attendees at a Helsinki meeting were treated to a black conference bag with white polka dots, or how this brightly dressed, chic lady could kick off her high heels and mount a chair to address the troops. Nor will they forget her fortitude as she maintained her unique blend of humour and no-nonsense attitude during her battle with cancer — continuing to lead meetings, guide students and juggle telephone conferences. It is up to us to make good on her legacy, by pursuing not only fame and fortune, but also real clinical utility.

Gertjan van Ommen
Gertjan van Ommen is in the Department of Human Genetics and Center of Medical Systems Biology, Leiden University Medical Center, 2333 ZC Leiden, the Netherlands.
e-mail: gjvo@lumc.nl

PERSPECTIVES

International network of cancer genome projects

The International Cancer Genome Consortium*

The International Cancer Genome Consortium (ICGC) was launched to coordinate large-scale cancer genome studies in tumours from 50 different cancer types and/or subtypes that are of clinical and societal importance across the globe. Systematic studies of more than 25,000 cancer genomes at the genomic, epigenomic and transcriptomic levels will reveal the repertoire of oncogenic mutations, uncover traces of the mutagenic influences, define clinically relevant subtypes for prognosis and therapeutic management, and enable the development of new cancer therapies.

The genomes of all cancers accumulate somatic mutations[1]. These include nucleotide substitutions, small insertions and deletions, chromosomal rearrangements and copy number changes that can affect protein-coding or regulatory components of genes. In addition, cancer genomes usually acquire somatic epigenetic 'marks' compared to non-neoplastic tissues from the same organ, notably changes in the methylation status of cytosines at CpG dinucleotides.

A subset of the somatic mutations in cancer cells confers oncogenic properties such as growth advantage, tissue invasion and metastasis, angiogenesis, and evasion of apoptosis[2]. These are termed 'driver' mutations. The identification of driver mutations will provide insights into cancer biology and highlight new drug targets and diagnostic tests. Knowledge of cancer mutations has already led to the development of specific therapies, such as trastuzumab for *HER2* (also known as *NEU* or *ERBB2*)-positive breast cancers[3] and imatinib, which targets BCR-ABL tyrosine kinase for the treatment of chronic myeloid leukaemia[4,5]. The remaining somatic mutations in cancer genomes that do not contribute to cancer development are called 'passengers'. These mutations provide insights into the DNA damage and repair processes that have been operative during cancer development, including exogenous environmental exposures[6,7]. In most cancer genomes, it is anticipated that passenger mutations, as well as germline variants not yet catalogued in polymorphism databases, will substantially outnumber drivers.

Large-scale analyses of genes in tumours have shown that the mutation load in cancer is abundant and heterogeneous[8–13]. Preliminary surveys of cancer genomes have already demonstrated their relevance in identifying new cancer genes that constitute potential therapeutic targets for several types of cancer, including *PIK3CA*[14], *BRAF*[15], *NF1* (ref. 10), *KDR*[10], *PIK3R1* (ref. 9), and histone methyltransferases and demethylases[16,17]. These projects have also yielded correlations between cancer mutations and prognosis, such as *IDH1* and *IDH2* mutations in several types of gliomas[13,18]. Advances in massively parallel sequencing technology have enabled sequencing of entire cancer genomes[19–22].

Following the launch of comprehensive cancer genome projects in the United Kingdom (Cancer Genome Project)[23] and the United States (The Cancer Genome Atlas)[24], cancer genome scientists and funding agencies met in Toronto (Canada) in October 2007 to discuss the opportunity to launch an international consortium. Key reasons for its formation were: (1) the scope is huge; (2) independent cancer genome initiatives could lead to duplication of effort or incomplete studies; (3) lack of standardization across studies could diminish the opportunities to merge and compare data sets; (4) the spectrum of many cancers is known to vary across the world; and (5) an international consortium will accelerate the dissemination of data sets and analytical methods into the user community.

Working groups were created to develop strategies and policies that would form the basis for participation in the ICGC. The goals of the consortium (Box 1) were released in April 2008 (http://www.icgc.org/files/ICGC_April_29_2008.pdf). Since then, working groups and initial member projects have further refined the policies and plans for international collaboration.

Bioethical framework

ICGC members agreed to a core set of bioethical elements for consent as a precondition of membership (Box 2). The Ethics and Policy

Box 1 | Goals of the ICGC

The goals of the ICGC are:

- To coordinate the generation of comprehensive catalogues of genomic abnormalities (somatic mutations) in tumours in 50 different cancer types and/or subtypes that are of clinical and societal importance across the globe.
- To ensure high quality by defining the catalogue for each tumour type or subtype to include the full range of somatic mutations, such as single-nucleotide variants, insertions, deletions, copy number changes, translocations and other chromosomal rearrangements, and to have the following features. (1) Comprehensiveness, such that most cancer genes with somatic abnormalities occurring at a frequency of greater than 3% are discovered. (2) High resolution, ideally at a single nucleotide level. (3) High quality, using common standards for pathology and technology. (4) Data from matched non-tumour tissue, to distinguish somatic from inherited sequence variants and aberrations. (5) Generate complementary catalogues of transcriptomic and epigenomic data sets from the same tumours.
- Make the data available to the entire research community as rapidly as possible, and with minimal restrictions, to accelerate research into the causes and control of cancer.
- Coordinate research efforts so that the interests and priorities of individual participants, self-organizing consortia, funding agencies and nations are addressed, including use of the burden of disease and the minimization of unnecessary redundancy in tumour analysis efforts.
- Support the dissemination of knowledge and standards related to new technologies, software, and methods to facilitate data integration and sharing with cancer researchers around the globe.

*A list of participants and their affiliations appears at the end of the paper.

Box 2 | Core bioethical elements

For prospective research, ICGC members should convey to potential participants, that:
- The ICGC is a coordinated effort among related scientific research projects being carried on around the world.
- Participation in the ICGC and its component projects is voluntary.
- Samples and data collected will be used for cancer research, which may include whole-genome sequencing.
- The patient's care will not be affected by their decision about participation.
- The samples collected will be in limited quantities; access to them will be tightly controlled and will depend on the policy and practices of the ICGC-member project. At least a small percentage of the samples may be shared with laboratories in other countries for the purposes of performing quality control studies.
- Data derived from the samples collected and data generated by the ICGC members will be made accessible to ICGC members and other international researchers through either an open or a controlled access database under terms and conditions that will maximize participant confidentiality.
- The researchers accessing data and samples will be required to affirm that they will not attempt to re-identify participants.
- There is a remote risk of being identified from data available on the databases.
- Once data are placed in open databases, those data cannot be withdrawn later.
- In controlled access databases the links to (local) data that can identify an individual will be destroyed after withdrawal. Data previously distributed will continue to be used.
- ICGC members agree not to make claims to possible intellectual property on primary data.
- No profit from eventual commercial products will be returned to subjects donating samples.

For retrospective research, the above guidelines remain the same, with the exception that where the individual is no longer a patient, there will not be a concern that their care could be affected by participation.

For research involving samples and data from deceased individuals:
- Where required by law or ethics, consent should always be obtained from the families of a deceased individual if their samples and data are to be used; if re-consent is not required, however, ethics review is sufficient.
- Ethics committee review should be sought for all research proposing the use of existing sample and data collections.
- Existing collections are a limited and valuable resource; access to them will be tightly controlled.

For research using anonymized samples, ethics review may be required in some jurisdictions.

Committee has created patient consent templates for both prospective collection and retrospective use of samples and data for ICGC projects. Differences in project-specific requirements and national legal frameworks may require some local amendments, while still reflecting the core principles of ICGC.

The ICGC recognizes a delicate balance between protecting participants' personal data and sharing these data to accelerate cancer research. Data access policies have been drawn up that are respectful of the rights of the donors, while allowing ICGC data derived from samples to be shared ethically among a wide research community. Two levels of access have been implemented. For data that cannot be used to identify individuals, 'open access' data sets are publicly available. These include data such as gender, age range, histology, normalized gene expression values, epigenetic data sets, somatic mutations, summaries of germline data, and study protocols. 'Controlled access' data sets contain germline genomic data and detailed clinical information that are associated to a unique individual whose personal identifiers have been removed. To access controlled data sets researchers must seek authorizations by contacting the Data Access Compliance Office (DACO) (http://www.icgc.org/daco). An independent International Data Access Committee (IDAC) oversees the work of the DACO and provides assistance with resolving issues that arise.

Pathology and clinical annotation

Large-scale genomic studies of human tumours rely on the availability of freshly frozen tumour tissue. To address the paucity of samples that meet ICGC standards, many projects have initiated prospective collections of high-quality source material. Accordingly, the ICGC recommended procedures to promote consistency of sample processing throughout the consortium and ensure a series of quality features such as high tissue integrity and tumour cell content. Each project will need to include diverse data types, such as environmental exposures, clinical history of participants, tumour histopathology, and clinical outcomes.

Tumours show considerable clinical and biological heterogeneity that has resulted in a variety of tumour classifications. Within the ICGC, special measures are taken to promote the consistency of diagnosis. These include the coordination of diagnostic criteria among groups investigating tumours that are related, and policies that all samples will be reviewed by at least two independent reference pathologists. Furthermore, images of the stained tumour sections (or blood smear or cytospins for haematological neoplasias) from which diagnoses were made, will be stored and made available to the community.

Although different tumour types may require specific procedures for tumour acquisition or compilation of clinical and environmental data, the ICGC has set guidelines about the use of common definitions and data standards. This will allow ICGC data users to identify correlations between tumour-specific molecular changes with clinical and histopathological data including prognosis, prediction of therapy response and tumour classification schemes for diagnosis.

Study design and statistical issues

To identify cancer-related genes, one needs to detect genes that are mutated at a higher frequency than the background mutation rate. Given that several driver genes have been found to be mutated at low frequencies, the ICGC will identify somatic mutations observed in at least 3% of tumours of a given subtype. The ICGC determined that 500 samples would be needed per tumour type (although for rare tumour types, a smaller sample size may be justified). In practice, the degree of heterogeneity of a given tumour type is difficult to know in advance, such that some particularly heterogeneous tumour types may require larger sample collections.

Cancer genome analyses

High-quality catalogues of somatic mutations from whole cancer genomes will ultimately be the ICGC standard. Shotgun sequencing using second generation technologies can detect all classes of somatic mutation implicated in cancer. Moreover, if the level of coverage is sufficient, comprehensive high-quality catalogues of somatic mutations from individual cancer genomes can be acquired with >90% sensitivity and >95% specificity. To achieve this, it will be necessary to sequence the genome of both the cancer and a normal tissue from the same individual to distinguish germline variants. Although a few genomes of this standard have already been generated, the cost and the continuing technology development will mean that interim analyses of particularly informative sectors of the genome will be carried out, for example of all coding exons and microRNAs.

For each individual cancer genome, the catalogue of somatic mutations will be supplemented by genome-wide information on the state of methylation of CpG dinucleotides. The optimal strategies and technologies to achieve this are not yet clear. Moreover, the genomes of individual cancers will be accompanied, where possible, by analyses of the transcriptome. Although conventional array-based approaches predominate at present, it is preferable that RNA sequencing becomes the standard as sequencing has a greater dynamic range[25] and provides further information including new transcripts and sequence variants[26].

ICGC data sets

The distributed nature of the consortium coupled with the large size of the data sets makes it cumbersome to store all data in a single

centralized repository. For this reason, the ICGC has adopted a 'franchise' database model for integrating the information and making it available to the public. Under this model, each member project releases tumour information by copying it into its local franchise database after it has been quality checked. Each franchise database shares a common schema to describe the specimens, the associated clinical information, and their genome characterization data. ICGC primary data files, are sent to the National Center for Biotechnology Information (NCBI) and/or the European Bioinformatics Institute (EBI) for archiving, while interpreted data sets, such as somatic mutation calls, are stored in franchise databases. The ICGC franchise databases and web portal use BioMart[27], a data federation technology originally developed for use in Ensembl[28], and since adopted for use by several model organism and genome databases. The management of the ICGC data flow is the responsibility of the ICGC Data Coordination Center (DCC) located at the Ontario Institute for Cancer Research.

The DCC also operates the ICGC data portal that allows researchers to access both open and controlled access portions of the ICGC data. The portal provides a variety of user interfaces that range from simple gene-oriented queries ('show me all the non-silent coding mutations identified in *PIK3R1* for all cancers') to queries that integrate genomic, clinical and functional information ('show me all members of the Toll-receptor pathway having deletions in stage III breast cancer'). These queries will be distributed across the franchise databases in a manner that is invisible to the user. The portal will also provide links to the primary files at the NCBI and EBI, interfaces for generating tabular reports, data dumps in common bioinformatics formats, and other visualizations including genome browser tracks, pathway diagrams and survival curves. The portal is available via a link at http://www.icgc.org.

At the time of this publication, the following cancer and reference data sets will be available through the ICGC web portal: (1) initial data releases from ICGC members for breast cancer (UK), liver cancer (Japan), and pancreatic cancer (Australia and Canada); (2) a whole genome data set of a metastatic melanoma cell line (COLO829)[6]; (3) open data sets from The Cancer Genome Atlas (TCGA) for glioblastoma multiforme (GBM) and serous cystadenocarcinoma of the ovary (see later); (4) whole exome somatic mutation data from 68 individuals with breast, colorectal, pancreatic cancer and GBM[11–13]; (5) links to the human reference genome (http://www.genomereference.org/) and gene annotations from the GENCODE project (http://www.sanger.ac.uk/gencode/) that includes the CCDS gene set[29]; (6) links to the single nucleotide polymorphism database (dbSNP)[30] and the HapMap[31] databases, providing access to common patterns of variation in reference population samples; (7) links to Reactome[32], a curated database of biological pathways in human; and (8) a set of reference gene models, mirrored from ENSEMBL[28].

The current version of the web portal provides an entry point to the open access data tier by interactive query as well as bulk download of data files. We expect that in mid-2010 both open access and controlled data will be available.

The ICGC recently established a bioinformatics analysis working group to compare pipelines, analytic methods, consistency within and among algorithms, and establish guidelines or best practices for the consortium. Over time, significant resources will be deployed to develop strategies to analyse the large complex data sets generated by ICGC member projects, and provide value-added views of cancer genomic data by integrating them with other biological and epidemiological data sets.

Data release and intellectual property policies

The data release policies of the ICGC are intended to maximize public benefit while, at the same time, protecting the interests and rights of sample donors and their relatives. Members of the ICGC are committed to the principles of rapid data release (with appropriate controlled access mechanisms), in concordance with the Toronto statement[33]. ICGC members encourage the scientific community to use any data that targets specific genes and mutations, without any restrictions. To allow ICGC members the opportunity to be the first to publish global analyses from data sets they generate, the consortium has also agreed that member projects may specify conditions that include a time limit during which other data users are asked to refrain from publishing global analyses (defined by several ICGC member projects as 100 tumours and matched controls), a provision referred to as a 'publication moratorium'. To allow time for a data set to be analysed and submitted for publication, ICGC members will have at most one year after released data sets reach the specified threshold before third parties are permitted to submit manuscripts describing global analyses. Further details on data release guidelines for data producers, users and reviewers are available http://www.icgc.org. Users of ICGC data are expected to respect these terms and to cite this manuscript and the source of pre-publication data, including the version of the data set. In cases of uncertainty, scientists using ICGC data are encouraged to contact the member projects to discuss publication plans.

ICGC members believe that maximum public benefit will be achieved if the data remain publicly accessible without patent restrictions, hence no claims to possible intellectual property derived from primary data (including somatic mutations) will be made. Users of ICGC data (including ICGC members) may elect to perform further research and to exercise their intellectual property rights on these downstream discoveries. If this occurs, users are expected to implement licensing policies that do not obstruct further research.

Initial ICGC projects

At present, ten countries and two European consortia have initiated cancer genome projects under the umbrella of the ICGC. The initial projects, listed in Supplementary Table 1, will analyse tumour types found around the globe and throughout the human body affecting a diversity of organs, including blood, brain, breast, kidney, liver, pancreas, stomach, oral cavity and ovary. Over time, the ICGC will investigate 50 or more types and subtypes of cancer in adults and children. In the case of tumours with several subtypes, analyses should be focused on subtypes that may be defined on pathological, molecular, aetiological or geographical differences. It is expected that some cancer types will be studied in parallel in different parts of the world, as the mutation profiles may differ among populations. The consortium has enabled the coordination of initial projects analysing similar cancers in different countries, and in some cases, the redirection of resources to launch new projects.

The Cancer Genome Atlas

TCGA is a comprehensive program in cancer genomics that is jointly supported and managed by the National Cancer Institute and the National Human Genome Research Institute of the US National Institutes of Health. TCGA began in 2006 as a pilot focused on three projects, glioblastoma multiforme (GBM), serous cystadenocarcinoma of the ovary, and lung squamous carcinoma, and has recently expanded to produce comprehensive genomic data sets for at least ten other cancers in the next two years. Given TCGA's contributions in launching the ICGC and cooperation to ensure that its policies (posted at http://cancergenome.nih.gov) are coordinated with those of the ICGC, TCGA's participation in the ICGC is considered to be equivalent to that of a full member. TCGA, however, is not able to join the ICGC formally at this time, because of technical and legal issues in the US related to the mechanisms of the distribution of controlled-access data, although such data are directly available to investigators at http://cancergenome.nih.gov/dataportal. The National Institutes of Health (NIH) policies relating to distribution of controlled-access data sets are being reviewed with the intent of enabling researchers to integrate and analyse across databases, for example, using the franchise model adopted by the ICGC. Meanwhile, TCGA

is ensuring that projects are coordinated and data sets are compatible with those of the consortium.

ICGC in the next decade

A large proportion of common cancers affecting patients around the world have been or will soon be selected for comprehensive cancer genome studies. Further efforts will be needed to leverage support and expertise to tackle the remaining tumour types, including rare cancers. The challenges of the ICGC are daunting owing to the scope of the initiative, the complexity that is inherent to the heterogeneity of cancer, and the limitations of current technologies to provide accurate long-range assemblies of highly rearranged chromosomes found in tumour cells. These challenges underscore the importance of continued international coordination and further engagement of the scientific community in the next decade.

Moving towards clinical applications

ICGC catalogues, which are expected to grow exponentially, will have immediate relevance in the cancer research community. Early insight into the biology of somatic mutations will come from functional studies in cell-based and animal models of tumours. Mutation screens in retrospective tumour banks linked to registries or clinical trials having significant clinical data will inform on the potential clinical utility of somatic mutations as biomarkers for prognosis or drug-response. Germline variants identified by ICGC projects may allow the discovery of genes predisposing to familial malignancies, such as *PALB2* and pancreatic cancer[12,34]. High throughput screens of RNA interference or small molecule libraries, and the adaptation of existing model systems, will have a major role in refining potential therapeutic candidates for further study[35].

Translating these discoveries into clinical practice will require more sophisticated clinical trials that take into account the increases in phenotypic subdivisions, further coordination to identify subjects having tumours with similar profiles, and increased use of biomarkers, genomic analyses, informatics and other technologies in the clinical development of new therapeutics. Given the tremendous potential for relatively low-cost genomic sequencing to reveal clinically useful information, we anticipate that in the not so distant future, partial or full cancer genomes will routinely be sequenced as part of the clinical evaluation of cancer patients and as part of their continuing clinical management. The successful and appropriate translation of cancer genome research into clinical practice will raise important social and ethical questions. It will be essential to combine the expertise of oncologists, biostatisticians, pathologists, geneticists, policy-makers and members of the biopharmaceutical industry to meet this challenge by developing new policies and clinical models that enable rapid translation of many new biomarkers and cancer targets into new clinical tests and therapeutic interventions that will benefit cancer patients.

1. Stratton, M. R., Campbell, P. J. & Futreal, P. A. The cancer genome. *Nature* **458,** 719–724 (2009).
2. Hanahan, D. & Weinberg, R. A. The hallmarks of cancer. *Cell* **100,** 57–70 (2000).
3. Slamon, D. J. *et al.* Use of chemotherapy plus a monoclonal antibody against HER2 for metastatic breast cancer that overexpresses HER2. *N. Engl. J. Med.* **344,** 783–792 (2001).
4. Druker, B. J. *et al.* Efficacy and safety of a specific inhibitor of the BCR-ABL tyrosine kinase in chronic myeloid leukemia. *N. Engl. J. Med.* **344,** 1031–1037 (2001).
5. Druker, B. J. *et al.* Activity of a specific inhibitor of the BCR-ABL tyrosine kinase in the blast crisis of chronic myeloid leukemia and acute lymphoblastic leukemia with the Philadelphia chromosome. *N. Engl. J. Med.* **344,** 1038–1042 (2001).
6. Pleasance, E. D. *et al.* A comprehensive catalogue of somatic mutations from a human cancer genome. *Nature* **463,** 184–190 (2010).
7. Pleasance, E. D. *et al.* A small-cell lung cancer genome with complex signatures of tobacco exposure. *Nature* **463,** 191–196 (2010).
8. Greenman, C. *et al.* Patterns of somatic mutation in human cancer genomes. *Nature* **446,** 153–158 (2007).
9. Cancer Genome Atlas Research Network. Comprehensive genomic characterization defines human glioblastoma genes and core pathways. *Nature* **455,** 1061–1068 (2008).
10. Ding, L. *et al.* Somatic mutations affect key pathways in lung adenocarcinoma. *Nature* **455,** 1069–1075 (2008).
11. Wood, L. D. *et al.* The genomic landscapes of human breast and colorectal cancers. *Science* **318,** 1108–1113 (2007).
12. Jones, S. *et al.* Core signaling pathways in human pancreatic cancers revealed by global genomic analyses. *Science* **321,** 1801–1806 (2008).
13. Parsons, D. W. *et al.* An integrated genomic analysis of human glioblastoma multiforme. *Science* **321,** 1807–1812 (2008).
14. Samuels, Y. *et al.* High frequency of mutations of the *PIK3CA* gene in human cancers. *Science* **304,** 554 (2004).
15. Davies, H. *et al.* Mutations of the *BRAF* gene in human cancer. *Nature* **417,** 949–954 (2002).
16. van Haaften, G. *et al.* Somatic mutations of the histone H3K27 demethylase gene *UTX* in human cancer. *Nature Genet.* **41,** 521–523 (2009).
17. Dalgliesh, G. L. *et al.* Systematic sequencing of renal carcinoma reveals inactivation of histone modifying genes. *Nature* **463,** 360–363 (2010).
18. Yan, H. *et al. IDH1* and *IDH2* mutations in gliomas. *N. Engl. J. Med.* **360,** 765–773 (2009).
19. Ley, T. J. *et al.* DNA sequencing of a cytogenetically normal acute myeloid leukaemia genome. *Nature* **456,** 66–72 (2008).
20. Mardis, E. R. *et al.* Recurring mutations found by sequencing an acute myeloid leukemia genome. *N. Engl. J. Med.* **361,** 1058–1066 (2009).
21. Shah, S. P. *et al.* Mutational evolution in a lobular breast tumour profiled at single nucleotide resolution. *Nature* **461,** 809–813 (2009).
22. Stephens, P. J. *et al.* Complex landscapes of somatic rearrangement in human breast cancer genomes. *Nature* **462,** 1005–1010 (2009).
23. Dickson, D. Wellcome funds cancer database. *Nature* **401,** 729 (1999).
24. Collins, F. S. & Barker, A. D. Mapping the cancer genome. Pinpointing the genes involved in cancer will help chart a new course across the complex landscape of human malignancies. *Sci. Am.* **296,** 50–57 (2007).
25. Mortazavi, A., Williams, B. A., McCue, K., Schaeffer, L. & Wold, B. Mapping and quantifying mammalian transcriptomes by RNA-Seq. *Nature Methods* **5,** 621–628 (2008).
26. Shah, S. P. *et al.* Mutation of *FOXL2* in granulosa-cell tumors of the ovary. *N. Engl. J. Med.* **360,** 2719–2729 (2009).
27. Haider, S. *et al.* BioMart Central Portal–unified access to biological data. *Nucleic Acids Res.* **37,** W23–W27 (2009).
28. Hubbard, T. J. *et al.* Ensembl 2009. *Nucleic Acids Res.* **37,** D690–D697 (2009).
29. Pruitt, K. D. *et al.* The consensus coding sequence (CCDS) project: identifying a common protein-coding gene set for the human and mouse genomes. *Genome Res.* **19,** 1316–1323 (2009).
30. Sherry, S. T. *et al.* dbSNP: the NCBI database of genetic variation. *Nucleic Acids Res.* **29,** 308–311 (2001).
31. International HapMap Consortium. A second generation human haplotype map of over 3.1 million SNPs. *Nature* **449,** 851–861 (2007).
32. Matthews, L. *et al.* Reactome knowledgebase of human biological pathways and processes. *Nucleic Acids Res.* **37,** D619–D622 (2009).
33. Toronto International Data Release Workshop Authors. Prepublication data sharing. *Nature* **461,** 168–170 (2009).
34. Jones, S. *et al.* Exomic sequencing identifies *PALB2* as a pancreatic cancer susceptibility gene. *Science* **324,** 217 (2009).
35. Chin, L. & Gray, J. W. Translating insights from the cancer genome into clinical practice. *Nature* **452,** 553–563 (2008).

Supplementary Information is linked to the online version of the paper at www.nature.com/nature.

Acknowledgements We thank research participants who are generously donating samples and data, as well as physicians and clinical staff contributing to sample annotation and collection. A complete list of organizations that support ICGC projects is in Supplementary Table 1.

Author Contributions See list of consortium authors below.

Author Information Reprints and permissions information is available at www.nature.com/reprints. The authors declare no competing financial interests. Correspondence and requests for materials should be addressed to T.J.H. (tom.hudson@oicr.on.ca).

International Cancer Genome Consortium

Executive committee Thomas J. Hudson[1,2] (Chairperson), Warwick Anderson[3], Axel Aretz[4], Anna D. Barker[5], Cindy Bell[6], Rosa R. Bernabé[7], M. K. Bhan[8], Fabien Calvo[9], Iiro Eerola[10], Daniela S. Gerhard[5], Alan Guttmacher[11], Mark Guyer[12], Fiona M. Hemsley[13], Jennifer L. Jennings[1], David Kerr[14,15], Peter Klatt[7], Patrik Kolar[10], Jun Kusuda[16], David P. Lane[13], Frank Laplace[17], Youyong Lu[18], Gerd Nettekoven[19], Brad Ozenberger[12], Jane Peterson[12], T.S. Rao[8], Jacques Remacle[10], Alan J. Schafer[20], Tatsuhiro Shibata[21], Michael R. Stratton[22], Joseph G. Vockley[5], Koichi Watanabe[23], Huanming Yang[24], Matthew M. F. Yuen[25]

Ethics and policy committee Bartha M. Knoppers[26] (Leader), Martin Bobrow[27], Anne Cambon-Thomsen[28], Lynn G. Dressler[29], Stephanie O. M. Dyke[22], Yann Joly[26], Kazuto Kato[30], Karen L. Kennedy[22], Pilar Nicolás[31], Michael J. Parker[32], Emmanuelle

Rial-Sebbag[28], Carlos M. Romeo-Casabona[31], Kenna M. Shaw[5], Susan Wallace[26], Georgia L. Wiesner[33,34], Nikolajs Zeps[35,36]

Tissue and clinical annotation working group Peter Lichter[37] (Leader), Andrew V. Biankin[38,39], Christian Chabannon[9,40], Lynda Chin[41,42], Bruno Clément[43], Enrique de Alava[44], Françoise Degos[45], Martin L. Ferguson[46], Peter Geary[47], D. Neil Hayes[48], Thomas J. Hudson[1,2], Amber L. Johns[38], Arek Kasprzyk[1], Hidewaki Nakagawa[49], Robert Penny[50], Miguel A. Piris[51], Rajiv Sarin[52], Aldo Scarpa[53,54], Tatsuhiro Shibata[21], Marc van de Vijver[55,56]

Technologies working group P. Andrew Futreal[22] (Leader), Hiroyuki Aburatani[57], Mónica Bayés[58,59], David D.L. Bowtell[60,61], Peter J. Campbell[22,62], Xavier Estivill[58,59], Daniela S. Gerhard[5], Sean M. Grimmond[63], Ivo Gut[64], Martin Hirst[65], Carlos López-Otín[66], Partha Majumder[67], Marco Marra[65], John D. McPherson[1,68], Hidewaki Nakagawa[49], Zemin Ning[22], Xose S. Puente[66], Yijun Ruan[69], Tatsuhiro Shibata[21], Michael R. Stratton[22], Hendrik G. Stunnenberg[70], Harold Swerdlow[22], Victor E. Velculescu[71], Richard K. Wilson[72,73], Hong H. Xue[74,75], Liu Yang[76]

Bioinformatics analyses working group Paul T. Spellman[77] (Leader), Gary D. Bader[78,79], Paul C. Boutros[1], Peter J. Campbell[22,62], Paul Flicek[80], Gad Getz[81], Roderic Guigó[82], Guangwu Guo[24], David Haussler[83], Simon Heath[64], Tim J. Hubbard[22], Tao Jiang[24], Steven M. Jones[65], Qibin Li[24], Nuria López-Bigas[84], Ruibang Luo[24], Lakshmi Muthuswamy[1], B. F. Francis Ouellette[1], John V. Pearson[63], Xose S. Puente[66], Victor Quesada[66], Benjamin J. Raphael[85], Chris Sander[86], Tatsuhiro Shibata[21], Terence P. Speed[87,88], Lincoln D. Stein[1], Joshua M. Stuart[89], Jon W. Teague[22], Yasushi Totoki[21], Tatsuhiko Tsunoda[49], Alfonso Valencia[90], David A. Wheeler[91], Honglong Wu[24], Shancen Zhao[24], Guangyu Zhou[24]

Data coordination and management working group Lincoln D. Stein[1] (Leader), Roderic Guigó[82], Tim J. Hubbard[22], Yann Joly[26], Steven M. Jones[65], Arek Kasprzyk[1], Mark Lathrop[64,92], Nuria López-Bigas[84], B. F. Francis Ouellette[1], Paul T. Spellman[77], Jon W. Teague[22], Gilles Thomas[93,94], Alfonso Valencia[90], Teruhiko Yoshida[21]

Data release, data tiers and publications working group Karen L. Kennedy[22] (Leader), Myles Axton[95], Stephanie O. M. Dyke[22], P. Andrew Futreal[22], Daniela S. Gerhard[5], Chris Gunter[96], Mark Guyer[12], Thomas J. Hudson[1,2], John D. McPherson[1,68], Linda J. Miller[97], Brad Ozenberger[12], Kenna M. Shaw[5]

Data coordination centre Arek Kasprzyk[1] (Leader), Lincoln D. Stein[1] (Leader), Junjun Zhang[1], Syed A. Haider[98], Jianxin Wang[1], Christina K. Yung[1], Anthony Cross[1], Yong Liang[1], Saravanamuttu Gnaneshan[1], Jonathan Guberman[1], Jack Hsu[1]

International data access committee Martin Bobrow[27] (Leader), Don R. C. Chalmers[99], Karl W. Hasel[6], Yann Joly[26], Terry S. H. Kaan[100], Karen L. Kennedy[22], Bartha M. Knoppers[26], William W. Lowrance[101], Tohru Masui[16], Pilar Nicolás[31], Emmanuelle Rial-Sebbag[28], Laura Lyman Rodriguez[12], Catherine Vergely[102], Teruhiko Yoshida[21]

Cancer genome projects: Pancreatic cancer (ductal adenocarcinoma) and ovarian cancer (serous adenocarcinoma) (Australia) Sean M. Grimmond[63] (Leader), Andrew V. Biankin[38,39], David D. L. Bowtell[60,61], Nicole Cloonan[63], Anna deFazio[103,104], James R. Eshleman[105], Dariush Etemadmoghadam[60,61], Brooke A. Gardiner[63], James G. Kench[38,106], Aldo Scarpa[53,54], Robert L. Sutherland[38], Margaret A. Tempero[107], Nicola J. Waddell[63], Peter J. Wilson[63]; **Pancreatic cancer (ductal adenocarcinomas) (Canada)** John D. McPherson[1,68] (Leader), Steve Gallinger[108,109], Ming-Sound Tsao[110,111], Patricia A. Shaw[112], Gloria M. Petersen[113], Debabrata Mukhopadhyay[114], Lynda Chin[41,42], Ronald A. DePinho[41,115], Sarah Thayer[116], Lakshmi Muthuswamy[1], Kamran Shazand[1], Timothy Beck[1], Michelle Sam[1], Lee Timms[1], Vanessa Ballin[1]; **Gastric cancer (intestinal- and diffuse-type) (China)** Youyong Lu[18] (Leader), Jiafu Ji[18], Xiuqing Zhang[24], Feng Chen[18], Xueda Hu[24], Guangyu Zhou[24], Qi Yang[24], Geng Tian[24], Lianhai Zhang[18], Xiaofang Xing[18], Xianghong Li[18], Zhenggang Zhu[117], Yingyan Yu[117], Jun Yu[118], Huanming Yang[24]; **Renal cancer (renal cell carcinoma; focus on but not limited to clear cell subtype) (European Union/France)** Mark Lathrop[64,92] (Leader), Jörg Tost[64,92], Paul Brennan[119], Ivana Holcatova[120], David Zaridze[121], Alvis Brazma[80], Lars Egevad[122], Egor Prokhortchouk[123], Rosamonde Elizabeth Banks[124], Mathias Uhlén[125], Anne Cambon-Thomsen[28], Juris Viksna[126], Fredrik Ponten[127], Konstantin Skryabin[128]; **Breast cancer (subtypes defined by an amplification of ER$^+$ HER ductal-type) (European Union/United Kingdom)** Michael R. Stratton[22] (Leader), P. Andrew Futreal[22], Ewan Birney[80], Ake Borg[129], Anne-Lise Børresen-Dale[130,131], Carlos Caldas[132], John A. Foekens[133], Sancha Martin[22], Jorge S. Reis-Filho[134], Andrea L. Richardson[135,136], Christos Sotiriou[137], Hendrik G. Stunnenberg[70], Gilles Thomas[93,94], Marc van de Vijver[55,56], Laura van't Veer[55]; **Breast cancer (subtype defined by an amplification of the *HER2* gene) (France)** Fabien Calvo[9] (Leader), Daniel Birnbaum[40], Hélène Blanche[92], Pascal Boucher[9], Sandrine Boyault[138], Christian Chabannon[9,40], Ivo Gut[64], Jocelyne D. Masson-Jacquemier[40], Mark Lathrop[64,92], Iris Pauporté[9], Xavier Pivot[139], Anne Vincent-Salomon[140], Eric Tabone[138], Charles Theillet[141], Gilles Thomas[93,94], Jörg Tost[64,92], Isabelle Treilleux[138]; **Liver cancer (hepatocellular carcinoma; secondary to alcohol and adiposity) (France)** Fabien Calvo[9] (Leader), Paulette Bioulac-Sage[142], Bruno Clément[43], Thomas Decaens[143,144], Françoise Degos[45], Dominique Franco[145], Ivo Gut[64], Marta Gut[92], Simon Heath[64], Mark Lathrop[64,92], Didier Samuel[146,147], Gilles Thomas[93,94], Jessica Zucman-Rossi[148]; **Paediatric brain tumours (medulloblastoma, paediatric pilocytic astrocytoma) (Germany)** Peter Lichter[37] (Leader), Roland Eils[37,149] (Leader), Benedikt Brors[37], Jan O. Korbel[80,150], Andrey Korshunov[151], Pablo Landgraf[152], Hans Lehrach[153], Stefan Pfister[37,154], Bernhard Radlwimmer[37], Guido Reifenberger[155], Michael D. Taylor[156,157], Christof von Kalle[158,159]; **Oral cancer (gingivobuccal) (India)** Partha P. Majumder[67] (Leader), Rajiv Sarin[52], T. S. Rao[8], M. K. Bhan[8]; **Rare pancreatic tumours (entero-pancreatic endocrine tumours and rare pancreatic exocrine tumours; intraductal papillary mucinous neoplasms, solid pseudopapillary tumours, mucinous cystic neoplasms and other rarer tumours) (Italy)** Aldo Scarpa[53,54] (Leader), Paolo Pederzoli[160], Rita T. Lawlor[54], Massimo Delledonne[161], Alberto Bardelli[162,163], Andrew V. Biankin[38,39], Sean M. Grimmond[63], Thomas Gress[164], David Klimstra[165], Giuseppe Zamboni[53]; **Liver cancer (hepatocellular carcinoma; virus associated) (Japan)** Tatsuhiro Shibata[21] (Leader), Yusuke Nakamura[49,166], Hidewaki Nakagawa[49], Jun Kusuda[16], Tatsuhiko Tsunoda[49], Satoru Miyano[166], Hiroyuki Aburatani[57], Kazuto Kato[30], Akihiro Fujimoto[49], Teruhiko Yoshida[21]; **Chronic lymphocytic leukaemia (with mutated and unmutated IgVH) (Spain)** Elias Campo[167] (Leader), Carlos López-Otín[66], Xavier Estivill[58,59], Roderic Guigó[82], Silvia de Sanjosé[168], Miguel A. Piris[51], Emili Montserrat[167], Marcos González-Díaz[44], Xose S. Puente[66], Pedro Jares[167], Alfonso Valencia[90], Heinz Himmelbaue[58], Victor Quesada[66], Silvia Bea[167]; **Breast cancer (triple negative/lobular/other) (United Kingdom)** Michael R. Stratton[22] (Leader), P. Andrew Futreal[22], Peter J. Campbell[22,62], Anne Vincent-Salomon[140], Andrea L. Richardson[135,136], Jorge S. Reis-Filho[134], Marc van de Vijver[55,56], Gilles Thomas[93,94], Jocelyne D. Masson-Jacquemier[40], Samuel Aparicio[169], Ake Borg[129], Anne-Lise Børresen-Dale[130,131], Carlos Caldas[132], John A. Foekens[133], Hendrik G. Stunnenberg[70], Laura van't Veer[55], Douglas F. Easton[170], Paul T. Spellman[77], Sancha Martin[22]; **The Cancer Genome Atlas (United States)** Anna D. Barker[5], Lynda Chin[41,42], Francis S. Collins[171], Carolyn C. Compton[5], Martin L. Ferguson[46], Daniela S. Gerhard[5], Gad Getz[81], Chris Gunter[96], Alan Guttmacher[11], Mark Guyer[12], D. Neil Hayes[48], Eric S. Lander[81], Brad Ozenberger[12], Robert Penny[50], Jane Peterson[12], Chris Sander[86], Kenna M. Shaw[5], Terence P. Speed[87,88], Paul T. Spellman[77], Joseph G. Vockley[5], David A. Wheeler[91], Richard K. Wilson[72,73]

Initial scientific planning committee Thomas J. Hudson[1,2] (Chairperson), Lynda Chin[41,42], Bartha M. Knoppers[26], Eric S. Lander[81], Peter Lichter[37], Lincoln D. Stein[1], Michael R. Stratton[22], Warwick Anderson[3], Anna D. Barker[5], Cindy Bell[6], Martin Bobrow[27], Wylie Burke[172], Francis S. Collins[171], Carolyn C. Compton[5], Ronald A. DePinho[41,115], Douglas F. Easton[170], P. Andrew Futreal[22], Daniela S. Gerhard[5], Anthony R. Green[173], Mark Guyer[12], Stanley R. Hamilton[174], Tim J. Hubbard[22], Olli P. Kallioniemi[175], Karen L. Kennedy[22], Timothy J. Ley[72,176], Edison T. Liu[69], Youyong Lu[18], Partha Majumder[67], Marco Marra[65], Brad Ozenberger[12], Jane Peterson[12], Alan J. Schafer[20], Paul T. Spellman[77], Hendrik G. Stunnenberg[70], Brandon J. Wainwright[177], Richard K. Wilson[72,73], Huanming Yang[24]

[1]Ontario Institute for Cancer Research, Toronto, Ontario M5G 0A3, Canada. [2]Departments of Medical Biophysics and Molecular Genetics, University of Toronto, Toronto, Ontario M5S 1A1, Canada. [3]National Health and Medical Research Council, Canberra, Australian Capital Territory 2601, Australia. [4]Project Management Agency, German Aerospace Center (DLR), 53175 Bonn, Germany. [5]National Cancer Institute, US National Institutes of Health, Bethesda, Maryland 20892, USA. [6]Genome Canada, Ottawa, Ontario K2P 1P1, Canada. [7]Secretariat of State for Research, Ministry of Science and Innovation, 28027 Madrid, Spain. [8]Department of Biotechnology, Ministry of Science & Technology, Government of India, New Delhi, Delhi 110003, India. [9]Institut National du Cancer, 92513 Boulogne-Billancourt, France. [10]Genomics and Systems Biology Unit, Health Research Directorate, European Commission, B-1049 Brussels, Belgium. [11]Eunice Kennedy Shriver National Institute of Child Health and Human Development, US National Institutes of Health, Bethesda, Maryland 20892, USA. [12]National Human Genome Research Institute, US National Institutes of Health, Bethesda, Maryland 20892, USA. [13]Cancer Research UK, London WC2A 3PX, UK. [14]Sidra Medical and Research Center, Qatar Foundation, Doha, Qatar. [15]Department of Clinical Pharmacology, University of Oxford, Oxford OX2 6HE, UK. [16]National Institute of Biomedical Innovation, Ibaraki, Osaka 567-0085, Japan. [17]Division of Molecular Life Sciences, Federal Ministry of Education and Research, 11055 Berlin, Germany. [18]Beijing Cancer Institute and Hospital, Peking University School of Oncology, 100142 Beijing, China. [19]German Cancer Aid, 53113 Bonn, Germany. [20]Wellcome Trust, London NW1 2BE, UK. [21]National Cancer Center Research Institute, Chuo-ku, Tokyo 104-0045, Japan. [22]Wellcome Trust Sanger Institute, Hinxton, Cambridge CB10 1SA, UK. [23]Yokohama Institute, RIKEN, Yokohama, Kanagawa 230-0045, Japan. [24]BGI-Shenzhen, Shenzhen, 518083 Guangdong, China. [25]The Hong Kong University of Science and Technology, Hong Kong, China. [26]Centre of Genomics and Policy, McGill University and Génome Québec Innovation Centre, Montreal, Québec H3A 1A4, Canada. [27]Department of Medical Genetics, Cambridge Institute for Medical Research, University of Cambridge, Cambridge CB2 0XY, UK. [28]U558, INSERM, 31073 Toulouse, France. [29]University of North Carolina School of Pharmacy, Division of Pharmaceutical Outcomes and Policy, Institute for Pharmacogenomics and Individualized Therapy, Chapel Hill, North Carolina 27599, USA. [30]Institute for Research in Humanities, Graduate School of Biostudies, Institute for Integrated Cell-Material Sciences, Kyoto University, Kyoto, Kyoto 606-8501, Japan. [31]Inter-University Chair in Law and the Human Genome, University of Deusto, Bilbao, 48007 Bizkaia, Spain. [32]The Ethox Centre, University of Oxford, Oxford OX3 7LF, UK. [33]Department of Genetics, Case Western Reserve University, Cleveland, Ohio 44106, USA. [34]Center for Human Genetics, University Hospitals Case Medical Center, Cleveland, Ohio 44106, USA. [35]St John of God Pathology, Subiaco, Western

Australia 6008, Australia. [36]Schools of Surgery and Pathology and Laboratory Medicine, The University of Western Australia, Nedlands, Western Australia 6009, Australia. [37]German Cancer Research Center, 69120 Heidelberg, Germany. [38]Garvan Institute of Medical Research, University of New South Wales, Darlinghurst, Sydney, New South Wales 2010, Australia. [39]Department of Surgery, Bankstown Hospital, Bankstown, Sydney, New South Wales 2200, Australia. [40]Institut Paoli-Calmettes, 13273 Marseille, France. [41]Belfer Institute for Applied Cancer Science, Dana-Farber Cancer Institute, Boston, Massachusetts 02115, USA. [42]Department of Dermatology, Harvard Medical School, Boston, Massachusetts 02115, USA. [43]U991, INSERM, 35043 Rennes, France. [44]Department of Hematology, Centro de Investigación del Cáncer, Hospital Universitario, Universidad de Salamanca, 37007 Salamanca, Spain. [45]Hôpital Beaujon, 92110 Clichy, France. [46]MLF Consulting, Arlington, Massachusetts 02474, USA. [47]Canadian Tumour Repository Network, Winnipeg, Manitoba R3M 0V5, Canada. [48]Department of Internal Medicine, Division of Medical Oncology, Lineberger Comprehensive Cancer Center, University of North Carolina, Chapel Hill, North Carolina 27599, USA. [49]Center for Genomic Medicine, RIKEN, Yokohama, Kanagawa 230-0045, Japan. [50]International Genomics Consortium, Phoenix, Arizona 85004, USA. [51]Molecular Pathology Programme, Spanish National Cancer Research Centre (CNIO), 28029 Madrid, Spain. [52]Advanced Centre for Treatment, Research and Education in Cancer, Tata Memorial Centre, Kharghar, Navi Mumbai, Maharashtra 410210, India. [53]Department of Pathology, University of Verona, 37134 Verona, Italy. [54]Center for Applied Research on Cancer (ARC-NET), Verona University Hospital, 37134 Verona, Italy. [55]Netherlands Cancer Institute, 1066 CX Amsterdam, The Netherlands. [56]Academic Medical Center, 1015 AZ Amsterdam, The Netherlands. [57]Research Center for Advanced Science and Technology, University of Tokyo, Meguro-ku, Tokyo 153-8904, Japan. [58]Center for Genomic Regulation, Pompeu Fabra University, 08003 Barcelona, Spain. [59]Public Health and Epidemiology Network Biomedical Research Center (CIBERESP), Barcelona, 08003 Catalonia, Spain. [60]Peter MacCallum Cancer Centre, Melbourne, Victoria 3002, Australia. [61]Department of Biochemistry and Molecular Biology, University of Melbourne, Parkville, Victoria 3010, Australia. [62]Department of Haematology, University of Cambridge, Cambridge CB2 2XY, UK. [63]Queensland Centre for Medical Genomics, Institute for Molecular Bioscience, The University of Queensland, Brisbane, Queensland 4067, Australia. [64]CEA/DSV/IG-Centre National de Genotypage, 91057 Evry, France. [65]Canada's Michael Smith Genome Sciences Centre, BC Cancer Agency, Vancouver, British Columbia V5Z 1L3, Canada. [66]Departamento de Bioquímica y Biología Molecular, Instituto Universitario de Oncología, Universidad de Oviedo, 33006 Oviedo, Spain. [67]National Institute of Biomedical Genomics, Kalyani, West Bengal 741251, India. [68]Department of Medical Biophysics, University of Toronto, Toronto, Ontario M5S 1A1, Canada. [69]Genome Institute of Singapore, Agency for Science, Technology and Research, Singapore 138672, Singapore. [70]Nijmegen Centre for Molecular Life Sciences, Radboud University Nijmegen, 6500 HB Nijmegen, The Netherlands. [71]Ludwig Center for Cancer Genetics and Therapeutics, Johns Hopkins Kimmel Cancer Center, Baltimore, Maryland 21231, USA. [72]The Genome Center, Washington University School of Medicine, St. Louis, Missouri 63108, USA. [73]Siteman Cancer Center, Washington University School of Medicine, St. Louis, Missouri 63108, USA. [74]Applied Genomics Center, Fok Ying Tung Graduate School, HKUST, Hong Kong, China. [75]Department of Biochemistry, The Hong Kong University of Science and Technology, Hong Kong, China. [76]Cancer Institute, Zhejiang University, 310009 Hangzhou, China. [77]Life Sciences Division, Lawrence Berkeley National Laboratory, Berkeley, California 94510, USA. [78]Donnelly Centre for Cellular and Biomolecular Research, University of Toronto, Toronto, Ontario M5S 3E1, Canada. [79]Banting and Best Department of Medical Research, University of Toronto, Toronto, Ontario M5S 3E1, Canada. [80]European Molecular Biology Laboratory-European Bioinformatics Institute, Hinxton, Cambridge CB10 1SD, UK. [81]Broad Institute of Harvard and MIT, Cambridge, Massachusetts 02142, USA. [82]Spanish National Bioinformatics Institute (INB) and Center for Genomic Regulation, Universitat Pompeu Fabra, 08003 Barcelona, Spain. [83]Howard Hughes Medical Institute and Center for Biomolecular Science and Engineering, University of California Santa Cruz, Santa Cruz, California 95064, USA. [84]Research Unit on Biomedical Informatics, Department of Experimental and Health Science, Pompeu Fabra University, 08003 Barcelona, Spain. [85]Department of Computer Science & Center for Computational Molecular Biology, Brown University, Providence, Rhode Island 02912, USA. [86]Computational Biology Center, Memorial Sloan-Kettering Cancer Center, New York, New York 10065, USA. [87]Walter and Eliza Hall Institute of Medical Research, Parkville, Victoria 3052, Australia. [88]Department of Statistics, University of California Berkeley, Berkeley, California 94720, USA. [89]Department of Biomolecular Engineering, University of California Santa Cruz, Santa Cruz, California 95064, USA. [90]Spanish National Bioinformatics Institute (INB) and Structural Biology and Biocomputing Programme, Spanish National Cancer Research Centre (CNIO), 28029 Madrid, Spain. [91]Human Genome Sequencing Center & Department of Molecular and Human Genetics, Baylor College of Medicine, Houston, Texas 77030, USA. [92]Fondation Jean Dausset, Centre d'Etude du Polymorphisme Humain, 75010 Paris, France. [93]Université Claude Bernard Lyon 1, 69622 Villeurbanne, France. [94]Fondation Synergie Lyon Cancer, 69008 Lyon, France. [95]Nature Genetics, New York, New York 10013-1917, USA. [96]HudsonAlpha Institute for Biotechnology, Huntsville, Alabama 35806, USA. [97]Nature and the Nature research journals, New York, New York 10013, USA. [98]Computer Laboratory, University of Cambridge, Cambridge CB3 0FD, UK. [99]Faculty of Law, University of Tasmania, Hobart, Tasmania 7001, Australia. [100]Faculty of Law, National University of Singapore, Singapore 259776, Singapore. [101]Consultant in Health Research Ethics and Policy, 34280 La Grande Motte, France. [102]ISIS 39 rue Camille Desmoulins, Institut Gustav Roussy, Pediatric Sce, 94805 Villejuif, France. [103]Department of Gynaecological Oncology, Westmead Hospital, Westmead, Sydney, New South Wales 2145, Australia. [104]Westmead Institute for Cancer Research, University of Sydney at the Westmead Millennium Institute, Westmead, Sydney, New South Wales 2145, Australia. [105]Sol Goldman Pancreatic Cancer Research Center, Johns Hopkins Medical Institutions, Baltimore, Maryland 21231, USA. [106]Department of Anatomical Pathology, Royal Prince Alfred Hospital, University of Sydney, Camperdown, Sydney, New South Wales 2050, Australia. [107]Helen Diller Family Comprehensive Cancer Center, University of California San Francisco, San Francisco, California 94115, USA. [108]Department of General Surgery, Toronto General Hospital, Toronto, ON M5G 2C4, Canada. [109]Samuel Lunenfeld Research Institute, Toronto, Ontario M5S 1A1, Canada. [110]Ontario Cancer Institute, University Health Network, Toronto, Ontario M5G 2M9, Canada. [111]Department of Laboratory Medicine and Pathobiology, University of Toronto, Toronto, Ontario M5S 1A1, Canada. [112]Department of Pathology, University Health Network, Toronto, Ontario M5G 2C4, Canada. [113]Department of Health Science Research, Mayo Clinic, Rochester, Minnesota 55905, USA. [114]Department of Biochemistry and Molecular Biology, Mayo Clinic, Rochester, Minnesota 55905, USA. [115]Department of Medicine and Genetics, Harvard Medical School, Boston, Massachusetts 02115, USA. [116]Department of Surgery, Harvard Medical School, Boston, Massachusetts 02115, USA. [117]Shanghai Ruijin Hospital, Shanghai Jiao Tong University School of Medicine, Shanghai 200025, China. [118]Institute of Digestive Disease, The Chinese University of Hong Kong, Hong Kong, China. [119]International Agency for Research on Cancer, 69372 Lyon, France. [120]Institute of Hygiene and Epidemiology, First Faculty of Medicine, Charles University in Prague, 121 08 Prague, Czech Republic. [121]Department of Epidemiology and Prevention, N. N. Blokhin Russian Cancer Research Centre, Moscow 115478, Russian Federation. [122]Karolinska Institutet, Karolinska University Hospital, SE-171 76 Stockholm, Sweden. [123]Bioengineering Center, Russian Academy of Sciences, Moscow 117312, Russian Federation. [124]Cancer Research UK Centre, Leeds Institute for Molecular Medicine, St James's University Hospital, Leeds LS9 7TF, UK. [125]Science for Life Laboratory, KTH Royal Institute of Technology, SE-100 44 Stockholm, Sweden. [126]Institute of Mathematics and Computer Science, University of Latvia, Riga LV-1459, Latvia. [127]Uppsala University, SE-751 05 Uppsala, Sweden. [128]Kurchatov Scientific Center, Moscow 123182, Russian Federation. [129]Department of Oncology, Lund University, SE-221 85 Lund, Sweden. [130]Institute for Cancer Research, Oslo University Hospital Radiumhospitalet, 0310 Oslo, Norway. [131]Faculty of Medicine, University of Oslo, 0316 Oslo, Norway. [132]Department of Oncology, University of Cambridge and Cancer Research UK Cambridge Research Institute, Li Ka Shing Centre, Cambridge CB2 0RE, UK. [133]Department of Medical Oncology, Erasmus MC Rotterdam, Josephine Nefkens Institute and Cancer Genomics Centre, 3015 CE Rotterdam, The Netherlands. [134]Breakthrough Breast Cancer Research Centre, Institute of Cancer Research, London SW3 6JB, UK. [135]Dana-Farber Cancer Institute, Boston, Massachusetts 02115, USA. [136]Department of Pathology, Brigham and Women's Hospital, Boston, Massachusetts 02115, USA. [137]Jules Bordet Institute, B-1000 Brussels, Belgium. [138]Centre Léon Bérard, 69373 Lyon, France. [139]Hôpital Jean Minjoz, 25030 Besançon, France. [140]Institut Curie, 75231 Paris, France. [141]Centre Val d'Aurelle Paul-Lamarque, 34298 Montpellier, France. [142]Hôpital Pellegrin, 33076 Bordeaux, France. [143]Hôpital Henri Mondor, 94010 Créteil, France. [144]U955, INSERM, 94000 Créteil, France. [145]Hôpital Antoine Béclère, 92141 Clamart, France. [146]Centre Hepato-Bilaire, AP-HP Hôpital Paul-Brousse, 94800 Villejuif, France. [147]U785, INSERM, 94800 Villejuif, France. [148]U674, INSERM, 75010 Paris, France. [149]BioQuant, Heidelberg University, 69120 Heidelberg, Germany. [150]Genome Biology Unit, European Molecular Biology Laboratory, 69126 Heidelberg, Germany. [151]Department of Neuropathology, Heidelberg University Hospital, 69120 Heidelberg, Germany. [152]Clinic for Pediatric Oncology, Hematology and Immunology, Heinrich-Heine University Hospital, 40225 Düsseldorf, Germany. [153]Max Planck Institute for Molecular Genetics, 14195 Berlin, Germany. [154]Department of Pediatric Hematology and Oncology, Heidelberg University Hospital, 69120 Heidelberg, Germany. [155]Institute of Neuropathology, Heinrich-Heine University, 40001 Düsseldorf, Germany. [156]Division of Neurosurgery, Hospital for Sick Children, Toronto, Ontario M5G 1X8, Canada. [157]The Arthur and Sonia Labatt Brain Tumour Research Centre, Hospital for Sick Children, Toronto, Ontario M5G 1X8, Canada. [158]National Center for Tumor Diseases, 69120 Heidelberg, Germany. [159]Division of Translational Oncology, German Cancer Research Center, 69120 Heidelberg, Germany. [160]Department of Surgery, University Hospital Trust of Verona, 37134 Verona, Italy. [161]Functional Genomics Center, Department of Biotechnology, University of Verona, 37134 Verona, Italy. [162]Laboratory of Molecular Genetics, Institute for Cancer Research and Treatment, University of Torino, 10060 Torino, Italy. [163]FIRC Institute of Molecular Oncology, 20139 Milan, Italy. [164]Department of Gastroenterology, Endocrinology, Metabolism and Infectiology, University of Marburg, 35043 Marburg, Germany. [165]Department of Pathology, Memorial Sloan-Kettering Cancer Center, New York, New York 10065, USA. [166]Human Genome Center, Institute of Medical Science, University of Tokyo, Minato-ku, Tokyo 108-8639, Japan. [167]Hospital Clínic, University of Barcelona, 08036 Barcelona, Spain. [168]Unit of Infections and Cancer, Cancer Epidemiology Research Programme, CIBER Epidemiología y Salud Pública, Institut Català d'Oncologia-IDIBELL, 08907 Hospitalet de Llobregat, Spain. [169]BC Cancer Research Centre, BC Cancer Agency, Vancouver, British Colombia V5Z 1L3, Canada. [170]Departments of Public Health and Primary Care and Oncology, University of Cambridge, Cambridge CB1 8RN, UK. [171]US National Institutes of Health, Bethesda, Maryland 20892, USA. [172]Department of Bioethics and Humanities, University of Washington, Seattle, Washington 98195, USA. [173]Cambridge Institute for Medical Research and Department of Haematology, University of Cambridge, Cambridge CB2 2XY, UK. [174]Pathology and Laboratory Medicine, The University of Texas M. D. Anderson Cancer Center, Houston, Texas 77030, USA. [175]Institute for Molecular Medicine Finland, University of Helsinki, FIN-00290 Helsinki, Finland. [176]Departments of Medicine and Genetics, Washington University School of Medicine, St. Louis, Missouri 63110, USA. [177]Institute for Molecular Bioscience, The University of Queensland, Brisbane, Queensland 4072, Australia.

ARTICLES

Genome remodelling in a basal-like breast cancer metastasis and xenograft

Li Ding[1,2]*, Matthew J. Ellis[3,4]*, Shunqiang Li[3], David E. Larson[1], Ken Chen[1], John W. Wallis[1,2], Christopher C. Harris[1], Michael D. McLellan[1], Robert S. Fulton[1,2], Lucinda L. Fulton[1,2], Rachel M. Abbott[1], Jeremy Hoog[3], David J. Dooling[1,2], Daniel C. Koboldt[1], Heather Schmidt[1], Joelle Kalicki[1], Qunyuan Zhang[2,5], Lei Chen[1], Ling Lin[1], Michael C. Wendl[1,2], Joshua F. McMichael[1], Vincent J. Magrini[1,2], Lisa Cook[1], Sean D. McGrath[1], Tammi L. Vickery[1], Elizabeth Appelbaum[1], Katherine DeSchryver[3], Sherri Davies[3], Therese Guintoli[3], Li Lin[3], Robert Crowder[3], Yu Tao[6], Jacqueline E. Snider[3], Scott M. Smith[1], Adam F. Dukes[1], Gabriel E. Sanderson[1], Craig S. Pohl[1], Kim D. Delehaunty[1], Catrina C. Fronick[1], Kimberley A. Pape[1], Jerry S. Reed[1], Jody S. Robinson[1], Jennifer S. Hodges[1], William Schierding[1], Nathan D. Dees[1], Dong Shen[1], Devin P. Locke[1], Madeline E. Wiechert[1], James M. Eldred[1], Josh B. Peck[1], Benjamin J. Oberkfell[1], Justin T. Lolofie[1], Feiyu Du[1], Amy E. Hawkins[1], Michelle D. O'Laughlin[1], Kelly E. Bernard[1], Mark Cunningham[1], Glendoria Elliott[1], Mark D. Mason[1], Dominic M. Thompson Jr[7], Jennifer L. Ivanovich[7], Paul J. Goodfellow[7], Charles M. Perou[8], George M. Weinstock[1,2], Rebecca Aft[7], Mark Watson[9], Timothy J. Ley[1,2,3,4], Richard K. Wilson[1,2,4] & Elaine R. Mardis[1,2,4]

Massively parallel DNA sequencing technologies provide an unprecedented ability to screen entire genomes for genetic changes associated with tumour progression. Here we describe the genomic analyses of four DNA samples from an African-American patient with basal-like breast cancer: peripheral blood, the primary tumour, a brain metastasis and a xenograft derived from the primary tumour. The metastasis contained two *de novo* mutations and a large deletion not present in the primary tumour, and was significantly enriched for 20 shared mutations. The xenograft retained all primary tumour mutations and displayed a mutation enrichment pattern that resembled the metastasis. Two overlapping large deletions, encompassing *CTNNA1*, were present in all three tumour samples. The differential mutation frequencies and structural variation patterns in metastasis and xenograft compared with the primary tumour indicate that secondary tumours may arise from a minority of cells within the primary tumour.

Basal-like breast cancer is characterized by the absence of oestrogen receptor (ER) expression, the lack of *ERBB2* gene amplification, and a high mitotic index. The consequent absence of approved targeted therapy options and frequently poor response to standard chemotherapy often result in a rapidly fatal clinical course. The disease also accounts for an elevated percentage of breast cancers in patients with African ancestry[1]. Clinical progress has been limited by a poor understanding of the genetic events responsible for this tumour subtype and by limited preclinical models to study the disease. Because basal-like breast cancer has a highly unstable genome, a key question is whether the fatal metastatic process is driven by mutations that occur after the tumour cells arrive at the distant site, or whether the primary tumour generates cells with a complete repertoire of somatic mutations required for metastatic growth. The rapid advancement of next-generation sequencing technologies allows comprehensive characterization of genomic changes, facilitating the comparison of multiple samples taken from the same patient to address the genetic basis for tumour progression and metastasis.

Case presentation and previous characterization of samples

A 44-year-old African-American woman was diagnosed with an ERBB2-negative and ER-negative inflammatory breast cancer. She was treated with neoadjuvant dose-dense chemotherapy[2], but significant residual tumour was present in the breast and axillary lymph nodes at mastectomy. This indicated chemotherapy resistance and she subsequently underwent radiation therapy. Eight months later she developed a cerebellar metastasis and, despite resection, rapidly succumbed to widely disseminated disease. A transplantable human-in-mouse (HIM) xenograft tumour line was generated from a sample of her primary tumour biopsied before treatment[3]. The xenograft in the mammary fat pad was locally invasive and produced metastatic deposits in lymph nodes and ovaries. Informed consent for full genome sequencing was obtained and DNA samples were prepared from her peripheral blood, primary tumour, brain metastasis and an early passage xenograft (harvested 101 days after initial engrafting into the mouse host). Application of the PAM50 intrinsic subtype algorithm identified the primary tumour, brain metastasis and xenograft line as basal-like subtype, with high risk of relapse (ROR) scores[4].

Sequence coverage and mutation analysis

Using a paired-end sequencing strategy, we generated 130.7, 124.9, 111.8 and 149.2 billion base pairs of sequence data from genomic DNA derived from blood, primary tumour, brain metastasis and

[1]The Genome Center at Washington University, [2]Department of Genetics, [3]Department of Medicine, [4]Siteman Cancer Center, [5]Division of Statistical Genomics, [6]Division of Biostatistics, [7]Department of Surgery and the Young Women's Breast Cancer Program, [9]Department of Pathology and Immunology, Washington University School of Medicine, St Louis, Missouri 63108, USA. [8]Department of Genetics, Lineberger Cancer Center, University of North Carolina, Chapel Hill, North Carolina 27599, USA.
*These authors contributed equally to this work.

xenograft samples, respectively, with corresponding haploid coverages of 38.8×, 29.0×, 32.0× and 23.8× (Supplementary Table 1). These genome-wide coverages were assessed by comparing single nucleotide variants (SNVs) detected by MAQ[5] with single nucleotide polymorphisms (SNPs) genotyped using Illumina 1M duo arrays for all tissues excluding the xenograft. Array data from the metastasis were used as a surrogate for monitoring the xenograft SNP coverage and confirmed bi-allelic detection of 98.27%, 96.79%, 96.17% and 88.77% of the heterozygous array SNPs in the normal, primary tumour, metastasis and xenograft sequence data sets, respectively (Supplementary Table 1).

The process for selecting somatic mutations is shown in Supplementary Table 2 and is detailed in Supplementary Information. Putative somatic SNVs and indels that overlap with coding sequences, splice sites and RNA genes were included as 'tier 1'. We combined tier 1 sites identified in all three tumour samples and obtained deep read count data for all four samples from Illumina and/or 454 platforms (Supplementary Information). On the basis of pathology review, the tumour cellularity estimates were 70% for the primary tumour and 90% for both the brain metastasis and xenograft. Using these estimates, we calculated the tumour read counts by proportionally removing the counts derived from the normal tissue reads from the counts obtained from primary tumour and metastasis reads (Supplementary Table 3a). Using the Illumina platform, we also generated 15.6 Gb (4.4× haploid coverage) of sequence data for the NOD/SCID mouse genome used as the host for the xenograft line. The mapping rates of NOD/SCID data to human and mouse C57BL/6 reference sequences were 3.17% and 95.85%, respectively. As the non-malignant contamination in xenograft is largely from murine cells (which do not significantly affect read mapping), no correction was applied for the xenograft data. Adjusted tumour read counts were used to calculate mutant allele frequencies. Somatic changes were validated by comparing mutant allele frequencies in the three tumour genomes against the germline DNA sample, combined with a manual review of ABI 3730 data from PCR products (Supplementary Information).

A total of 50 somatic sites, including 28 missense, 11 silent, 2 splice site, 1 RNA, 1 nonsense, 4 insertions and 3 deletions, were validated in at least one of the three tumour genomes. Of coding point mutations, the observed nonsynonymous/synonymous ratio of 2.64:1 (29:11) is not significantly different from that expected by chance[6] ($P = 0.51$), indicating that the majority of coding mutations do not confer a selective advantage to the basal tumour. This is similar to the nonsynonymous/synonymous ratio reported in the small-cell lung cancer cell line NCI-H209[7], but higher than the ratio reported in the melanoma cell line COLO-829[8].

Mutation spectrum in basal breast tumour

We investigated the spectrum of DNA sequence changes in this basal tumour and found that 55% (22 out of 40) of coding point mutations represent C•G→T•A transitions. A similar frequency of C•G→T•A transitions (56% (18 out of 32)) was observed in a lobular breast tumour recently reported[9] (Fig. 1a). In addition, 15% (6 out of 40) of coding point mutations representing C•G→A•T transversions were detected in the basal tumour, but none was found in the lobular tumour. The statistical significance of these observations should be explored with the comparative analysis of a larger number of basal and lobular breast tumours. Moreover, the observed C•G→T•A transition frequency is notably higher than those observed in a previous breast cancer study[10] ($P = 0.027$; Fig. 1b). A set of extremely high-confidence tier 1–4 mutations (somatic score >55 and average mapping quality >79) was used to explore the genome-wide mutation spectrum. We found that mutations at A•T bases are significantly expanded in the genome-wide set compared to the coding mutations, especially for A•T→G•C transitions ($P = 0.0065$). This is consistent with the higher A•T content in non-coding sequences than in coding sequences. Comparison to the whole-genome mutation spectrum reported for the melanoma cell line (COLO-829)[8] and a small-cell lung cancer cell line (NCI-H209)[7] indicates that the tumour genome under study shows no sign of tobacco or ultraviolet influence. We then compared the fraction of the three classes of guanine mutations occurring at CpG dinucleotides in primary tumour, brain metastasis and xenograft and found that the frequencies of G→A mutations are 27.54%, 27.60% and 28.05% in each respective tumour, significantly higher than both the genome average of 4.45% ($P < 10^{-10}$) and the frequency reported in NCI-H209 ($P < 10^{-10}$; Fig. 1c).

Distribution of mutations among tumours

Common mutations detected in three tumour genomes. Of the 50 validated point mutations and small indels, 48 are detectable in all three tumours. We performed a statistical enrichment test that takes the variations of different platforms, experiments and primer pairs into consideration (Supplementary Information). These 48 sites consist of 20 sites with relatively comparable frequencies across tumours, 26 sites significantly enriched (false discovery rate (FDR) ≤ 0.05) in the metastasis and/or xenograft, and two sites with significant enrichment (FDR ≤ 0.05) in the primary tumour (Fig. 2 and Table 1). The affected genes and the likely consequences of these mutations are summarized in Table 1 and Supplementary Table 3b.

Mutations with comparable frequencies in three tumours. We detected a *JAK2* mutation (I166T), residing in the FERM domain, which is different from the previously reported activating mutations in myeloproliferative diseases, often found in the pseudokinase domain[11]. Screening of an additional 116 breast tumours identified another mutation (R1122P) in the kinase domain of JAK2 from a luminal B-type breast cancer. A splice site mutation (e8-1) was found in *IRAK2*. We performed a polymerase chain reaction with reverse transcription (RT–PCR) experiment using RNAs from the brain metastasis and xenograft and found that the first 30 nucleotides of exon 8 (*IRAK2*, NM_001570) were skipped and an internal exonic AG site was used as a splice acceptor, resulting in an in-frame deletion. A missense

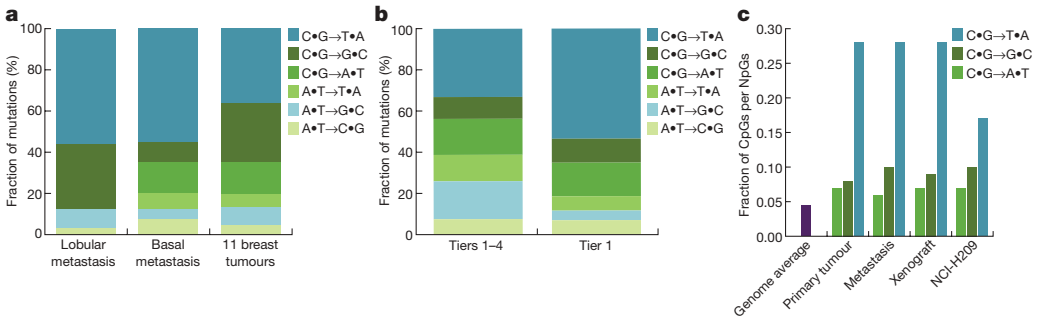

Figure 1 | Mutational signatures in the basal breast tumour. a, Fraction of mutations in each of the transition and transversion categories in the metastasis of a lobular breast tumour[9], the metastasis of the basal breast tumour under study, and the 11 breast tumours reported previously[29] from which 1,104 coding mutations identified in the discovery set were used in the analysis. **b**, Fraction of mutations in each of the transition and transversion categories in 43 tier 1 mutations and 3,204 tier 1–4 mutations in the metastasis under study. **c**, Fraction of guanine mutations at CpGs in primary tumour, metastasis, xenograft and NCI-H209 as reported previously[7].

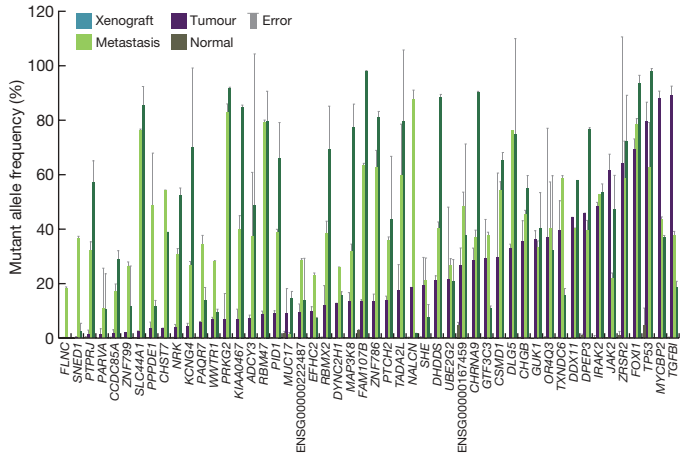

Figure 2 | Mutant allele frequency from deep read count data. The mutant allele frequency of each somatic mutation is shown. Mutations were validated using both 454 and Illumina sequencing. Each bar represents the average of the frequency yielded by the two technologies for a single primer pair and the error bars represent the standard deviation. Data were considered only if there were at least 200 reads from Illumina sequencing and at least 20 reads from 454 sequencing. If no error bar exists, then data were only available from a single sequencing platform.

mutation (A401S) in *CSMD1* was found in all three tumours. Loss of *CSMD1* expression is associated with poor survival in invasive ductal breast carcinoma[12] and it is frequently deleted in colorectal adenocarcinoma and head/neck carcinomas[13]. We also identified three missense (E608K, T1456R, and Q2204R) and one nonsense (Q3005*) mutations in *CSMD1* in four breast cancers out of 116 screened. A binomial test shows that *CSMD1* is significantly mutated in breast cancer ($P = 0.022$ and FDR = 0.197; Supplementary Table 4).

Mutations highly enriched in metastasis and/or xenograft. A missense mutation (A681E) in *NRK*, a protein kinase involved in activating JNK, was found to be present in all three tumours, but at 8- and 13-fold increased allele frequencies in the metastasis and xenograft, respectively (Fig. 2 and Table 1). Two somatic mutations (S424C and Q521*) in *NRK* have been previously reported in breast cancer[14]. The missense mutation (P461L) identified in the carboxy terminus of MAP3K8 was present at a roughly sixfold increase in the xenograft compared to the primary tumour. C-terminal truncation of MAP3K8 has been shown to activate this oncogenic kinase[15,16], raising the possibility that this C-terminal substitution (P461L) is an activating mutation.

Another missense mutation (K1017N) in *PTPRJ*, a protein tyrosine phosphatase, had a mutant allele frequency of 32% in the metastasis and 57% in the xenograft compared with just 1.3% in the primary tumour. This K1017N mutation in *PTPRJ* is among the most highly enriched mutations in both the metastasis (FDR = 0.00035) and xenograft (FDR = 0.00022). The mutation site is in the juxtamembrane domain (a basic residue motif) and is in close proximity to the tyrosine-protein phosphatase domain (amino acids 1041–1298). Reference 17 reported that the PTPRJ charged peptide (amino acids 1013–1024) is responsible for interaction with its substrates, such as ERK1/2. The K1017N mutation found in the basal tumour and the K1016A mutation described in ref. 17 both change a basic residue to a neutral residue, indicating that these two mutations may be functionally similar. A missense mutation (F299V) in *WWTR1*, assigned as deleterious by SIFT[18], was detected at 28% mutant allele frequency in metastasis, but only at 7% and 10% in primary tumour and xenograft, respectively (Fig. 2 and Table 1). WWTR1, a 14-3-3 binding protein with a PDZ binding motif, has been shown to modulate mesenchymal stem cell differentiation[19]. Overexpression of *WWTR1* has also been implicated in promoting the migration, invasion and tumorigenesis of breast cancer cells[20].

Another point mutation (R258Q) was identified in *CHGB* (chromogranin B) encoding a tyrosine-sulphated secretory protein. A SNP at the same position was reported to dbSNP in January 2009 for a Yoruba sample. It was also assigned as a germline site in another African-American with breast cancer when we genotyped this mutation in 112 additional primary tumours and 73 metastatic tumours of various expression classes (Supplementary Information). To investigate this variant further, 84 cancer-free African-American women with an average age of 71.2 years (low risk for developing breast cancer) and 38 early-onset African-American breast cancer patients with an average age of 35.6 years were genotyped. The results indicated that 8 out of 84 controls and 3 out of 38 cases carried the variant allele, indicating that this variant is unlikely to be a breast cancer susceptibility allele.

Three validated indels were enriched in the metastasis and/or xenograft. One was the 1-bp insertion in exon 4 of the *TP53* gene, which creates a frameshift mutation (Q167fs) in the DNA binding domain and results in a truncated protein. We found the *TP53* mutation to be significantly enriched in the xenograft, whereas it was present at a relatively constant frequency in primary tumour and metastasis (Fig. 2 and Table 1).

Mutations enriched in the primary tumour. A nonsense mutation (Q2222*) in *MYCBP2* and a missense mutation (E576K) in *TGFBI*, both found in all three tumours, had higher mutant allele frequencies in the primary tumour (88% for *MYCBP2* and 89% for *TGFBI*) than in the metastasis (44% for *MYCBP2* and 38% for *TGFBI*) or the xenograft (37% for *MYCBP2* and 18% for *TGFBI*) (Fig. 2 and Table 1).

***De novo* mutations identified in the metastasis.** Two *de novo* mutations were discovered in the metastatic tumour, neither of which was detected in the primary or xenograft tumour genomes. One was a missense mutation (T708I) in *SNED1*, with a mutant allele frequency of 37%; the other was a silent mutation (N2483) in *FLNC* with a mutant allele frequency of 18% (Fig. 2 and Table 1). Because the xenograft line, without these two mutations, exhibits metastatic lesions in ovarian, lymphoid and subcutaneous tissue (data not shown), it is unlikely that these mutated genes are essential to the metastatic process.

Elevated copy number alterations in metastasis and xenograft

The cnvHMM algorithm (K.C., X.S., E.R.M., L.D. and R.K.W., unpublished) was applied to the aligned sequence reads to detect regions of copy number alterations in all three tumours. Using pathology-based purity estimates for the primary tumour and brain metastasis, we calculated the read depth contributed from the tumour cells alone and then computed the copy number for all genomic positions. Read depth correction was not applied to the xenograft, as stated earlier. We subsequently compared the copy number data from all three tumours with those from peripheral blood, to identify genomic segments with significant copy number alterations (CNAs) (Supplementary Information). A total of 516.5 Mb, 640.4 Mb and 754.5 Mb were amplified, whereas 342.5 Mb, 383.1 Mb and 562.5 Mb were deleted, in primary tumour, metastasis and xenograft, respectively (Supplementary Table 5–7). Moreover, 96.11% and 93.98% of CNA sequences in the primary tumour were also found in CNA segments in the metastasis and xenograft, respectively, indicating that most primary tumour CNAs are preserved during disease progression and engraftment. On the other hand, only 80.65% of metastasis and 61.29% of xenograft CNA sequences overlap with primary tumour CNAs. Furthermore, 155 regions with focal copy number segments (≤2 Mb) were detected in the primary tumour, but only 101 and 97 regions in the metastasis and xenograft (Supplementary Tables 8–10). Our result also shows that 111 (average span = 745,183 bp) and 99 (average span = 799,395 bp) focal copy number segments (≤2Mbp) in the primary tumour overlap with broader copy number segments in the metastasis (average span = 2,245,546 bp) and xenograft (average span = 3,565,456 bp), indicating possible expansion of primary focal

Table 1 | Summary of point mutations and small indels

Chr	Start	Allele change	Gene	Amino acid change	Mutant allele frequency (%)				Copy number			Enrichment FDR	
					N	T	M	X	T	M	X	M:T	X:T
1	26062702	G>A	*PAQR7*	p.A72	0.17	5.78	34.55	13.70	2	2	2	9.00×10^{-4}	0.011
1	26646672	G>A	*DHDDS*	p.R159H	0.14	21.12	40.24	88.29	2	2	2	5.73×10^{-5}	2.46×10^{-5}
1	43684654	G>A	*KIAA0467*	p.G2119R	0.13	7.00	40.02	84.84	2	2	2	0.001	5.98×10^{-5}
1	45068225	C>G	*PTCH2*	p.W293S	0.02	13.70	36.03	43.61	2	2	2	0.085	0.381
1	152723308	delGCAACTTTTCATT	*SHE*	p.LPFKG476in_frame_delW	0.19	19.28	21.33	7.69	4.61	5.34	6.92	0.820	0.065
1	226395989	C>A	*GUK1*	p.P11Q	0.01	36.29	33.12	40.17	3.66	3.96	4.64	0.374	0.365
1	242935580	A>T	*PPPDE1*	p.T151S	0.12	3.39	48.57	11.47	3.45	3.71	4.38	0.012	0.063
2	24994872	G>A	*ADCY3*	p.H163	0.06	7.10	37.49	48.71	3.17	3.24	3.78	0.007	0.029
2	56273320	delG	*CCDC85A*	p.E161fs	0.16	1.71	17.11	28.78	2.9	3.24	3.34	0.002	0.006
2	197349569	G>C	*GTF3C3*	p.R474G	0.11	29.42	37.75	11.08	1.4	1.31	1.24	0.316	0.065
2	229835724	C>T	*PID1*	p.S14	0.11	8.95	38.89	66.13	2	2	1.36	0.001	0.166
2	241641282	C>T	*SNED1*	p.T708I	0.04	0.32	36.52	2.30	2	2	2	1.58×10^{-4}	0.719
3	10236363	G>T	*IRAK2*	e8-1	0.38	48.37	52.69	53.33	2	2	2	0.156	0.762
3	139505123	G>A	*TXNDC6*	p.R221W	0.29	39.50	58.62	15.81	2	2	2	0.039	0.012
3	150728323	A>C	*WWTR1*	p.F299V	0.03	6.87	28.14	9.53	2	2	2	1.43×10^{-4}	0.020
4	40051165	C>A	*CHRNA9*	p.D437E	0.10	28.38	36.82	90.26	2	2	2	0.073	9.67×10^{-5}
4	40134827	delG	*RBM47*	p.I280fs	0.05	8.62	79.15	79.74	2	2	2	0.030	0.124
4	82232630	C>T	*PRKG2*	p.R709	0.11	6.99	82.99	91.51	2	2	2	0.083	0.094
5	135422725	G>A	*TGFBI*	p.E576K	0.17	89.09	37.58	18.45	2	2	2	3.34×10^{-6}	3.23×10^{-5}
5	169466048	C>T	*FOXI1*	p.S170F	0.15	69.28	78.33	93.61	2	2	2	0.473	0.009
7	100463999	G>C	*MUC17*	p.S861T	1.69	9.22	1.46	14.43	2	2.76	4.04	0.073	0.816
7	128284099	C>T	*FLNC*	p.N2483	0.11	0.17	18.21	0.16	2.54	2.8	2.93	0.002	0.193
7	148400407	G>A	*ZNF786*	p.F130	0.13	13.61	62.86	81.04	2.51	2.85	3.54	3.01×10^{-4}	3.23×10^{-5}
8	3232441	C>A	*CSMD1*	p.A409S	0.04	29.75	54.22	65.18	2	2	2	0.355	0.141
8	8477326	C>T	ENSG00000222487	NULL	0.11	9.61	28.43	13.74	2	2	2.67	0.120	0.787
9	5040714	T>C	*JAK2*	p.I166T	0.09	61.63	21.93	47.40	2.83	2.67	2.84	0.246	0.999
9	107137789	G>A	*SLC44A1*	p.A132T	0.08	2.59	76.14	85.31	2	1.29	1.19	1.43×10^{-4}	1.05×10^{-4}
10	14603968	C>T	*FAM107B*	p.R237Q	2.65	13.53	63.25	97.88	3.7	4.04	4.76	3.29×10^{-6}	8.54×10^{-8}
10	30789749	C>T	*MAP3K8*	p.P461L	0.11	13.33	31.72	77.47	3.44	3.71	4.21	0.002	9.67×10^{-5}
10	79240899	G>A	*DLG5*	p.D1474	0.07	32.94	76.10	74.72	2	2	2	6.12×10^{-5}	0.011
11	12496610	insATGGAG	*PARVA*	p.338in_frame_insDG	0.00	1.41	10.75	10.58	2	2	2	0.347	0.365
11	48128224	A>T	*PTPRJ*	p.K1017N	0.20	1.25	32.08	57.23	2	2	2.99	3.48×10^{-4}	2.20×10^{-4}
11	102687902	G>A	*DYNC2H1*	p.R3867Q	0.06	12.81	25.78	15.69	2	2	2	0.002	0.023
12	31122692	T>G	*DDX11*	p.V33G	0.02	44.35	40.39	57.88	1.49	1.37	1.24	0.316	0.386
13	76628331	G>A	*MYCBP2*	p.Q2222*	0.10	87.84	43.76	36.95	2	2	2	0.004	0.003
13	100688137	A>T	*NALCN*	p.D468E	0.16	18.60	87.66	1.65	2	2.74	2.92	0.004	0.216
14	19285546	G>T	*OR4Q3*	p.L40	0.22	36.94	40.31	32.28	2	2	2	0.313	0.107
16	66569387	T>G	*DPEP3*	p.R262S	0.84	45.61	39.43	76.59	2	2.9	3.02	0.293	6.93×10^{-4}
16	82828230	C>A	*KCNG4*	p.G121	0.04	4.15	26.82	69.89	2.43	3.09	3.49	0.083	0.259
17	7519157	insG	*TP53*	p.Q167fs	4.61	79.40	62.62	97.96	2	2	2	0.085	0.003
17	32904736	C>T	*TADA2L*	p.R339W	0.12	17.49	59.92	79.47	2	2	2	0.002	0.002
19	12363315	G>A	*ZNF799*	p.H299	0.17	2.05	26.23	11.81	2	2	3.06	0.062	0.618
19	16006577	insA	ENSG00000167459	p.I38fs	4.82	26.53	48.47	37.74	2	2	3.06	0.286	0.809
20	5851563	G>A	*CHGB*	p.R258Q	0.14	35.64	45.50	54.87	2.57	2.86	3.64	0.057	0.005
21	45015744	G>A	*UBE2G2*	p.I158	0.12	21.57	26.72	20.89	2	2	2	0.522	0.728
X	15731812	C>G	*ZRSR2*	p.A95G	1.01	64.01	58.66	72.08	2.51	2.77	2.99	0.137	0.969
X	43893087	C>G	*EFHC2*	e15-1	0.01	9.88	23.15	7.35	2	2.68	2.82	0.114	0.381
X	46318872	insA	*CHST7*	p.T188fs	0.19	3.67	54.36	38.84	2	2.68	2.82	0.073	0.058
X	105040331	C>A	*NRK*	p.A681E	0.12	4.08	30.84	52.45	2	2	2	0.085	0.017
X	129374039	A>G	*RBMX2*	p.K169E	0.30	11.88	38.36	69.46	2	2.65	2.77	0.002	0.003

Gene sets from Ensembl build 54 and GenBank (downloaded in May 2009) were used for annotation of mutations. Enrichment FDR represents the false discovery rate of the significance of the variant frequency change between the two samples. M, metastasis; N, peripheral blood; T, primary tumour; X, xenograft.
* Nonsense mutation.

regions or selection of new adjacent events during disease progression and in the mouse host. Sequence depth-based copy number analysis shows overall the highest concordance with other platforms, including the array CGH and Illumina SNP array, and also provided the highest concordance of copy number (correlation coefficients: 0.89–0.97) between primary tumour, metastasis and xenograft (Supplementary Table 11).

Common and unique structural variations in three tumours

We used BreakDancer[21] to detect structural variants in sequencing data from paired end libraries (Supplementary Table 12) and applied a set of thresholds to identify putative somatic structural events.

Deletions, insertions and inversions. Breakpoint-containing contigs from the three tumour samples that were not present in the matched normal genome were successfully assembled for 137 deletions, 15 insertions and 38 inversions using the TIGRA assembler (L.C., K.C., J.W.W., E.R.M., R.K.W., L.D. and G.M.W., unpublished), suggesting that they were putative somatic events. We then re-mapped individual reads to these assembled contigs to screen out germline structural variants and to confirm somatic structural variants (Supplementary Information), resulting in the detection of 59 deletions and 18 inversions. PCR primers were designed successfully to validate 73 out of 77 putative structural variant events and the resulting amplicons were sequenced by either the Roche 454 or ABI 3730 platform. Subsequently, 28 deletions and 6 inversions were validated as somatic events (Table 2). Among them, a 46,462-bp heterozygous deletion in *FBXW7* removes the last 10 exons and a portion of the first exon of NM_018315, probably inactivating FBXW7. FBXW7 targets cyclin E and mTOR for ubiquitin-mediated degradation[22,23]. Numerous cancer-associated mutations in *FBXW7* have been previously reported, and loss of FBXW7 function causes chromosomal instability and tumorigenesis[24]. Two overlapping deletions (538,467 bp and 515,465 bp in length) on chromosome 5, affecting *CTNNA1* along with *LRRTM2*, *MATR3*, *SNORA74A* and *SIL1*, were also validated. This result is consistent with the detection of a focal copy number deletion encompassing this region in both metastasis (copy number = 0.65) and xenograft (copy number = 0.03) (Fig. 3 and Supplementary Tables 9 and 10). Careful examination of

Table 2 | Validated structural variations

Type	Tumour source	Chromosome A	Breakpoint A	Orientation A	Chromosome B	Breakpoint B	Orientation B	Event size (bp)	Gene
Translocation	T,M,X	1	245548334	Minus	2	64855174	Plus	–	*ZNF496*
Translocation	T,M	1	245548342	Plus	6	144243130	Plus	–	*ZNF496, C6orf94*
Translocation	T,M,X	2	64855565	Plus	6	144243118	Minus	–	*C6orf94*
Translocation	T,M,X	2	165126335	Plus	16	4537866	Plus	–	*GRB14*
Translocation	T,M,X	4	188855443	Plus	9	139022260	Plus	–	*ABCA2*
Translocation	T,M,X	12	10874022	Plus	14	99382256	Minus	–	*EML1*
Translocation	T,M	19	17188977	Minus	3	188010735	Plus	–	*USE1*
Inversion	T,M,X	1	35703682	–	1	35732148	–	28,465	*KIAA0319L*
Inversion	T,M,X	1	95919529	–	1	95920940	–	1,410	–
Inversion	T,M,X	1	204459097	–	1	204461297	–	2,200	–
Inversion	T,M,X	1	204459547	–	1	204460581	–	1,033	–
Inversion	T,M,X	4	177886041	–	4	177890171	–	4,129	*VEGFC*
Inversion	T,M,X	19	17800861	–	19	17801858	–	996	*JAK3*
Deletion	M	1	29389213	–	1	29416133	–	26,919	*MECR*
Deletion	T,M,X	1	76496719	–	1	76496797	–	79	*ST6GALNAC3*
Deletion	T,M,X	1	88291885	–	1	88292292	–	406	–
Deletion	T,M,X	2	18629189	–	2	19196656	–	567,466	*NT5C1B*
Deletion	T,M,X	2	64853205	–	2	65010694	–	157,488	–
Deletion	T,M,X	2	128745303	–	2	128898612	–	153,308	*HS6ST1*
Deletion	T,M,X	4	1203395	–	4	1265560	–	62,164	*CTBP1*
Deletion	T,M,X	4	135737399	–	4	135738718	–	1,318	–
Deletion	T,M,X	4	147221480	–	4	147294628	–	73,147	*AK057233*
Deletion	T,M,X	4	153446894	–	4	153493357	–	46,462	*FBXW7*
Deletion	T,M,X	5	15572469	–	5	15572649	–	179	*FBXL7*
Deletion	T,M,X	5	130743604	–	5	130743718	–	113	*CDC42SE2*
Deletion	T,M,X	5	138131495	–	5	138669963	–	538,467	*CTNNA1, LRRTM2, MATR3, SNORA74A, SIL1*
Deletion	T,M,X	5	138141753	–	5	138657219	–	515,465	*CTNNA1, LRRTM2, MATR3, SNORA74A, SIL1*
Deletion	T,M,X	6	39689264	–	6	39689652	–	387	*KIF6*
Deletion	T,M,X	7	999743	–	7	999984	–	240	–
Deletion	T,M,X	7	135419232	–	7	135419453	–	220	–
Deletion	T,M,X	8	32597100	–	8	32706664	–	109,563	*NRG1*
Deletion	T,M,X	8	116552846	–	8	116634665	–	81,818	*TRPS1*
Deletion	T,M,X	8	136595795	–	8	136596285	–	489	*KHDRBS3*
Deletion	T,M,X	9	2746534	–	9	2746735	–	200	–
Deletion	T,M,X	10	77142378	–	10	77142881	–	502	*C10orf11*
Deletion	T,M,X	11	115974418	–	11	115974688	–	269	–
Deletion	T,M,X	11	125479377	–	11	125479744	–	366	–
Deletion	T,M,X	17	24451601	–	17	24475255	–	23,653	*MYO18A*
Deletion	T,M,X	17	73733446	–	17	73733547	–	100	*BIRC5*
Deletion	T,M,X	18	46765510	–	18	46768017	–	2,507	*ELAC1*
Deletion	T,M,X	X	149511547	–	X	149548642	–	37,094	*MTM1*

M, metastasis; T, primary tumour; X, xenograft.

this region in the aligned sequence reads for the primary tumour confirms the existence of copy number deletion. Loss of *CTNNA1* was shown to result in global loss of cell adhesion in human breast cancer cells[25] and increased *in vitro* tumorigenic characteristics[26], indicating that this bi-allelic deletion has functional importance. A 109,563-bp heterozygous deletion on chromosome 8 was assembled and validated in all three tumours. This event removed three exons of *NRG1*, which encodes a peptide growth factor that binds to ERBB3 and ERBB4. Notably, a 26,919-bp deletion in *MECR* was only identified, assembled and validated in the metastasis, suggesting its *de novo* nature in this sample.

Translocations. Of the 112 assembled putative translocations, 34 passed manual review using Pairoscope graphs (D.E.L., C.C.H., E.R.M., L.D. and R.K.W., unpublished), and 19 with an assembly score greater than our experimentally supported cutoff of 10 were included in Supplementary Table 13. Seven translocations were experimentally validated (Table 2). One validated translocation t(4;9)(188855443;139022258), assembled in all three tumours, involved a long terminal repeat (LTR) from the ERVL-MaLR family on chromosome 4 and *ABCA2* on chromosome 9. The translocation removes the final exon of the *ABCA2* gene (NM_001606). Two other validated translocations, identified in all three tumours, are t(1;2)(245548338;64855172) and t(2;6)(64855607;144243116) (Supplementary Fig. 1). Noticeably, the breakpoints on chromosome 2 for these two translocations are only separated by 393 bp in a TcMar-Tigger repeat. The chromosome 1 breakpoint of t(1;2)(245548338;64855172) is in intron 5 of NM_032752 in *ZNF496*. We expect the translation of *ZNF496* to continue through exon 5 into intron 5 due to lack of a splice acceptor site. On the other hand, t(2;6)(64855565;144243116) involves *FAM164B* on chromosome 6 and the translocation contig retains three exons of XM_928657. We have also validated t(1:6)(245548342;144243110) (not detected by BreakDancer), the breakpoints of which are only 4 bp and 6 bp away from the breakpoints identified on chromosomes 1 and 6 for t(1;2)(245548338;64855172) and t(2;6)(64855607;144243116), respectively (Supplementary Fig. 1). This translocation is found in both the primary tumour and the metastasis, but apparently is lost in the xenograft (Supplementary Fig. 1 and Fig. 4). Sequencing of two PCR products generated using two primer pairs from chromosomes 1 and 6 demonstrated the presence of two forms of genomic fusion: one includes chromosomes 1 and 6 and the other includes chromosomes 1, 2 and 6. The former is only present in the primary tumour and the metastasis.

Discussion

Our comprehensive analysis of this sample set identified 50 novel somatic point mutations and small indels in coding sequences, RNA genes and splice sites as well as 28 large deletions, 6 inversions and 7 translocations. In terms of functional annotation, a hierarchy can be suggested. The first level includes somatic changes likely to be functional, such as the small indel in *TP53*, the large heterozygous deletion in *FBXW7* and the bi-allelic deletion in *CTNNA1*. The second level consists of nonsynonymous mutations in genes previously noted to be targeted for somatic mutation in cancer or found to be recurrently mutated in this study, although the exact mutations are novel and their functional importance requires further investigation (*JAK2*, *PTCH2*, *CSMD1* and *NRK*). The third level contains mutations known to be related to signal transduction in the malignant cells and/or found to be enriched during disease progression (*MAP3K8*,

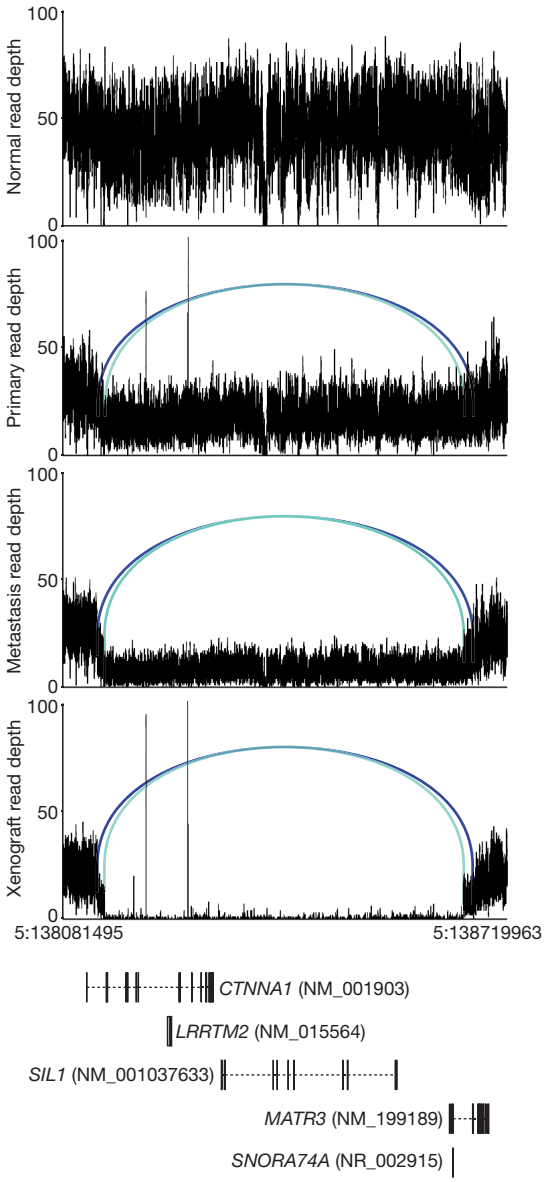

Figure 3 | Two overlapping *CTNNA1* deletions on chromosome 5 in three tumours. A graph of sequence depths, read pairs and genes in a 638,468-bp region containing two overlapping deletions. The top four panels display the read depths at each base, and the reads within the region whose mates mapped at an abnormal distance are displayed as blue bars, with matched pairs connected by arcs. Two different shades of blue indicate the two separate allelic deletion events (538,467 bp and 515,465 bp in length). The bottom panel displays genes annotated in this genomic region.

PTPRJ and *WWTR1*). The final level, by far the largest group, awaits the acquisition of new data. Analysis of germline variants for over 500 classic tumour suppressor genes and oncogenes[27] identified a large number of SNPs, none of which was an unequivocal hereditary breast cancer susceptibility allele (data not shown).

The wide range of mutant allele frequencies suggests considerable genetic heterogeneity in the cellular population at the primary site. The mutation frequency range narrowed in brain metastasis and xenograft, indicating that the metastatic and transplantation processes selected for cells carrying a distinct subset of the primary tumour mutation repertoire. The overlap between the mutation frequency changes seen in the metastatic and xenograft samples argues that cellular selection during xenograft formation is similar to that during metastasis. Moreover, it suggests that the changes were not therapy-related, as the xenograft was established before any treatment. GO annotation of enriched mutations suggests that transcription factor activity is

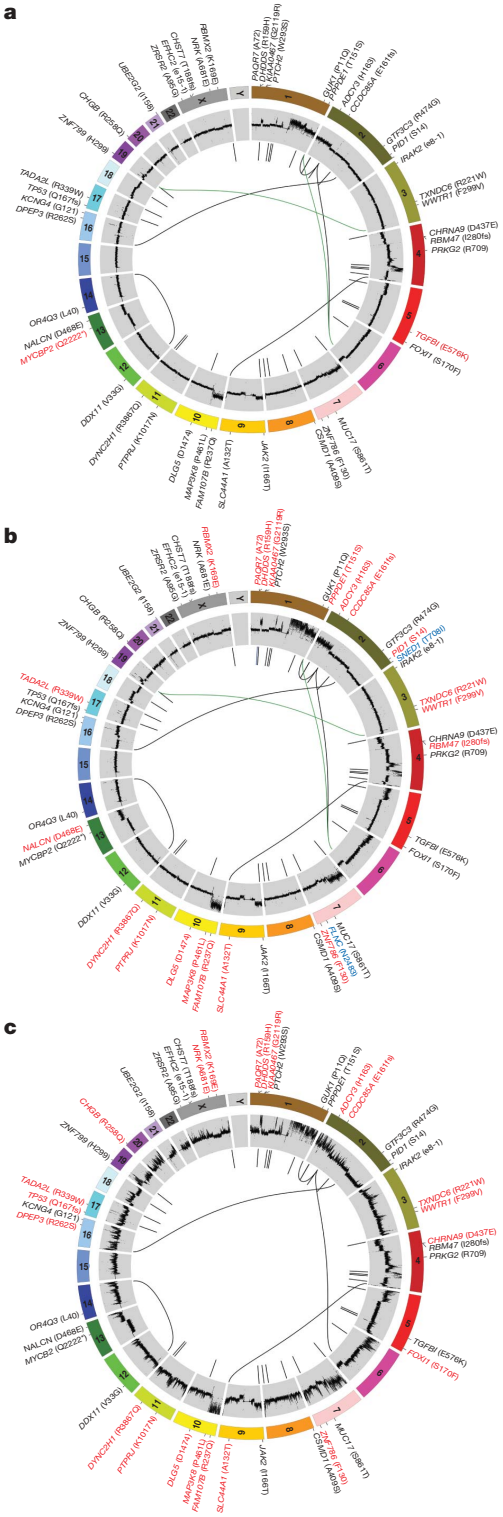

Figure 4 | Circos plots for the primary tumour, metastasis and xenograft genomes. **a**–**c**, Circos[30] plots display the validated tier 1 somatic mutations, DNA copy number and validated structural rearrangements in the primary tumour (**a**), metastasis (**b**) and xenograft (**c**). Mutations enriched in the primary tumour are labelled in red in panel **a**; mutations enriched in the metastasis or xenograft are in red in panels **b** and **c**. Mutations and the large deletion unique to the metastasis are in blue (**b**). Translocations only present in primary tumour and metastasis are in green. All shared events are in black. The copy number difference between the tumour and normal is shown (scale: −4 to 4). No purity-based copy number corrections were used for plotting.

possibly selected for in the xenograft (Supplementary Table 14). In contrast to our observation of only two new tier 1 mutations at the metastatic site, sequencing of an indolent metastatic lobular breast tumour showed that the great majority of the mutations detected were completely novel when compared to the primary tumour[9]. However, in this instance, the metastatic process evolved over 9 years, as opposed to less than 1 year in the case we describe here. Another difference relative to the lobular cancer genome, where no structural variants were validated, was that paired-end sequencing detected 41 structural variations within this basal-like tumour genome. Our study of a primary tumour–metastasis–xenograft trio therefore demonstrates that, although additional somatic mutations, copy number alterations and structural variations do occur during the clinical course of the disease, most of the original mutations and structural variants present in the primary tumour are propagated. The preservation of all primary mutations in the xenograft suggests that early passage xenograft lines are valid for functional and therapeutic studies. However, the altered mutation frequency and elevated degree of copy number alterations suggest caution when interpreting the results of such experiments.

The first completed basal-like breast cancer genome is highly complex, as would be anticipated for a tumour type associated with chromosomal instability and DNA repair defects. Indeed, this cancer genome, in comparison with the two AML (acute myeloid leukemia) cases published recently[27,28], revealed a 3–4-fold increase in high-confidence SNVs genome-wide, suggesting a much greater background mutation rate. Future studies should extend our analysis approach of primary, metastatic and normal tissue trios and include affected individuals with diverse geographic origins to produce a complete catalogue of recurrent somatic and inherited variants associated with the development of this common malignancy.

METHODS SUMMARY

Illumina reads from peripheral blood, primary tumour, metastasis and xenograft were aligned to NCBI build36 using MAQ[5] and coverage levels were defined by comparison of SNPs identified by Illumina 1M duo arrays to SNVs called by MAQ. Somatic mutations were identified using our in-house programs glfSomatic and a modified version of the Samtools indel caller (http://samtools.sourceforge.net/). Putative variants were manually reviewed and then validated by Illumina, 3730 or 454 sequencing. Structural variations were identified using BreakDancer[21], manually reviewed and validated by a combination of localized Illumina read assembly, PCR and either 3730 or 454 sequencing. A complete description of the materials and methods used to generate this data set and results is provided in the Supplementary Information.

Received 24 November 2009; accepted 11 March 2010.

1. Carey, L. A. *et al.* Race, breast cancer subtypes, and survival in the Carolina Breast Cancer Study. *J. Am. Med. Assoc.* **295,** 2492–2502 (2006).
2. Citron, M. L. *et al.* Randomized trial of dose-dense versus conventionally scheduled and sequential versus concurrent combination chemotherapy as postoperative adjuvant treatment of node-positive primary breast cancer: first report of Intergroup Trial C9741/Cancer and Leukemia Group B Trial 9741. *J. Clin. Oncol.* **21,** 1431–1439 (2003).
3. Kuperwasser, C. *et al.* Reconstruction of functionally normal and malignant human breast tissues in mice. *Proc. Natl Acad. Sci. USA* **101,** 4966–4971 (2004).
4. Parker, J. S. *et al.* Supervised risk predictor of breast cancer based on intrinsic subtypes. *J. Clin. Oncol.* **27,** 1160–1167 (2009).
5. Li, H., Ruan, J. & Durbin, R. Mapping short DNA sequencing reads and calling variants using mapping quality scores. *Genome Res.* **18,** 1851–1858 (2008).
6. Bardelli, A. *et al.* Mutational analysis of the tyrosine kinome in colorectal cancers. *Science* **300,** 949 (2003).
7. Pleasance, E. D. *et al.* A small-cell lung cancer genome with complex signatures of tobacco exposure. *Nature* **463,** 184–190 (2010).
8. Pleasance, E. D. *et al.* A comprehensive catalogue of somatic mutations from a human cancer genome. *Nature* **463,** 191–196 (2010).
9. Shah, S. P. *et al.* Mutational evolution in a lobular breast tumour profiled at single nucleotide resolution. *Nature* **461,** 809–813 (2009).
10. Sjoblom, T. *et al.* The consensus coding sequences of human breast and colorectal cancers. *Science* **314,** 268–274 (2006).
11. Mullighan, C. G. *et al.* JAK mutations in high-risk childhood acute lymphoblastic leukemia. *Proc. Natl Acad. Sci. USA* **106,** 9414–9418 (2009).
12. Kamal, M. *et al.* Loss of CSMD1 expression is associated with high tumour grade and poor survival in invasive ductal breast carcinoma. *Breast Cancer Res. Treat.* doi: 10.1007/s10549-009-0500-4 (2009).
13. Toomes, C. *et al.* The presence of multiple regions of homozygous deletion at the CSMD1 locus in oral squamous cell carcinoma question the role of CSMD1 in head and neck carcinogenesis. *Genes Chromosom. Cancer* **37,** 132–140 (2003).
14. Stephens, P. *et al.* A screen of the complete protein kinase gene family identifies diverse patterns of somatic mutations in human breast cancer. *Nature Genet.* **37,** 590–592 (2005).
15. Gandara, M. L., Lopez, P., Hernando, R., Castano, J. G. & Alemany, S. The COOH-terminal domain of wild-type Cot regulates its stability and kinase specific activity. *Mol. Cell. Biol.* **23,** 7377–7390 (2003).
16. Clark, A. M., Reynolds, S. H., Anderson, M. & Wiest, J. S. Mutational activation of the MAP3K8 protooncogene in lung cancer. *Genes Chromosom. Cancer* **41,** 99–108 (2004).
17. Sacco, F. *et al.* Tumor suppressor density-enhanced phosphatase-1 (DEP-1) inhibits the RAS pathway by direct dephosphorylation of ERK1/2 kinases. *J. Biol. Chem.* **284,** 22048–22058 (2009).
18. Ng, P. C. & Henikoff, S. SIFT: Predicting amino acid changes that affect protein function. *Nucleic Acids Res.* **31,** 3812–3814 (2003).
19. Hong, J. H. *et al.* TAZ, a transcriptional modulator of mesenchymal stem cell differentiation. *Science* **309,** 1074–1078 (2005).
20. Chan, S. W. *et al.* A role for TAZ in migration, invasion, and tumorigenesis of breast cancer cells. *Cancer Res.* **68,** 2592–2598 (2008).
21. Chen, K. *et al.* BreakDancer: an algorithm for high-resolution mapping of genomic structural variation. *Nature Methods* **6,** 677–681 (2009).
22. Zhang, W. & Koepp, D. M. Fbw7 isoform interaction contributes to cyclin E proteolysis. *Mol. Cancer Res.* **4,** 935–943 (2006).
23. Mao, J. H. *et al.* FBXW7 targets mTOR for degradation and cooperates with PTEN in tumor suppression. *Science* **321,** 1499–1502 (2008).
24. Welcker, M. & Clurman, B. E. FBW7 ubiquitin ligase: a tumour suppressor at the crossroads of cell division, growth and differentiation. *Nature Rev. Cancer* **8,** 83–93 (2008).
25. Bajpai, S., Feng, Y., Krishnamurthy, R., Longmore, G. D. & Wirtz, D. Loss of α-catenin decreases the strength of single E-cadherin bonds between human cancer cells. *J. Biol. Chem.* **284,** 18252–18259 (2009).
26. Plumb, C. L. *et al.* Modulation of the tumor suppressor protein α-catenin by ischemic microenvironment. *Am. J. Pathol.* **175,** 1662–1674 (2009).
27. Mardis, E. R. *et al.* Recurring mutations found by sequencing an acute myeloid leukemia genome. *N. Engl. J. Med.* **361,** 1058–1066 (2009).
28. Ley, T. J. *et al.* DNA sequencing of a cytogenetically normal acute myeloid leukaemia genome. *Nature* **456,** 66–72 (2008).
29. Wood, L. D. *et al.* The genomic landscapes of human breast and colorectal cancers. *Science* **318,** 1108–1113 (2007).
30. Krzywinski, M. *et al.* Circos: an information aesthetic for comparative genomics. *Genome Res.* **19,** 1639–1645 (2009).

Supplementary Information is linked to the online version of the paper at www.nature.com/nature.

Acknowledgements We thank the many members of The Genome Center and Siteman Cancer Center at Washington University in St Louis for support. This work was funded by grants to R.K.W. from Washington University in St Louis and the National Human Genome Research Institute (NHGRI U54 HG003079), and grants to M.J.E. from the National Cancer Institute (NCI 1 U01 CA114722-01), the Susan G Komen Breast Cancer Foundation (BCTR0707808), and the Fashion Footwear Charitable Foundation, Inc. NCI U10 CA076001 and a Breast Cancer Research Foundation grant awarded to the American College of Surgeons Oncology Group supported the acquisition of samples for recurrence testing. The tissue procurement core was supported by an NCI core grant to the Siteman Cancer Center (NCI 3P50 CA68438). The Human and Mouse Linked Evaluation of Tumors Core was supported by the Institute of Clinical and Translational Sciences at Washington University (CTSA grant UL1 RR024992). We also thank Illumina, Inc. for their support and role in the Washington University Cancer Genome Initiative.

Author Contributions E.R.M., L.D., R.S.F., M.J.E., T.J.L. and R.K.W. designed the experiments. L.D. and M.J.E. led data analysis. L.D., D.E.L., K.C., J.W.W., C.C.H., M.D.M., D.C.K., Q.Z., H.S., J.K., L.C., L.L., M.C.W., N.D.D., D.S., D.M.T., J.L.I., P.J.G., J.S.H., W.S., G.M.W. and Y.T. performed data analysis. D.E.L., C.C.H., J.W.W., J.F.M. and L.D. prepared figures and tables. R.S.F., L.L.F., R.M.A., J.H., K.D.D., C.C.F., K.A.P., J.S.Re., J.S.Ro., V.J.M., L.C., S.D.M., T.L.V., E.A., K.D., S.D., T.G., L.L., R.C., J.E.S., D.P.L., M.E.W., M.C., G.E., M.D.M., D.M.T., J.L.I. and P.J.G. performed laboratory experiments. S.L. and M.J.E. created the xenograft line. M.J.E., M.W. and R.A. provided samples. D.J.D., S.M.S., A.F.D., G.E.S., C.S.P., J.M.E., J.B.P., B.J.O., J.T.L., F.D., A.E.H., M.D.O. and K.E.B. provided informatics support. L.D., M.J.E., E.R.M. and R.K.W. wrote the manuscript. T.J.L., D.E.L., M.C.W., D.C.K. and C.M.P. critically read and commented on the manuscript.

Author Information The sequence data and high-quality variants have been deposited in the dbGaP database under the accession number phs000245.v1.p1. Reprints and permissions information is available at www.nature.com/reprints. The authors declare no competing financial interests. Correspondence and requests for materials should be addressed to R.K.W. (rwilson@wustl.edu).

Vol 464|15 April 2010|doi:10.1038/nature08943

ARTICLES

Molecular basis of infrared detection by snakes

Elena O. Gracheva[1]*, Nicholas T. Ingolia[2,3,4]*, Yvonne M. Kelly[1], Julio F. Cordero-Morales[1], Gunther Hollopeter[1]†, Alexander T. Chesler[1], Elda E. Sánchez[5], John C. Perez[5], Jonathan S. Weissman[2,3,4] & David Julius[1,2]

Snakes possess a unique sensory system for detecting infrared radiation, enabling them to generate a 'thermal image' of predators or prey. Infrared signals are initially received by the pit organ, a highly specialized facial structure that is innervated by nerve fibres of the somatosensory system. How this organ detects and transduces infrared signals into nerve impulses is not known. Here we use an unbiased transcriptional profiling approach to identify TRPA1 channels as infrared receptors on sensory nerve fibres that innervate the pit organ. TRPA1 orthologues from pit-bearing snakes (vipers, pythons and boas) are the most heat-sensitive vertebrate ion channels thus far identified, consistent with their role as primary transducers of infrared stimuli. Thus, snakes detect infrared signals through a mechanism involving radiant heating of the pit organ, rather than photochemical transduction. These findings illustrate the broad evolutionary tuning of transient receptor potential (TRP) channels as thermosensors in the vertebrate nervous system.

Venomous pit vipers detect warm-blooded prey through their ability to sense infrared (750 nm–1 mm wavelength) radiation. Superimposition of thermal and visual images within the snake's brain enables it to track animals with great precision and speed. Biophysical studies suggest that this system is exquisitely sensitive, such that vipers can detect prey at distances of up to 1 m. Infrared sensation may also be important for predator avoidance and thermoregulatory behaviour[1–3].

The western diamondback rattlesnake (*Crotalus atrox*) is a highly evolved viper whose ability to detect infrared radiation is unmatched by other snakes. Infrared detection is mediated by specialized loreal pit organs located between the eye and nostril on either side of the viper's face (Fig. 1a)[4]. Suspended within each of these hollow chambers is a thin membrane that serves as an infrared antenna (Fig. 1b). The membrane is rich in mitochondria, highly vascularized, and densely innervated by primary afferent nerve fibres from the trigeminal branch of the somatosensory system (Supplementary Fig. 1a)[5–8]. These fibres convey infrared signals from the pit organ to the optic tectum of the brain, where they converge with input from other sensory modalities[9–11]. Some members of the non-venomous *Pythonidae* and *Boidae* families (pythons and boas, respectively) also detect infrared radiation, albeit with 5–10-fold lower sensitivity than *Crotalinae* vipers[3,12,13]. Pythons and boas possess labial pit organs, which are distributed over the snout and lack the complex architecture seen in loreal pits of vipers (Supplementary Fig. 1b). Nonetheless, they are similarly vascularized and innervated by trigeminal fibres, but at lower density[5,14–16]. Thus, relative sensitivities of these snake species to infrared radiation probably reflect molecular and anatomical differences of this specialized sensory system. Although the role of the pit organ as an infrared sensor is well established, fundamental questions remain about its mechanism of stimulus detection. For example, it is unclear whether the membrane itself contains the infrared sensor, or whether the sensor is expressed by the closely apposed nerve fibres. Moreover, the molecular identity of the infrared sensor is unknown, and thus how its intrinsic biophysical characteristics account for the physiological properties of the pit organ has yet to

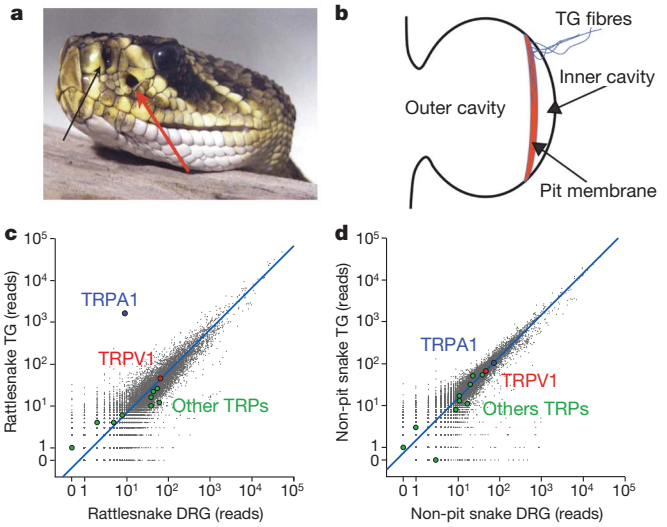

Figure 1 | Anatomy of the pit organ and comparison of gene expression in snake sensory ganglia. a, Rattlesnake head showing location of nostril and loreal pit organ (black and red arrows, respectively) (from Wikimedia Commons). **b**, Schematic of pit organ structure showing innervation of pit membrane suspended within hollow cavity. **c**, **d**, Number of mRNA-Seq reads from snake ganglia that align to the chicken proteome. TRPA1 and TRPV1 are highlighted, as are other TRP channels. Blue line indicates expected number of sequencing reads for genes with similar expression levels in the two samples based on the total number of aligned reads from each. Signals <20 reads are within statistical noise and therefore scored as non-expressed sequences. Rattlesnake refers to *C. atrox* (**c**), non-pit refers to a combination of Texas rat (*Elaphe obsoleta lindheimeri*) and western coachwhip (*Masticophis flagellum testaceus*) snakes (**d**).

[1]Department of Physiology, [2]Department of Cellular and Molecular Pharmacology, [3]Howard Hughes Medical Institute, [4]California Institute for Quantitative Biosciences, University of California, San Francisco, California 94158-2517, USA. [5]Natural Toxins Research Center, Texas A&M University- Kingsville, Texas 78363, USA. †Present address: Department of Biology, University of Utah, 257 South 1400 East, Salt Lake City, Utah 84112-0840, USA.
*These authors contributed equally to this work.

be established. Also at issue is whether *Crotalinae*, *Pythonidae* and *Boidae* snakes use similar molecular strategies for sensing infrared radiation.

In principle, an infrared receptor could detect photons directly, similar to photochemical activation of opsins in the eye, or indirectly through heating of tissue within the pit, leading to activation of a thermoreceptor[1]. Because the pit receives direct input from the somatosensory, rather than the visual system[9], it seems likely that infrared signals are detected through a thermotransduction, rather than a phototransduction mechanism. Consistent with this, heat-activated membrane currents from rattlesnake trigeminal neurons have been described, although their functional properties have not been extensively characterized[6,17].

Snakes, particularly pit vipers, are inconvenient subjects for physiological and behavioural studies. They are also genetically intractable organisms for which annotated genomic information is scarce, limiting molecular studies of infrared detection. We therefore used transcriptome profiling to identify pit-enriched sensory transducers, yielding the snake orthologue of the 'wasabi receptor', TRPA1, as a candidate infrared detector. This channel is highly enriched in trigeminal neurons that innervate the pit and, when heterologously expressed, exhibits robust heat-sensitivity. Thus, TRPA1 has been evolutionarily selected to function as a specialized and highly sensitive heat receptor in the pit, whereas in mammals it functions primarily as a detector of chemical irritants and inflammatory agents[18]. Our results demonstrate that the pit membrane serves as a passive antenna for radiant heat, transducing thermal energy to heat-sensitive channels on embedded nerve fibres.

Exploiting specialization of pit vipers

In most sensory systems, specialized receptor cells detect relevant stimuli and transmit signals to adjacent nerve fibres. In the somatosensory system, however, bare nerve endings are themselves detectors of thermal, mechanical or chemical stimuli[19]. Indeed, trigeminal ganglia (TG) of pit-bearing snakes are unusually large compared to those of mammals, and send a thick bundle of afferents directly to the pit on the ipsilateral side of the face (Supplementary Fig. 1a)[20,21]. We therefore reasoned that snake TG should express proteins dedicated to pit function, and that such proteins should be less abundant in dorsal root ganglia (DRG), which provide somatosensory input to the trunk. Because mammalian TG and DRG gene expression profiles are more-or-less equivalent[22,23], marked differences in snakes should reflect functional specialization associated with infrared detection. Remarkably, a pair-wise comparison of transcriptomes from rattlesnake TG versus DRG highlighted a single gene encoding an orthologue of the TRPA1 ion channel (Fig. 1c). Whereas other members of the TRP channel family (for example, the capsaicin- and heat-activated receptor, TRPV1) showed equivalent expression in these ganglia, TRPA1 was enriched 400-fold in TG.

If TRPA1 is of unique functional importance to infrared sensing, then snakes lacking pit organs (non-pit species) should not show a disparity in TRPA1 expression between TG and DRG. Indeed, transcriptomes from two non-pit species—Texas rat and western coachwhip snakes—showed no obvious outliers for either ganglion (Fig. 1d). Consistent with this, transcriptome comparison from TG of rattlesnake versus non-pit snakes again identified *TRPA1* as the only differentially expressed gene (Supplementary Fig. 1c). In stark contrast to non-pit snakes and other vertebrates, *TRPA1* transcripts were absent from rattlesnake DRG (Supplementary Fig. 1d), further supporting a specific role for this channel in TG/pit function. Lastly, we did not detect opsin-like sequences in TG of any snake species examined.

Unique expression of TRPA1 in viper TG

Vertebrate somatosensory ganglia contain anatomically and functionally diverse neuronal subpopulations[24]. In general, neurons having the largest soma diameters are involved in the detection of innocuous sensations, such as light touch, whereas small to medium diameter neurons constitute most nociceptors that detect noxious stimuli. In mammals, TRPA1 is expressed by ~25% of all somatosensory neurons, preferentially nociceptors that also express TRPV1 (refs 25, 26). We observed a very different anatomical profile in rattlesnakes, where most TG neurons were medium-to-large diameter, 59.9 ± 9.7% (mean ± s.d.) of which expressed TRPA1 (Fig. 2a, b) (also see later). Consistent with our transcriptome analysis, no TRPA1 signal was observed in rattlesnake DRG (Fig. 2a, c). We also examined the distribution of TRPV1, which in rodent TG or DRG is expressed by 40–60% of neurons, predominantly nociceptors[26,27]. In rattlesnake TG or DRG, TRPV1 was expressed by only 13 ± 4.1% or 14.5 ± 5.7% of neurons, respectively, most with small diameters (Fig. 2a, c). Thus, pit viper TG is unique among vertebrates, reflecting adaptation for infrared detection.

Snake TRPA1 is a heat-activated channel

Mammalian TRPA1 is activated by allyl isothiocyanate (AITC), the pungent agent from wasabi and other mustard plants[25,28]. AITC and other electrophilic irritants gate the channel through an unusual mechanism involving covalent modification of cysteine residues within the cytoplasmic amino terminus[29,30]. Rattlesnake and rat snake TRPA1 show 81% identity with one another and 63% identity with human TRPA1, and contain three conserved N-terminal cysteines required for activation by electrophiles (Supplementary Fig. 2). Indeed, when expressed in HEK293 cells, TRPA1 from either snake species responded to AITC, demonstrating functionality of the cloned channels (Fig. 3a).

If TRPA1 is important for infrared sensing, then it should respond to thermal stimuli in a temperature range consistent with sensitivity

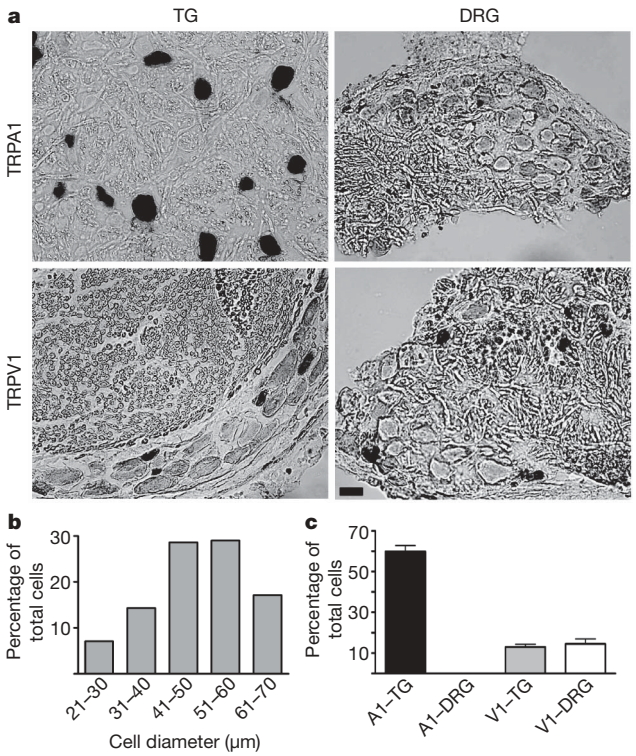

Figure 2 | Expression of TRPA1 and TRPV1 in rattlesnake sensory ganglia. **a**, *In situ* hybridization showing expression of TRPA1 or TRPV1 in tissue sections from rattlesnake TG or DRG, as indicated. Scale bar, 20 μm. **b**, Quantification of neuronal cell size (diameter) determined from histological sections of rattlesnake TG ($n = 70$ cells from five independent sections). **c**, Quantitative analysis of cells within TG or DRG that express *TRPA1* or *TRPV1* transcripts (mean ± s.d.; $n = 448$ neurons from 11 independent sections for *TRPA1*, and $n = 151$ neurons from 5 independent sections for *TRPV1*).

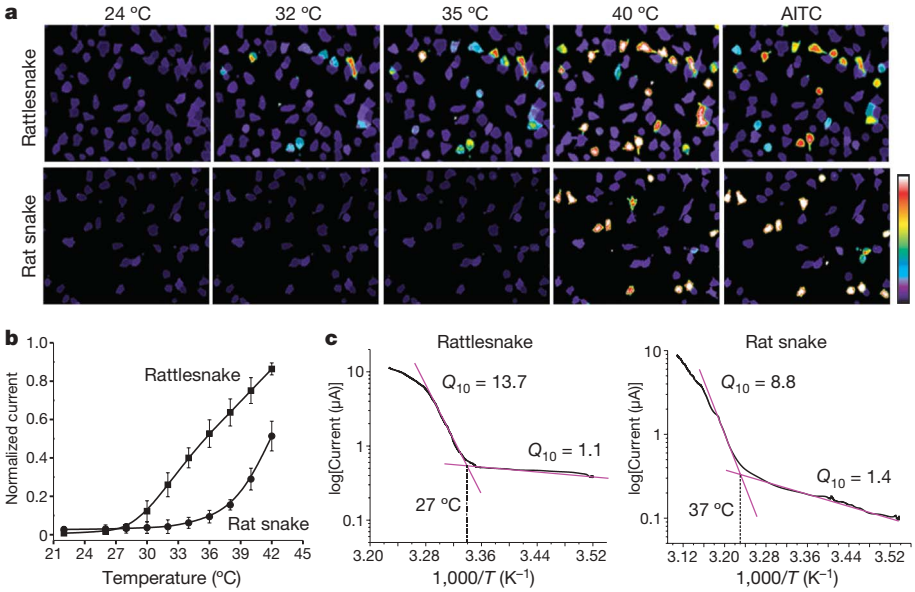

Figure 3 | Functional analysis of snake TRPA1 channels. a, HEK293 cells expressing cloned rattlesnake or rat snake TRPA1 channels were analysed for heat or mustard oil (200 μM AITC; 24 °C)-evoked responses using calcium imaging; colour bar indicates relative change in fluorescence ratio, with purple and white denoting the lowest and highest cytoplasmic calcium, respectively ($n \geq 105$ cells per channel). **b**, Relative heat response profiles of rattlesnake and rat snake channels expressed in oocytes (response at each temperature was normalized to the maximal response at 45 °C; holding potential (V_H) = −80 mV; $n \geq 6$). Data show mean ± s.d. **c**, Arrhenius plots show thermal thresholds and Q_{10} values for baseline and evoked responses of rattlesnake (left) and rat snake (right) TRPA1 channels, as indicated (temperature ramp of 1 °C s^{-1}).

of the pit, which detects changes in ambient temperature above ~30 °C (ref 17). Indeed, rattlesnake TRPA1 was inactive at room temperature, but robustly activated above 28.0 ± 2.5 °C (Fig. 3a and Supplementary Fig. 3a). Interestingly, rat snake TRPA1 was also heat-sensitive, albeit with a substantially higher threshold of 36.3 ± 0.6 °C. To assess thermal response profiles in greater detail, we measured heat-evoked membrane currents in voltage-clamped *Xenopus* oocytes expressing snake channels. Consistent with calcium imaging data, rattlesnake TRPA1 showed extremely robust and steep responses to heat with a threshold of 27.6 ± 0.9 °C (Q_{10} = 13.7), whereas the rat snake channel responded with a higher threshold of 37.2 ± 0.7 °C (Q_{10} = 8.8) (Fig. 3b, c and Supplementary Fig. 3b). Thus, although the rat snake channel is heat-sensitive, its thermal response properties make it less well suited to act as an infrared sensor than the pit viper channel. Instead, TRPA1, in conjunction with TRPV1, may contribute to cutaneous and somatic thermosensation in non-pit snakes, consistent with the higher activation thresholds of rat snake versus rattlesnake TRPA1. The rattlesnake channel did not respond to cold (12 °C) (not shown).

TRPA1 channels have been characterized from several vertebrate species, including fish[31], all of which are activated by AITC, but not heat (Supplementary Fig. 4). TRPA1-like channels are also found in invertebrate organisms, including *Drosophila melanogaster*, whose genome contains three *TRPA1* orthologues. One of these (d*TrpA1*) is heat-sensitive[32,33], and in our experimental conditions shows a thermal threshold of 33.7 ± 1.0 °C (Supplementary Fig. 5). Relative to rat TRPA1, which responds to AITC with a half-maximum effective concentration (EC_{50}) of 11 μM, the rattlesnake and rat snake orthologues are less sensitive, showing robust responses at concentrations ≥500 μM and with significantly slower activation. The relative sensitivities of these channels to heat versus AITC are clearly shown by comparing current–voltage profiles (Supplementary Fig. 3b). This inverse relationship between heat- and AITC-sensitivity probably underscores the relative contribution of TRPA1 to thermo- versus chemosensation in different organisms. Taken together, our bioinformatics, and anatomical and functional results strongly indicate that TRPA1 serves as an infrared detector in the pit viper.

Ancient snakes use TRPA1 to sense infrared radiation

Ancient (pythons and boas) and modern (pit vipers) snakes are separated by a long evolutionary distance (>30 million years) and show substantial differences in pit architecture and sensitivity[34,35]. We therefore asked whether they use the same molecule to detect heat. In sensory ganglia of royal python (*Python regius*) and amazon tree boa (*Corallus hortulanus*), *TRPA1*, again, stood out as the major differentially expressed transcript, being 65- and 170-fold more abundant in TG than DRG for pythons and boas, respectively (Fig. 4a, b). Moreover, comparison of transcript ratios from rattlesnake and python showed that TRPA1 stands alone as a highly TG-specific molecule (Supplementary Fig. 6a). In contrast to pit vipers, TRPA1 was expressed in DRG of python and boa, but only at relatively modest levels, comparable to that of other TRP channels. Surprisingly, *TRPV1* transcripts were not observed above background levels in pythons (Fig. 4a), suggesting that TRPA1 or another heat-sensitive channel underlies somatic thermosensation in this species.

Dendrogram analysis of snake TRPA1 channels shows that they constitute a closely related subfamily of heat-sensitive orthologues (Fig. 4c). Moreover, the position of boa and python sequences supports the hypothesis that these species represent an evolutionarily ancient branch of snakes that is independent of modern snakes such as pit vipers or rat snakes.

Expression of cloned python and boa TRPA1 in oocytes showed that both are heat-activated channels with modest sensitivity to AITC (Fig. 4d and Supplementary Fig. 6b, c). Interestingly, we found that python and boa channels exhibited a slightly higher thermal threshold compared to rattlesnake TRPA1 (32.7 ± 1.3 °C and 29.6 ± 0.7 °C, respectively, versus 27.6 ± 0.9 °C for rattlesnake), consistent with differential sensitivity of these snakes to infrared radiation. As in the case of the rattlesnake channel, python and boa TRPA1 were substantially more sensitive to heat than chemical agonists, as evidenced by relatively small responses to AITC (Supplementary Fig. 6b, c).

Endogenous TRPA1 subserves infrared detection

To assess the contribution of TRPA1 to neuronal heat sensitivity, we chose pythons as a convenient (that is, non-venomous) pit-bearing

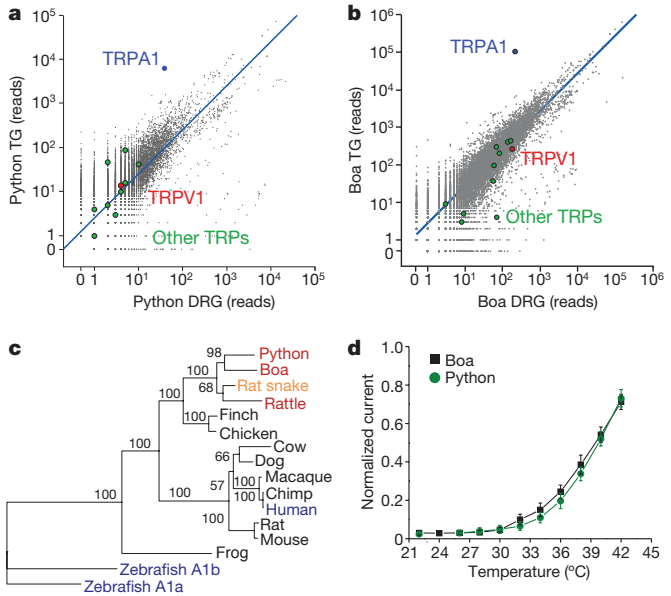

Figure 4 | Analysis of TRPA1 from python and boa. **a**, **b**, Transcriptome profiling of ancient snakes. Number of mRNA-Seq reads from python (**a**) and boa (**b**) ganglia that align to the chicken proteome, as described in Fig. 1. **c**, Phylogenetic tree of TRPA1 channel protein sequences with bootstrap values from 100 trials. Red denotes heat-sensitive channels with a lower thermal threshold than rat snake (orange). Blue indicates non-heat-sensitive channels according to this study. **d**, Relative heat response profiles for python and boa TRPA1 as measured in oocytes (recorded and normalized as described in Fig. 3b). Data show mean ± s.d.

species for functional studies. Anatomically, python TG resemble those of rattlesnakes, consisting primarily of large and medium diameter neurons, most of which (73.1 ± 7.8%) express TRPA1 (Fig. 5a and Supplementary Fig. 7a, b). Consistent with this, most (78.2 ± 14.0%) neurons from python TG were heat-sensitive and exhibited a threshold of 28.0 ± 2.2 °C (Fig. 5b). Moreover, all heat-sensitive neurons responded to 500 μM AITC (not shown), confirming expression of functional TRPA1 channels in these cells. No capsaicin-sensitive neurons were observed in python TG cultures, consistent with our bioinformatics profile showing lack of TRPV1 in these ganglia.

TG from control rat snake more closely resembled those of mammals in the relative proportion of small, medium and large diameter neurons. Compared to pit-bearing species, TRPA1 was expressed by a restricted cohort (13.3 ± 5.7%) of rat snake TG neurons that included mostly small and medium diameter cells (Fig. 5a and Supplementary Fig. 7a). Unlike pythons, rat snake TG contained a considerable proportion (27.3 ± 4.4%) of TRPV1-positive neurons (Supplementary Fig. 7a), suggesting that both TRPA1 and TRPV1 contribute to heat sensation in this species. Neurons from rat snake TG also showed a lower prevalence (~20%) of heat- and AITC-sensitivity compared to pythons, and responders were confined to the medium/small diameter subpopulation (Supplementary Fig. 7b). Notably, rat snake neurons responded at higher temperatures, binning into two distinct populations with thresholds of 36.2 ± 1.8 °C and 38.7 ± 1.4 °C ($P < 0.025$), the former being AITC-sensitive and the latter being capsaicin-sensitive (Fig. 5b and Supplementary Fig. 7c). Taken together, our results indicate that TRPA1 underlies infrared and somatic heat sensation in pit-bearing snakes, whereas TRPA1 and TRPV1 contribute to somatic thermosensation in rat

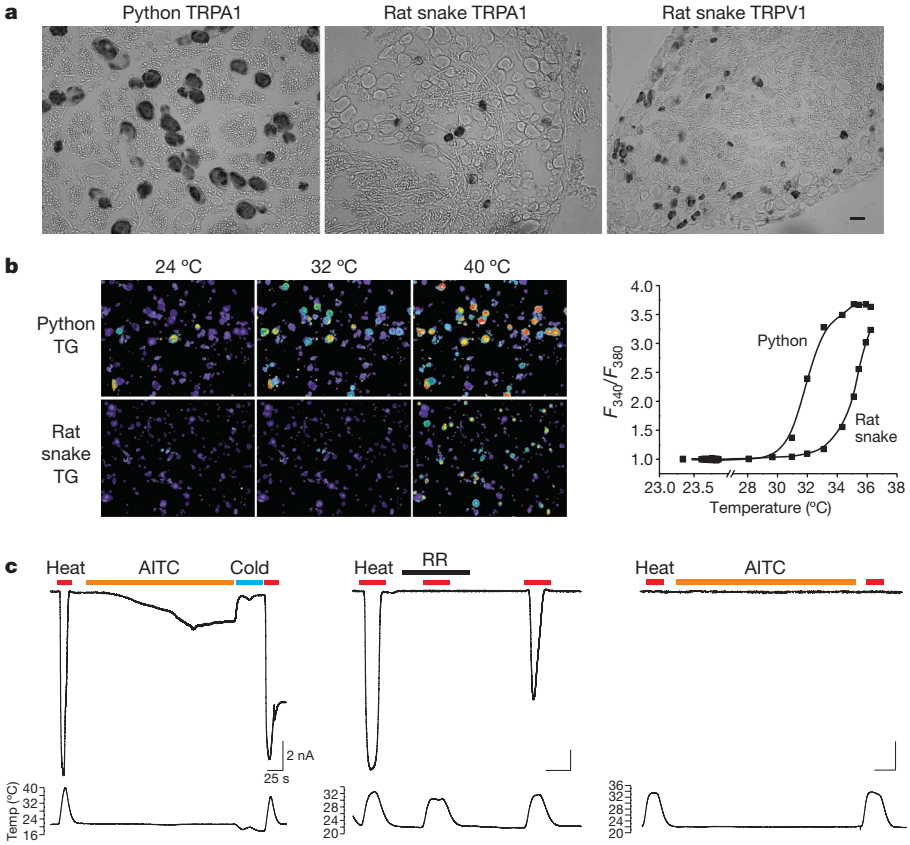

Figure 5 | Functional analysis of snake sensory neurons. **a**, Expression of TRPA1 or TRPV1 transcripts in python and rat snake TG. Scale bar, 40 μm. **b**, Thermal sensitivity of python and rat snake TG neurons as measured by calcium imaging. Temperature ramps (24 to 46 °C) were applied by continuous perfusion to assess thresholds (colour scale as in Fig. 3a). Corresponding temperature-response profiles are shown at the right ($n = 5$ and 26 neurons, respectively). Thresholds (28.0 ± 0.7 and 36.2 ± 0.6; $P < 0.0001$) were determined from an average of 43 and 89 neurons from python and rat snake, respectively (10 independent fields each). **c**, Patch-clamp recordings from python neurons showing robust heat- and AITC-evoked currents that were suppressed by cold (left) and blocked by ruthenium red (RR, 10 μM) (centre) ($n > 45$). A minority of neurons was insensitive to heat and AITC (right) ($n > 8$).

snakes. Furthermore, the functional properties and tissue distribution of rattlesnake TRPV1 (Supplementary Fig. 8 and Fig. 2a, c) make it a likely candidate for mediating somatic thermosensation in this species.

Finally, patch-clamp recording verified the presence of heat-sensitive membrane currents in snake neurons. Most python TG neurons showed enormous heat-evoked currents bearing the hallmarks of TRPA1 channels, including blockade by ruthenium red, inward rectification, and desensitization (Fig. 5c and Supplementary Fig. 7d). Like heterologously expressed python TRPA1, these responses were attenuated (~50%) by the mammalian TRPA1 antagonist HC-030031 (not shown). Consistent with our calcium imaging results, heat-sensitive python TG neurons also responded to AITC and showed a thermal threshold of $29.5 \pm 1.7\ ^{\circ}C$. A more restricted population of medium diameter neurons were insensitive to heat or AITC (Fig. 5c), although they showed robust action potential firing after depolarization (not shown). In contrast with pythons, the activation threshold for heat-sensitive rat snake neurons was substantially higher ($35.6 \pm 1.2\ ^{\circ}C$) (Supplementary Fig. 7d).

Discussion

Four vertebrate families possess specialized sensory organs devoted to the detection of infrared radiation: pit viper, python, and boa families of snakes, as well as vampire bats[2,36]. Here we delineate the mechanism whereby three of these families sense infrared radiation, starting with the pit viper as the paragon of this unique sensory modality. We accomplished this by taking an unbiased transcriptome profiling approach in which minimal assumptions were made about the molecular specialization of the pit and associated neural structures. This represents a powerful, sensitive and quantitative version of the classic plus–minus screen for identifying organ-specific genes. We exploited this technology to address a problem vexed by a paucity of tissue and lack of genomic information.

In vertebrates, temperature sensation is mediated through activation of TRP channels that detect heat or cold[37]. In invertebrate organisms, such as flies (*Drosophila*), activation of TRP channels also contributes to temperature detection[32,33], whereas in worms (*Caenorhabditis elegans*), thermosensation is suggested to involve a phototransduction-like pathway involving activation of cyclic nucleotide-gated channels[38,39]. Our analysis suggests that the pit organ detects infrared radiation through a TRP channel-based process, rather than an opsin-like pathway, consistent with thermal, rather than photochemical signal transduction.

Identification of snake TRPA1 as an infrared sensor is interesting from an evolutionary perspective because previously identified vertebrate TRPA1 orthologues function primarily as detectors of chemical irritants[18], and possibly cold[40,41]. Thus, snake TRPA1 is functionally more like its invertebrate counterparts, despite their greater sequence diversity. Recent observations suggest that among TRP channels, TRPA1 orthologues show particularly rapid evolution in invertebrate species, where they display a range of heat sensitivities and contribute differentially to thermosensation[42,43]. Our findings indicate that this functional diversification extends to vertebrate channels, as well. Although the evolutionary relationship among snake species is a subject of continuing study and debate[34,44], our phylogenetic analysis indicates that ancient and modern snakes have independently adapted TRPA1 as an infrared sensor through convergent evolution. The cloned rattlesnake channel is the most heat-sensitive (that is, lowest thermal activation threshold and highest Q_{10}), in keeping with the greater infrared acuity of pit vipers compared to pythons or boas[3]. At the same time, differences in thermosensitivity among snake TRPA1 channels can differ by as little as $2\ ^{\circ}C$ (for example, rattlesnake versus boa), suggesting that other cellular or anatomical factors contribute to physiological and behavioural differences in stimulus detection. Finally, the relative contributions of TRPA1 and other heat-sensitive channels (such as TRPV1) to somatic thermosensation probably differ among snake species, depending on thermal thresholds and expression patterns.

Sensory systems evolve rapidly to accommodate variations in environmental niche, such as those affecting climate and predator–prey relationships[45,46]. TRPA1 channels have undergone particularly fascinating evolutionary perturbation and selection to function as thermo- or chemoreceptors in organisms of very different lineage, indicative of their unique physiological plasticity throughout the animal kingdom. Thus, TRPA1 and other TRP channels provide new genetic and physiological markers with which to delineate evolutionary relationships among vertebrate and invertebrate species.

METHODS SUMMARY

Complementary DNA libraries were sequenced on Illumina Genome Analyser II and aligned to chicken RefSeq protein database. The unrooted phylogenetic tree was constructed from multiple sequence alignments using PhyML (version 3.0). Bootstrapping was performed with 100 trials. Adult snake tissue was fixed with paraformaldehyde for chromogenic *in situ* hybridization histochemistry. Rattlesnakes were provided by the Natural Toxins Research Center, Texas A&M University-Kingsville; boas, pythons and rat snakes were obtained from Glades Herp Farm. Animal husbandry and euthanasia procedures were approved by the University of California, San Francisco (UCSF) or University of Texas Institutional Animal Care and Use Committee. Cloned channels were transiently expressed in HEK293 cells and subjected to calcium imaging using Fura-2/AM ratiometric dye. Snake TG neurons were cultured as previously described[17]. Oocytes from *Xenopus laevis* were cultured, injected with 5 ng RNA, and analysed 2–5 days after injection by two-electrode voltage-clamp (TEVC) as described[47]. Membrane currents were recorded under the whole-cell patch-clamp configuration and thermal stimulation applied with a custom-made Peltier device (Reid-Dan Electronics). Temperature thresholds represent the point of intersection between linear fits to baseline and the steepest component of the Arrhenius profile, as described[48].

Full Methods and any associated references are available in the online version of the paper at www.nature.com/nature.

Received 23 September 2009; accepted 24 February 2010.
Published online 14 March; corrected 15 April 2010 (see full-text HTML version for details).

1. Bullock, T. H. & Cowles, R. B. Physiology of an infrared receptor: the facial pit of pit vipers. *Science* **115,** 541–543 (1952).
2. Campbell, A. L., Naik, R. R., Sowards, L. & Stone, M. O. Biological infrared imaging and sensing. *Micron* **33,** 211–225 (2002).
3. Ebert, J. *Infrared Sense in Snakes – Behavioural and Anatomical Examinations* (Crotalus atrox, Python regius, Corallus hortulanus). Dr rer. nat. thesis, Rheinische Friedrich Wilhelms Univ. Bonn (2007).
4. Barrett, R., Maderson, P. F. A. & Meszler, R. M. in *Biology of Reptilia* (ed. Parsons, T. S.) Ch. 4, 277–300 (Academic Press, 1970).
5. Ebert, J. & Schmitz, A. in *Herpetologia Bonnensis II* (eds Vences, M. Kohler, J., Ziegler T. & Bohme, W.) 215–217 (2006).
6. Terashima, S. & Liang, Y. F. Temperature neurons in the crotaline trigeminal ganglia. *J. Neurophysiol.* **66,** 623–634 (1991).
7. Amemiya, F., Ushiki, T., Goris, R. C., Atobe, Y. & Kusunoki, T. Ultrastructure of the crotaline snake infrared pit receptors: SEM confirmation of TEM findings. *Anat. Rec.* **246,** 135–146 (1996).
8. Bleichmar, H. & De Robertis, E. Submicroscopic morphology of the infrared receptor of pit vipers. *Z. Zellforsch. Mikrosk. Anat.* **56,** 748–761 (1962).
9. Hartline, P. H., Kass, L. & Loop, M. S. Merging of modalities in the optic tectum: infrared and visual integration in rattlesnakes. *Science* **199,** 1225–1229 (1978).
10. Newman, E. A. & Hartline, P. H. Integration of visual and infrared information in bimodal neurons in the rattlesnake optic tectum. *Science* **213,** 789–791 (1981).
11. Molenaar, G. J. The sensory trigeminal system of a snake in the possession of infrared receptors. II. The central projections of the trigeminal nerve. *J. Comp. Neurol.* **179,** 137–151 (1978).
12. de Cock Buning, T., Terashima, S. & Goris, R. C. Python pit organs analyzed as warm python pit organs analyzed as warm receptors. *Cell. Mol. Neurobiol.* **1,** 271–278 (1981).
13. Warren, J. W. & Proske, U. Infrared receptors in the facial pits of the Australian python Morelia spilotes. *Science* **159,** 439–441 (1968).
14. Kishida, R., Amemiya, F., Kusunoki, T. & Terashima, S. A new tectal afferent nucleus of the infrared sensory system in the medulla oblongata of Crotaline snakes. *Brain Res.* **195,** 271–279 (1980).
15. Kishida, R., de Cock Buning, T. & Dubbeldam, J. L. Primary vagal nerve projections to the lateral descending trigeminal nucleus in boidae (*Python molurus* and *Boa constrictor*). *Brain Res.* **263,** 132–136 (1983).
16. Noble, G. K. & Schmidt, A. The structure and function of facial and labial pits of snakes. *Proc. Am. Phil. Soc.* **77,** 263–288 (1937).

17. Pappas, T. C., Motamedi, M. & Christensen, B. N. Unique temperature-activated neurons from pit viper thermosensors. *Am. J. Physiol. Cell Physiol.* **287,** C1219–C1228 (2004).
18. Bautista, D. M. *et al.* TRPA1 mediates the inflammatory actions of environmental irritants and proalgesic agents. *Cell* **124,** 1269–1282 (2006).
19. Julius, D. & Basbaum, A. I. Molecular mechanisms of nociception. *Nature* **413,** 203–210 (2001).
20. Molenaar, G. J. An additional trigeminal system in certain snakes possessing infrared receptors. *Brain Res.* **78,** 340–344 (1974).
21. Schroeder, D. M. & Loop, M. S. Trigeminal projections in snakes possessing infrared sensitivity. *J. Comp. Neurol.* **169,** 1–13 (1976).
22. Eng, S. R., Dykes, I. M., Lanier, J., Fedtsova, N. & Turner, E. E. POU-domain factor Brn3a regulates both distinct and common programs of gene expression in the spinal and trigeminal sensory ganglia. *Neural Dev.* **2,** 3 (2007).
23. Su, A. I. *et al.* A gene atlas of the mouse and human protein-encoding transcriptomes. *Proc. Natl Acad. Sci. USA* **101,** 6062–6067 (2004).
24. Woolf, C. J. & Ma, Q. Nociceptors–noxious stimulus detectors. *Neuron* **55,** 353–364 (2007).
25. Jordt, S. E. *et al.* Mustard oils and cannabinoids excite sensory nerve fibres through the TRP channel ANKTM1. *Nature* **427,** 260–265 (2004).
26. Kobayashi, K. *et al.* Distinct expression of TRPM8, TRPA1, and TRPV1 mRNAs in rat primary afferent neurons with aδ/c-fibers and colocalization with trk receptors. *J. Comp. Neurol.* **493,** 596–606 (2005).
27. Tominaga, M. *et al.* The cloned capsaicin receptor integrates multiple pain-producing stimuli. *Neuron* **21,** 531–543 (1998).
28. Bandell, M. *et al.* Noxious cold ion channel TRPA1 is activated by pungent compounds and bradykinin. *Neuron* **41,** 849–857 (2004).
29. Macpherson, L. J. *et al.* Noxious compounds activate TRPA1 ion channels through covalent modification of cysteines. *Nature* **445,** 541–545 (2007).
30. Hinman, A., Chuang, H. H., Bautista, D. M. & Julius, D. TRP channel activation by reversible covalent modification. *Proc. Natl Acad. Sci. USA* **103,** 19564–19568 (2006).
31. Prober, D. A. *et al.* Zebrafish TRPA1 channels are required for chemosensation but not for thermosensation or mechanosensory hair cell function. *J. Neurosci.* **28,** 10102–10110 (2008).
32. Hamada, F. N. *et al.* An internal thermal sensor controlling temperature preference in *Drosophila*. *Nature* **454,** 217–220 (2008).
33. Viswanath, V. *et al.* Opposite thermosensor in fruitfly and mouse. *Nature* **423,** 822–823 (2003).
34. Krochmal, A. R., Bakken, G. S. & LaDuc, T. J. Heat in evolution's kitchen: evolutionary perspectives on the functions and origin of the facial pit of pitvipers (Viperidae: Crotalinae). *J. Exp. Biol.* **207,** 4231–4238 (2004).
35. Safer, A. B. & Grace, M. S. Infrared imaging in vipers: differential responses of crotaline and viperine snakes to paired thermal targets. *Behav. Brain Res.* **154,** 55–61 (2004).
36. Kishida, R., Goris, R. C., Terashima, S. & Dubbeldam, J. L. A suspected infrared-recipient nucleus in the brainstem of the vampire bat, *Desmodus rotundus*. *Brain Res.* **322,** 351–355 (1984).
37. Jordt, S. E., McKemy, D. D. & Julius, D. Lessons from peppers and peppermint: the molecular logic of thermosensation. *Curr. Opin. Neurobiol.* **13,** 487–492 (2003).
38. Komatsu, H., Mori, I., Rhee, J. S., Akaike, N. & Ohshima, Y. Mutations in a cyclic nucleotide-gated channel lead to abnormal thermosensation and chemosensation in *C. elegans*. *Neuron* **17,** 707–718 (1996).
39. Ramot, D., MacInnis, B. L. & Goodman, M. B. Bidirectional temperature-sensing by a single thermosensory neuron in *C. elegans*. *Nature Neurosci.* **11,** 908–915 (2008).
40. Story, G. M. *et al.* ANKTM1, a TRP-like channel expressed in nociceptive neurons, is activated by cold temperatures. *Cell* **112,** 819–829 (2003).
41. Caspani, O. & Heppenstall, P. A. TRPA1 and cold transduction: an unresolved issue? *J. Gen. Physiol.* **133,** 245–249 (2009).
42. Wang, G. *et al. Anopheles gambiae* TRPA1 is a heat-activated channel expressed in thermosensitive sensilla of female antennae. *Eur. J. Neurosci.* **30,** 967–974 (2009).
43. Matsuura, H., Sokabe, T., Kohno, K., Tominaga, M. & Kadowaki, T. Evolutionary conservation and changes in insect TRP channels. *BMC Evol. Biol.* **9,** 228 (2009).
44. Dong, S. & Kumazawa, Y. Complete mitochondrial DNA sequences of six snakes: phylogenetic relationships and molecular evolution of genomic features. *J. Mol. Evol.* **61,** 1432 (2005).
45. Liman, E. R. Use it or lose it: molecular evolution of sensory signaling in primates. *Pflugers Arch.* **453,** 125–131 (2006).
46. Myers, B. R., Sigal, Y. M. & Julius, D. Evolution of thermal response properties in a cold-activated TRP channel. *PLoS One* **4,** e5741 (2009).
47. Chuang, H. H., Neuhausser, W. M. & Julius, D. The super-cooling agent icilin reveals a mechanism of coincidence detection by a temperature-sensitive TRP channel. *Neuron* **43,** 859–869 (2004).
48. DeCoursey, T. E. & Cherny, V. V. Temperature dependence of voltage-gated H^+ currents in human neutrophils, rat alveolar epithelial cells, and mammalian phagocytes. *J. Gen. Physiol.* **112,** 503–522 (1998).

Supplementary Information is linked to the online version of the paper at www.nature.com/nature.

Acknowledgements We thank A. Priel for advice and assistance with calcium imaging and electrophysiology, C. Chu for help with sequencing, J. Poblete for technical assistance, and the staff of the Natural Toxins Research Center serpentarium for animal husbandry. We thank P. Garrity for providing the d*TrpA1* cDNA. This work was supported by a Ruth L. Kirschstein National Research Service Award (GM080853) (N.T.I.), a NIH Institutional Research Service Award in Molecular and Cellular Basis of Cardiovascular Disease (A.T.C.), the Howard Hughes Medical Institute (J.S.W.), and grants from the National Institutes of Health, including NCRR Viper grant P40 RR018300-06 (E.E.S. and J.C.P.), P01 AG010770 (J.S.W.) and NS047723 and NS055299 (D.J.).

Author Contributions E.O.G., J.F.C.-M. and N.T.I. designed and performed experiments and analysed data. N.T.I. and J.S.W. developed analytical tools and analysed data. Y.M.K., G.H. and A.T.C. performed experiments and/or provided reagents and analysed data. E.E.S. and J.C.P. supervised snake husbandry and handling. E.O.G., Y.M.K., J.F.C.-M. and D.J. wrote the manuscript with discussion and contributions from all authors. J.S.W. and D.J. provided advice and guidance throughout. D.J. initiated and supervised the project.

Author Information Deep sequencing data are archived under GEO accession number GSE19911. GenBank accession numbers are GU562965 (*Python regius* TRPA1), GU562966 (*Elaphe obsoleta lindheimeri* TRPA1), GU562967 (*Crotalus atrox* TRPA1), GU562968 (*Crotalus atrox* TRPV1), and GU562969 (*Corallus hortulanus* TRPA1). Reprints and permissions information is available at www.nature.com/reprints. The authors declare no competing financial interests. Correspondence and requests for materials should be addressed to D.J. (julius@cmp.ucsf.edu or david.julius@ucsf.edu).

METHODS

Deep sequencing and analysis. Sequencing libraries were prepared from poly A^+ RNA using the Illumina mRNA-Seq Sample Prep Kit according to the manufacturer's instructions. Libraries were then sequenced on the Illumina Genome Analyser II using two 36-cycle sequencing kits to read 80 nucleotides of sequence from a single end of each insert, by standard protocols. Between 2.4 and 12.5 million inserts were sequenced for each sample.

Sequences were aligned to the chicken RefSeq protein database (NCBI version 2.1) using the blastx tool from NCBI blast (version 2.2.21), which aligns a six-frame translation of each query against a protein database. The alignment was performed with a word size of four amino acids and a window size of five; a maximum E value of 1×10^{-5} was required. For each read that aligned to the chicken proteome, a set of optimal hits was collected based on alignments whose bit score was within 0.2 of the highest bit score reported for that sequencing read. Each RefSeq alignment for a given sequencing read was converted to an Entrez Gene identifier and redundant alignments for a single read (which correspond to alignments against different isoforms of the same protein) were collapsed. The number of optimally aligning reads was then counted for each gene; in some cases a single read counted towards several genes. Multiple sequence alignment was performed with MUSCLE v3.70 and the tree was built from the MSA using PhyML 3.0. The multiple sequence alignment of all TRPA1 amino acid sequences was constructed using MUSCLE (version 3.70) using the default parameters. The unrooted phylogenetic tree was constructed from this multiple sequence alignment using PhyML (version 3.0) with default parameters and maximum likelihood estimation of the gamma shape parameter and the fraction of invariant sites. Bootstrapping was performed with 100 trials.

***In situ* hybridization histochemistry.** Adult snakes were euthanized with beuthanasia-D (1 ml per 4.5 kg body weight). TG and DRG tissue were dissected and fixed in 4% paraformaldehyde in PBS for 5 days. Cryostat sections (12–15-μm thick) were processed and probed with a digoxigenin-labelled cRNA. Probes were generated by T7/T3 *in vitro* transcription reactions using a 2.9-kb fragment of *TRPA1* cDNA (nucleotides 153–3024) and 1.9-kb fragment of *TRPV1* cDNA (nucleotides 417–2387). Signal was developed with alkaline phosphatase-conjugated anti-digoxigenin Fab fragments according to the manufacturer's instructions.

Channel cloning. Functional cDNAs were amplified from single-stranded DNA, generated by reverse transcriptase reaction, using the following primers: rattlesnake *TRPA1*, non-pit *TRPA1* and royal python *TRPA1* (forward: 5′-GAAT GACCAGGAGCTGTATC-3′; reverse: 5′-AGCCAGCTTGACTGGAATTG-3′); rattlesnake *TRPV1* (forward: 5′-CAGGTGAGGTGAGTCCTTCGTAAC-3′; reverse: 5′-TGAATGACGCAGATGGGGGTC-3′).

Calcium imaging. All tested channels were transiently expressed in HEK293 cells with the use of Lipofectamin 2000 (Invitrogen), and cells were maintained in medium containing ruthenium red (3 μM). Calcium imaging of HEK293 cells using Fura-2/AM was performed on coverslips coated with Matrigel (BD). Fluorescent images were acquired with Metaflour software (Molecular Device) and analysed using Graph Pad Prism 4.

Culture of sensory neurons. Snake were anaesthetized using isofluorane and then decapitated. TGs were isolated and cultured as previously described[17]. In brief, dissected ganglia were first placed in ice-cold DMEM/F12 solution. Cells were dissociated from trigeminal ganglia by treatment with collagenase (1 mg ml^{-1}, 50 min, 28 °C) and trypsin (10 min, room temperature) followed by mechanical dissociation with plastic pipette. Dissociated cells were centrifuged at 1,000*g* for 10 min and then diluted with DMEM/F12, 10% FBS, penicillin/streptomycin and 2 mM glutamine. Cells were plated onto the Matrigel-precoated coverslips. Cells were maintained at 28 °C in 7% CO_2, 93% air for 6–48 h.

Oocyte electrophysiology. Surgically extracted oocytes from *Xenopus laevis* (Nasco) were cultured and analysed 2–5 days after injection by TEVC as previously described[47]. Oocytes were injected with 5 ng RNA and whole-cell currents measured after 24–72 h using a Geneclamp 500 amplifier (Axon Instruments, Inc.). Microelectrodes were pulled from borosilicate glass capillary tubes to obtain resistances of 0.3–0.07 MΩ. Bath solution contained 10 mM HEPES, 120 mM NaCl, 2 mM KCl, 0.2 mM EGTA, 1 mM $CaCl_2$ and 2 mM $MgCl_2$ buffered to a final pH of 7.4 with NaOH. Data were analysed using pCLAMP10 software.

Patch-clamp recording. Membrane currents were recorded using gap free protocol at −60 mV under the whole-cell configuration of the patch-clamp technique using Axopatch 200B amplifier (Axon Instruments). Membrane currents were digitized online using a Digidata 1440A interface board and pCLAMP 10.2 software (Axon Instruments). Sampling frequency was set to 5 kHz, and the low-pass filter was set to 1 kHz. Patch electrodes were fabricated from borosilicate glass with a resistance of 2–4 MΩ. The bath solution contained (mM): 130 NaCl, 3 KCl, 1.2 $MgSO_4$, 2 $CaCl_2$, 10 HEPES, 10 glucose, adjusted to pH 7.4. The perfusion solution was the same as the bath solution but with 0.2 mM $CaCl_2$ to reduce the desensitization process. The pipette solution contained (mM): 130 $CsMeSO_4$, 20 CsCl, 9 NaCl, 0.2 EGTA, 10 HEPES, 1 MgATP, and adjusted to pH 7.2. Thermal stimulation was applied with a custom-made Peltier device (Reid-Dan Electronics) that heated or cooled the flowing perfusate stream. Temperature was measured using a thermistor placed adjacent to the cell.

Determination of thermal threshold. Temperature thresholds represent the point of intersection between linear fits to baseline and the steepest component of the Arrhenius profile. Values are derived from averages of individual curves; $n \geq 6$. Arrhenius curve were obtained by plotting the current on a log-scale against the reciprocal of the absolute temperature. Q_{10} was used to characterize the temperature dependence of the ionic current as calculated using the following equation:

$$Q_{10} = \left[\frac{R_2}{R_1}\right]^{10/(T_2 - T_1)}$$

where R_2 is the current at the higher temperature T_2, and R_1 is the current at the lower temperature T_1 (ref 48).

ARTICLES

Real-time tRNA transit on single translating ribosomes at codon resolution

Sotaro Uemura[1,2], Colin Echeverría Aitken[1,3]†, Jonas Korlach[4], Benjamin A. Flusberg[4], Stephen W. Turner[4] & Joseph D. Puglisi[1,3]

Translation by the ribosome occurs by a complex mechanism involving the coordinated interaction of multiple nucleic acid and protein ligands. Here we use zero-mode waveguides (ZMWs) and sophisticated detection instrumentation to allow real-time observation of translation at physiologically relevant micromolar ligand concentrations. Translation at each codon is monitored by stable binding of transfer RNAs (tRNAs)—labelled with distinct fluorophores—to translating ribosomes, which allows direct detection of the identity of tRNA molecules bound to the ribosome and therefore the underlying messenger RNA (mRNA) sequence. We observe the transit of tRNAs on single translating ribosomes and determine the number of tRNA molecules simultaneously bound to the ribosome, at each codon of an mRNA molecule. Our results show that ribosomes are only briefly occupied by two tRNA molecules and that release of deacylated tRNA from the exit (E) site is uncoupled from binding of aminoacyl-tRNA site (A-site) tRNA and occurs rapidly after translocation. The methods outlined here have broad application to the study of mRNA sequences, and the mechanism and regulation of translation.

During translation, the ribosome progressively coordinates the dynamic interplay of tRNA and protein factors to decipher individual codons of an mRNA molecule and synthesize protein. The ribosome contains three tRNA-binding sites corresponding to three adjacent codons[1]. As it elongates, the ribosome repetitively selects aminoacylated tRNA molecules at the A site, orienting them for peptide-bond formation with peptidyl tRNA positioned in the P site. Peptidyl transfer is followed by the coordinated movement of the A- and P-site tRNAs into the P and E sites, respectively, thus preparing the deacylated tRNA for dissociation from the ribosome. During this translocation step, which is catalysed by the GTPase EF-G, the ribosome simultaneously steps along the mRNA, positioning the next codon in the A site and preparing to select another aminoacylated tRNA.

Although dynamic changes in ligand occupancy and positioning in the A, P and E sites are intimately tied to the mechanism of translation[2–5], the timing and relation of aminoacylated tRNA arrival at the A site, as a ternary complex with EF-Tu•GTP, and dissociation of deacylated tRNA from the E site remain unknown. Single-molecule fluorescence methods have recently probed dynamics during translation, such as the selection of tRNA during elongation and ribosomal conformational changes (reviewed in ref. 6). However, traditional single-molecule fluorescence only allows observation of fluorescent ligands in the nanomolar range, well below the physiological micromolar concentration of most components of the translational apparatus.

Real-time translation in ZMWs

ZMWs (Fig. 1a) are nanophotonic confinement structures consisting of circular holes of diameter 50–200 nm in a metal cladding film deposited on a solid, transparent substrate[7]. In conjunction with laser-excited fluorescence, ZMWs provide observation volumes on the order of zeptolitres (10^{-21} l), three to four orders of magnitude smaller than far-field excitation volumes. This drastically reduces the background signal from freely diffusing fluorescent molecules, allowing the observation of fluorescent ligands in the micromolar range. Advances in fabrication[8], surface chemistry[9] and detection instrumentation[10] have allowed direct monitoring of DNA polymerization in ZMWs[11]. The binding of labelled ligands to an enzyme immobilized in a ZMW is detected as pulses of fluorescent light. Here we adapt this instrumentation to the study of translation. Using ZMWs, we observe real-time selection and transit of fluorescently labelled tRNAs at micromolar concentrations (Fig. 1b) on single ribosomes during multiple rounds of translation elongation.

Binding of tRNA on single ribosomes was tracked using tRNAs that were specifically dye-labelled at their elbow positions without affecting their function[12,13]. Ribosomes were immobilized in ZMWs as 70S initiation complexes—containing fMet-(Cy3)tRNA^{fMet}—assembled on biotinylated mRNAs, which were tethered to the biotin–polyethylene glycol (PEG)-derivatized bottom of ZMWs through neutravidin-biotin linkages; mRNAs contained 5′-UTR (untranslated region) and Shine-Dalgarno sequences from the T4 gene 32, an initiation codon and coding sequence of 3–12 codons, terminated by a stop (UAA) codon followed by four phenylalanine codons (Figs 2a and 3a). Cy3 fluorescence from an immobilized complex confirmed the presence of initiator tRNA and marked a properly assembled and immobilized ribosome in a ZMW. The number of ribosome complexes immobilized per individual ZMW surface increased at higher concentrations of ribosomal complex, obeying Poisson statistics, and, as expected, could be blocked by addition of free biotin (Supplementary Fig. 1). Ellipsometry and ZMW experiments in the absence of ribosomes confirmed minimal non-specific surface adsorption of translational components (100 μM tRNA, 1 μM EF-Tu and EF-G) (Supplementary Fig. 2).

To confirm the use of ZMWs for investigating translation, we used fluorescence resonance energy transfer (FRET)—a sensitive distance

[1]Department of Structural Biology, Stanford University School of Medicine, Stanford, California 94305-5126, USA. [2]Japan Science and Technology Agency, 4-1-8, Honcho, Kawaguchi, Saitama 332-0012, Japan. [3]Biophysics Program, Stanford University School of Medicine, Stanford, California 94305-5126, USA. [4]Pacific Biosciences, Inc., 1505 Adams Drive, Menlo Park, California 94025-1451, USA. †Present address: Department of Biophysics and Biophysical Chemistry, John Hopkins University School of Medicine, 725 N. Wolfe Street, WBSB 713, Baltimore, Maryland 21205-2185, USA.

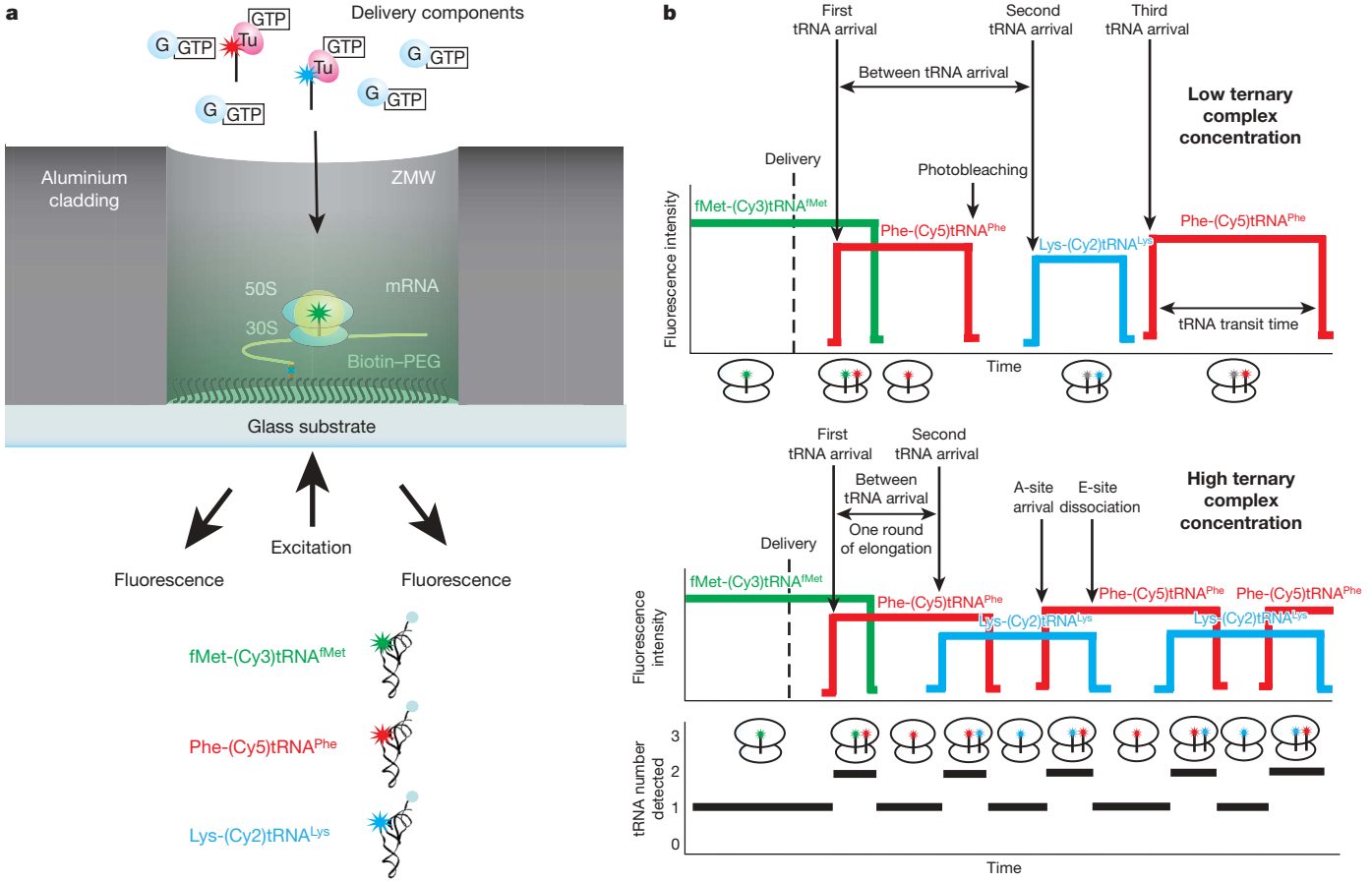

Figure 1 | Translation in ZMWs. a, Experimental setup. ZMWs are cylindrical nanostructures with varying diameters (~50–200 nm). The aluminium side wall and quartz bottom surfaces are derivatized to allow specific biotin–streptavidin interactions on the quartz surface and to block non-specific interactions of molecules with ZMWs[9,11]. Ribosomal complexes are specifically immobilized in the bottom of derivatized ZMWs using biotinylated mRNAs. Ternary complexes Cy5-labelled Phe-tRNA^{Phe}-EF-Tu(GTP) and Cy2-labelled Lys-tRNA^{Lys}-EF-Tu(GTP), along with EF-G(GTP), are delivered to a ZMW surface-immobilized, initial ribosome complex containing Cy3-labelled fMet-tRNA^{fMet}. Fluorescence is excited by illumination at 488, 532 and 642 nm, and Cy2, Cy3 and Cy5 fluorescence are simultaneously detected using previously described instrumentation[10,11]. **b**, Expected signal sequence. Initiation complexes are detected by fluorescence of fMet-(Cy3)tRNA^{fMet} bound at an initiation codon. Fluorescent tRNAs are delivered as ternary complexes. Arrival of Phe-(Cy5)tRNA^{Phe} or Lys-(Cy2)tRNA^{Lys} at the ribosomal A site is marked by a red or blue fluorescent pulse. At low concentrations of ternary complex, tRNA arrival times are slow (much longer than 1 s), and Cy5- or Cy2-labelled tRNAs can photobleach on the ribosome while waiting for translocation. In the absence of photobleaching, the length of a pulse represents the transit time of that tRNA on the ribosome. At high concentrations of ternary complex, tRNA arrival times are fast (much less than 1 s), and fluorescent pulses are overlapped, which indicates simultaneous occupancy by two tRNA molecules. The tRNA occupancy count is shown below the schematic trace.

indicator—to observe the path of incoming A-site tRNA accommodation on the ribosome. We have previously used traditional single-molecule total internal reflection fluorescence (TIRF) to detect FRET between fMet-(Cy3)tRNA^{fMet} in the P site and Phe-(Cy5)tRNA^{Phe} in the A site[12,13]. We repeated these experiments using ZMW-immobilized ribosome complexes and excitation at 532 nm. Using FRET values calibrated in ZMWs, we matched the values and timescales observed in previous tRNA–tRNA FRET experiments at tRNA concentrations up to 600 nM, more than 20-fold higher than previously measured (Supplementary Figs 3 and 4). Consistent with previous single-molecule studies, bimolecular arrival rates of ternary complex to surface-bound ribosomes were decreased by an order of magnitude compared with bulk rates, but unimolecular rates were unaffected. Decreased association rates are likely due to steric and surface effects[14], but ribosomal function is clearly maintained. These results confirmed the functionality of ZMW-immobilized ribosomes and our ability to detect fluorescent tRNA-binding events on individual ribosomes at ternary complex concentrations greater than 100 nM.

Detecting tRNA binding in real time. The basic steps of translation were then observed through direct detection of fluorescently labelled tRNA binding on single ribosomes immobilized in ZMWs. We monitored the binding of ternary complexes Phe-(Cy5)tRNA^{Phe}•EF-Tu•GTP and unlabelled Lys-tRNA^{Lys}•EF-Tu•GTP or labelled Lys-(Cy2)tRNA^{Lys}•EF-Tu•GTP to ribosomes programmed by mRNAs encoding four amino acids (MFFF or MFKF) (Fig. 2a, b); ZMWs were illuminated simultaneously with 488-, 532- and 642-nm excitation. Initiated ribosomes were identified by the presence of fMet-(Cy3)-tRNA^{fMet}; subsequent real-time arrival and occupation of tRNAs on translating ribosomes were detected as fluorescent pulses of appropriate colour[10].

Each tRNA pulse marks the arrival and accommodation of that tRNA within the ribosomal A site. The arrival time of the first elongator tRNA encoded by the mRNA marks the transition of ribosomes into elongation. The time between subsequent tRNA pulse arrivals delineates one round of translational elongation and arrival of tRNA at the next codon (Fig. 1b). This time should depend on the concentration of EF-G, which controls the rate of translocation to the next codon. The duration of each tRNA pulse represents the transit time of that tRNA through the A, P and E sites, followed by dissociation from the ribosome. At the low (<50 nM) factor and tRNA concentrations normally used for single-molecule experiments, photobleaching of ribosome-bound tRNA can also terminate a pulse. Because each pulse describes binding of one tRNA molecule on the ribosome, full

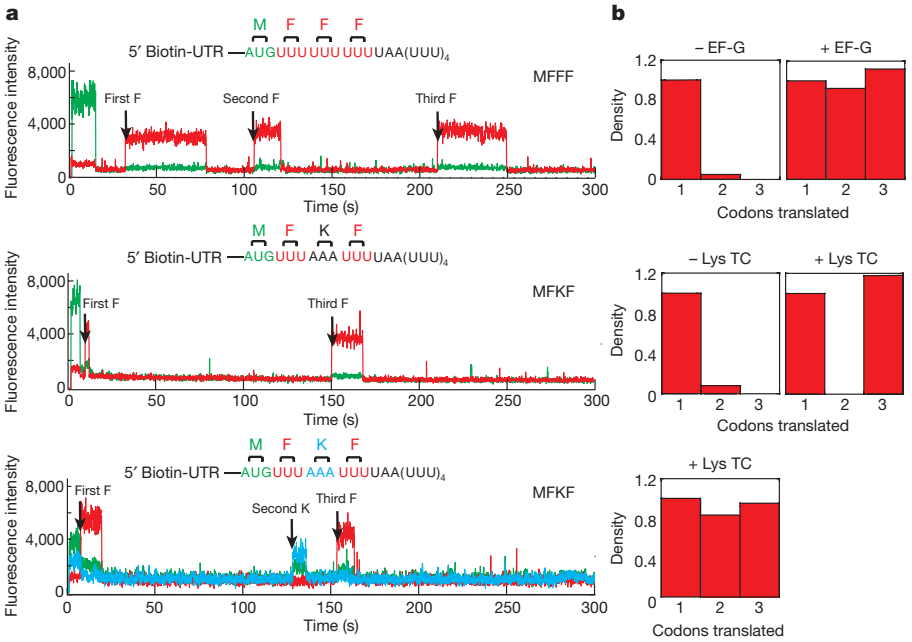

Figure 2 | Monitoring translation by fluorescent tRNA-binding events. **a**, Representative single-ZMW traces of ribosomes translating MFFF mRNA (top) and MFKF mRNA (bottom) in the presence of 30 nM EF-G and 30 nM ternary complex. F, Phe-tRNA^{Phe}; K, Lys-tRNA^{Lys}. **b**, The number of fluorescent pulses observed in ZMWs depends on the presence of EF-G and ternary complex. Event histograms for the three experiments in the absence ($n = 341$) and presence ($n = 304$) of 30 nM EF-G (top), and in the absence ($n = 278$) and presence ($n = 297$) of 30 nM unlabelled Lys-tRNA^{Lys} ternary complex (middle) and presence ($n = 355$) of 30 nM Lys (Cy2)tRNA^{Lys} ternary complex (bottom). Histograms are normalized by the number of ribosomes showing single events.

translation is detected as a series of pulses corresponding to the number and sequential identity of codons in the mRNA.

To define the order and identity of these pulses, initial experiments were performed at concentrations of 30 nM EF-G/30 nM ternary complex, with translation times of about 20 s per codon, which allows P-site tRNAs to photobleach (average lifetime 13.7 s) before the arrival of A-site tRNA. In the absence of EF-G, translation of the MFFF message stalls upon arrival of the first tRNA^{Phe} (Fig. 2b). Cy3 fluorescence is followed only by a single red pulse, indicating binding of a single Phe-(Cy5)tRNA^{Phe} and no subsequent translocation (Fig. 2b). In the presence of 30 nM EF-G, three distinct red fluorescent pulses are observed (Fig. 2a, b). The number of fluorescent tRNA pulses is similarly sensitive to the identity of the A-site codon and the presence of correct ternary complex. Translation of the MFKF mRNA in the presence of EF-G but absence of Lys-tRNA^{Lys} ternary complex results in a single fluorescence pulse following the Cy3 signal, whereas two red pulses are observed upon addition of unlabelled Lys-tRNA^{Lys} ternary complex; finally, two red pulses separated by a blue pulse are observed upon inclusion of fluorescently labelled Lys-(Cy2)tRNA^{Lys} ternary complex. In all traces, brief single-frame (100 ms) bursts in fluorescence can be observed (Fig. 2a). These events were only observed in the presence of 70S ribosomal complexes, and likely represent non-cognate ternary complex sampling at an A-site codon (see below). These results confirm our ability to track translation through sequential stable tRNA-binding events.

Monitoring translation in real time. These tRNA-binding signals were then used to observe full translation of distinct heteropolymeric mRNAs encoding 13 amino acids (M(FK)$_6$ and M(FKK)$_4$). The sequence of the mRNA is readily distinguished from the pattern of fluorescent pulses (Fig. 3a). The number of events observed relates the number of codons translated on each mRNA. At 200-nM ternary complex and 500-nM EF-G, ribosomes translate the entire mRNA (Fig. 3b, red bars). The duration of most tRNA pulses is not limited by photobleaching at these high concentrations, which suggests that the lifetime of each tRNA signal provides a signal for its transit time on the ribosome (see below). Addition of erythromycin, which binds to the exit tunnel of the ribosome[15], blocks translation at six to eight amino acids[16], as expected (Fig. 3b). These data strongly support the direct link between the pattern of tRNA pulses observed in the ZMW and translation.

The arrival of tRNAs at single ribosomes tracks the dynamic composition of the translational apparatus in real time. First tRNA arrival events are fast, as they do not depend on translocation. As predicted, the time between subsequent tRNA arrivals decreases with increasing EF-G concentrations between 30 and 500 nM (Fig. 3c). For codons 2–12, the tRNA transit time is also strongly dependent on EF-G, as it represents at least two rounds of peptide-bond formation and translocation (Fig. 3d). Inhibition of EF-G by fusidic acid, which stabilizes EF-G•GDP on the ribosome after translocation[17], lengthens the transit time by 3.3-fold (Fig. 3d). Arrival of the ribosome at the UGA stop codon after translation of 12 codons leads to a long pulse from the remaining tRNA in the P site of the stalled ribosome. The dwell time for this last tRNA is 4.9-fold longer than for preceding pulses, which emphasizes that photobleaching of the P-site tRNA is not a significant problem using our approach at high-factor concentrations: at 500 nM EF-G, the mean lifetime (4.1 s) of tRNAs bound to the ribosome is significantly shorter than the photobleaching lifetime (17.3 s) observed in experiments at lower concentrations. While paused on the stop codon, tRNA sampling events are observed with short lifetimes (~50 ms for Phe-(Cy5)tRNA^{Phe} or Lys-(Cy2)tRNA^{Lys}) (Fig. 4a, b), which are clearly distinguishable from real tRNA transit events of more than 1 s. These sampling events are consistent with non-cognate ternary-complex interaction[4] with the A site, and their frequency is proportional to ternary-complex concentration (Fig. 4c). All trends discussed above were independent of mRNA sequence.

The total translation time for different mRNAs is characterized by the arrival times of tRNAs at different codons. As expected, translation rates depend on the concentrations of ternary complex and EF-G. For the M(FK)$_6$ mRNA (Fig. 3e), translation rates increased from 0.08 to 0.4 s^{-1} for EF-G concentrations ranging from 30 and 500 nM (200 nM ternary complex). Likewise, increasing the concentration of ternary complex also increased the overall translation rate. At the highest concentrations of ternary complex and EF-G, the translation rate was nearly one codon per second, approaching that obtained using cell extracts *in vitro*[18]. When 30S pre-initiation complexes are immobilized in ZMWs and translation is initiated by addition of 50S subunits, ternary complex and EF-G—requiring initiation before protein synthesis (Supplementary Fig. 5)—the overall translation rate is unaffected, except for a delay (12 s) in arrival of the first tRNA. This delay is consistent with the timescale of 50S subunit joining during initiation[19], before progression to elongation.

Our approach allows analysis of translational rates at each codon of an mRNA molecule. Arrival of the first tRNA is independent of EF-G concentration, as expected. However, the first EF-G catalysed translocation of the ribosome may become the slowest step in elongation, as revealed by the time between arrivals of tRNA molecules

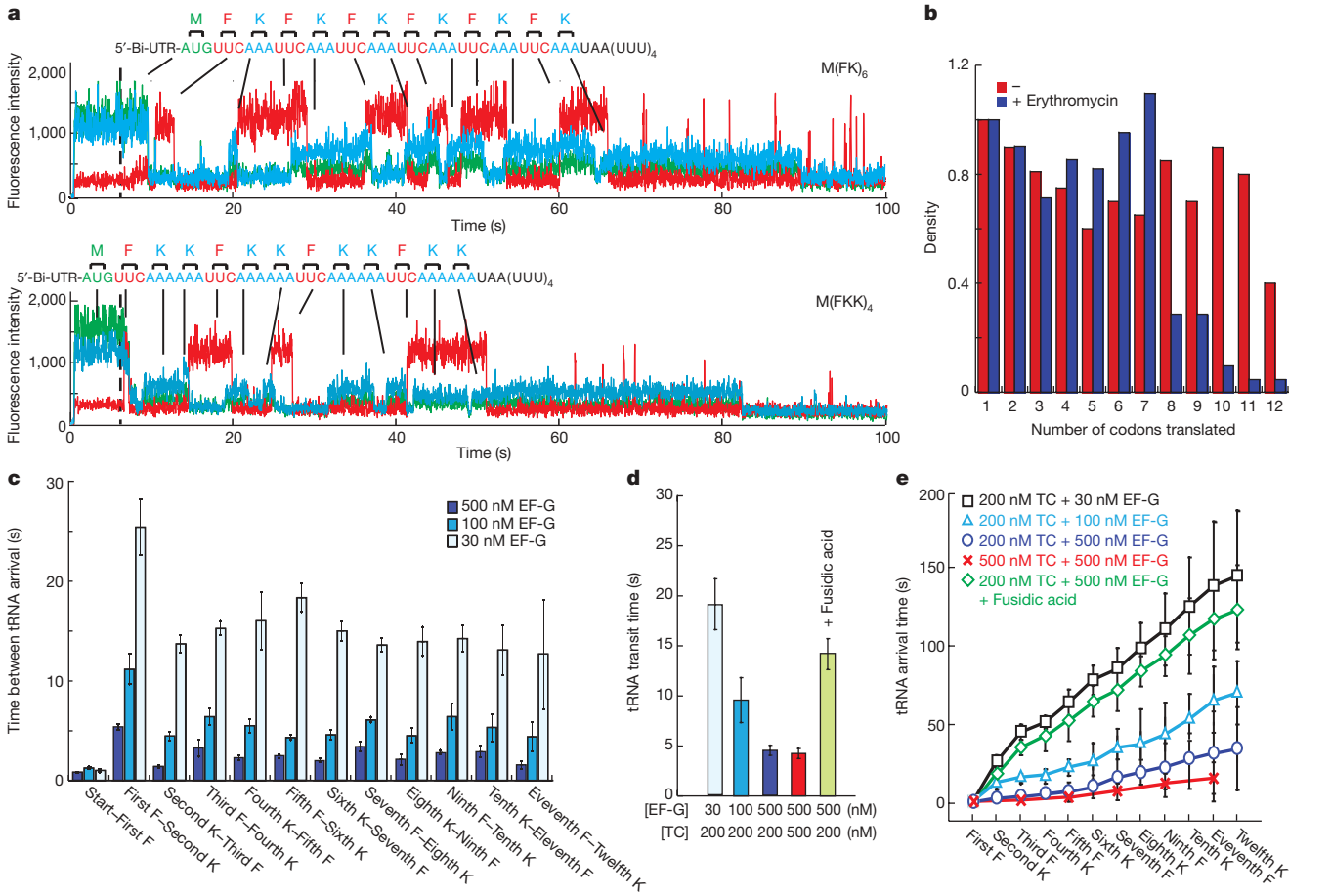

Figure 3 | Real-time translation at near-physiological concentrations. **a**, Two heteropolymeric mRNAs encoding 13 amino acids were used: $M(FK)_6$ and $M(FKK)_4$. Translation was observed in the presence of 200 nM Phe-(Cy5)$tRNA^{Phe}$, 200 nM Lys-(Cy2)$tRNA^{Lys}$ ternary complex and 500 nM EF-G as a series of fluorescent pulses that mirror the mRNA sequence. A long Cy2 pulse is observed upon arrival of the ribosome at the stop codon. Brief sampling pulses (<100 ms) of both Lys-(Cy2)$tRNA^{Lys}$ and Phe-(Cy5)$tRNA^{Phe}$ ternary complex are observed after arrival at the stop codon. **b**, Event histograms for translation of $M(FK)_6$ showing translation out to 12 elongation codons (red, $n = 381$). In the presence of 1 μM erythromycin, translation (blue, $n = 201$) is stalled at codon 8 of the mRNA. **c**, Analysis of translation rates at each codon in $M(FK)_6$. Mean times between tRNA arrival events are plotted for translation in the presence of 200 nM ternary complex and 30, 100 and 500 nM EF-G. **d**, Overall tRNA transit mean times for codons 2–12 at (from left) 200 nM ternary complex (TC) and 30, 100 or 500 nM EF-G; 500 nM ternary complex and 500 nM EF-G; and 200 nM ternary complex and 500 nM EF-G in the presence of 1 μM fusidic acid. **e**, Cumulative mean translation times for each codon in $M(FK)_6$ at 200 nM ternary complex and 30, 100 or 500 nM EF-G; 500 nM ternary complex and 500 nM EF-G; and 200 nM ternary complex and 500 nM EF-G in the presence of 1 μM fusidic acid. All error bars are 95% confidence intervals from single-exponential fits.

(Fig. 3e). This first EF-G-catalysed translocation step is about two-fold slower than subsequent translocation events, at all EF-G concentrations and for all mRNAs tested (Supplementary Fig. 5). A similar trend in elongation rate was previously observed by following the global conformation of single translating ribosomes[28]. Codons after position 3 are all translated with similar rates in $M(FK)_6$ until the long stall at the final stop codon. Slight differences in overall translation rates are observed for distinct mRNA sequences, with MF_{12} translated most slowly and $M(FKK)_4$ most rapidly (Supplementary Fig. 5). The hydrophobic character of the poly(phe) peptide may inhibit translation of the MF_{12} mRNA.

To define the mechanism linking tRNA arrival at the A site and release from the E site, we used these signals to measure the real-time tRNA occupancy of the ribosome during translation. Although at least two tRNA molecules must occupy the ribosome during peptide-bond formation[2–6], the ribosome contains three tRNA-binding sites (A, P and E), and stable tRNA occupancy in the E site after translocation would cause accumulation of three tRNA molecules on the ribosome. The arrival of tRNA in the A site may signal tRNA departure from the E site, or dissociation from the E site may occur spontaneously upon translocation. In our single-molecule traces, overlapping fluorescence pulses denote multiple tRNA molecules simultaneously bound to the ribosome, whereas appearance and departure of fluorescence indicates tRNA arrival and dissociation (Fig. 1b). During translation of the $M(FK)_6$, at 200 nM Phe-(Cy5)$tRNA^{Phe}$ and Lys-(Cy2)$tRNA^{Lys}$ ternary complex and 500 nM EF-G, most (82.2%) consecutive Cy5 and Cy2 pulses are overlapping, which indicates that two tRNA molecules occupy the ribosome simultaneously during translation.

Dynamic tRNA occupancy during translation. To determine the real-time occupancy of the ribosome at each codon, we post-synchronized 381 traces according to the arrival of aminoacylated tRNA at each codon (Fig. 5a). In this formulation, two-dimensional colour plots reveal the time-dependent tRNA occupancy of hundreds of single ribosomes during each elongation cycle along the mRNA.

This analysis shows that EF-G driven translocation controls the number of tRNA molecules on the ribosome. At 30 nM EF-G, the two-tRNA state lasts approximately 6.3 s at each codon, consistent with the estimated time for translocation. Increasing the concentrations of EF-G to 500 nM shortens the lifetime of the two-tRNA bound state of the ribosome from 6.3 s to 1.5 s (Fig. 5b). These trends are observed at different codons and for distinct mRNA sequences (Supplementary Fig. 6), confirming the generality of the conclusions. The two-tRNA state is not followed by a three-tRNA state; even at high concentrations of both EF-G and ternary complex, ribosomes occupied by three tRNA molecules are almost never observed (1.7%),

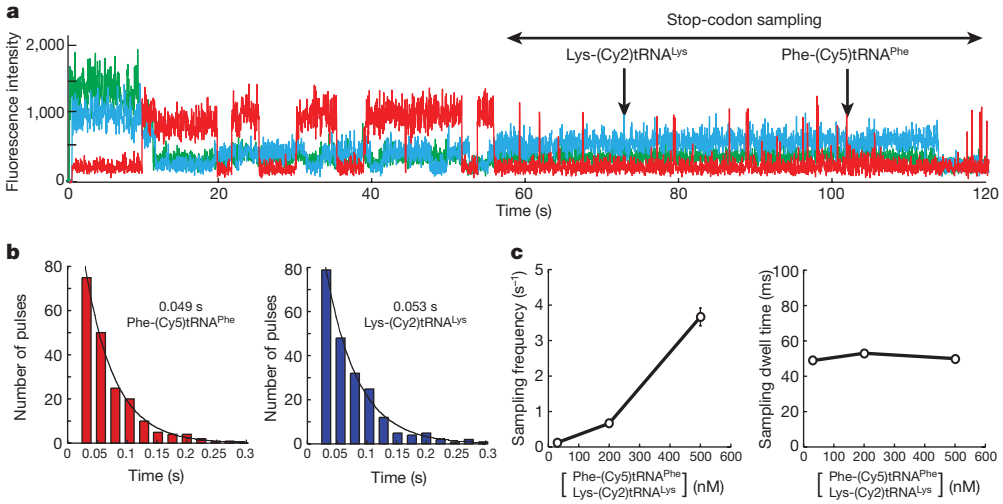

Figure 4 | A-site sampling on ribosomes stalled at the stop codon. **a**, Fast sampling events at the stop codon position of the $M(FK)_6$ template were observed in the presence of 200 nM Phe-(Cy5)tRNA^{Phe}, 200 nM Lys-(Cy2)tRNA^{Lys} ternary complex and 500 nM EF-G. **b**, Dwell-time histograms of individual sampling pulses of Phe-(Cy5)tRNA^{Phe} (left) and Lys-(Cy2)tRNA^{Lys} (right). Both histograms are well approximated by a single exponential fit. **c**, Mean frequency of fast sampling increased linearly with ternary complex concentration (left), whereas mean sampling dwell time did not depend on ternary complex concentration (right). Error bars are 95% confidence intervals from single-exponential fits.

which would be consistent with decreased E-site affinity upon A-site tRNA arrival. However, departure of E-site tRNA is not linked to arrival of the next tRNA at the A site in our experiments, as correlation analysis shows no connection between E-site tRNA departure events and A-site arrivals ($r = 0.04$). Instead, these results suggest that EF-G binding and subsequent GTP hydrolysis drive the tRNA from the A/P, P/E hybrid states to the P and E sites, at which point the E-site tRNA rapidly dissociates. Consistent with this model, fusidic-acid-stalled EF-G (GDP) in the A site inhibits arrival of the next tRNA, and inhibits each round of elongation, but does not affect the rate of tRNA dissociation from the E site (Fig. 5b).

The results presented here demonstrate that translation can be observed in real time using single ribosomes immobilized in ZMWs. The application of ZMWs to the observation of translating ribosomes allows the sensitivity and precision of single-molecule measurements at near physiological micromolar concentrations of both tRNA and protein factors (Supplementary Fig. 7). By using specifically dye-labelled tRNAs, long-lived binding events to mRNA-programmed ribosomes are readily observed and distinguished from transient sampling. The sequence of tRNA-binding events reveals the encoding mRNA sequence. Full translation requires the presence of both EF-G and the appropriate ternary complexes. Ribosome-directed antibiotics interfere with translation as predicted by their mechanism of action: fusidic acid blocks release of EF-G from the ribosome, slowing elongation, whereas erythromycin blocks elongation beyond seven amino acids. The dynamics of tRNA-binding events at each codon revealed slow initiation and long pauses upon encountering the stop codon; sampling of ternary complex at the stop codon of stalled ribosomes is observed. Translation at micromolar concentrations of factors and ligands is efficient and rapid, avoiding limitations of dye photobleaching, and allows correlation of bimolecular binding events on single ribosomes.

The mechanism by which tRNAs transit through the ribosome during decoding, peptide-bond formation and translocation was explored using our approach. Various models for the interplay of the A and E sites have been proposed. Recent dynamic and structural studies suggest that EF-G interaction within the A site may control the conformation of the E site[20]. The ability to probe tRNA dynamics on the ribosome at high ternary complex and factors concentrations in ZMWs allowed us to determine the time-dependent composition of the ribosome at each codon during translation. These results show unambiguously that tRNA release from the E site is rapid once translocation has occurred and is uncorrelated with the arrival of the next tRNA. This is consistent with a model of transient E-site occupancy after translocation[21,22].

Three tRNA molecules are rarely observed on translating ribosomes, and only at high micromolar concentrations of ternary complex, where arrival of the third tRNA molecule in the A site is rapid.

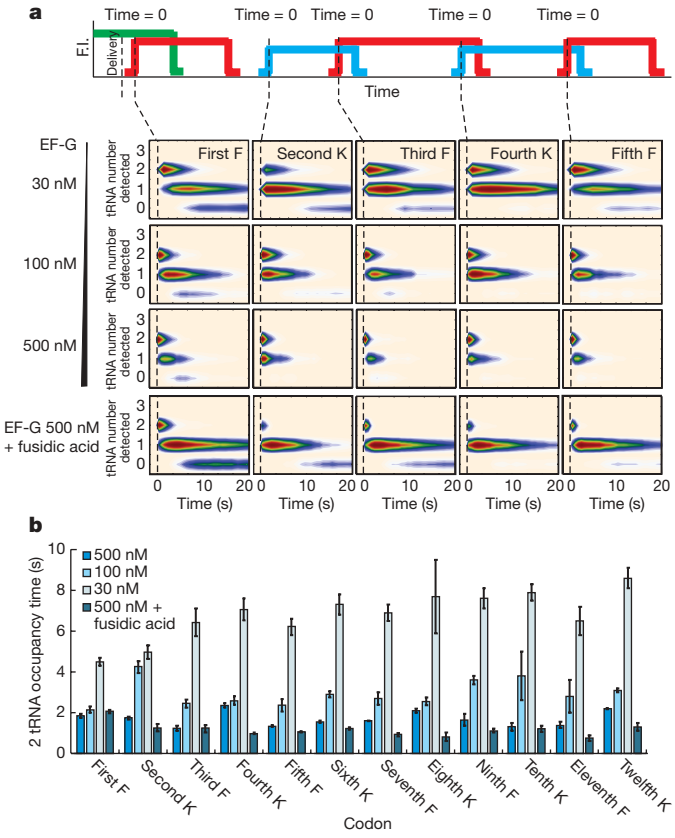

Figure 5 | Monitoring the dynamic tRNA occupancy of translating ribosomes. **a**, Post-synchronization plots for time-resolved tRNA occupancy at codons 2–6 during translation of $M(FK)_6$. Two-dimensional histograms are post-synchronized in time with respect to each tRNA transit event (First F to fifth F; F, Phe-tRNA^{Phe}; K, Lys-tRNA^{Lys}) at 500, 100 and 30 nM EF-G, and at 500 nM EF-G in the presence of fusidic acid. **b**, tRNA occupancy mean time at 500, 100 and 30 nM EF-G, and at 500 nM EF-G in the presence of fusidic acid. Error bars are 95% confidence intervals from single-exponential fits.

These data agree with dynamic investigations of the E site that show coupling of E-site opening, in particular the L1 stalk[23–25], with translocation and E-site occupancy. Rapid dissociation of the E-site tRNA upon translocation is also consistent with the fast rates required for efficient elongation. Occupancy by three tRNA molecules occurs when a slow E-site dissociation event is coincident with rapid tRNA arrival in the A site (Supplementary Fig. 7). Slow E-site dissociation delays subsequent rounds of elongation, and may be important in rare translational events, such as frameshifting[26].

Future perspectives

The real-time system outlined here has broad application to the study of translation. The dynamic events underlying translational fidelity and ribosomal movement are probed directly at each codon during translation, allowing rare translational events to be uncovered. Time-resolved analysis of compositional changes in the ribosome can be extended to initiation, elongation and release-factor binding and can be merged with FRET signals to correlate ligand binding and ribosomal conformational changes. Eukaryotic translational systems can be readily substituted to probe the dynamics of translational control and regulation. This approach allows the direct detection of mRNA coding sequence, and may allow the observation of translational events involved in the regulation of protein synthesis, such as frameshifting.

METHODS SUMMARY

Sample preparation. *Escherichia coli* ribosomal subunits and factors were prepared and purified as described[12,13]. $tRNA^{fMet}$, $tRNA^{Phe}$ and $tRNA^{Lys}$ were labelled with fluorescent dyes at their elbow positions (U8 or U47), purified and aminoacylated using previously described approaches[12,13]. Ribosome initiation complexes were assembled by combining 0.5-μM 30S subunits pre-incubated with stoichiometric S1, 0.5-μM 50S subunits, 5 μM 5′-biotinyated mRNA, 1 μM fMet-(Cy3)$tRNA^{fMet}$, 2 μM IF2 and 4 mM GTP in a polymix buffer (50 mM Tris-acetate (pH 7.5), 100 mM potassium chloride, 5 mM ammonium acetate, 0.5 mM calcium acetate, 5 mM magnesium acetate, 0.5 mM EDTA, 5 mM putrescine-HCl and 1 mM spermidine) and incubating at 37 °C for 5 min.
ZMW assay. The ZMW surface was derivatized with 1 μM neutravidin for 2 min and rinsed with the polymix buffer to remove unbound neutravidin. After rinsing, ribosome initiation complexes (diluted tenfold in polymix buffer containing 2 μM IF2 and 4 mM GTP) were delivered to the ZMW surface and incubated for 5 min at room temperature, after which the surface was rinsed with polymix buffer containing 2 μM IF2 and 4 mM GTP, as well as an oxygen scavenging system[27] (250 nM protocatechuate dioxygenase, 2.5 mM PCA (3,4-dihydroxybenzoic acid) and 1 mM Trolox). Real-time delivery solutions were prepared in polymix buffer and contained 2 μM IF2, 4 mM GTP, 30–500 nM EF-G and 30–500 nM ternary complex (one or more of the following: Phe-(Cy5)$tRNA^{Phe}$, Lys-(Cy2)$tRNA^{Lys}$ or Lys-$tRNA^{Lys}$, pre-assembled with 15 μM EF-Tu and 4 mM GTP), as well as the protocatechuate dioxygenase oxygen scavenging system.

Full Methods and any associated references are available in the online version of the paper at www.nature.com/nature.

Received 22 January 2010; accepted 18 February 2010.

1. Green, R. & Noller, H. F. Ribosomes and translation. *Annu. Rev. Biochem.* **66,** 679–716 (1997).
2. Moazed, D. & Noller, H. F. Intermediate states in the movement of transfer RNA in the ribosome. *Nature* **342,** 142–148 (1989).
3. Hausner, T. P., Geigenmüller, U. & Nierhaus, K. H. The allosteric three-site model for the ribosomal elongation cycle. New insights into the inhibition mechanism of aminoglycosides, thiostrepton, and viomycin. *J. Biol. Chem.* **263,** 13103–13111 (1988).
4. Rodnina, M. W. & Wintermeyer, W. Fidelity of aminoacyl-tRNA selection on the ribosome: kinetic and structural mechanisms. *Annu. Rev. Biochem.* **70,** 415–435 (2001).
5. Agirrezabala, X. *et al.* Visualization of the hybrid state of tRNA binding promoted by spontaneous racheting of the ribosome. *Mol. Cell* **32,** 190–197 (2008).
6. Marshall, R. A., Aitken, C. E., Dorywalska, M. & Puglisi, J. D. Translation at the single-molecule level. *Annu. Rev. Biochem.* **77,** 177–203 (2008).
7. Levene, M. J. *et al.* Zero-mode waveguides for single-molecule analysis at high concentrations. *Science* **299,** 682–686 (2003).
8. Foquet, M. *et al.* Improved fabrication of zero-mode waveguides for single-molecule detection. *J. Appl. Phys.* **103,** 034301 (2008).
9. Korlach, J. *et al.* Selective aluminum passivation for targeted immobilization of single DNA polymerase molecules in zero-mode waveguide nanostructures. *Proc. Natl Acad. Sci. USA* **105,** 1176–1181 (2008).
10. Lundquist, P. M. *et al.* Parallel confocal detection of single molecules in real time. *Opt. Lett.* **33,** 1026–1028 (2008).
11. Eid, J. *et al.* Real-time DNA sequencing from single polymerase molecules. *Science* **323,** 133–138 (2009).
12. Blanchard, S. C., Gonzalez, R. L. Jr, Kim, H. D., Chu, S. & Puglisi, J. D. tRNA selection and kinetic proofreading in translation. *Nature Struct. Mol. Biol.* **11,** 1008–1014 (2004).
13. Blanchard, S. C., Kim, H. D., Gonzalez, R. L. Jr, Puglisi, J. D. & Chu, S. tRNA dynamics on the ribosome during translation. *Proc. Natl Acad. Sci. USA* **101,** 12893–12898 (2004).
14. Chan, V., Graves, D. J. & McKenzie, S. E. The biophysics of DNA hybridization with immobilized oligonucleotide probes. *Biophys. J.* **69,** 2243–2255 (1995).
15. Schlunzen, F. *et al.* Structural basis for the interaction of antibiotics with the peptidyl transferase centre in eubacteria. *Nature* **413,** 814–821 (2001).
16. Tenson, T., Lovmar, M. & Ehrenberg, M. The mechanism of action of macrolides, lincosamides and streptogramin B reveals the nascent peptide exit path in the ribosome. *J. Mol. Biol.* **330,** 1005–1014 (2003).
17. Bodley, J. W. & Godtfredsen, W. O. Studies on translocation. XI. Structure-function relationships of the fusidane-type antibiotics. *Biochem. Biophys. Res. Commun.* **46,** 871–877 (1972).
18. Underwood, K. A., Swartz, J. R. & Puglisi, J. D. Quantitative polysome analysis identifies limitations in bacterial cell-free protein synthesis. *Biotechnol. Bioeng.* **91,** 425–435 (2005).
19. Marshall, R. A., Aitken, C. E. & Puglisi, J. D. GTP hydrolysis by IF2 guides progression of the ribosome into elongation. *Mol. Cell* **35,** 37–47 (2009).
20. Gao, Y. G. *et al.* The structure of the ribosome with elongation factor G trapped in the posttranslocational state. *Science* **326,** 694–699 (2009).
21. Lill, R. & Wintermeyer, W. Destabilization of codon-anticodon interaction in the ribosomal exit site. *J. Mol. Biol.* **196,** 137–148 (1987).
22. Semenkov, Y. P., Rodnina, M. V. & Wintermeyer, W. The ''allosteric three-site model'' of elongation cannot be confirmed in a well-defined ribosome system from *Escherichia coli*. *Proc. Natl Acad. Sci. USA* **93,** 12183–12188 (1996).
23. Cornish, P. V. *et al.* Following movement of the L1 stalk between three functional states in single ribosomes. *Proc. Natl Acad. Sci. USA* **106,** 2571–2576 (2009).
24. Fei, J., Kosuri, P., MacDougall, D. D. & Gonzalez, R. L. Jr. Coupling of ribosomal L1 stalk and tRNA dynamics during translation elongation. *Mol. Cell* **30,** 348–359 (2008).
25. Fei, J. *et al.* Allosteric collaboration between elongation factor G and the ribosomal L1 stalk directs tRNA movements during translation. *Proc. Natl Acad. Sci. USA* **106,** 15702–15707 (2009).
26. Sanders, C. L. & Curran, J. F. Genetic analysis of the E site during RF2 programmed frameshifting. *RNA* **13,** 1483–1491 (2007).
27. Aitken, C. E., Marshall, R. A. & Puglisi, J. D. An oxygen scavenging system for improvement of dye stability in single-molecule fluorescence experiments. *Biophys. J.* **94,** 1826–1835 (2008).
28. Aitken, C. E. & Puglisi, J. D. Following the intersubunit conformation of the ribosome during translation in real time. *Nat. Struct. Mol. Biol.* (in the press).

Supplementary Information is linked to the online version of the paper at www.nature.com/nature.

Acknowledgements This work was supported by National Institutes of Health grant GM51266 (to J.D.P.). We thank T. Funatsu, A. Tsai and A. Petrov for encouragement and discussions. We thank J. Gray for performing ellipsometry experiments.

Author Contributions S.U. performed all experiments and data analysis. S.U., C.E.A. and J.D.P. discussed results and wrote the manuscript. S.W.T., J.K. and B.A.F. provided technical expertise with instrumentation and data processing.

Author Information Reprints and permissions information is available at www.nature.com/reprints. The authors declare competing financial interests: details accompany the full-text HTML version of the paper at www.nature.com/nature. Correspondence and requests for materials should be addressed to J.D.P. (puglisi@stanford.edu).

METHODS

Instrumentation. Instrumentation[10] and chips containing 3,000 individual ZMWs[8] were used and prepared as described previously[11]. Specific immobilization of ribosome complexes in ZMWs was achieved by surface passivation using polyphosphonate with biotin–PEG–silane[9]. ZMW diameters were in the range 120–135 nm. Cy2, Cy3 and Cy5 fluorescence was detected upon simultaneous excitation at 488, 532 and 642 nm. Each laser power for three excitations was 0.5 $\mu W\,\mu m^{-2}$ for all three colour experiments, but 2.5 $\mu W\,\mu m^{-2}$ for two colour experiments (Fig. 2a). Each dye lifetime was 17.3 s for Phe-(Cy5)$tRNA^{fMet}$ in the P site, 22.5 s for fMet-(Cy3)$tRNA^{fMet}$ in the P site and 16.5 s for fMet-(Cy2)$tRNA^{fMet}$ in the P site.

Data collection and analysis. Data were collected on a highly parallel confocal fluorescence detection instrument, using prism-based dispersion optics and an electron-multiplying charge-coupled device camera[10]. Fluorescence traces were recorded at a rate of 30 frames per second for 3 min, with the exception experiments using MFF, MFKF mRNAs and those at 30 nM EF-G for $M(FK)_6$ mRNA, which were recorded at a rate of 100 frames per second for 5 min. Using custom software written in Matlab (MathWorks), fluorescence traces that displayed Cy3 fluorescence corresponding to an fMet-(Cy3)$tRNA^{fMet}$ molecule and co-localized with the arrival of labelled ternary complex upon delivery were analysed to extract individual tRNA transit times, time between tRNA arrivals and tRNA occupancy within single ribosomes. Data from individual molecules ($n > 200$ molecules for all experiments) were accumulated into statistical distributions to extract mean estimates for the above-described values.

Vol 464|15 April 2010|doi:10.1038/nature09007

LETTERS

An image of an exoplanet separated by two diffraction beamwidths from a star

E. Serabyn[1], D. Mawet[1] & R. Burruss[1]

Three exoplanets around the star HR 8799 have recently been discovered by means of differential imaging with large telescopes[1]. Bright scattered starlight limits high-contrast imaging to large angular offsets, currently of the order of ten diffraction beamwidths, $10\lambda/D$, of the star (where λ is the wavelength and D is the aperture diameter[1–5]). Imaging faint planets at smaller angles calls for reducing the starlight and associated photon and speckle noise before detection, while efficiently transmitting nearby planet light. To carry out initial demonstrations of reduced-angle high-contrast coronagraphy, we installed a vortex coronagraph[6–9] capable of reaching small angles behind a small, well-corrected telescope subaperture that provides low levels of scattered starlight[10,11]. Here we report the detection of all three HR 8799 planets with the resultant small-aperture (1.5 m) system, for which only $2\lambda/D$ separate the innermost planet from the star, with a final noise level within a factor of two of that given by photon statistics. Similar well-corrected small-angle coronagraphs should thus be able to detect exoplanets located even closer to their host stars with larger ground-based telescopes[12–15], and also allow a reduction in the size of potential space telescopes aimed at the imaging of very faint terrestrial planets.

To provide low scatter (which decreases with the variance of the wavefront error), we used the Palomar well-corrected subaperture[10], a clear, 1.5-m-diameter, off-axis subaperture on the Hale telescope that provides root-mean-square wavefront errors of about 85–100 nm (compared to about 200–250 nm with the adaptive optics system coupled to the full telescope). Performance was further improved by reducing non-common-path wavefront errors arising from the non-coincidence of the science and wavefront-sensor cameras. These include differential pointing and focus between the cameras, and quasi-static scattered-light speckles that degrade off-axis contrast. The instrumental pointing needed under best atmospheric conditions, about $0.02\lambda/D$ of the mask centre[16], was achieved with upgraded mirror actuation in the Palomar adaptive optics system, and the non-common-path focus error was reduced by minimizing residual light in the post-coronagraphic-mask pupil (Lyot) plane. Finally, the quasi-static speckle contribution was reduced from about 110 nm to about 40 nm using the science camera as a secondary wavefront sensor in a phase retrieval algorithm[17]. To reject the stellar diffraction pattern, we use phase-based coronagraphic masks, because transparent phase masks can transmit planetary light at small angular offsets from stars. The vortex phase mask (see Supplementary Information), which applies an azimuthal phase spiral in the focal plane, is expected to have close to ideal performance[18], and so we developed and installed a K_s-band (2.15 μm) vector vortex mask in the Palomar infrared camera[19].

Figure 1 shows the high-quality point spread function provided by the Palomar well-corrected subaperture on HR 8799—a nearly perfect Airy pattern with a Strehl ratio of approximately 0.91 ± 0.008—as well as the doughnut-shaped post-vortex residual stellar point spread function. The high stability of the point spread function provided by the well-corrected subaperture even in the face of relatively poor seeing (1.6″) allows us to remove the residual point spread function by means of reference star subtraction (using the "locally optimized combination of images" LOCI algorithm[20]). In the resultant fully reduced image of HR 8799, shown in Fig. 2, all three of its known planets have been detected, including the innermost 'd' planet, located about $2\lambda/D$ from the star for the well-corrected subaperture. Figure 2b also shows the resultant azimuthally averaged beam profiles and noise curves (in contrast units) for each step in the process. Comparing the two point spread function profiles (solid curves), a raw coronagraphic peak-to-peak stellar rejection ratio of approximately 50 is seen, consistent with the Strehl ratio. The black dashed curve shows the intensity variations of the raw, non-coronagraphic point spread function, relative to the azimuthal average. The red dashed curve, showing the 4σ post-vortex, post-phase-retrieval semi-static speckle noise (with $1\sigma < 10^{-4}$ beyond $2.5\lambda/D$) shows that the residual speckle noise is roughly an order of magnitude below both the coronagraphically attenuated starlight and the variations in the non-coronagraphic point spread function. Moreover, the relative flatness of the semi-static speckle contrast between about 1 and 2.8 arcseconds is suggestive of the beginnings of a central well-corrected "dark hole" region[21]

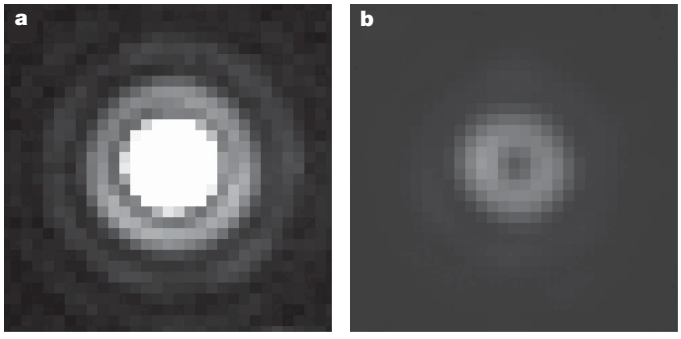

Figure 1 | Pre- and post-vortex stellar point spread functions. a, The K_s-band raw (non-coronagraphic) stellar point spread function obtained on HR 8799 with the Palomar well-corrected subaperture on 11 July 2009. Even with 1.6″ seeing during the observations, the post-correction Strehl ratio was both very good and very stable, 0.91 ± 0.008 (root mean square). **b**, The residual post-coronagraph point spread function for HR 8799, on the same intensity scale. With no discontinuities other than on the optical axis, vortex masks provide a clear 2π field of view around the star. The observed peak-to-peak stellar rejection ratio is around 50, consistent with the Strehl ratio. The star was re-centred on the vortex mask roughly once per minute, to keep the residual doughnut pattern symmetrical, resulting in alignment of the stellar position to the vortex axis at the 3–5 milliarcsecond level. Our K_s-band, topological charge 2, vector vortex mask was manufactured at JDS Uniphase using polymeric liquid crystal technology[9,19].

[1]Jet Propulsion Laboratory, California Institute of Technology, 4800 Oak Grove Drive, Pasadena, California 91109, USA.

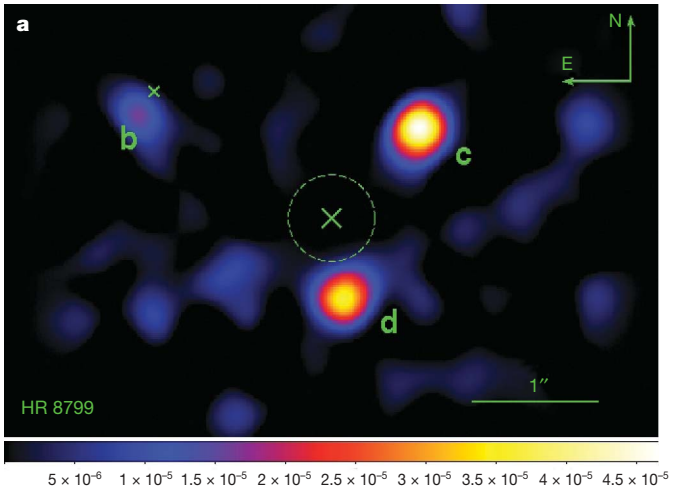

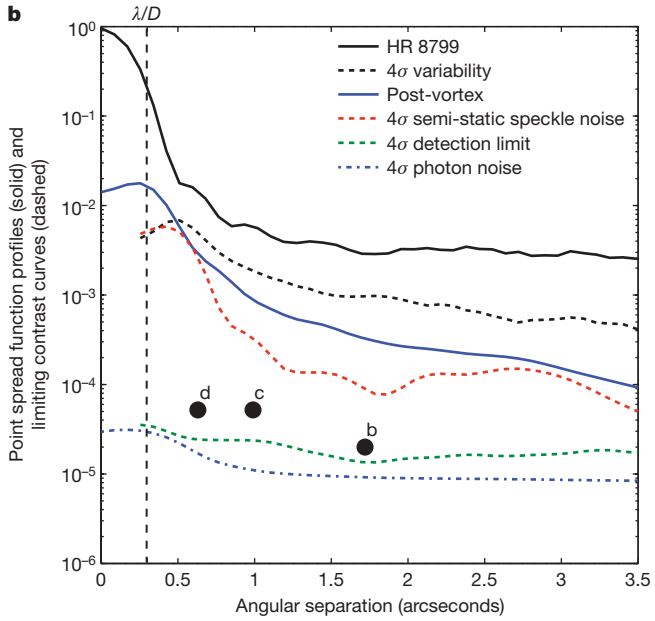

Figure 2 | Final image of HR 8799 and concomitant stellar point spread function profiles and limiting contrast curves. a, Final calibrated image of the HR 8799 system obtained with the K_s-band vector vortex coronagraph on the well-corrected subaperture. The residual point spread function subtraction was performed with the LOCI algorithm[20] using two reference stars (SAO 91022 and 108402) with V and K magnitudes similar to HR 8799. The exposure time for each star was 800 s. The stellar position is marked with a large cross, and the central 300 milliarcseconds ($1\lambda/D$) radius region inside the dashed circle is blanked out. The position of HR 8799b during the 1998 Hubble observations[2] is shown by the small cross. Off-axis astrometry errors are dominated by plate scale and orientation uncertainties resulting from the limited numbers of reference binary stars observed until now. **b**, Azimuthally averaged point spread function profiles and limiting contrast curves. The black solid curve is the azimuthally averaged non-coronagraphic point spread function profile, and the blue solid curve is the azimuthal average of the post-coronagraph residual point spread function profile. The black dashed curve gives the 4σ azimuthal variations in the non-coronagraphic point spread function. The red dashed curve shows the radial dependence of the post-vortex semi-static speckle 4σ noise level after the modified Gerchberg–Saxton phase retrieval algorithm[17] (obtained from the blue solid curve by subtracting the median-filtered residual point spread function). The green dashed curve shows the azimuthally averaged 4σ detection limit after reference-star subtraction with LOCI, and the blue dashed curve shows the 4σ photon noise estimated from the residual stellar flux and background. Flux accuracies are limited mostly by speckle variations and the reference-star subtraction procedure; in comparison, photometric errors due to Strehl ratio and atmospheric transmission variations are minor.

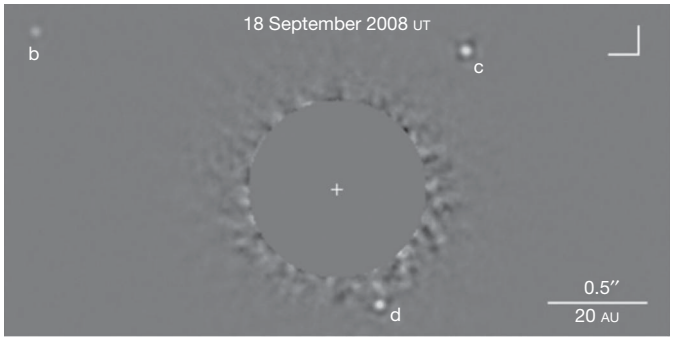

Figure 3 | Keck K_s-band image of HR 8799. UT, Universal Time. The central blanked-off region has a radius of around 0.44″ or about $10\lambda/D$. The positions from this image[1] are [1.525″, 0.796″] for b, [−0.659″, 0.708″] for c and [−0.221″, −0.581″] for d, with errors on each coordinate of ±0.003″. The K_s magnitudes[1] are 14.05 ± 0.08 for b; 13.13 ± 0.08 for c and 13.11 ± 0.12 for d. Image courtesy of C. Marois and the National Research Council Canada and Keck Observatory.

coincident with the domain of influence of the adaptive optics system's deformable mirror (which should extend to about 2.4 arcseconds). The green dashed curve shows our final 4σ contrast detection limit after the last step of reference star subtraction with the LOCI algorithm. A relatively flat 4σ detection limit of around 2×10^{-5} is seen at most radii beyond our inner cut-off of $1\lambda/D$, owing to the contribution of the background. This contrast level corresponds to an equivalent 1σ wavefront error of around 7 nm root-mean-square, slightly more than an order of magnitude below the starting value. Our final detection limit is also within a factor of two of the statistical photon noise expected from the coronagraphically attenuated starlight and the background, given by the blue dashed curve. On bright stars under good seeing conditions, contrasts several times better than this should be possible with the well-corrected subaperture.

Large telescopes currently typically reach contrasts of about 10^{-4} to 10^{-5} at smallest angular separations from stars of the order of $10\lambda/D$. Detections closer to stars with much less demanding contrast differences are of course possible[11,22]. The Keck discovery images[1] (for example Fig. 3) provide a very good example of current capabilities. In Fig. 3, an inner region with a radius of around 0.44″, or about $10\lambda/D$, is blanked out as inaccessible. Our ability to detect planets at contrasts of a few 10^{-5} in to around $1\lambda/D$ (see Fig. 2; note that the theoretical half-power transmission[7,18] of a vortex is about $0.9\lambda/D$) is thus clearly a step forward, demonstrating that a small aperture can reach smallest angles (about 300 milliarcseconds) comparable to those that the largest telescopes can reach, by combining a coronagraph intrinsically capable of reaching small angles with a high degree of wavefront correction, so as to push the contrast profile both inward and downward.

Table 1 gives the measured positions and fluxes of the three detected HR 8799 planets, and Fig. 2 shows the decade-long orbital shift of HR 8799b relative to the published Hubble Space telescope image[2]. The inner 'c' and 'd' planets were not detected by Hubble, and our positional error bars are not yet small enough to detect significant orbital motions for planets 'c' and 'd' relative to more recent images from large ground-based telescopes, because astrometric accuracy is inversely proportional to telescope diameter. On the other hand, the ability to image

Table 1 | Planet positions and fluxes

	Radius (arcsec)	Position angle (degrees)	RA offset (arcsec)	Dec. offset (arcsec)	K_s flux (mag)
B	1.728 ± 0.095	62.9 ± 1.5	1.539 ± 0.042	0.787 ± 0.061	14.0 ± 0.5
C	0.998 ± 0.059	315.9 ± 1.5	−0. 695 ± 0.053	0.717 ± 0.053	12.8 ± 0.2
D	0.643 ± 0.035	197.5 ± 1.5	−0.193 ± 0.065	−0.613 ± 0.034	13.0 ± 0.3

RA, right ascension. Dec., declination.

planets roughly an order of magnitude closer to stars in terms of diffraction beamwidths will clearly ease the search for faint planets around nearby stars. In particular, a small-angle coronagraph and a current-generation adaptive optics system could enable smaller (for example, 1.5–4 m) ground-based telescopes to carry out high-contrast disk[23] and exoplanet observations, especially important for time-intensive surveys.

Of course, next-generation adaptive optics systems on large ground-based telescopes[12–15] will be needed to reap the full benefits of small-angle coronagraphs. Reaching the smallest possible angles is important both because reflected-light planets increase in brightness closer to stars, and because observing young planets still in formation requires access to more distant stars. Reaching the smallest possible angles is also important for potential space-based telescopes aiming at terrestrial exoplanets, because it allows the telescopes to be smaller and more affordable. For example, even a 2-m space telescope with an innermost angle of about $1.5\lambda/D$ at $\lambda = 0.6\,\mu$m can access potential planets within approximately one astronomical unit of stars to a distance of about 10 parsecs, a volume which encompasses several hundred stars, thus providing a reasonable possibility of uncovering nearby terrestrial analogues.

Received 21 November 2009; accepted 26 February 2010.

1. Marois, C. *et al.* Direct imaging of multiple planets orbiting the star HR8799. *Science* **322,** 1348–1352 (2008).
2. Lafreniere, D., Marois, C., Doyon, R. & Barman, T. HST/NICMOS detection of HR8799b in 1998. *Astrophys. J.* **694,** L148–L152 (2009).
3. Fukagawa, M. *et al.* H-band image of a planetary companion around HR 8799 in 2002. *Astrophys. J.* **696,** L1–L5 (2009).
4. Metchev, S., Marois, C. & Zuckerman, B. Pre-discovery 2007 image of the HR 8799 planetary system. *Astrophys. J.* **705,** L204–L207 (2009).
5. Biller, B. *et al.* An imaging survey for extrasolar planets around 45 close, young stars with the simultaneous differential imager at the Very Large Telescope and MMT. *Astrophys. J.* **173** (Suppl.), 143–165 (2007).
6. Foo, G., Palacios, D. M. & Swartzlander, G. A. Jr. Optical vortex coronagraph. *Opt. Lett.* **30,** 3308–3310 (2005).
7. Mawet, D., Riaud, P., Absil, O. & Surdej, J. Annular groove phase mask coronagraph. *Astrophys. J.* **633,** 1191–1200 (2005).
8. Swartzlander, G. A. Jr *et al.* Astronomical demonstration of an optical vortex coronagraph. *Opt. Express* **16,** 10200–10297 (2008).
9. Mawet, D. *et al.* Optical vectorial vortex coronagraphs using liquid crystal polymers: theory, manufacturing and laboratory demonstration. *Opt. Express* **17,** 1902–1918 (2009).
10. Serabyn, E. *et al.* Extreme adaptive optics imaging with a clear and well-corrected off-axis telescope subaperture. *Astrophys. J.* **658,** 1386–1391 (2007).
11. Serabyn, E. *et al.* Imaging faint brown dwarf companions close to bright stars with a small, well-corrected telescope aperture. *Astrophys. J.* **696,** 40–46 (2009).
12. Macintosh, B. A. *et al.* The Gemini Planet Imager: from science to design to construction. *Proc. SPIE* **7015,** 701518 (2008).
13. Beuzit, J.-L. *et al.* SPHERE: a planet finder instrument for the VLT. *Proc. SPIE* **7014,** 701418 (2008).
14. Hodapp, K. W. *et al.* HiCIAO: the Subaru Telescope's new high-contrast coronographic imager for adaptive optics. *Proc. SPIE* **7014,** 701419 (2008).
15. Bouchez, A. H. *et al.* The PALM-3000 high-order adaptive optics system for Palomar Observatory. *Proc. SPIE* **7015,** 70150Z (2008).
16. Jenkins, C. Optical vortex coronagraphs on ground-based telesopes. *Mon. Not. R. Astron. Soc.* **384,** 515–524 (2008).
17. Bikkannavar, S., Ohara, C. & Troy, M. Autonomous phase retrieval control for calibration of the Palomar Adaptive Optics system. *Proc. SPIE* **7015,** 70155K (2008).
18. Guyon, O., Pluzhnik, E. A., Kuchner, M. J., Collins, B. & Ridgway, S. T. Theoretical limits on extrasolar terrestrial planet detection with coronagraphs. *Astrophys. J.* **167** (Suppl.), 81–99 (2006).
19. Mawet, D. *et al.* The Vector Vortex Coronagraph: laboratory results and first light at Palomar Observatory. *Astrophys. J.* **709,** 53–57 (2010).
20. Lafrenière, D., Marois, C. & Doyon, R. Nadeau, D. & Artigau, É. A new algorithm for point-spread function subtraction in high-contrast imaging: a demonstration with angular differential imaging. *Astrophys. J.* **660,** 770–780 (2007).
21. Malbet, F., Yu, J. W. & Shao, M. High-dynamic-range imaging using a deformable mirror for space coronography. *Publ. Astron. Soc. Pacif.* **107,** 386–398 (1995).
22. Boccaletti, A., Chauvin, G., Baudoz, P. & Beuzit, J.-L. Coronagraphic near-IR photometry of AB Doradus C. *Astron. Astrophys.* **482,** 939–943 (2008).
23. Mawet, D., Serabyn, E., Stapelfeldt, K. & Crepp, J. Imaging the debris disk of HD 32297 with a phase-mask coronagraph at high Strehl ratio. *Astrophys. J.* **702,** L47–L50 (2009).

Supplementary Information is linked to the online version of the paper at www.nature.com/nature.

Acknowledgements This work was carried out at the Jet Propulsion Laboratory, California Institute of Technology, under contract with the National Aeronautics and Space Administration, and is based on observations obtained at the Hale Telescope, Palomar Observatory, as part of a continuing collaboration between the California Institute of Technology, NASA/JPL, and Cornell University. We thank the staff of the Palomar Observatory and both the JPL and Caltech Palomar Adaptive Optics (PALAO) teams, as well as our colleagues at JDS Uniphase, where our vortex masks are manufactured.

Author Contributions All authors contributed equally to this work.

Author Information Reprints and permissions information is available at www.nature.com/reprints. The authors declare no competing financial interests. Correspondence and requests for materials should be addressed to E.S. (gene.serabyn@jpl.nasa.gov).

LETTERS

Random numbers certified by Bell's theorem

S. Pironio[1,2]*, A. Acín[3,4]*, S. Massar[1]*, A. Boyer de la Giroday[5], D. N. Matsukevich[6], P. Maunz[6], S. Olmschenk[6], D. Hayes[6], L. Luo[6], T. A. Manning[6] & C. Monroe[6]

Randomness is a fundamental feature of nature and a valuable resource for applications ranging from cryptography and gambling to numerical simulation of physical and biological systems. Random numbers, however, are difficult to characterize mathematically[1], and their generation must rely on an unpredictable physical process[2–6]. Inaccuracies in the theoretical modelling of such processes or failures of the devices, possibly due to adversarial attacks, limit the reliability of random number generators in ways that are difficult to control and detect. Here, inspired by earlier work on non-locality-based[7–9] and device-independent[10–14] quantum information processing, we show that the non-local correlations of entangled quantum particles can be used to certify the presence of genuine randomness. It is thereby possible to design a cryptographically secure random number generator that does not require any assumption about the internal working of the device. Such a strong form of randomness generation is impossible classically and possible in quantum systems only if certified by a Bell inequality violation[15]. We carry out a proof-of-concept demonstration of this proposal in a system of two entangled atoms separated by approximately one metre. The observed Bell inequality violation, featuring near perfect detection efficiency, guarantees that 42 new random numbers are generated with 99 per cent confidence. Our results lay the groundwork for future device-independent quantum information experiments and for addressing fundamental issues raised by the intrinsic randomness of quantum theory.

The characterization of true randomness is elusive. There exist statistical tests used to verify the absence of certain patterns in a stream of numbers[16,17], but no finite set of tests can ever be considered complete, as there may be patterns not covered by such tests. For example, certain pseudo-random number generators are deterministic in nature, yet produce results that satisfy all the randomness tests[18]. At a more fundamental level, there is no such thing as true randomness in the classical world: any classical system admits in principle a deterministic description and thus appears random to us as a consequence of a lack of knowledge about its fundamental description. Quantum theory is, on the other hand, fundamentally random; yet, in any real experiment the intrinsic randomness of quantum systems is necessarily mixed-up with an apparent randomness that results from noise or lack of control of the experiment. It is therefore unclear how to certify or quantify unequivocally the observed random behaviour even of a quantum process.

These considerations are of direct relevance to applications of randomness, and in particular cryptographic applications. Imperfections in random number generators[2–6,18] (RNGs) can introduce patterns undetected by statistical tests but known to an adversary. Furthermore, if the device is not trusted but viewed as a black box prepared by an adversary, no existing RNGs can establish the presence of private randomness. Indeed, one can never exclude the possibility that the numbers were generated in advance by the adversary and copied into a memory located inside the device.

Here we establish a fundamental link between the violation of Bell inequalities and the unpredictable character of the outcomes of quantum measurements and show, as originally proposed in ref. 14, that the non-local correlations of quantum states can be used to generate certified private randomness. The violation of a Bell inequality[15] guarantees that the observed outputs are not predetermined and that they arise from entangled quantum systems that possess intrinsic randomness. For simplicity, we consider the Clauser–Horn–Shimony–Holt (CHSH) form of Bell inequality[19], but our approach is general and applies to any Bell inequality. We thus consider two separate systems that can each be measured in two different ways, with a measurement on each system resulting in one of two values (Fig. 1). The binary variables x and y describe the type of measurement performed on each system, resulting in respective binary measurement outcomes a and b. We quantify the Bell inequality violation through the CHSH correlation function[19]

$$I = \sum_{x,y} (-1)^{xy} [P(a=b|xy) - P(a\neq b|xy)] \qquad (1)$$

where $P(a=b|xy)$ is the probability that $a=b$ when settings (x, y) are chosen, and $P(a\neq b|xy)$ is defined analogously. Systems that admit a local, hence deterministic[20], description satisfy $I\leq 2$. Certain measurements performed on entangled states, however, can violate this inequality.

In order to estimate the Bell violation, the experiment is repeated n times in succession. The measurement choices (x, y) for each trial are generated by an identical and independent probability distribution $P(xy)$. We denote the final output string after the n runs $r=(a_1, b_1; \ldots; a_n, b_n)$ and the input string $s=(x_1, y_1; \ldots; x_n, y_n)$. An estimator $\hat{I}$ of the CHSH expression, equation (1), determined from the observed data is given by

$$\hat{I} = \frac{1}{n}\sum_{x,y} (-1)^{xy} [N(a=b,xy) - N(a\neq b,xy)]/P(xy) \qquad (2)$$

where $N(a=b, xy)$ is the number of times that the measurements x, y were performed and that the outcomes a and b were found equal after n realizations, and where $N(a\neq b, xy)$ is defined analogously.

The randomness of the output string r can be quantified by the min-entropy[21] $H_\infty(R|S) = -\log_2[\max_r P(r|s)]$, where $P(r|s)$ is the conditional probability of obtaining the outcomes r when the measurements s are made and the maximum is taken over all possible values of the output string r. We show (Supplementary Information A) that the min-entropy of the outputs r is bounded by

$$H_\infty(R|S) \geq nf\left(\hat{I}-\varepsilon\right) \qquad (3)$$

[1]Laboratoire d'Information Quantique, CP 225, Université Libre de Bruxelles, Bvd Du Triomphe, 1050 Bruxelles, Belgium. [2]Group of Applied Physics, University of Geneva, 1211 Geneva, Switzerland. [3]ICFO-Institut de Ciencies Fotoniques, Mediterranean Technology Park, 08860 Castelldefels (Barcelona), Spain. [4]ICREA-Institucio Catalana de Recerca i Estudis Avançats, 08010 Barcelona, Spain. [5]Cavendish Laboratory, Cambridge University, Cambridge CB3 0HE, UK. [6]Joint Quantum Institute, University of Maryland Department of Physics and National Institute of Standards and Technology, College Park, Maryland 20742, USA.
*These authors contributed equally to this work.

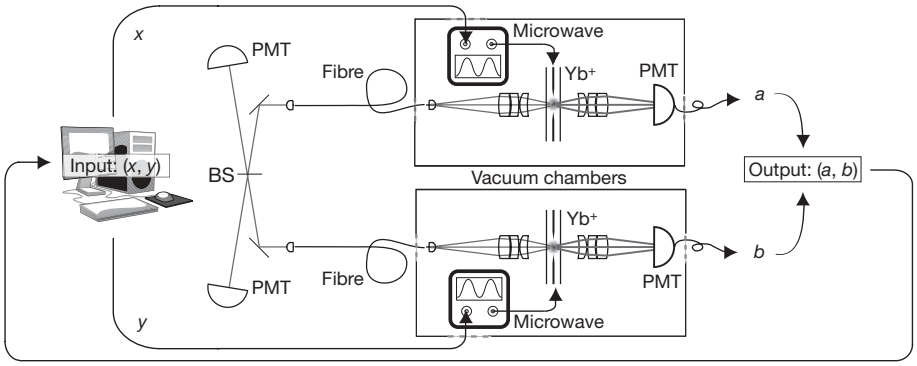

Figure 1 | Experimental realization of private random number generator using two $^{171}Yb^{+}$ qubits trapped in independent vacuum chambers. Each atom emits a single photon (to the left) that is entangled with its host atomic qubit and coupled into optical fibres; the interference of the photons on the beamsplitter (BS) and subsequent coincidence detection on photomultiplier tubes (PMT) herald the entanglement of the atomic qubits[26]. After the qubits are entangled, binary random inputs (x, y) are fed to microwave oscillators that coherently rotate each qubit in one of two ways before measurement[26]. Each qubit is finally measured through fluorescence that is collected by the PMTs[25] (right), resulting in the binary outputs (a, b). Abstractly, we can view this scheme as composed of two black boxes that receive inputs x, y and produce outputs a, b. In our theoretical analysis, no hypotheses are made about the internal working of the devices, but the classical and quantum information flowing in and out of the boxes is restricted (dashed lines). In particular, the two boxes are free to communicate before inputs are introduced (to establish shared entanglement), but are no longer allowed to interact during the measurement process. Moreover, the values of the inputs are revealed to the boxes only at the beginning of the measurement process. In the experiment, no active measures are taken to control the flow of information in and out of the systems. However, once the atoms are entangled, direct interaction between them is negligible. In addition, the value of the chosen measurement bases (x, y), obtained by combining the outputs of several random number generators, is unlikely to be correlated to the state of the atoms before the measurement microwave pulses are applied. The conditions for the bound (equation (3)) on the entropy of the outputs should thus be satisfied.

with probability greater than $1-\delta$, where $\varepsilon = O\left(\sqrt{-\log\delta/(q^2 n)}\right)$ is a statistical parameter and $q = \min_{x,y} P(xy)$ is the probability of the least probable input pair. The function $f(I)$ is obtained using semidefinite programming[22,23] and presented in Fig. 2. To derive the bound given as equation (3), we make the following assumptions: (1) the two observed systems satisfy the laws of quantum theory; (2) they are separated and non-interacting during each measurement step i; and (3) the inputs x_i, y_i are generated by random processes that are independent and uncorrelated from the systems and their value is revealed to the systems only at step i (Fig. 1). Other than these assumptions, no constraints are imposed on the states, measurements, or the dimension of the Hilbert space. We do not even assume that the system behaves identically and independently for each trial; for instance, the devices may have an internal memory (possibly quantum), so that the ith measurement can depend on the previous $i-1$ results and measurement settings. Any value of the min-entropy smaller than that given by equation (3) is incompatible with quantum theory. The observed CHSH quantity $\hat{I}$ thus provides a bound (Fig. 3) on the randomness produced by the quantum devices, independent of any apparent randomness that could arise from noise or limited control over the experiment.

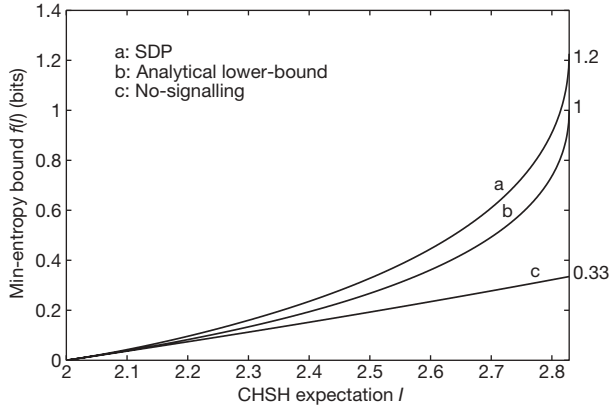

Figure 2 | Plot of the function $f(I)$ bounding the output randomness. The function $f(I)$ can be interpreted as a bound on the min-entropy per use of the system for a given CHSH expectation I, in the asymptotic limit of large n where finite statistics effects (the parameter ε in equation (3)) can be neglected. The function $f(I)$ (curve a) is derived through semidefinite programming using the techniques of refs 22 and 23 (semidefinite programming is a numerical method that is guaranteed to converge to the exact result). Curve b corresponds to the analytical lower-bound $f(I) \geq -\log_2\left[1-\log_2\left(1+\sqrt{2-\frac{I^2}{4}}\right)\right]$. Curve c corresponds to the minimal value $f(I) = -\log_2(3/2 - I/4)$ of the min-entropy implied by the no-signalling principle alone. The function $f(I)$ starts at zero at the local threshold value $I = 2$. Systems that violate the CHSH inequality ($I > 2$), on the other hand, satisfy $f(I) > 0$, that is, have a positive min-entropy.

This result can be exploited to construct a novel RNG where the violation of a Bell inequality guarantees that the output is random and private from any adversary, even in a device-independent scenario[12,13] where the internal workings of the two quantum devices are unknown or not trusted (Supplementary Information B). Some amount of randomness at the inputs is necessary to perform the statistical tests used to estimate the Bell inequality violation. Hence what we describe here is a randomness expansion scheme[14], where a small private random seed is expanded into a longer private random string. The randomness used to choose the inputs needs not be divulged and can be used subsequently for another task. The final random string, the concatenation of the input and output random strings, is thus manifestly longer than the initial one. However, when n becomes sufficiently large, a catalysis effect is possible wherein a seed string of length $O\left(\sqrt{n}\log\sqrt{n}\right)$ produces a much longer random output string of entropy $O(n)$, as illustrated in Fig. 3 (Supplementary Information B). This is possible because I can be adequately estimated without consuming much randomness by using the same input pair most of the time (for example, $(x, y) = (0, 0)$) while only seldom sampling from the other possibilities, in which case $q \ll 1$. This follows from the fact that the CHSH expression depends only the conditional probabilities $P(ab|xy)$, which can be estimated even if x, y are not uniformly distributed.

Although the final output string may not be uniformly random (it may not even pass one of the usual statistical tests[16,17] of randomness), we are guaranteed that its entropy is bounded by equation (3). With the help of a small private random seed, the output string can then be classically processed using a randomness extractor[24] to convert it into a string of size $nf\left(\hat{I}-\varepsilon\right)$ that is nearly uniform and uncorrelated to

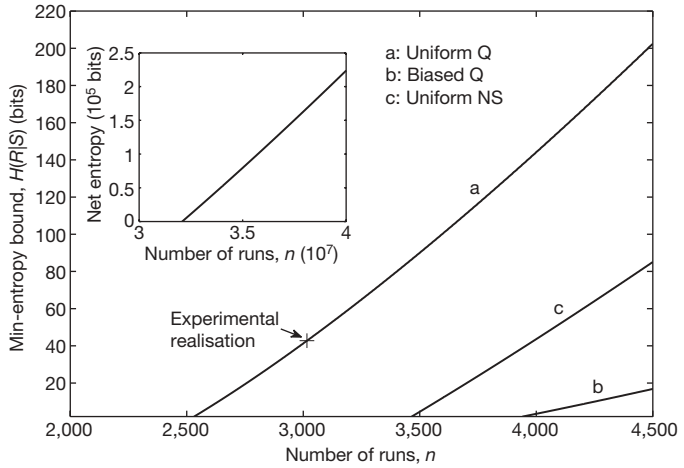

Figure 3 | Bound $nf(I)$ on the minimum entropy produced versus the number of trials n for an observed CHSH violation of $\hat{I}=2.414$, and a confidence level $1-\delta=99\%$. The amount of randomness given by the bound (equation (3)) depends on the probability with which the inputs of each trial (x_i, y_i) are chosen through the parameter $q=\min_{x,y}[P(x,y)]$, where $P(x, y)$ is the probability distribution of the inputs. We have plotted the bounds on the entropy implied by quantum theory for a uniform choice of inputs $[P(x, y)=1/4]$ (curve a) and for a biased choice of inputs given by $P(00)=1-3q$, $P(01)=P(10)=P(11)=q$, where $q=\alpha n^{-1/2}$ with $\alpha=11$ (curve b). For a given number n of uses of the devices, the uniform choice of inputs leads to more randomness in the outputs. On the other hand, biased inputs require less randomness to be generated, and the net amount of randomness produced (given by the difference between the output and input entropy) becomes positive for sufficiently large n. Curve c represents the bound on the entropy implied by the no-signalling principle alone for a uniform choice of inputs. Note that in all cases, a minimal number of uses of the devices (a few thousand) is required to guarantee that some randomness has been produced at the confidence level $1-\delta=99\%$ The inset shows the net amount of entropy produced (output entropy minus input entropy) for the biased choice of inputs with the observed CHSH violation.

the information of an adversary. The bound, equation (3), establishes security of our randomness expansion protocol against an adversary that measures his side-information before the randomness extraction step; for example, against an adversary that has only a short-lived or bounded quantum memory. This is because it applies when conditioned to any measurement performed by the adversary. However, our protocol is not yet proven to be universally composable against a full quantum adversary, that is, secure against an adversary that stores his side-information in a quantum memory which can be measured at a later stage. A universally composable proof would also cover the situation in which the adversary tries to estimate the random numbers after getting partial information about them. Proving universally composable security of our protocol would also probably lead to much more efficient randomness expansion schemes. Note that the fact that the bound, equation (3), holds for devices that have an internal memory is a significant advance over the device-independent protocols[9,12,13] proposed so far. It is the crucial feature that makes our protocol practical.

The experimental realization of this scheme requires the observation of a Bell inequality with the detection loophole closed (near-perfect detection of every event), so that the outputs r cannot be deterministically reproduced. The two individual systems should also be sufficiently separated so that they do not interact, but it is not necessary for the two subsystems to be space-like separated (Supplementary Information C).

We realize this situation with two $^{171}Yb^{+}$ atomic ion quantum bits (qubits)[25] confined in two independent vacuum chambers separated by about 1 m. The qubit levels within each atom are entangled through a probabilistic process whereby each atom is entangled with emitted photons and the interference and coincident detection of the two photons heralds successful preparation of a near-maximal entangled state of the two remote atomic qubits through entanglement swapping[26], as described in Fig. 1 and Supplementary Information D. The binary values a and b correspond to subsequent measurement results of each qubit obtained through standard atomic fluorescence techniques (detection error $<3\%$)[25], and every event is recorded. The respective binary measurement bases x and y are chosen randomly and set by coherent qubit rotation operations before measurement. Direct interaction between the atoms is negligible and classical microwave and optical fields used to perform rotations and measurements on one atom have no influence on the other atom (we perform statistical tests to verify that the measurement data are compatible with this hypothesis; Supplementary Information D.4). To estimate the value of the CHSH inequality, we accumulate $n=3{,}016$ successive entanglement events over the period of about one month, summarized in Supplementary Information D.1 and Table 1. The observed CHSH violation of $\hat{I}=2.414$ represents a substantial improvement over previous results[26,27]. The probability that a local theory, possibly including an internal memory of past events[28], could produce such a violation is $P(\hat{I}\geq 2.414)\leq 0.00077$ (Supplementary Information D.3).

In the experiment, we chose a uniform random distribution of the initial input measurement bases, $P(x, y)=1/4$, to minimize the number of runs required to obtain a meaningful bound on the output entropy (Fig. 3). The observed CHSH violation implies that at least $H(R|S)>42$ new random bits are generated in the experiment with a 99% confidence level. This is the first time that one can certify that new randomness is produced in an experiment without a detailed model of the devices. We rely only on a high-level description (atoms confined to independent vacuum chambers separated by one metre) to ensure the absence of interaction between the two subsystems when the measurements are performed. As no active measures are taken in our experiment to control this interaction, these new random bits cannot be considered private in the strongest adversarial device-independent scenario. The level of security provided by our experiment will nevertheless be sufficient for many applications, as it guarantees that almost all failure modes of the devices will be detected. The current experiment does not reach the catalysis regime mentioned above, owing to the low success probability of heralded entanglement generation (2×10^{-8}) (ref. 26). However, it should be possible to exceed the catalysis threshold by improving the photon-collection efficiency through the use of nearby optical collection elements or optical cavities[29].

Stepping back to the more conceptual level, we note that equation (3) relates the random character of quantum theory to the violation of Bell inequalities. This bound can be modified for a situation where we assume only the no-signalling principle instead of the entire quantum formalism (Figs 2 and 3 and Supplementary Information A.3). Such a bound lays the basis for addressing in a statistically significant way one of the most fundamental questions raised by quantum theory: whether our world is compatible with determinism (but then necessarily allows signalling between space-like separated

Table 1 | Experimental results

Inputs (x, y)	Rotations (φ_x, φ_y)	$N(0, 0; x, y)$	$N(0, 1; x, y)$	$N(1, 0; x, y)$	$N(1, 1; x, y)$	Total events	$P(a=b\|xy)$
0, 0	0°, 45°	293	94	70	295	752	0.782
0, 1	0°, 135°	298	70	74	309	751	0.808
1, 0	90°, 45°	283	69	64	291	707	0.812
1, 1	90°, 135°	68	340	309	89	806	0.195

Observed number of events $N(a, b; x, y)$ for which the measurement on one atom gave outcome a and the measurement on the other atom gave outcome b, given the binary choices of the measurement bases (x, y) corresponding to $\pi/2$ qubit rotations with phase angles (φ_x, φ_y) on the equator of the Bloch sphere. The last column gives the fraction of events where $a=b$ given each input. If the experiment is interpreted as consisting of identical and independent realizations (an assumption not made elsewhere in this paper), the data then indicate a CHSH observable of $I=\sum_{x,y}(-1)^{xy}[P(a=b|xy)-P(a\neq b|xy)]=2.414\pm 0.058$, significantly beyond the local-deterministic threshold of $I=2$.

regions), or is inherently random (if signalling between space-liked separated regions is deemed impossible).

Received 25 November 2009; accepted 18 February 2010.

1. Knuth, D. *The Art of Computer Programming* Vol. 2, *Seminumerical Algorithms* (Addison-Wesley, 1981).
2. Jennewein, T., Achleitner, U., Weihs, G., Weinfurter, H. & Zeilinger, A. A fast and compact quantum random number generator. *Rev. Sci. Instrum.* **71,** 1675–1680 (2000).
3. Stefanov, A., Gisin, N., Guinnard, O., Guinnard, L. & Zbinden, H. Optical quantum random number generator. *J. Mod. Opt.* **47,** 595–598 (2000).
4. Dynes, J. F., Yuan, Z. L., Sharpe, A. W. & Shields, A. J. A high speed, postprocessing free, quantum random number generator. *Appl. Phys. Lett.* **93,** 031109 (2008).
5. Atsushi, U. *et al.* Fast physical random bit generation with chaotic semiconductor lasers. *Nature Photon.* **2,** 728–732 (2008).
6. Fiorentino, M., Santori, C., Spillane, S. M., Beausoleil, R. G. & Munro, W. J. Secure self-calibrating quantum random-bit generator. *Phys. Rev. A* **75,** 032334 (2007).
7. Ekert, A. K. Quantum cryptography based on Bell's theorem. *Phys. Rev. Lett.* **67,** 661–663 (1991).
8. Barrett, J., Hardy, L. & Kent, A. No signaling and quantum key distribution. *Phys. Rev. Lett.* **95,** 010503 (2005).
9. Masanes, L. Universally composable privacy amplification from causality constraints. *Phys. Rev. Lett.* **102,** 140501 (2009).
10. Mayers, D. & Yao, A. in *FOCS '98: Proceedings of the 39th Annual Symposium on Foundations of Computer Science* 503–509 (IEEE Computer Society, Washington DC, 1998).
11. Magniez, F., Mayers, D., Mosca, M. & Ollivier, H. in *Proceedings of ICALP 2006* Part I (eds Bugliesi, M. *et al.*) 72–83 (Lecture Notes in Computer Science 4051, Springer, 2006).
12. Acin, A. *et al.* Device-independent security of quantum cryptography against collective attacks. *Phys. Rev. Lett.* **98,** 230501 (2007).
13. Pironio, S. *et al.* Device-independent quantum key distribution secure against collective attacks. *N. J. Phys.* **11,** 045021 (2009).
14. Colbeck, R. *Quantum and Relativistic Protocols for Secure Multi-Party Computation.* PhD dissertation, Univ. Cambridge (2007).
15. Bell, J. S. *Speakable and Unspeakable in Quantum Mechanics: Collected Papers on Quantum Philosophy* (Cambridge Univ. Press, 2004).
16. The Marsaglia Random Number CDROM including the Diehard Battery of Tests of Randomness. Available at ⟨http://www.stat.fsu.edu/pub/diehard/⟩ (2008).
17. Rukhin, A. *et al. A Statistical Test Suite for Random and Pseudorandom Number Generators for Cryptographic Applications* (Special Publication 800–22 Revision 1, National Institute of Standards and Technology, 2008); available at ⟨http://csrc.nist.gov/publications/PubsSPs.html⟩.
18. Matsumoto, M. & Nishimura, T. Mersenne twister: a 623-dimensionally equidistributed uniform pseudo-random number generator. *ACM Trans. Model. Comput. Simul.* **8,** 3–30 (1998).
19. Clauser, J. F., Horne, M. A., Shimony, A. & Holt, R. A. Proposed experiment to test local hidden-variable theories. *Phys. Rev. Lett.* **23,** 880–884 (1969).
20. Fine, A. Hidden variables, joint probability, and the Bell inequalities. *Phys. Rev. Lett.* **48,** 291–295 (1982).
21. Koenig, R., Renner, R. & Schaffner, C. The operational meaning of min- and max-entropy. *IEEE Trans. Inf. Theory* **55,** 4337–4347 (2009).
22. Navascues, M., Pironio, S. & Acin, A. A convergent hierarchy of semidefinite programs characterizing the set of quantum correlations. *N. J. Phys.* **10,** 073013 (2008).
23. Navascues, M., Pironio, S. & Acin, A. Bounding the set of quantum correlations. *Phys. Rev. Lett.* **98,** 010401 (2007).
24. Nisan, N. & Ta-Shma, A. Extracting randomness: a survey and new constructions. *J. Comput. Syst. Sci.* **58,** 148–173 (1999).
25. Olmschenk, S. *et al.* Manipulation and detection of a trapped Yb^+ hyperfine qubit. *Phys. Rev. A* **76,** 052314 (2007).
26. Matsukevich, D. N., Maunz, P., Moehring, D. L., Olmschenk, S. & Monroe, C. Bell inequality violation with two remote atomic qubits. *Phys. Rev. Lett.* **100,** 150404 (2008).
27. Rowe, M. A. *et al.* Experimental violation of a Bell's inequality with efficient detection. *Nature* **409,** 791–794 (2001).
28. Gill, R. D. in *Mathematical Modelling in Physics, Engineering and Cognitive Sciences* Vol. 5, *Proceedings of the International Conference on Foundations of Probability and Physics – 2* (ed. Khrennikov, A.) 179–206 (Växjö Univ. Press., Växjö, 2003).
29. Luo, L. *et al.* Protocols and techniques for a scalable atom-photon quantum network. *Fortschr. Phys.* **57,** 1133–1152 (2009).

Supplementary Information is linked to the online version of the paper at www.nature.com/nature.

Acknowledgements We thank R. Colbeck for sharing his PhD thesis with us. This work was supported by the Swiss NCCR Quantum Photonics, the European ERC-AG QORE, the European projects QAP and COM-PAS, the ERC starting grant PERCENT, the Spanish MEC FIS2007-60182 and Consolider-Ingenio QOIT projects, Generalitat de Catalunya, Caixa Manresa, Fundacio Cellex Barcelona, the Interuniversity Attraction Poles Photonics@be Programme (Belgian Science Policy), the Brussels-Capital Region through the project CRYPTASC and a BB2B Grant, the US Army Research Office with funds from IARPA, the National Science Foundation (NSF) Physics at the Information Frontier Program, and the NSF Physics Frontier Center at JQI.

Author Contributions S.P., A.A., S.M. and A.B.d.I.G. developed the theoretical aspects of this work. D.N.M., P.M., S.O., D.H., L.L., T.A.M. and C.M. performed the experiments.

Author Information Reprints and permissions information is available at www.nature.com/reprints. The authors declare no competing financial interests. Correspondence and requests for materials should be addressed to A.A. (antonio.acin@icfo.es).

LETTERS

Catastrophic cascade of failures in interdependent networks

Sergey V. Buldyrev[1,2], Roni Parshani[3], Gerald Paul[2], H. Eugene Stanley[2] & Shlomo Havlin[3]

Complex networks have been studied intensively for a decade, but research still focuses on the limited case of a single, non-interacting network[1–14]. Modern systems are coupled together[15–19] and therefore should be modelled as interdependent networks. A fundamental property of interdependent networks is that failure of nodes in one network may lead to failure of dependent nodes in other networks. This may happen recursively and can lead to a cascade of failures. In fact, a failure of a very small fraction of nodes in one network may lead to the complete fragmentation of a system of several interdependent networks. A dramatic real-world example of a cascade of failures ('concurrent malfunction') is the electrical blackout that affected much of Italy on 28 September 2003: the shutdown of power stations directly led to the failure of nodes in the Internet communication network, which in turn caused further breakdown of power stations[20]. Here we develop a framework for understanding the robustness of interacting networks subject to such cascading failures. We present exact analytical solutions for the critical fraction of nodes that, on removal, will lead to a failure cascade and to a complete fragmentation of two interdependent networks. Surprisingly, a broader degree distribution increases the vulnerability of interdependent networks to random failure, which is opposite to how a single network behaves. Our findings highlight the need to consider interdependent network properties in designing robust networks.

Today's networks are becoming increasingly dependent on one another. Diverse infrastructures such as water supply, transportation, fuel and power stations are coupled together. We show that owing to this coupling, interdependent networks are extremely sensitive to random failure, such that a random removal of a small fraction of nodes from one network can produce an iterative cascade of failures in several interdependent networks. Electrical blackouts frequently result from a cascade of failures between interdependent networks, and the problem has been dramatically exemplified by the several large-scale blackouts that have occurred in recent years. In this Letter, we demonstrate a cascade of failures using real-world data from a power network and an Internet network (a supervisory control and data acquisition system) that were implicated in the blackout that affected much of Italy on 28 September 2003[20]. These two networks feature a bidirectional dependence such that power stations depend on communication nodes for control and communication nodes depend on power stations for their electricity supply.

Figure 1 shows the two networks and the connections between them, based on the real geographical locations. The figure exemplifies a situation in which an initial failure of only one power station may lead to an iterative cascade of failures that causes both networks to become fragmented. For an isolated single network, a significant number of the network nodes must be randomly removed before the network breaks down. However, when taking into account the dependencies between the networks, removal of only a small fraction of nodes can result in the complete fragmentation of the entire system.

To model interdependent networks, we consider for simplicity, and without loss of generality, two networks, A and B, with the same number of nodes, N. The functioning of node A_i ($i = 1, 2, \ldots, N$), in network A, depends on the ability of node B_i, in network B, to supply a critical resource, and vice versa. If node A_i stops functioning owing to attack or failure, node B_i stops functioning. Similarly, if node B_i stops functioning then node A_i stops functioning. We denote such a dependence by a bidirectional link, $A_i \leftrightarrow B_i$, that defines a one-to-one correspondence between nodes of network A and nodes of network B. Within network A, the nodes are randomly connected by A-links with degree distribution $P_A(k)$, where the degree, k, of each node is defined as the number of A-links connected to that node in network A. Analogously, within network B, the nodes are randomly connected by B-links with degree distribution $P_B(k)$ (Fig. 2).

We begin by randomly removing a fraction, $1 - p$, of the nodes of network A and removing all the A-links connected to these removed nodes (Fig. 2a). Owing to the dependence between the networks, all the nodes in network B that are connected to the removed A-nodes by $A \leftrightarrow B$ links must also be removed (Fig. 2b). Any B-links connected to the removed B-nodes are then also removed. As nodes and links are sequentially removed, each network begins to fragment into connected components, which we call clusters. The clusters in network A and the clusters in network B are different because each network is connected differently. A set of nodes, a, in network A and the corresponding set of nodes, b, in network B form a mutually connected set if (1) each pair of nodes in a is connected by a path that consists of nodes belonging to a and links of network A, and (2) each pair of nodes in b is connected by a path that consists of nodes belonging to b and links of network B. We call a mutually connected set a mutually connected cluster if it cannot be enlarged by adding other nodes and still satisfy the conditions above. Only mutually connected clusters are potentially functional.

To identify these mutually connected clusters, we first define the a_1-clusters as the clusters of network A remaining after a fraction $1 - p$ of the A-nodes are removed as the result of an attack or malfunction (Fig. 2b). This state of the networks is the first stage in the cascade of failures. Next we define the b_1-sets as the sets of B-nodes that are connected to a_1-clusters by $A \leftrightarrow B$ links. According to the definition of mutually connected clusters, all the B-links connecting different b_1-sets must be removed. Because the two networks are connected differently, each b_1-set may split into several clusters, which we define as b_2-clusters (Fig. 2c). The b_1-sets that do not split, and hence coincide with a_1-clusters, are mutually connected. This state of the networks is the second stage in the cascade of failures. In the third stage, we determine all the a_3-clusters (Fig. 2d), in a similar way, and in the fourth stage we determine all the b_4-clusters. We

[1]Department of Physics, Yeshiva University, 500 West 185th Street, New York, New York 10033, USA. [2]Center for Polymer Studies and Department of Physics, Boston University, Boston, Massachusetts 02215, USA. [3]Minerva Center and Department of Physics, Bar-Ilan University, 52900 Ramat-Gan, Israel.

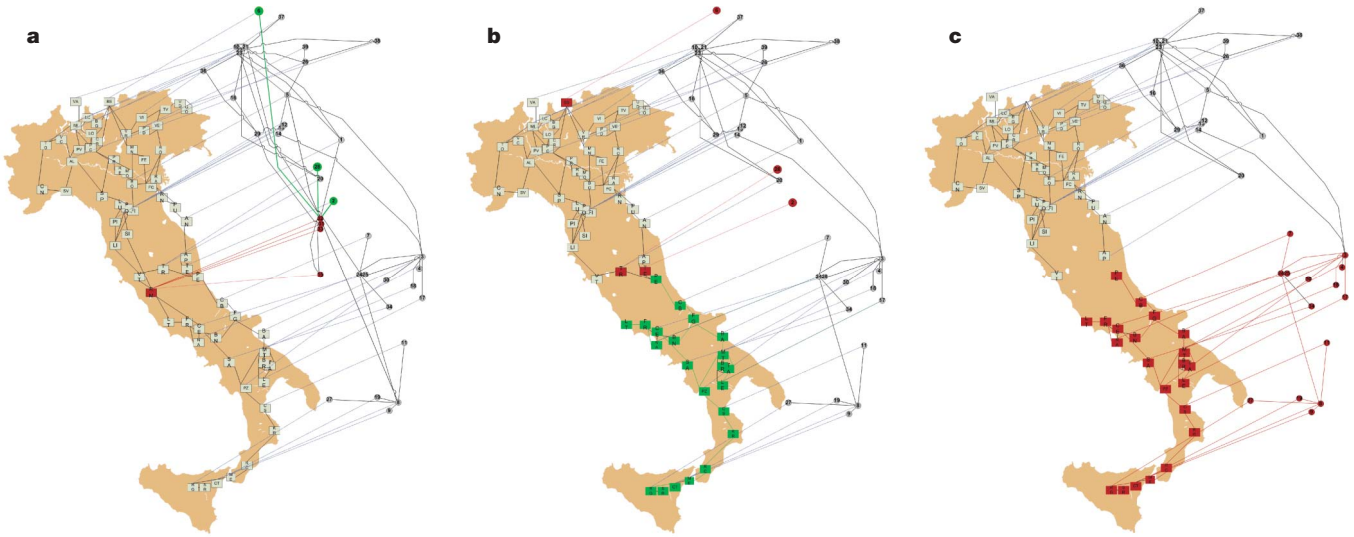

Figure 1 | Modelling a blackout in Italy. Illustration of an iterative process of a cascade of failures using real-world data from a power network (located on the map of Italy) and an Internet network (shifted above the map) that were implicated in an electrical blackout that occurred in Italy in September 2003[20]. The networks are drawn using the real geographical locations and every Internet server is connected to the geographically nearest power station. **a**, One power station is removed (red node on map) from the power network and as a result the Internet nodes depending on it are removed from the Internet network (red nodes above the map). The nodes that will be disconnected from the giant cluster (a cluster that spans the entire network) at the next step are marked in green. **b**, Additional nodes that were disconnected from the Internet communication network giant component are removed (red nodes above map). As a result the power stations depending on them are removed from the power network (red nodes on map). Again, the nodes that will be disconnected from the giant cluster at the next step are marked in green. **c**, Additional nodes that were disconnected from the giant component of the power network are removed (red nodes on map) as well as the nodes in the Internet network that depend on them (red nodes above map).

continue this process until no further splitting and link removal can occur (Fig. 2d). We find that this process leads to a percolation phase transition for the two interdependent networks at a critical threshold, $p = p_c$, which is significantly larger than the equivalent threshold for a single network. As in classical network theory[21–25], we define the giant mutually connected component to be the mutually connected cluster spanning the entire network. Below p_c there is no giant mutually connected component, whereas above p_c a giant mutually connected cluster exists.

Our insight based on percolation theory is that when the network is fragmented, the nodes belonging to the giant component connecting a finite fraction of the network are still functional, whereas the nodes that are part of the remaining small clusters become non-functional. Therefore, for interdependent networks only the giant mutually connected cluster is of interest. The probability that two neighbouring A-nodes are connected by A↔B links to two neighbouring B-nodes scales as $1/N$ (Supplementary Information). Hence, at the end of the cascade process of failures, above p_c only very small mutually connected clusters and one giant mutually connected cluster exist, in contrast to traditional percolation, wherein the cluster size distribution obeys a power law. When the giant component exists, the interdependent networks preserve their functionality; if it does not exist, the networks split into small fragments that cannot function on their own.

We apply our model first to the case of two Erdős–Rényi networks[21–23] with average degrees $\langle k_A \rangle$ and $\langle k_B \rangle$. We remove a random fraction, $1 - p$, of the nodes in network A and follow the iterative process of forming a_1-, b_2-, a_3-, …, b_{2k}- and a_{2k+1}-clusters as

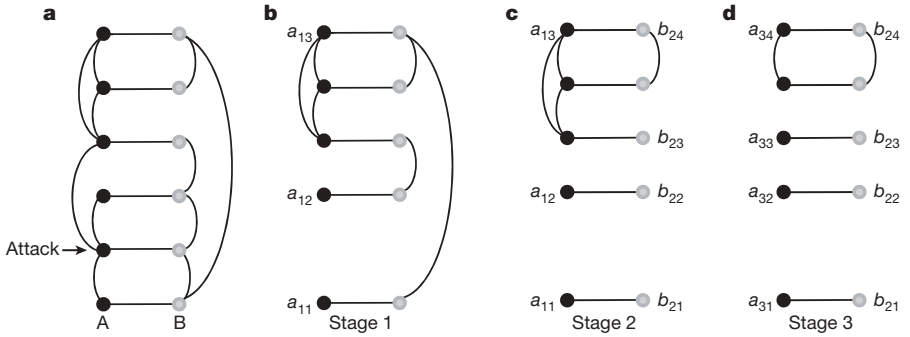

Figure 2 | Modelling an iterative process of a cascade of failures. Each node in network A depends on one and only one node in network B, and vice versa. Links between the networks are shown as horizontal straight lines, and A-links and B-links are shown as arcs. **a**, One node from network A is removed ('attack'). **b**, Stage 1: a dependent node in network B is also eliminated and network A breaks into three a_1-clusters, namely a_{11}, a_{12} and a_{13}. **c**, Stage 2: B-links that link sets of B-nodes connected to separate a_1-clusters are eliminated and network B breaks into four b_2-clusters, namely b_{21}, b_{22}, b_{23} and b_{24}. **d**, Stage 3: A-links that link sets of A-nodes connected to separate b_2-clusters are eliminated and network A breaks into four a_3-clusters, namely a_{31}, a_{32}, a_{33} and a_{34}. These coincide with the clusters b_{21}, b_{22}, b_{23} and b_{24}, and no further link elimination and network breaking occurs. Therefore, each connected b_2-cluster/a_3-cluster pair is a mutually connected cluster and the clusters b_{24} and a_{34}, which are the largest among them, constitute the giant mutually connected component.

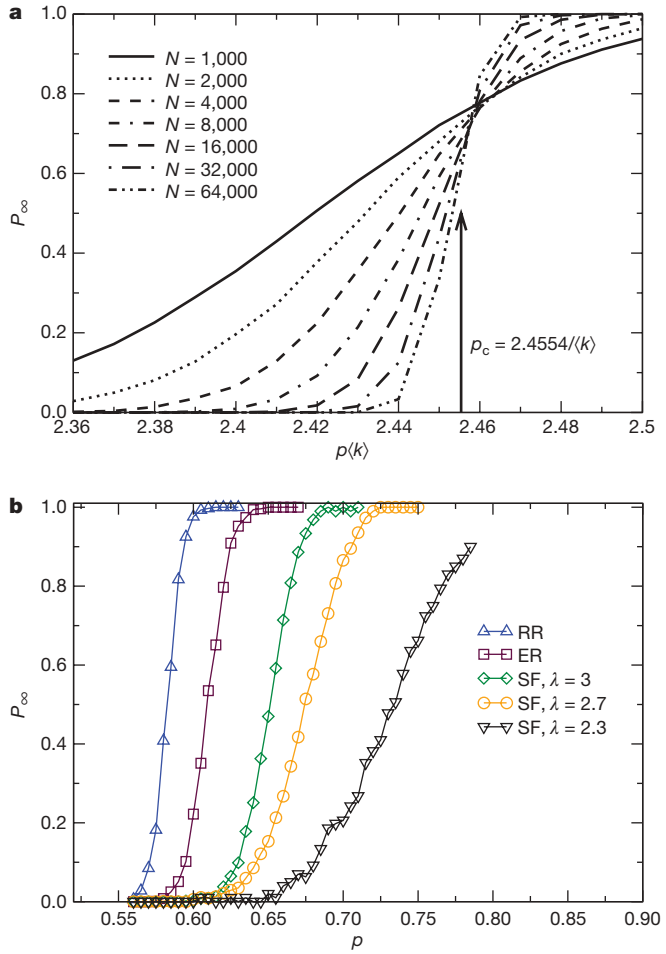

Figure 3 | Numerical validation of theoretical results. a, Numerical simulations of coupled Erdős–Rényi networks with $\langle k\rangle = \langle k_A\rangle = \langle k_B\rangle$ and a finite number of nodes, N. The probability of existence of the giant mutually connected component, P_∞, is shown as function of p for different values of N. As $N\to\infty$, the curves converge to a step function. The theoretical prediction of p_c is shown by the arrow. **b**, Simulation results for P_∞ as a function of p for coupled scale-free (SF) networks with $\lambda = 3$, 2.7, 2.3, coupled Erdős–Rényi (ER) networks and coupled random regular (RR) networks, all with an average degree of $\langle k\rangle = 4$ and $N = 50{,}000$. The simulation results agree with our analytical results. We note that the broader the distribution, the higher the value of p_c.

described above. After each stage, n, in the cascade of failures, we determine the fraction of nodes, μ_n, in the largest a_n- or b_n-cluster. At the end of the process, μ_n converges to μ_∞, the probability that a randomly chosen node belongs to the mutually connected largest cluster. As $N\to\infty$, the probability μ_∞ converges to a well defined function, $\mu_\infty(p)$, which has a single step discontinuity at the threshold $p = p_c$, where it changes from zero for $p < p_c$ to $\mu_\infty(p_c) > 0$ for $p = p_c$ (Supplementary Information). This behaviour is characteristic of a first-order phase transition, quite different from a second-order phase transition such as that characterizing percolation of a single network, where $\mu_\infty(p)$ is a continuous function at $p = p_c$. For a finite N and p close to p_c, the giant mutually connected component exists in a particular network realization with probability $P_\infty(p, N)$. As $N\to\infty$, $P_\infty(p, N)$ converges to a Heaviside step function, $\Theta(p - p_c)$, which discontinuously changes value from zero for $p < p_c$ to one for $p > p_c$ (Fig. 3a). Our simulation results for the value of p_c (Fig. 3a) agree with the analytical results presented below.

For two interdependent scale-free networks[2] with power-law degree distributions, $P_A(k) = P_B(k) \propto k^{-\lambda}$, we find that the existence criteria for the giant component are quite different from those in a single network. For a single scale-free network with $\lambda \leqslant 3$, a giant component exists for every non-zero value of p. However, for interdependent scale-free networks, the giant component does not exist below the critical value $p_c \neq 0$, even for $2 < \lambda \leqslant 3$.

In the case of a single network, p_c is smaller for a broader degree distribution. In sharp contrast, for interdependent networks a broader degree distribution results in a larger value of p_c because high-degree nodes of one network can depend on low-degree nodes of the other. The hubs (defined as nodes of exceptionally large degree) that have a dominant role in the robustness of a single network become vulnerable when a cascade of failures occurs in two interdependent networks. Moreover, a broader distribution with the same average degree implies that there are more low-degree nodes. Because the low-degree nodes are more easily disconnected, the advantage of a broad distribution for a single network becomes a disadvantage for interdependent networks. In Fig. 3b, we demonstrate this behaviour by comparing simulation results for several scale-free networks with different λ values, an Erdős–Rényi network and a random regular network, all with an average degree of $\langle k\rangle = 4$. The simulation results are in full agreement with our analytical results and show that p_c is indeed higher for a broader distribution.

Next we analytically solve our model of interconnected networks using the mathematical technique of generating functions. We will define generating functions for network A; similar equations describe network B. As in refs 24–26, we will introduce generating functions of the degree distributions, $G_{A0}(z) = \sum_k P_A(k) z^k$. Analogously, we will introduce generating functions of the underlying branching processes, $G_{A1}(z) = G'_{A0}(z)/G'_{A0}(1)$.

Random removal of fraction, $1 - p$, of nodes will change the degree distribution of the remaining nodes, so the generating function of the new distribution is equal to the generating function of the original distribution with argument $1 - p(1 - z)$ (ref. 24). We denote the subsets of nodes remaining after the random removal of $1 - p$ nodes as $A_0 \subset A$ and $B_0 \subset B$, and note that there is one-to-one correspondence between nodes in A_0 and nodes in B_0, established by $A \leftrightarrow B$ links. As the total number of nodes in network A is N, the number of nodes in A_0 and B_0 is $N_0 = pN$. The fraction of nodes that belong to the giant component of network A_0 is $g_A(p) = 1 - G_{A0}[1 - p(1 - f_A)]$ (refs 25, 26), where f_A is a function of p that satisfies the transcendental equation $f_A = G_{A1}[1 - p(1 - f_A)]$. Analogous equations exist for network B.

Using the generating function approach, we find that the fraction, μ_n, of the nodes in the giant component after stage n in the cascade of failures obeys a simple recursion relation (Supplementary Information). We find good agreement between simulations and theory (Supplementary Fig. 1).

To determine the final size of the giant mutually connected component, we recall that the fraction of nodes in the giant mutually connected component, μ_∞, is the limit of the sequence μ_n as $n\to\infty$. This limit must satisfy the equations $\mu_{2m+1} = \mu_{2m} = \mu_{2m-1}$ because the cluster is not further fragmented. This condition leads to the following system of two unknowns, x and y (Supplementary Information), where $\mu_\infty = x g_B(x) = y g_A(y)$:

$$\begin{cases} x = g_A(y)p \\ y = g_B(x)p \end{cases} \quad (1)$$

The system of equations (1) has one trivial solution, $x = 0$ and $y = 0$, for any p value, corresponding to the giant mutually connected component being of zero size. If p is large enough, there also exists a solution such that the giant mutually connected component is of non-zero size. We can easily exclude y from these equations and obtain a single equation

$$x = g_A[g_B(x)p]p \quad (2)$$

which can be solved graphically (Supplementary Fig. 2) as the intersection of the straight line $y = x$ and the curve $y = g_A[g_B(x)p]p$. When p is small enough, the curve increases very slowly and does not intersect the straight line (except at the origin, which intersection corresponds to

the trivial solution). A nontrivial solution first emerges in the critical case ($p = p_c$), in which the line touches the curve at a single point, $x = x_c$, where they have equal derivatives. Therefore, we have the condition

$$1 = p^2 \frac{dg_A}{dx}[pg_B(x)] \frac{dg_B}{dx}(x)\Big|_{x=x_c,\, p=p_c} \quad (3)$$

which, together with equation (2), yields the solution for p_c and the critical size of the giant mutually connected component, $\mu_\infty(p_c) = x_c g_B(x_c)$.

In the case of two Erdős–Rényi networks[21–23], the problem can be solved explicitly. Then, $G_{A1}(x) = G_{A0} = \exp[\langle k_A\rangle(x-1)]$, $G_{B1} = G_{B0} = \exp[\langle k_B\rangle(x-1)]$ and the system of transcendental equations (2) and (3) for the critical value of $p = p_c$ can be expressed in terms of elementary functions (Supplementary Information). In the simple case with $\langle k_A\rangle = \langle k_B\rangle = \langle k\rangle$, the critical parameters can be expressed in terms of the nontrivial root $f = f_A = f_B = 0.28467$ of the equation $f = \exp[(f-1)/2f]$. We find that $p_c = [2\langle k\rangle f(1-f)]^{-1} = 2.4554/\langle k\rangle$ and that $\mu_\infty(p_c) = (1-f)/(2\langle k\rangle f) = 1.2564/\langle k\rangle$. Our simulations of Erdős–Rényi networks agree with our theory (Fig. 3a).

We also find that the known result for a single scale-free network, namely that $p_c \to 0$ as $N \to \infty$ for $\lambda \le 3$, is not valid for two scale-free interdependent networks, where instead p_c is finite for any $\lambda > 2$. Analysis of the behaviour of the generating functions as $z \to 1$ shows that as $x \to 0$ the right-hand side of equation (2) can be approximated by a power law, Cx^η (see Supplementary Information for a detailed derivation), where C is constant and

$$\eta = 1/(3-\lambda_A)(3-\lambda_B)$$

For $2 < \lambda_A < 3$ and $2 < \lambda_B < 3$, $\eta > 1$. Thus, the curve $y = g_A[g_B(x)p]p$ always passes below $y = x$ as $x \to 0$ and for sufficiently small values of p we do not have a non-trivial solution (Supplementary Fig. 2), which means that the giant mutually connected component is absent. Hence, we have a percolation phase transition at some finite $p = p_c > 0$ (Fig. 3b).

The model presented here captures the important phenomenon of a cascade of failures in interdependent networks that results in the first-order percolation phase transition. The model can be generalized to the case of three or more interdependent networks, to the case in which the A ↔ B links connecting the networks are unidirectional rather than bidirectional, and to the case in which a node from network A can depend on more than one node from network B. All these generalizations can be treated analytically by using generating functions, provided the networks are randomly connected and uncorrelated.

Note added in proof: After this work was completed, we learned of the independent work of E. Leicht and R. de Souza, also addressing the challenges of interacting networks.

Received 22 December 2009; accepted 17 February 2010.

1. Watts, D. J. & Strogatz, S. H. Collective dynamics of 'small-world' networks. *Nature* **393,** 440–442 (1998).
2. Barabási, A.-L. & Albert, R. Emergence of scaling in random networks. *Science* **286,** 509–512 (1999).
3. Albert, R. & Barabási, A.-L. Statistical mechanics of complex networks. *Rev. Mod. Phys.* **74,** 47–97 (2002).
4. Pastor-Satorras, R. & Vespignani, A. *Evolution and Structure of the Internet: A Statistical Physics Approach* (Cambridge Univ. Press, 2006).
5. Dorogovtsev, S. N. & Mendes, J. F. F. *Evolution of Networks: From Biological Nets to the Internet and WWW* (Oxford Univ. Press, 2003).
6. Barrat, A., Barthelemy, M. & Vespignani, A. *Dynamical Processes on Complex Networks* (Cambridge Univ. Press, 2009).
7. Cohen, R. & Erez, K. ben-Avraham, D. & Havlin, S. Resilience of the Internet to random breakdown. *Phys. Rev. Lett.* **85,** 4626–4628 (2000).
8. Newman, M. E. J., Barabsi, A.-L. & Watts, D. J. (eds) *The Structure and Dynamics of Networks* (Princeton Univ. Press, 2006).
9. Newman, M. E. J. The structure and function of complex networks. *Phys. Rev. E* **64,** 026118 (2001).
10. Goh, K. I., Kahng, B. & Kim, D. Universal behavior of load distribution in scale-free networks. *Phys. Rev. Lett.* **87,** 278701 (2001).
11. Callaway, D. S., Newman, M. E. J., Strogatz, S. H. & Watts, D. J. Network robustness and fragility: percolation on random graphs. *Phys. Rev. Lett.* **85,** 5468–5471 (2000).
12. Song, C. *et al.* Self-similarity of complex networks. *Nature* **433,** 392–395 (2005).
13. Motter, A. E. & Lai, Y. C. Cascade-based attacks on complex networks. *Phys. Rev. E* **66,** 065102(R) (2002).
14. Boccaletti, S. *et al.* Complex networks: structure and dynamics. *Phys. Rep.* **424,** 175–308 (2004).
15. Peerenboom, J., Fischer, R. & Whitfield, R. Recovering from disruptions of interdependent critical infrastructures, in *Proc. CRIS/DRM/IIIT/NSF Workshop Mitigat. Vulnerab. Crit. Infrastruct. Catastr. Failures* (2001).
16. Rinaldi, S., Peerenboom, J. & Kelly, T. Identifying, understanding, and analyzing critical infrastructure interdependencies. *IEEE Contr. Syst. Mag.* **21,** 11–25 (2001).
17. Laprie, J. C., Kanoun, K. & Kaniche, M. Modeling interdependencies between the electricity and information infrastructures. *SAFECOMP-2007* **4680,** 54–67 (2007).
18. Kurant, M. & Thiran, P. Layered complex networks. *Phys. Rev. Lett.* **96,** 138701 (2006).
19. Panzieri, S. & Setola, R. Failures propagation in critical interdependent infrastructures. *Int. J. Model. Ident. Contr.* **3,** 69–78 (2008).
20. Rosato, V. *et al.* Modelling interdependent infrastructures using interacting dynamical models. *Int. J. Crit. Infrastruct.* **4,** 63–79 (2008).
21. Erdős, P. & Rényi, A. On random graphs I. *Publ. Math.* **6,** 290–297 (1959).
22. Erdős, P. & Rényi, A. The evolution of random graphs. *Publ. Math. Inst. Hung. Acad. Sci.* **5,** 17–61 (1960).
23. Bollobás, B. *Random Graphs* (Academic, 1985).
24. Newman, M. E. J. Spread of epidemic disease on networks. *Phys. Rev. E* **66,** 016128 (2002).
25. Shao, J. *et al.* Fractal boundaries of complex networks. *Europhys. Lett.* **84,** 48004 (2008).
26. Shao, J., Buldyrev, S. V., Braunstein, L. A., Havlin, S. & Stanley, H. E. Structure of shells in complex networks. *Phys. Rev. E* **80,** 036105 (2009).

Supplementary Information is linked to the online version of the paper at www.nature.com/nature.

Acknowledgements We thank R. Burk for discussions that led the authors to focus on the interesting new scientific principles governing the catastrophic collapse of coupled networks. We also thank V. Rosato for providing the Italy 2003 blackout data. S.V.B. thanks the Office of Academic Affairs of Yeshiva University for funding the Yeshiva University high-performance computer cluster and acknowledges the partial support of this research through the Dr. Bernard W. Gamson Computational Science Center at Yeshiva College. S.V.B., G.P. and H.E.S. thank the Office of Naval Research for support. S.H. thanks the European EPIWORK project and the Israel Science Foundation for financial support. We thank E. Leicht and R. de Souza for discussing their unpublished work with us.

Author Contributions S.V.B., R.P., G.P., H.E.S. and S.H. all participated equally in the conceptual design of the model, the theoretical analysis, the computer simulations and the writing of the paper.

Author Information Reprints and permissions information is available at www.nature.com/reprints. The authors declare no competing financial interests. Correspondence and requests for materials should be addressed to S.V.B. (buldyrev@yu.edu).

LETTERS

Phosphate oxygen isotopic evidence for a temperate and biologically active Archaean ocean

Ruth E. Blake[1], Sae Jung Chang[1] & Aivo Lepland[2,3]

Oxygen and silicon isotope compositions of cherts[1–3] and studies of protein evolution[4] have been interpreted to reflect ocean temperatures of 55–85 °C during the early Palaeoarchaean era (~3.5 billion years ago). A recent study combining oxygen and hydrogen isotope compositions of cherts, however, makes a case for Archaean ocean temperatures being no greater than 40 °C (ref. 5). Ocean temperature can also be assessed using the oxygen isotope composition of phosphate. Recent studies show that ^{18}O:^{16}O ratios of dissolved inorganic phosphate ($\delta^{18}O_P$) reflect ambient seawater temperature as well as biological processing that dominates marine phosphorus cycling at low temperature[6,7]. All forms of life require and concentrate phosphorus, and as a result of biological processing, modern marine phosphates have $\delta^{18}O_P$ values typically between 19–26‰ (VSMOW)[7,8], highly evolved from presumed source values of ~6–8‰ that are characteristic of apatite in igneous rocks[9,10] and meteorites[11]. Here we report oxygen isotope compositions of phosphates in sediments from the 3.2–3.5-billion-year-old Barberton Greenstone Belt in South Africa. We find that $\delta^{18}O_P$ values range from 9.3‰ to 19.9‰ and include the highest values reported for Archaean rocks. The temperatures calculated from our highest $\delta^{18}O_P$ values and assuming equilibrium with sea water with $\delta^{18}O = 0$‰ (ref. 12) range from 26 °C to 35 °C. The higher $\delta^{18}O_P$ values are similar to those of modern marine phosphate and suggest a well-developed phosphorus cycle and evolved biologic activity on the Archaean Earth.

Geochemical fingerprints of early life[13–15] and ancient ocean chemistry may be found in the relatively well-preserved rocks of the Barberton Greenstone Belt—3.2–3.5 billion years old—in southern Africa[16] (Supplementary Figs 1 and 2). The Barberton Greenstone Belt comprises a sequence of volcanic rocks, inter-layered with volumetrically minor sedimentary units consisting of cherts, banded iron formations and variably silicified terrigenous and volcaniclastic sediments[16], which have experienced only low-grade metamorphism[17]. The cherts have been variably interpreted to be of hydrothermal origin, sedimentary precipitates, the products of early diagenetic replacement of pyroclastic sediments, or derived from the interaction of seafloor sediments with silica-saturated Archaean sea water[1,18–20].

A longstanding controversy exists over the interpretation of the oxygen-isotope compositions of Precambrian cherts and the co-existing phosphates that systematically decrease with increasing age[1,2]. Low $\delta^{18}O$ values of Barberton cherts have been attributed to (1) diagenetic /hydrothermal alteration by low-$\delta^{18}O$ fluids[19,20], (2) equilibrium with $\delta^{18}O = 0$‰ sea water and very high (55–85 °C) ocean temperatures[1] or (3) equilibrium with $\delta^{18}O = -10$‰ sea water and low (<40 °C) ocean temperatures[5]. Modelled variations in $\delta^{30}Si$ values of cherts were initially interpreted to support high-temperature (~70 °C) oceans 3.5 billion years ago on the basis of the temperature dependence of silica solubility[3]. A more recent study[21] however, challenges this interpretation and suggests that $\delta^{30}Si$ values do not record high-temperature early Archaean oceans, but rather the influence of hydrothermal fluids.

The new $\delta^{18}O$ analyses of Barberton phosphates and derived temperatures presented here come from outcrop samples of sedimentary units (cherts, banded iron formations, silicified tuffs and silicified sandstone) at various stratigraphic levels (Supplementary Information). Thin-section analyses revealed the presence of discrete phosphate phases only in some samples, consistent with generally low P_2O_5 content ranging from <0.01 to 0.04 wt% (Supplementary

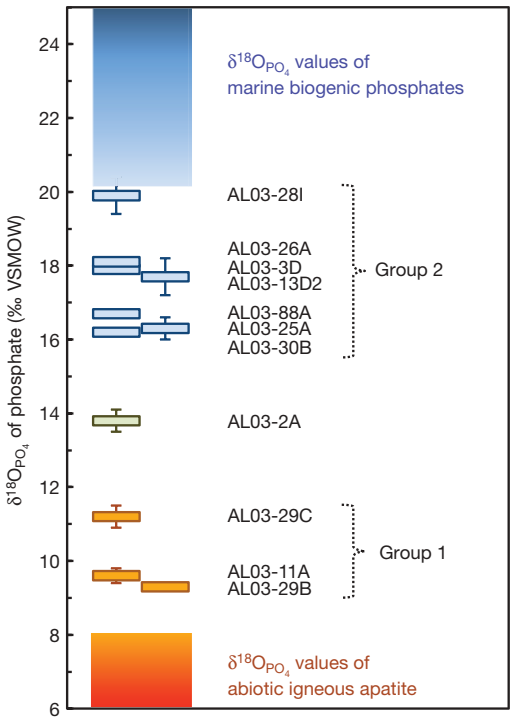

Figure 1 | Comparison of $\delta^{18}O_P$ values from Barberton sediments with modern marine phosphates[7,8] and igneous phosphates[9,10]. Isotopically heavy Group 2 samples have modern-day marine phosphate $\delta^{18}O_P$ values of 17.7–19.9‰ and record biological processing and equilibrium with cool ocean surface waters. Group 1 samples have been affected by secondary veining (Fig. 2a) and their low $\delta^{18}O_P$ values of 9.3–11.2‰ record high-temperature phosphate. Data points between Groups 1 and 2 and in the lower range of Group 2 may reflect mixtures of secondary hydrothermal–metamorphic apatite and primary sedimentary phosphate not fully resolved by our petrographic and sequential extraction methods. Error bars represent standard deviation based on replicate mass spectrometric analyses of single samples (Supplementary Table 1).

[1]Yale University, Department of Geology and Geophysics, New Haven, Connecticut 06520-8109, USA. [2]Geological Survey of Norway, 7491 Trondheim, Norway. [3]Tallinn Technical University, Institute of Geology, 19086 Tallinn, Estonia.

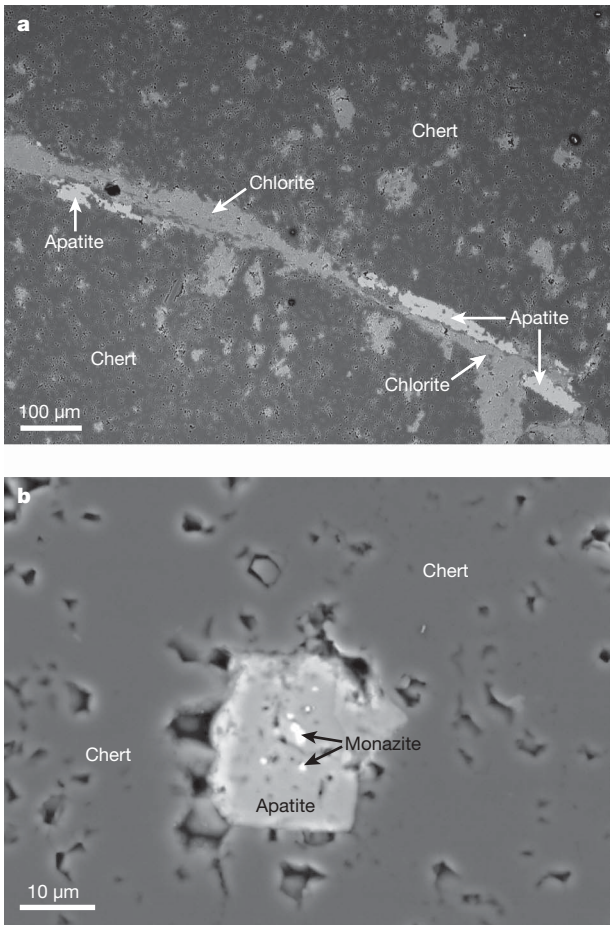

Figure 2 | Back-scattered electron images of phosphate phases in Barberton sediments. **a**, Apatite in cross-cutting chlorite vein in AL03-29B. Samples affected by such secondary veining contain isotopically light phosphate formed during hydrothermal or metamorphic alteration. **b**, Apatite crystal with monazite inclusion in AL03-28C. Disseminated, apatite crystals not related to veins have been identified in some samples, particularly ferruginous cherts and banded iron formations. Phosphate is isotopically heavy in such samples, reflecting a sedimentary origin and cool ambient sea water.

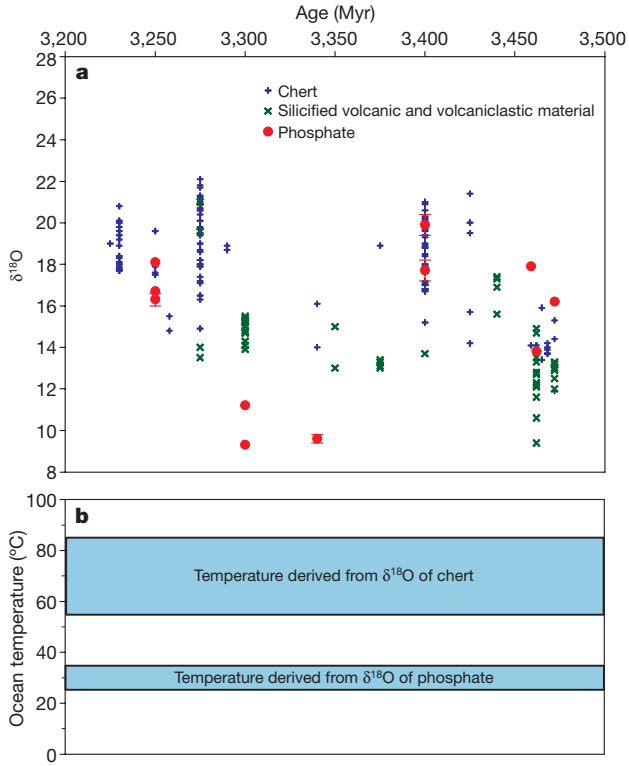

Figure 3 | Comparison of $\delta^{18}O$ values of Barberton phosphates and cherts. Comparison of $\delta^{18}O$ values of Barberton phosphates (this study) and cherts and silicified volcanic and volcaniclastic materials[1] (**a**) with estimates of ocean temperature derived from $\delta^{18}O$ values of chert and phosphate (**b**). If phosphate and chert co-precipitated in equilibrium with the same sea water, phosphate should be >8‰ lighter than co-existing chert ($\Delta^{18}O_{chert\text{-}phosphate}$ >8‰) at seawater temperatures below 70 °C (refs 1, 2, 26). But the $\Delta^{18}O_{chert\text{-}phosphate}$ is considerably smaller, indicating isotopic disequilibrium between phosphate and cherts. This disequilibrium can be explained by decoupled formation in a thermally stratified ocean: phosphate $\delta^{18}O$ records biological processing and equilibrium with cooler surface waters, while chert $\delta^{18}O$ records hydrothermal influence and warmer conditions at the sea floor (Fig. 4). The error bars represent standard deviation based on replicate mass spectrometric analyses of single samples (Supplementary Table 1).

Table 1). Phosphate was extracted from powdered whole-rock samples, purified and converted to silver phosphate for oxygen-isotope analysis using the method of ref. 22 (see Methods). All oxygen-isotope data are reported relative to the Vienna Standard Mean Ocean Water (VSMOW) in per mil (‰).

Previous studies reporting $\delta^{18}O$ analyses of trace amounts of phosphate do not specify the mode of occurrence of PO_4 (such as apatite or other mineral phosphates or organophosphorus). We tested Barberton samples explicitly for the presence of condensed or organic phosphates using ^{18}O-labelled water to prepare extractant solutions. We also used a sequential extraction method and microanalysis technique that provided insight into the occurrence and specific associations (such as apatite veins and PO_4 associated with iron), of the small amounts of PO_4 present in most samples (Methods and Supplementary Table 1).

The $\delta^{18}O_P$ values of Barberton sediments range from 9.3‰ to 19.9‰ (Fig. 1 and Supplementary Table 1) and can be divided into two groups: 9.3–11.2‰ (Group 1) and 16.2–19.9‰ (Group 2), with one value of 13.8‰ that falls between the two defined groups. Phosphate in Group 1 samples could be extracted almost entirely using 10 M nitric acid (HNO_3), whereas the fraction of PO_4 extracted with 6 M hydrochloric acid (HCl) was only 2.4–10.6% of the total PO_4. This result suggests that phosphate in Group 1 samples is present as apatite, which is consistent with petrographic observations that identify the presence of relatively large apatite crystals in cross-cutting veinlets within Group 1 samples (Fig. 2a).

Group 2 samples are typically rich in iron (Fe_2O_3 from 8–50 wt%) with the exception of AL03-3D and AL03-30B. Phosphate has a well-known strong affinity for iron oxides in marine and aquatic systems[23]. Iron oxides have been shown to record $\delta^{18}O_P$ values of dissolved inorganic phosphate in ambient sea water[7] with no measurable fractionation between dissolved inorganic phosphate and iron-oxide-bound PO_4 (Supplementary Table 2). Consistent with a high iron-oxide content, HCl was more effective than HNO_3 for the extraction of PO_4 from Group 2 samples, presumably owing to the formation of Fe–Cl^{n+}(aq) complexes that increase iron solubility. The amount of PO_4 extracted from iron-rich Group 2 samples by 6 M HCl was greater than 63% of the total PO_4 with the exception of sample AL03-30B. This result suggests that phosphate in Group 2 samples is predominantly associated with iron oxides (for example, adsorbed, occluded and/or co-precipitated), although phosphorus and Fe abundances are not linearly correlated in all samples. Minor phosphate in some Group 2 samples occurs as disseminated apatite crystals that occasionally contain inclusions of monazite (Fig. 2b). Trace amounts of monazite and xenotime that are present in some samples would be insoluble in both HNO_3 and HCl solutions.

$\delta^{18}O_P$ values of 9.3–11.2‰ for Group 1 phosphates are close to, but slightly higher than, the range reported for igneous and metamorphic apatites[9,10] (Fig. 1). These relatively low $\delta^{18}O_P$ values,

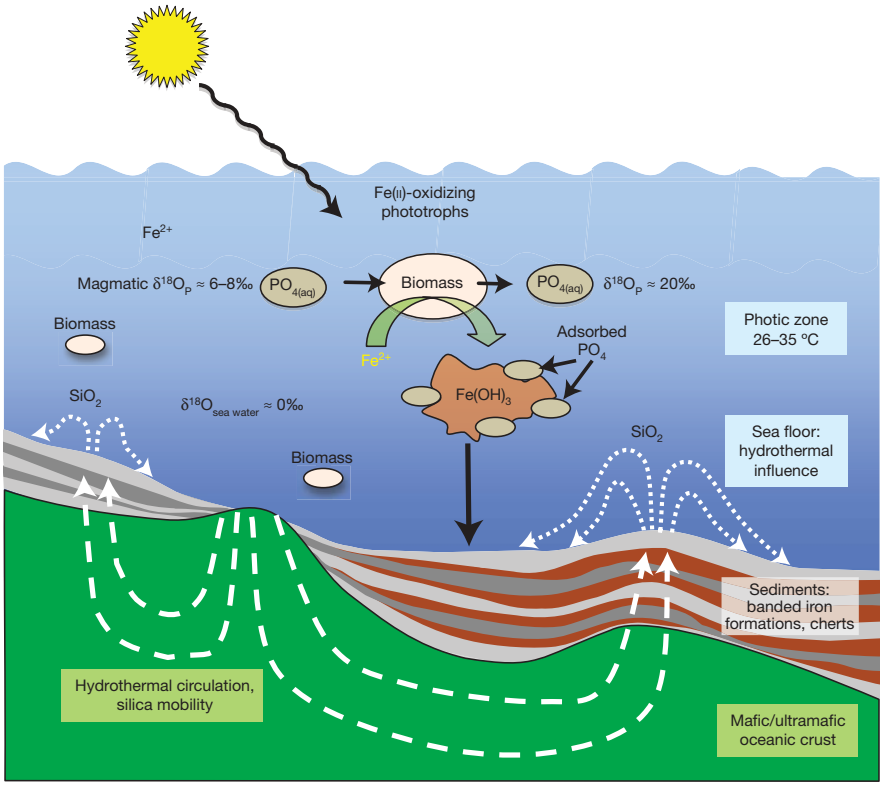

Figure 4 | Sketch of possible phosphorus cycling and phosphate–iron oxide interactions in a thermally stratified Archaean ocean. Biologically processed dissolved phosphate, perhaps involving Fe^{2+} oxidizing anoxygenic phototrophs, records equilibrium $\delta^{18}O_P$ values with cooler ocean surface waters. Dissolved phosphate is scavenged by iron oxides and is carried along with sinking biomass from the photic zone to the shallow and deep sea floor, where some cherts are formed under higher-temperature conditions.

together with evidence for secondary veining and phosphate mobility (Fig. 2a), indicate that Group 1 phosphates are mainly formed from hydrothermal or metamorphic fluids. The $\delta^{18}O_P$ value of 9.3‰ for sample AL03-29B was the lowest of all the samples analysed in this study and thus may represent an end-member value for PO_4 derived from secondary fluids.

$\delta^{18}O_P$ values of 16.2‰ to 19.9‰ for phosphate in Group 2 are close to those of modern marine phosphate[7,8] (Fig. 1). Karhu and Epstein[2] reported a similarly high $\delta^{18}O_P$ value of 17.9‰ for one Barberton chert sample, but this measurement was dismissed as anomalous. Several high $\delta^{18}O_P$ values among Group 2 samples, however, demonstrate that such phosphates are not anomalous but instead probably common, and may be typical for primary sedimentary phosphate in Barberton sediments. The range in $\delta^{18}O_P$ of Group 2 samples can be explained by minor interactions with secondary fluids that variably shifted $\delta^{18}O_P$ to slightly lower values.

Ocean temperatures calculated from O isotope proxies using chert or phosphate depend on the value used for $\delta^{18}O$ of water ($\delta^{18}O_W$). It has been suggested that in the absence of glacial periods, $\delta^{18}O_W$ of sea water has remained constant near a value of about 0‰ over geologic time[12] (see more detailed discussion in Supplementary Information). Oxygen isotope and trace element compositions and alteration patterns in volcanic rocks from the Barberton Greenstone Belt have also been interpreted to reflect ~0‰ Archaean seawater $\delta^{18}O$ values[20,24]. In contrast, it has been proposed that the $\delta^{18}O_W$ of sea water has evolved to present-day values relatively systematically over time from values as low as −10‰ to −13‰ in the Archaean[5,25].

If Group 2 phosphates with the highest $\delta^{18}O_P$ values (17.7 to 19.9‰) formed in isotopic equilibrium with 0‰ sea water, the calculated[26] Archaean ocean temperature ranges from 26 °C to 35 °C. A calculation using the proposed $\delta^{18}O_W$ values of −10‰ to −13‰ and $\delta^{18}O_P$ values of 17.7–19.9‰ gives unrealistic ocean temperatures (−8 to −30°C), so such low $\delta^{18}O_W$ values of Archaean sea water are not compatible with the $\delta^{18}O_P$ record. $\delta^{18}O_W$ values as low as −8.0‰ are compatible with our highest $\delta^{18}O_P$ values at very cold ocean temperatures (1 °C). A more temperate 30 °C ocean would yield a minimum $\delta^{18}O_W$ value of −1.2‰, as constrained by $\delta^{18}O_P$.

If both chert and phosphate precipitated in equilibrium with the same sea water and retained their primary isotopic compositions, the $\delta^{18}O$ values of cherts should be >8‰ higher than co-existing phosphates at temperatures <70 °C (refs 1, 2, 26). Thus, chert formed in equilibrium with 0‰ sea water and phosphates having $\delta^{18}O_P$ values of 17.7–19.9‰ would, at <70 °C, have $\delta^{18}O$ values higher than 26–28‰. No $\delta^{18}O$ values higher than 22.1‰ have been reported for Barberton cherts[1,5], and in some units, phosphates are isotopically heavier than co-occurring cherts[2] (Fig. 3a).

The disequilibrium between Barberton phosphates and cherts can be explained either by extensive secondary overprinting that has led to non-equilibrium resetting of primary $\delta^{18}O$ values, or by decoupling of initial formation of phosphates and cherts. The ability of phosphates to retain primary $\delta^{18}O_P$ values through burial diagenesis and over geologic timescales is evident in the recording of palaeotemperatures and seasonal fluctuations in $\delta^{18}O_P$ by fossil apatites[8,27]. Exchange of sedimentary phosphates with heavy diagenetic/metamorphic fluids or fluids that evolved in the presence of isotopically heavy cherts could potentially result in ^{18}O enrichment of reworked phosphates. This, however, would cause phosphate $\delta^{18}O$ values to shift towards, but not exceed, co-occurring chert values, and thus would not account for the isotopic compositions of some sedimentary units for which phosphate $\delta^{18}O$ values are higher than those of coexisting cherts[2] (Fig. 3a).

At low to moderate temperatures, only biological processes have been shown to cause large shifts in $\delta^{18}O_P$ values of dissolved inorganic PO_4 (refs 6 and 7) and apatite[8] that can account for the evolution of $\delta^{18}O_P$ from igneous PO_4 source values by as much as 15–20‰, to reach modern-marine values in the range 18–26‰. Hence we propose that high $\delta^{18}O_P$ values of 17.7–19.9‰ in Barberton phosphates are the

result of the exchange of oxygen between dissolved PO_4 and sea water ($\delta^{18}O_W = 0‰$) at low temperatures (26–35 °C), driven by enzymatic catalysis and microbial metabolism of phosphorus in the Archaean ocean.

Since the discovery of anoxygenic phototrophs capable of using Fe^{2+} as an electron donor[28], it has been suggested that such organisms could have been responsible for the widespread accumulation of banded iron formations before the oxygenation of Earth's oceans and atmosphere[29]. In the vicinity of Fe oxyhydroxides, produced either as a by-product of anoxygenic photosynthesis, or by alternative abiotic mechanisms involving dissolved O_2 or ultraviolet photolysis in surface waters, any dissolved phosphate would be rapidly adsorbed[30]. The oxygen-isotope ratio of PO_4 scavenged by Fe-oxyhydroxide particles as well as that of degrading biomass carried from the photic zone to the sea floor would reflect the biological cycling and temperature regime of surface waters[7]. Thus, the observed isotopic disequilibrium between phosphates and co-existing cherts can be explained by decoupled formation of these phases, with cherts being possibly affected by hydrothermal processes at the sea floor[19–21] regardless of water depth. Accordingly, high phosphate $\delta^{18}O$ would record low-temperature biological processing and equilibrium with cooler surface waters, while some chert $\delta^{18}O$ values could record warmer seafloor conditions (Fig. 4). Such thermal stratification would be best developed in deeper-water settings, which, in the Barberton Greenstone Belt, are characterized by accumulation of ferruginous cherts and banded iron formations, consistent with typically high $\delta^{18}O_P$ values in ferruginous sediments. Near modern-day $\delta^{18}O$ values of 17.7–19.9‰ for dissolved marine phosphate in Barberton sediments thus provide new evidence that the Archaean ocean was cool and that the marine phosphate reservoir and biological cycling of phosphorus had already evolved significantly by 3.5 billion years ago.

METHODS SUMMARY

This study was made possible by newly developed techniques with which to measure $\delta^{18}O_P$ that reduce sample requirements from ~50 μmol to only 5 μmol PO_4 and allow quantitative precipitation of small amounts of silver phosphate from a large and complex rock matrix. Phosphate was sequentially extracted from whole-rock samples using HNO_3 and HCl, purified by recrystallization and ion resin exchange, then converted to silver phosphate for oxygen isotope analysis. Isotope analyses were carried out at the Earth System Center for Stable Isotope Studies (ESCSIS) at Yale using a Thermo-Chemolysis Elemental Analyser (TC/EA, 1,350 °C) coupled to a Delta +XL continuous-flow isotope ratio monitoring mass spectrometer (Thermo-Finnigan) with precision of ±0.2–0.3‰. Phosphate oxygen-isotope ratios were calibrated against conventional fluorination using three silver phosphate standards according to published methods[22]. The $\delta^{18}O_P$ value of a KH_2PO_4 internal laboratory standard ($14.4 \pm 0.5‰$, s.d., $n = 5$) treated with the same phosphate extraction, purification and precipitation methods as the samples is at the accepted value ($14.2 \pm 0.3‰$, s.d., $n = 5$) (Supplementary Table 1), demonstrating that the sample purification process does not introduce artefacts.

Full Methods and any associated references are available in the online version of the paper at www.nature.com/nature.

Received 10 May 2009; accepted 18 February 2010.

1. Knauth, L. P. & Lowe, D. R. High Archean climatic temperature inferred from oxygen isotope geochemistry of cherts in the 3.5 Ga Swaziland Supergroup, South Africa. *Geol. Soc. Am. Bull.* **115,** 566–580 (2003).
2. Karhu, J. & Epstein, S. The implication of the oxygen isotope records in coexisting cherts and phosphates. *Geochim. Cosmochim. Acta* **50,** 1745–1756 (1986).
3. Robert, F. & Chaussidon, M. A palaeotemperature curve for the Precambrian oceans based on silicon isotopes in cherts. *Nature* **443,** 969–972 (2006).
4. Gaucher, E. A., Govindarajan, S. & Ganesh, O. K. Paleotemperature trend for Precambrian life inferred from resurrected proteins. *Nature* **451,** 704–707 (2008).
5. Hren, M. T., Tice, M. M. & Chamberlain, C. P. Oxygen and hydrogen isotope evidence for a temperate climate 3.42 billion years ago. *Nature* **462,** 205–208 (2009).
6. Blake, R. E., O'Neil, J. R. & Surkov, A. V. Biogeochemical cycling of phosphorus: insights from oxygen isotope effects of phosphoenzymes. *Am. J. Sci.* **305,** 596–620 (2005).
7. Colman, A. S., Blake, R. E., Karl, D. M., Fogel, M. L. & Turekian, K. K. Marine phosphate oxygen isotopes and organic matter remineralization in the oceans. *Proc. Natl Acad. Sci. USA* **102,** 13023–13028 (2005).
8. Shemesh, A., Kolodny, Y. & Luz, B. Oxygen isotope variations in phosphate of biogenic apatites. II. Phosphorite rocks. *Earth Planet. Sci. Lett.* **64,** 405–416 (1983).
9. Taylor, H. P. & Epstein, S. Relationship between O^{18}/O^{16} ratios in coexisting minerals of igneous and metamorphic rocks. Part I. Principles and experimental results. *Geol. Soc. Am. Bull.* **73,** 461–480 (1962).
10. Markel, D., Kolodny, Y., Luz, B. & Nishri, A. Phosphorus cycling and phosphorus sources in Lake Kinneret: tracing by oxygen isotopes in phosphate. *Isr. J. Earth Sci.* **43,** 165–178 (1994).
11. Greenwood, J. P., Blake, R. E. & Coath, C. D. Ion microprobe measurements of $^{18}O/^{16}O$ ratios of phosphate minerals in the Martian meteorites ALH84001 and Los Angeles. *Geochim. Cosmochim. Acta* **67,** 2289–2298 (2003).
12. Muehlenbachs, K. & Clayton, R. N. Oxygen isotope composition of the oceanic crust and its bearing on seawater. *J. Geophys. Res.* **81,** 4365–4369 (1976).
13. Walsh, M. M. & Lowe, D. R. Filamentous microfossils from the 3,500-Myr-old Onverwacht Group, Barberton Mountain Land, South Africa. *Nature* **314,** 530–532 (1985).
14. Byerly, G. R., Lowe, D. R. & Walsh, M. M. Stromatolites from the 3,300–3,500-Myr Swaziland Supergroup, Barberton Mountain Land, South Africa. *Nature* **319,** 489–491 (1986).
15. Furnes, H., Banerjee, N. R., Muehlenbachs, K., Staudigel, H. & de Wit, M. Early life recorded in Archean pillow lavas. *Science* **304,** 578–581 (2004).
16. Lowe, D. R. & Byerly, G. R. in *Earth's Oldest Rocks* (eds van Kranendonk, M. J., Smithies, R. H. & Bennet, V. C.) 481–526 (Elsevier, Developments in Precambrian Geology 15, 2007).
17. Tice, M. M., Bostick, B. C. & Lowe, D. R. Thermal history of the 3.5–3.2 Ga Onverwacht and Fig Tree Groups, Barberton greenstone belt, South Africa, inferred by Raman microspectroscopy of carbonaceous material. *Geology* **32,** 37–40 (2004).
18. Lowe, D. R. in *Geologic Evolution of the Barberton Greenstone Belt, South Africa* (eds Lowe, D. R. & Byerly, G. R.) *Geol. Soc. Am. Spec. Pap.* **329,** 83–114 (1999).
19. Hofmann, A. & Bolhar, R. Carbonaceous cherts in the Barberton Greenstone Belt and their significance for the study of early life in the Archean record. *Astrobiology* **7,** 355–388 (2007).
20. Hofmann, A. & Harris, C. Silica alteration zones in the Barberton greenstone belt: a window into subseafloor processes 3.5–3.3 Ga ago. *Chem. Geol.* **257,** 221–239 (2008).
21. van den Boorn, S. H. J. M., van Bergen, M. J., Nijman, W. & Vroon, P. Z. Dual role of seawater and hydrothermal fluids in Early Archean chert formation: evidence from silicon isotopes. *Geology* **35,** 939–942 (2007).
22. Vennemann, T. W., Fricke, H. C., Blake, R. E., O'Neil, J. R. & Colman, A. Oxygen isotope analysis of phosphates: a comparison of techniques for analysis of Ag_3PO_4. *Chem. Geol.* **185,** 321–336 (2002).
23. Berner, R. A. Phosphate removal from sea water by adsorption on volcanogenic ferric oxides. *Earth Planet. Sci. Lett.* **18,** 77–86 (1973).
24. Smith, H. S., O'Neil, J. R. & Erlank, A. J. in *Archean Geochemistry* (eds Kroner, A., Hanson, G. N. & Goodwin, A. M.) 115–137 (Springer, 1984).
25. Jaffrés, J. B. D., Shields, G. A. & Wallmann, K. The oxygen isotope evolution of seawater: a critical review of a long-standing controversy and an improved geological water cycle model for the past 3.4 billion years. *Earth Sci. Rev.* **83,** 83–122 (2007).
26. Longinelli, A. & Nuti, S. Revised phosphate-water isotopic temperature scale. *Earth Planet. Sci. Lett.* **19,** 373–376 (1973).
27. Kolodny, Y., Luz, B. & Navon, O. Oxygen isotope variations in phosphate of biogenic apatites. I. Fish bone apatite—rechecking the rules of the game. *Earth Planet. Sci. Lett.* **64,** 398–404 (1983).
28. Widdel, F. *et al.* Ferrous iron oxidation by anoxygenic phototrophic bacteria. *Nature* **362,** 834–836 (1993).
29. Kappler, A., Pasquero, C., Konhauser, K. O. & Newman, D. K. Deposition of banded iron formations by anoxygenic phototrophic Fe(II)-oxidizing bacteria. *Geology* **33,** 865–868 (2005).
30. Bjerrum, C. J. & Canfield, D. E. Ocean productivity before about 1.9 Gyr ago limited by phosphorus adsorption onto iron oxides. *Nature* **417,** 159–162 (2002).

Supplementary Information is linked to the online version of the paper at www.nature.com/nature.

Acknowledgements We thank M. Kastner and J. R. O'Neil for editorial suggestions and G. Olack and K. Fornash for technical assistance with isotopic analyses.

Author Contributions R.B. and A.L. conceived the study; A.L. performed field work, sample collection, petrographic and chemical analyses; S.J.C. and R.B. developed methods of sequential PO_4 extraction, purification, micro-precipitation and PO_4 oxygen isotope analysis. All authors contributed to the interpretation of results and the writing and editing of the manuscript.

Author Information Reprints and permissions information is available at www.nature.com/reprints. The authors declare no competing financial interests. Correspondence and requests for materials should be addressed to R.B. (ruth.blake@yale.edu).

METHODS

Extraction and purification of PO_4. Phosphate was extracted sequentially from 2–31 g of powdered rock using 10 M HNO_3 (4–7 ml per gram of sample), followed by 6 M HCl (4–11 ml per gram of sample) with continuous agitation on a reciprocal shaker for three and seven days, respectively. The use of HNO_3 and HCl as opposed to hydrofluoric acid and citrate-dithionite-bicarbonate solution[31,32] avoided excessive dissolution of silica and introduction of iron species, respectively, which interfere with subsequent steps in the purification and precipitation of silver phosphate (Ag_3PO_4). Following each extraction, acidic supernatants were separated from residual solids by centrifugation at ~1,950*g* for 20 min, then residual solids were rinsed with deionized water (4–10 ml per gram of sample). The concentrations of PO_4 in acid extractant and rinse solutions were determined colorimetrically[33], and then solutions were pooled for subsequent purification steps.

A single purification method cannot normally achieve separation of extracted phosphate from all contaminants (such as Si, Fe, organic matter). Thus, a combination of several purification steps was used as follows: (1) two rounds of magnesium-induced co-precipitation (MAGIC) of PO_4, (2) micro-precipitation of ammonium phosphomolybdate (APM), (3) recrystallization of APM as magnesium ammonium phosphate (MAP), (4) cation resin, (5) anion resin, (6) second cation resin and (7) final micro-precipitation of Ag_3PO_4.

The MAGIC treatment was adapted from ref. 34 to concentrate extracted phosphate in a <30 ml volume and simultaneously remove interfering ions (for example, Cl^-). Acid solutions containing 5–10 μmol PO_4 were diluted to ~700 ml, which also increased the pH. Solutions were then amended with $Mg(NO_3)_2{\cdot}6H_2O$ to achieve an approximate seawater concentration of 55 mM and 5 M NaOH was added to raise the pH to ~10 to induce Mg- and Fe-hydroxide precipitation. Next, samples were centrifuged for 20 min at 2,600*g* and 25 °C, followed by measurement of the PO_4 concentration of the supernatant to ensure complete co-precipitation/adsorption of PO_4. The residual PO_4/Mg- and Fe-hydroxide pellet was dissolved in a minimum of 10 M HNO_3 (<30 ml) with shaking (reciprocal shaker) at room temperature (21 ± 1 °C) until the pellet dissolved completely. ^{18}O-labelled water, which was added to 10 M HNO_3 solutions, was not incorporated into dissolved phosphate (that is, no phosphate–water exchange occurred) at room temperature (21 ± 1 °C) over a 115-day period (Supplementary Table 3). Thus, the approximately 1-week dissolution period did not introduce artefacts. The dissolved pellet solution was then diluted to ~100 ml in preparation for the second round of MAGIC.

APM and MAP micro-precipitations were adapted from refs 27 and 35. To precipitate 5–10 μmol phosphate as APM, it is critical to constrain the volume of sample solutions below ~5 ml. Thus, the dissolved pellet solution volume was reduced by evaporation below 60 °C for up to 10 h. Oxygen isotope exchange between dissolved PO_4 and water in 10 M HNO_3 at 70 °C is negligible for up to 22 h (Supplementary Table 3). Next, ammonium nitrate (NH_4NO_3) was added to give a NH_4NO_3/PO_4 ratio of 120:1 (by weight). Sample tubes were then heated to 48 °C, followed by slow addition of ~1 ml of ammonium molybdate reagent (100 g MoO_3, 400 ml of 69% HNO_3, 80 ml of 28.0–30.0% NH_4OH and 1 litre distilled water) with constant mixing until yellow APM crystals were formed. After ~30 min, additional reagent (total 7 ml) was added rapidly. APM crystals were allowed to develop overnight at room temperature, then collected and rinsed with 5% (w/w) NH_4NO_3 using a vacuum filtration system and 0.2 μm Gelman Supor filters. APM crystals were dissolved with ~1 ml of ammonium citrate reagent (5 g citric acid, 70 ml of 28.0–30.0% NH_4OH, and 150 ml distilled water) plus deionized water. For MAP precipitation, the initial sample volume was constrained to <2 ml. Magnesia reagent (63.08 g l^{-1} $Mg(NO_3)_2{\cdot}6H_2O$, 149.63 g l^{-1} NH_4NO_3 and 1:50 (by volume) of 28.0–30.0% NH_4OH) was added after adjusting the sample pH to <7 with 10 M HNO_3 to give a ratio of 0.25 ml magnesia reagent per milligram PO_4. Samples were constantly swirled while slowly adding 1:1 (by volume) NH_4OH, until white MAP crystals were formed. After ~30 min, 1 ml of 1:1 (by volume) NH_4OH was added to rapidly precipitate the remaining MAP, which was left to digest overnight at room temperature. MAP crystals were filtered and rinsed with 1:20 (by volume) NH_4OH and then dissolved with ~0.5 ml of 1 M HNO_3 plus deionized water. Next, samples were adjusted to ~pH 5 by addition of 1 M NaOH then loaded onto cation resin columns (Bio-Rad AG50W-X8, H^+ form, 100–200 mesh). Following sample elution, the cation resin was rinsed carefully with deionized water to remove all dissolved PO_4. Next, anion resin treatment followed the methods of ref. 36 as adapted from ref. 37. Samples were adjusted to pH 4–6 by addition of 1 M NaOH, then loaded onto anion resin columns (Bio-Rad AG1-X8, OH^- form, 200–400 mesh; converted to HCO_3^- form with 1 M $NaHCO_3$). Phosphate was eluted from columns using ~30 ml of 0.2 M $NaHCO_3$ at a flow rate of 1 ml min^{-1}. This allowed separation of the phosphate peak from interfering anion peaks. The eluted phosphate peak fractions were treated again with cation resin (H^+ form, ~1 ml resin per 5 ml sample) in batch mode for several hours to remove excess carbonate (evolved as CO_2 gas). The sample solution was next filtered through glass wool and the resin was rinsed with deionized water. Next, sample volume was reduced to ~0.5 ml by evaporation below 60 °C in preparation for the micro-precipitation of silver phosphate.

Micro-precipitation of silver phosphate. Sample solution and rinse water (~1 ml) were transferred to a micro-precipitation vessel. 0.75 ml of Ag-ammine reagent (0.067 M $AgNO_3$, 0.12 M NH_4NO_3 and 0.43 M NH_4OH) was added for every 5 μmol of dissolved PO_4. For samples containing more than 5 μmol PO_4, additional Ag-ammine reagent was added to maintain a Ag:P ratio close to 10. The vessels were incubated overnight at 50 °C to promote formation of large Ag_3PO_4 crystals, which are easier to manipulate in subsequent steps. Ag_3PO_4 crystals were rinsed with deionized water followed by ethanol and dried at 60 °C overnight. Yields of phosphate were above 96%. We tested selected samples (AL03-13D2 and AL03-28I) for the presence of condensed or organophosphates using ^{18}O-labelled waters ($\delta^{18}O_W = -6‰$ and +114.4‰) to prepare extractant solutions. The $\delta^{18}O_P$ values of these samples were identical within error (Supplementary Table 1). This result indicates that incorporation of oxygen from water into PO_4 during the hydrolysis of any phosphoesters or condensed forms such as polyphosphate that may have been present was negligible. Isotope analyses were carried out at the Earth System Center for Stable Isotope Studies (ESCSIS) at Yale using a Thermo-Chemolysis Elemental Analyser (TC/EA, 1,350 °C) coupled to a Delta +XL continuous-flow isotope ratio monitoring mass spectrometer (Thermo-Finnigan) with precision of ±0.2–0.3‰. Phosphate oxygen-isotope ratios were calibrated against conventional fluorination using three silver phosphate standards according to published methods[22].

31. Ruttenberg, K. C. Development of a sequential extraction method for different forms of phosphorus in marine sediments. *Limnol. Oceanogr.* **37,** 1460–1482 (1992).
32. Poulton, S. W. & Canfield, D. E. Development of a sequential extraction procedure for iron: implications for iron partitioning in continentally derived particulates. *Chem. Geol.* **214,** 209–221 (2005).
33. Murphy, J. & Riley, J. P. A modified single solution method for the determination of phosphate in natural waters. *Anal. Chim. Acta* **27,** 31–36 (1962).
34. Karl, D. M. & Tien, G. MAGIC: A sensitive and precise method for measuring dissolved phosphorus in aquatic environments. *Limnol. Oceanogr.* **37,** 105–116 (1992).
35. Tudge, A. P. A method of analysis of oxygen isotopes in orthophosphate—its use in the measurement of paleotemperatures. *Geochim. Cosmochim. Acta* **18,** 81–93 (1960).
36. Liang, Y. *Oxygen Isotope Studies of Biogeochemical Cycling of Phosphorus* PhD thesis, Yale Univ. (2005).
37. Colman, S. A. *The Oxygen Isotope Composition of Dissolved Inorganic Phosphate and the Marine Phosphorus Cycle* PhD thesis, Yale Univ. (2002).

LETTERS

Périgord black truffle genome uncovers evolutionary origins and mechanisms of symbiosis

Francis Martin[1], Annegret Kohler[1], Claude Murat[1], Raffaella Balestrini[2], Pedro M. Coutinho[3], Olivier Jaillon[4–6], Barbara Montanini[7], Emmanuelle Morin[1], Benjamin Noel[4–6], Riccardo Percudani[7], Bettina Porcel[4–6], Andrea Rubini[8], Antonella Amicucci[9], Joelle Amselem[10], Véronique Anthouard[4–6], Sergio Arcioni[8], François Artiguenave[4–6], Jean-Marc Aury[4–6], Paola Ballario[11], Angelo Bolchi[7], Andrea Brenna[11], Annick Brun[1], Marc Buée[1], Brandi Cantarel[3], Gérard Chevalier[12], Arnaud Couloux[4–6], Corinne Da Silva[4–6], France Denoeud[4–6], Sébastien Duplessis[1], Stefano Ghignone[2], Benoît Hilselberger[1,10], Mirco Iotti[13], Benoît Marçais[1], Antonietta Mello[2], Michele Miranda[14], Giovanni Pacioni[15], Hadi Quesneville[10], Claudia Riccioni[8], Roberta Ruotolo[7], Richard Splivallo[16], Vilberto Stocchi[9], Emilie Tisserant[1], Arturo Roberto Viscomi[7], Alessandra Zambonelli[13], Elisa Zampieri[2], Bernard Henrissat[3], Marc-Henri Lebrun[17], Francesco Paolocci[8], Paola Bonfante[2], Simone Ottonello[7] & Patrick Wincker[4–6]

The Périgord black truffle (*Tuber melanosporum* Vittad.) and the Piedmont white truffle dominate today's truffle market[1,2]. The hypogeous fruiting body of *T. melanosporum* is a gastronomic delicacy produced by an ectomycorrhizal symbiont[3] endemic to calcareous soils in southern Europe. The worldwide demand for this truffle has fuelled intense efforts at cultivation. Identification of processes that condition and trigger fruit body and symbiosis formation, ultimately leading to efficient crop production, will be facilitated by a thorough analysis of truffle genomic traits. In the ectomycorrhizal *Laccaria bicolor*, the expansion of gene families may have acted as a 'symbiosis toolbox'[4]. This feature may however reflect evolution of this particular taxon and not a general trait shared by all ectomycorrhizal species[5]. To get a better understanding of the biology and evolution of the ectomycorrhizal symbiosis, we report here the sequence of the haploid genome of *T. melanosporum*, which at ~125 megabases is the largest and most complex fungal genome sequenced so far. This expansion results from a proliferation of transposable elements accounting for ~58% of the genome. In contrast, this genome only contains ~7,500 protein-coding genes with very rare multigene families. It lacks large sets of carbohydrate cleaving enzymes, but a few of them involved in degradation of plant cell walls are induced in symbiotic tissues. The latter feature and the upregulation of genes encoding for lipases and multicopper oxidases suggest that *T. melanosporum* degrades its host cell walls during colonization. Symbiosis induces an increased expression of carbohydrate and amino acid transporters in both *L. bicolor* and *T. melanosporum*, but the comparison of genomic traits in the two ectomycorrhizal fungi showed that genetic predispositions for symbiosis—'the symbiosis toolbox'—evolved along different ways in ascomycetes and basidiomycetes.

The 125-megabase (Mb) genome of *T. melanosporum* is the largest sequenced fungal genome to date[6], but no evidence for whole-genome duplication or large scale dispersed segmental duplications was observed (Supplementary Table 1 and Supplementary Information section 2). The approximately fourfold larger size of the truffle genome compared with other sequenced ascomycetes is accounted for by multi-copy transposable elements (TE) which constitute about 58% of the assembled genome (Fig. 1, Supplementary Figs 5, 6 and 8, Supplementary Information section 3). Estimated insertion times suggest a major wave of retrotransposition at <5 million years ago (Supplementary Fig. 7). TEs are not uniformly spread across the genome, but are clustered in gene-poor or gene-lacking regions (Fig. 1 and Supplementary Fig. 8). The expansion of regions between blocks of protein-coding genes results from an increased density of TEs. The proliferation of TEs within the truffle genome may result from its low effective population size[7] during postglaciation migrations[8] (Supplementary Information section 2.5).

The predicted proteome is in the lower range of sequenced filamentous fungi[6], as only 7,496 protein-coding genes were identified (Supplementary Information section 4). They are mainly located in TE-poor regions and the gene density is heterogeneous when compared with that of other ascomycetes (Fig. 1, Supplementary Figs 8 and 9). Among the predicted proteins, only 3,970, 5,596 and 5,644 showed significant sequence similarity to proteins from *Saccharomyces cerevisiae*, *Neurospora crassa* and *Aspergillus niger*, respectively (Supplementary Fig. 10). This agrees with the predicted ancient separation (>450 Myr ago) of the Pezizomycetes from the other ancestral fungal lineages (Supplementary Fig. 4)[9]. Of the ~5,650 *T. melanosporum* genes that have an orthologue, very few show conservation of neighbouring orthologues (synteny) in at least one of the other species (Supplementary Fig. 11, Supplementary

[1]INRA, UMR 1136, INRA-Nancy Université, Interactions Arbres/Microorganismes, 54280 Champenoux, France. [2]Istituto per la Protezione delle Piante del CNR, sez. di Torino and Dipartimento di Biologia Vegetale, Università degli Studi di Torino, Viale Mattioli, 25, 10125 Torino, Italy. [3]Architecture et Fonction des Macromolécules Biologiques, UMR 6098 CNRS-Universités Aix-Marseille I & II, 13288 Marseille, France. [4]CEA, IG, Genoscope, 2 rue Gaston Crémieux CP5702, F-91057 Evry, France. [5]CNRS, UMR 8030, 2 rue Gaston Crémieux, CP5706, F-91057 Evry, France. [6]Université d'Evry, F-91057 Evry, France. [7]Dipartimento di Biochimica e Biologia Molecolare, Università degli Studi di Parma, Viale G.P. Usberti 23/A, 43100 Parma, Italy. [8]CNR-IGV Istituto di Genetica Vegetale, Unità Organizzativa di Supporto di Perugia, via Madonna Alta, 130, 06128 Perugia, Italy. [9]Dipartimento di Scienze Biomolecolari, Università degli Studi di Urbino, Via Saffi 2 - 61029 Urbino (PU), Italy. [10]INRA, Unité de Recherche Génomique Info, Route de Saint-Cyr, 78000 Versailles, France. [11]Dipartimento di Genetica e Biologia Molecolare & IBPM (CNR), Università La Sapienza, Roma, Piazzale, A. Moro 5, 00185 Roma, Italy. [12]INRA, UMR Amélioration et Santé des Plantes, INRA-Université Blaise Pascal, INRA – Clermont-Theix, 63122 Saint-Genes-Champanelle, France. [13]Dipartimento di Protezione e Valorizzazione Agroalimentare, Università degli Studi di Bologna, 40 126 Bologna, Italy. [14]Dipartimento di Biologia di Base ed Applicata, [15]Dipartimento di Scienze Ambientali, Università degli Studi dell'Aquila, Via Vetoio Coppito 1 - 67100 L'Aquila, Italy. [16]University of Goettingen, Molecular Phytopathology and Mycotoxin Research, Grisebachstrasse 6, D-37077 Goettingen, Germany. [17]INRA, UMR BIOGER-CPP, INRA-Grignon, av Lucien Brétignières - 78850 Thiverval Grignon, France.

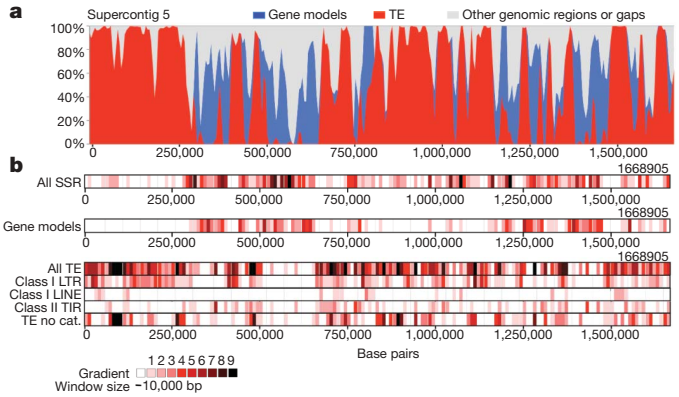

Figure 1 | Genomic landscape of *T. melanosporum*. **a**, The area chart quantifies the distribution of transposable elements (TE) and protein-coding genes (Gene models) along supercontig 5. The *y* axis represents the percentage of base pairs corresponding to TE (red), genes (blue), and other regions and gaps (white) in 10,000-bp sliding windows. **b**, Heat maps display the distribution of selected elements, including simple sequence repeats (SSR), gene models, all TE, long terminal repeat retrotransposons (class I LTR), long interspersed elements (class I LINE), terminal inverted repeats (class II TIR), and unknown TE classes (TE no cat.). Abundance of TE, protein-coding genes and other sequences is represented by a colour scale from 0 (white) to ≥9 occurrences (black) per 10 kbp window.

Information section 5.2). The *T. melanosporum* genome shows a structural organization strikingly different from other sequenced ascomycetes; the largest syntenic region (with *Coccidioides immitis*) only contains 99 genes with 39 orthologues (Supplementary Fig. 12). TE proliferation probably facilitated genome rearrangements. Some regions of meso-synteny were however detected, suggesting that *T. melanosporum* could be used for assessing the genome organization of ancestral ascomycete clades.

Expression of most predicted genes was detected in free-living mycelium, ectomycorrhizal (ECM) root tips and/or fruiting body by custom oligoarrays, expressed-sequence-tag pyrosequencing and Illumina RNA-Seq (Supplementary Information sections 2.4 and 8, Supplementary Table 2, Supplementary Fig. 26). Only a low proportion of transcripts (7.6%) is differentially expressed (fold-ratio ≥4.0, $P < 0.05$) in either ectomycorrhiza or fruiting body by comparison to free-living mycelium (Table 1, Supplementary Table 4). Only 61 transcripts unique to ectomycorrhiza, fruiting body or free-living mycelium were detected (Supplementary Table 5). A few transcripts coding for a H-type lectin, an arabinogalactan protein, a LysM-domain containing protein, major facilitator superfamily (MFS) transporters, laccase/tyrosinase, a lipase and polysaccharide-degrading enzymes are strikingly enriched (>1,000-fold) in symbiotic tissues (Table 1). They may play a role in adhesion to host cells, detoxication of plant defence metabolites, nutrient exchange, and colonization of root apoplast through the deconstruction of cell walls.

A process that is crucial to the success of ECM interactions is the mutualistic exchange of nutrients between the microsymbiont and its host plant. A comparison with other fungi revealed that the total number of predicted transporters is lower in *T. melanosporum* (381 members) compared with *L. bicolor* (491 members) as well as with saprotrophic and pathogenic ascomycetes (481–781 members) (Supplementary Table 26). However, 64 predicted membrane transporters showed an upregulated expression in truffle ectomycorrhizas, suggesting increased fluxes of carbohydrates, oligopeptides, amino acids and polyamines at the symbiotic interface (Supplementary Table 27). PFAM classification of fungal genes induced in symbiotic tissues of either *L. bicolor* or *T. melanosporum* ECM root tips revealed strikingly divergent fungal symbiotic proteomes (Supplementary Fig. 15). However, the PFAM categories corresponding to the MFS transporters (PFAM00083), aquaporin-related major intrinsic proteins (PFAM00230) and amino acid permeases (PFAM000324) were among the most strongly overrepresented in genes that were transcriptionally upregulated in both *L. bicolor* and *T. melanosporum* ectomycorrhizas.

Orthologous genes (that is, reciprocal best hits, BLASTP e-value $\leq 10^{-5}$) significantly induced in the symbiosis represent only 1.5% and

Table 1 | The most highly upregulated transcripts in *T. melanosporum*/*Corylus avellana* ECM root tips

SEQ_ID	ECM level	FB level	FLM level	ECM/FLM ratio	FB/FLM ratio	Definition	Size (AA)	Location	TMD
GSTUMT00012772001	13,262	731	1	**13,262**	731	H-type lectin	279	C	0
GSTUMT00012792001	11,423	250	1	**11,423**	250	Fasciclin-like arabinogalactan protein	414	S	0
GSTUMT00012437001	19,542	180	2	**9,796**	90	Lipase/esterase	346	S	0
GSTUMT00009894001	18,205	2	2	**7,721**	1	Cytochrome P450	396	M	0
GSTUMT00008973001	10,866	2	2	**6,213**	1	Endoglucanase GH5	342	C	0
GSTUMT00008992001	19,305	9	4	**4,538**	2	Laccase	586	S	0
GSTUMT00006890001	5,436	3,787	2	**2,636**	1,836	Sporulation-induced protein	481	C	0
GSTUMT00010076001	2,063	1	1	**2,063**	1	Tyrosinase	604	C	0
GSTUMT00003538001	3,588	2,818	2	**2,050**	1,610	FAD oxidoreductase	564	C	0
GSTUMT00012780001	6,542	44	4	**1,745**	12	LysM domain protein	87	S	0
GSTUMT00009016001	6,737	3,257	5	**1,432**	692	DUF1479-domain protein	379	C	0
GSTUMT00005760001	12,966	989	9	**1,401**	107	Major facilitator superfamily (MFS) permease*	142	S	2
GSTUMT00007927001	1,073	593	1	**1,073**	593	Hypothetical protein	306	C	0
GSTUMT00008954001	19,493	35	18	**1,066**	2	MFS permease	496	C	10
GSTUMT00000763001	902	2	1	**902**	2	Cytochrome P450	397	M	0
GSTUMT00002130001	1,534	1	2	**833**	1	β-Glucan synthesis-associated protein SKN1	575	M	1
GSTUMT00006579001	14,241	8,701	22	**662**	404	DUF1479-domain protein	426	M	0
GSTUMT00010279001	7,848	1,926	12	**651**	160	DUF2235-domain protein	403	C	0
GSTUMT00000499001	49,524	634	77	**644**	8	Phosphatidylserine decarboxylase	316	C	0
GSTUMT00012667001	1,151	7	2	**575**	3	Hypothetical protein	883	C	2
GSTUMT00009500001	2,529	2,846	6	403	453	*Tuber*-specific protein	86	M	0

Upregulation in ectomycorrhizal root tips and fruiting body is assessed by comparing transcript profiles to those from free-living mycelium. Ectomycorrhizal root tips were sampled from five-month-old common hazel (*Corylus avellana* L.) plantlets. Values are the means of seven, four and five biological replicates for free-living mycelium (FLM), ectomycorrhizal root tips (ECM) and fruiting body (FB), respectively. Based on the statistical analysis, a gene was considered significantly upregulated if it met two criteria: (1) *t*-test *P* value <0.05 (ArrayStar, DNASTAR); (2) mycorrhiza or fruiting body versus free-living mycelium fold change ≥4; 571 genes (7.6% of the total gene repertoire) showed an upregulated expression. The highest signal intensity value observed on these arrays was 65,189 arbitrary units. Signals below the cut-off values (100 arbitrary units) were assigned a signal intensity value of 1. Bold font emphasises upregulation in symbiosis. AA, amino acid; C, predicted as cytosolic; S, predicted as secreted; M, predicted mitochondrial protein; TMD, no. of transmembrane domain.
* Truncated sequence. See Supplementary Information section 8 for details.

Table 2 | Orthologous symbiosis upregulated genes of *L. bicolor* and *T. melanosporum*

Tuber gene models	*Lb* gene models (protein ID)	Percentage identity	Putative function	*Tm*- Hazel ECM/FLM ratio	*Lb*-poplar ECM/FLM ratio	*Lb*-Douglas fir ECM/FLM ratio
GSTUMT00008973001	303005	61	Cellulase CBM1-GH5	**6,213**	4	6
GSTUMT00008992001	229839	31	Laccase	**4,538**	8	19
GSTUMT00002130001	239682	38	β-Glucan synthesis-associated protein	**833**	6	4
GSTUMT00005583001	314483	45	MFS permease	**55**	6	8
GSTUMT00005380001	306393	39	DUF1996	**54**	12	22
GSTUMT00005614001	249535	33	Sugar (and other) transporter	**35**	5	8
GSTUMT00010098001	300838	41	Amino acid permease	**33**	18	13
GSTUMT00012011001	247019	36	GH28 pectinase	**29**	5	6
GSTUMT00001268001	308894	35	Hypothetical protein	**23**	5	5
GSTUMT00009221001	187852	37	MFS permease	**7**	8	6
GSTUMT00003668001	256686	53	Sugar (and other) transporter	**6**	12,548	16,648
GSTUMT00000861001	186401	45	Sulphate transporter	**6**	6	5
GSTUMT00010105001	162486	43	Hypothetical protein	**5**	7	5
GSTUMT00007281001	152257	40	Amino oxidase	**5**	5	4

Table shows genes upregulated in ectomycorrhizas (ECM) compared to free-living mycelia (FLM). ECM of *T. melanosporum* were sampled on roots of five-month-old common hazel (*Corylus avellana* L.) plantlets, whereas ECM of *L. bicolor* were sampled on roots of nine-month-old Douglas fir (*Pseudotsuga menziesii*) seedlings or three-month old poplar (*P. trichocarpa*) plantlets[4]. Orthologous genes have been identified by BLASTP (reciprocal best hits, e-value $\leq 10^{-5}$). Transcript profiling was performed on FLM and ECM root tips. Values are the means of seven and four biological replicates, respectively. Based on the statistical analysis, a gene was considered significantly upregulated if it met two criteria: (1) *t*-test *P* value <0.05 (ArrayStar, DNASTAR); (2) ECM versus FLM fold change ≥4. Bold font emphasises upregulation in *Tuber* symbiosis. *Lb*, *L. bicolor*; *Tm*, *T. melanosporum*; MFS, major facilitator superfamily. See Supplementary Information section 8 for details.

4.1% of the ectomycorrhiza-upregulated genes in both *T. melanosporum* and *L. bicolor*, respectively. Most of these rare transcripts code for membrane transporters involved in sugar, amino acid or sulphate uptake (Table 2). This transcriptome trait appears to be a hallmark of the mycorrhizal symbiosis. The resulting increased nutrient flux probably explains the beneficial effect of the symbionts on the growth of their host seedlings (Supplementary Information section 1 and Supplementary Fig. 3). Other overrepresented PFAM categories displayed different patterns in the two symbionts. None of the effector-like small secreted MiSSP proteins specifically expressed in *L. bicolor* ectomycorrhizas[4] were detected among ectomycorrhiza-regulated *T. melanosporum* transcripts.

One of the most striking characteristics of the *T. melanosporum* genome is the almost complete absence of highly similar gene pairs. Of the predicted 7,496 protein-coding genes, only seven pairs share >90% amino-acid identity in their coding sequence, whereas 30 pairs share >80% identity (Supplementary Information section 5.3, Fig. 2). This feature was also observed in the ascomycetous saprotroph *N. crassa*[10]. In striking contrast to the ECM *L. bicolor*[4], multigene families in *T. melanosporum* are limited in number and comprise only 19% of the predicted proteome; most families have only two members (Supplementary Fig. 13). The rate of gene family gain is much lower than the rate of gene loss and among the 11,234 gene families found in ascomycetes, 5,695 appear to be missing in *T. melanosporum* (Supplementary Information section 5.4, Fig. 2). This compact gene coding space may reflect the genome organization of an ascomycete common ancestor, as the Pezizomycetes clade is the earliest diverging lineage within the Pezizomycotina (Supplementary Fig. 4). By comparison to other ascomycetes, gene families predicted to encode metabolite transporters (for example, amino acid and sugar permeases) and secondary metabolism enzymes (such as polyketide synthases and cytochrome P450s) are much smaller. Only 465 genes encoded by expanding gene families of *L. bicolor* are also found in the *T. melanosporum* genome (BLASTP, e-value $\leq 10^{-5}$) and 154 orthologues are shared between expanding gene families of both symbionts. None of them is differentially expressed in ectomycorrhizas. Differences in gene family expansion, in particular dynamic repertoires of genes encoding symbiosis-regulated effector-like proteins and sugar-cleaving enzymes (see below), are probably responsible for different symbiotic traits between *T. melanosporum* and *L. bicolor*, such as altered host specificity. The compact genome of *T. melanosporum* might be a product of selection for specialization; this is because genome expansion, as observed in *L. bicolor*, is probably driven by selection on the symbiont to exploit a diversity of encountered substrates provided by multiple potential hosts and by their diverse soils[4,5].

The volatiles released by truffles are attractive to rodents and truffle flies[11], which disperse their spores, but also to humans who consider this elusive mushroom a delicacy. *T. melanosporum* is the first sequenced fungus producing highly flavoured hypogeous fruiting bodies (Supplementary Information section 6.4, Fig. 3). Genomic signatures of the long-standing (>2,000-year-old) reputation of the

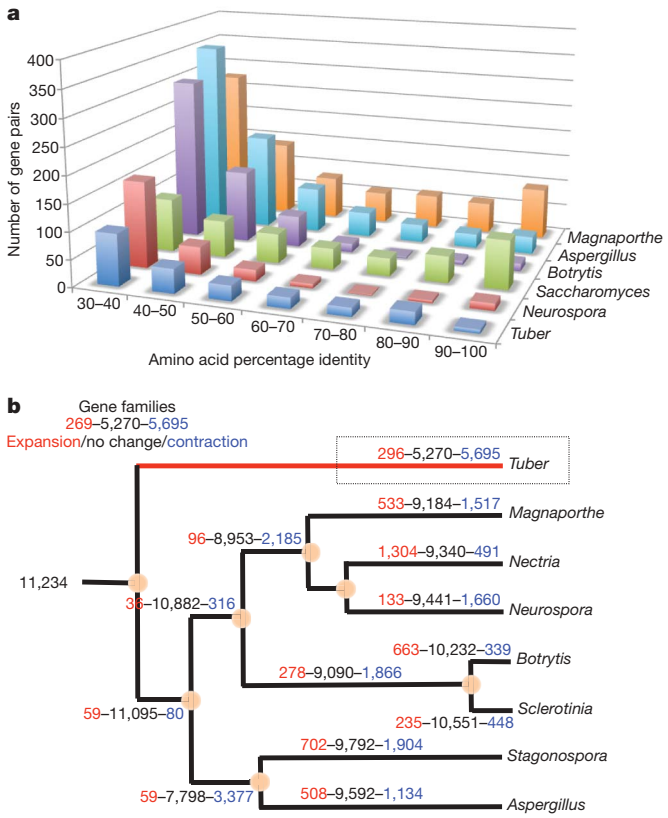

Figure 2 | Genome redundancy in the truffle genome. a, The percentage of amino-acid identity of the top-scoring self-matches for protein-coding genes in *T. melanosporum, Saccharomyces cerevisiae, Aspergillus nidulans, Neurospora crassa, Magnaporthe grisea,* and *Botrytis cinerea.* For each fungus, the protein-coding regions for each gene were compared with those of every other gene in the same genome using BLASTX. **b**, The figure represents the total number of protein families in each species or node. The numerals on branches show numbers of expanded (left, red), unchanged (middle, black) or contracted (right, blue) protein families along lineages by comparison to the putative pan-proteome.

black truffle as a gastronomic delicacy are its extremely low allergenic potential (Supplementary Fig. 18), coupled with the lack of key mycotoxin biosynthetic enzymes (Supplementary Information section 6.2, Supplementary Table 14), and the preferential overexpression of various flavour-related enzymes in the fruiting body (Supplementary Figs 19–21). Among the latter are specific subsets of sulphur assimilation and S-amino acid interconversion enzymes. These include cystathionine lyases known to promote the side-formation of methyl sulphide volatiles abundant in truffles[12] as well as various enzymes involved in amino acid degradation through the Ehrlich pathway which are giving rise to known truffle volatiles and flavours, for example, 2-methyl-1-butanal (Fig. 3, Supplementary Information section 6.4, Supplementary Figs 20 and 21). Also notable, given the subterranean habitat of this fungus, is the presence of various putative light-sensing components (Supplementary Information section 6.6), which might be involved in light avoidance mechanisms and/or in the control of seasonal developmental variations, especially those related to fruiting body formation and sexual reproduction.

The analysis of genes implicated in the mating process, including pheromone response, meiosis and fruiting body development showed that most sex-related components identified in other ascomycetes are also present in *T. melanosporum* (Supplementary Table 11). Sexual reproduction in ascomycete filamentous fungi is partly controlled by two different mating-type (*MAT*) genes that establish sexual compatibility[13]: one *MAT* gene codes for a protein with an α-box domain, whereas the other encodes a high mobility group (HMG) DNA binding protein (Supplementary Information section 6.5). It was widely believed that *T. melanosporum* was a homothallic or even an exclusively selfing species[14]. The sequenced Mel28 strain contains the HMG locus, and the opposite linked *MAT*α locus was identified in another natural isolate (Supplementary Fig. 22), confirming recent hints that *T. melanosporum* is heterothallic and thus an obligate outcrossing species[15]. This result has major implications for truffle cultivation, which will be improved by the use of host plants harbouring truffle strains of opposite mating types. In most ascomycetes, the genomic regions flanking the *MAT* locus show an extended conservation[13], but there is no synteny of the *MAT* loci between *T. melanosporum* and other sequenced fungi (Supplementary Fig. 23).

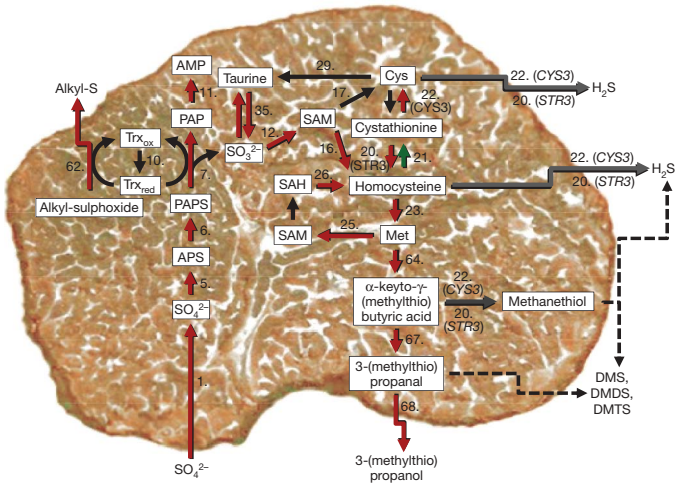

Figure 3 | Outline of sulphur metabolism in *T. melanosporum* fruiting body. Numbers identify enzymes and gene models as specified in Supplementary Table 15. Reactions (arrows) catalysed by enzymes whose mRNAs are upregulated in fruiting bodies are shown in red; mRNAs downregulated by at least twofold in fruiting bodies, or whose expression levels differ by less than twofold compared to free-living mycelia and ectomycorrhizas are represented by green and black arrows, respectively. Off-pathway cystathionine-γ-lyase (no. 22)- and cystathionine β-lyase (no. 20)-supported reactions, and spontaneous (non-enzymatic) breakdown reactions are indicated by grey and dashed arrows, respectively. APS, adenosine phosphosulphate; PAPS, phosphoadenosine phosphosulphate; PAP, phosphoadenosine phosphate; Trx, thioredoxin; SAM, S-adenosylmethionine; SAH, S-adenosylhomocysteine; DMS, dimethylsulphide; DMDS, dimethyl-disulphide; DMTS, dimethyl-trisulphide.

To determine whether *T. melanosporum* sugar-cleaving capabilities resemble those of other fungi, we have undertaken a comparison of the glycoside hydrolase (GH) and polysaccharide lyase (PL) repertoires[16] of 18 completely sequenced fungi (Fig. 4). As expected for a symbiotic fungus living in the root apoplast, *T. melanosporum* has a relatively small number of GH-encoding genes (91 members; Supplementary Tables 23 and 24); much fewer than phytopathogens (for example, *Magnaporthe grisea*, *Fusarium graminearum*) and saprotrophs (for example, *N. crassa*, *Podospora anserina*). The *T. melanosporum* GH repertoire bears some similarity with that of *L. bicolor*[4], especially a reduced spectrum of enzymes targeting the plant cell wall compared to saprobes, culminating in both fungi with the absence of cellulases from families GH6 and GH7. There are however significant differences in the spectrum of enzymes present in these two symbiotic fungi. For instance, *T. melanosporum* has hemicellulases from families GH10 and GH43, whereas *L. bicolor* has none. Similarly, *T. melanosporum* has a family GH45 cellulase that is absent from the *L. bicolor* genome. Other differences include different strategies to cleave pectin: whereas *L. bicolor* utilizes six hydrolytic GH28 pectinases, *T. melanosporum* has only two, but these are complemented by three pectin lyases and a pectin methylesterase that are missing in *L. bicolor*. Both fungi have a set of proteins, few in number, bearing cellulose-binding domains, but differences appear here too: the single cellulose-binding CBM1 motif of *L. bicolor* is appended to a GH5 endoglucanase, whereas *T. melanosporum* has two CBM1 motifs attached to a GH61 enzyme and to a protein of unknown function. GH61 enzymes have been reported to display weak cellulolytic activity[17].

An extended comparison with other sequenced fungi (Fig. 4) shows that *T. melanosporum* clusters neither with *L. bicolor* nor with saprotrophic ascomycetes, most probably because of its limited overall number of GHs and PLs that make it closer to yeasts and fungi that do not interact with plants, but rather with animals (*Cryptococcus neoformans*, *Malassezia globosa*). Differences between the enzyme repertoires of *T. melanosporum* and *L. bicolor* suggest differences in the mode of interaction of the two symbionts with their respective host plants. A striking difference is the presence of an invertase gene in *T. melanosporum*, whereas *L. bicolor* has none and is therefore completely dependent on its host for its provision of glucose[5]. In contrast, *T. melanosporum* could access and hydrolyse the plant-derived sucrose. This would suggest that although both fungi develop symbiotic relationships with plants, *T. melanosporum* is probably less dependent than *L. bicolor*. The overall pattern of induction of genes coding for enzymes acting on polysaccharides is similar in both *L. bicolor* and *T. melanosporum* symbiotic transcriptomes, although a larger number of carbohydrate-cleaving enzyme transcripts are upregulated for some families—for example, GH16 (β-1,6-glucanases), GH18 (chitinases) and GT20 (α,α-trehalose-phosphate synthase) in *L. bicolor* (Supplementary Table 25 and Supplementary Fig. 24). Intriguingly, a GH5 cellulase and a GH28 pectinase are among the rare transcripts that are highly upregulated in both *L. bicolor* and *T. melanosporum* ectomycorrhizas, suggesting that they play a key role in the symbiosis. On the other hand, the β-glucan synthesis-associated protein present in both ectomycorrhizas is involved in fungal cell wall remodelling[16] and may play a role in the alteration of cell wall surface during infection to conceal the hyphae from the host.

The ability to establish ECM symbioses is a widespread characteristic of various ascomycetes and basidiomycetes[3]. The truffle genome reveals features of an ancestral fungal lineage that diverged from other lineages >450 Myr ago[9]. Despite their similar symbiotic structures and similar beneficial effects on plant growth, the ascomycete *T. melanosporum* and the basidiomycete *L. bicolor* encode strikingly

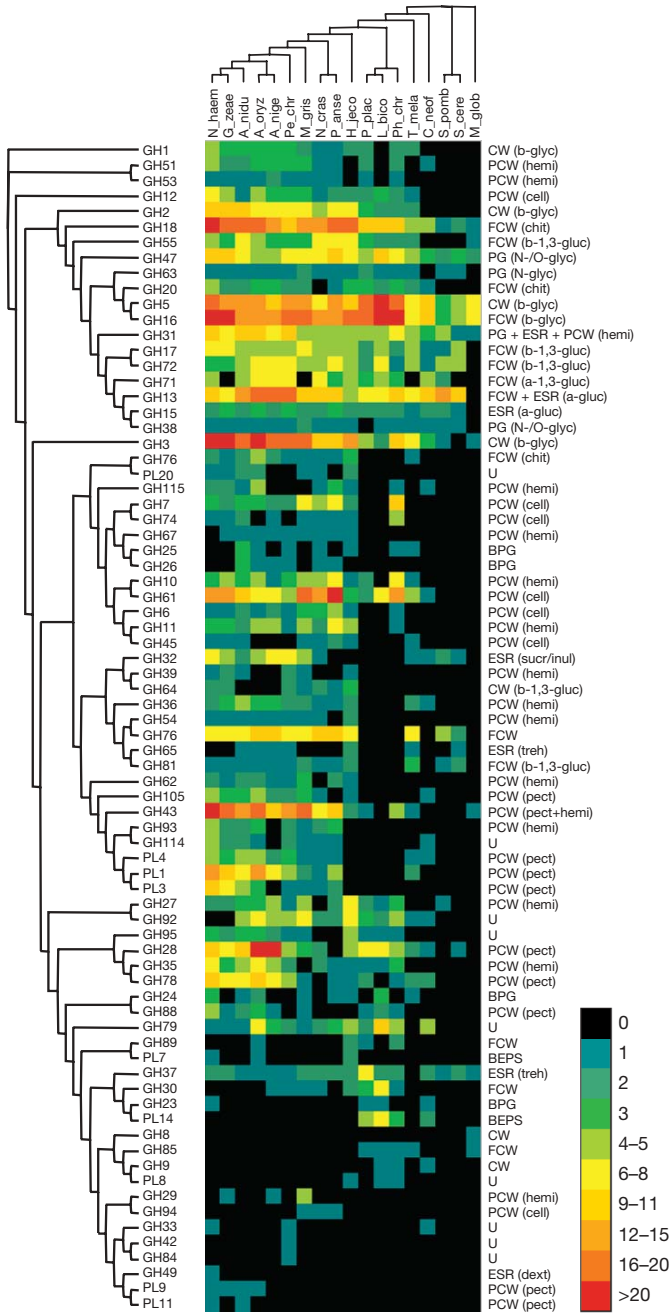

Figure 4 | Double clustering of the carbohydrate-cleaving families from representative fungal genomes. Top tree: the fungi named are *Aspergillus nidulans* (A_nidu), *Aspergillus niger* (A_nige), *Aspergillus oryzae* (A_oryz), *Cryptococcus neoformans* (C_neof), *Gibberella zeae* (G_zeae), *Hypocrea jecorina* (H_jeco), *Laccaria bicolor* (L_bico), *Magnaporthe grisea* (M_gris), *Malassezia globosa* (M_glob), *Nectria haematococca* (N_haem), *Neurospora crassa* (N_cras), *Penicillium chrysogenum* (Pe_chr), *Phanerochaete chrysosporium* (Ph_chr), *Podospora anserina* (P_anse), *Postia placenta* (P_plac), *Saccharomyces cerevisiae* (S_cere), *Schizosaccharomyces pombe* (S_pomb), and *Tuber melanosporum* (T_mela). Left tree: the enzyme families are represented by their class (GH, glycoside hydrolase; PL, polysaccharide lyase) and family number according to the carbohydrate-active enzyme database[16]. Right side: known substrate of CAZy families (most common forms in brackets): BPG, bacterial peptidoglycan; BEPS, bacterial exopolysaccharides; CW, cell wall; ESR, energy storage and recovery; FCW, fungal cell wall; PCW, plant cell wall; PG, protein glycosylation; U, undetermined; a-gluc, α-glucans (including starch/glycogen); b-glyc, β-glycans; b-1,3-gluc, β-1,3-glucan; cell, cellulose; chit, chitin/chitosan; dext, dextran; hemi, hemicelluloses; inul, inulin; N-glyc, N-glycans; N-/O-glyc, N- / O-glycans; pect, pectin; sucr, sucrose; and tre, trehalose. Abundance of the different enzymes within a family is represented by a colour scale from 0 (black) to ≥20 occurrences (red) per species.

different proteomes—compact with very few multigene families, versus large with many expanded multigene families—and symbiosis-regulated genes. Effector-like proteins, such as the *L. bicolor* ECM-induced SSP MiSSP7 (ref. 4), are not expressed in *T. melanosporum* ectomycorrhizas. On the basis of our results, the ECM symbiosis appears as an ancient innovation that developed several times during the course of Mycota evolution using different 'molecular toolkits'[18]. Sequencing of the *T. melanosporum* genome has provided unprecedented insights into the molecular bases of symbiosis, sex and fruiting in a most popular representative of the only lifestyle not yet addressed by Ascomycota genomics[19]. This sequencing will be a major step in moving truffle research into the realm of ecosystem science, and a deeper understanding of the genome of the Périgord black truffle is expected to have substantial social and cultural impact.

METHODS SUMMARY

A whole-genome shotgun strategy was adopted for sequencing and assembling the *T. melanosporum* genome (Supplementary Information section 2). All genomic DNA was obtained from the homokaryotic haploid strain Mel28. All data were generated by paired-end sequencing of cloned 3 kb and 10 kb inserts using Sanger technology. The pool of data available for the assembly consisted of 1,262,177 reads, with ~1,250 Mb of sequence. The data were assembled using the ARACHNE assembler. The 4,464 contigs (N50 = 62 kb) were assembled in 398 supercontigs (N50 = 638 kb) corresponding to 124.946 Mb of sequence. The main genome scaffolds were at a depth of 10. Assemblies and annotations are available at INRA (http://mycor.nancy.inra.fr/IMGC/TuberGenome/) and Genoscope (www.genoscope.cns.fr/tuber).

The GAZE pipeline selected a best representative gene model for each locus on the basis of expressed-sequence-tag support and similarity to known proteins from other organisms, and predicted 7,496 protein-coding gene models (Supplementary Information section 4). All predicted genes were annotated using Gene Ontology and KEGG pathways. Protein domains were predicted using InterProScan. Gene families were built from proteins using Tribe-MCL.

Single dye labelling of cDNAs, hybridization procedures, data acquisition, background correction and normalization of custom-exon expression arrays were performed at the NimbleGen facilities following their standard protocol. A Student *t*-test with false discovery rate was applied to the data using the ARRAYSTAR software (DNASTAR). Transcripts with a significant *P* value (<0.05) and ≥4-fold change in transcript level were considered as differentially expressed in ECM root tips or fruiting body.

Received 20 August 2009; accepted 28 January 2010.
Published online 28 March 2010.

1. Mello, A., Murat, C. & Bonfante, P. Truffles: much more than a prized and local fungal delicacy. *FEMS Microbiol. Lett.* **260,** 1–8 (2006).
2. Hall, I. R., Brown, G. T. & Zambonelli, A. *Taming the Truffle. The History, Lore, and Science of the Ultimate Mushroom* (Timber Press, Portland, 2007).
3. Smith, S. E. & Read, D. J. *Mycorrhizal Symbiosis* 3rd edn (Academic, 2008).
4. Martin, F. *et al.* The genome of *Laccaria bicolor* provides insights into mycorrhizal symbiosis. *Nature* **452,** 88–92 (2008).
5. Martin, F. & Selosse, M. A. The *Laccaria* genome: a symbiont blueprint decoded. *New Phytol.* **180,** 296–310 (2008).
6. Galagan, J. E., Henn, M. R., Ma, L. J., Cuomo, C. A. & Birren, B. Genomics of the fungal kingdom: insights into eukaryotic biology. *Genome Res.* **15,** 1620–1631 (2005).
7. Lynch, M. & Conery, J. S. The origins of genomic complexity. *Science* **302,** 1401–1404 (2003).
8. Murat, C. *et al.* Polymorphism at the ribosomal DNA ITS and its relation to postglacial re-colonization routes of the Perigord truffle *Tuber melanosporum*. *New Phytol.* **164,** 401–411 (2004).
9. Taylor, J. W. & Berbee, M. L. Dating divergences in the fungal tree of life: review and new analyses. *Mycologia* **98,** 838–849 (2006).
10. Galagan, J. E. & Selker, E. U. RIP: the evolutionary cost of genome defense. *Trends Genet.* **20,** 417–423 (2004).
11. Maser, C., Claridge, A. W. & Trappe, J. M. *Trees, Truffles and Beasts* (Rutgers Univ. Press, 2008).
12. Liu, M., Nauta, A., Francke, C. & Siezen, R. J. Comparative genomics of enzymes in flavor-forming pathways from amino acids in lactic acid bacteria. *Appl. Environ. Microbiol.* **74,** 4590–4600 (2008).
13. Fraser, J. A. & Heitman, J. Evolution of fungal sex chromosomes. *Mol. Microbiol.* **51,** 299–306 (2004).
14. Bertault, G., Raymond, M., Berthomieu, A., Callot, G. & Fernandez, D. Trifling variation in truffles. *Nature* **394,** 734 (1998).
15. Riccioni, C. *et al. Tuber melanosporum* outcrosses: analysis of the genetic diversity within and among its natural populations under this new scenario. *New Phytol.* **180,** 466–478 (2008).

16. Cantarel, B. L. *et al.* The Carbohydrate-Active EnZymes database (CAZy): an expert resource for glycogenomics. *Nucleic Acids Res.* **37,** D233–D238 (2009).
17. Karkehabadi, S. *et al.* The first structure of a glycoside hydrolase family 61 member, Cel61B from *Hypocrea jecorina*, at 1.6 Å resolution. *J. Mol. Biol.* **383,** 144–154 (2008).
18. Hibbett, D. S. & Matheny, P. B. Relative ages of ectomycorrhizal mushrooms and their plant hosts. *BMC Biol.* **7,** 13 (2009).
19. Soanes, D. M. *et al.* Comparative genome analysis of filamentous fungi reveals gene family expansions associated with fungal pathogenesis. *PLoS One* **3,** e2300 (2008).

Supplementary Information is linked to the online version of the paper at www.nature.com/nature.

Acknowledgements We thank the late L. Riousset and C. Dupré for providing the Mel28 isolate, and acknowledge F. Le Tacon and J. Weissenbach for continuous support. The genome sequencing of *T. melanosporum* was funded by the Génoscope, Institut de Génomique, CEA, and Agence Nationale de la Recherche (ANR). Genome annotation and transcriptome analysis were supported by INRA, the European FP6 Network of Excellence EVOLTREE, Région Lorraine, the ANR FungEffector project, Fondazione Cariparma, Compagnia di San Paolo-Torino, the Italian Ministry of Education, University and Research (MIUR), Regione Umbria and Instituto Pasteur Fondazione Cenci Bolognetti. We thank D. Hibbett and J. Heitman for comments on an early draft of the manuscript, and J. Plett for a critical reading of the paper.

Author Contributions B.H., M.-H.L., F.P., P. Bonfante, S.O. and P.W. contributed equally to this work as senior authors; A.K., C.M., R.B., P.M.C., O.J., B.M., E.M., B.N., R.P., B.P. and A.R. contributed equally to this work as second authors. F.M. initiated the project and coordinated the genome annotation, data analysis and manuscript preparation; P.W. coordinated the sequencing and automated annotation at Genoscope. F.M. and S.O. wrote the manuscript with input from P. Bonfante. R.B., P.M.C., B.H., O.J., A.K., M.H.L., B.M., E.M., C.M., B.N., F.P., R.P., A.R. and P.W. also made substantial contributions (listed in alphabetical order). All other authors are members of the genome sequencing consortium and contributed annotation, analyses or data throughout the project, and are listed in alphabetical order. We also thank A. Bonfigli, M. Buffalini, S. Colafarina, T. Flutre, S. Kamal, P. Ceccaroli, C. Roux, R. Saltarelli, S. von Pall di Tolna and O. Zarivi for their assistance in annotation.

Author Information Genome assemblies together with predicted gene models and annotations have been deposited at DNA Data Bank of Japan/European Molecular Biology Laboratory/GenBank under the project accession numbers CABJ01000001–CABJ01004455 (whole genome shotgun sequencing data) and FN429986–FN430383 (scaffolds and annotations). The complete expression dataset is available as series (accession number GSE17529) at the Gene Expression Omnibus at NCBI. The authors declare no competing financial interests. Correspondence and requests for materials should be addressed to F.M. (fmartin@nancy.inra.fr).

LETTERS

Dissection of genetically complex traits with extremely large pools of yeast segregants

Ian M. Ehrenreich[1,2,3], Noorossadat Torabi[1,4], Yue Jia[1,3], Jonathan Kent[1], Stephen Martis[1], Joshua A. Shapiro[1,2,3], David Gresham[1]†, Amy A. Caudy[1] & Leonid Kruglyak[1,2,3]

Most heritable traits, including many human diseases[1], are caused by multiple loci. Studies in both humans and model organisms, such as yeast, have failed to detect a large fraction of the loci that underlie such complex traits[2,3]. A lack of statistical power to identify multiple loci with small effects is undoubtedly one of the primary reasons for this problem. We have developed a method in yeast that allows the use of much larger sample sizes than previously possible and hence permits the detection of multiple loci with small effects. The method involves generating very large numbers of progeny from a cross between two *Saccharomyces cerevisiae* strains and then phenotyping and genotyping pools of these offspring. We applied the method to 17 chemical resistance traits and mitochondrial function, and identified loci for each of these phenotypes. We show that the level of genetic complexity underlying these quantitative traits is highly variable, with some traits influenced by one major locus and others by at least 20 loci. Our results provide an empirical demonstration of the genetic complexity of a number of traits and show that it is possible to identify many of the underlying factors using straightforward techniques. Our method should have broad applications in yeast and can be extended to other organisms.

Genome-wide association studies (GWAS) have recently detected many trait loci in humans[4]. Despite the large number of loci that have been identified by GWAS, case studies, such as human height[5], have shown that we remain unable to explain the genetic basis of complex traits in our population[2]. Controlled crosses in model organisms can shed light on this problem by elucidating basic principles that govern the genetic basis of trait variation. However, akin to the problem in humans, mapping studies in model organisms typically detect only a fraction of the loci underlying heritable traits, implying that they lack statistical power[3].

Very large mapping populations are needed to dissect comprehensively the genetic basis of highly complex traits. In many cases, genotyping and phenotyping on a sufficient scale will not be feasible without the use of methods that examine pools of individuals. One such method, bulk segregant analysis (BSA), was first proposed nearly twenty years ago as an expeditious approach for mapping quantitative trait loci (QTLs)[6], and its modern implementations are commonly used to map major effect QTLs and Mendelian loci[7–11]. However, BSA has yet to be effectively used to dissect a highly complex trait, even though simulations indicate that it should be capable of detecting numerous small-effect loci with high resolution when $>10^5$ cross progeny are used (Supplementary Figs 1 and 2). We have developed a powerful extension of BSA that can be used to map complex traits in yeast comprehensively. Extreme QTL mapping (X-QTL) has three key steps. The first is the generation of segregating populations of very large size. The second is selection-based phenotyping of these populations to recover large numbers of progeny with extreme trait values. This can be accomplished, for example, by selection for drug resistance or by cell sorting. The final step is quantitative measurement of pooled allele frequencies across the genome, by either microarray-based genotyping or massively parallel sequencing.

To generate the pools of segregants that form the starting point for X-QTL, we implemented the Synthetic Genetic Array (SGA) marker scheme[12,13], which enables the recovery of MAT**a** haploids from a cross of appropriately marked parental strains (Fig. 1a, b). We used the *Saccharomyces cerevisiae* strains BY4716 (hereafter referred to as BY), a laboratory strain, and RM11-1a (hereafter referred to as RM), a wine strain, as the progenitors of the pools. We crossed these strains to form a diploid, sporulated the diploid, and selected for $\sim 10^7$ unique BY×RM MAT**a** haploid segregants. We designed an allele-specific genotyping microarray with isothermal probes[14] that assays ~18,000 single nucleotide polymorphisms (SNPs) between BY and RM. We tested the array by hybridizing the haploid and diploid progenitor strains, as well as multiple MAT**a** pools, and found that we could discriminate the parental strains and reproducibly identify deviations in allele frequencies associated with the SGA markers and other loci in the segregating pools (Fig. 1c–e). Comparable results were obtained by sequencing pools to ~180× coverage with the Illumina Genome Analyzer (Fig. 1e).

We first used X-QTL to map the genetic basis of sensitivity to 4-nitroquinoline (4-NQO), a DNA damaging agent. We previously showed that sensitivity to 4-NQO is a complex trait in the BY×RM cross[15]. BY×RM segregants show varying degrees of sensitivity, and the parental strains are both intermediate relative to their progeny, suggesting contributions of multiple alleles from each parent. Conventional QTL mapping with 123 genotyped segregants detected a single significant locus on chromosome 12, and subsequent experiments identified an amino acid substitution in the DNA repair gene *RAD5* as the underlying causative polymorphism. A backcrossing strategy identified a smaller contributing effect of a polymorphism in the gene *MKT1*. The BY allele of *RAD5* and the RM allele of *MKT1* conferred 4-NQO resistance, but these loci did not fully explain the observed 4-NQO responses of the segregants, implying that additional loci must exist.

To map the genetic basis of sensitivity to 4-NQO using X-QTL, we first plated segregating pools across a range of drug doses to find a highly selective 4-NQO concentration. We then conducted 4-NQO selections at this concentration, while in parallel growing control populations on rich medium without the drug. 4-NQO-resistant and control pools were harvested, and the extracted DNA was hybridized to genotyping microarrays. To identify loci that confer resistance to 4-NQO, we scanned the genome for locations at which allele frequencies in selected pools were significantly different from the

[1]Lewis-Sigler Institute for Integrative Genomics, [2]Department of Ecology and Evolutionary Biology, [3]Howard Hughes Medical Institute, [4]Department of Molecular Biology, Princeton University, Princeton, New Jersey 08540, USA. †Present address: Center for Genomics and Systems Biology, New York University, New York, New York 10003, USA.

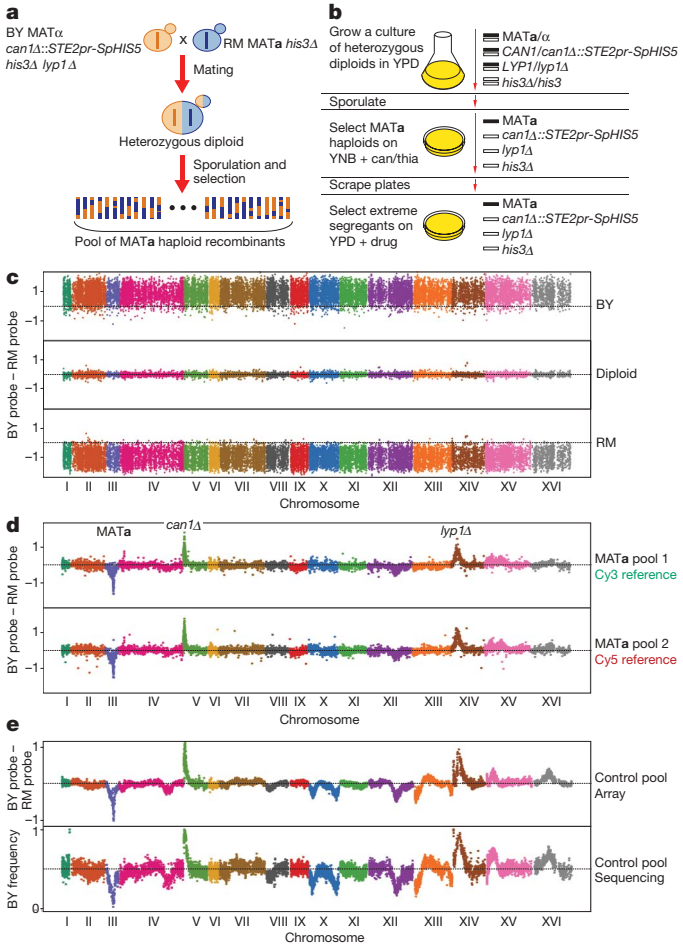

Figure 1 | X-QTL design and quantitative allele frequency measurement in DNA pools. **a**, **b**, The crossing design used for X-QTL is shown in **a**, whereas the selection scheme used to generate segregating pools is shown in **b**. can/thia, canavanine/thialysine. **c**–**e**, Genotyping of parental strains (**c**), two segregating pools (**d**) and an unselected control pool grown on rich medium (**e**) is shown. Dotted lines at zero indicate no difference between the $\log_{10}$ ratios of the BY and RM allele-specific probes. Enrichment of the BY allele is indicated by deviations above 0 and enrichment of the RM allele is indicated by deviations below 0. For the segregating pools, both the control loci involved in MAT**a** selection and the dye used for reference labelling are denoted. In **d**, we use a dye-swap experiment to show that the dye used for labelling does not cause any bias in allele frequency measurement. Panels **d** and **e** differ in that **d** shows a MAT**a** pool before plating on rich medium and **e** shows a MAT**a** pool after 2 days of growth on rich medium. In **e**, the same pool was hybridized to the genotyping microarray and was sequenced to ~180× coverage with the Illumina Genome Analyzer. The results in **c** and **d** are plots of raw data with no sites removed, whereas in **e** raw data was plotted with sites more than 1.5 standard deviations away from the local average of the 10 nearest data points removed for clarity.

control pools (Supplementary Methods). Using this approach, we identified 14 loci in the 4-NQO selection at a false discovery rate (FDR) of 0.05. Similar deviations in allele frequency in the selected pools were observed when the genotyping step was carried out by either arrays or short-read sequencing (X-QTL-seq; Supplementary Fig. 3).

We examined whether the loci identified by X-QTL for 4-NQO resistance correspond to real biological effects. Using X-QTL, we observed peaks at *RAD5* and *MKT1*, with both loci selected in the expected direction (Fig. 2). We confirmed that the peak overlapping *RAD5* was actually due to this gene by repeating the BY×RM cross with an RM parent strain that had the BY version of *RAD5*. When 4-NQO resistance was mapped in the selected pool with *RAD5* fixed, the resulting segregating pool showed increased resistance to 4-NQO,

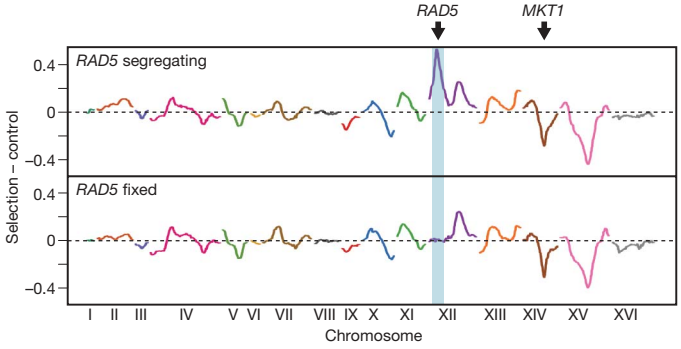

Figure 2 | X-QTL detection of loci for 4-NQO resistance. Results for 4-NQO resistance with *RAD5* segregating (top) and fixed (bottom) are shown. The difference between the average of the selections and the average of the controls generated on the same day is plotted, with enrichment of the BY allele indicated by deviations above 0 and enrichment of the RM allele indicated by deviations below 0. Sliding window averages (50 kb) are plotted. Arrows point to *MKT1* and *RAD5*. The *RAD5* fixed population was generated by using a RM parent strain in which the $RAD5^{RM}$ allele was replaced with a $RAD5^{BY}$ allele. This strain was constructed by crossing strain EAY1467 (ref. 15) to the RM parent strain used for X-QTL.

and no *RAD5* peak was observed by X-QTL (Fig. 2). Next, we isolated 96 individual progeny from the same cross used to generate the segregating pools, phenotyped them for 4-NQO sensitivity, and genotyped them at the 14 loci identified by X-QTL. Nine of the loci showed significant effects in this independent data set ($P < 0.05$), five of which were highly significant ($P < 0.001$). The loci jointly explained 59% of the phenotypic variance in 4-NQO sensitivity in an additive model (Supplementary Fig. 4). Because we measured the heritability of this trait to be 0.84, the loci explained 70% of the genetic variance, indicating that we have explained most of the genetic basis of this trait with the loci detected by X-QTL.

We next applied X-QTL to resistance to 16 diverse chemical agents (Supplementary Table 1), including a detergent and a number of antifungal compounds, using the same methodology that was used for 4-NQO. At a global FDR of 0.05, we mapped 177 total loci for these 16 traits. We detected between 1 and 24 peaks in pools selected on these agents. Including 4-NQO, we detect an average of 11 peaks per trait, suggesting high genetic complexity for many traits. The 17 traits show marked differences in their genetic architectures (Fig. 3 and Supplementary Fig. 5). At the simpler end of the range, resistance to cadmium chloride, copper sulphate and ethanol is controlled by one major locus for each trait (Fig. 3a). At the other extreme, we identified more than 20 loci in the diamide, hydrogen peroxide and sodium dodecyl sulphate selections (Fig. 3b). Other traits show intermediate levels of complexity (Fig. 3c, d).

We compared the 191 peaks detected across the 17 traits. The genome was divided into 20-kilobase (kb) bins, and all loci within a bin were grouped together. Using this procedure, we found 123 distinct loci (Fig. 3e). Of these, 82 loci (~67%) were trait-specific. For instance, a peak was detected at *RAD5* on chromosome XII only in our analysis of resistance to 4-NQO. Similarly, the major locus for copper sulphate resistance, which was previously mapped in a screen for QTLs involved in resistance to small molecules in the BY×RM cross[16], coincides with the location of the *CUP1* genes on chromosome VIII and was detected only in the copper sulphate selection. Of the 41 remaining loci, 40 were detected for 2 to 5 traits, and 1 locus, which overlaps *MKT1*, was detected for 8 different compounds. An amino acid polymorphism in *MKT1* is known to be involved in a large number of trait differences between BY and other strains, including 4-NQO resistance[15], sensitivity to dipropyldopamine and phenylephrine[17], high temperature growth[18], sporulation efficiency[19], gene expression[20], and growth of petite colonies[21]. Our results suggest that in addition to these previously studied phenotypes, *MKT1* also has a broadly pleiotropic effect on drug resistance under the conditions of

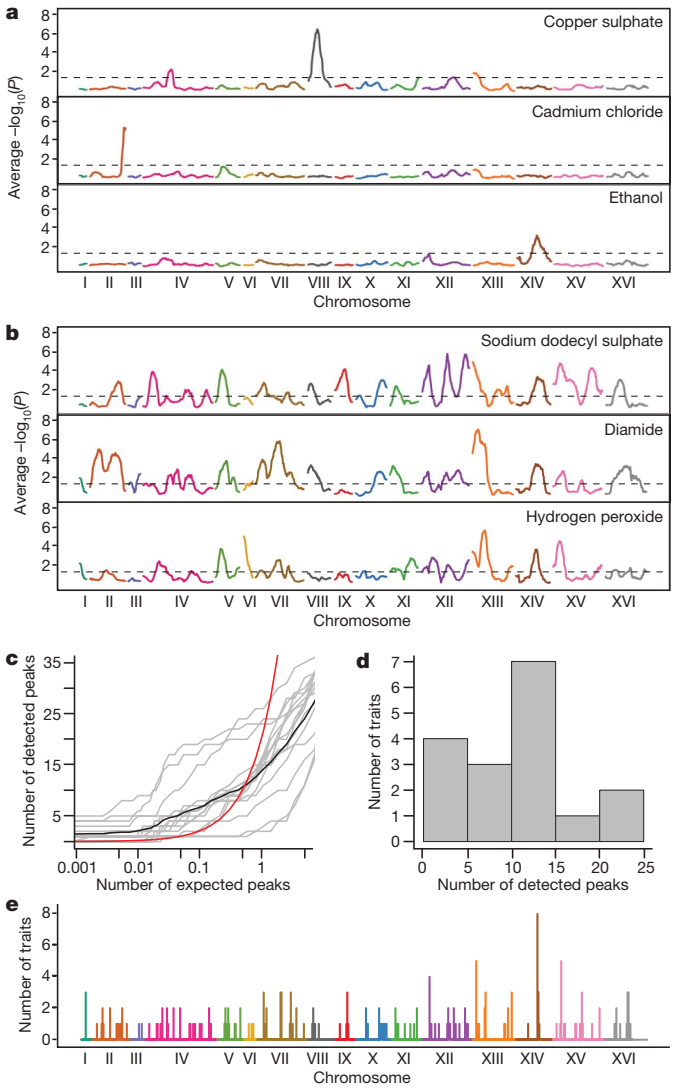

Figure 3 | Genetic architecture of chemical resistance traits. a–e, Examples of genetically simple traits (**a**), examples of genetically complex traits (**b**), relationship between the number of expected and detected peaks (**c**), the number of loci detected per trait (**d**), and a map of compound-specific and pleiotropic loci across the genome (**e**). In **a** and **b** the $-\log_{10}(P)$ values are shown for *t*-tests comparing selected samples to control samples. The sliding averages within 50-kb windows for these tests are plotted. Peaks above the dashed lines in **a** and **b** are significant at an FDR of 0.05. In **c**, the average relationship between expected and detected peaks is plotted as a black line and the trait-specific relationships are plotted as grey lines. The red line plots the theoretical relationship between expected and detected peaks at an FDR of 0.05. The expected counts were generated from permutations of the chemical resistance data set. The histogram in **d** was made using loci significant at a global FDR of 0.05. In **e**, detected loci were grouped within 20-kb windows across the genome.

our study. Furthermore, our results suggest that X-QTL detects loci at a fine resolution, as the locations of the peaks corresponding to *MKT1* and *RAD5* were estimated to be within 2 kb of these genes themselves (Supplementary Table 2). The loci we have detected across 17 compounds thus provide a foundation for comprehensively studying the molecular mechanisms that shape phenotypic variation in response to chemical agents among yeast strains.

Selections for resistance to chemical agents permit only one extreme tail of the phenotype distribution to be sampled. Additional insights can be gained from selections where both high and low extreme segregants can be recovered. Fluorescence-activated cell sorting (FACS) provides a straightforward approach to such two-tailed selections, as large numbers of individuals exhibiting high and low values for a stain or reporter can easily be recovered. To pilot this approach, we used the dye Mitotracker red, which stains cells depending on the mitochondrial proton gradient and mitochondrial volume. We harvested a MAT**a** pool, stained it with Mitotracker red, and then sorted out extreme cells by FACS. We sorted a population of $\sim 5 \times 10^6$ cells and selected 3×10^4 cells from each tail. These selected cells were then grown up on agar plates with rich medium to generate enough cells from which to extract DNA. DNA pools from both tails, as well as from a subsample of the whole population, were hybridized to the genotyping microarray.

Comparison of the high and low extremes found multiple major peaks at an FDR of 0.05 (Fig. 4). These peaks showed similar heights but opposite directions in the two tails. The location of one of the peaks provided a strong candidate for the causal gene. The peak on chromosome XII spans *HAP1*, a zinc finger transcription factor involved in response to oxygen. *HAP1* was previously shown to be a hotspot for *trans* regulation of gene expression differences in the BY×RM cross[22,23]. BY has a partially functional allele of *HAP1* due to a Ty transposon insertion in the *HAP1* coding region[24], whereas RM has a fully functional *HAP1* allele. Consistent with *HAP1*'s function, segregants carrying the RM allele of *HAP1* show increased oxidative capacity based on X-QTL mapping. Comparison of BY with a partially functional *HAP1* to BY with a fully functional *HAP1* shows that *HAP1* has a causal role in variation in Mitotracker red staining (Supplementary Fig. 6).

X-QTL represents a powerful method for rapidly and cost-effectively mapping the multiple QTLs underlying a trait difference between two yeast strains. We have used X-QTL to demonstrate empirically that many traits have a highly complex genetic basis. These results are consistent with previous studies in yeast, such as those focused on transcript levels[3], protein abundance[25] and sensitivity to chemical agents[16], in which genetic complexity was inferred from trait distributions and a lack of mapped loci, rather than from direct detection of multiple loci as we have accomplished here. Our results agree with those from the comprehensive genetic dissection of a small number of traits in other model organisms, such as bristle number in *Drosophila*[26] and flowering time in maize[27], which have shown that dozens of loci can underlie a difference between two individuals. Notably, whereas these studies required substantial labour, time and resources, X-QTL is a quick and easy approach to achieve a comparable level of genetic dissection. The levels of complexity observed here (for example, 14 loci explaining 70% of the genetic variance for 4-NQO resistance) are still markedly lower than those seen for some human traits in GWAS (for example, 40 loci explaining 5% of the variance for height[2,5]). One obvious explanation is the difference in experimental designs (line crosses versus population association studies), but differences in genetic architectures among species and traits may also contribute. The comprehensive genetic dissection of complex traits by X-QTL makes it possible to answer empirically many of the basic questions about the genetic architecture of complex traits, including

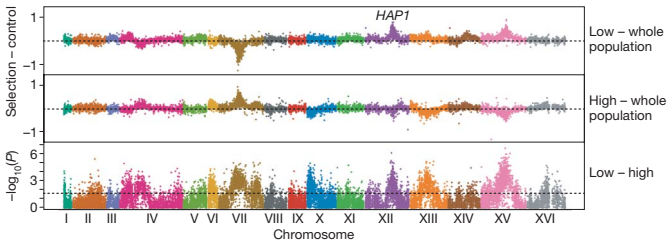

Figure 4 | X-QTL mapping of mitochondrial activity by cell sorting. Segregants were stained with the dye Mitotracker red. The comparisons of high and low pools to the entire population are shown, in addition to $-\log_{10}(P)$ values for the difference between these groups. The dashed lines in the high or low minus control plots indicate zero difference in a comparison, whereas the dashed line in the low minus high plot indicates the probe-level threshold for an FDR of 0.05.

the number of loci underlying a trait and the distribution of their allele frequencies in a population. High-resolution mapping of these loci also enables identification of the underlying genes and sequence variants, as well as investigation of allelic effect sizes and genetic interactions. We anticipate that general insights from such studies will be applicable to understanding the genetics of complex traits in other organisms, including humans, and that variants of X-QTL can be developed for other species.

METHODS SUMMARY

Microarray hybridizations. DNA was extracted from segregating pools using Qiagen Genomic-tip 100/G columns. DNA was labelled using array comparative genomic hybridization reagents from Invitrogen and Cy3- or Cy5-labelled dUTP from Enzo. Hybridization, scanning and feature extraction were done using Agilent equipment and software. Normalization of arrays was done using the rank invariant method within the Agilent software.

Statistical analysis. For a given SNP, the difference in $\log_{10}$ ratios of the intensities of the BY and RM allele-specific probes on a single array was computed, and this metric was used in downstream analyses. In cases where a SNP was represented by two probe sets, the probe sets were used as separate data points. For the drug selections, selection and control experiments were compared using *t*-tests with equal variances. A regression-based peak-finding approach was then used, which scans the genome for locations where the slope in $-\log_{10}(P)$ values changes signs. Significance levels were determined by permutation (Fig. 3c). For the Mitotracker red study, the high- and low-staining pools were compared using *t*-tests with equal variances. QVALUE[28] was then used to determine an FDR based on the observed *P* values.

Full Methods and any associated references are available in the online version of the paper at www.nature.com/nature.

Received 10 November 2009; accepted 16 February 2010.

1. Plomin, R., Haworth, C. M. A. & Davis, O. S. P. Common disorders are quantitative traits. *Nature Rev. Genet.* **10,** 872–878 (2009).
2. Manolio, T. A. *et al.* Finding the missing heritability of complex diseases. *Nature* **461,** 747–753 (2009).
3. Brem, R. B. & Kruglyak, L. The landscape of genetic complexity across 5,700 gene expression traits in yeast. *Proc. Natl Acad. Sci. USA* **102,** 1572–1577 (2005).
4. Hindorff, L. A. *et al.* Potential etiologic and functional implications of genome-wide association loci for human diseases and traits. *Proc. Natl Acad. Sci. USA* **106,** 9362–9367 (2009).
5. Visscher, P. M. Sizing up human height variation. *Nature Genet.* **40,** 489–490 (2008).
6. Michelmore, R. W., Paran, I. & Kesseli, R. V. Identification of markers linked to disease-resistance genes by bulked segregant analysis: a rapid method to detect markers in specific genomic regions by using segregating populations. *Proc. Natl Acad. Sci. USA* **88,** 9828–9832 (1991).
7. Wolyn, D. J. *et al.* Light-response quantitative trait loci identified with composite interval and eXtreme array mapping in *Arabidopsis thaliana*. *Genetics* **167,** 907–917 (2004).
8. Brauer, M. J., Christianson, C. M., Pai, D. A. & Dunham, M. J. Mapping novel traits by array-assisted bulk segregant analysis in *Saccharomyces cerevisiae. Genetics* **173,** 1813–1816 (2006).
9. Segrè, A. V., Murray, A. W. & Leu, J. Y. High-resolution mutation mapping reveals parallel experimental evolution in yeast. *PLoS Biol.* **4,** e256 (2006).
10. Lai, C. Q. *et al.* Speed-mapping quantitative trait loci using microarrays. *Nature Methods* **4,** 839–841 (2007).
11. Schneeberger, K. *et al.* SHOREmap: simultaneous mapping and mutation identification by deep sequencing. *Nature Methods* **6,** 550–551 (2009).
12. Tong, A. H. *et al.* Systematic genetic analysis with ordered arrays of yeast deletion mutants. *Science* **294,** 2364–2368 (2001).
13. Tong, A. H. & Boone, C. High-throughput strain construction and systematic synthetic lethal screening in *Saccharomyces cerevisiae*. In *Yeast Gene Analysis* 2nd edn *Methods in Microbiology* Vol. 36, 369–707 (Elsevier, 2007).
14. Gresham, D. *et al.* Optimized detection of sequence variation in heterozygous genomes using DNA microarrays with isothermal-melting probes. *Proc. Natl Acad. Sci. USA* **107,** 1482–1487 (2010).
15. Demogines, A., Smith, E., Kruglyak, L. & Alani, E. Identification and dissection of a complex DNA repair sensitivity phenotype in Baker's yeast. *PLoS Genet.* **4,** e1000123 (2008).
16. Perlstein, E. O., Ruderfer, D. M., Roberts, D. C., Schreiber, S. L. & Kruglyak, L. Genetic basis of individual differences in the response to small-molecule drugs in yeast. *Nature Genet.* **39,** 496–502 (2007).
17. Kim, H. S. & Fay, J. C. A combined cross analysis reveals genes with drug-specific and background-dependent effects on drug sensitivity in *Saccharomyces cerevisiae*. *Genetics* **183,** 1141–1151 (2009).
18. Steinmetz, L. M. *et al.* Dissecting the architecture of a quantitative trait locus in yeast. *Nature* **416,** 326–330 (2002).
19. Deutschbauer, A. M. & Davis, R. W. Quantitative trait loci mapped to single-nucleotide resolution in yeast. *Nature Genet.* **37,** 1333–1340 (2005).
20. Smith, E. N. & Kruglyak, L. Gene-environment interaction in yeast gene expression. *PLoS Biol.* **6,** e83 (2008).
21. Dimitrov, L. N., Brem, R. B., Kruglyak, L. & Gottschling, D. E. Polymorphisms in multiple genes contribute to the spontaneous mitochondrial genome instability of *Saccharomyces cerevisiae* S288C strains. *Genetics* **183,** 365–383 (2009).
22. Brem, R. B., Yvert, G., Clinton, R. & Kruglyak, L. Genetic dissection of transcriptional regulation in budding yeast. *Science* **296,** 752–755 (2002).
23. Yvert, G. *et al.* Trans-acting regulatory variation in *Saccharomyces cerevisiae* and the role of transcription factors. *Nature Genet.* **35,** 57–64 (2003).
24. Gaisne, M., Becam, A. M., Verdiere, J. & Herbert, C. J. A 'natural' mutation in *Saccharomyces cerevisiae* strains derived from S288c affects the complex regulatory gene *HAP1* (*CYP1*). *Curr. Genet.* **36,** 195–200 (1999).
25. Foss, E. J. *et al.* Genetic basis of proteome variation in yeast. *Nature Genet.* **39,** 1369–1375 (2007).
26. Mackay, T. F. & Lyman, R. F. *Drosophila* bristles and the nature of quantitative genetic variation. *Phil. Trans. R. Soc. Lond. B* **360,** 1513–1527 (2005).
27. Buckler, E. S. *et al.* The genetic architecture of maize flowering time. *Science* **325,** 714–718 (2009).
28. Storey, J. D. & Tibshirani, R. Statistical significance for genomewide studies. *Proc. Natl Acad. Sci. USA* **100,** 9440–9445 (2003).

Supplementary Information is linked to the online version of the paper at www.nature.com/nature.

Acknowledgements The authors are grateful to members of the Kruglyak laboratory for comments on this manuscript; D. Botstein, J. Gerke, G. Lang and E. Perlstein for input regarding experiments; J. Bloom, L. Parsons, D. Sangurdekar and J. Storey for advice regarding analyses; and E. Alani for sharing the EAY1467 strain. This work was supported by NIH grant R37 MH59520, a James S. McDonnell Centennial Fellowship, and the Howard Hughes Medical Institute (L.K.), a NIH postdoctoral fellowship F32 HG51762 (I.M.E.), and NIH grant P50 GM071508 to the Center for Quantitative Biology at the Lewis-Sigler Institute of Princeton University.

Author Contributions Experiments were designed by I.M.E., A.A.C. and L.K. Strains were constructed by I.M.E., Y.J., S.M. and A.A.C. Microarrays were designed by I.M.E. and D.G. Experiments were performed by I.M.E., N.T., Y.J., J.K., S.M. and A.A.C. Simulation scripts were written by I.M.E. and J.A.S. Analyses were conducted by I.M.E. The manuscript was written by I.M.E. and L.K., and incorporates comments by all other authors.

Author Information Reprints and permissions information is available at www.nature.com/reprints. The authors declare no competing financial interests. Correspondence and requests for materials should be addressed to L.K. (leonid@genomics.princeton.edu).

METHODS

Construction of segregating pools. To construct segregating pools, we use the Synthetic Genetic Array (SGA) marker system[12,13]. In our cross, we use a BY parent that is MATα *can1Δ::STE2pr-SpHIS5 lyp1Δ his3Δ1* and an RM parent that is MAT**a** $AMN1^{BY}$ *his3Δ0::NatMX ho::HphMX*. These strains were crossed and a diploid zygote was recovered.

To create the segregating pools, a single colony of the diploid progenitor was inoculated into 100 ml YPD and grown to stationary phase. The diploid culture was spun down and the supernatant was decanted. The diploid pellet was then resuspended in 200 ml Spo++ sporulation medium (http://www.genomics.princeton.edu/dunham/sporulationdissection.htm). The sporulation was kept at room temperature (~22 °C) with shaking and monitored for the fraction of diploids that had sporulated. Once more than 50% of the diploids had sporulated, the culture was deemed suitable for downstream use.

The next step in the generation of segregating pools was to select for MAT**a** haploids. Fifty millilitres of the sporulation were spun down and then the supernatant was decanted. The pellet was resuspended in 1 ml water. Three-hundred microlitres β-glucoronidase (Sigma; G7770) were added to the preparation and the mixture was incubated at 30 °C for 1 h. Approximately 50 μl of glass beads (Sigma; G8772) were then added and the sample was vortexed for 2 min. The sample was incubated for an additional hour at 30 °C, followed by a second round of vortexing for 2 min. Water was added to the sample so that the total volume was 20 ml. The spore preparation was spread onto YNB + canavanine/thialysine (Sigma; C9758 for canavanine (L-canavanine sulphate salt); A2636 for thialysine (*S*-(2-aminoethyl)- L-cysteine hydrochloride)), with 100 μl of sample going onto each plate. The plates were incubated at 30 °C. MAT**a** haploids typically grew up after ~2 days.

The final step in pool creation was to mix together MAT**a** segregants selected on different plates. Ten millilitres of water were poured onto a plate and a sterile spreader was used to remove the segregants from the plate. The cell mixtures from each plate were then pipetted off the plates into a separate container. The pool was spun down and the water decanted. For drug selections, the cell pellet was resuspended in 1.5 ml YPD per scraped plate. The segregant pool was incubated at 30 °C for 1 h. One-hundred microlitres of this segregant pool was then spread onto each selection or control plate. For sorting of Mitotracker red-stained cells, haploid segregants selected on YNB + canavanine/thialysine were scraped from plates and inoculated into YNB + canavanine liquid medium at a concentration of around $\sim 3 \times 10^6$ cells ml^{-1}. The cells were grown for approximately three generations to a density of $\sim 2 \times 10^7$ cells ml^{-1}.

Drug selections with segregating pools. X-QTL should be most powerful when selections are stringent, as this implies that one is enriching for segregants that are phenotypically extreme and are likely to possess multiple alleles that affect a trait in the same direction. For cell sorting, such selections are straightforward, as individual cells exhibiting a trait value within a specified range can be isolated. For chemical resistance mapping, achieving a stringent selection is slightly more challenging, as a whole population of cells is plated and one can only enrich for segregants with high trait values.

Drug selections with segregating pools require finding the optimal concentration to use for a particular compound before X-QTL mapping. To do this, we plate segregating pools across a range of concentrations. The concentration at which we start to resolve individual colonies on plates is the concentration that we use for X-QTL mapping. The fact that we observe $\sim 5 \times 10^2$ to $\sim 5 \times 10^3$ individual colonies when we plate more than 10^6 individuals implies that we are selecting far into the resistance tail of the phenotype distribution. Final concentrations used for the chemical selections are in Supplementary Table 1. After selection was completed, several replicate selection plates were scraped, pooled and frozen at −80 °C. Control experiments were also conducted by plating segregating pools on YPD without any drug added, and pools were collected and stored in the same manner as the selections.

We attempted to combine MAT**a** selections with our chemical resistance selections by incorporating a chemical of interest into our YNB + canavanine/thialysine plates. We found that this approach worked far worse than separating the selection of MAT**a** haploids and the selection of resistant segregants into two steps.

Microarray description. We designed our array using 21,994 BY and RM allele-specific probe pairs. These pairs cover 17,566 SNPs that differentiate BY and RM, at an average spacing of one marker every ~700 bp. The BY-specific probes were designed as part of a separate study of optimal probe design parameters for DNA genotyping arrays and were chosen to minimize the variance in T_m values across probes[14]. For this study, we used the previously designed BY-specific probes and made an additional probe specific to the RM sequence. To maximize the sensitivity of our genotyping array, probes were chosen to have the interrogated SNP within the middle five bases of a given probe. Our custom two-colour microarray was manufactured by Agilent.

DNA extraction, labelling and microarray hybridization. DNA was extracted from parental strains and segregating pools using Genomic-tip 100/G columns (Qiagen; 10243). DNA was labelled using the BioPrime Array CGH Genomic Labeling Module (Invitrogen; 18095-012) with the sample being labelled with Cy3 dUTP and the reference being labelled with Cy5 dUTP in most cases. We used a BY/RM diploid as the reference for all hybridizations. Hybridization intensities were extracted and normalized using the rank invariant method in the Agilent Feature Extraction software package.

Comparison of microarray data to sequencing data. DNA from the same control and 4-NQO-selected segregating pools was hybridized to the microarray and sequenced on the Illumina Genome Analyzer using 75-bp reads. Two biological replicate control and two biological replicate 4-NQO-selected pools were sequenced. Except for one of the replicate controls that was sequenced in a single lane, each sample was sequenced in two lanes. To analyse the Genome Analyser data, sequencing reads were mapped to the BY genome using ELAND and the Illumina EXPORT files were converted into SAM format using SAMTOOLS[29]. The PILEUP function in SAMTOOLS was used to reformat the sequence data. Sequence data at polymorphic sites included on the genotyping microarray were extracted from the PILEUP file and only these sites were analysed. The polymorphic sites were subjected to a quality filter, with only sites having a quality score of 10 or higher used. The coverage was ~60× per site in each lane. Supplementary Fig. 3 shows only one lane (~60×) of sequence data from a 4-NQO selection, four aggregated lanes of sequence data (~240×) from both 4-NQO selections, and a single microarray. Even at 60× sequencing coverage, peaks are discernible, although the variance in measured allele frequencies is high. 240× coverage provides results comparable to the genotyping microarray. Our results suggest that both X-QTL and X-QTL-seq are useful approaches to genetic mapping in pools of cross progeny.

Mapping results for drug traits. Before analysis, each array was subjected to a quality check that both allele-specific probes for a given probe set had successfully hybridized. Bad probe sets were excluded from downstream analyses. We conducted separate analyses for the drug selection and FACS-based selection experiments.

The difference in the $\log_{10}$ ratios of the intensities of the BY and RM allele-specific probes on a single array was computed for a given SNP, and this metric was used in downstream analyses. In cases where a SNP was represented by two probe sets, the probe sets were used as separate data points. For the drug selections, *t*-tests were conducted comparing results from two independent selection experiments to results from 13 independent control experiments. *t*-tests were conducted with the variances of the two groups set to be equal. The $-\log_{10}(P)$ values were then used for unsupervised peak calling. We found that an approach that scanned the genome for inflection points in the slope of the average $-\log_{10}(P)$ values worked best. By definition, a peak is a point at which the slope of the data changes sign. When scanning $-\log_{10}(P)$ values, which are always positive, a peak is represented by a positive to negative sign change.

To identify inflection points, we first smoothed the data by averaging the $-\log_{10}(P)$ values within 50-kb sliding windows. We then scanned the genome chromosome-by-chromosome by resistance trait using sliding window linear regression. We fit linear regressions over 100-kb sliding windows and used the slope of these regressions to estimate the locations of peaks. A special case was allowed at the ends of chromosomes in which peaks were recorded if the slope was negative at the top of the chromosome or positive at the bottom of the chromosome. The average $-\log_{10}(P)$ value at estimated peaks was recorded and used for thresholding. The same approach was used to analyse 1,000 permutations of the chemical resistance data set, in which two randomly chosen arrays ('selections') were compared to 13 randomly chosen arrays ('controls'). A requirement was set on the permuted data sets that the selection arrays never be biological replicates of the same real trait selection. Because of uncertainty about what constitutes a distinct peak under cases of close linkage, we set a requirement that two peaks could not occur within 200 kb of each other. Increasing or decreasing this proximity threshold results in a slightly different number of called peaks, but does not affect the general findings of the paper. Inflection points detected in the permutations were used to set an empirical FDR threshold of 0.05. We used a global FDR threshold, as opposed to a trait-level FDR, as most observed expected–observed peak relationships at the trait level were very close to the global relationship (Fig. 3d). Average $-\log_{10}(P)$ plots, as well as significant peaks, are provided for each trait in Supplementary Fig. 5a–q.

For the FACS experiment, three low, three high and three whole-population biological replicates were generated. Because of the small number of arrays in the experiment, permutations were unlikely to be useful for setting an empirical FDR threshold. Furthermore, because the data structure of the FACS experiment, which used two tails of the segregant distribution, was different from the drug selections, which used only one tail of the segregant distribution, we could not use the drug selections in permutations of the FACS data. For these reasons, we

used QVALUE[28], which estimates the FDR using the distribution of *P* values in an experiment, to determine probes that were significant at an FDR of 0.05. We show this threshold in Fig. 4.

All analyses were conducted in R.

29. Li, H. *et al.* The Sequence Alignment/Map format and SAMtools. *Bioinformatics* **25,** 2078–2079 (2009).

LETTERS

APCDD1 is a novel Wnt inhibitor mutated in hereditary hypotrichosis simplex

Yutaka Shimomura[1]*, Dritan Agalliu[3]*, Alin Vonica[4]*, Victor Luria[1,2]*, Muhammad Wajid[1], Alessandra Baumer[5], Serena Belli[6], Lynn Petukhova[1], Albert Schinzel[5], Ali H. Brivanlou[4], Ben A. Barres[3] & Angela M. Christiano[1,2]

Hereditary hypotrichosis simplex is a rare autosomal dominant form of hair loss characterized by hair follicle miniaturization[1,2]. Using genetic linkage analysis, we mapped a new locus for the disease to chromosome 18p11.22, and identified a mutation (Leu9Arg) in the adenomatosis polyposis down-regulated 1 (*APCDD1*) gene in three families. We show that APCDD1 is a membrane-bound glycoprotein that is abundantly expressed in human hair follicles, and can interact *in vitro* with WNT3A and LRP5—two essential components of Wnt signalling. Functional studies show that APCDD1 inhibits Wnt signalling in a cell-autonomous manner and functions upstream of β-catenin. Moreover, APCDD1 represses activation of Wnt reporters and target genes, and inhibits the biological effects of Wnt signalling during both the generation of neurons from progenitors in the developing chick nervous system, and axis specification in *Xenopus laevis* embryos. The mutation Leu9Arg is located in the signal peptide of APCDD1, and perturbs its translational processing from the endoplasmic reticulum to the plasma membrane. APCDD1(L9R) probably functions in a dominant-negative manner to inhibit the stability and membrane localization of the wild-type protein. These findings describe a novel inhibitor of the Wnt signalling pathway with an essential role in human hair growth. As APCDD1 is expressed in a broad repertoire of cell types[3], our findings indicate that APCDD1 may regulate a diversity of biological processes controlled by Wnt signalling.

Hair follicle miniaturization is a degenerative process that proportionally reduces the dimensions of the epithelial and mesenchymal compartments of the hair follicle, and leads to the conversion of thick, terminal hair to fine, vellus hair[4]. It is most commonly observed in androgenetic alopecia, but is also characteristic of a rare, autosomal dominant form of hair loss, known as hereditary hypotrichosis simplex[1] (HHS; OMIM accession 146520) (Supplementary Note). To gain insight into the molecular underpinnings of hair follicle miniaturization and identify a gene underlying HHS, we performed a linkage study in two Pakistani families (HHS1 and HHS2) (Fig. 1a–d and Supplementary Fig. 1a–l). After excluding the *CDSN* locus on chromosome 6 (ref. 5), we used Affymetrix 10K single nucleotide polymorphism (SNP) arrays for genotyping. Linkage analysis using a dominant model yielded a maximum log odds ratio (lod) score of $Z = 4.6$ on chromosome 18p11.22 (Supplementary Fig. 1m). We narrowed the candidate interval to a 1.8-megabase (Mb) region (Fig. 1e) containing eight genes, four pseudogenes and three predicted transcripts (Supplementary Fig. 1n). Direct sequencing identified a heterozygous mutation 26T>G (Leu9Arg) in the signal peptide of the *APCDD1* gene (Supplementary Fig. 1o)[6]. The Leu9Arg mutation cosegregated with the disease phenotype in both families, and was absent in 200 unrelated, unaffected controls and in the SNP databases (Supplementary Fig. 1p; data not shown). Unexpectedly, we identified the identical *APCDD1* mutation in an Italian family with autosomal dominant HHS, which had previously been mapped to the same region of chromosome 18p11.22 (Supplementary Fig. 2)[7], providing independent genetic evidence in support of this finding.

APCDD1 was abundantly expressed in both the epidermal and dermal compartments of the human hair follicle, consistent with a role in hair follicle miniaturization. APCDD1 messenger RNA and protein were present in human scalp skin by reverse transcription PCR (RT–PCR) (Supplementary Fig. 3a), and a western blot using an APCDD1 antibody (Fig. 1l). APCDD1 mRNA and protein were highly expressed in the hair follicle dermal papilla, the matrix, and the hair shaft (Fig. 1f–j). Apcdd1 orthologues are conserved throughout vertebrate evolution (Supplementary Fig. 4a, b), suggesting that a role in mouse (also called Drapc1)[3] and human hair follicle growth emerged recently in mammalian species.

Several lines of evidence led us to postulate that APCDD1 may function as a negative regulator of Wnt signalling, including the observation that it is a direct target gene of Wnt/β-catenin[6]; its similarity in expression pattern with another Wnt inhibitor, Wise[8]; the abundance of Wnt inhibitors in the hair follicle[9]; and the conservation of 12 cysteine residues (Supplementary Fig. 4a), a structural motif important for interaction between Wnt ligands and their receptors[10,11].

To test whether APCDD1 is an inhibitor of Wnt signalling, we first determined whether APCDD1 interacts with ligands and receptors of the canonical Wnt pathway. No interaction was found with FZD2, FZD8 and DKK4 (data not shown). In contrast, the extracellular domain of APCDD1 (APCDD1ΔTM) co-precipitated with recombinant tagged forms of WNT3A and LRP5, two proteins important for hair follicle induction[12] (Fig. 2a and Supplementary Figs 3b and 5), suggesting that APCDD1 can modulate the Wnt pathway by potential interactions with WNT3A and LRP5 at the cell surface. To determine the effect of APCDD1 on Wnt signalling, we performed TOP/FOP-flash (T-cell factor (TCF)-responsive and negative control luciferase reporter) Wnt reporter assays in HEK293T cells. Reporter activity induced by WNT3A alone, or in combination with LRP5 and FZD2, was downregulated ~2-fold by APCDD1 in a dose-dependent manner (Fig. 2b), indicating that APCDD1 inhibits the Wnt/β-catenin pathway.

To determine whether APCDD1 can function as a Wnt inhibitor *in vivo*, we selected two systems in which the role of the Wnt/β-catenin pathway has been well-defined: neuronal specification in the developing

[1]Department of Dermatology, [2]Department of Genetics and Development, Columbia University, College of Physicians and Surgeons, 630 West 168th Street, VC15 204A, New York, New York 10032, USA. [3]Department of Neurobiology, Stanford University, Stanford, California 94305, USA. [4]The Laboratory of Vertebrate Embryology, The Rockefeller University, New York, New York 10065, USA. [5]Institute of Medical Genetics, University of Zurich, Schwerzenbach CH-8603, Switzerland. [6]Struttura Semplice Genetica Medica APSS, Trento 138100, Italy.
*These authors contributed equally to this work.

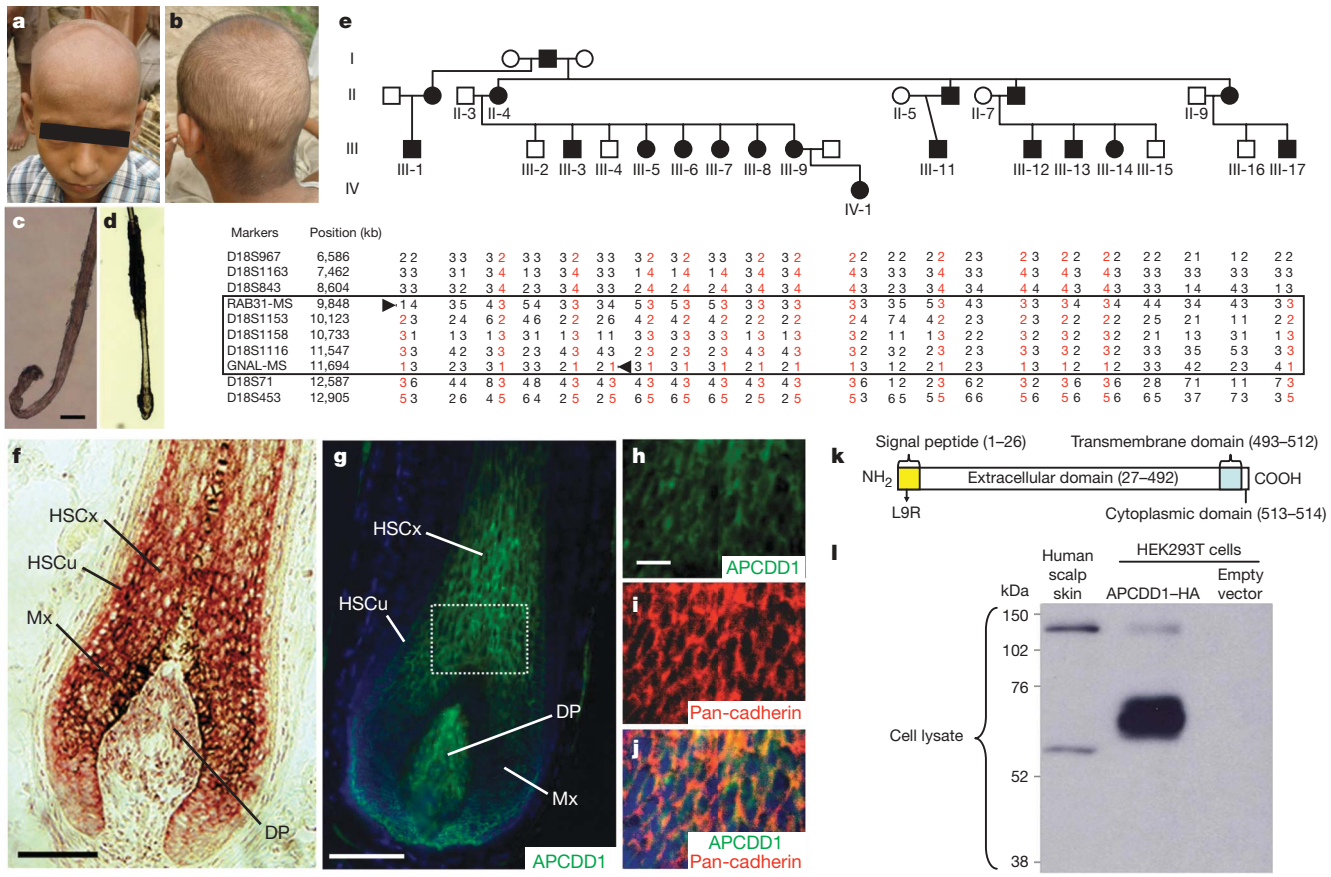

Figure 1 | The HHS phenotype maps on chromosome 18p11.2 at a point mutation in the *APCDD1* gene. **a–d**, Clinical appearance of HHS patients (**a**, **b**) and their hair shafts (**c**, **d**). Scale bar, 100 μm. **e**, Haplotype analysis of a Pakistani family, HHS1. The linked haplotype is indicated in red. The critical recombination events are indicated by black arrowheads. kb, kilobases. **f**, *In situ* hybridization with an *APCDD1* antisense mRNA probe in human hair follicles. *APCDD1* is present in the dermal papilla (DP), matrix (Mx), hair shaft cortex (HSCx), and cuticle (HSCu) of the hair follicle. **g–j**, Immunofluorescence in human HFs with a mouse polyclonal anti-APCDD1 antibody (Abnova). The expression of APCDD1 protein in the HSCx (white box in **g**) overlaps with that of E- and P-cadherin (pan-cadherin) (**h–j**). Counterstaining with DAPI is shown in blue (**g**, **j**). Scale bars, 100 μm (**f**, **g**) and 20 μm (**h**). **k**, Schematic of APCDD1 protein and the position of the Leu9Arg mutation. **l**, A western blot with the mouse polyclonal anti-APCDD1 antibody (Abnova) from cell lysates of human scalp skin shows two fragments around 58 and 130 kDa in size. A similar pattern was observed with the haemagglutinin (HA)-tagged wild-type APCDD1 overexpressed in HEK293T cells.

spinal cord[13–15] and axis determination in the frog[16,17]. In the chick spinal cord, a Wnt/β-catenin gradient promotes proliferation of neural progenitors and generation of some neuronal classes[13–15]. Transfection of the Wnt reporter TOP::eGFP (T cell factor responsive enhanced green fluorescent protein reporter) in the chick neural tube showed strong activation of the pathway in the dorsal and intermediate progenitors, as previously shown[15]. However, overexpression of APCDD1 strongly reduced eGFP expression levels (Supplementary Fig. 6a–d), decreased the number of $SOX3^+$ neural progenitors by ~20–30%, and also decreased various neuronal subtypes of dorsal and ventral origin (Fig. 3a–e and Supplementary Fig. 7a–d). This effect was stronger with mouse Apcdd1 (mApcdd1), a closer orthologue of the chick protein (Supplementary Figs 8a–i and 9a–e). These findings are consistent with the hypothesis that APCDD1 functions as a Wnt inhibitor.

The maternal Wnt pathway is required for the formation of dorsal and anterior structures in early *Xenopus* embryos[18,19]. Overexpression of APCDD1 in dorsal blastomeres ($n = 35$) reduced the anterior structures, such as the eyes and cement gland, at the tadpole stage (Fig. 4a, b), consistent with maternal Wnt inhibition. APCDD1 also inhibited transcription of the siamois (*sia*) reporter gene (Fig. 2c), activated by the maternal Wnt pathway[20]. A zygotic Wnt pathway is subsequently activated on the ventral side of the embryo[21], and its inhibition produces secondary axes with incomplete heads[16,17]. Ventral overexpression of APCDD1 induced secondary axes ($n = 43$, 28% duplicated axes; Fig. 4c, d), consistent with an inhibitory effect on zygotic Wnt signalling. The inhibition of Wnt activity by APCDD1 was also seen in transcription assays with *wnt8* RNA, but not *β-catenin* (Fig. 2c), indicating that it acts upstream of β-catenin.

We next investigated which domain of APCDD1 mediates its activity and in which cell APCDD1 exerts its function. First, western blot of APCDD1 expressed in HEK293T cells showed that the protein is glycosylated and forms a dimer (Supplementary Fig. 10a–c). Second, misexpression of mApcdd1ΔTM (lacking the transmembrane domain) in the chick neural tube mimicked the effects observed with wild-type mApcdd1 (Supplementary Figs 8j–r and 9f–j), suggesting that the Wnt inhibitory activity resides in the extracellular domain. Third, APCDD1 could affect either the signalling cell, by regulating Wnt secretion[22], or the receiving cell. In *Xenopus* transcription assays, *wnt8* RNA injected in one cell activated the *sia* reporter in an adjacent cell. Human *APCDD1* RNA inhibited transcription when co-injected with the *sia* reporter, but not with *wnt8* (Fig. 4h), suggesting that APCDD1 inhibits Wnt signalling cell-autonomously in the receiving cell. Last, because wild-type APCDD1 contains a transmembrane domain (Fig. 1k), and was localized to the plasma membrane (Fig. 2h and Supplementary Fig. 11a, c, f, i), we tested whether APCDD1 undergoes cleavage to generate a diffusible inhibitor (APCDD1ΔTM); however, it was undetectable in the medium of transfected cells (Supplementary Fig. 10d). Collectively, these data show that APCDD1 is probably a membrane-tethered Wnt inhibitor that acts as a dimer at the surface of the Wnt-receiving cell.

The Leu9Arg mutation disrupts the hydrophobic core of the signal peptide critical for co-translational processing (Supplementary

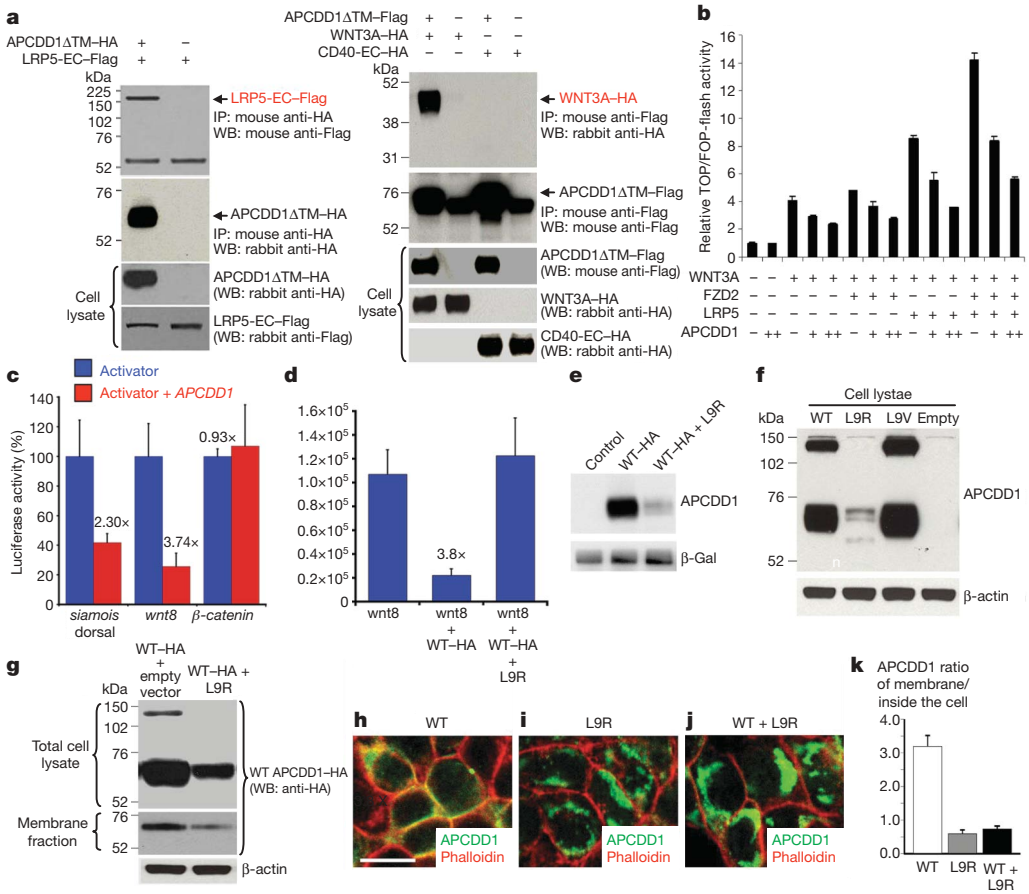

Figure 2 | Wild-type, but not Leu9Arg mutant APCDD1, inhibits canonical Wnt signalling. **a**, Co-immunoprecipitation assays show that the extracellular domain of APCDD1 (APCDD1ΔTM) strongly interacts with the extracellular domain of LRP5 (LRP5-EC) and WNT3A. The extracellular domain of a non-Wnt related single transmembrane receptor CD40 (CD40-EC) was used as a negative control. IP, immunoprecipitation; WB, western blot. **b**, TOP/FOP-flash reporter assays in HEK293T cells. TOP-flash, TCF-β-catenin reporter (active); FOP-flash, scrambled consensus reporter (inactive). **c**, Effect of APCDD1 overexpression on transcriptional activity of the Wnt-specific *sia* reporter gene induced by wnt8 or β-catenin in *Xenopus*. *APCDD1* (1 ng RNA) inhibited *wnt8*- (50 pg RNA), but not *β-catenin*-(1 ng RNA) induced transcription. The number above the column indicates fold repression by *APCDD1*. **d**, The Leu9Arg mutant APCDD1 has a dominant-negative effect on wild-type APCDD1 in *Xenopus*. Activity of the *sia* reporter gene induced by *wnt8* RNA (50 pg) was inhibited by co-injection of wild-type *APCDD1* RNA (1 ng), but not by co-expression of wild-type and the Leu9Arg mutant. **e**, Western blot of APCDD1 levels in *Xenopus* embryos. APCDD1(L9R) affects wild-type protein levels in *Xenopus* embryos. Coexpressed β-Galactosidase (β-Gal) is used as a loading control. **f**, Western blot analysis of lysates from HEK293T cells transfected with wild-type, APCDD1(L9R) or APCDD1(L9V). **g**, The expression level of HA-tagged wild-type APCDD1 (WT–HA) is decreased by co-expression with APCDD1(L9R). β-actin was used as a normalization control (**f**, **g**). **h–j**, Immunofluorescence in transfected HEK293T cells with an APCCD1 antibody (green). The cell membrane was labelled with rhodamine–phalloidin (red). Scale bar, 20 μm. **k**, Quantification of subcellular localization of APCDD1 isoforms. Error bars represent mean ± s.e.m. ($n = 20$ cells per group). Wild type versus Leu9Arg, $P < 8 \times 10^{-7}$; wild type versus wild type + Leu9Arg, $P < 3 \times 10^{-6}$; Leu9Arg versus wild type + Leu9Arg, $P = 0.99$. The reported *P*-values are adjusted with the Bonferroni correction.

Fig. 4b, c)[23]. We analysed protein stability and localization by western blotting and immunofluorescence in two cell lines (HEK293T or Bend3.0) transfected with either wild-type APCDD1 or two different mutant forms (pathogenic mutation, Leu9Arg, and conservative substitution, Leu9Val). Two fragments (68 kilodalton (kDa) and 130 kDa) were detected in lysates of the wild-type and APCDD1(L9V)-transfected cells, whereas only a faint 68 kDa fragment was detected in the Leu9Arg mutant (Fig. 2f). In addition, wild-type or APCDD1(L9V) protein was localized to the cell membrane, whereas APCDD1(L9R) was retained within the endoplasmic reticulum (ER) (Fig. 2h, i and Supplementary Fig. 11a–j). Furthermore, unlike the wild-type isoform, amino-terminally GFP-tagged APCDD1(L9R) could not be cleaved to localize at the membrane (Supplementary Fig. 11l–n). Finally, when the wild-type and APCDD1(L9R) were either co-transfected in cells or injected into *Xenopus* embryos, some wild-type protein was degraded (Fig. 2e, g), and the rest was sequestered in the ER along with the Leu9Arg isoform (Fig. 2j, k and Supplementary Fig. 11k, o–r). Therefore, the Leu9Arg mutation probably functions in a dominant-negative manner, to destabilize the wild-type protein and prevent it from reaching the plasma membrane.

We next tested whether the Leu9Arg mutation affects APCDD1 protein function *in vivo*. In the chick neural tube, expression of APCDD1(L9R) only weakly inhibited eGFP transcription from the Wnt reporter (Supplementary Fig. 6e, f), and had no effect on SOX3 neural progenitors and neuronal subtypes (Fig. 3f–j and Supplementary Fig. 7e–h), in contrast to wild-type or APCDD1(L9V) (Supplementary Fig. 7m–u). Moreover, APCDD1(L9R) was able to block wild-type protein function *in vivo* when they were co-transfected (Fig. 3k–o and Supplementary Fig. 7i–l), indicative of a dominant-negative effect. The same results were observed in *Xenopus*, where the inhibitory effect of wild-type APCDD1 on wnt8-induced transcription was blocked by co-expression of the Leu9Arg mutant (Fig. 2d).

We then determined the consequences of *Xenopus* apcdd1 (Xapcdd1) protein depletion on axis formation in *Xenopus* embryos. *Xapcdd1* mRNA is expressed maternally throughout development, with the highest levels in animal (future ectoderm) and marginal (future mesoderm) cells of stage ten embryos (Supplementary Fig. 12). Depletion of Xapcdd1 protein with a specific translation-blocking morpholino oligonucleotide (MO) (Supplementary Fig. 13) resulted in loss of anterior and dorsal structures (Fig. 4e and Supplementary Table 1).

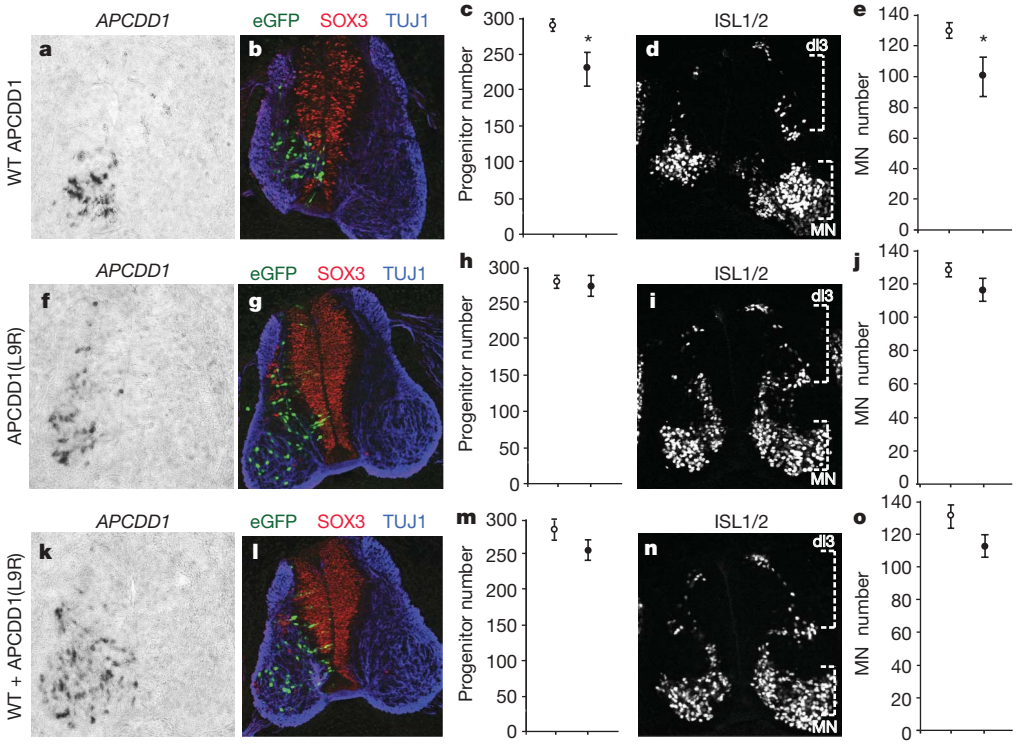

Figure 3 | Overexpression of wild-type APCDD1, but not the Leu9Arg mutant, inhibits progenitor proliferation and neuronal specification in the chick spinal cord. Transfection of wild-type, Leu9Arg or both APCDD1 isoforms is visualized by eGFP fluorescence (**b**, **g**, **l**; green) and *in situ* for human *APCDD1* (**a**, **f**, **k**). SOX3 labels neural progenitors in red and TUJ1 labels neurons in blue (**b**, **g**, **l**). Misexpression of wild-type, but not Leu9Arg or a combination of both APCDD1 isoforms, reduces the number of SOX3$^+$ neural progenitors. Immunofluorescence for ISL1/2$^+$ (**d**, **i**, **n**; motor neurons (MNs), ventral ISL1/2$^+$ cells; dorsal dI3 interneurons, dorsal ISL1/2$^+$ cells) shows that MNs are only reduced in the wild-type APCDD1 electroporation. The D3 interneuron population is reduced in all conditions. Plots of SOX3$^+$ progenitors (**c**, **h**, **m**) and ISL1/2$^+$ MNs (**e**, **j**, **o**) in control (open circles) and transfected embryos (closed circles). Error bars represent mean ± s.e.m. ($n = 40$ embryos for wild-type APCDD1, $n = 35$ embryos for APCDD1(L9R) and $n = 28$ embryos for wild-type and APCDD1(L9R); Student's *t*-test, $*P < 0.05$).

This phenotype was rescued by injection of either MO-resistant 5′ mutant *Xapcdd1* RNA, or of dominant-negative *wnt8* RNA (Fig. 4f, g and Supplementary Table 1), which inhibit zygotic Wnt signalling[24].

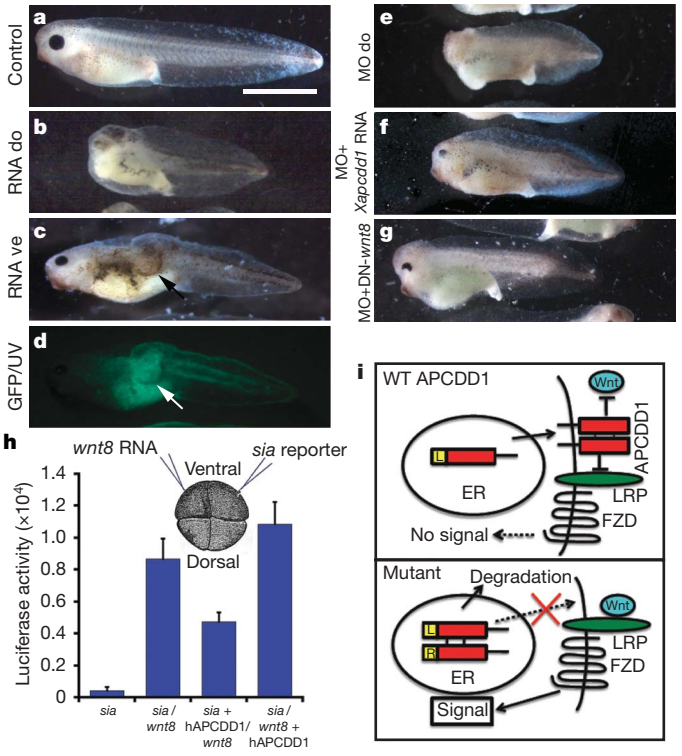

Figure 4 | APCDD1 inhibits the Wnt pathway in *Xenopus* embryos. **a**, **b**, Dorsal (do) overexpression of human APCDD1 (hAPCDD1) reduces axial and anterior structures (**b**). Scale bar, 4 mm (**a**). **c**, **d**, Ventral (ve) overexpression of hAPCDD1 produces a secondary axis (arrow in **c**) in cell autonomous fashion (GFP tracer under ultraviolet (UV) light, arrow in **d**). **e**–**g**, Phenotype of Xapcdd1 protein depletion and its rescue. Dorsal depletion by MO produced a ventralized phenotype (**e**), which was rescued by *Xapcdd1* RNA (**f**) and by dominant-negative *wnt8* RNA (DN-*wnt8*) (**g**). **h**, APCDD1 is required in the signal-receiving cells. *wnt8* RNA and *siamois* reporter gene were injected in adjacent cells. hAPCDD1 inhibited signalling only when co-injected with the reporter. +, Coexpression in the same cell; /, expression in different cells. **i**, Potential mechanism of action for wild-type and mutant APCDD1. Top, wild-type APCDD1 (L) is processed in the ER and localized at the cell membrane, where it may inhibit Wnt signalling by interacting with Wnt and LRP proteins. Bottom, when wild-type and APCDD1(L9R) (R) are co-expressed, wild-type APCDD1 is retained and degraded in the ER with the mutant, thus activating the Wnt signalling pathway.

Therefore, the loss-of-function phenotype is consistent with ectopic activation on the dorsal side of zygotic Wnt activity, and supports the notion that endogenous APCDD1 is a Wnt inhibitor.

In conclusion, we suggest that APCDD1 may prevent formation of the Wnt receptor complex (Fig. 4i) as it interacts *in vitro* with LRP5 and WNT3A. The Leu9Arg mutant is unable to repress Wnt-responsive genes, by trapping the wild-type protein in the ER where it may undergo degradation (Fig. 4i).

Our findings underscore the requirement for controlled regulation of the Wnt signalling pathway in hair follicle morphogenesis and cycling[25]. It is known that perturbation of Wnt signaling in mouse models leads to increased hair follicle density when Wnt signaling is constitutively activated in the epidermis[26], and a loss of hair when Lef1 is deleted[27]. We postulate that in HHS, Wnt signalling is indirectly

increased through the loss of the inhibitory function of APCDD1 in both the epidermal and dermal compartments of the hair follicle, although the lack of HHS scalp samples precluded us from verifying this assumption. This notion is supported by mice with targeted ablation of another Wnt inhibitor, klotho (*Kl*), which show a reduction in hair follicle density due to indirect upregulation of Wnt signalling and a depletion of hair follicle bulge stem cells[28]. As APCDD1 is expressed in both epidermal hair follicle cells and the dermal papilla, we postulate that the simultaneous deregulation of Wnt signalling in both compartments may lead to a proportional reduction in organ size of the hair follicle, resulting in miniaturization.

Our study provides the first genetic evidence, to our knowledge, that mutations in a Wnt inhibitor result in hair loss in humans. APCDD1 may be implicated in polygenic hair follicle disorders as well, because it resides within linkage intervals on chromosome 18 in families with androgenetic alopecia[29] as well as alopecia areata[30]. Furthermore, because APCDD1 is expressed in a broad range of cell types[3], our findings raise the possibility that APCDD1 is involved in other Wnt-regulated processes, such as morphogenesis, stem-cell renewal, neural development and cancer.

METHODS SUMMARY

Linkage analysis. Genome-wide SNP-based genotyping was performed using the Affymetrix Human Mapping 10K 2.0 Array. Quality control and data analysis was performed with Genespring GT (Agilent software). SNPs that violated a Mendelian inheritance pattern were removed from the data set before analysis. Haplotypes were inferred from raw genotype data. By analysing haplotypes rather than individual SNPs, type I error introduced by linkage disequilibrium between markers is mitigated. Finally, haplotypes were analysed for linkage under the assumption of a fully penetrant disease gene with a frequency of 0.001 transmitted by a dominant mode of inheritance.

Mutation analysis. Using the genomic DNA of the family members, all exons and exon-–intron boundaries of the human *APCDD1* gene were amplified by PCR with the gene-specific primers (Supplementary Table 2). The PCR products were directly sequenced in an ABI Prism 310 Automated Sequencer, using the ABI Prism Big Dye Terminator Cycle Sequencing Ready Reaction Kit (PE Applied Biosystems). The mutation 26T>G disrupts a DdeI restriction enzyme site, which was used to screen the family members and control individuals.

Full Methods and any associated references are available in the online version of the paper at www.nature.com/nature.

Received 21 March 2009; accepted 3 February 2010.

1. Toribio, J. & Quinones, P. A. Hereditary hypotrichosis simplex of the scalp. Evidence for autosomal dominant inheritance. *Br. J. Dermatol.* **91,** 687–696 (1974).
2. Ibsen, H. H., Clemmensen, O. J. & Brandrup, F. Familial hypotrichosis of the scalp. Autosomal dominant inheritance in four generations. *Acta Derm. Venereol.* **71,** 349–351 (1991).
3. Jukkola, T., Sinjushina, N. & Partanen, J. *Drapc1* expression during mouse embryonic development. *Gene Expr. Patterns* **4,** 755–762 (2004).
4. Trüeb, R. M. Molecular mechanisms of androgenetic alopecia. *Exp. Gerontol.* **37,** 981–990 (2002).
5. Betz, R. C. *et al.* A gene for hypotrichosis simplex of the scalp maps to chromosome 6p21.3. *Am. J. Hum. Genet.* **66,** 1979–1983 (2000).
6. Takahashi, M. *et al.* Isolation of a novel human gene, *APCDD1*, as a direct target of the β-Catenin/T-cell factor 4 complex with probable involvement in colorectal carcinogenesis. *Cancer Res.* **62,** 5651–5656 (2002).
7. Baumer, A., Belli, S., Trüeb, R. M. & Schinzel, A. An autosomal dominant form of hereditary hypotrichosis simplex maps to 18p11.32-p11.23 in an Italian family. *Eur. J. Hum. Genet.* **8,** 443–448 (2000).
8. O'Shaughnessy, R. F., Yeo, W., Gautier, J., Jahoda, C. A. & Christiano, A. M. The WNT signalling modulator, Wise, is expressed in an interaction-dependent manner during hair-follicle cycling. *J. Invest. Dermatol.* **123,** 613–621 (2004).
9. Bazzi, H., Fantauzzo, K. A., Richardson, G. D., Jahoda, C. A. & Christiano, A. M. The Wnt inhibitor, Dickkopf 4, is induced by canonical Wnt signaling during ectodermal appendage morphogenesis. *Dev. Biol.* **305,** 498–507 (2007).
10. Kawano, Y. & Kypta, R. Secreted antagonists of the Wnt signalling pathway. *J. Cell Sci.* **116,** 2627–2634 (2003).
11. Nakamura, T. & Matsumoto, K. The functions and possible significance of Kremen as the gatekeeper of Wnt signalling in development and pathology. *J. Cell. Mol. Med.* **12,** 391–408 (2008).
12. Kishimoto, J., Burgeson, R. E. & Morgan, B. A. Wnt signaling maintains the hair-inducing activity of the dermal papilla. *Genes Dev.* **14,** 1181–1185 (2000).
13. Megason, S. G. & McMahon, A. P. A mitogen gradient of dorsal midline Wnts organizes growth in the CNS. *Development* **129,** 2087–2098 (2002).
14. Lei, Q. *et al.* Wnt signaling inhibitors regulate the transcriptional response to morphogenetic Shh-Gli signaling in the neural tube. *Dev. Cell* **11,** 325–337 (2006).
15. Yu, W., McDonnell, K., Taketo, M. M. & Bai, C. B. Wnt signaling determines ventral spinal cord cell fates in a time-dependent manner. *Development* **135,** 3687–3696 (2008).
16. Leyns, L., Bouwmeester, T., Kim, S. H., Piccolo, S. & De Robertis, E. M. Frzb-1 is a secreted antagonist of Wnt signaling expressed in the Spemann organizer. *Cell* **88,** 747–756 (1997).
17. Wang, S., Krinks, M., Lin, K., Luyten, F. P. & Moos, M. Jr. Frzb, a secreted protein expressed in the Spemann organizer, binds and inhibits Wnt-8. *Cell* **88,** 757–766 (1997).
18. Niehrs, C. Regionally specific induction by the Spemann–Mangold organizer. *Nature Rev. Genet.* **5,** 425–434 (2004).
19. Heasman, J. Patterning the early *Xenopus* embryo. *Development* **133,** 1205–1217 (2006).
20. Brannon, M., Gomperts, M., Sumoy, L., Moon, R. T. & Kimelman, D. A β-catenin/XTcf-3 complex binds to the *siamois* promoter to regulate dorsal axis specification in *Xenopus*. *Genes Dev.* **11,** 2359–2370 (1997).
21. Smith, J. C., Price, B. M., Green, J. B., Weigel, D. & Herrmann, B. G. Expression of a *Xenopus* homolog of *Brachyury (T)* is an immediate-early response to mesoderm induction. *Cell* **67,** 79–87 (1991).
22. Kadowaki, T., Wilder, E., Klingensmith, J., Zachary, K. & Perrimon, N. The segment polarity gene porcupine encodes a putative multitransmembrane protein involved in Wingless processing. *Genes Dev.* **10,** 3116–3128 (1996).
23. Pidasheva, S., Canaff, L., Simonds, W. F., Marx, S. J. & Hendy, G. N. Impaired cotranslational processing of the calcium-sensing receptor due to signal peptide missense mutations in familial hypocalciuric hypercalcemia. *Hum. Mol. Genet.* **14,** 1679–1690 (2005).
24. Hoppler, S., Brown, J. D. & Moon, R. T. Expression of a dominant-negative Wnt blocks induction of MyoD in *Xenopus* embryos. *Genes Dev.* **10,** 2805–2817 (1996).
25. Blanpain, C. & Fuchs, E. Epidermal homeostasis: a balancing act of stem cells in the skin. *Nature Rev. Mol. Cell Biol.* **10,** 207–217 (2009).
26. Gat, U., DasGupta, R., Degenstein, L. & Fuchs, E. *De novo* hair follicle morphogenesis and hair tumors in mice expressing a truncated β-catenin in skin. *Cell* **95,** 605–614 (1998).
27. van Genderen, C. *et al.* Development of several organs that require inductive epithelial-mesenchymal interactions is impaired in LEF-1-deficient mice. *Genes Dev.* **8,** 2691–2703 (1994).
28. Liu, H. *et al.* Augmented Wnt signaling in a mammalian model of accelerated aging. *Science* **317,** 803–806 (2007).
29. Hillmer, A. M. *et al.* Genome-wide scan and fine-mapping linkage study of androgenetic alopecia reveals a locus on chromosome 3q26. *Am. J. Hum. Genet.* **82,** 737–743 (2008).
30. Martinez-Mir, A. *et al.* Genomewide scan for linkage reveals evidence of several susceptibility loci for alopecia areata. *Am. J. Hum. Genet.* **80,** 316–328 (2007).

Supplementary Information is linked to the online version of the paper at www.nature.com/nature.

Acknowledgements We are grateful to the family members for their participation in this study, and to H. Lam and M. Zhang for technical assistance. We appreciate the collaboration and discussions with R. M. Bernstein, R. M. Trüeb and members of the A.M.C. laboratory. We thank S. Ishii and J. Miyazaki for supplying the pCXN2.1 vector. We thank C. Jahoda, A. Tomlinson, A. Salic, C. Extavour, L. Shapiro, B. Honig, D. Petrey, R. Vallee, G. Di Paolo and G. Karsenty for discussions and comments on the manuscript, and P. Ducy for sharing reagents. This work was supported in part by USPHS NIH grant R01AR44924 from NIH/NIAMS (A.M.C.). Y.S. is supported by a Research Career Development Award from the Dermatology Foundation. The work in B.A.B.'s laboratory (D.A. and B.A.B.) was supported by grants from the Myelin Repair Foundation and the National Multiple Sclerosis Society (grant RG 3936A7/1). The work in A.H.B.'s laboratory (A.V. and A.H.B.) was supported by NIH grants R01 HD032105 (A.H.B.) and R03HD057334 (A.V.).

Author Contributions A.M.C. and B.A.B. are equally contributing senior authors. The study was conceived, designed and supervised by A.M.C.; laboratory work, phenotyping and sample ascertainment were performed by Y.S., D.A., A.V., V.L., M.W. and A.B.; statistical analyses were performed by L.P.; different aspects of clinical genetics, phenotyping and mutation screening assays were made by M.W., Y.S., A.H.B., S.B., A.S. and A.M.C.; and Y.S., D.A., A.V., V.L., A.H.B., B.A.B. and A.M.C. had considerable input in the experimental design and contributed to the preparation and editing of the manuscript.

Author Information Data have been deposited at NCBI under accession codes NM_153000 (*APCDD1* mRNA) and NP_694545 (APCDD1 protein). Reprints and permissions information is available at www.nature.com/reprints. The authors declare no competing financial interests. Correspondence and requests for materials should be addressed to A.M.C. (amc65@columbia.edu).

METHODS

Clinical details and DNA extraction. Informed consent was obtained from all subjects and approval for this study was provided by the Institutional Review Board of Columbia University. The study was conducted in adherence to the Declaration of Helsinki Principles. Peripheral blood samples were collected from the family members as well as unrelated healthy control individuals of Pakistani and European origin (200 individuals each). Genomic DNA was isolated from these samples using the PUREGENE DNA isolation kit (Gentra System).

Genotyping. Genomic DNA from members of two Pakistani families was amplified by PCR using Platinum PCR SuperMix (Invitrogen) and primers for microsatellite markers on chromosome 18p11. The amplified products were analysed on 8% polyacrylamide gels.

Mutation analysis of the *APCDD1* gene. Exon 1 and the adjacent boundary sequences of the *APCDD1* gene were amplified using Platinum Taq DNA Polymerase High Fidelity (Invitrogen). Owing to the high G/C content, dimethylsuphoxide (DMSO) (final 5%) and $MgSO_4$ (final 1.6 mM) were added to the PCR reaction. Other exons, as well as the exon–intron boundaries of the *APCDD1* gene, were amplified using Platinum PCR SuperMix (Invitrogen). Primer sequences are shown in Supplementary Table 2.

To screen for the mutation 26T>G (Leu9Arg), a part of exon 1 and intron 1 of the *APCDD1* gene was amplified by PCR using Platinum Taq DNA Polymerase High Fidelity (Invitrogen) and the following primers: forward (5′-CCAGAGC AGGACTGGAAATG-3′) and reverse (5′-CGCCAAGGGGACAGTGTAG-3′). The amplified PCR products, 191 base pairs in size, were digested with DdeI at 37 °C overnight, and run on 2.0% agarose gels.

Cell culture. HEK293T (human embryonic kidney) and Bend3.0 cells were cultured in DMEM; GIBCO) supplemented with 10% FBS (GIBCO), 100 international units (IU) ml^{-1} penicillin and 100 μg ml^{-1} streptomycin. For transfection experiments in HEK293T cells, dishes were coated with a coating medium containing 0.01 mg ml^{-1} of fibronectin (Sigma) and 0.03 mg ml^{-1} of type I collagen (Sigma) before seeding the cells in to prevent detachment of the cells.

Anti-APCDD1 antibodies. A mouse polyclonal anti-human APCDD1 antibody was purchased from Abnova. This antibody was raised against the full-length hAPCDD1 protein. We performed epitope-mapping using three truncated glutathione *S*-transferase (GST)–APCDD1 proteins (amino acid residues 1–171, 166–336 and 331–514), and confirmed that the epitope of the antibody exists between residues 166 and 336 of the hAPCDD1, which corresponds to the middle portion of the extracellular domain (data not shown). This antibody recognized hair shaft and dermal papilla in human hair follicles (Fig. 1g–j), which finely overlapped with the signals detected by *in situ* hybridization (Fig. 1f). An affinity-purified rabbit polyclonal anti-mApcdd1 antibody was produced by immunizing rabbits with the synthetic peptide, CQRPSDGSSPDRPEKRATSY (corresponding to the carboxy terminus of the extracellular domain of the mApcdd1 protein, residues 441–459) conjugated to keyhole limpet haemocyanin (KLH; Pierce). This region is completely conserved among mouse and human APCDD1 proteins. The antibody was affinity-purified from the serum using the Sulfolink immobilization column (Pierce). This antibody strongly recognized hAPCDD1 protein in western blots and immunofluorescence.

RT–PCR in human scalp skin and plucked hairs. Total RNA was isolated from scalp skin and plucked scalp hairs of healthy control individuals using the RNeasy Minikit (Qiagen). Two micrograms of total RNA was reverse-transcribed with oligo-dT primers and SuperScript III (Invitrogen). The complementary DNAs were amplified by PCR using Platinum PCR SuperMix and primer pairs for *APCDD1*, *APCDD1L*, keratin 15 (*KRT15*), *LRP5*, *WNT3A*, and β-2 microglobulin (*B2M)* genes (Supplementary Table 2). Primers for the *KRT15*, *LRP5* and *WNT3A* genes were designed as described previously[31,32]. PCR products were run on 1.5% agarose gels.

Expression vectors. cDNA sequences for human *APCDD1*, *WNT3A*, *CD40* and *LRP5* were amplified by PCR using primers and templates shown in Supplementary Table 2. The amplified products were subcloned into the mammalian expression vector pCXN2.1 (ref. 33), a slightly modified version of pCXN2 (ref. 34) with several cloning sites. The expression construct for the full-length human LRP5 was provided by P. Ducy. To generate the expression construct for mouse Fzd2, the full-length open reading frame of Fzd2 was purchased from Invitrogen (clone ID 6411627), which was subcloned into the NotI sites of the pCXN2.1 vector. To introduce a Flag-tag between amino acids 35 and 36 of the APCDD1 protein, the N-terminal region of the APCDD1 was PCR-amplified using a forward primer (APCDD1-F-XhoI in Supplementary Table 2) and a reverse primer (APCDD1-R-Flag-AvrII: 5′-AAAACCTAGGCTTATCGTC GTCATCCTTGTAATCATGAGACCTGCTGTCTGGAT-3′), which was followed by digestion with restriction enzymes XhoI and AvrII. The C-terminal region of the APCDD1 and the truncated APCDD1 proteins with the C-terminal HA-tag were obtained through digestion of the pCXN2.1-Wt-APCDD1-HA and pCXN2.1-APCDD1-ΔTM-HA constructs with restriction enzymes AvrII and NheI. These two fragments were ligated with the AvrII site, and subsequently subcloned into the XhoI and NheI sites of the pCXN2.1 vector. To generate expression constructs for N-terminal GFP-tagged APCDD1 protein, the coding region of the *APCDD1* and the rabbit β-globin 3′-flanking sequences were cut out from the pCXN2.1-APCDD1 constructs with restriction enzymes XhoI and BamHI, and subcloned in frame into the pEGFP-C1 vector (Clontech). The templates were also subcloned into the XhoI and BamHI sites of pBluescript-SK (−) vector (Stratagene). pGEM *wnt8* (from R. Harland), the *sia* luciferase reporter gene (from D. Kimmelman), and pSP36 β-catenin (from B. M. Gumbiner) have been previously described.

To generate a *Xenopus* expression vector for *Xenopus apcdd1*, we used a full-length cDNA clone (BC080377, from Open Biosystems) as a template and amplified the open reading frame with the primers shown in Supplementary Table 2. The PCR product was inserted as a ClaI/SalI fragment in CS2+2XHA (A. Vonica), resulting in CS2+Xapcdd1–HA.

The full-length mouse Apcdd1 cDNA was amplified by RT–PCR from brain endothelial cells using the First Strand Synthesis Kit and High Fidelity Amplification Kit (Roche Applied Science) with primers shown in Supplementary Table 2, and then subcloned into pCRII-TOPO (Invitrogen) and pCAGGS[34] vectors for *in vitro* transcription and chick neural tube electroporations, respectively. The Apcdd1ΔTM isoform containing the extracellular domain of mApcdd1 (residues 1–486) was amplified by PCR from the full-length cDNA using primers shown in Supplementary Table 2 and subcloned into pCAGGS vector for chick electroporation.

Chick neural tube electroporations. The full-length wild-type, APCDD1(L9R), APCDD1(L9V), mApcdd1 or mApcdd1ΔTM isoforms were subcloned into the pCAGGS vector and transfected into the chick neural tube (stage 12–13) together with nuclear GFP vector (pCIG) using *in ovo* electroporation as described[35]. The chick embryos were grown for 3–4 more days in the 39 °C incubator, fixed with 4% paraformaldehyde (PFA), 0.1 M phosphate buffer, washed and cryoprotected as described[35] before being processed for *in situ* hybridization or immunofluorescence. For the Wnt reporter assays, the TOP::eGFP reporter (M38 TOP::eGFP from Addgene) was transfected alone or in combination with wild-type APCDD1 or APCDD1(L9R). The chick embryos were grown for 12 h in the 39 °C incubator, fixed with 4% PFA, 0.1M phosphate buffer for 30 min, washed and cryoprotected as described[35], before being processed for immunofluorescence.

Cell counts and statistical analysis. Spinal cord $SOX3^+$ progenitors, $ISL1/2^+$ ventral motor neurons, $ISL1/2^+$ dorsal interneurons and $CHX10^+$ V2a interneurons were counted from eight independent 12-μm thick sections of chick spinal cord from each transfected embryo. The nucleus stained with the transcription factor was considered one cell for this purpose. The cells were counted from both the electroporated side and the opposite control side. The plots were created using Sigma plot with values representing the mean for each embryo. Statistical significance was determined using the Student's *t*-test.

Transient transfections and western blots in cultured cells and human scalp skin. HEK293T or Bend3.0 cells were plated in 60-mm dishes the day before transfection. Expression plasmids of APCDD1 were transfected with FuGENE 6 (Roche Applied Science) at 60% confluency for HEK293 cells, or with Targefect_HUVEC for Bend3.0 cells. The total amount of transfected plasmids was adjusted with the empty pCXN2.1 vector. The cells were cultured 48 h after transfection in Opti-MEM (GIBCO). The cells were collected and homogenized by sonication in homogenization buffer (25 mM HEPES-NaOH, pH 7.4, 10 mM $MgCl_2$, 250 mM sucrose and Complete Mini Protease Inhibitor Cocktail (Roche Applied Science)). The cell debris was removed by centrifugation at 800*g* for 10 min at 4 °C, and the supernatant was collected as cell lysates. N-glycosidase (PNGase F) treatment and extraction of membrane fraction were performed as described previously[33]. The cultured medium with Complete Mini Protease Inhibitor Cocktail was centrifuged at 300*g* for 5 min at 4 °C. The supernatant was purified with 0.45 μm syringe filters (Thermo Fisher Science), and concentrated using Amicon Ultra-15 Centrifugal Filter Unit with Ultracel-10 Membrane (Millipore) according to the manufacturer's recommendations. Total cell lysates from human scalp skin were extracted by homogenization in 50 mM Tris-HCl, pH 8.0, 150 mM NaCl, 1.0% NP40, 0.5% sodium deoxycholate, 0.1% SDS and Complete Mini Protease Inhibitor Cocktail. All samples were mixed with an equal amount of Laemmli Sample Buffer (Bio-Rad Laboratories) containing 5% β-mercaptoethanol, boiled at 95 °C for 5 min, and analysed by 10% SDS–PAGE. Western blots were performed as described previously[36]. The primary antibodies used were rabbit polyclonal anti-HA (diluted 1:4,000; Abcam), rabbit polyclonal anti-APCDD1 (1:20,000), mouse polyclonal anti-APCDD1 (1:1,000; Abnova), mouse monoclonal anti-Flag M2 (1:1,000; Sigma), and rabbit polyclonal anti-β-actin (1:10,000; Sigma).

Wnt reporter assays in HEK293T cells. HEK293T cells were seeded in 12-well dishes the day before transfection. One-hundred nanograms of either TOP-flash (active) or FOP-flash (inactive) Wnt reporter vector (gifts from P. Ducy) was transfected into each well along with constructs for WNT3A (200 ng), FZD2 (100 ng), LRP5 (100 ng), and/or wild-type APCDD1–HA (300 ng or 800 ng) using Lipofectamine 2000 (Invitrogen). A construct for the β-galactosidase reporter (100 ng) was also transfected for normalization of transfection efficiency. The cells were lysed 36 h after transfection and the signals were assayed as described previously[9]. The Wnt activity was measured based on the ratio of TOP/FOP luciferase activity. The results represent triplicate determination of a single experiment that is representative of a total of five similar experiments.

Co-immunoprecipitation assays. Expression plasmids (total 4 μg) were transfected into HEK293T cells seeded on 60-mm dishes with FuGENE 6 (Roche Applied Science) at 60% confluency. Twenty-four hours after the transfection, the cells were collected and homogenized in lysis buffer (20 mM Tris-HCl, pH 7.5, 137 mM NaCl, 10% Glycerol, 2 mM EDTA, 0.5% Triton X-100, and Complete Mini Protease Inhibitor Cocktail). Total cell lysates were collected by centrifugation at 16,000 *g* for 15 min at 4 °C. The samples were incubated with either mouse monoclonal anti-Flag M2 agarose gel (Sigma) or mouse monoclonal anti-HA agarose gel (Sigma) for 3 h at 4 °C. The agarose beads were washed with lysis buffer five times. The precipitated proteins were eluted with NuPAGE lithium dodecyl sulphate (LDS) sample buffer containing Sample Reducing Agent (Invitrogen), incubated at 75 °C for 10 min, and separated on 10% NuPAGE gels (Invitrogen). Western blots were performed using anti-HA (Abcam) and anti-Flag M2 antibodies (Sigma).

GST pulldown assays. To express the GST-fusion APCDD1 protein in bacteria, the extracellular domain of hAPCDD1 (residues 28–486) was PCR-amplified (Supplementary Table 2), and subcloned in-frame into the EcoRI and XhoI sites of pGEX-4T-3 vector (GE Healthcare Life Sciences). Expression of GST-fusion proteins was induced in DH5α (Invitrogen) by the addition of 0.1 mM isopropyl-β-D-thiogalactopyranoside at 37 °C for 3 h, and the fusion proteins were isolated from bacterial lysates by affinity chromatography with Glutathione Sepharose beads (GE Healthcare Life Sciences). LRP5-EC–Flag, WNT3A–HA or CD40-EC–HA were overexpressed in HEK293T cells. GST pulldown assays were performed as described previously[37]. The antibodies used were rabbit polyclonal anti-GST (1:3,000; Santa Cruz Biotechnology), anti-HA (Abcam) and anti-Flag M2 (Sigma).

***In situ* hybridization.** A part of the human *APCDD1* cDNA (GenBank Accession number, NM_153000: nucleotides 338–1899) was cloned into pCRII-TOPO vector (Invitrogen). The antisense and sense digoxigenin (DIG)-labelled complementary RNA probes were synthesized from the linearized vectors with T7 and SP6 RNA polymerases (Roche Applied Science), respectively. *In situ* hybridization on dissected human hair follicles was performed following the methods described previously with minor modifications[38]. *In situ* hybridizations on chick spinal cord sections were performed as described[39]. The antisense mouse *Apcdd1* mRNA was generated using the *in vitro* transcription kit (Roche) with T7 RNA polymerase. The antisense chick *SIM1* mRNA was generated using the T3 RNA polymerase.

Indirect immunofluorescence. Indirect immunofluorescence on cultured cells and fresh frozen sections of individually dissected hair follicles was performed as described previously[36]. Indirect immunofluorescence on HEK293T and Bend3.0 cells was performed 48 h after the APCDD1 expression constructs were transfected. For some stainings, the cell membrane was labelled with rhodamine–phalloidin (Invitrogen). The primary antibodies used were mouse polyclonal anti-APCDD1 (diluted 1:1,000; Abnova), rabbit polyclonal anti-APCDD1 (1:4,000), rabbit polyclonal anti-pan-cadherin (1:200; Invitrogen), and goat polyclonal anti-calnexin (1:200; Santa Cruz Biotechnology). Immunofluorescence on chick spinal cord sections was performed as described[40]. The monoclonal antibodies against NKX2.2, PAX6, PAX7, EN1 and EVX1 were purchased from DSHB; rabbit anti-OLIG2 (Chemicon), rabbit anti-SOX3 (provided by S. Wilson), rabbit anti-CHX10, guinea pig anti-ISL1/2, sheep anti-GFP (Biogenesis) and mouse anti-β3-tubulin (TUJ1; Covance) were used as described[40].

Quantification of subcellular localization of APCDD1 protein. On the basis of the results of immunofluorescence with a rabbit polyclonal anti-APCDD1 antibody in HEK293T cells transfected with APCDD1-expression constructs, we measured the subcellular localization of APCDD1 proteins. The cell outline was visualized using rhodamine–phalloidin (Invitrogen). Images were processed in Image J (http://rsbweb.nih.gov/ij/), splitting the channels. First, the outline of the cell was used to measure the signal within the whole cell. Second, scaling the cell frame down, the signal inside the cell was measured. For each cell, the following values were recorded: (1) the adjusted total signal in the cell (the level of fluorescence, relative to the background); (2) the adjusted signal inside the cell; (3) the adjusted signal in the membrane; and (4) the ratio between adjusted signal in the membrane and inside the cell. The adjusted signal (S_{adj}) was calculated by subtracting the background signal and then normalizing to the background (B) signal levels in an empty area of equal size within the same image. $S_{adj} = (S - B)/B$. For example, a reported signal $S_{adj} = 5$ indicates five times stronger than the background[41–43]. Data are represented as average ± s.e.m. *P*-values are reported using heteroscedastic two-tailed *t*-tests, applying the Bonferroni correction to take into account the three-way comparisons (wild type versus Leu9Arg; wild type versus wild type plus Leu9Arg; Leu9Arg versus wild type plus Leu9Arg). All reported values are measured in 20 cells per condition.

***Xenopus* embryo manipulations.** *Xenopus laevis* embryos were obtained by *in vitro* fertilization, cultured in 0.1× MMR and staged as described previously[44]. *APCDD1* RNA was produced from the pBluescript-SK (−)-human APCDD1 constructs using the mMessage Machine *in vitro* T7 transcription kit (Ambion). For full length *Xapcdd1* RNA expression, the vector (pCMV-SPORT6) was restricted with XbaI and transcribed with the mMessage Machine *in vitro* SP6 transcription kit (Ambion). For *Xapcdd1-HA* expression, CS2+Xapcdd1–HA was restricted with NotI and transcribed with the same kit. RNA and reporter DNA injections were done at the four-cell stage. For the effect of APCDD1 on anteroposterior patterning, *APCDD1* RNA (1 ng) was injected in the marginal zone of both dorsal blastomeres at the four-cell stage. For the ventral effect of APCDD1, one ventral blastomere was injected in the marginal zone at the four-cell stage[45].

MO techniques. Translation-blocking MO (AS1 MO) was designed and synthesized by GeneTools, with the sequence: 5′-**T**GGTAGTTCAGCTCCAGAA TGTCCT-3′, where the nucleotide in bold is the first one in the open reading frame. The efficiency and specificity of the MO was tested on the full-length mRNA (wild-type *Xapcdd1* in Supplementary Fig. 13) and the *Xapcdd1-HA* mRNA lacking the 5′ untranslated region to which AS1 MO binds (5′ mutant *Xapcdd1* in Supplementary Fig. 13). RNA preincubation with MO and *in vitro* translation were performed as described previously[46], using the Promega Reticulocyte Lysate System for translation in the presence of [S35]-Met. MO was injected at the four-cell stage in both dorsal blastomeres (30 ng), alone or together with *Xapcdd1* RNA (300 pg) or dominant-negative *wnt8* RNA (300 pg). Embryos were scored for the dorsoanterior index at stage 41.

Transcription assays. Injected embryos were collected at stage nine and processed for luciferase assays (Promega) as described[45]. The *sia* reporter gene[21] was injected at 100 pg DNA. All assays were in triplicate, and each experiment was repeated three times.

RT–PCR in *Xenopus* embryos. Radioactive RT–PCR was performed as described previously[47]. mRNA was purified from whole embryos, or from fragments cut with a hair knife, at the indicated stages with RNA-Bee (Tel-Test), before reverse transcription with SuperScript III (Invitrogen), using poly-dT as priming oligonucleotide. The primers used for PCR were ODC (ornithine decarbocylase): sense, 5′-CGAAGGCTAAAGTTGCAG-3′, antisense, 5′-AATG GATTTCAGAGACCA-3′; *goosecoid*: sense, 5′-TCTTATTCCAGAGGAACC-3′, antisense, 5′-ACA ACTGGAAGCACTGGA-3′; *Xapcdd1*: sense, 5′-CTGGAG CTGAACTACCATGG-3′, antisense, 5′-TGACCCTCGATGTTTGGAGGC-3′.

Western blot in *Xenopus* embryo. *Xenopus* embryos were injected at the four-cell stage with 1 ng RNA of wild-type human APCDD1 alone or together with 1 ng Leu9Arg mutant RNA. Injections also contained 1 ng *LacZ* RNA as loading control. Embryos were retrieved at stage ten, homogenized in NP 40 extract buffer, mixed with LDS sample buffer and run on NuPage 4–12% gels (Invitrogen). After transfer to PVDF membrane, blots were incubated with rabbit polyclonal anti-APCDD1 (1:10,000) or anti-β-galactosidase (1:1,000; ProSci) antibodies, and stained with ECL Western Blotting Reagent (GE Healthcare).

31. Pasternack, S. M. *et al.* G protein-coupled receptor P2Y5 and its ligand LPA are involved in maintenance of human hair growth. *Nature Genet.* **40,** 329–334 (2008).
32. Königshoff, M. *et al.* Functional Wnt signaling is increased in idiopathic pulmonary fibrosis. *PLoS One* **3,** e2142 (2008).
33. Noguchi, K., Ishii, S. & Shimizu, T. Identification of p2y9/GPR23 as a novel G protein-coupled receptor for lysophosphatidic acid, structurally distant from the Edg family. *J. Biol. Chem.* **278,** 25600–25606 (2003).
34. Niwa, H., Yamamura, K. & Miyazaki, J. Efficient selection for high-expression transfectants with a novel eukaryotic vector. *Gene* **108,** 193–199 (1991).
35. Briscoe, J., Pierani, A., Jessell, T. M. & Ericson, J. A homeodomain protein code specifies progenitor cell identity and neuronal fate in the ventral neural tube. *Cell* **101,** 435–445 (2000).
36. Bazzi, H. *et al.* Desmoglein 4 is expressed in highly differentiated keratinocytes and trichocytes in human epidermis and hair follicle. *Differentiation* **74,** 129–140 (2006).
37. Shimomura, Y., Aoki, N., Ito, K. & Ito, M. Gene expression of Sh3d19, a novel adaptor protein with five Src homology 3 domains, in anagen mouse hair follicles. *J. Dermatol. Sci.* **31,** 43–51 (2003).
38. Aoki, N. *et al.* A novel type II cytokeratin, mK6irs, is expressed in the Huxley and Henle layers of the mouse inner root sheath. *J. Invest. Dermatol.* **116,** 359–365 (2001).
39. Schaeren-Wiemers, N. & Gerfin-Moser, A. A single protocol to detect transcripts of various types and expression levels in neural tissue and cultured cells: *in situ*

hybridization using digoxigenin-labelled cRNA probes. *Histochemistry* **100,** 431–440 (1993).
40. Agalliu, D. & Schieren, I. Heterogeneity in the developmental potential of motor neuron progenitors revealed by clonal analysis of single cells in vitro. *Neural Dev.* **4,** 2 (2009).
41. Hanson, M. G. & Landmesser, L. T. Normal patterns of spontaneous activity are required for correct motor axon guidance and the expression of specific guidance molecules. *Neuron* **43,** 687–701 (2004).
42. Luria, V., Krawchuk, D., Jessell, T. M., Laufer, E. & Kania, A. Specification of motor axon trajectory by ephrin-B:EphB signaling: symmetrical control of axonal patterning in the developing limb. *Neuron* **60,** 1039–1053 (2008).
43. Luria, V. & Laufer, E. Lateral motor column axons execute a ternary trajectory choice between limb and body tissues. *Neural Dev.* **2,** 13 (2007).
44. Nieuwkoop, P. D. & Faber, J. *Normal Table of* Xenopus laevis (North Holland Publishing, 1967).
45. Vonica, A. & Gumbiner, B. M. Zygotic Wnt activity is required for *Brachyury* expression in the early *Xenopus laevis* embryo. *Dev. Biol.* **250,** 112–127 (2002).
46. Taylor, M. F., Paulauskis, J. D., Weller, D. D. & Kobzik, L. *In vitro* efficacy of morpholino-modified antisense oligomers directed against tumor necrosis factor-α mRNA. *J. Biol. Chem.* **271,** 17445–17452 (1996).
47. Wilson, P. A. & Melton, D. A. Mesodermal patterning by an inducer gradient depends on secondary cell–cell communication. *Curr. Biol.* **4,** 676–686 (1994).

Vol 464|15 April 2010|doi:10.1038/nature08895

LETTERS

Functional genomic screen for modulators of ciliogenesis and cilium length

Joon Kim[1], Ji Eun Lee[1], Susanne Heynen-Genel[2], Eigo Suyama[2], Keiichiro Ono[3], KiYoung Lee[3,4], Trey Ideker[3], Pedro Aza-Blanc[2] & Joseph G. Gleeson[1]

Primary cilia are evolutionarily conserved cellular organelles that organize diverse signalling pathways[1,2]. Defects in the formation or function of primary cilia are associated with a spectrum of human diseases and developmental abnormalities[3]. Genetic screens in model organisms have discovered core machineries of cilium assembly and maintenance[4]. However, regulatory molecules that coordinate the biogenesis of primary cilia with other cellular processes, including cytoskeletal organization, vesicle trafficking and cell–cell adhesion, remain to be identified. Here we report the results of a functional genomic screen using RNA interference (RNAi) to identify human genes involved in ciliogenesis control. The screen identified 36 positive and 13 negative ciliogenesis modulators, which include molecules involved in actin dynamics and vesicle trafficking. Further investigation demonstrated that blocking actin assembly facilitates ciliogenesis by stabilizing the pericentrosomal preciliary compartment (PPC), a previously uncharacterized compact vesiculotubular structure storing transmembrane proteins destined for cilia during the early phase of ciliogenesis. The PPC was labelled by recycling endosome markers. Moreover, knockdown of modulators that are involved in the endocytic recycling pathway affected the formation of the PPC as well as ciliogenesis. Our results uncover a critical regulatory step that couples actin dynamics and endocytic recycling with ciliogenesis, and also provides potential target molecules for future study.

Cilium assembly and disassembly are interconnected with several complex cellular processes such as cell cycle, cell polarization and cell migration, suggesting that there may be large numbers of ciliogenesis modulators[1,5]. In accordance with this, recent proteomic analyses together with comparative genomics and bioinformatics studies have identified over a thousand cilia- or basal body-associated proteins, referred to as the ''ciliome''[6,7]. Although these approaches can provide a comprehensive list of candidates, the discovery of key regulators of ciliogenesis, which could reveal potential therapeutic targets, requires functional analysis. Thus we developed a high-throughput assay using small interfering RNA (siRNA) to evaluate the functional impact of 7,784 therapeutically relevant genes across the human genome (Supplementary Table 1). The screen was based on an *in vitro* ciliogenesis model: serum starvation-induced ciliogenesis in telomerase-immortalized human retinal pigmented epithelial (htRPE) cells. Enhanced green fluorescent protein (EGFP)-tagged Smoothed (Smo), a transmembrane protein that accumulates in primary cilia[8], was used as a cilium marker for automated quantification of ciliated cells (Supplementary Fig. 1 a–c). Sensitivity of the screen strategy was assessed by siRNAs targeting KIF3A, a critical protein for cilium assembly (Supplementary Fig. 1d). We selected a screen condition suitable for identifying both positive and negative modulators: siRNA transfection was performed at a reduced (suboptimal) cell density to detect these dynamic ranges of ciliogenesis activity, and ciliation was assessed after 48 h of serum starvation (Supplementary Fig. 1e, f).

The primary screen identified 153 positive modulator hits and 79 negative modulator hits (Supplementary Table 1 and Supplementary Fig. 2a). We next performed a confirmation screen with the following modifications: (1) optimal cell density for ciliogenesis (confluent at the time of serum starvation) was used to minimize the selection of siRNAs that influence ciliogenesis indirectly through an effect on cell density, (2) cilium length was measured for validating negative modulators because length increase was a highly specific indicator for enhanced ciliogenesis, where optimal ciliogenesis condition was used (Supplementary Fig. 2b). The confirmation screen identified 40 positive and 13 negative modulators, which are associated with various molecular processes (Supplementary Table 2 and Supplementary Fig. 3). Notably, the screen hits include *INPP5E*, a gene recently identified as mutated in a human ciliopathy, Joubert syndrome[9]. A positive modulator *Agtpbp1* (formerly *Nna1*) is mutated in *Purkinje cell degeneration* (*pcd*) mice, which exhibit ciliopathy phenotypes: retinal degeneration and defective spermatogenesis[10]. Although the library was selected for therapeutically relevant genes and thus not highly representative of ciliome genes (tending to be structural), we did confirm 12 genes encoding ciliome proteins (Supplementary Table 3 and Supplementary Fig. 3).

We rescreened the confirmed positive modulators using anti-acetylated tubulin immunofluorescence as a cilium marker, and found four genes that did not affect cilium assembly (Supplementary Table 3 and Supplementary Fig. 3). The confirmed negative modulators were further classified according to silencing phenotypes observed in the absence of serum starvation. Silencing of five genes facilitated ciliogenesis even without serum starvation (Supplementary Table 3 and Supplementary Fig. 3).

Among the ciliogenesis modulators with high confirmation screen scores (Supplementary Table 2) are two gelsolin (GSN) family proteins GSN and AVIL, which regulate cytoskeletal actin organization by severing actin filaments[11]. Depletion of GSN proteins by two independent siRNAs significantly reduced ciliated cell numbers, indicating that actin filament severing is involved in ciliogenesis (Fig. 1a–c). In contrast, silencing of actin-related protein ACTR3 (also called ARP3), which is a major constituent of the ARP2/3 complex that is necessary for nucleating actin polymerization at filament branches[12], caused a significant increase in cilium length (Fig. 1a, d, e) and also facilitated ciliogenesis independently of serum starvation (Fig. 1f). These observations indicate an inhibitory role of branched actin network formation in ciliogenesis.

[1]Departments of Neurosciences and Pediatrics, Institute for Genomic Medicine, Howard Hughes Medical Institute, University of California San Diego, La Jolla, California 92093, USA. [2]High Content Screening and Functional Genomics Core, Sanford-Burnham Medical Research Institute, La Jolla, California 92037, USA. [3]Departments of Medicine and Bioengineering, University of California San Diego, La Jolla, California 92093, USA. [4]Department of Biomedical Informatics, Ajou University School of Medicine, Suwon 443-749, Korea.

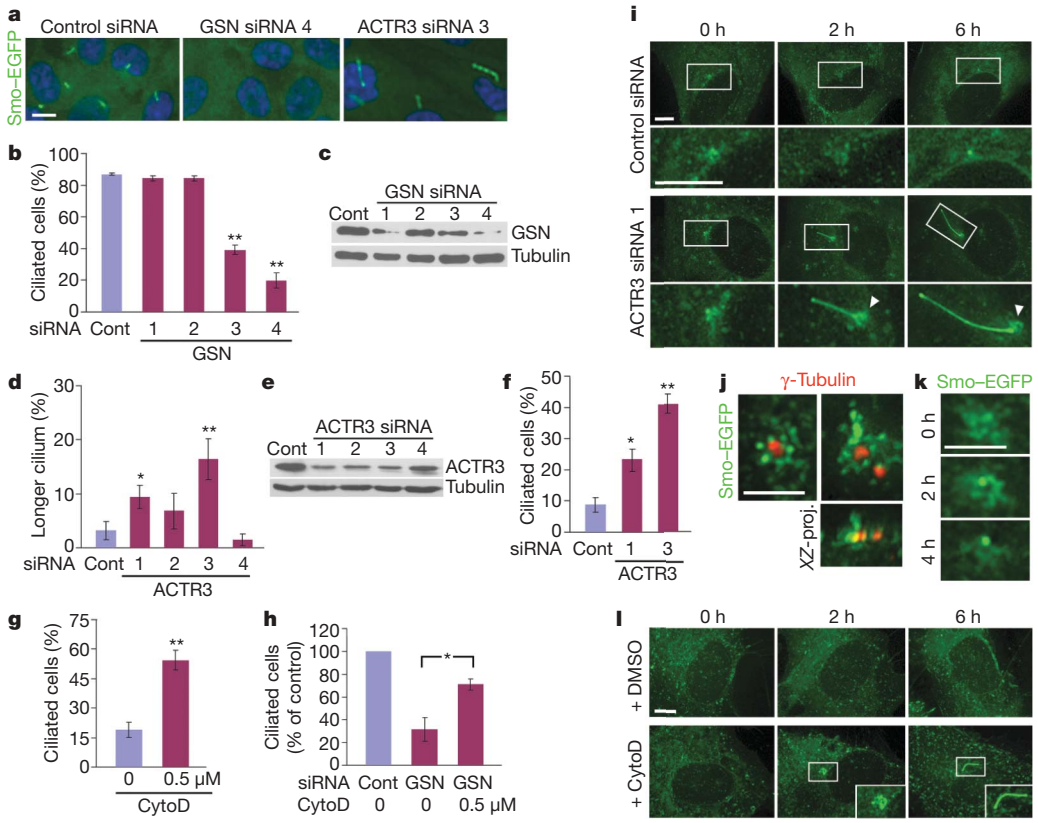

Figure 1 | Regulators of actin dynamics modulate cilium assembly. **a**, **b**, GSN knockdown reduced ciliated cell numbers. **a**, **d**, ACTR3 knockdown increased the number of cells with longer cilium (>6 μm). **c**, **e**, Western blots showing protein levels (note that GSN siRNA 1 (**c**) was cytotoxic). **f**, ACTR3 knockdown induced ciliogenesis without serum starvation. **g**, Cytochalasin D treatment for 8 h increased ciliated cell numbers without serum starvation. **h**, Ciliogenesis defect by GSN knockdown was rescued by 8 h cytochalasin D treatment. **i**, Live imaging of htRPE–Smo–EGFP cells after 60 h siRNA transfection. Arrowheads, the pericentrosomal preciliary compartment (PPC) at the ciliary base. **j**, Morphology of PPC. Gamma-tubulin labels the centrosome. **k**, Live imaging of a PPC-positive cell in serum-free medium. **l**, Live cell imaging in serum-free medium containing dimethylsulphoxide (DMSO) or cytochalasin D. Values, mean ± s.d. ($n = 4$ (**b**, **d**), 2 (**f**) and 3 (**g**, **h**)). Cont, control; CytoD, cytochalasin D. Student's *t*-test: *, $P < 0.05$; **, $P < 0.01$. Scale bars, 10 μm (**a**); 5 μm (**i**, **l**); 2.5 μm (**j**, **k**).

To examine the link between actin dynamics and ciliogenesis, we treated htRPE cells with actin polymerization inhibitor cytochalasin D, which facilitated ciliogenesis independently of serum starvation and promoted cilium elongation (Fig. 1g and Supplementary Fig. 4). The ciliogenic effect of cytochalasin D was also observed in HEK293T cells (Supplementary Fig. 5a, b). Moreover, cytochalasin D treatment significantly rescued the ciliogenesis defect caused by GSN knockdown (Fig. 1h). Cytochalasin D facilitated ciliogenesis at doses below that which affects stress fibre formation, excluding the possibility of global actin cytoskeleton rearrangement in ciliogenesis control (Supplementary Fig. 5c). Involvement of actin dynamics in ciliogenesis is further supported by the finding that α-PARVIN (PARVA), a component of the focal adhesion complex regulating actin cytoskeletal dynamics and cell signalling[13], exhibits knockdown phenotypes similar to that of ACTR3 (Supplementary Fig. 6).

To identify the mechanism of altered ciliogenesis, we performed time-course live imaging. Notably, a number of non-ciliated htRPE cells transfected with ACTR3 siRNAs (14/30 cells) developed pronounced primary cilia (2.9 ± 0.9 μm in length) within 2 h of serum starvation, whereas none of the control cells (0/30 cells) displayed cilia longer than 1.5 μm (Fig. 1i and Supplementary Fig. 7a). Furthermore, faster cilium elongation after the initiation of ciliogenesis was observed in ACTR3-depleted cells (mean cilium extension rate for the first 6 h after serum starvation: ACTR3 depleted cells, $0.75 \pm 0.27\ \mu m\ h^{-1}$ ($n = 17$); control cells, $0.11 \pm 0.06\ \mu m\ h^{-1}$ ($n = 6$)). These observations indicate that slow progression of ciliogenesis in htRPE cells is not the result of slow transduction of serum starvation-mediated ciliogenic signal or unavailability of core cilium assembly machineries, but is ascribed to the presence of an inhibitory regulation involving ACTR3.

Earlier electron microscopic studies found small vesicles tightly associated with the centriole initiating cilium assembly in fibroblasts and smooth muscle cells[14,15]. This indicates that ciliogenesis in non-polarized cells could be initiated by vesicle docking to the basal body, whereas basal body docking to the apical plasma membrane initiates ciliogenesis in polarized epithelial cells. More recent studies have also reported that the biogenesis of ciliary membrane that is coordinated with axoneme assembly may involve fusion of transport vesicles at the base of cilia[16,17]. Smo–EGFP allowed us to visualize transport vesicles targeted to the ciliary base. Interestingly, a subset of htRPE–Smo–EGFP cells (~10%: 42/434 interphase cells) cultured in the presence of serum exhibited compact Smo–EGFP-positive vesiculotubular structures (termed here PPCs) tightly associated with the centrosome (Fig. 1j). In these cells, ciliogenesis occurred at the PPC during 4 h live imaging (Fig. 1k). Notably, an attenuation of Smo–EGFP-positive PPC was observed after the initiation of ciliogenesis (Fig. 2k and Supplementary Fig. 7b, control cells). After 4 h of serum starvation (when cilia are detected in ~20% of cells), 3.4% of total cilia (17/500 cilia) were accompanied by PPCs, indicating that the transition of the PPC to cilia occurs over the course of hours. PPC-positive cilia were rarely observed after 24 h serum starvation (2/500 cilia), confirming that the PPC is a transient structure (Supplementary Fig. 8a). Smo–EGFP showed similar transient structures in mouse inner medullary collecting duct (IMCD) cells (Supplementary Fig. 8b).

Notably, the majority of newly formed cilia (13/17 cilia) displaying mature lengths (4.5 ± 1.9 μm) in ACTR3-depleted live cells maintained pronounced PPC at the ciliary base (Fig. 1i and Supplementary Fig. 7b), although the PPC eventually disappeared after 24 h serum starvation as in the control (Supplementary Fig. 8a). Moreover, facilitated ciliogenesis

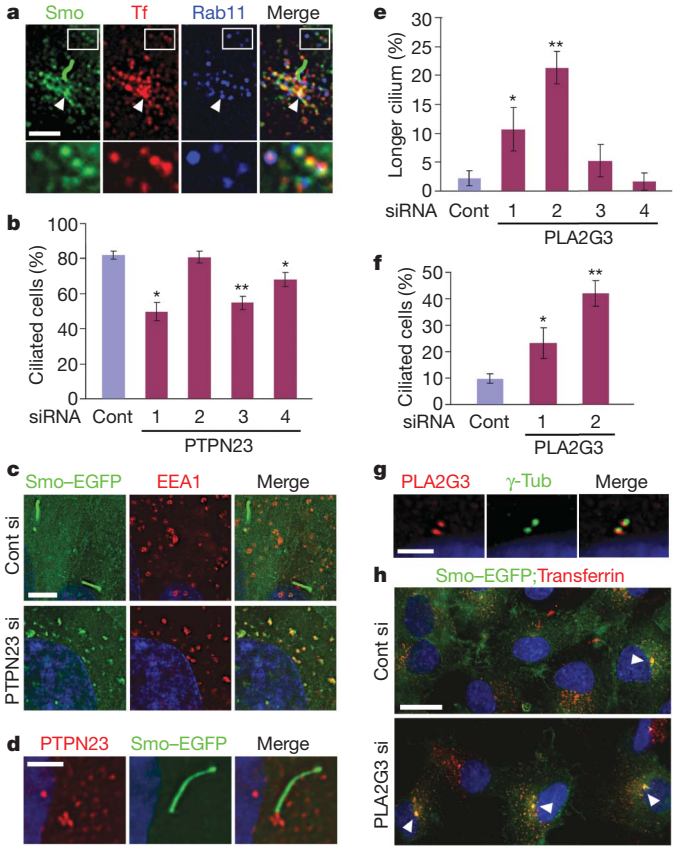

Figure 2 | Endocytic recycling pathway is linked to ciliogenesis. **a**, PPC overlapping with endocytosed transferrin–alexa 594 and Rab11 (arrowhead). **b**, PTPN23 knockdown decreased the number of ciliated cells. **c**, PTPN23 knockdown caused an accumulation of Smo–EGFP on EEA1-positive early endosomes. **d**, PTPN23 immunofluorescence was detected at the ciliary base. **e**, PLA2G3 knockdown increased the number of cells with longer cilia (>6 μm). **f**, PLA2G3 knockdown induced ciliogenesis without serum starvation. **g**, Pericentriolar localization of PLA2G3. **h**, PLA2G3 knockdown increased the number of cells exhibiting recycling endosomes concentrated at high levels around the centrosome (arrowheads). γ-Tub, γ-tubulin. Values, mean ± s.d. ($n = 4$ (**b**, **e**) and 3 (**f**)). Student's *t*-test: *, $P < 0.05$, **, $P < 0.01$. Scale bars, 2.5 μm (**a**, **d**, **g**); 5 μm (**c**); 20 μm (**h**).

in cytochalasin D-treated cells was preceded by a promotion of PPC formation (16 PPC positive cells/30 live-imaged cells treated with cytochalasin D for 2 h versus 5 PPC-positive cells/30 control cells; Fig. 1l). Short-term live imaging showed that cytochalasin D also affects the stability of the pre-existing PPC (Supplementary Fig. 9). These observations indicate that actin network formation may negatively modulate ciliogenesis by destabilizing the PPC, a potential temporary reservoir of lipid and membrane proteins for efficient ciliogenesis.

Recycling endosomes are a dynamic vesiculotubular compartment, exporting endocytosed membrane proteins and lipids to the cell surface via vesicular intermediates[18]. We found that the PPC extensively overlaps with a subset of recycling endosomes concentrated around the centrosome: the PPC was labelled by endocytosed transferrin and recycling endosome marker Rab11 (Fig. 2a and Supplementary Fig. 10). PTPN23, a non-transmembrane tyrosine phosphatase, has been implicated in cargo sorting at early endocytic compartments[19], and is one of the high-scored hits. Silencing of PTPN23 significantly reduced the number of ciliated cells (Fig. 2b and Supplementary Fig. 11). In addition, PTPN23 knockdown caused an accumulation of Smo–EGFP on the early endosomes marked by EEA1 (Fig. 2c). The PPC was not observed in the cells exhibiting early endosomal Smo–EGFP accumulation (0/80 cells; Supplementary Fig. 12). Supporting the link between recycling endosomes and ciliogenesis, knockdown of ASAP1 (not included in the initial screen library), a gene required for pericentrosomal enrichment of recycling endosomes[20], caused a decrease in the number of ciliated cells (Supplementary Fig. 13a, b, c). These observations indicate that a trafficking pathway connecting endocytic compartments to the PPC is involved in cilium assembly. Pharmacological blocking of endocytic degradation pathway to lysosomes using concanamycin A did not block PPC formation or ciliogenesis, indicating that the endocytic recycling pathway is specifically involved in ciliogenesis (Supplementary Fig. 13d). Detection of PTPN23 immunoreactivity at the basal bodies further supported a direct role for PTPN23 in ciliary vesicle targeting (Fig. 2d).

Among the unexpected screen hits was PLA2G3, a secreted phospholipase[21]. Involvement of cytoplasmic phospholipase A2 enzymes in intracellular vesicle trafficking has been suggested on the basis of their potential for introducing membrane curvature[22]. Depletion of PLA2G3 facilitated cilium extension and induced ciliogenesis independently of serum starvation, indicating that PLA2G3 is a negative ciliogenesis regulator (Fig. 2e, f and Supplementary Fig. 14). Confirming this result, application of oleyloxyethyl phosphorylcholine (OPC), an inhibitor for secreted phospholipase[23], increased the number of ciliated cells (Supplementary Fig. 15a). Notably, PLA2G3 immunofluorescence was detected at the centriole pair (Fig. 2g). In accord with its localization, knockdown of PLA2G3 significantly increased the number of cells displaying recycling endosomes concentrated at high levels around the centrosome (17.4 ± 1.4% in control cells and 48.2 ± 2.7% in PLA2G3-depleted cells examined after 56 h transfection without serum starvation; Student's *t*-test, $P = 0.006$; Fig. 2h). The majority of pericentrosomal recycling endosomes in PLA2G3-depleted cells (122/153) were associated with the PPC or cilia. Overexpressed PLA2G3 exhibited an extensive co-localization with endocytosed transferrin and inhibited ciliogenesis (Supplementary Fig. 14d–f). These results further demonstrate the link between endocytic recycling pathway and ciliogenesis. Moreover, higher intensities of Smo–EGFP fluorescence was observed in cilia from cells depleted of PLA2G3, demonstrating an inhibitory role for PLA2G3 in ciliary membrane protein targeting (Supplementary Fig. 15b, c).

The fact that both axoneme assembly and ciliary membrane biogenesis were facilitated by inhibition of actin polymerization

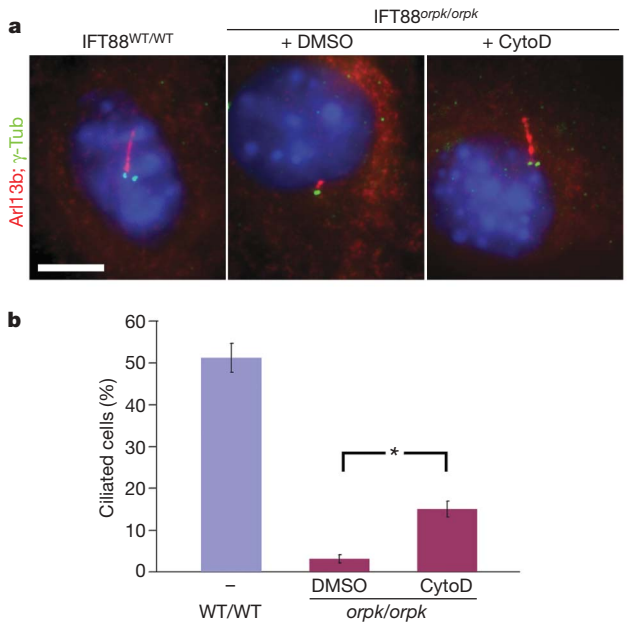

Figure 3 | Pharmacological rescue of ciliary defect on IFT88 mutant cells. **a**, Cytochalasin D treatment for 16 h partially rescued cilium elongation defect caused by hypomorphic IFT88 mutation. **b**, Percentage of cells with the primary cilium longer than 1.5 μm. WT, wild type. Values, mean ± s.d. ($n = 3$). Student's *t*-test: *, $P < 0.05$. Scale bar, 5 μm.

(Supplementary Fig. 16) prompted us to test if cytochalasin D treatment could rescue ciliogenesis defect caused by loss-of-function mutation in core ciliogenesis machinery. IFT88 transports molecules required for cilium assembly[4], and cells carrying homozygous *IFT88* hypomorphic mutation (*orpk/orpk*) fail to grow cilia with normal length[24]. Notably, 16 h cytochalasin D treatment partially, but significantly, rescued ciliogenesis defect of *IFT88* mutant cells (Fig. 3). A recent study showed that IFT particles are associated with recycling endosomes and are implicated in the recycling of T-cell receptors in lymphocytes[25]. Thus it is likely that cytochalasin D facilitates ciliary recruitment of IFT particles through the endocytic recycling pathway. Cytochalasin D can interfere with many cellular processes involving actin polymerization, and thus is unlikely to be useful for ciliopathy treatment. However, small molecules specifically targeting actin modulators implicated in ciliogenesis might be good candidates for ciliopathy treatment.

In summary, our high-throughput functional screen identified modulators of ciliogenesis with diverse molecular functions, connecting ciliogenesis with other basic cellular processes. Furthermore, we discovered several proteins involved in the control of cilium length, a key determinant of normal cilium function. We anticipate that the development of small molecules that target these proteins will provide novel strategies for the treatment of the ciliopathies.

METHODS SUMMARY

Cell culture. htRPE cells were maintained in DMEM:F12 (Dulbecco's modified Eagle medium) supplemented with 10% fetal bovine serum. Plasmid DNA harbouring mouse Smo–EGFP fusion gene was transfected to htRPE cells and a stable cell line (htRPE–Smo–EGFP) was established by G418 selection. For ciliogenesis induction, culture medium was replaced with DMEM (without supplement) when cells are ~90% confluent, and cultured for 48 h before fixation. Overexpressed Smo–EGFP was targeted to ciliary membrane independent of Sonic hedgehog.

siRNA library screen. An arrayed library containing 31,111 unique siRNAs targeting 7,784 human genes (Ambion; human druggable genome siRNA library V3.1; including siRNAs targeting 665 kinases, 101 kinase modulators, 231 phosphatases, 307 ligases, 57 lipases, 444 signalling molecules and 426 cytoskeleton-interacting proteins) was screened in duplicates. High-throughput imaging was done using an IC100 automated microscope system (Beckman Coulter), and the images were analysed by CytoShop software. For a confirmation screen, re-arrayed 913 siRNAs targeting 232 primary screen hits were tested in quadruplicates.

Full Methods and any associated references are available in the online version of the paper at www.nature.com/nature.

Received 10 November 2009; accepted 4 February 2010.

1. Gerdes, J. M., Davis, E. E. & Katsanis, N. The vertebrate primary cilium in development, homeostasis, and disease. *Cell* **137,** 32–45 (2009).
2. Eggenschwiler, J. T. & Anderson, K. V. Cilia and developmental signaling. *Annu. Rev. Cell Dev. Biol.* **23,** 345–373 (2007).
3. Fliegauf, M., Benzing, T. & Omran, H. When cilia go bad: cilia defects and ciliopathies. *Nature Rev. Mol. Cell Biol.* **8,** 880–893 (2007).
4. Rosenbaum, J. L. & Witman, G. B. Intraflagellar transport. *Nature Rev. Mol. Cell Biol.* **3,** 813–825 (2002).
5. Christensen, S. T. *et al.* The primary cilium coordinates signaling pathways in cell cycle control and migration during development and tissue repair. *Curr. Top. Dev. Biol.* **85,** 261–301 (2008).
6. Inglis, P. N., Boroevich, K. A. & Leroux, M. R. Piecing together a ciliome. *Trends Genet.* **22,** 491–500 (2006).
7. Gherman, A., Davis, E. E. & Katsanis, N. The ciliary proteome database: an integrated community resource for the genetic and functional dissection of cilia. *Nature Genet.* **38,** 961–962 (2006).
8. Corbit, K. C. *et al.* Vertebrate Smoothened functions at the primary cilium. *Nature* **437,** 1018–1021 (2005).
9. Bielas, S. L. *et al.* Mutations in *INPP5E*, encoding inositol polyphosphate-5-phosphatase E, link phosphatidyl inositol signaling to the ciliopathies. *Nature Genet.* **41,** 1032–1036 (2009).
10. Fernandez-Gonzalez, A. *et al. Purkinje cell degeneration* (*pcd*) phenotypes caused by mutations in the axotomy-induced gene, *Nna1*. *Science* **295,** 1904–1906 (2002).
11. Silacci, P. *et al.* Gelsolin superfamily proteins: key regulators of cellular functions. *Cell. Mol. Life Sci.* **61,** 2614–2623 (2004).
12. Cooper, J. A. & Schafer, D. A. Control of actin assembly and disassembly at filament ends. *Curr. Opin. Cell Biol.* **12,** 97–103 (2000).
13. Sepulveda, J. L. & Wu, C. The parvins. *Cell. Mol. Life Sci.* **63,** 25–35 (2006).
14. Sorokin, S. Centrioles and the formation of rudimentary cilia by fibroblasts and smooth muscle cells. *J. Cell Biol.* **15,** 363–377 (1962).
15. Archer, F. L. & Wheatley, D. N. Cilia in cell-cultured fibroblasts. II. Incidence in mitotic and post-mitotic BHK 21-C13 fibroblasts. *J. Anat.* **109,** 277–292 (1971).
16. Nachury, M. V. *et al.* A core complex of BBS proteins cooperates with the GTPase Rab8 to promote ciliary membrane biogenesis. *Cell* **129,** 1201–1213 (2007).
17. Yoshimura, S. *et al.* Functional dissection of Rab GTPases involved in primary cilium formation. *J. Cell Biol.* **178,** 363–369 (2007).
18. Maxfield, F. R. & McGraw, T. E. Endocytic recycling. *Nature Rev. Mol. Cell Biol.* **5,** 121–132 (2004).
19. Doyotte, A., Mironov, A., McKenzie, E. & Woodman, P. The Bro1-related protein HD-PTP/PTPN23 is required for endosomal cargo sorting and multivesicular body morphogenesis. *Proc. Natl Acad. Sci. USA* **105,** 6308–6313 (2008).
20. Inoue, H., Ha, V. L., Prekeris, R. & Randazzo, P. A. Arf GTPase-activating protein ASAP1 interacts with Rab11 effector FIP3 and regulates pericentrosomal localization of transferrin receptor-positive recycling endosome. *Mol. Biol. Cell* **19,** 4224–4237 (2008).
21. Valentin, E. *et al.* Novel human secreted phospholipase A(2) with homology to the group III bee venom enzyme. *J. Biol. Chem.* **275,** 7492–7496 (2000).
22. Brown, W. J., Chambers, K. & Doody, A. Phospholipase A2 (PLA2) enzymes in membrane trafficking: mediators of membrane shape and function. *Traffic* **4,** 214–221 (2003).
23. Hope, W. C., Chen, T. & Morgan, D. W. Secretory phospholipase A2 inhibitors and calmodulin antagonists as inhibitors of cytosolic phospholipase A2. *Agents Actions* **39** (Spec No), C39–C42 (1993).
24. Yoder, B. K. *et al.* Polaris, a protein disrupted in *orpk* mutant mice, is required for assembly of renal cilium. *Am. J. Physiol. Renal Physiol.* **282,** F541–F552 (2002).
25. Finetti, F. *et al.* Intraflagellar transport is required for polarized recycling of the TCR/CD3 complex to the immune synapse. *Nature Cell Biol.* **11,** 1332–1339 (2009).

Supplementary Information is linked to the online version of the paper at www.nature.com/nature.

Acknowledgements The screen was performed at the Functional Genomics Core (LJINCC grant P30 NS057096 to S. Lipton) with technical assistance from A. Cortez and E. Sisman and with imaging support from the UCSD Microscopy Core (P30 NS047101 and P30 CA23100). We thank P. A. Beachy for the Smo–EGFP plasmid and J. F. Reiter for IFT88$^{orpk/orpk}$ MEFs. We thank C. Kintner, V. M. Fowler, S. J. Field and S. Ferro-Novick for discussion. This work was supported by grants from NARSAD (Young Investigator Award to J.K.), NINDS (RO1 NS052455 to J.G.G.), the NIH (GM070743 to T.I. and K.L.), the Korea Food and Drug Administration (10182KFDA992 to K.L.) and the Brain Research Center of the 21st Century Frontier Research Program (M103KV010008-07K2201-00810 to K.L.). J.G.G. is an investigator of the Howard Hughes Medical Institute.

Author Contributions J.G.G. conceived and directed the project. J.K., S.H.-G. and P.A.-B. designed the screen and J.K., S.H.-G. and E.S. performed the screen. J.K., K.O., K.L. and T.I. analysed the screen data. J.K. designed the follow-up experiments and J.K. and J.E.L. performed the experiments. J.K. interpreted the results and J.K. and J.G.G. wrote the paper with contributions from S.H.-G. and P.A.-B.

Author Information Reprints and permissions information is available at www.nature.com/reprints. The authors declare competing financial interests: details accompany the full-text HTML version of the paper at www.nature.com/nature. Correspondence and requests for materials should be addressed to J.G.G. (jogleeson@ucsd.edu).

METHODS

Primary screen. Assay plates (384-well plate with optical bottom; Greiner) were spotted with 1 μl of 0.5 μM siRNA using the Velocity 11-Bravo Pipettor with a 384 ST head. To acquire high-quality primary screen data, four unique siRNAs were typically used to knockdown each gene and all siRNAs were tested individually in duplicate. KIF3A siRNAs were included in all the plates as a positive control. Reverse transfection was performed using Lipofectamine RNAiMAX: final siRNA concentration was 10 nM. htRPE–Smo–EGFP cells were suspended in DMEM:F12 supplemented with 10% FBS, and seeded onto assay plates using the Matrix-Well Mate (4,000 cells in 40 μl medium for each well). Culture medium was replaced with DMEM 24 h after transfection using the TiterTek-MAP-C, and cells were incubated for additional 48 h before fixation.

Imaging and image analysis. Image acquisition of the siRNA screen was performed on the IC100 imaging system (Beckman Coulter) equipped with an ORCA-ER scientific camera (Hamamatsu) and a multi-plate handling BRT system (Beckman Coulter). Images were acquired using a Nikon Plan Fluor ×20 0.5 NA objective. Six fields were acquired throughout each well at two wavelengths: nuclear DAPI and GFP. CytoShop HCS analysis software (Beckman Coulter) was used to perform image segmentation and cytometry. The nucleus of each cell was identified from the DAPI images using CytoShop's 'Nuclear Segmentation' algorithm that included an 'open' morphological operation to separate touching nuclei. Equidistance tessellation lines were drawn between the centroids of the identified nuclei, effectively breaking up the images into cellular regions. Cilia detection was performed on the GFP images using CytoShop's 'GPCR Segmentation' algorithm. An Object Extraction Correlation radius of 30 pixels was set, inside which pixels were assumed to belong to the cytoplasm of the cell. The object scale for the aggregate (cilia) detection was iteratively adjusted to 8 pixels (average object = cilia size) and the minimum intensity peak height was set to 15 (minimum difference in intensity between cilia object and neighbouring image intensities). The number of detected aggregates (cilia) was then reported for each cell object and used to determine the percentage of cells per well that were cilia positive. Plate-to-plate variability was normalized by a control-based method: Normalized percent inhibition (NPI) = (mean of negative control − *X*i)/(mean of negative control − mean of positive control) × 100, where *X*i is the means of ciliated cell count (%) for each siRNA, negative control is mock transfection and positive control is KIF3A siRNA ($n = 4$ per plate). Threshold for selecting active siRNAs was ± 1.5 s.d. from the overall mean. Genes were defined as primary screen hits if at least two independent siRNAs showed NPI values above the threshold. Data from toxic siRNAs that decreased cell count by 2 ≥ s.d. from overall mean were excluded, and additional invalid data ascribed to cell toxicity or out-of-focus images were excluded through manual inspection.

Confirmation screen. For a confirmation screen, htRPE–Smo–EGFP cells (6,500 cells per well) were transfected and serum-starved as in the primary screen. The confirmation screen was based on measurement of (1) the percentage of ciliated cells for positive modulators and (2) mean cilium size (pixel sum, arbitrary unit) for negative modulators. For plate normalization, quantification data was converted to *Z* scores using 48 unique non-targeting siRNAs included to each plate as references: *Z* score = (*X*i − median of 48 control siRNAs)/1.4826 × MAD of 48 control siRNAs, where *X*i is quantification data and MAD is median absolute deviation. Genes were defined as confirmation screen hits if at least two siRNAs showed *Z* scores ≤ −2 (for positive modulators) or ≥ 1.15 (for negative modulators). Target sequences for selected siRNAs used for the follow-up studies are given in Supplementary Table 4.

Hit classification. To identify genes required for Smo–EGFP targeting to cilia without affecting ciliogenesis, the confirmed positive modulators were rescreened: htRPE cells were transfected with siRNAs (two best-scored siRNAs for each gene), serum-starved as above and examined by anti-acetylated-tubulin immunofluorescence staining (Supplementary Table 3). To classify further the confirmed negative modulators, htRPE–Smo–EGFP cells were transfected with siRNAs (two best scored siRNAs for each gene) for 3 days without serum starvation (Supplementary Table 3).

Immunofluorescence and western blotting. For indirect immunofluorescence, cells were fixed in either methanol or 4% paraformaldehyde (PFA) depending on antigen. Cells for anti-acetylated tubulin staining were incubated on ice for 45 min before fixation to destroy cytoskeletal microtubules. Primary antibodies used for immunofluorescence are: mouse anti-acetylated-tubulin (Sigma), rabbit anti-Glu-tub (Chemicon), mouse anti-EEA1 (BD Transduction Laboratory), mouse anti-Rab11 (BD Transduction Laboratory), mouse anti-PTPN23 (Abnova), mouse anti-PLA2G3 (Abnova), rabbit-anti-Arl13b (a gift from T. Caspary), and rabbit anti-gamma-tubulin (Sigma). Alexa 488- or Alexa 594-conjugated secondary antibodies (Molecular Probes) were applied for 1 h at room temperature. For immunoblotting, cells were extracted with RIPA lysis buffer 2.5 days after transfection and boiled with SDS sample buffer. Same volumes of lysates were loaded for paired experiments. Primary antibodies used for western blotting are: mouse anti-GSN (Genetex), rabbit anti-ACTR3 (Sigma), rabbit anti-PARVA (Cell Signaling), mouse anti-PTPN23 (Abnova) and mouse anti-PLA2G3 (Abnova). Bound antibodies were detected using horseradish peroxidase-conjugated secondary antibodies (Pierce). Membranes were stripped and re-blotted with anti-alpha-tubulin antibody (Sigma).

Live cell imaging. htRPE–Smo–EGFP cells were transfected with siRNAs for 2.5 days in the presence of 10% serum and then non-ciliated cells were live-imaged for 6 h in serum-free medium (Fig. 1i). Images (2 μm *Z*-stack) were acquired using an Olympus IX70 microscope and a cooled charge-coupled device system with temperature and CO_2 control.

Internalization of transferrin. Cells were incubated with iron-saturated human transferrin-AlexaFluor594 (30 μg ml^{-1}; Invitrogen) in serum-free medium for 45 min at 37 °C. Cells were rinsed quickly three times with ice-cold DMEM containing 10% FBS and incubated for 5 min at 37 °C to clear transferrin–alexaFluor 594 from the plasma membrane and early endosomes. Cells were fixed with 4% PFA on ice.

Pharmacological studies. Cytochalasin D (Sigma) resuspended in DMSO was applied to cells at various conditions (see text and figure legends). Concanamycin A (Sigma) resuspended in DMSO was applied to cells at 2 μM in the absence of serum for final 16 h before fixation. OPC (BIOMOL) resuspended in ethanol was applied to cell at 25 μM for final 36 h before fixation in the presence of 10% serum (OPC was cytotoxic when treated at 25 μM in the absence of serum). For a vehicle control, an equivalent amount of DMSO or ethanol was added to cells.

Fluorescence intensity measurement. Exposure was set to minimum and EGFP fluorescence was imaged using an Olympus IX70 microscope and a cooled charge-coupled device system. Small areas including cilium were excised from the images and placed in a panel using Adobe Photoshop 7.0 software. Maximum pixel intensity of EGFP fluorescence from each cilium was measured using ImageJ software.

Cell counting and statistics. The total numbers of cells counted are: >2,000 (Figs 1b and 2b), >500 (Figs 1d, f and 2e, f) and >300 (Figs 1g, h and 3b). Binucleated cells were excluded from the counting for Fig. 3b. Data from follow-up studies were analysed by two-tailed, paired Student's *t*-test using *t*-test calculation software (GraphPad).

Vol 464|15 April 2010|doi:10.1038/nature08878

LETTERS

Therapeutic antibody targeting of individual Notch receptors

Yan Wu[1]*, Carol Cain-Hom[2]*, Lisa Choy[2], Thijs J. Hagenbeek[2], Gladys P. de Leon[7], Yongmei Chen[1], David Finkle[4], Rayna Venook[4], Xiumin Wu[5], John Ridgway[5], Dorreyah Schahin-Reed[6], Graham J. Dow[2]†, Amy Shelton[2], Scott Stawicki[1], Ryan J. Watts[6], Jeff Zhang[8], Robert Choy[8], Peter Howard[8], Lisa Kadyk[8], Minhong Yan[5], Jiping Zha[3], Christopher A. Callahan[3], Sarah G. Hymowitz[7] & Christian W. Siebel[2]

The four receptors of the Notch family are widely expressed transmembrane proteins that function as key conduits through which mammalian cells communicate to regulate cell fate and growth[1,2]. Ligand binding triggers a conformational change in the receptor negative regulatory region (NRR) that enables ADAM protease cleavage[3,4] at a juxtamembrane site that otherwise lies buried within the quiescent NRR[5,6]. Subsequent intramembrane proteolysis catalysed by the γ-secretase complex liberates the intracellular domain (ICD) to initiate the downstream Notch transcriptional program. Aberrant signalling through each receptor has been linked to numerous diseases, particularly cancer[7], making the Notch pathway a compelling target for new drugs. Although γ-secretase inhibitors (GSIs) have progressed into the clinic[8], GSIs fail to distinguish individual Notch receptors, inhibit other signalling pathways[9] and cause intestinal toxicity[10], attributed to dual inhibition of Notch1 and 2 (ref. 11). To elucidate the discrete functions of Notch1 and Notch2 and develop clinically relevant inhibitors that reduce intestinal toxicity, we used phage display technology to generate highly specialized antibodies that specifically antagonize each receptor paralogue and yet cross-react with the human and mouse sequences, enabling the discrimination of Notch1 versus Notch2 function in human patients and rodent models. Our co-crystal structure shows that the inhibitory mechanism relies on stabilizing NRR quiescence. Selective blocking of Notch1 inhibits tumour growth in pre-clinical models through two mechanisms: inhibition of cancer cell growth and deregulation of angiogenesis. Whereas inhibition of Notch1 plus Notch2 causes severe intestinal toxicity, inhibition of either receptor alone reduces or avoids this effect, demonstrating a clear advantage over pan-Notch inhibitors. Our studies emphasize the value of paralogue-specific antagonists in dissecting the contributions of distinct Notch receptors to differentiation and disease and reveal the therapeutic promise in targeting Notch1 and Notch2 independently.

To enable independent antagonism of Notch1 and Notch2, we used phage display to generate antibodies targeting the NRRs. Previous studies proposed that antibody targeting of the NRR might stabilize the 'off' conformation[6], and the report of mouse monoclonal antibody antagonists against the human Notch3 NRR supports this approach[12]. As an important advance, each of our synthetic antibodies, anti-NRR1 and anti-NRR2, is a clinically relevant, fully human IgG1 selected to (1) potently inhibit its cognate paralogue but not other Notch receptors, (2) bind the human orthologue for therapeutic targeting, and (3) bind the mouse orthologue for dissecting receptor-specific functions in mouse models. Each antibody bound highly specifically to its cognate receptor but not to any of the other receptors, measured by enzyme-linked immunosorbent assay (ELISA), surface plasmon resonance (SPR) and flow cytometry (Fig. 1a, b and Supplementary Figs 1, 2). Each antibody bound with similar high affinities (K_d = 1.3–3.1 nM) to both the human and mouse sequences of only the targeted NRR (Fig. 1a, b).

We assayed signalling *in vitro* using a co-culture assay with one cell line expressing the Notch ligand Jagged1 (Jag1) and a second expressing Notch1 or Notch2. Anti-NRR1 inhibited signalling in the Notch1 cells in a dose-dependent manner. Complete inhibition, equivalent to the background signal seen without induction (−Jag1) or in the presence of a GSI (DAPT), occurred between 80 and 400 ng ml^{-1} of antibody (Fig. 1c, left). Addition of purified NRR1 but not NRR2 antigen rescued signalling inhibited by anti-NRR1, confirming that inhibition reflected specific binding of anti-NRR1 to NRR1 (Fig. 1c, left). Using Notch2-expressing cells to assay anti-NRR2 activity, we observed similarly potent and specific inhibition of Notch2 signalling (Fig. 1c, right). Both antibodies inhibited signalling induced through the ligands Jag1, Jag2, Delta-like1 (Dll1) and Dll4, and thus inhibition occurs irrespective of the ligand (Supplementary Fig. 3).

To determine whether anti-NRR1 and anti-NRR2 function as receptor-specific inhibitors *in vivo*, we investigated the development of T cells and splenic marginal zone B (MZB) cells because each depends distinctly on Notch1 or Notch2, respectively[13–15]. Treating mice with anti-NRR1, but not anti-NRR2, significantly reduced thymus weights and cellularity (Supplementary Fig. 4). Relative to the anti-gD control (77.5%), anti-NRR1 dramatically reduced the $CD4^+/CD8^+$ population (5.9%) whereas anti-NRR2 did not (80%) (Fig. 1d). In contrast, treatment with anti-NRR2 nearly eliminated $CD21^{hi}CD23^{lo/-}$ MZB cells, reducing the population more than lymphotoxin-β receptor (LTβR)–Fc fusion protein[16], a positive control (Fig. 1e). Anti-NRR1 did not significantly reduce the MZB population and thus appears not to affect Notch2 signalling, consistent with *in vitro* data (Supplementary Fig. 5). Our results demonstrate that anti-NRR1 and anti-NRR2 are potent paralogue-specific inhibitors of signalling from Notch1 and Notch2, respectively.

To understand the molecular basis of anti-NRR1 antagonistic activity, we determined the 2.2 Å crystal structure of the antibody Fab fragment bound to human NRR1 (Fig. 1f, g and Supplementary Table 1). The NRR consists of three Lin-Notch repeats (LNRs) juxtaposed with the heterodimerization (HD) domain, in turn comprised of amino- and carboxy-terminal subdomains. Our structure of NRR1

Departments of [1]Antibody Engineering, [2]Molecular Biology, [3]Pathology, [4]Translational Oncology, [5]Tumor Biology and Angiogenesis, [6]Neurodegeneration, [7]Structural Biology, Genentech, Inc., 1 DNA Way, South San Francisco, California 94080, USA. [8]Exelixis Inc., 210 East Grand Avenue, PO Box 511, South San Francisco, California 94083-0511, USA.
†Present address: Department of Biology, Stanford University, Stanford, California 94305, USA.
*These authors contributed equally to this work.

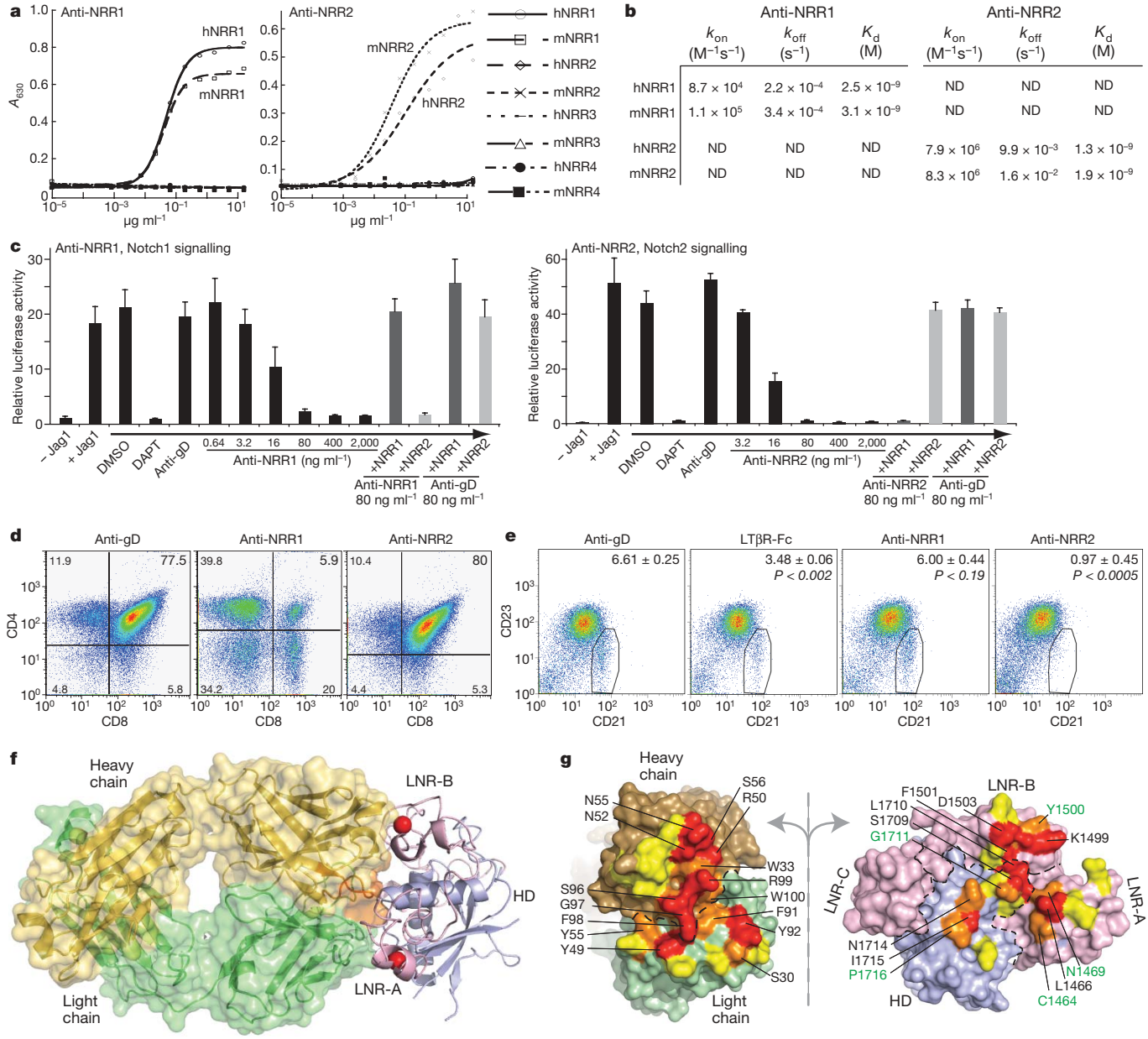

Figure 1 | Anti-NRR1 and anti-NRR2 specifically antagonize their cognate receptors. **a**, ELISA measuring antibody binding to purified NRR protein fragments from each of the human (h) and murine (m) Notch receptors. **b**, SPR binding constants; ND, not detectable. **c**, Co-culture assays of Notch1 (left) or Notch2 (right) signalling, induced with Jag1-expressing cells (+Jag1). −Jag1, control for no induction; DMSO, dimethyl sulfoxide alone; DAPT, 5 μM in DMSO; anti-gD, isotype control antibody, 2,000 ng ml^{-1}; the last four assays in each panel included 80 ng ml^{-1} of the indicated antibody plus purified NRR1 or NRR2. Values reflect Notch reporter gene signalling relative to control reporter, normalized to the DAPT values (mean ± coefficient of variation (CV), $n = 5$–6). **d**, **e**, Anti-NRR1 and anti-NRR2 function as receptor-specific inhibitors *in vivo*. Thymus or spleen cells from mice treated with the indicated reagents were harvested for flow cytometry of CD4$^+$/CD8$^+$ T cells (**d**) or splenic MZB cells (**e**). Numbers represent the mean percentages ± s.d. ($n = 3$) of cells within the boxed gates; representative dot plots are shown. **f**, Side-view of the 2.2 Å structure of the anti-NRR1 Fab–NRR1 complex showing anti-NRR1 binding across the face of NRR1, bridging the LNR and HD domains; LNR-C is hidden from view behind the complex. The Fab heavy and light chains are yellow and green, respectively, whereas the LNR and HD subdomains are pink and blue, respectively; heavy chain CDR3 residues that bury surface area upon binding NRR1 are orange. **g**, Open-book view of the interface between anti-NRR1 Fab (left) and human NRR1 (right). Residue colouring symbolizes the extent to which the solvent accessible surface area is buried by complex formation (25–49%, yellow; 50–75%, orange; > 75%, red). Residues buried by ≥ 50% are labelled, with identical residues in the Notch1 and Notch2 NRRs in green.

in complex with anti-NRR1 seems very similar to the previously described compact, autoinhibited NRR structures[5,6]. The epitope is dispersed across the NRR face, spanning residues in LNR-A, LNR-B and HD-C, consistent with domain swap experiments (Supplementary Fig. 6). Despite the ~45% sequence identity between NRR1 and NRR2, only 29% of the epitope residues are identical, revealing the basis of anti-NRR1 specificity for Notch1 over Notch2 (Fig. 1g and Supplementary Fig. 7). The Fab heavy chain contacts LNR-B, the final helix in the HD-C domain, and the periphery of LNR-A, whereas the light chain contacts the connecting loop before the final helix in the HD domain and LNR-A. CDR H3 nestles into the interface between LNR-B and HD, with R99 from H3 packing against L1710 from the HD domain and forming a hydrogen bond to the backbone carbonyl of LNR-B residue F1501. This structure suggests an inhibitory mechanism in which anti-NRR1 functions as a molecular clamp between the LNR-AB region and the HD domain, stabilizing the autoinhibited NRR1 and interfering with the conformational changes required for receptor activation.

To determine whether anti-NRR1 can directly inhibit growth of cancer cells, we initially focused on T-cell acute lymphoblastic

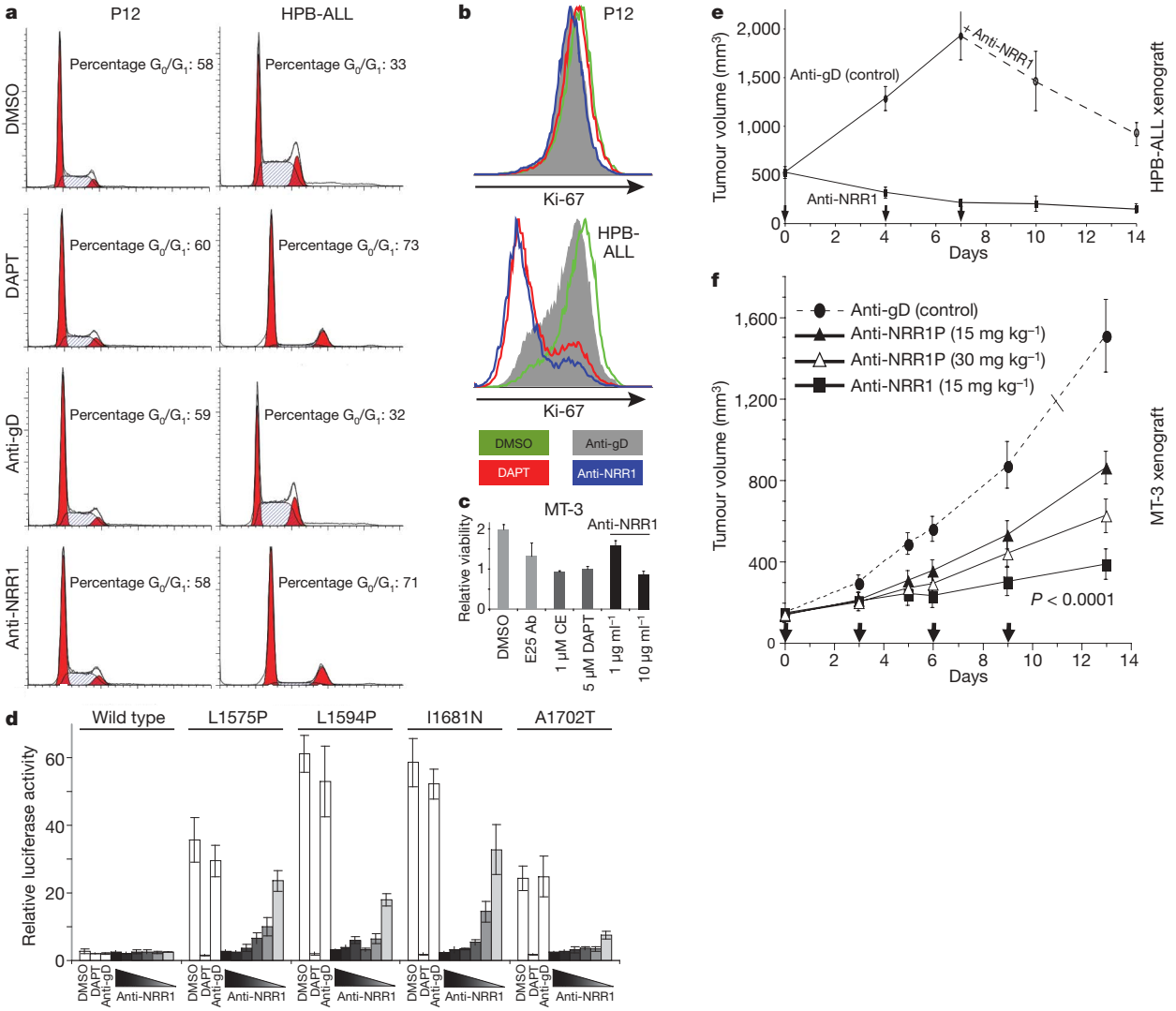

Figure 2 | Anti-NRR1 inhibits growth of Notch1-driven cancer cells and blocks signalling through mutationally destabilized NRRs. a, **b**, Anti-NRR1 causes a G_0/G_1 block of T-ALL cell cycling and proliferation. P12-Ichikawa (control, resistant to GSIs) and HPB-ALL (sensitive to GSIs) cells were treated with the indicated reagents, and cell cycling (DNA content) (**a**) or proliferation (Ki-67) (**b**) were assessed. **c**, Anti-NRR1 decreases viability of MT-3 colon cancer cells. MT-3 cells were treated with the indicated reagents (E25, 10 μg ml^{-1} isotype control antibody; CE, compound E GSI), and viability was assessed by measuring ATP levels (normalized to the DAPT cultures; mean ± CV, $n = 8$). **d**, Co-culture assays demonstrating that anti-NRR1 inhibits signalling of mutationally-activated Notch1 receptors. NRR1 point mutations listed at top. Anti-NRR1, fivefold serial dilutions from 50 to 0.016 μg ml^{-1} (mean ± CV, $n = 4$). **e**, **f**, Effects of anti-NRR1 in HPB-ALL and MT-3 xenografts. Mice carrying established tumours were dosed (arrows) with the indicated antibodies (anti-NRR1P, low affinity parent of anti-NRR1 before affinity maturation) and tumour volumes were measured (mean ± s.e.m.). In (**e**), mice in the anti-gD group were switched on day 7 to anti-NRR1 dosing (days seven and 10). $n = 15$ for anti-gD; $n = 17$ for anti-NRR1. In **f**, $n = 9$.

leukaemia (T-ALL). Over half of T-ALL patients carry activating Notch1 mutations, the most frequent class comprised of amino acid substitutions in the NRR that destabilize the autoinhibited conformation and activate ligand-independent signalling[17,18]. Screens measuring T-ALL cell line growth have identified several that are sensitive to GSI treatment[17]. One such cell line, HPB-ALL, expresses Notch1 with both an activating mutation (L1575P) in the NRR and a PEST domain truncation, which prolongs signalling[17]. As a control T-ALL line expected to be resistant to GSIs (and thus anti-NRR1), we examined P12-Ichikawa (P12) cells. Although P12 cells express Notch1 that is constitutively activated by a 12 amino acid insertion between the NRR and the transmembrane domain, they are resistant to GSIs because they have acquired additional genetic changes that bypass the need for Notch signalling[17,19]. Treatment of HPB-ALL cells with DAPT or anti-NRR1 significantly increased the percentage of cells in the G_0/G_1 phases of the cell cycle and reduced staining for the proliferation marker Ki-67 (also known as Mki67; Fig. 2a, b). Both drugs also decreased HPB-ALL cell size and increased apoptosis (Supplementary Figs 8 and 9), both effects correlating with inhibition of Notch1 activation (Supplementary Fig. 10). As expected, neither drug affected the GSI-resistant P12 cells. These results demonstrate that anti-NRR1 can directly inhibit T-ALL cell growth *in vitro*.

These effects of anti-NRR1 on HPB-ALL cells also suggested that anti-NRR1 inhibits signalling through Notch1 with a NRR point mutation. Given that T-ALL NRR mutations lie in and destabilize the very domain that anti-NRR1 targets, we tested whether different NRR mutations affected anti-NRR1 antagonism. We chose L1594P and L1575P, two of the most common T-ALL mutations, as well as I1681N, one of the strongest activating mutations[18]. In a reporter assay, anti-NRR1 inhibited signalling activated by each of these three NRR mutations (Fig. 2d) as well as a PEST domain truncation, representative of the other common cluster of T-ALL mutations (Supplementary Fig. 11)[17]. Also, anti-NRR1 binding to the NRR was not affected by another activating NRR mutation (L1597H), as

judged by SPR and ELISA assays (data not shown). Together with the observation that none of the known T-ALL NRR point mutations fall within the anti-NRR1 epitope (Supplementary Fig. 12), these results suggest that the ability of anti-NRR1 to inhibit mutant signalling will apply to the majority of the known NRR1 point mutations in T-ALL.

To identify additional oncology indications for anti-NRR1, we screened a panel of ~45 cancer cell lines for anti-NRR1 sensitivity and identified a human colon cancer line, MT-3. Anti-NRR1 and GSIs decreased MT-3 viability in a dose-dependent and ligand-independent manner (Fig. 2c) that correlated with decreases in ICD levels and target gene expression (data not shown). This ligand-independence suggested that MT-3 cells have an endogenous mechanism for activating Notch1 signalling. Sequencing the NRR and PEST domain exons revealed a single point mutation, A1702T, at the same position as A1702P, a known activating mutation in T-ALL[17]. A1702T activated Notch1 signalling independent of ligand and to a similar extent as L1575P (Fig. 2d). Thus, MT-3 growth appears at least partly driven by Notch1 mutational activation.

We used xenograft models to examine the ability of anti-NRR1 to inhibit tumour growth *in vivo*. In the HBP-ALL model, anti-NRR1 caused regression of well-established tumours (Fig. 2e). In contrast, tumours from mice in the anti-gD control group grew rapidly; when these animals were switched to dosing with anti-NRR1 on day seven, we again observed tumour regression, particularly notable given the large initial tumour volume. In the MT-3 colon cancer model, anti-NRR1 also clearly slowed tumour growth (Fig. 2f and Supplementary Fig. 13). Inhibition depended on antibody affinity, as anti-NRR1P, the parent antibody of anti-NRR1 before affinity maturation (K_d approximately 200 nM compared to 3 nM for anti-NRR1), did not inhibit tumour growth as strongly as anti-NRR1 (Fig. 2f). These results establish that anti-NRR1 can inhibit the growth of Notch1-dependent tumours *in vivo*.

Signalling induced by Dll4 through Notch1 and perhaps Notch4 plays a key role in angiogenesis by regulating endothelial cell fate choice[20]. We found that anti-NRR1, like a GSI and anti-Dll4 antagonist, affected lumen-like sprouting from human umbilical vein endothelial cells (HUVECs) (Supplementary Fig. 14)[21]. Likewise, systemic delivery of anti-NRR1 dramatically disrupted retinal vasculature development in neonate mice, generating a dense, compact vascular network (Fig. 3a) correlating with increased proliferation (data not shown). These observations mimic those found following inhibition of Dll4 or γ-secretase using this same model[21] and are consistent with results from the mouse corneal pocket assay (data not shown). These anti-angiogenic effects resulted from specific blocking of Notch1 (as opposed to the Notch1 and Notch4 inhibition expected from a GSI), indicating that (1) Notch1 inhibition alone is sufficient and (2) Notch4 inhibition is not necessary to disrupt mammalian angiogenesis.

To determine whether anti-NRR1 is sufficient to inhibit tumour growth through an anti-angiogenic mechanism, we tested mouse xenograft models using the Calu-6 and HM7 cell lines, chosen because their growth is sensitive to anti-angiogenic reagents *in vivo*[21] but not to Notch inhibition *in vitro* (data not shown). In the Calu-6 model, anti-NRR1 caused a decrease in tumour volume, similar to that observed following anti-VEGF treatment (Fig. 3b). We also observed growth inhibition by anti-NRR1 in the aggressively growing HM7 model (Fig. 3d, e). Consistent with reports that selective blocking of Dll4 (refs 21, 22) increases tumour CD31 staining and generates poorly functioning tumour vasculature, anti-NRR1 increased CD31 staining in Calu-6 tumour sections (Fig. 3c and Supplementary Fig. 15). Taken together, our results indicate that the anti-tumour effects exerted by anti-NRR1 in these models probably reflect a disruption of tumour angiogenesis.

A hurdle to the therapeutic application of pan-Notch inhibitors has been toxicity in the intestinal crypt marked by a decrease of proliferative cells and an increase of secretory goblet cells[10]. However, genetic disruption of Notch1 or Notch2 suggested that this

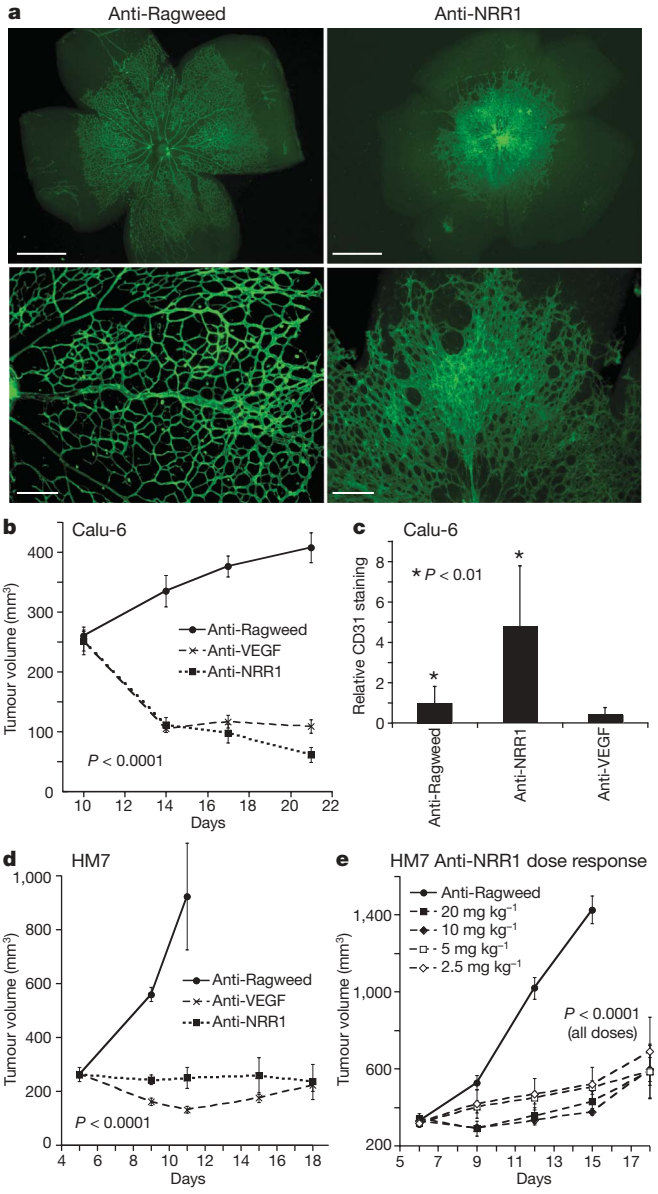

Figure 3 | Anti-NRR1 is an anti-angiogenic agent that inhibits tumour growth. a, Mouse neonate retinal assay for endothelial cell sprouting and angiogenesis. Retinal vasculature from mouse neonates treated with the indicated antibodies was visualized following isolectin perfusion. Top panels, scale bar = 1 mm. Bottom panels, scale bar = 0.2 mm. **b**, **d**, **e**, Graphs for human tumour xenograft models (Calu-6, human anaplastic carcinoma, probably lung; HM7, human colon carcinoma) showing tumour volume following dosing twice per week with the indicated antibodies (mean ± s.e.m., $n = 10$ in **b**, **d**; $n = 5$ in **e**; P values for anti-Ragweed vs anti-NRR1). Anti-NRR1 at 20 mg kg^{-1} except where indicated otherwise. **c**, Quantification of endothelial cell density. Relative anti-CD31 staining was used to score for endothelial cells in tumour sections from the model in (**b**) (normalized to the anti-Ragweed control; mean ± s.d.; $n = 8$ image fields).

goblet cell metaplasia required inhibition of both receptors[11], as would be expected following treatment with GSIs but not receptor-specific inhibitors. We found that mice treated with either anti-NRR1 or anti-NRR2 maintained weight, but mice treated with anti-NRR1 plus anti-NRR2 lost nearly 20% of their body weight within 6 days (Fig. 4a). Consistent with previously reported effects of GSIs[10], intestinal crypts from mice treated with both antibodies showed severe goblet cell metaplasia (Fig. 4b). In contrast, anti-NRR2 alone did not detectably affect intestinal morphology or expression of Hes1, a marker of pathway activity. Surprisingly, we found that Notch1 inhibition alone was sufficient to induce some

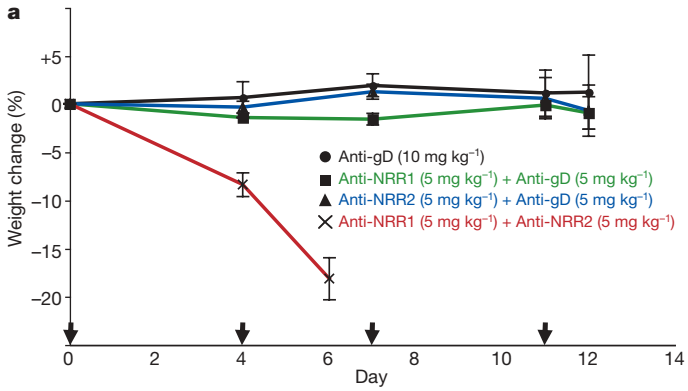

c

Ki-67–positive crypt cells (%)

Anti-gD	Anti-NRR1	Anti-NRR2	Anti-NRR1 + Anti-NRR2
69	52	65	35

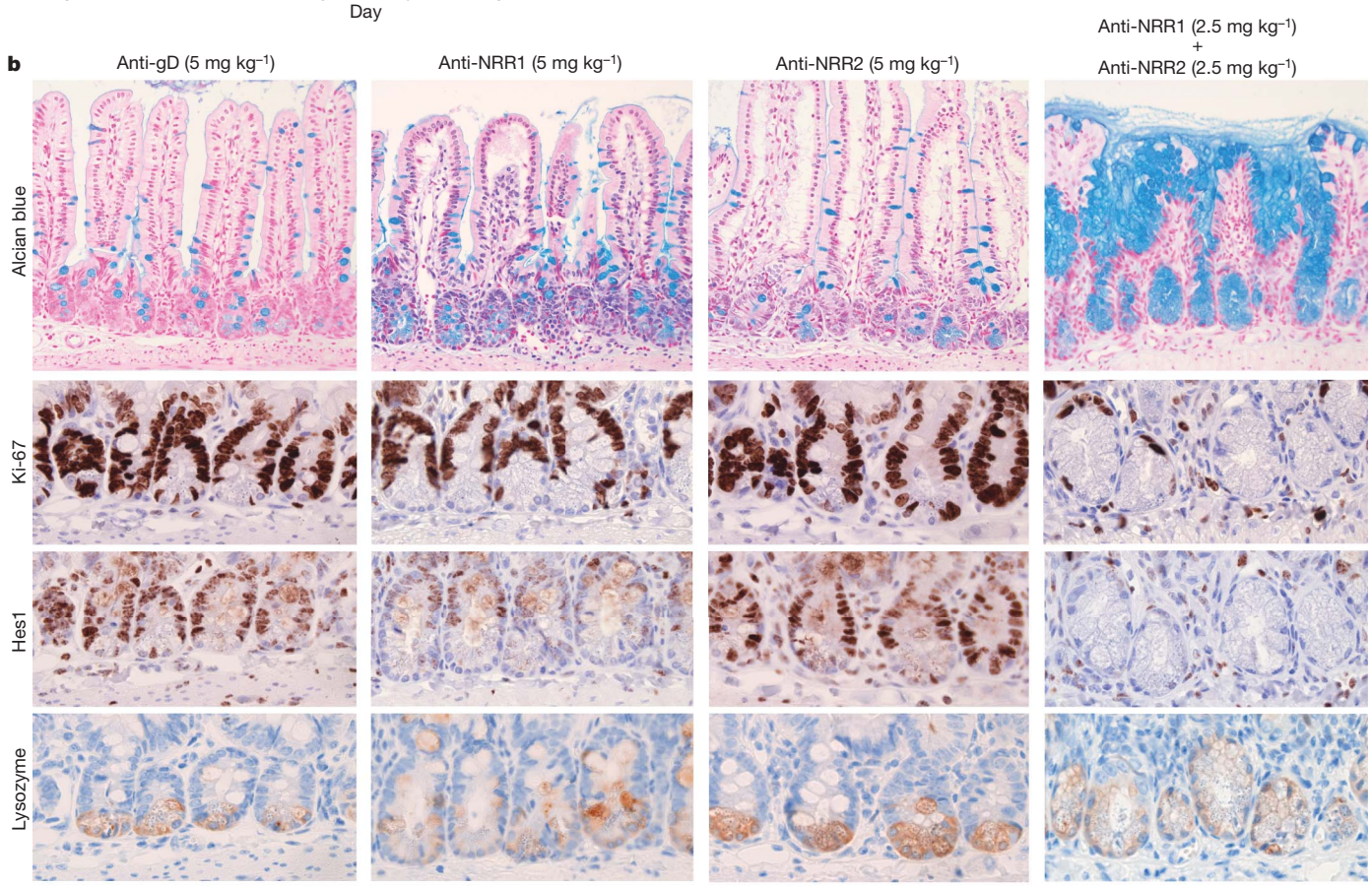

Figure 4 | Selective antibody blocking of Notch1 or Notch2 avoids severe goblet cell metaplasia associated with pan-Notch inhibition. **a**, Change in total body weight (mean ± s.d., $n = 3$) in adult mice dosed (arrows) with the indicated antibodies. **b**, Immunohistochemical analyses of small intestines, using Alcian blue for mucin to mark secretory goblet cells, anti-Ki-67 staining for proliferation, anti-Hes1 staining for expression of a Notch pathway target, and lysozyme for Paneth cells. Mice were dosed as in (**a**) at the indicated concentrations, and tissues were harvested on day 12. **c**, Quantification of Ki-67 staining.

goblet cell metaplasia; however, this effect was mild relative to that observed following dual inhibition of Notch1 and Notch2 (Fig. 4b, c). Our results indicate that Notch1 and Notch2 function redundantly in intestinal cell differentiation, although inhibition of Notch1 but not Notch2 is sufficient to reveal a partial phenotype. In reducing or avoiding the goblet cell metaplasia that is a hallmark of a general Notch block, our receptor-specific inhibitors represent a clear breakthrough over existing pan-Notch inhibitors such as GSIs.

Anti-NRR1 and anti-NRR2 stand among the strongest therapeutic candidates for treating indications linked to aberrant Notch signalling, particularly in cancer, immunology and regenerative medicine. Compared to pan-Notch inhibitors such as GSIs or stapled peptides[23], our fully human antibodies offer the advantages of an improved safety profile, paralogue-specific inhibition and a clinically established drug format. Anti-NRR1 holds the promise of simultaneously targeting cancers by directly inhibiting cancer cell growth and disrupting tumour angiogenesis. As anti-DLL4 blocking antibodies are entering the clinic because of anti-angiogenic effects, our Notch1 inhibitor may also directly affect tumour cell viability in Notch1-driven cancers and blocks both ligand-dependent and -independent activation. Similarly, Notch2 has been implicated in many cancers[7,24], and anti-NRR2 stands as a candidate for treating melanomas[25–28] and some B-cell leukaemias[29,30], both linked to the *Notch2* gene by amplification, overexpression or mutation. Our characterizations of anti-NRR1 and anti-NRR2 make a compelling case for adding these Notch receptor-specific antibodies to the arsenal of cancer therapeutics.

METHODS SUMMARY

Human phage libraries with diversities in the H1, H2, H3 and L3 regions were used for panning. Fab fragments were identified by ELISA/DNA sequencing and reformatted to express IgGs. NRR proteins were purified following expression in mammalian or insect cells. A BIAcore-3000 instrument was used to determine

binding affinities. Co-culture assays used NIH-3T3 cells stably transfected with Jag1 plus NIH-3T3 cells stably transfected with Notch1 (or transiently transfected with mutant Notch1 expression plasmids; the Notch2 assay used U87MG cells) and transiently co-transfected with a TP-1 (Notch responsive promoter) firefly luciferase reporter and a constitutively expressed *Renilla* luciferase reporter. T and MZB cell development were analysed by flow cytometry with anti-CD8-phycoerythrin (PE)-Cy5 and anti-CD4-allophycocyanin (APC) or anti-B220-APC, anti-CD5-peridinin chlorophyll protein (PerCP), anti-CD23-PE and anti-CD21-fluorescein (FITC), respectively. The NRR1-Fab structure was solved by molecular replacement to 2.2 Å and refined to an R and R_{free} of 22.2 and 27.2%, respectively. For cycling, DNA content was determined in 7–8-day cultures by flow cytometry after propidium iodide staining and analysed using ModFit. Proliferation was measured by flow cytometry using anti-Ki-67-FITC. MT-3 viability was assessed after 1 week using CellTiter-Glo (Promega). Xenografted tumour cells were implanted in the flank of immunocompromised mice. Mice were dosed intraperitoneally twice per week. Tumour angiogenesis was examined with anti-CD31, normalized to total cell number using DAPI. Retinal angiogenesis used CD1 neonates, injected intraperitoneally 1 and 3 days after birth, with retinas analysed 2 days later using biotinylated isolectin B4 to visualize vasculature. Intestinal studies used 12-week-old BALB/c mice. Histochemical identification of intestinal cell types used Alcian blue. Proliferation was assessed using anti-Ki-67. Areas of $\geq 100{,}000\ \mu m^2$, containing $\geq 1{,}000$ crypt cells, were analysed for the percentages of Ki-67-positive epithelial cells. Notch activity and Paneth cells were visualized using anti-Hes1 and anti-lysozyme, respectively.

Full Methods and any associated references are available in the online version of the paper at www.nature.com/nature.

Received 30 June 2009; accepted 28 January 2010.

1. Aster, J. C., Pear, W. S. & Blacklow, S. C. Notch signaling in leukemia. *Annu. Rev. Path.* **3,** 587–613 (2008).
2. Kopan, R. & Ilagan, M. X. G. The canonical Notch signaling pathway: unfolding the activation mechanism. *Cell* **137,** 216–233 (2009).
3. Mumm, J. S. *et al.* A ligand-induced extracellular cleavage regulates γ-secretase-like proteolytic activation of Notch1. *Mol. Cell* **5,** 197–206 (2000).
4. Brou, C. *et al.* A novel proteolytic cleavage involved in Notch signaling: the role of the disintegrin-metalloprotease TACE. *Mol. Cell* **5,** 207–216 (2000).
5. Gordon, W. R. *et al.* Structural basis for autoinhibition of Notch. *Nature Struct. Mol. Biol.* **14,** 295–300 (2007).
6. Gordon, W. R. *et al.* Structure of the Notch1-negative regulatory region: implications for normal activation and pathogenic signaling in T-ALL. *Blood* **113,** 4381–4390 (2009).
7. Koch, U. & Radtke, F. Notch and cancer: a double-edged sword. *Cell. Mol. Life Sci.* **64,** 2746–2762 (2007).
8. Shih, I.-M. & Wang, T.-L. Notch signaling, γ-secretase inhibitors, and cancer therapy. *Cancer Res.* **67,** 1879–1882 (2007).
9. Beel, A. J. & Sanders, C. Substrate specificity of γ-secretase and other intramembrane proteases. *Cell. Mol. Life Sci.* **65,** 1311–1334 (2008).
10. van Es, J. H. *et al.* Notch/γ-secretase inhibition turns proliferative cells in intestinal crypts and adenomas into goblet cells. *Nature* **435,** 959–963 (2005).
11. Riccio, O. *et al.* Loss of intestinal crypt progenitor cells owing to inactivation of both Notch1 and Notch2 is accompanied by derepression of CDK inhibitors p27Kip1 and p57Kip2. *EMBO Rep.* **9,** 377–383 (2008).
12. Li, K. *et al.* Modulation of Notch signaling by antibodies specific for the extracellular negative regulatory region of Notch3. *J. Biol. Chem.* **283,** 8046–8054 (2008).
13. Saito, T. *et al.* Notch2 is preferentially expressed in mature B cells and indispensable for marginal zone B lineage development. *Immunity* **18,** 675–685 (2003).
14. Radtke, F. *et al.* Deficient T cell fate specification in mice with an induced inactivation of Notch1. *Immunity* **10,** 547–558 (1999).
15. Witt, C. M., Won, W.-J., Hurez, V. & Klug, C. A. Notch2 haploinsufficiency results in diminished B1 B cells and a severe reduction in marginal zone B cells. *J. Immunol.* **171,** 2783–2788 (2003).
16. Ettinger, R., Browning, J. L., Michie, S. A., van Ewijk, W. & McDevitt, H. O. Disrupted splenic architecture, but normal lymph node development in mice expressing a soluble lymphotoxin-β receptor-IgG1 fusion protein. *Proc. Natl Acad. Sci. USA* **93,** 13102–13107 (1996).
17. Weng, A. P. *et al.* Activating mutations of NOTCH1 in human T cell acute lymphoblastic leukemia. *Science* **306,** 269–271 (2004).
18. Malecki, M. J. *et al.* Leukemia-associated mutations within the NOTCH1 heterodimerization domain fall into at least two distinct mechanistic classes. *Mol. Cell. Biol.* **26,** 4642–4651 (2006).
19. Palomero, T. *et al.* Mutational loss of PTEN induces resistance to NOTCH1 inhibition in T-cell leukemia. *Nature Med.* **13,** 1203–1210 (2007).
20. Phng, L. K. & Gerhardt, H. Angiogenesis: a team effort coordinated by Notch. *Dev. Cell* **16,** 196–208 (2009).
21. Ridgway, J. *et al.* Inhibition of Dll4 signalling inhibits tumour growth by deregulating angiogenesis. *Nature* **444,** 1083–1087 (2006).
22. Noguera-Troise, I. *et al.* Blockade of Dll4 inhibits tumour growth by promoting non-productive angiogenesis. *Nature* **444,** 1032–1037 (2006).
23. Moellering, R. E. *et al.* Direct inhibition of the NOTCH transcription factor complex. *Nature* **462,** 182–188 (2009).
24. Leong, K. G. & Karsan, A. Recent insights into the role of Notch signaling in tumorigenesis. *Blood* **107,** 2223–2233 (2006).
25. Jönsson, G. *et al.* Genomic profiling of malignant melanoma using tiling-resolution array CGH. *Oncogene* **26,** 4738–4748 (2007).
26. Hoek, K. *et al.* Expression profiling reveals novel pathways in the transformation of melanocytes to melanomas. *Cancer Res.* **64,** 5270–5282 (2004).
27. Massi, D. *et al.* Evidence for differential expression of Notch receptors and their ligands in melanocytic nevi and cutaneous malignant melanoma. *Mod. Pathol.* **19,** 246–254 (2005).
28. Qin, J.-Z. *et al.* p53-independent NOXA induction overcomes apoptotic resistance of malignant melanomas. *Mol. Cancer Ther.* **3,** 895–902 (2004).
29. Lee, S.-y. *et al.* Gain-of-function mutations and copy number increases of Notch2 in diffuse large B-cell lymphoma. *Cancer Sci.* **100,** 920–926 (2009).
30. Trøen, G. *et al. NOTCH2* mutations in marginal zone lymphoma. *Haematologica* **93,** 1107–1109 (2008).

Supplementary Information is linked to the online version of the paper at www.nature.com/nature.

Acknowledgements We acknowledge the Notch scientists at Genentech and Exelixis for support throughout this project. In particular, we thank the following contributors at Exelixis: S.-H. Lin, L. Doukhan, S. Weiss, N. Benin and R. Mercer for protein production, purification and analysis, R. Funke for cloning and sequencing and D. Buckley and J. Greve for scientific discussions and guidance. We thank the Genentech protein expression group, R. Vij and J.-A. Hongo for help with antibody characterization, F. Bazan and C. Sanchez-Irizarry for stimulating discussions and critically reading the manuscript, J. Eastham-Anderson for morphometric analysis of the intestines, Y. Shang for making mutant Notch1 expression plasmids, S. Seshagiri for MT-3 sequencing, E. Quan for initial work with T-ALL lines, S. Chaudhuri for cloning and antibody characterization, and G. Plowman for insights and guidance. We appreciate the important contributions of F. de Sauvage, who helped initiate this collaborative project and provided guidance throughout. The Advanced Light Source and Berkeley Center for Structural Biology are supported by the Department of Energy, National Institutes of Health, and the National Institute of General Medical Sciences.

Author Contributions Y.W., Y.C. and S.S. generated the phage display antibodies and performed the *in vitro* binding experiments. G.P.d.L. purified and crystallized the NRR1-Fab complex. S.G.H. solved and analysed the structure, made the structure figures and wrote the corresponding section of the paper, D.F. and R.V. performed the MT-3 xenograft experiment, X.W. performed the Calu-6 and HM7 xenograft experiments, J.R. performed the HUVEC experiments and M.Y. supervised these experiments; Ji.Z. and C.A.C. analysed intestinal pathology; C.C.-H., L.C. and T.J.H. performed the experiments characterizing antibody activity *in vitro* and *in vivo*, C.C.-H. also analysed CD31 staining in the Calu-6 model, L.C. also analysed signalling from mutant receptors, T.J.H. also analysed T-ALL growth, including the HPB-ALL xenograft, L.C. and A.S. analysed T-ALL growth *in vitro*, G.J.D. performed the domain swap experiments, D.S.-R. performed the neonate retina experiments and R.J.W. supervised these experiments; Je.Z. purified and characterized antigens, R.C. developed *in vitro* signalling assays, P.H. developed cell-binding assays and L.K. supervised the work at Exelixis. C.W.S. supervised the experiments and wrote the paper.

Author Information Coordinates for the co-crystal structure have been assigned pdb accession code 3L95. Reprints and permissions information is available at www.nature.com/reprints. The authors declare competing financial interests: details accompany the full-text HTML version of the paper at www.nature.com/nature. Correspondence and requests for materials should be addressed to C.W.S. (csiebel@gene.com).

METHODS

Antibody generation. Human phage antibody libraries with synthetic diversities in the selected complementary determining regions (H1, H2, H3, L3), mimicking the natural diversity of the human IgG repertoire, were used for panning. Fab fragments were displayed bivalently on the surface of M13 bacteriophage particles[31]. NRR fragments were expressed as secreted proteins fused to epitope tags (Flag or 6×His) using the baculovirus expression vector system or 293T cells, purified to >90% purity using affinity chromatography and tested for lack of aggregation using light scattering. The sequences of the NRR antigens were as follows: Flag–Human–Notch1–NRR–6×His, KDDDDKGSGVINGCKGKPCKNGGTCAVAS NTARGFICKCPAGFEGATCENDARTCGSLRCLNGGTCISGPRSPTCLCLGPF TGPECQFPASSPCLGGNPCYNQGTCEPTSESPFYRCLCPAKFNGLLCHILDY SFGGGAGRDIPPPLIEEACELPECQEDAGNKVCSLQCNNHACGWDGGDCS LNFNDPWKNCTQSLQCWKYFSDGHCDSQCNSAGCLFDGFDCQRAEGQC NPLYDQYCKDHFSDGHCDQGCNSAECEWDGLDCAEHVPERLAAGTLVVV VLMPPEQLRNSSFHFLRELSRVLHTNVVFKRDAHGQQMIFPYYGREEELRK HPIKRAAEGWAAPDALLGQVKASLLPGGSEGGRRRRELDPMDVRGSIVYLE IDNRQCVQASSQCFQSATDVAAFLGALASLGSLNIPYKIEAVQSETVEPPPPA QEFGLVPRGSGHHHHHH; Flag–Mouse–Notch1–NRR–6×His, KDYKDDDD KLEVINGCRGKPCKNGGVCAVASNTARGFICRCPAGFEGATCENDARTCG SLRCLNGGTCISGPRSPTCLCLGSFTGPECQFPASSPCVGSNPCYNQGTCEPT SENPFYRCLCPAKFNGLCHILDYSFTGAGRDIPPPQIEEACELPECQVDAGN KVCNLQCNNHACGWDGGDCSLNFNDPWKNCTQSLQCWKYFSDGHCDS QCNSAGCLFDGFDCQLTEGQCNPLYDQYCKDHFSDGHCDQGCNAECEW DGLDCAEVPERLAAGTLVLVVLLPPDQLRNNSFHFLRELSHVLHTNVVFKR DAQGQQMIFPYYGHEEELRKHPIKRSTVGWATSSLLPGTSGGRQRRELDP MDIRGSIVYLEIDNRQCVQSSQCFQSATDVAAFGALASLGSLNIPYKIEAVKS EPVEPPLPSQGSGHHHHHH; Flag–Human–Notch2–NRR–6×His, KDDDDK GSGDVCPQMPCLNGGTCAVASNMPDGFICRCPPGFSGARCQSSCGQVKC RKGEQCVHTASGPRCFCPSPRDCESGCASSPCQHGGSCHPQRQPPYYSCQ CAPPFSGSRCELYTAPPSTPPATCLSQYCADKARDGVCDEACNSHACQWD GGDCSLTMENPWANCSSPLPCWDYINNQCDELCNTVECLFDNFECQGNS KTCKYDKYCADHFKDNHCNQGCNSEECGWDGLDCAADQPENLAEGTLV IVVLMPPEQLLQDARSFLRALGTLLHTNLRIKRDSQGELMVYPYYGEKSAAM KKQRMTRRSLPGEQEQEVAGSKVFLEIDNRQCVQDSDHCFKNTDAAAALLA SHAIQGTLSYPLVSVVSESLTPERTEFGLVPRGSGHHHHHH; Mouse–Notch2–NRR–Flag, ADVCPQKPCLNGGTCAVASNMPDGFICRCPPGFSGARCQSSCGQ VKCRRGEQCIHTDSGPRCFCLNPKDCESGCASNPCQHGGTCYPQRQPPHYS CRCPPSFGGSHCELYTAPTSTPPATCQSQYCADKARDGICDEACNSHACQW DGGDCSLTMEDPWANCTSTLRCWEYINNQCDEQCNTAECLFDNFECQRN SKTCKYDKYCADHFKDNHCDQGCNSEECGWDGLDCASDQPENLAEGTLII VVLLPPEQLLQDSRSFLRALGTLLHTNLRIKQDSQGALMVYPYFGEKSAAMK KQKMTRRSLPEEQEQEQEVIGSKIFLEIDNRQCVQDSDQCFKNTDAAAALLA SHAIQGTLSYPLVSVFSELESPRNARRAGSGDYKDDDDKENLYFQ.

Nunc 96-well MaxiSorp immunoplates were coated overnight at 4 °C with NRR1 or NRR2 protein (10 μg ml^{-1}) and blocked for 1 h with PBST buffer (PBS, 0.05% Tween 20) plus 1% BSA. The libraries were added and incubated overnight at room temperature. Plates were washed with PBST buffer, bound phage were eluted with 50 mM HCl and 500 mM NaCl for 30 min, and the eluate was neutralized with an equal volume of 1 M Tris base. Recovered phage were amplified using *Escherichia coli* XL-1 blue cells. During subsequent selection rounds, the binding time was decreased to 2 h as the stringency of plate washing increased[32]. Phage antibodies that bound to both human and murine forms of the targeted NRRs were identified by ELISA and DNA sequencing. Antibody clones were reformatted to express full-length IgGs by cloning the light chain (V_L) and heavy chain (V_H) regions into LPG3 and LPG4 vectors, respectively. Antibodies were transiently expressed in mammalian cells and purified using protein A[33].

SPR with a BIAcore-3000 instrument was used to determine antibody binding affinities[32]. For Notch1, anti-NRR1 was coated directly on CM5 biosensor chips to achieve approximately 400 response units (RU), and purified human or murine NRR1 was injected; for Notch2, purified human (6× His epitope tag) or mouse (Fc epitope tag) NRR2 was coated on the chips, and anti-NRR2 was injected. Injections were done in PBST buffer at 25 °C with a flow rate of 30 μl min^{-1}. Association and dissociation rates were calculated using a simple one–one Langmuir binding model (BIAcore Evaluation Software version 3.2).

Phagemids displaying monovalent Fab[31] served as the library template for grafting V_L and V_H variable domains for affinity maturation using a soft randomization strategy[32]. Stop codons were incorporated in CDR-L3. Three combinations of CDR loops (H1/H2/L3, H3/L3 or L1/L2/L3) were selected for randomization. Affinity-matured clones were selected by sorting against NRR protein, first on plates (one round) and then in solution (four rounds)[31]. A high-throughput, single-point, competitive phage ELISA was used to screen rapidly for high-affinity clones[34].

ELISA. Serial dilutions of antibodies were incubated for 1 h at room temperature on 96-well Maxisorp plates coated with 1 μg of purified human or mouse NRR proteins, each tagged with 6×His except for human NRR2, which was tagged with human Fc. The plates were washed, and bound antibodies were detected with anti-human antibody HRP conjugates. The signal was developed with one component TMB substrate and measured at 630 nm. Data were plotted using a four-parameter nonlinear regression curve-fitting program (KaleidaGraph, Synergy Software).

Notch reporter assays. NIH-3T3 cells stably transfected with Notch1 or transiently transfected with Notch expression plasmids were co-transfected with a Notch-responsive TP-1 (12X CSL) firefly luciferase reporter and a constitutively expressed *Renilla* luciferase reporter (pRL-CMV, Promega) to control for transfection efficiency. Antibodies, *N*-[*N*-(3,5-difluorophenylacetyl)-L-alanyl]-*S*-phenylglycine *tert*-butyl ester (DAPT) (5 μM) or compound E (1 μM) (both from EMD) were added together with the ligand-expressing cells (NIH-3T3 cells stably transfected with Jag1 under control of the CMV promoter) 6–18 h after transfection. Luciferase activities were measured after 20 h of co-culture (Promega, Dual Glo Luciferase). Typically, four to eight replicates were analysed for each condition, and values were expressed as relative luciferase units (firefly signal divided by the *Renilla* signal). For the Notch2 signalling assay, U87MG cells (which predominantly express Notch2 as well as a low level of Notch1) were used in place of NIH3T3-Notch1 cells. As noted in the text or figure legends, the NIH-3T3-based assay was also performed in a 'transient' format in which an expression plasmid encoding the Notch receptor to be tested was transiently transfected together with the luciferase reporter plasmids.

T cell and marginal zone B cell analysis. BALB/c mice (Jackson Labs) at 12 weeks old were injected intraperitoneally every 4 days for 2 weeks with 5 mg kg^{-1} of anti-gD, anti-NRR1 or anti-NRR2 or 10 mg kg^{-1} of LTβR-Fc. Thymocytes were stained with anti-CD8-PE-Cy5 and anti-CD4-APC (BD Biosciences)[35,36] and splenocytes with anti-B220-APC, anti-CD5-PerCP, anti-CD23-PE and anti-CD21-FITC (BD Biosciences)[13], and flow cytometry was performed using a FACSCalibur (BD Biosciences) or a LSRII (BD Biosciences), with FACSDiva (BD Biosciences) and FlowJo (Tree Star) software.

Co-crystallization of Notch1 NRR and Fab. The Fab fragment of anti-NRR1 was expressed in *E. coli*, purified using Protein G-sepharose, and eluted with 0.58% acetic acid. Fab-containing fractions were then purified using a SP HiTrap column (GE Healthcare) with 20 mM MES pH 5.5 and a NaCl gradient. Human Notch NRR1 (residues A1449–P1729 with deletion of residues R1623–M1670 in the S1 loop) with the addition of a C-terminal 6×His tag was expressed in SF9 insect cells. NRR1 containing medium was separated from cells by centrifugation and purified using a 10 ml Ni-NTA Superflow (Qiagen) column. NRR1 was eluted with 500 mM NaCl and 300 mM imidazole in 20 mM Tris, pH 8.0. Fractions containing the NRR1 were pooled, and NRR1 was further purified by size exclusion chromatography (S-75, Pharmacia). NRR1-Fab complexes were prepared with a molar excess of Fab. The protein complex was purified using sizing column chromatography (S-200, Pharmacia) in 150 mM NaCl, 20 mM Tris-Bis, pH 6.5. Fractions containing complex were pooled and concentrated to approximately 6 mg ml^{-1} for crystallization trials. Crystals grew in sitting drops from a 1:1 mixture of protein and well solution (300 mM diammonium sulphate, 20% polyethylene glycol 5000 MME, 100 mM Tris pH 7.5) at 19 °C. Microseeding was used to control nucleation and crystal size. Crystals (0.2 mm × 0.15 mm × 0.1 mm) were cryo-protected in Paratone-N (Qiagen). Crystallographic data were collected at beamline 5.0.2 of the Advanced Light Source (Supplementary Table 1) and processed with XDS. The structure was solved by molecular replacement with the program PHASER (CCP4) using the structure of human Notch 2 NRR (PDB code 2OO4) and a variant of the humanized Fab 4D5 (ref. 37) as a search model followed by refinement with REFMAC5 (CCP4). NCS restraints were applied on the light chain Fv, heavy chain Fv, light chain constant domain, heavy chain constant domain and NRR1 residues 1461–1726 throughout refinement. The final model has excellent geometry with 99.2% of all residues in the most favoured or additional allowed regions of a Ramachandran plot and only 0.8% in either the generously allowed or disallowed regions. Structure figures were made with PyMOL (www.pymol.org).

Cell cycle, proliferation and apoptosis assays. Cells were plated at 5 × 10^5 ml^{-1} in growth medium and treated with DAPT or the equivalent volume of vehicle (dimethyl sulfoxide, DMSO), 10 μg ml^{-1} anti-gD (isotype control antibody) or 10 μg ml^{-1} anti-NRR1. Cells were split to 5 × 10^5 ml^{-1} every 2–3 days and retreated with drugs. After 7–8 days in culture, cells were fixed in 70% ethanol and stained with propidium iodide. DNA content was determined by flow cytometry and cell cycle analysis was performed using ModFit software (Verity).

For analysis of proliferation using Ki-67, T-ALL cells were maintained in Iscove's modified Dulbecco's medium supplemented with 8% fetal calf serum (FCS, Sigma). Cultures were inoculated with 1 × 10^6 cells and treated for 9 days

with 5 μM DAPT or an equivalent volume of DMSO, 10 μg ml^{-1} anti-gD or 10 μg ml^{-1} anti-NRR1; at days 4 and 7, cells were split 1:4 and 2:5, respectively. Intracellular staining using anti-Ki-67-FITC (BD Biosciences) was performed using the Cytofix/Cytoperm Fixation/Permeabilization kit (BD Biosciences) according to the manufacturer's instructions.

To analyse MT-3 growth *in vitro*, 1×10^4 cells were plated in wells of a 96-well plate in RPMI 1640 with 10% FCS and allowed to attach overnight. Cultures were then grown without FCS for 5 hours before the medium was changed to RPMI 1640 with 2.5% FCS and drugs were added. Medium was refreshed every 2–3 days. Viability was assayed after 1 week using CellTiter-Glo (Promega).

Immunoblotting. T-ALL cell lines were treated with 5 μM DAPT or an equivalent volume of DMSO, 50 μg ml^{-1} anti-gD antibody, or 10 or 50 μg ml^{-1} anti-NRR1 antibody for 48 h, with the addition of 10 μM MG132 for the last 3 h. Cells were lysed in 0.2% NP-40, 10 mM HEPES pH 7.9, 10 mM KCl, 1 mM EDTA, 10% glycerol, and 1× HALT protease inhibitor cocktail (Pierce). Nuclei were recovered by centrifugation and subsequently lysed in 1× RIPA buffer with protease inhibitor cocktail. Immunoblotting was performed using anti-Notch1 V1744 and anti-CREB antibodies from Cell Signaling Technologies.

***In vivo* tumour studies.** Animal studies were conducted in accordance with the Guide for the Care and Use of Laboratory Animals, published by the National Academy Press (2006). The Institutional Animal Care and Use Committee (IACUC) of Genentech approved all protocols. HPB-ALL cells (20×10^6), cultured in Iscove's modified Dulbecco's medium with 8% FCS (Sigma), were diluted in 200 μl 50% Matrigel (BD Biosciences)/50% PBS and implanted subcutaneously in $\gamma c^{-/-} \times Rag2^{-/-}$ mice[38]. When tumours reached 500 mm^3, mice were randomized into groups of equal average tumour volume, and treated with intraperitoneal doses of antibody. Tumour volumes were measured in two dimensions (length and width) using UltraCal-IV calipers (Model 54-10-111, Fred V. Fowler Company) and calculated using the formula: tumour volume = (length × width^2) × 0.5.

MT-3 cells, obtained from Deutsche Sammlung von Mikroorganismen und Zellkulturen (DSMZ), were cultured in RPMI 1640 media plus 1% L-glutamine with 10% FCS (Invitrogen). Cells (5×10^6 in 0.2 ml) were implanted in the right flank of 8-week-old female NCR nude mice (Taconic Farms). When tumours reached 82−227 mm^3, mice were treated as described above.

Calu-6 (human anaplastic carcinoma, probably lung) and HM7 (human colon carcinoma) tumour cell lines were grown in Ham's F12, low glucose DMEM 1:1 supplemented with 10% v/v FCS, 1% v/v penicillin/streptomycin, 2 mM L-glutamine and 1 μg ml^{-1} Fungizone (Invitrogen). Cells were suspended at a concentration of 1×10^8 or 1×10^9 cells ml^{-1} and injected (100 μl per mouse) subcutaneously into the dorsal flank of Balb/c nude mice (Harlan Sprague Dawley). When tumours reached a volume of 250–300 mm^3, cohorts of ten mice were randomly divided into groups. The transplanted tumours were measured twice weekly along the longest axis and the perpendicular axis, and tumour volumes were calculated. The mean tumour volumes were compared using Dunnett's *t*-test implemented in the JMPTM Statistical Analysis System (version 5.1 for Windows; SAS Institute), at a level of $P < 0.05$. Tumours were sectioned by cryostat to 7 μm, fixed with acetone and stained with DAPI (Invitrogen), hamster anti-CD31 (Serotec) and an anti-hamster Cy3 secondary antibody (Jackson ImmunoResearch). Slides were mounted with Fluorescent Mounting Medium (Dako). Images were taken with a Zeiss Axioskop2 microscope and analysed by ImageJ for area of DAPI stain and Cy3 staining. To normalize for cell number, the values for Cy3 stain were divided by the corresponding areas of DAPI stain. The ratio determined for the anti-ragweed control was set at a value of 1.

Neonatal retinal assay for angiogenesis. As described[21], CD1 neonates (Charles River) were injected intraperitoneally at 1 and 3 days after birth with either 10 mg kg^{-1} of ragweed control antibody or 20 mg kg^{-1} of anti-NRR1. Retinas were harvested 2 days later and fixed with 4% paraformaldehyde. After blocking with 5% BSA, 0.5% Triton X-100 for 1 h, followed by 1 M sodium citrate for 10 min, biotinylated isolectin B4 (Sigma) and anti-Ki-67 antibody (NeoMarkers) were added for incubation at 4 °C overnight. Retinas were subsequently washed and stained with streptavidin-Alexa 488 and Cy3-conjugated goat anti-rabbit in 1% BSA, 0.5% Triton X-100, before mounting and imaging using an epifluorescence microscope.

Histology and immunohistochemistry of mouse intestine tissue. BALB/c mice (Jackson Labs) at 12 weeks old were injected intraperitoneally twice per week, and small intestine samples were harvested on day 12. Formalin-fixed and paraffin-embedded tissues were sectioned at 3 μm thickness. Histochemical identification of intestinal cell types was performed with Alcian blue as recommended by the manufacturer (PolyScientific). For anti-Ki-67 staining, sections were pretreated with Target Retrieval Solution (S1700, DAKO), and incubated with rabbit anti-Ki-67 (1:200, clone SP6, Neomarkers). Secondary goat anti-rabbit at 7.5 μg ml^{-1} (Vector labs) was detected with the Vectastain ABC Elite Kit (Vector labs). Ki-67-stained sections were counterstained with Mayer's haematoxylin. Crypt areas of at least 100,000 μm^2, which contained at least 1,000 crypt cells, were analysed to determine the proliferative index, expressed as the percentages of Ki-67-positive crypt epithelial cells in the crypt areas examined. For anti-lysozyme staining, sections were processed on the Discovery XT platform (Ventana Medical Systems) using CC1m epitope recovery conditions, OmniMap-rabbit detection and Ventana haematoxylin II/with blueing counterstain. For HES-1 staining, anti-rat HES-1 (clone NM1, MBL International) was followed by TSA-HRP.

31. Lee, C. V. *et al.* High-affinity human antibodies from phage-displayed synthetic Fab libraries with a single framework scaffold. *J. Mol. Biol.* **340,** 1073–1093 (2004).
32. Liang, W.-C. *et al.* Function blocking antibodies to Neuropilin-1 generated from a designed human synthetic antibody phage library. *J. Mol. Biol.* **366,** 815–829 (2007).
33. Carter, P. *et al.* Humanization of an anti-p185HER2 antibody for human cancer therapy. *Proc. Natl Acad. Sci. USA* **89,** 4285–4289 (1992).
34. Sidhu, S. S. *et al.* Phage-displayed antibody libraries of synthetic heavy chain complementarity determining regions. *J. Mol. Biol.* **338,** 299–310 (2004).
35. Hagenbeek, T. J. & Spits, H. T-cell lymphomas in T-cell-specific Pten-deficient mice originate in the thymus. *Leukemia* **22,** 608–619 (2008).
36. Hagenbeek, T. J. *et al.* The loss of PTEN allows TCR αβ lineage thymocytes to bypass IL-7 and pre-TCR-mediated signaling. *J. Exp. Med.* **200,** 883–894 (2004).
37. Eigenbrot, C., Randal, M., Presta, L., Carter, P. & Kossiakoff, A. A. X-ray structures of the antigen-binding domains from three variants of humanized anti-p185HER2 antibody 4D5 and comparison with molecular modeling. *J. Mol. Biol.* **229,** 969–995 (1993).
38. Kirberg, J., Berns, A. & Boehmer, H. V. Peripheral T cell survival requires continual ligation of the T cell receptor to major histocompatibility complex-encoded molecules. *J. Exp. Med.* **186,** 1269–1275 (1997).

Vol 464|15 April 2010|doi:10.1038/nature08871

LETTERS

Chemoprevention of colorectal cancer by targeting APC-deficient cells for apoptosis

Ling Zhang[1]*, Xiaoyang Ren[1]*, Eckhard Alt[2], Xiaowen Bai[2], Shaoyi Huang[1], Zhengming Xu[1], Patrick M. Lynch[3], Mary P. Moyer[5], Xian-Feng Wen[1] & Xiangwei Wu[1,4]

Cancer chemoprevention uses natural, synthetic, or biological substances to reverse, suppress, or prevent either the initial phase of carcinogenesis or the progression of neoplastic cells to cancer[1]. It holds promise for overcoming problems associated with the treatment of late-stage cancers. However, the broad application of chemoprevention is compromised at present by limited effectiveness and potential toxicity. To overcome these challenges, here we developed a new chemoprevention approach that specifically targets premalignant tumour cells for apoptosis. We show that a deficiency in the adenomatous polyposis coli (*APC*) gene and subsequent activation of β-catenin lead to the repression of cellular caspase-8 inhibitor c-FLIP (also known as CFLAR) expression through activation of c-Myc, and that all-*trans*-retinyl acetate (RAc) independently upregulates tumour necrosis factor-related apoptosis-inducing ligand (TRAIL) death receptors and suppresses decoy receptors. Thus, the combination of TRAIL and RAc induces apoptosis in APC-deficient premalignant cells without affecting normal cells *in vitro*. In addition, we show that short-term and non-continuous TRAIL and RAc treatment induce apoptosis specifically in intestinal polyps, strongly inhibit tumour growth, and prolong survival in multiple intestinal neoplasms C57BL/6J-*Apc*^{Min}/J (*Apc*^{Min}) mice. With our approach, we further demonstrate that TRAIL and RAc induce significant cell death in human colon polyps, providing a potentially selective approach for colorectal cancer chemoprevention by targeting APC-deficient cells for apoptosis.

TRAIL (also known as TNFSF10 or Apo2L), is a membrane-bound TNF family ligand[2,3]. Although TRAIL induces apoptosis in cancer cells, it does not harm normal cells[4,5]. To test the response of premalignant tumour cells to TRAIL, we isolated primary adenoma cells from intestinal polyps (benign adenomas) of *Apc*^{Min} mice[6–8]. We also isolated intestinal epithelial cells from wild-type mice as controls (Supplementary Fig. 1a). TRAIL treatment did not induce any apoptosis in the isolated epithelial cells (Fig. 1a and Supplementary Fig. 1b). Previous reports indicate that certain retinoids synergize TRAIL-induced apoptosis in some cancer cell lines by inducing either TRAIL or its death receptors[9–11]. We explored the effect of RAc on TRAIL sensitivity in isolated primary adenoma and normal epithelial cells. Although RAc alone had no effect on the survival of either normal cells from control mice or adenoma cells, it specifically sensitized the adenoma cells to TRAIL-induced cell death (Fig. 1a and Supplementary Fig. 1b). These results show that RAc and TRAIL synergistically induce apoptosis in intestinal adenoma cells derived from *Apc*^{Min} mice.

The major difference between adenoma cells and normal cells is the loss of the wild-type *APC* allele in adenoma cells[12]. To test the role of APC in cell sensitivity to TRAIL and RAc, we knocked down APC expression in an immortalized normal human colon epithelial cell line, NCM356, using *APC* small interfering RNA (*APC*-siRNA) (Fig. 1b). We observed that APC knockdown and treatment with TRAIL and RAc resulted in caspase 8 cleavage and an increase in caspase 3/7 activity (Fig. 1c and Supplementary Fig. 1c). Furthermore, the caspase 8 inhibitor Z-IETD blocked caspase 3/7 activity (Supplementary Fig. 1c), suggesting that caspase 8 processing resulted in its activation. Similar results were obtained using an immortalized normal human bronchial epithelial cell line (BEAS-2B-BW1799 or BW1799) (Supplementary Fig. 2). These results demonstrate that APC deficiency is

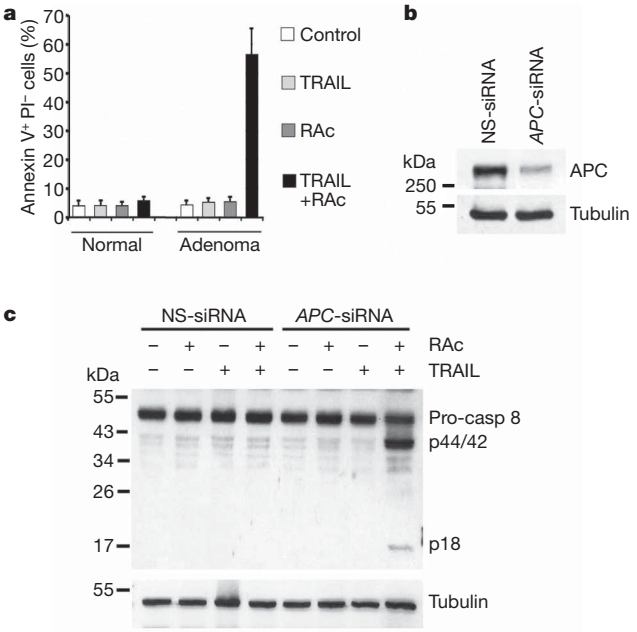

Figure 1 | TRAIL and RAc induce apoptosis in APC-deficient cells. **a**, Primary epithelial cells were isolated from normal mouse intestine and polyps from *Apc*^{Min} mice, and treated with TRAIL (50 ng ml^{-1} for 24 h), RAc (6.8 ng ml^{-1} for 48 h), or both (RAc for 48 h then TRAIL for 24 h). Cells were stained with annexin V–FITC (fluorescein isothiocyanate) and propidium iodide (PI). Early apoptotic cells (annexin V-positive, PI-negative) were counted. The data represent results from three independent experiments. Mean and s.d. are shown. **b**, Immortalized normal human colon epithelial cells (NCM356) were transfected with either non-specific (NS)-siRNA or *APC*-siRNA, and APC protein was detected 48 h after transfection by western blotting. **c**, The transfected NCM356 cells were treated and collected, and both full-length pro-caspase 8 and cleaved forms (p44/42 and p18) were detected by western blotting.

[1]Department of Head and Neck Surgery, [2]Department of Molecular Pathology, [3]Department of Gastroenterology, Hepatology and Nutrition, and [4]Department of Molecular and Cellular Oncology, The University of Texas M. D. Anderson Cancer Center, 1515 Holcombe Boulevard, Houston, Texas 77030, USA. [5]INCELL Corporation, San Antonio, Texas 78249, USA.
*These authors contributed equally to this work.

the key factor in sensitizing normal cells to apoptosis induced by the combination of TRAIL and RAc.

Inactivation of *APC* leads to stabilization and nuclear translocation of β-catenin, and to transcriptional activation of target genes, such as *c-Myc* (also known as *MYC*) and cyclin D1 (*CCDN1*)[13]. To investigate the signalling events in the APC pathway required for sensitizing cells to TRAIL and RAc, we transfected either stabilized β-catenin[14] or full-length *c-Myc* into NCM356 cells (Supplementary Fig. 3a, b). The expression of either β-catenin mutant or c-Myc led to TRAIL- and RAc-mediated caspase 8 cleavage and activation (Fig. 2a and Supplementary Fig. 3c). Transfection of cyclin D1 had no effect on TRAIL- and RAc-induced apoptosis in NCM356 and other cells (data not shown). We then determined the requirement of c-Myc for sensitizing cells to TRAIL and RAc. APC knockdown led to an increase in c-Myc expression, as expected. Co-transfection of *c-Myc*-siRNA blocked APC deficiency-mediated c-Myc induction and caspase 8 cleavage/activation in response to TRAIL and RAc (Fig. 2b and Supplementary Fig. 3c). We further confirmed these observations using independent siRNAs (Supplementary Fig. 4). These results indicate that the effect of APC on the cell response to TRAIL and RAc is largely dependent on APC/β-catenin-mediated activation of c-Myc.

Other studies have shown that c-Myc directly suppresses c-FLIP expression, and that this activity correlates with TRAIL sensitivity[15]. NCM356 cells expressed readily detectable c-FLIP, and transfection of c-Myc resulted in a significant decrease in c-FLIP expression and caspase 8 cleavage (Fig. 2c). Direct suppression of c-FLIP expression by *c-FLIP*-siRNA led to caspase 8 cleavage and activation in NCM356 cells treated with TRAIL and RAc. Rescue of c-FLIP expression by transfection of a c-FLIP expression plasmid prevented c-Myc-induced caspase 8 processing and activation in response to TRAIL and RAc (Fig. 2c and Supplementary Fig. 3c). Similar results were obtained in BW1799 cells (Supplementary Fig. 5). In addition to suppressing c-FLIP expression, c-Myc could also act on mitochondria to facilitate TRAIL-induced apoptosis[16]. To test this possibility, we performed rescue experiments using BCL2 and BCL-XL (also known as BCL2L1). Overexpression of either BCL2 or BCL-XL did not inhibit c-Myc-mediated caspase 8 processing and activation in response to TRAIL and RAc (Fig. 2c and Supplementary Fig. 3c). These results indicate that APC deficiency sensitizes normal cells to TRAIL and RAc by suppressing c-FLIP expression through the activation of β-catenin and c-Myc.

Previous reports have shown that certain retinoids sensitize some cancer cells to TRAIL-induced apoptosis by upregulating either TRAIL or the TRAIL receptors DR4 and DR5 (also known as TNFRSF10A and TNFRSF10B, respectively)[9, 10]. To test the effect of RAc on normal cells in our setting, we examined the expression of TRAIL receptors in NCM356, BW1779 and CRL1831 (another immortalized normal human colon epithelial cell line) cells after RAc treatment. Although RAc did not induce TRAIL expression (data not shown), it induced DR4 or DR5 expression in these cells (Fig. 2d and Supplementary Fig. 6a). Notably, RAc strongly suppressed DcR1 (also known as TNFRSF10C) expression in these cells (Fig. 2d and Supplementary Fig. 6a). In addition, DcR2 (TNFRSF10D) expression was inhibited by RAc in NCM356 cells (Fig. 2d). We further showed that RAc caused similar changes in messenger RNA levels in NCM356 cells (Supplementary Fig. 6b), suggesting that RAc modulates TRAIL receptor expression at the levels of mRNA.

Overexpression of DR5 sensitized APC-knockdown cells to TRAIL-induced caspase 8 cleavage and activation (Fig. 2e and Supplementary Fig. 6c). Pretreatment of APC-knockdown cells with a DcR1-neutralizing antibody to block the TRAIL–DcR1 interaction also partially induced caspase 8 cleavage and activation after TRAIL treatment, and this effect was further enhanced in DR5-transfected cells (Fig. 2e and Supplementary Fig. 6c). Similar results were obtained in BW1799 cells (Supplementary Fig. 6d, e). These data indicate that both induction of DR5 and suppression of DcR1 contribute to the effect of RAc in sensitizing APC-deficient cells to apoptosis.

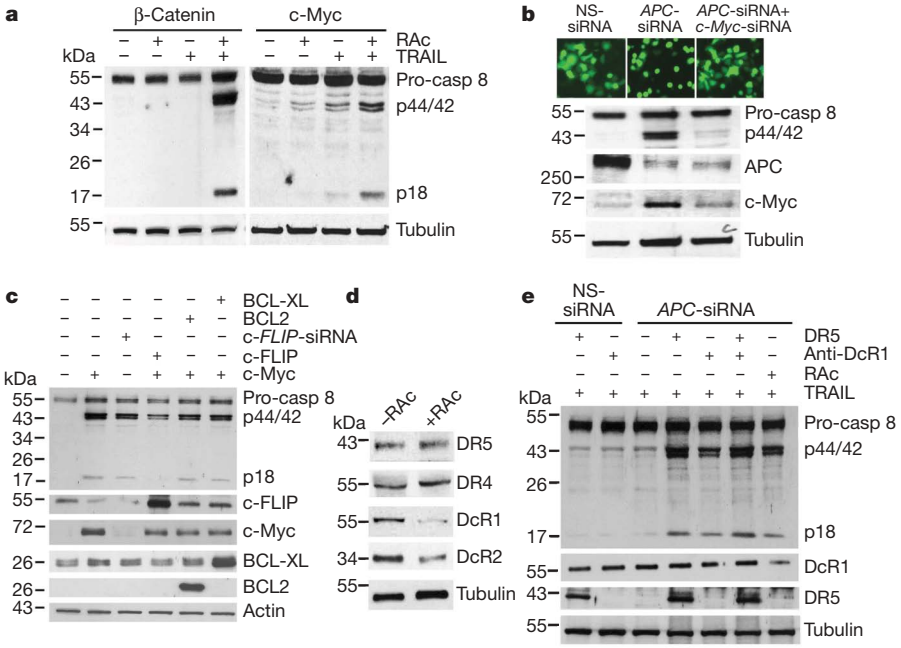

Figure 2 | Downregulation of c-FLIP by APC/β-catenin-mediated activation of c-Myc and modulation of TRAIL receptor expression by RAc contribute to the activation of TRAIL signalling. **a**, NCM356 cells were transfected with either β-catenin or c-Myc and treated with TRAIL, RAc or both. Cleavage of caspase 8 was detected by western blotting. **b**, NCM356 cells were transfected with non-specific siRNA, *APC*-siRNA (GFP tagged), or *APC*-siRNA plus *c-Myc*-siRNA. The transfected cells were treated with RAc and TRAIL, and photographs were taken (original magnification, ×20). The expression of APC, c-Myc and caspase 8 was detected by western blotting. **c**, NCM356 cells were transfected with c-Myc, *c-FLIP*-siRNA, c-Myc and c-FLIP, c-Myc and BCL2, or c-Myc and BCL-XL. The transfected cells were treated with RAc and TRAIL. The expression of c-Myc, c-FLIP, BCL2, BCL-XL and caspase 8 was detected by western blotting. **d**, NCM356 cells were treated with RAc for 48 h, and the expression of DR4, DR5, DcR1 and DcR2 was detected by western blotting. **e**, NCM356 cells were transfected with non-specific siRNA or *APC*-siRNA, with/without DR5, and with/without pre-treatment with an anti-DcR1 antibody. Transfected cells were treated with TRAIL alone or with TRAIL and RAc, as indicated. Cleavage of caspase 8 was detected by western blotting.

We next tested the effect of TRAIL and RAc in Apc^{Min} mice *in vivo*. We first treated the 3-month-old Apc^{Min} mice with TRAIL and low-dose RAc for 15 treatment cycles over 6 weeks. We observed that TRAIL and RAc significantly inhibited the growth of intestinal polyps as compared to controls (Fig. 3a). Histological analysis of tumours and adjacent normal tissues in treated mice showed that many cells in tumours, but not in normal tissues, contain condensed nuclei, suggesting that cells in the tumours are dying (Fig. 3b). This observation was confirmed by TUNEL (terminal deoxynucleotidyl transferase biotin-dUTP nick end labelling) analysis (Fig. 3b). When the total numbers and sizes of the polyps were compared 1 month after the 6-week treatment period, the treated mice showed on average a four- to fivefold decrease in the total number of polyps relative to the mice treated with PBS control (Fig. 3c). The reduction in large polyps ($\geq$2 mm) was much more pronounced (to about 1/30 of control) (Fig. 3c). These data demonstrate that the combination of TRAIL and RAc induces apoptosis specifically in *Apc*-defective polyps and effectively suppresses the tumour growth.

Biochemically, the accumulation of soluble β-catenin and induction of c-Myc expression were seen in the polyps of Apc^{Min} mice but not in normal tissue (Supplementary Fig. 7a). c-FLIP protein was readily detectable in normal tissue, whereas it was significantly reduced in polyps (Supplementary Fig. 7a). Consistent with our *in vitro* observations, RAc induced DR5 expression and repressed DcR1 in both the polyps in Apc^{Min} mice (Supplementary Fig. 7b).

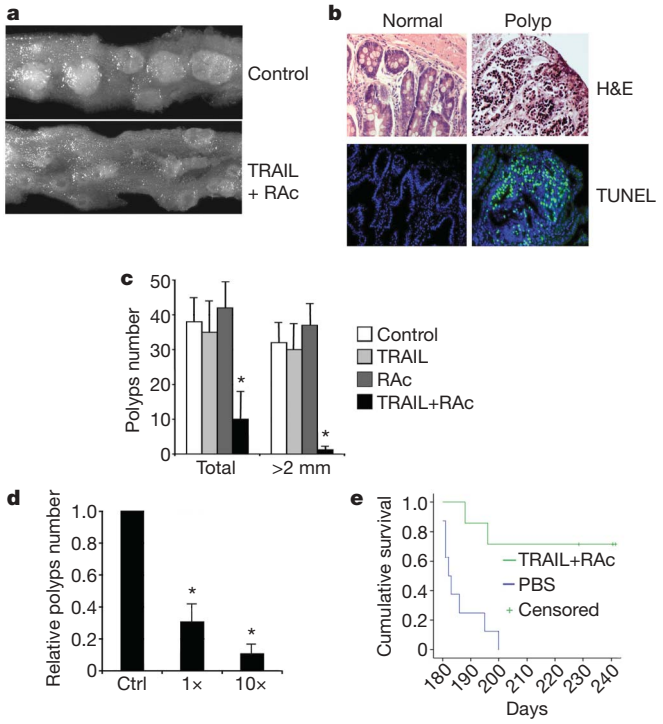

Figure 3 | Treatment with TRAIL and RAc induces cell death in the polyps, inhibits tumour growth, and promote survival in Apc^{Min} mice. **a**, The Apc^{Min} mice were treated with either PBS control or TRAIL plus RAc for 15 treatment cycles. Intestinal polyps were examined 1 month after the treatment and photographs were taken. Original magnification, ×1. **b**, The polyp samples and adjacent sections were stained by H&E and TUNEL assay. Surrounding normal tissue was used as the control. Representative photographs are shown. Original magnification, ×20. **c**, Intestinal polyps in the entire intestinal track were examined and counted. Each treatment group contained 5–7 mice. Mean and s.d. are shown. *$P < 0.001$. **d**, The Apc^{Min} mice were treated with either 1× or 10× doses of TRAIL and RAc for two cycles within a week. The intestinal polyps in the entire intestinal track were examined and counted. Each treatment group contained 5–7 mice. Mean and s.d. are shown. Ctrl, control. *$P < 0.001$. **e**, Kaplan–Meier survival analysis of Apc^{Min} mice. Apc^{Min} mice at 4 months were treated with TRAIL (3 mg kg^{-1}) plus RAc (68 μg kg^{-1}) or with control PBS every 3 weeks for 5 cycles. The endpoint was reached either when mice were moribund or at day 243. Mean survival time was 212.8 ± 5.9 days in the TRAIL plus RAc group (7 mice), and 186 ± 2.6 days in the PBS-treated group (8 mice), with log-rank test $P \leq 0.001$. All statistical analyses were performed using SPSS software (version 16.0).

Because TRAIL and RAc together target APC-deficient cells for apoptosis, this combination has the potential to achieve chemoprevention in short-term therapy. To test this, we applied two short consecutive TRAIL and RAc treatment cycles to Apc^{Min} within a week and analysed the intestinal tumours 2 weeks after treatment. After only two treatments, we observed a 69% reduction in the number of polyps when 3 mg kg^{-1} TRAIL and 68 μg kg^{-1} RAc were injected into Apc^{Min} mice (Fig. 3d). The tumour numbers were further reduced to 10% of the control when tenfold higher doses of TRAIL and RAc were used (Fig. 3d). These data indicate that short-term treatment with TRAIL and RAc is capable of inhibiting growth of premalignant cells in Apc^{Min} mice. To test the effect of TRAIL and RAc treatment on the survival of Apc^{Min} mice, we applied five non-consecutive TRAIL and RAc treatments to Apc^{Min} mice within 4 months (average 1 treatment every 3 weeks). All mice in the control group treated with PBS died within 7 months; however, five of the seven treated mice survived beyond 8 months ($P \leq 0.001$) (Fig. 3e), demonstrating that non-continuous TRAIL and RAc treatment yields a long-term survival benefit for Apc^{Min} mice. Although it is likely that the two early deaths in the treatment group resulted from a late start in treatment, it cannot be ruled out that intrinsic resistance, heterogeneity, genetic or epigenetic changes of premalignant cells can influence the effect of TRAIL treatment. Further study will provide a more in-depth assessment.

As a first step to demonstrating the efficacy and relevance of TRAIL and RAc treatment in humans, we treated biopsy samples of both normal and tumour regions from consenting familial adenomatous polyposis (FAP) patients under organ culture conditions as reported[17,18]. A cross-section of normal colon tissue showed a round and defined structure of individual villus consisting of a monolayer of colon epithelial cells and membrane β-catenin staining pattern, whereas dysplastic colon polyps showed much larger villi, bigger nuclei, an irregular structure consisting of several epithelial layers, and enhanced nuclear β-catenin staining (Fig. 4a). Treatment of normal tissue slices with TRAIL and RAc did not induce significant cell death, whereas the same treatment in the polyp samples resulted in significant cell death, as detected by TUNEL assay (Fig. 4a). Quantification of TUNEL-positive cells showed that TRAIL and RAc killed an average of 57% of the cells in the human colon polyps (Fig. 4b). These results verify that TRAIL and RAc are effective against human polyps from FAP patients *in vitro*, and that our approach holds promise for the chemoprevention of colon cancer in humans.

A major concern in chemoprevention is potential toxicity associated with treatment. We have shown that TRAIL and RAc target the APC–β-catenin–c-Myc signalling pathway for apoptosis. Because activation of β-catenin is involved in stem cell self-renewal and maintenance in adult tissues[19], TRAIL and RAc could possibly interact in a detrimental way with stem cells. To investigate this, we first tested the effect of TRAIL and RAc on intestinal stem cells (ISCs) in Apc^{Min} mice. Using the putative ISC marker leucine-rich-repeat-containing G-protein-coupled receptor 5 (Lgr5)[20], we noted that most of the Lgr5-positive cells in the normal sections were located at the bottom of the crypt as reported[20] (Fig. 4c). Staining of active caspase 3 showed extensive staining in tumour sections, similar to the findings shown in Fig. 3b (Fig. 4c). More importantly, no staining was detected in serial sections from the normal region, including Lgr5$^+$ cells in the crypt regions where the ISC resides (Fig. 4c). We also studied the effect of long-term TRAIL and RAc treatment on tissue-resident stem cells isolated from pararenal adipose tissue (mice adipose-tissue-derived stem cells, or mASCs) of Apc^{Min} mice[21] (Supplementary Fig. 8). We found no detectable effect on morphology (data not shown), neural differentiation (data not shown), proliferation and apoptosis, senescence, osteogenesis and adipogenesis both *in vitro* and *in vivo* (Supplementary Figs 9 and 10). Taken together, these

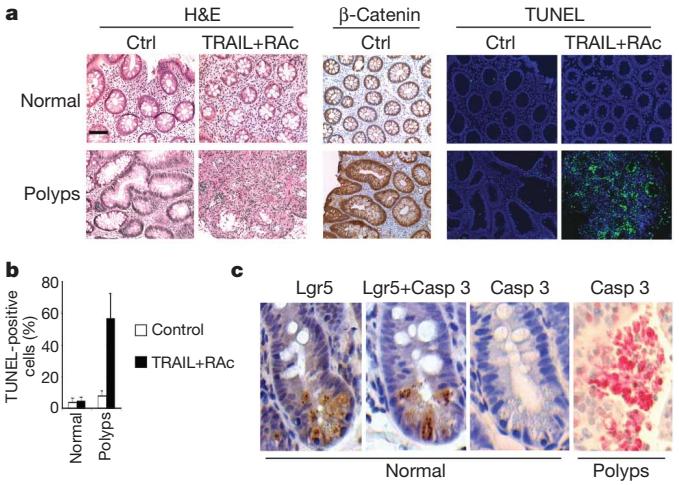

Figure 4 | Effect of TRAIL and RAc on human colon polyps and ISCs. a, Tissue slices from both the normal region and colon polyps from FAP patients were treated with RAc (6.8 ng ml^{-1}) for 48 h and then with TRAIL (100 ng ml^{-1}) for a further 24 h (TRAIL+RAc). The samples treated with vehicle were used as controls. H&E staining, β-catenin staining, and TUNEL assay (green) were performed. Nuclei were revealed by DAPI (4′,6-diamidino-2-phenylindole) staining (blue). Scale bar, 100 μm. Representative photographs are shown. **b**, TUNEL-positive cells (green) were counted and compared to the number of nuclei in several fields under a microscope. Mean and s.d. are shown. The data are derived from samples of four patients. **c**, *Apc*^{Min} mice were treated with five non-continuous cycles of TRAIL and RAc. Both the normal tissue and polyps of the intestine were serially sectioned and stained with Lgr5 (brown), activated caspase 3 (red), or both. Many serial sections were analysed and representative photographs are shown. Original magnification, ×60.

results indicate that TRAIL and RAc exert no negative effect on stem cells (ISCs and mASCs) in mice.

In summary, we discovered a synergistic interaction among TRAIL, RAc and tumour suppressor APC, which results in the specific induction of apoptosis in APC-deficient cells by TRAIL and RAc (Supplementary Fig. 11). Induction of apoptosis represents a most potent cellular mechanism against cancer, and selectively eliminating premalignant tumour cells by TRAIL and RAc is an effective method of chemoprevention. More notably, we demonstrate that the chemopreventive effect of TRAIL and RAc can be achieved by short-term intermittent and non-continuous treatment cycles. Thereby, the potential side effects and costs often associated with long-term treatment could be minimized and controlled.

METHODS SUMMARY

Recombinant soluble human TRAIL was prepared according to a published method[22]. For TRAIL and RAc treatment, the cells were first treated with RAc (6.8 ng ml^{-1}) for 48 h, and then TRAIL (50 or 500 ng ml^{-1}) was added. Cell viability was determined using the Annexin V-FITC Apoptosis Detection Kit (Sigma). Caspase 3/7 activity was measured using the Apo-ONE Homogeneous Caspase 3/7 assay kit (Promega). Transfection and western blotting were performed as described previously[23]. The apoptotic cells in tumour samples were detected by TUNEL assay using an apoptosis detection kit (R&D Systems) or by caspase 3 staining using an anti-cleaved caspase 3 antibody (Cell Signaling). *Apc*^{Min} mice were purchased from the Jackson Laboratory. For treatment, *Apc*^{Min} mice at 3 months of age were first given RAc by intraperitoneal (i.p.) injection at 68 μg kg^{-1}. After 48 h, an i.p. injection of TRAIL was given at 3 mg kg^{-1}. After 24 h, RAc was injected again, followed by TRAIL injection. The procedure was repeated for 6 weeks, resulting in a total of 15 treatment cycles. Whole intestines were collected immediately after euthanasia and opened longitudinally so that polyps could be counted and measured. Tissues were processed either by formalin fixation or by being frozen in liquid nitrogen for tissue protein extraction, haematoxylin and eosin (H&E) staining, immunohistochemical analysis, and TUNEL assay. All animal experiments were reviewed and approved by the Institutional Animal Care and Use Committee of The University of Texas M. D. Anderson Cancer Center. Fresh human tissue samples were obtained from consenting FAP patients according to an Institutional Review Board-approved protocol.

Full Methods and any associated references are available in the online version of the paper at www.nature.com/nature.

Received 12 October 2009; accepted 3 February 2010.
Published online 28 March 2010.

1. Sporn, M. B., Dunlop, N. M., Newton, D. L. & Smith, J. M. Prevention of chemical carcinogenesis by vitamin A and its synthetic analogs (retinoids). *Fed. Proc.* **35,** 1332–1338 (1976).
2. Pitti, R. M. *et al.* Induction of apoptosis by Apo-2 ligand, a new member of the tumor necrosis factor cytokine family. *J. Biol. Chem.* **271,** 12687–12690 (1996).
3. Wiley, S. R. *et al.* Identification and characterization of a new member of the TNF family that induces apoptosis. *Immunity* **3,** 673–682 (1995).
4. Koschny, R., Walczak, H. & Ganten, T. M. The promise of TRAIL-potential and risks of a novel anticancer therapy. *J. Mol. Med.* **85,** 923–935 (2007).
5. Ashkenazi, A. Directing cancer cells to self-destruct with pro-apoptotic receptor agonists. *Nature Rev. Drug Discov.* **7,** 1001–1012 (2008).
6. Moser, A. R., Pitot, H. C. & Dove, W. F. A dominant mutation that predisposes to multiple intestinal neoplasia in the mouse. *Science* **247,** 322–324 (1990).
7. Su, L. K. *et al.* Multiple intestinal neoplasia caused by a mutation in the murine homolog of the APC gene. *Science* **256,** 668–670 (1992).
8. Fodde, R. *et al.* A targeted chain-termination mutation in the mouse Apc gene results in multiple intestinal tumors. *Proc. Natl Acad. Sci. USA* **91,** 8969–8973 (1994).
9. Altucci, L. *et al.* Retinoic acid-induced apoptosis in leukemia cells is mediated by paracrine action of tumor-selective death ligand TRAIL. *Nature Med.* **7,** 680–686 (2001).
10. Sun, S. Y., Yue, P., Hong, W. K. & Lotan, R. Augmentation of tumor necrosis factor-related apoptosis-inducing ligand (TRAIL)-induced apoptosis by the synthetic retinoid 6-[3-(1-adamantyl)-4-hydroxyphenyl]-2-naphthalene carboxylic acid (CD437) through up-regulation of TRAIL receptors in human lung cancer cells. *Cancer Res.* **60,** 7149–7155 (2000).
11. Jin, F. *et al.* Activation of nuclear factor-κB contributes to induction of death receptors and apoptosis by the synthetic retinoid CD437 in DU145 human prostate cancer cells. *Cancer Res.* **65,** 6354–6363 (2005).
12. Yang, K. *et al.* A mouse model of human familial adenomatous polyposis. *J. Exp. Zool.* **277,** 245–254 (1997).
13. Polakis, P. The many ways of Wnt in cancer. *Curr. Opin. Genet. Dev.* **17,** 45–51 (2007).
14. Chen, D. *et al.* SKI activates Wnt/beta-catenin signaling in human melanoma. *Cancer Res.* **63,** 6626–6634 (2003).
15. Ricci, M. S. *et al.* Direct repression of FLIP expression by c-myc is a major determinant of TRAIL sensitivity. *Mol. Cell. Biol.* **24,** 8541–8555 (2004).
16. Nieminen, A. I., Partanen, J. I., Hau, A. & Klefstrom, J. c-Myc primed mitochondria determine cellular sensitivity to TRAIL-induced apoptosis. *EMBO J.* **26,** 1055–1067 (2007).
17. Willson, J. K., Bittner, G. N., Oberley, T. D., Meisner, L. F. & Weese, J. L. Cell culture of human colon adenomas and carcinomas. *Cancer Res.* **47,** 2704–2713 (1987).
18. Hasson, E. *et al.* Solid tissues can be manipulated *ex vivo* and used as vehicles for gene therapy. *J. Gene Med.* **7,** 926–935 (2005).
19. Nusse, R. Wnt signaling and stem cell control. *Cell Res.* **18,** 523–527 (2008).
20. Barker, N. *et al.* Identification of stem cells in small intestine and colon by marker gene *Lgr5*. *Nature* **449,** 1003–1007 (2007).
21. Bai, X., Sadat, S., Gehmert, S., Alt, E. & Song, Y. H. VEGF receptor Flk-1 plays an important role in c-kit expression in adipose tissue derived stem cells. *FEBS Lett.* **581,** 4681–4684 (2007).
22. Ren, X., Xu, Z., Myers, J. N. & Wu, X. Bypass NFκB-mediated survival pathways by TRAIL and Smac. *Cancer Biol. Ther.* **6,** 1031–1035 (2007).
23. Deng, Y., Ren, X., Yang, L., Lin, Y. & Wu, X. A JNK-dependent pathway is required for TNFα-induced apoptosis. *Cell* **115,** 61–70 (2003).

Supplementary Information is linked to the online version of the paper at www.nature.com/nature.

Acknowledgements We thank H. Yang for technical support, R. Lotan for the BW1799 cells, and W. El-Deiry for DR5 expression plasmid; and M. Chambers, J. Yate, L. Ingram, D. Chow and G. Reyes for their involvement in IRB approval and human tissue acquisition. We also thank J. Vykoukal, A. E. Kadala and D. Malone for their help in editing the manuscript. This work was supported by NIH grant AI063063 and Institutional Funds from M. D. Anderson Cancer Center (to X.W.), and in part by Alliance of Cardiovascular Researchers grant 543102 (to E.A.).

Author Contributions X.W. designed and supervised the experiments, and also analysed the data and wrote the paper. X.R. initiated the experiments, and L.Z. performed most of the experiments and participated in designing experiments and analysing data. E.A. designed the mASC experiments and edited and partially wrote the paper. X.B. performed experiments in mASCs. S.H., Z.X. and X.-F.W. helped perform the experiments. P.M.L. provided human tumour samples. M.P.M. provided cell lines.

Author Information Reprints and permissions information is available at www.nature.com/reprints. The authors declare no competing financial interests. Correspondence and requests for materials should be addressed to X.W. (xwwu@mdanderson.org).

METHODS

Cell lines and transfection. Primary mouse intestinal epithelial cells and adenoma cells were isolated from either normal C57/B6 mice or Apc^{Min} mice as reported[24]. In brief, the small intestine or polyps were cut into 2–3-mm segments. The tissues were transferred to a 15-ml tube, washed at least 10 times in 10 ml of fresh Hank's buffered salt solution (HBSS) with vigorous shaking, and diced into $<1\text{-mm}^3$ pieces using a sharp scalpel blade. The tissue pieces were transferred to a 15-ml tube with 10 ml DMEM containing 100 U ml^{-1} penicillin and 100 μg ml^{-1} streptomycin. The mixtures were allowed to settle under gravity for 1 min, and all but a small amount at the bottom was carefully removed. This procedure was repeated five times. The mixtures were then washed with DMEM three times and the pellet was resuspended in the epithelial cell medium containing equal volumes of DMEM and Ham's F12 medium with the following additives: 5 μg ml^{-1} insulin, 10 ng ml^{-1} epidermal growth factor, 20 mM 4-(2-hydroxyethyl)-1-piperazineethanesulfonic acid (HEPES), 2 mM glutamine, 100 U ml^{-1} penicillin, 100 μg ml^{-1} streptomycin, 0.2% D-glucose, and 2% FBS. CRL1831 cells were obtained from the American Type Culture Collection (ATCC). NCM356 cells were obtained from INCELL and grown in A52 medium supplemented with 30 μg ml^{-1} bovine pituitary extract, 8 μg ml^{-1} vitamin C, 2 mM glutamine and 1 nM dexamethasone. A52 was custom made without folic acid, which was added at concentrations of 25, 50, 75 and 150 nM before use. BW1799 cells were provided by R. Lotan and maintained in keratinocyte-SFM medium (Gibco).

Antibodies and other materials. Anti-full-length and anti-cleaved caspase 8, anti-cleaved caspase 3, anti-c-FLIP, anti-DR5, anti-BCL2 and anti-BCL-XL antibodies were purchased from Cell Signaling Technology. Anti-c-Myc and anti-cytokeratin-20 (CK-20) antibodies were purchased from Santa Cruz Biotechnology. Anti-APC was obtained from Calbiochem. Anti-β-actin and anti-α-tubulin were purchased from Sigma. Anti-DcR1 and anti-DcR2 antibodies were purchased from Imgenex. Anti-DR4 antibody was obtained from Upstate. Anti-β-catenin antibody was purchased from BD Transduction Laboratories. FITC-conjugated anti-mouse CD14 and CD31 and phycoerythrin (PE)-conjugated anti-mouse CD44 and CD90 antibodies were purchased from BD Pharmingen. Anti-Lgr5 antibody was obtained from Abcam. Recombinant soluble TRAIL was prepared according to published results[22]. RAc was purchased from Sigma.

Plasmids and vector-based siRNA construction. The c-Myc, β-catenin, BCL2 and BCL-XL expression plasmids were described previously[14,23,25]. The DR5 expression plasmid was provided by W. El-Deiry. The full-length *c-FLIP* cDNA was generated by reverse-transcription PCR of total RNA from HeLa cells. All siRNAs except *APC*-siRNA(2) and *c-Myc*-siRNA(2) were generated in pSUPER as described elsewhere[23]. The target sequence of human *APC* is 5′-GGA AGTATTGAAGATGAAG-3′, of human *c-FLIP* is 5′-AGAGGTAAGCTGTCTG TCG-3′, and of human *c-Myc* is 5′-TTCAAGAGA-3′. The *APC*-siRNA(2) and *c-Myc*-siRNA(2) were purchased from Open Biosystems with target sequences of 5′-GCTGTGAAATTCACAGTAATA-3′ and 5′-CCGAGAACAGTTGAAACAC AAA-3′, respectively.

Quantitative PCR. Total RNA was extracted using Trizol reagent according to the manufacturer's instructions (Invitrogen). The cDNA was prepared using the SuperScript cDNA Synthesis Kit (Invitrogen). Quantitative PCR was performed using the SYBR Green Quantitative PCR kit from Thermo Scientific in a Bio-Rad C1000TM Thermal Cycler following the manufacturer's protocol. Amplification was carried out in a total volume of 20 μl for 40 cycles of 15 s at 95 °C, 20 s at 60 °C, and 30 s at 72 °C. Samples were run in triplicate and their relative expression was determined by normalizing expression of each target *GAPDH*. These were then compared with the normalized expression in control untreated sample to calculate a fold-change value. Primer sequences were as follows: human *GAPDH*, 5′-TGCACCACCAACTGCTTAGC-3′ and 5′-GGCATGGACTGT GGTCATGAG-3′; human *DR4*, 5′- TGTACGCCCTGGAGTGACAT-3′ and 5′-CACCAACAGCAACGGAACAA-3′; human *DR5*, 5′-CACTCACTGGAATG ACCTCCTTT-3′ and 5′-GTGCAGGGACTTAGCTCCACTT-3′; human *DcR1*, 5′-CCCTAAAGTTCGTCGTCGTCAT-3′ and 5′-GGGCAGTGGTGGCAGAG TA-3′; and human *DcR2*, 5′-ACAGAGGCGCAGCCTCAA-3′ and 5′-ACG GGTTACAGGCTCCAGTATATT-3′.

***Ex vivo* organ cultures.** Paired tumour and adjacent normal samples from consenting patients (male and female) undergoing colonoscopy at the MD Anderson Cancer Center Gastrointestinal Oncology and Digestive Diseases endoscopy and surgical unit were collected, transferred to research laboratory in cold media, and processed within 1 h in a sterile tissue culture hood. The culture condition is modified on the basis of previous reports[17,18]. In brief, the culture medium consists of a 1:1 mixture of DMEM and Ham's F12 with 5% FCS, 10 mM HEPES, 0.5% dimethylsulphoxide (DMSO), 0.5 μg ml^{-1} hydrocortisone, 1% MEM vitamins solution, 5 μg ml^{-1} insulin, 5 μg ml^{-1} transferin, 5 ng ml^{-1} selenium, 100 U ml^{-1} penicillin, 100 μg ml^{-1} streptomycin, 15 μg ml^{-1} gentamicin and 15 μg ml^{-1} ciproxin. The tissue was washed five times in culture media, and placed in a sterile glass dish where all necrotic and visible connective tissue was removed. Tissue was sliced gently into very thin pieces using a blade, placed in a 6-well tissue culture dish with 1 ml of growth media, and incubated at 37 °C, 5% CO_2 for 24 h. Plates were inspected visually for contamination and the media was pulled off and replaced every 2 days. After 1 day in culture, the tissue slices were subject to various treatment protocols.

Isolation and culture of adipose tissue-derived stem cells. Subcutaneous adipose tissue was obtained from three mice (one wild-type and two Apc^{Min}) or from Apc^{Min} mice that had received five cycles of TRAIL and RAc treatment within 4 months following our institutional guidelines. Cells were isolated from adipose tissue as described previously[26,27]. Adipose tissue was minced and incubated for 90 min at 37 °C on a shaker with Liberase Blendzyme 3 (Roche) at a concentration of 4 U g^{-1} fat tissue in PBS. The digested tissue was sequentially filtered through 100-μm and 40-μm filters (Fisher Scientific) and centrifuged at 450*g* for 5 min. The supernatant containing adipocytes and debris was discarded; the pelleted cells were washed twice with HBSS (Cellgro) and finally resuspended in stem cell growth medium (SCGM), which contained αMEM (Cellgro), 20% FBS (Atlanta Biologicals), 2 mM glutamine (Cellgro), and 100 U ml^{-1} penicillin with 100 μg ml^{-1} streptomycin (Cellgro). Cells adhering to plastic were designated as mASCs and grown in Nunclon culture flasks (Nunc) at 37 °C in a humidified atmosphere containing 5% CO_2, followed by daily washes to remove red blood cells and non-attached cells. After the mASCs became confluent (passage 0), cells were digested and seeded at a density of 3,000 cells cm^{-2} (passage 1).

Assays of mASCs. For *in vitro* treatment assays, mASCs were cultured in the presence TRAIL (50 ng ml^{-1}), or RAc (6.8 ng ml^{-1}), or both, for 2 months (about 60 doublings). To study the effect of TRAIL and RAc treatment *in vivo*, mASCs were collected from Apc^{Min} mice that had received five treatment cycles of TRAIL (3 mg kg^{-1}) and RAc (68 μg kg^{-1}) in 4 months. Cell proliferation was determined by counting live cells. Apoptosis was measured by Annexin V staining (BD Biosciences) using a FACSCalibur flow cytometer (Becton Dickinson) and Cell Quest software (Becton Dickinson). Cell senescence was determined by β-galactosidase activity at pH 6 using the Senescent Cells Staining Kit (Cell Signaling) according to the provided protocol. Osteogenic differentiation of mASCs was induced in osteogenic medium containing high-glucose DMEM supplemented with 10% FBS, 0.1 μM dexamethasone, 200 μM L-ascorbic acid, and 10 mM β-glycerol phosphate (Sigma). The medium was changed every 3 days for 2 weeks. In the control experiment, mASCs were cultured in control medium containing high-glucose DMEM plus 10% FBS for 2 weeks. To assess mineralization, calcium deposits in cultures were stained with Alizarin Red S (Sigma). The osteogenic efficiency was then determined using an Osteogenesis Quantitation Kit (Chemicon) following the manufacture's instructions. The adipogenic ability of mASCs was induced in adipogenic medium for up to 2 weeks as described previously[26,27]. The adipogenic medium contained low-glucose DMEM supplemented with 10% FBS, 2 mM L-glutamine, 100 U ml^{-1} penicillin, 100 μg ml^{-1} streptomycin (Cellgro), 100 μM L-ascorbic acid, 1 μM dexamethasone, 0.5 mM 1-methyl-3-isobutylxanthine, 100 μM indomethacin, and 10 μg ml^{-1} insulin (Sigma). mASCs of the control group were cultured in low-glucose DMEM plus 10% FBS (control media). The medium was changed every 3 days. Adipogenesis of cells was assessed by incubating cells with Oil Red O solution (Sigma) to stain neutral lipids in the cytoplasm. The adipogenic efficiency of mASCs was then determined using the Adipogenesis Quantitation Kit (Chemicon) according to the protocol provided by the manufacturer.

Immunohistochemistry and immunofluorescence staining. Tissues in paraffin block were sectioned at 4-μM thickness. After deparaffinization, antigen retrieval was performed using citrate buffer (Vector lab) heated in a pressure cooker for 25 min and then cooled to room temperature. Blocking of endogenous peroxides was accomplished by incubating sections in 3% hydrogen peroxide (Sigma) for 5 min. Antibodies were incubated with sections overnight at 4 °C. Immunostaining was performed by using DAB (3,3′-diaminobenzidine) or AEC (3-amino-9-ethylcarbazole) (Dako) according to the manufacturer's instructions. Sections were counterstained with haematoxylin for 1 min, rinsed in water and a coverslip was permanently added for light microscopy.

The mASCs cultured on glass coverslips were washed three times with PBS and fixed with 4% paraformaldehyde (PFA) for 10 min at room temperature. Cells were then washed three times with PBS alone or PBS containing 0.3% Triton X-100 (Sigma), and blocked by treatment with 10% donkey serum for 30 min at room temperature. Cells were then incubated with primary antibodies FITC-conjugated anti-mouse CD14 and CD31 or PE-conjugated anti-mouse CD44 and CD90 in a humidified chamber for 1 h at 37 °C. Thereafter, DAPI was used to stain the cell nuclei. The images of cells were taken under a fluorescence microscope.

Statistical analysis. The two-tailed Student's *t*-test or one-way analysis of variance (ANOVA) was used to compare differences between groups. Values with $P < 0.05$ were considered statistically significant. Survival analyses were performed using SPSS software (Version 16.0).

24. Evans, G. S., Flint, N., Somers, A. S., Eyden, B. & Potten, C. S. The development of a method for the preparation of rat intestinal epithelial cell primary cultures. *J. Cell Sci.* **101,** 219–231 (1992).
25. Wu, X. & Levine, A. J. p53 and E2F–1 cooperate to mediate apoptosis. *Proc. Natl Acad. Sci. USA* **91,** 3602–3606 (1994).
26. Bai, X. *et al.* Electrophysiological properties of human adipose tissue-derived stem cells. *Am. J. Physiol. Cell Physiol.* **293,** C1539–C1550 (2007).
27. Gimble, J. & Guilak, F. Adipose-derived adult stem cells: isolation, characterization, and differentiation potential. *Cytotherapy* **5,** 362–369 (2003).

Vol 464|15 April 2010|doi:10.1038/nature08978

LETTERS

Migrastatin analogues target fascin to block tumour metastasis

Lin Chen[1]*, Shengyu Yang[1]*, Jean Jakoncic[2], J. Jillian Zhang[1] & Xin-Yun Huang[1]

Tumour metastasis is the primary cause of death of cancer patients. Development of new therapeutics preventing tumour metastasis is urgently needed. Migrastatin is a natural product secreted by *Streptomyces*[1,2], and synthesized migrastatin analogues such as macroketone are potent inhibitors of metastatic tumour cell migration, invasion and metastasis[3–6]. Here we show that these migrastatin analogues target the actin-bundling protein fascin to inhibit its activity. X-ray crystal structural studies reveal that migrastatin analogues bind to one of the actin-binding sites on fascin. Our data demonstrate that actin cytoskeletal proteins such as fascin can be explored as new molecular targets for cancer treatment, in a similar manner to the microtubule protein tubulin.

To understand the molecular basis by which migrastatin analogues inhibit tumour cell migration and tumour metastasis, we pursued the biochemical identification of the protein target for macroketone. We took an affinity protein purification approach using synthesized biotin-labelled macroketone[4] (Fig. 1a). Biotin-conjugated macroketone inhibited 4T1 breast tumour cell migration with a similar potency (50% inhibitory concentration (IC_{50}) $\approx$ 300 nM) to that of the non-biotinylated macroketone ($IC_{50} \approx 100$ nM)[4]. 4T1 tumour cell extracts were incubated with biotin-conjugated macroketone or with free biotin. Strepavidin-conjugated agarose beads were added. After extensive washes, bound proteins were eluted and resolved by SDS–PAGE. A protein of about 58 kDa was specifically detected in the sample from affinity-purified proteins with biotin-conjugated macroketone, but not in the sample with free biotin (Fig. 1b). This roughly 58-kDa protein was identified by mass spectrometry and by peptide sequence as mouse fascin 1. Fascin is the primary actin cross-linker in filopodia and is required to crosslink the actin filaments maximally into straight, compact, rigid bundles[7–12]. Elevated expressions of fascin messenger RNA and protein in cancer cells have been correlated with an aggressive clinical course, poor prognosis and shorter survival[13–21].

Next we verified that macroketone does indeed interact directly with fascin. We purified recombinant glutathione *S*-transferase (GST)-tagged fascin to homogeneity from *Escherichia coli* (Supplementary Fig. 1a). Purified fascin, but not GST control, interacted specifically with biotin-conjugated macroketone (Fig. 1c). Moreover, an excess of non-biotinylated macroketone efficiently competed with the binding between fascin and biotin-conjugated macroketone (Supplementary Fig. 1b). Another migrastatin analogue, macrolactam, also competed with biotin-conjugated macroketone for binding to fascin. Taken together, these data demonstrate that fascin is a protein target of macroketone.

We then examined the biochemical effect of macroketone on the activity of fascin. We have used three different approaches to investigate the effect. First, we used purified recombinant fascin protein and investigated its actin-bundling activity with the F-actin pelleting assay[9]. In this low-speed centrifugation assay, the pellets contain bundles of F-actin polymers[9]. Purified fascin increased the amounts of F-actin bundles in the pellets (Fig. 1d, e). Although macroketone alone had no effect on the formation of F-actin bundles, macroketone significantly decreased the fascin-induced bundling of F-actin polymers (Fig. 1d, e). Second, we used fluorescence microscopy to reveal the fascin-regulated F-actin filament bundles in the absence and presence of macroketone (Supplementary Fig. 2a, b). The addition of fascin induced the formation of F-actin bundles, as revealed by the staining of F-actin filaments with rhodamine-conjugated phalloidin (Supplementary Fig. 2a). In contrast, in the presence of macroketone, the formation of F-actin bundles was largely (more than 80%) inhibited (Supplementary Fig. 2a, b). Third, we used electron microscopy to examine the actin bundles (Fig. 1f and Supplementary Fig. 2c). This examination revealed that macroketone decreased the thickness of the bundles. These data demonstrate that macroketone inhibits the actin-bundling activity of fascin.

To reveal the structural basis for the inhibition of fascin function by migrastatin analogues, we solved the X-ray crystal structures of fascin in the absence and presence of a migrastatin analogue (Fig. 2). We determined the native fascin structure and the structure of the fascin–macroketone complex at 1.8 Å and 2.7 Å, respectively (Fig. 2 and Supplementary Table 1). The overall structure of fascin has four β-trefoil folds, with each β-trefoil comprising six two-stranded β-hairpins (Fig. 2a–c, Supplementary Figs 3–5 and Supplementary Tables 2–4). This structure is similar to one fascin structure deposited in the protein structural database (Supplementary Fig. 6). The overall domain arrangement of the fascin–macroketone complex is very similar to that of the native fascin (Fig. 2d). The bound macroketone molecule sits at the surface of trefoil 4, on the side facing the cleft between trefoils 4 and 1 (Fig. 2d, e and Supplementary Fig. 7). Macroketone is held in place by interaction with the side chains of His 392, Glu 391, Ala 488, Lys 471 and His 474 as well as the α carbon of Asp 473 (Fig. 2d, e and Supplementary Fig. 8). His 392 and His 474 contribute to the binding of macroketone through hydrogen bonds (Fig. 2e). The interaction between fascin and macroketone is further stabilized by the van der Waals force between the macrolide ring carbon and residues Glu 391, Ala 488, Lys 471 and Asp 473 (Fig. 2e). These structural data are consistent with our previous structure–activity studies on migrastatin analogues showing that the macrolide ring, instead of the lengthy side chain of migrastatin, was important for the inhibitory function on tumour cell migration[4].

The structure of the fascin–macroketone complex immediately suggests a possible biochemical mechanism by which macroketone inhibits the actin-bundling activity of fascin. The macroketone binding site is one of the actin-binding sites on fascin (Fig. 3a). We therefore propose that macroketone binding interferes with the binding of actin filament to fascin. Fascin functions as a monomer to

[1]Department of Physiology, Cornell University Weill Medical College, New York, New York 10065, USA. [2]Brookhaven National Laboratory, National Synchrotron Light Source, Upton, New York 11973, USA.
*These authors contributed equally to this work.

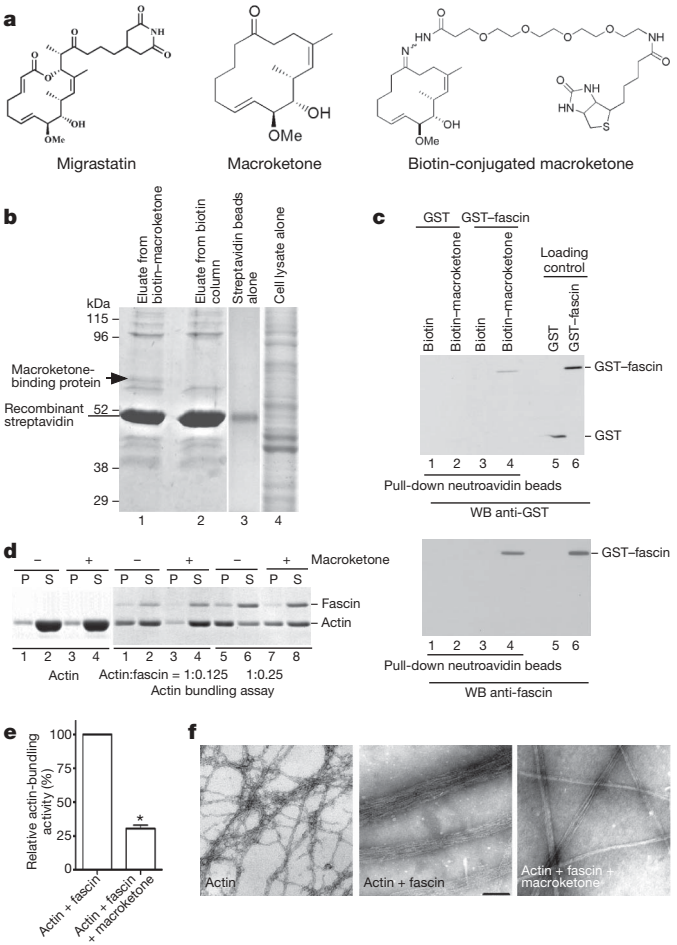

Figure 1 | Identification of fascin as a macroketone target. **a**, Diagram of the structures of migrastatin, one of its analogues (the macroketone core) and the biotin-conjugated macroketone core. **b**, Coomassie blue stain of the SDS–PAGE gel after protein affinity purification. The arrow indicates the band identified as mouse fascin 1. **c**, Direct interaction of fascin with macroketone. Neutroavidin-agarose beads with biotin-conjugated macroketone (10 μM) or biotin (10 μM) were mixed with GST–fascin or GST. WB, western blot. Data are representative of three experiments with similar results. **d**, Assay of the actin-bundling activity with a low-speed co-sedimentation assay. Polymerized F-actin (1 μM) was incubated with 0.125 μM or 0.25 μM purified fascin in the presence or absence of macroketone (10 μM). Supernatants (S) or pellets (P) were analysed by SDS–PAGE followed by Coomassie blue staining. The result shown is representative of five experiments with similar outcomes. **e**, Quantification of F-actin bundling assays from **d**. Results are means and s.d. ($n = 5$; asterisk, $P < 0.05$). **f**, Electron microscopy of fascin-induced F-actin bundles in the presence or absence of macroketone. F-actin (1 μM) was incubated with fascin (0.125 μM) in the presence or absence of macroketone (10 μM). Representative images are shown. Scale bar, 50 nm.

bundle actin filaments, and it has been proposed that fascin has two actin-binding sites for this bundling activity[22]. Previous mutagenesis studies implied that both the amino and carboxy termini of fascin contribute to actin binding. Our crystal structure implicates that the N and C termini constitute one of the actin-binding sites (Fig. 3a). Both the N and C termini are located in the same cleft (Fig. 3a). Furthermore, a stretch of residues (29–42) at the N terminus, which has similarity to an actin-binding site of MARCKS (myristoylated alanine-rich C-kinase substrate)[23], is also facing the trefoil 1–4 cleft (Fig. 3a). Moreover, the actin-bundling activity of fascin is negatively regulated by a protein kinase C phosphorylation site (Ser 39) within the N-terminal region[22] (Fig. 3a). Taken together, these data suggest that this cleft is one of the actin-binding sites.

To investigate this hypothesis that the macroketone-binding site overlaps with one of the actin-binding sites, we mutated five residues

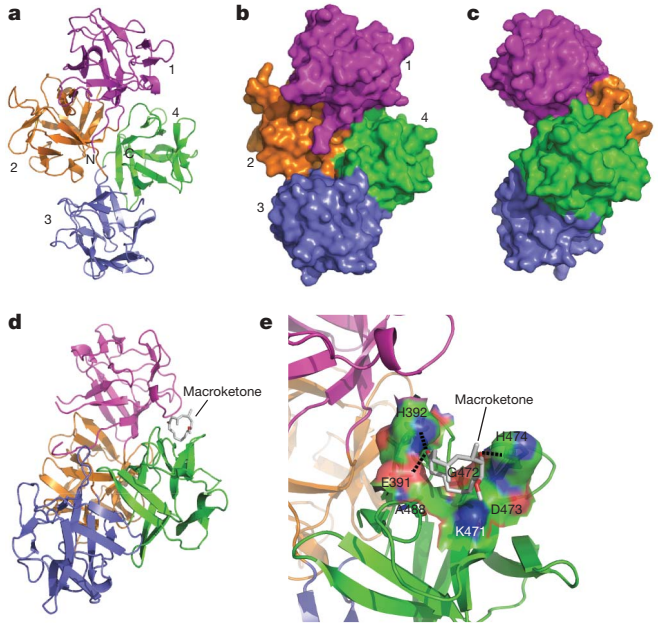

Figure 2 | X-ray crystal structures of fascin and of the complex of fascin and macroketone. **a**, Structure of fascin shown as a ribbon diagram, viewed from the N-terminal and C-terminal plane. The four β-trefoil domains are coloured magenta (trefoil 1), orange (trefoil 2), blue (trefoil 3) and green (trefoil 4). **b**, Surface presentation of fascin structure viewed in **a**. **c**, View of fascin turned clockwise 90° along the *y* axis relative to the view in **b**. **d**, Overall structure of the complex of fascin and macroketone. The macroketone molecule is shown as a white stick model. **e**, Macroketone-binding site. Residues involved in interactions with macroketone are shown as surface, and hydrogen bonds are shown as dashed lines.

involved in macroketone binding and examined the actin-bundling activity of those fascin mutants (Fig. 3b–d). We found that mutations of His 392, Lys 471 and Ala 488 did indeed decrease the actin-bundling activity of fascin (Fig. 3c, d). These data show that residues involved in macroketone binding are involved in actin bundling. We also examined the sensitivity of the actin-bundling activity of Glu 391 and His 474 to macroketone (mutants His 392, Lys 471 and Ala 488 were not tested because of their defective actin-bundling activity). As shown in Fig. 3e, f, mutation of His 474 to Ala rendered fascin resistant to macroketone treatment. Moreover, this His 474 to Ala mutant fascin did not bind to biotin–macroketone (Fig. 3g). Taken together, our data demonstrate that several fascin residues (such as His 392, Lys 471 and Ala 488) involved in macroketone binding also contribute to actin binding. Hence, the macroketone binding site is one of the actin-binding sites.

To critically evaluate further the possibility that macroketone inhibits fascin to decrease tumour cell migration, invasion and metastasis, it would be best to have a fascin mutant that does not bind to macroketone but retains its actin-bundling activity. This mutant fascin should confer resistance to macroketone in tumour cell migration, invasion and metastasis. Our data above showed that His 474 is essential for macroketone binding but not for actin bundling (Fig. 3). To confirm that the fascin His474Ala mutant could support tumour cell migration, invasion and metastasis, we used RNA interference to downregulate fascin protein levels in 4T1 mouse mammary tumour cells. Whereas two fascin short hairpin RNAs (shRNAs) knocked down the fascin protein levels, a control shRNA did not (Supplementary Fig. 9a). Fascin shRNA-treated cells grew at rates comparable to those of control shRNA-treated cells and non-transfected 4T1 cells in full growth medium (Supplementary Fig. 9b), suggesting that fascin is not required for the proliferation of breast tumour cells *in vitro*. This is consistent with our previous observation that migrastatin analogues had no effect on tumour cell proliferation and primary tumour growth in mouse models[5]. A Boyden-chamber cell migration

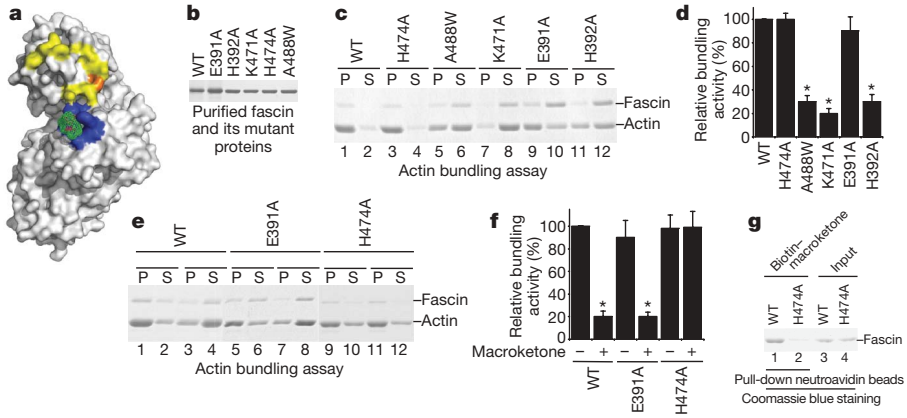

Figure 3 | Macroketone-binding site overlaps with one of the actin-binding sites. **a**, Surface presentation of the structure of the complex of fascin and macroketone. Residues involved in macroketone binding are shown in blue. Sequences (residues 29–42) homologous to the MARCKS actin-binding site are coloured yellow, and the protein kinase C phosphorylation site (Ser 39) is coloured orange. Macroketone is shown as a green mesh. **b**, Coomassie blue stain of purified fascin and its mutant proteins. WT, wild type. **c**, Actin bundling assay for the wild-type fascin and its mutants. P, pellet; S, supernatant. **d**, Quantification of data in **c**. Results are means and s.d. ($n = 3$, $P < 0.05$). **e**, Sensitivity to macroketone. Wild-type fascin and the E391A and H474A mutants of fascin were assayed for their actin-bundling activity in the absence or presence of macroketone (10 μM). **f**, Quantification of data in **e**. Results are means and s.d. ($n = 3$, $P < 0.05$). **g**, H474A fascin mutant protein fails to bind biotin–macroketone. The residual H474A protein pulled down by biotin–macroketone (lane 2) was aggregates bound to the beads.

assay showed that treatment with fascin shRNA, but not with the control shRNA, decreased the serum-induced migration of 4T1 cells (Supplementary Fig. 9c). Moreover, this inhibitory effect of fascin shRNA could be rescued by transfection of human fascin cDNA (there are two nucleotide changes without amino-acid changes in this specific region) (Fig. 4a). This rescued migration was sensitive to macroketone (Fig. 4a). Although mutations of His 474 to either Lys (*Drosophila* fascin has a Lys in the corresponding position) or Ala in human fascin also rescued the migration of 4T1 cells treated with fascin siRNAs (Fig. 4a), these rescued migrations were not inhibited by macroketone (Fig. 4a and Supplementary Fig. 9d). In addition, we performed rescue experiments of fascin shRNA-treated 4T1 cells with villin, another actin-bundling protein. From *Drosophila* genetic studies, villin partly rescued the phenotypes of fascin mutations during *Drosophila* oogenesis[24]. Villin did not bind macroketone *in vitro*, and overexpression of villin in fascin shRNA-treated 4T1 cells partly rescued the migration, which was insensitive to macroketone (Supplementary Fig. 9e). Similarly, expression of human wild-type fascin and the His474Ala fascin mutant in fascin shRNA-treated mouse 4T1 cells rescued tumour cell invasion (Fig. 4b). The rescued invasion by wild-type fascin but not by His474Ala mutant fascin was sensitive to macroketone (Fig. 4b and Supplementary Fig. 9f). Moreover, fascin

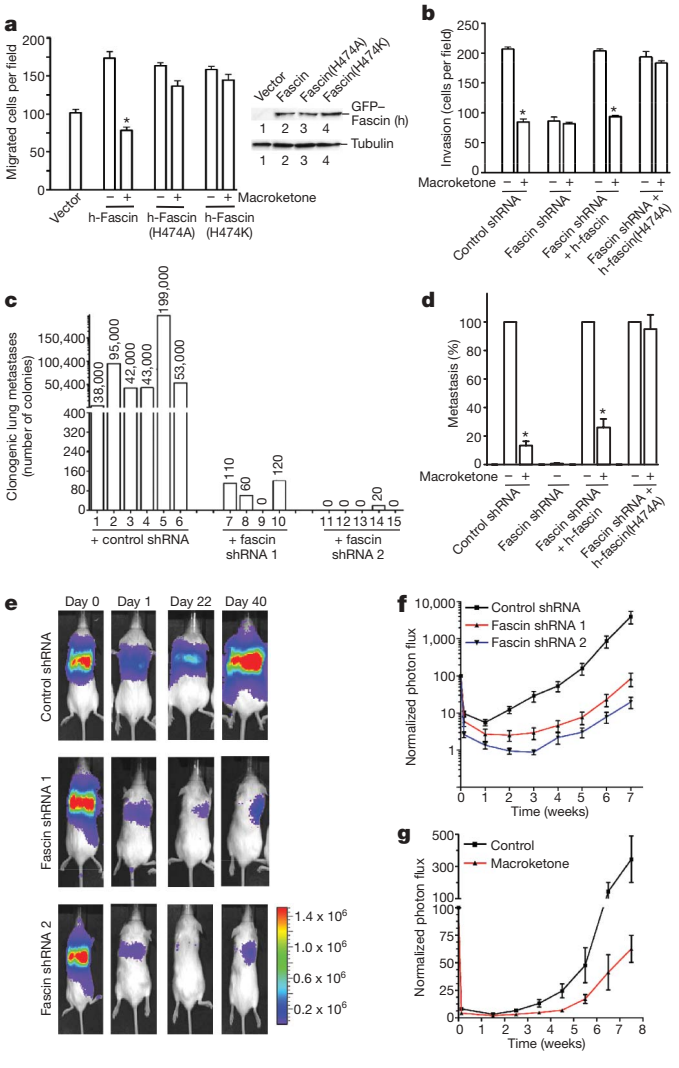

Figure 4 | Fascin His 474 mutation renders tumour cell migration, invasion and metastasis resistant to macroketone. **a**, Left: Boyden-chamber cell migration assay of mouse fascin shRNA 2-treated 4T1 cells transfected with various mutants of GFP–human fascin (h-fascin) in the presence or absence of macroketone (10 μM). Right: overexpression of various fascin mutants in mouse fascin shRNA-2-treated 4T1 cells. Results are means and s.d. ($n = 5$, $P < 0.05$). **b**, *In vitro* Matrigel invasion assay with mouse fascin shRNA-treated 4T1 cells overexpressing wild-type human fascin or fascin(H474A) mutant in the presence or absence of macroketone (10 μM). Results are means and s.d. ($n = 5$, $P < 0.05$). **c**, Total number of metastatic colonies in lungs of individual mice four weeks after injection of 4T1 cells expressing control shRNA and two fascin shRNAs. The numbers 1 to 15 on the *x* axis are mouse identification numbers. **d**, Tumour metastasis assay with mouse fascin shRNA-treated 4T1 cells overexpressing wild-type human fascin or fascin(H474A) mutant in the presence or absence of macroketone (10 mg kg^{-1}). Comparison of the fascin shRNA group with the control shRNA group. Results are means and s.d. ($n = 5$~6, $P < 0.05$). **e**, Representative non-invasive bioluminescence images of mice at the indicated times after injection of human MDA-MB-231 cells expressing control shRNA and two fascin shRNAs. **f**, Normalized photon flux of non-invasive bioluminescence images of mice at the indicated times after injection of human MDA-MB-231 cells expressing control shRNA and two fascin shRNAs. Results are means ± s.d. **g**, Normalized photon flux of non-invasive bioluminescence images of mice at the indicated times after injection of human MDA-MB-231 cells in the presence or absence of macroketone (10 mg kg^{-1}). Results are means ± s.d.

His474Ala mutation conferred macroketone resistance in tumour metastasis (Fig. 4c, d). Treatment with fascin shRNA abolished 4T1 tumour cell metastasis in mouse models (Fig. 4c, d). Macroketone significantly inhibited metastasis in mice injected with control shRNA-treated cells. Wild-type human fascin-rescued 4T1 cells metastasized to the lung, and this metastasis was inhibited by macroketone (Fig. 4d). In contrast, although re-expression of His474Ala mutant fascin rescued the tumour metastasis, this metastasis was insensitive to macroketone (Fig. 4d). These results further confirm that fascin is the protein target for macroketone in its inhibition of tumour cell migration, invasion and metastasis.

Mindful of the clinical potential of fascin inhibitors for human cancer treatments, we further investigated the inhibition of lung colonization of human breast tumour cells in immune-deficient mouse models by fascin inhibitors such as fascin shRNAs and macroketone. First, MDA-MB-231 cells were retrovirally infected with a triple-fusion protein reporter construct encoding herpes simplex virus thymidine kinase 1, green fluorescent protein (GFP) and firefly luciferase (TGL)[25,26]. These cells were injected into the tail vein of immunodeficient mice (NOD-SCID mice). The colonization of the lung by tumour cells was monitored by non-invasive bioluminescence imaging (Fig. 4e, f and Supplementary Fig. 10a–d)[20]. A substantial attenuation of the bioluminescence signal was observed within the first few days, indicating that cells that failed to metastasize were not able to survive (Fig. 4e, f). Progressively increasing signals after two weeks in mice with control shRNA-treated tumour cells indicated that cells had succeeded in metastasizing and proliferating (Fig. 4e, f). The presence of fascin shRNA-treated cells in the lung was much less than in control shRNA-treated cells (Fig. 4e, f). Fascin shRNA treatments therefore significantly inhibited the lung colonization. Second, we have also shown here that macroketone could effectively block the lung colonization of human breast tumours in an animal model. As shown in Fig. 4g, macroketone decreased the lung colonization of MDA-MB-231 cells by more than 80%. Taken together, our data demonstrate the feasibility of using the inhibitors of fascin (such as macroketone and the siRNAs) as therapeutic agents for treating metastatic breast tumours.

Fascin mRNA transcript and protein levels are significantly elevated in clinically aggressive tumours[17,27]. Overexpression of fascin leads to increases in cell migration and invasion[28,29]. We analysed a microarray gene expression data set with 137 breast cancer samples and 16 normal breast samples from patients treated at the Memorial Sloan-Kettering Cancer Center. Breast tumour samples showed increased fascin expression in comparison with normal samples. Moreover, we observed a high level of fascin transcripts in an oestrogen receptor (ER)-negative group of patients (Supplementary Fig. 11a) and a progesterone receptor (PR)-negative group of patients (Supplementary Fig. 11b). Immunohistology staining with an anti-fascin antibody confirmed that fascin protein was upregulated in ER-negative tumours (Supplementary Fig. 11c), whereas ER-positive tumour cells were negative for fascin staining (note that endothelia of vessels are fascin positive). We also analysed fascin mRNA expression levels in the Rosetta microarray data set of 295 breast cancer patients[30]. Similarly, we found that the levels of fascin transcripts were significantly higher in ER-negative and PR-negative tumours (Supplementary Fig. 11d, e).

Overexpression of fascin contributes to a more aggressive clinical course of cancer[16]. The Rosetta data set contains detailed clinical follow-up information on breast cancer patients. We therefore evaluated the clinical and pathological associations of fascin expression in breast cancer patients. Kaplan–Meier analyses showed that higher expression of fascin was associated with lower overall survival (Supplementary Fig. 11f) and lower metastasis-free survival (Supplementary Fig. 11g). These data highlight the correlation between higher fascin expression and metastasis and death in human breast cancer patients.

METHODS SUMMARY

Affinity purification. 4T1 tumour cells were lysed and the cell extract was then mixed with biotin-labelled macroketone or free biotin for 2 h at 4 °C with gentle rotation. Recombinant streptavidin-agarose beads (Pierce) were added to the cell extract and the incubation was continued for a further 2 h with gentle rotation. The mixtures were then loaded onto a Poly-Prep chromatography column. After extensive washing with cell lysis buffer, samples were eluted with elution buffer. The eluate was further concentrated with Centricon P-20 (Millipore) and separated by SDS–PAGE. The gel was stained with Coomassie blue and the indicated band was cut out for mass spectrometry and peptide sequencing analyses.

Breast tumour metastasis in mice. All animal work was performed in compliance with the Institutional Animal Care and Use Committee of Weill Medical College. Spontaneous 4T1 mouse breast tumour metastasis assay was performed as described previously[5,26]. In experimental lung metastasis experiments, NOD-SCID immunodeficient mice were used. MDA-MB-231 human breast tumour cells expressing the TGL reporter were trypsinized and washed with PBS. Subsequently 10^6 cells in 0.2 ml of PBS were injected into the lateral tail vein. Luciferase-based, non-invasive bioluminescent imaging and analysis were performed with an IVIS Imaging System (Xenogen).

Crystallization and structure determination. To obtain crystals of the fascin–macroketone complex, the protein was incubated for 1 h at room temperature (20–25 °C) in the protein buffer supplemented with 2 mM macroketone. Crystallization was performed at 20 °C with the vapour-diffusion hanging-drop method. Fascin crystallized in 100 mM HEPES pH 8.0, 16% PEG4000, 1% propan-2-ol. Both crystals (fascin without or with macroketone) belong to space group *C*2. X-ray diffraction data were recorded at National Synchrotron Light Source beamlines X6A and X4C at Brookhaven National Laboratory. A partial structure was initially solved by the MR-SAD method with a selenomethionine derivative sample that diffracted to 2.1 Å and a fraction of the 1DFC Protein Data Bank (PDB) file. This model was subsequently extended by iterative model building and refinement cycles with COOT and REFMAC5.

Full Methods and any associated references are available in the online version of the paper at www.nature.com/nature.

Received 24 September 2009; accepted 4 March 2010.

1. Nakae, K. *et al.* Migrastatin, a novel 14-membered lactone from *Streptomyces* sp. MK929–43F1. *J. Antibiot. (Tokyo)* **53,** 1228–1230 (2000).
2. Woo, E. J. *et al.* Migrastatin and a new compound, isomigrastatin, from *Streptomyces platensis*. *J. Antibiot. (Tokyo)* **55,** 141–146 (2002).
3. Njardarson, J. T., Gaul, C., Shan, D., Huang, X. Y. & Danishefsky, S. J. Discovery of potent cell migration inhibitors through total synthesis: lessons from structure–activity studies of (+)-migrastatin. *J. Am. Chem. Soc.* **126,** 1038–1040 (2004).
4. Gaul, C. *et al.* The migrastatin family: discovery of potent cell migration inhibitors by chemical synthesis. *J. Am. Chem. Soc.* **126,** 11326–11337 (2004).
5. Shan, D. *et al.* Synthetic analogues of migrastatin that inhibit mammary tumor metastasis in mice. *Proc. Natl Acad. Sci. USA* **102,** 3772–3776 (2005).
6. Ju, J. *et al.* Evaluation of new migrastatin and dorrigocin congeners unveils cell migration inhibitors with dramatically improved potency. *Bioorg. Med. Chem. Lett.* **18,** 5951–5954 (2008).
7. Otto, J. J., Kane, R. E. & Bryan, J. Formation of filopodia in coelomocytes: localization of fascin, a 58,000 dalton actin cross-linking protein. *Cell* **17,** 285–293 (1979).
8. Bryan, J. & Kane, R. E. Separation and interaction of the major components of sea urchin actin gel. *J. Mol. Biol.* **125,** 207–224 (1978).
9. Yamashiro-Matsumura, S. & Matsumura, F. Purification and characterization of an F-actin-bundling 55-kilodalton protein from HeLa cells. *J. Biol. Chem.* **260,** 5087–5097 (1985).
10. Vignjevic, D. *et al.* Formation of filopodia-like bundles *in vitro* from a dendritic network. *J. Cell Biol.* **160,** 951–962 (2003).
11. Vignjevic, D. *et al.* Role of fascin in filopodial protrusion. *J. Cell Biol.* **174,** 863–875 (2006).
12. Adams, J. C. Roles of fascin in cell adhesion and motility. *Curr. Opin. Cell Biol.* **16,** 590–596 (2004).
13. Maitra, A. *et al.* Immunohistochemical validation of a novel epithelial and a novel stromal marker of pancreatic ductal adenocarcinoma identified by global expression microarrays: sea urchin fascin homolog and heat shock protein 47. *Am. J. Clin. Pathol.* **118,** 52–59 (2002).
14. Pelosi, G. *et al.* Independent value of fascin immunoreactivity for predicting lymph node metastases in typical and atypical pulmonary carcinoids. *Lung Cancer* **42,** 203–213 (2003).
15. Hashimoto, Y., Shimada, Y., Kawamura, J., Yamasaki, S. & Imamura, M. The prognostic relevance of fascin expression in human gastric carcinoma. *Oncology* **67,** 262–270 (2004).
16. Hashimoto, Y., Skacel, M. & Adams, J. C. Roles of fascin in human carcinoma motility and signaling: prospects for a novel biomarker? *Int. J. Biochem. Cell Biol.* **37,** 1787–1804 (2005).

17. Yoder, B. J. *et al.* The expression of fascin, an actin-bundling motility protein, correlates with hormone receptor-negative breast cancer and a more aggressive clinical course. *Clin. Cancer Res.* **11,** 186–192 (2005).
18. Zigeuner, R., Droschl, N., Tauber, V., Rehak, P. & Langner, C. Biologic significance of fascin expression in clear cell renal cell carcinoma: systematic analysis of primary and metastatic tumor tissues using a tissue microarray technique. *Urology* **68,** 518–522 (2006).
19. Rodriguez-Pinilla, S. M. *et al.* Prognostic significance of basal-like phenotype and fascin expression in node-negative invasive breast carcinomas. *Clin. Cancer Res.* **12,** 1533–1539 (2006).
20. Minn, A. J. *et al.* Genes that mediate breast cancer metastasis to lung. *Nature* **436,** 518–524 (2005).
21. Wu, J. M. *et al.* Heterogeneity of breast cancer metastases: comparison of therapeutic target expression and promoter methylation between primary tumors and their multifocal metastases. *Clin. Cancer Res.* **14,** 1938–1946 (2008).
22. Ono, S. *et al.* Identification of an actin binding region and a protein kinase C phosphorylation site on human fascin. *J. Biol. Chem.* **272,** 2527–2533 (1997).
23. Mosialos, G. *et al.* Epstein–Barr virus infection induces expression in B lymphocytes of a novel gene encoding an evolutionarily conserved 55-kilodalton actin-bundling protein. *J. Virol.* **68,** 7320–7328 (1994).
24. Cant, K. & Cooley, L. Single amino acid mutations in *Drosophila* fascin disrupt actin bundling function *in vivo*. *Genetics* **143,** 249–258 (1996).
25. Minn, A. J. *et al.* Distinct organ-specific metastatic potential of individual breast cancer cells and primary tumors. *J. Clin. Invest.* **115,** 44–55 (2005).
26. Yang, S., Zhang, J. J. & Huang, X. Y. Orai1 and STIM1 are critical for breast tumor cell migration and metastasis. *Cancer Cell* **15,** 124–134 (2009).
27. Grothey, A., Hashizume, R., Sahin, A. A. & McCrea, P. D. Fascin, an actin-bundling protein associated with cell motility, is upregulated in hormone receptor negative breast cancer. *Br. J. Cancer* **83,** 870–873 (2000).
28. Hashimoto, Y., Parsons, M. & Adams, J. C. Dual actin-bundling and protein kinase C-binding activities of fascin regulate carcinoma cell migration downstream of Rac and contribute to metastasis. *Mol. Biol. Cell* **18,** 4591–4602 (2007).
29. Vignjevic, D. *et al.* Fascin, a novel target of β-catenin-TCF signaling, is expressed at the invasive front of human colon cancer. *Cancer Res.* **67,** 6844–6853 (2007).
30. van 't Veer, L. J. *et al.* Gene expression profiling predicts clinical outcome of breast cancer. *Nature* **415,** 530–536 (2002).

Supplementary Information is linked to the online version of the paper at www.nature.com/nature.

Acknowledgements J.J.Z. and X.Y.H. dedicate this paper to the memory of Yonghong Zhang, who died of cancer on 12 September 2009. We are grateful to W. Gerald (deceased) at Memorial Sloan-Kettering Cancer Center for letting us examine his DNA microarray data on human breast tumour samples for the fascin expression. We thank S. Almo for the fascin plasmid; S. Danishefsky and colleagues for the biotin-conjugated macroketone used in the initial exploration of the conditions for protein purification; members of the J. Massagué laboratory for teaching the use of the IVIS Imaging system; the personnel at the beamlines X6A and X4C of the National Synchrotron Light Source for the beamtime and for assistance; and D. Eliezer, T. Maack, L. Palmer, H. Wu and members of our laboratory for critically reading the manuscript. We thank S. Almo and his colleagues, H. Wu and J. Wu, for help with the crystallization experiments. This work was supported by grants from the National Institutes of Health (CA136837) and the Department of Defense (W81XWH-06-1-0362).

Author Contributions L.C., S.Y., J.J.Z. and X.Y.H. conceived the project. L.C. and S.Y. performed the experiments. S.Y. and J.J. determined the structures. L.C., S.Y., J.J.Z. and X.Y.H. analysed the data and wrote the paper.

Author Information The coordinates and structure factors of crystal structures of fascin and the fascin–macroketone complex have been deposited in the Protein Data Bank under accession numbers 3LLP and 3LNA, respectively. Reprints and permissions information is available at www.nature.com/reprints. The authors declare no competing financial interests. Correspondence and requests for materials should be addressed to X.Y.H. (xyhuang@med.cornell.edu).

METHODS

Materials. Mouse 4T1 mammary tumour cells and human MDA-MB-231 breast tumour cells were obtained from the American Type Culture Collection and have been described previously[31,32]. 4T1 cells were cultured in RPMI 1640 medium supplemented with 10% FBS. MDA-MB-231 cells were cultured in DMEM supplemented with 10% FBS. Macroketone and biotin-conjugated macroketone were custom synthesized by outside companies.

Affinity purification. 4T1 tumour cells were lysed in cell lysis buffer (50 mM Tris-HCl pH 7.4, 150 mM NaCl, 1% Nonidet P40, 0.1% SDS, and protease inhibitors: 1 mM phenylmethylsulphonyl fluoride, 10 μg ml^{-1} leupeptin, pepstatin and aprotinin). The cell extract was then mixed with biotin-labelled macroketone or free biotin for 2 h at 4 °C with gentle rotation. Streptavidin beads (Pierce) were added to the cell extract and the incubation was continued for a further 2 h with gentle rotation. The mixtures were then loaded onto the Poly-Prep chromatography column. After extensive washing with cell lysis buffer (with the NaCl concentration increased to 300 mM), samples were eluted three times with elution buffer (0.1 M glycine-HCl pH 2.8). The eluate was further concentrated with Centricon P-20 (Millipore) and separated by SDS–PAGE. The gel was stained with Coomassie blue and the indicated band was cut out for mass spectrometry and peptide sequencing analyses.

RNA interference. RNA-mediated interference of fascin was performed in 4T1 mouse breast tumour and MDA-MB-231 human breast tumour cells with pSUPER vector (Oligoengine). The target sequences of the two pairs of mouse fascin were 5′-GGTGGGCAAAGATGAGCTC-3′ and 5′-GTGGAGCGTGCA CATCGCC-3′. The target sequences of the two pairs of human fascin were 5′-GGTGGGCAAGGACGAGCTC-3′ and 5′-GCCTGAAGAAGAAGCAGAT-3′. Control shRNA was a shRNA that targets a LacZ sequence.

***In vitro* wound-healing assay.** Cell migration assays were performed as described previously[32,33]. Cells were allowed to form a confluent monolayer in a 24-well plate coated with gelatin, before being wounded. The wound was made by scraping a conventional pipette tip across the monolayer. Migration was induced by the addition of medium supplemented with 10% FBS. When the wound for the positive control had closed, cells were fixed with 3.7% formaldehyde and stained with crystal violet staining solution.

Boyden-chamber cell migration assay. Cells (5×10^4) suspended in starvation medium were added to the upper chamber of an insert (6.5 mm diameter, 8 μm pore size; Becton Dickinson), and the insert was placed in a 24-well dish containing starvation medium with or without 10% FBS[32,33]. When used, inhibitors were added to both chambers. Migration assays were performed for 4–6 h and cells were fixed with 3.7% formaldehyde. Cells were stained with crystal violet staining solution, and cells on the upper side of the insert were removed with a cotton swab. Three randomly selected fields (×10 objectives) on the lower side of the insert were photographed, and the migrated cells were counted. Migration was expressed as either the average number of migrated cells in a field or as a percentage of the migrated cells in the positive control. The percentage of migrated cells, P, was calculated with the formula $P = 100 \times (M - M_{nc})/M_{pc}$, where M is the number of migrated cells, M_{nc} is the number of migrated cells in negative controls, and M_{pc} is the number of migrated cells in positive controls.

Cell invasion assay. Cells (10^5) suspended in starvation medium were added to the upper chamber of a Matrigel-coated insert (6.5 mm diameter, 8 μm pore size; Becton Dickinson), and the insert was placed in a 24-well dish containing medium with or without serum. When used, inhibitors were added to both chambers. Invasion assays were performed for 16 h and cells were fixed with 3.7% formaldehyde. Cells were stained with crystal violet staining solution, and cells on the upper side of the insert were removed with a cotton swab. Three randomly selected fields (10× objectives) on the lower side of the insert were photographed, and the cells on the lower surface of the insert were counted.

Protein expression and purification. Recombinant GST–fascin fusion protein was produced in BL21 *Escherichia coli*. A 1-litre culture was grown to an attenuance at 600 nm (D_{600}) of 1.0 and then induced by the addition of 0.3 mM isopropyl β-D-thiogalactoside (IPTG) for 12 h at 25 °C. Cells were flash frozen and then lysed by sonication in Tris-buffered saline. The supernatant was then incubated with glutathione-Sepharose for 2 h at 4 °C. After extensive washing, GST–fascin was eluted and concentrated with a Centricon Plus-20 (Millipore). To remove the GST tag from the fusion protein, beads were incubated overnight at 4 °C with thrombin. The supernatant was collected and concentrated.

GST–fascin and biotin–macroketone interaction. Purified recombinant fascin protein or control protein were incubated with biotin–macroketone for 2 h at 4 °C. Proteins associated with biotin–macroketone were precipitated with Ultralink-immobilized Streptavidin-agarose (Pierce). After extensive washing, bound proteins were eluted with SDS sample buffer and resolved by 10% SDS–PAGE.

F-actin bundling assay. Actin-bundling activity was measured by low-speed centrifugation assay and fluorescence microscopy. In the low-speed centrifugation assay, monomeric rabbit G-actin was induced to polymerize at room temperature in F-actin buffer (20 mM Tris-HCl pH 8, 1 mM ATP, 1 mM dithiothreitol (DTT), 2 mM $MgCl_2$, 100 mM KCl). Recombinant fascin proteins or control buffer were subsequently incubated with F-actin for 60 min at room temperature and centrifuged for 30 min at 10,000*g* in an Eppendorf 5415D table-top centrifuge. Both supernatants and pellets were dissolved in an equivalent volume of SDS sample buffer, and the amount of actin was determined by SDS–PAGE. We measured the intensities of fascin proteins in Coomassie-stained gels and then calculated the relative actin-bundling activity, P, by the following formula: $P = 100 \times M_p/M_{pc}$, where M_p is the percentage of actin present in the pellet when mixed with different concentrations of fascin protein, calculated by (intensity in pellet)/(intensity in pellet + intensity in supernatant), and M_{pc} is the percentage of actin present in the pellet when mixed with 0.25 μM fascin, which is used at a saturated concentration determined in our control experiment.

In fluorescence microscopy, monomeric G-actin was polymerized as described earlier. F-actin was mixed with recombinant fascin protein in F-buffer (100 mM KCl, 2 mM $MgCl_2$, 1 mM ATP, 20 mM Tris-HCl pH 8.0) and incubated at room temperature for 30 min. Actin was then labelled by adding 5% rhodamine–phalloidin to the mixture. The samples were mounted between a slide and a coverslip coated with polylysine and imaged by fluorescence microscopy. Three randomly selected fields (×10 objectives) were photographed, and the bundles were counted. The number of bundles per field was expressed as the mean ± s.d.

Immunofluorescence microscopy. Cells cultured on gelatin-coated glass coverslips were fixed for 10 min at room temperature with 3.7% formaldehyde in PBS, permeabilized with 0.1% Triton X-100 for 5 min, and then washed three times with PBS. To block non-specific binding, the cells were incubated for 30 min with a solution of PBS containing 1% BSA and then incubated for 1 h with primary antibody at appropriate dilutions. After incubation with primary antibody, cells were washed three times with PBS and incubated with fluorescence-conjugated secondary antibody (Molecular Probes). The coverslips were then fixed onto slides and imaged with a Zeiss fluorescence microscope.

Electron microscopy. Samples were absorbed for 2 min onto freshly glow-discharged, carbon-coated copper grids and stained with 2% uranyl acetate. Grids were examined with a Zeiss electron microscope at an accelerating voltage of 80 kV.

4T1 breast tumour metastasis in mice. All animal work was performed in compliance with the guidelines of the Institutional Animal Care and Use Committee of the Weill Medical College. The spontaneous 4T1 mouse breast tumour metastasis assay was conducted as described previously[31,34]. Female BALB/c mice (6–8 weeks old) were purchased from the Jackson Laboratory. 4T1 tumour cells (10^5) were injected subcutaneously into the abdominal mammary gland area of mice by using 0.1 ml of a single-cell suspension in PBS on day 0. The dosage of tumour implantation was determined empirically to give rise to tumours about 10 mm in diameter in untreated wild-type mice within 21–23 days. Starting on day 7, when the tumours averaged about 4–5 mm in diameter, test compounds or control PBS saline were given every day by intraperitoneal injection at 10 mg kg^{-1} per mouse until day 25. On day 28, the mice were killed. This dosage regimen was well tolerated with no signs of overt toxicity. Each group included five mice. Primary tumours were measured with electronic calipers on the day that the mice were killed. Numbers of metastatic 4T1 cells in lungs were determined by the clonogenic assay. In brief, lungs were removed from each mouse on day 28, finely minced and digested for 2 h at 37 °C in 5 ml of enzyme cocktail containing PBS and 1 mg ml^{-1} collagenase type IV, on a platform rocker. After incubation, samples were filtered through 70-μm nylon cell strainers and washed twice with PBS. Resulting cells were suspended, plated with a series of dilutions in 10-cm tissue culture dishes in RPMI1640 medium containing 60 μM thioguanine for clonogenic growth. Because 4T1 tumour cells are resistant to 6-thioguanine, metastasized tumour cells formed foci after 14 days, at which time they were fixed with methanol and stained with 0.03% methylene blue for counting.

MDA-MB-231 human breast tumour lung colonization in mice. NOD-SCID immunodeficient mice were used for experimental lung colonization experiments. MDA-MB-231 human breast tumour cells expressing the TGL reporter were trypsinized and washed with PBS. This artificial TGL reporter gene encodes a triple fusion protein with herpes simplex virus 1 thymidine kinase fused to the N terminus of enhanced GFP and firefly luciferase fused to the C terminus of GFP[34,35]. Subsequently, 10^6 cells in 0.2 ml PBS were injected into the lateral tail vein. Luciferase-based, non-invasive bioluminescent imaging and analysis were performed with an IVIS Imaging System (Xenogen).

Microarray gene expression analysis. Gene expression data for fascin were extracted from each tumour sample and mean-centred across all samples for each. Tissues from primary breast cancers were obtained from therapeutic procedures performed as part of routine clinical management at Memorial Sloan-Kettering

Cancer Center (MSKCC). All research procedures with human tissue were approved by the MSKCC institutional review board[36]. Tissues were snap-frozen in liquid nitrogen and stored at −80 °C. Each sample was examined histologically with haematoxylin/eosin-stained cryostat sections. Regions were dissected manually from the frozen block to provide a consistent tumour cell content of more than 70% in tissues used for analysis. Total RNA was extracted from frozen tissue by homogenization in guanidinium isothiocyanate-based buffer (Trizol; Invitrogen), purified with RNAeasy (Qiagen) and examined for quality by denaturing agarose-gel electrophoresis. Complementary DNA was synthesized from RNA with a T7-promoter-tagged oligo(dT) primer. RNA target was synthesized from cDNA by *in vitro* transcription, and labelled with biotinylated nucleotides (Enzo Biochem). Gene expression analysis was performed with HG-U133A and U133B oligonucleotide microarrays in accordance with the manufacturer's instructions (Affymetrix). To identify differential gene expression, we used two different measures: fold change (ratio) between the normalized means of each group of samples, and a Student's *t*-test. The microarray data had previously been deposited at Gene Expression Omnibus (GEO) under accession number GSE2603.

Human fascin 1 expression and purification. Recombinant human fascin 1 was expressed as a GST fusion protein in *E. coli*. Typically, 1 litre of 2YT medium with antibiotic was inoculated overnight with 3 ml of BL21/DE3 culture transformed with pGEX4T-Fascin1 plasmid and grown at 37 °C until D_{600} reached about 0.8. The culture was then transferred to 22 °C and 0.1 mM IPTG was added for induction. After induction overnight, the bacteria were harvested by centrifugation at 5,000 r.p.m. for 10 min. The bacteria pellet was snap-frozen with liquid nitrogen and suspended in 30 ml of PBS supplemented with 0.2 mM PMSF, 1 mM DTT, 1% Triton X-100 and 1 mM EDTA. After sonication, the suspension was centrifuged at 15,000 r.p.m. for 60 min to remove the cell debris. The supernatant was then incubated for 2 h with 4 ml of glutathione beads (Sigma) at 4 °C. After extensive washing with PBS, the beads were resuspended in 10 ml of thrombin cleavage buffer (20 mM Tris-HCl pH 8.0, 150 mM NaCl, 2 mM $CaCl_2$, 1 mM DTT). Human fascin 1 was released from the beads by incubation overnight with 40–100 U of thrombin at 4 °C. After centrifugation, 0.2 mM PMSF was added to the supernatant to inactivate the remnant thrombin activity. The fascin protein was further purified with a Superdex 200 gel-filtration column and concentrated with Centricon to about 80 mg ml^{-1}. The typical yield from a 1-litre culture was about 40 mg.

Crystallization and structure determination. The concentrated protein stock solution was diluted with the protein buffer (20 mM Tris-HCl pH 8.0, 40 mM KBr, 0.5 mM EDTA, 1 mM DTT) to 15 mg ml^{-1} before crystallization. To obtain crystals of the fascin–macroketone complex, the protein was incubated for 1 h at room temperature in the protein buffer supplemented with 2 mM macroketone. Crystallization was performed at 20 °C with the vapour-diffusion hanging-drop method. Fascin crystallized in 100 mM HEPES pH 8.0, 16% PEG4000, 1% propan-2-ol. Both crystals (fascin without or with macroketone) belong to space group *C*2. Crystals were transferred briefly to the cryo-solution, which consisted of the crystallization solution supplemented with 15% glycerol, then flash-cooled in liquid nitrogen. X-ray diffraction data were recorded at National Synchrotron Light Source beamline X6A and X4C at Brookhaven National Laboratory. A partial structure was initially solved by the MR-SAD method with a selenomethionine derivative sample that diffracted to 2.1 Å and a fraction of the 1DFC PDB file. This model was subsequently extended by iterative model building and refinement cycles using COOT[37] and REFMAC5 (ref. 38). The fascin structure was solved by the molecular replacement method with the selenomethionine MR-SAD structure as a starting model and finally refined by following the same procedure. The diffraction of some fascin crystals was markedly improved by an 'annealing' process involving one freeze–thaw–freeze treatment. A 1.8 Å data set obtained from an annealed crystal rendered a markedly improved electronic density map, which was unambiguous throughout almost the entirety of both molecules in the asymmetric unit. The asymmetric unit contains two mostly complete molecules with the exception of four highly flexible loops (residues 1–7, 49–54 and 245–247 in chain A, and residues 1–7 and 300–303 in chain B) with poorly defined electron density. For the crystals of the complex of fascin and macroketone, one of the two molecules in the asymmetric unit is relatively disordered. An approximately 4σ peak was observed in the difference density map (Supplementary Fig. 7) near the surface of β-trefoil 4 of molecule A, on the side facing the cleft between trefoil 4 and trefoil 1. The ring structure was easily discernible in the difference map, and densities for the side chains were missing. The approximate orientation of the macroketone molecule was derived by fitting the macrolide ring into the density while keeping in mind the possible polar interactions between macroketone and fascin.

Statistical analysis. Data are expressed as means and s.d. and were analysed with Student's *t*-test; significance is defined as $P < 0.05$.

31. Shan, D. *et al.* Synthetic analogues of migrastatin that inhibit mammary tumor metastasis in mice. *Proc. Natl Acad. Sci. USA* **102,** 3772–3776 (2005).
32. Yang, S. & Huang, X. Y. Ca^{2+} influx through L-type Ca^{2+} channels controls the trailing tail contraction in growth factor-induced fibroblast cell migration. *J. Biol. Chem.* **280,** 27130–27137 (2005).
33. Shan, D. *et al.* The G protein $G\alpha_{13}$ is required for growth factor-induced cell migration. *Dev. Cell* **10,** 707–718 (2006).
34. Yang, S., Zhang, J. J. & Huang, X. Y. Orai1 and STIM1 are critical for breast tumor cell migration and metastasis. *Cancer Cell* **15,** 124–134 (2009).
35. Ponomarev, V. *et al.* A novel triple-modality reporter gene for whole-body fluorescent, bioluminescent, and nuclear noninvasive imaging. *Eur. J. Nucl. Med. Mol. Imaging* **31,** 740–751 (2004).
36. Doane, A. S. *et al.* An estrogen receptor-negative breast cancer subset characterized by a hormonally regulated transcriptional program and response to androgen. *Oncogene* **25,** 3994–4008 (2006).
37. Emsley, P. & Cowtan, K. Coot: model-building tools for molecular graphics. *Acta Crystallogr. D* **60,** 2126–2132 (2004).
38. Vagin, A. A. *et al.* REFMAC5 dictionary: organization of prior chemical knowledge and guidelines for its use. *Acta Crystallogr. D* **60,** 2184–2195 (2004).

LETTERS

Evidence of RNAi in humans from systemically administered siRNA via targeted nanoparticles

Mark E. Davis[1], Jonathan E. Zuckerman[1], Chung Hang J. Choi[1], David Seligson[2,3], Anthony Tolcher[5], Christopher A. Alabi[1]†, Yun Yen[6], Jeremy D. Heidel[7] & Antoni Ribas[2,4]

Therapeutics that are designed to engage RNA interference (RNAi) pathways have the potential to provide new, major ways of imparting therapy to patients[1,2]. Long, double-stranded RNAs were first shown to mediate RNAi in *Caenorhabditis elegans*[3], and the potential use of RNAi for human therapy has been demonstrated by the finding that small interfering RNAs (siRNAs; approximately 21-base-pair double-stranded RNA) can elicit RNAi in mammalian cells without producing an interferon response[4]. We are at present conducting the first in-human phase I clinical trial involving the systemic administration of siRNA to patients with solid cancers using a targeted, nanoparticle delivery system. Here we provide evidence of inducing an RNAi mechanism of action in a human from the delivered siRNA. Tumour biopsies from melanoma patients obtained after treatment show the presence of intracellularly localized nanoparticles in amounts that correlate with dose levels of the nanoparticles administered (this is, to our knowledge, a first for systemically delivered nanoparticles of any kind). Furthermore, a reduction was found in both the specific messenger RNA (M2 subunit of ribonucleotide reductase (*RRM2*)) and the protein (RRM2) levels when compared to pre-dosing tissue. Most notably, we detect the presence of an mRNA fragment that demonstrates that siRNA-mediated mRNA cleavage occurs specifically at the site predicted for an RNAi mechanism from a patient who received the highest dose of the nanoparticles. Together, these data demonstrate that siRNA administered systemically to a human can produce a specific gene inhibition (reduction in mRNA and protein) by an RNAi mechanism of action.

A major challenge with the use of siRNAs in mammals is their intracellular delivery to specific tissues and organs that express the target gene. The first demonstrations of siRNA-mediated gene silencing in mammals through systemic administration were accomplished using naked siRNA and methods of administration not compatible with clinical application[5–7]. Since then, several delivery vehicles have been combined with siRNAs to improve their delivery in animal models[1,2]. A recent study provided direct evidence for the siRNA mechanism of action by using a modified 5′-RACE (rapid amplification of complementary DNA ends) PCR technique providing positive identification of the specific mRNA cleavage product[8]. Human clinical trials with synthetic siRNAs began in 2004, using direct intraocular siRNA injections for patients with blinding choroidal neovascularization (CNV). Subsequently, other clinical trials have initiated[2] and early clinical data are beginning to appear[9,10]. Although there are animal studies that do support the possibility of an RNAi mechanism of action from administered siRNA[11], other animal data from siRNAs injected into the eyes of mice for the treatment of CNV suggest non-RNAi mechanisms of action for CNV suppression[12]. At this time, no direct evidence for an RNAi mechanism of action in humans from siRNA administered either locally or systemically has been reported.

We are at present conducting the first, to our knowledge, siRNA clinical trial that uses a targeted nanoparticle-delivery system (clinical trial registration number NCT00689065)[13]. Patients with solid cancers refractory to standard-of-care therapies are administered doses of targeted nanoparticles on days 1, 3, 8 and 10 of a 21-day cycle by a 30-min intravenous infusion. The nanoparticles consist of a synthetic delivery system (Fig. 1a) containing: (1) a linear, cyclodextrin-based polymer (CDP), (2) a human transferrin protein (TF) targeting ligand displayed on the exterior of the nanoparticle to engage TF receptors (TFR) on the surface of the cancer cells, (3) a hydrophilic polymer (polyethylene glycol (PEG) used to promote nanoparticle stability in biological fluids), and (4) siRNA designed to reduce the expression of the RRM2 (sequence used in the clinic was previously denoted siR2B+5)[14]. The TFR has long been known to be upregulated in malignant cells[15], and RRM2 is an established anti-cancer target[16]. These nanoparticles (clinical version denoted as CALAA-01) have been shown to be well tolerated in multi-dosing studies in non-human primates[17]. Although a single patient with chronic myeloid leukaemia has been administered siRNA by liposomal delivery[18], our clinical trial is the initial human trial to systemically deliver siRNA with a targeted delivery system and to treat patients with solid cancer[13].

To ascertain whether the targeted delivery system can provide effective delivery of functional siRNA to human tumours, we investigated biopsies from three patients from three different dosing cohorts; patients A, B and C, all of whom had metastatic melanoma and received CALAA-01 doses of 18, 24 and 30 mg m^{-2} siRNA, respectively. Given the highly experimental nature of this protocol, the regulatory process at both the local and federal levels explicitly precluded a provision for mandatory biopsies in all patients. Therefore, biopsies were obtained on a voluntary basis. Biopsies in these three patients were collected after the final dose of cycle 1 (denoted A_{post}, B_{post} and $C1_{post}$) and compared to archived tissue (denoted A_{pre}, B_{pre} and $C1_{pre}$). Patient C continued therapy beyond one cycle and provided another set of biopsy material ($C2_{pre}$ that was obtained approximately 1 month after the final dose of cycle 1, and $C2_{post}$ that was collected on the day of the final dose of cycle 2). Because of the limited sample amount, only immunohistochemistry (IHC) and staining for the nanoparticles could be performed on the $C1_{pre}$ and $C1_{post}$ samples, and protein (for western blot analyses) was only available from the $C2_{pre}$ and $C2_{post}$ samples. Details of this clinical trial will be reported elsewhere when completed.

[1]Chemical Engineering, California Institute of Technology, Pasadena, California 91125, USA. [2]Jonsson Comprehensive Cancer Center, [3]Department of Pathology, David Geffen School of Medicine, [4]Department of Medicine, Division of Hematology Oncology, David Geffen School of Medicine, University of California, Los Angeles, California 90095, USA. [5]START - South Texas Accelerated Research Therapeutics, LLC, 4383 Medical Drive, 4th Floor, San Antonio, Texas 78229, USA. [6]Department of Medical Oncology and Therapeutics Research, City of Hope Comprehensive Cancer Center, 1500 E. Duarte Road, Duarte, California 91010, USA. [7]Calando Pharmaceuticals, 201 South Lake Avenue, Suite 703, Pasadena, California 91101, USA. †Present address: Department of Chemical Engineering, Massachusetts Institute of Technology, Cambridge, Massachusetts 02139, USA.

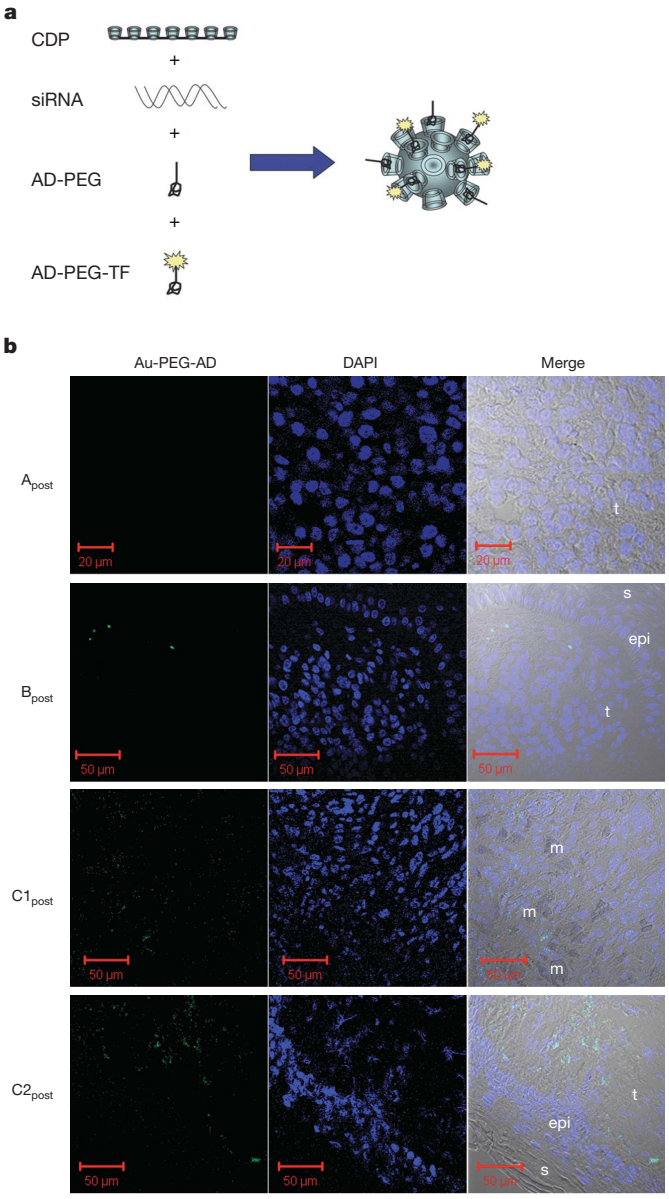

Figure 1 | Detection of targeted nanoparticles in human tumours. **a**, Schematic representation of the targeted nanoparticles. The polyethylene glycol (PEG) molecules are terminated with adamantane (AD) that form inclusion complexes with surface cyclodextrins to decorate the surface of the nanoparticle with PEG for steric stabilization and PEG-TF for targeting. **b**, Confocal images of post-treatment biopsy sections from patients A, B and C. Left, Au-PEG-AD stain; middle, DAPI stain; right, merged images of the left and right panels with the bright field. epi, epidermis, m, melanophage; s, skin side; t, tumour side.

The targeted nanoparticles (about 70-nm diameter) were administered intravenously, as they are designed to circulate and then to accumulate and permeate in solid tumours[13]. Within the tumour, the TF-targeting ligand assists in directing the nanoparticles into tumour cells overexpressing TFR[19]. To detect the nanoparticles in tumour cells, sections of the tumour tissue were stained for the presence of the nanoparticles using a 5-nm gold particle that is capped with thiolated PEG containing adamantane (AD) at the end distal to the thiol (AD-PEG-Au) to allow for multivalent binding to the cyclodextrins (Supplementary Scheme 2). The function of the stain has been previously confirmed using other cyclodextrin-containing particles[20], and is demonstrated here for the targeted nanoparticles carrying siRNA *in vitro* (Supplementary Fig. 1) and *in vivo* (Supplementary Figs 2 and 3). Transmission electron microscopy (TEM) images of the nanoparticles confirm that in mice, the nanoparticles are intracellular (Supplementary Fig. 2). Samples A, B and C1, analysed in a blinded fashion, demonstrated a heterogeneous distribution of nanoparticles only in post-dosing tumour tissue (Fig. 1 for post-dosing and Supplementary Fig. 4 for pre-dosing). The nanoparticles can localize intracellularly in tumour tissue and are not found in the adjacent epidermis (Fig. 1). In these biopsies TEM images were dominated by melanosomes[21] inhibiting the identification of the nanoparticles (data not shown). Samples $C1_{post}$ and $C2_{post}$ show the highest number and intensity of stained regions, B_{post} shows a decreased amount of staining relative to samples $C1_{post}$ and $C2_{post}$ (Fig. 1b), A_{post} does not show the presence of the stain (Fig. 1b), and all the pre-dosing samples are completely negative for the stain (Supplementary Fig. 4). This is the first example of a dose-dependent accumulation of targeted nanoparticles in tumours of humans from systemic injections for nanoparticles of any type.

Tumour *RRM2* mRNA levels were measured by quantitative real-time reverse-transcriptase polymerase chain reaction (qRT–PCR) and were performed in a blinded fashion[22]. Reduction in *RRM2* mRNA is observed in the post-treatment samples (Fig. 2). Because samples A_{pre} and B_{pre} are from tissues collected many months before the initiation of siRNA treatment, the fraction of the overall reduction in mRNA observed in A_{post} and B_{post} attributable to the nanoparticle treatment cannot be directly ascertained. Unfortunately, we were not able to perform PCR on the C1 samples. However, the PCR data from the $C2_{pre}$ and $C2_{post}$ samples (collected 10 days apart) provide direct evidence for *RRM2* mRNA reduction by the treatment of the patient with the nanoparticles.

To ascertain whether the RRM2 protein level is reduced in the tumour because of the siRNA treatment, IHC and western blotting were used as previously described in mice[23]. Because RRM2 protein expression is largely restricted to the late G1/early S phase of the cell cycle, not all of the tumour cells will be expressing RRM2. Figure 3 shows IHC data for RRM2 and TFR proteins in $C1_{pre}$ and $C1_{post}$ samples (IHC analyses were performed in a blinded fashion and ten random regions of each sample were analysed). Considerable reduction in RRM2 is observed (mean scoring of RRM2 from the ten sections was reduced fivefold) after treatment, whereas TFR levels are slightly increased (mean scoring of TFR from the ten sections was increased 1.2-fold) in the $C1_{pre}$ and $C1_{post}$ samples. The low level of RRM2 that is observed by IHC in the $C1_{post}$ sample is maintained in the $C2_{pre}$ and $C2_{post}$ samples (by IHC). Western blot analyses of the $C2_{pre}$ and $C2_{post}$ samples show a reduction in the level of the RRM2 protein that is due to the siRNA treatment (*RRM2* mRNA reductions exceeded the reduction levels obtained from protein but this could be due to post-transcriptional mechanisms that have been observed

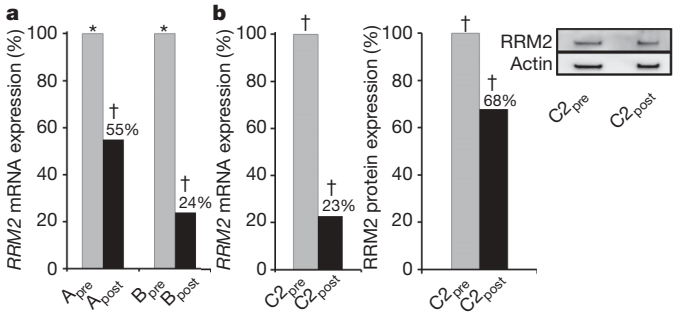

Figure 2 | RRM2 mRNA and protein expression in tumour tissue. **a**, qRT–PCR analysis of *RRM2* mRNA levels in samples from patients A and B before and after dosing. *RRM2* mRNA levels are normalized to TATA box binding protein (*TBP*) mRNA levels. Results are presented as the percentage of the pre-dosing *RRM2*/*TBP* mRNA levels for each patient. **b**, qRT–PCR and western blot analysis of RRM2 protein expression from patient samples $C2_{pre}$ and $C2_{post}$. The bar graph shows the average volume of western blot bands from two independent experiments; one representative blot is pictured. Asterisk denotes archived samples; dagger symbol denotes samples obtained during the trial.

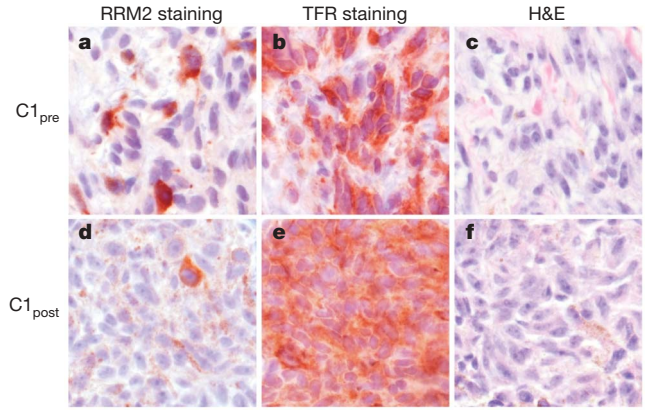

Figure 3 | RRM2 and TFR protein expression in $C1_{pre}$ and $C1_{post}$ samples. **a–f**, Photomicrographs of malignant melanoma belonging to pre-treatment (**a–c**) and post-treatment (**d–f**) samples. Protein expression is represented as brick-red (Nova Red) chromagen staining in immunohistochemically treated slides (RRM2 (**a**, **d**) and TFR (**b**, **e**)). The same tissues are also stained with haematoxylin and eosin (H&E; **c**, **f**). Brown, diffuse, finely granular colour seen in the post-treatment images (**d–f**) is the endogenous pigment of this lightly melanized tumour. Original magnification used, ×40.

previously[24]). The decreases in the RRM2 mRNA and protein observed after treatment (Fig. 2b) suggest the siRNA treatment remains effective after several cycles of dosing. The IHC data from patient A do not show changes in RRM2 expression after dosing, whereas results from patient B are indicative of reductions in maximal RRM2 expression (IHC scoring of the regions of maximal expression showed a 1.5-fold decrease), but the overall mean expression levels remained relatively constant (IHC scoring of the ten sections).

To demonstrate that the siRNA delivered by the targeted nanoparticles can engage the RNAi machinery, the mRNA cleavage products were characterized using a modified 5′-RNA-ligand-mediated RACE (5′-RLM-RACE) PCR technique (Fig. 4). An *RRM2* mRNA fragment—the 5′ end of which matches the predicted cleavage site (ten base pairs (bp) from the 5′ end of the antisense strand)—was detected in the $C2_{pre}$ and $C2_{post}$ samples, but not in B_{post} and A_{post} or their corresponding pre-treatment samples. RACE does not provide a quantitative measure of the amount of the fragments so the intensities of the bands cannot be correlated with the amounts in the tissue samples. The presence of this *RRM2* mRNA fragment from patient C indicates that siRNA delivered by targeted nanoparticles can engage the RNAi machinery in a solid human tumour and induce the desired mRNA cleavage. Furthermore, this result indicates that at least a portion of the RRM2 mRNA and protein reductions observed from the C2 samples are due to a bona fide RNAi mechanism. The presence of the *RRM2* mRNA fragment in the $C2_{pre}$ sample suggests that siRNA can provide an RNAi mechanism for several weeks (mRNA cleavage in the $C2_{pre}$ sample must originate from cycle one dosing) as the RRM2 protein levels remained relatively constant when compared to the $C1_{post}$ sample (IHC). We have shown that the length of the RNAi effects of delivered siRNA in both cells and animals (mice) is dependent on the doubling time of the cells being analysed (longer inhibition times with longer cell doubling times)[25]. Gene silencing by siRNA can occur on the timescale observed here, approximately 1 month, provided the cell doubling times are long[25]. Patient C had stable disease between these biopsies, and these mostly quiescent tumours have very slow growth kinetics that would be suitable to experience lengthy RNAi effects[25]. Furthermore, we do not know how long the nanoparticles reside within the cells and release siRNA. Because the nanoparticles are observed in the sample $C1_{post}$ and not the sample $C2_{pre}$, they must disassemble within 1 month. Thus, the pharmacodynamics of the RNAi effects could be due to the combination of the nanoparticle disassembly time and the time that the siRNA resides within the RNAi machinery.

When taken together, the data presented here provide the first, to our knowledge, mechanistic evidence of RNAi in a human from an

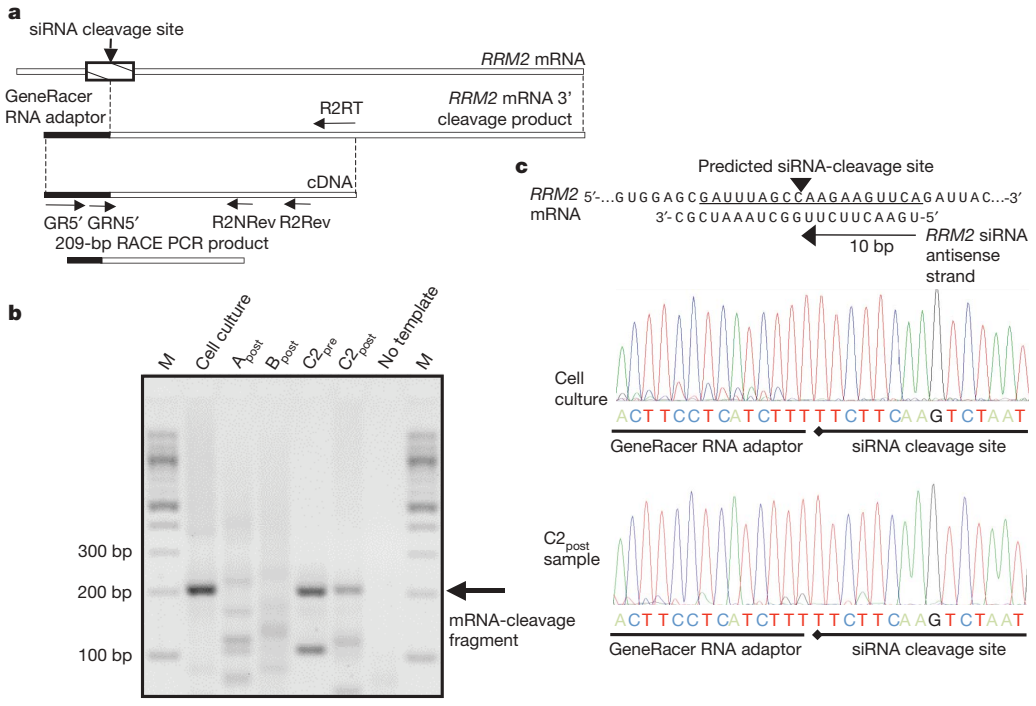

Figure 4 | 5′-RLM-RACE detection of siRNA-induced mRNA cleavage fragment. **a**, Schematic depicting the location of the predicted anti-*RRM2* siRNA cleavage site and the primers used for PCR amplification of the cleavage fragment. GR5′, GeneRacer 5′ primer; GRN5′, GeneRacer 5′ nested primer; R2RT, *RRM2* gene-specific reverse-transcriptase primer; R2Rev, *RRM2* gene-specific reverse primer; R2NRev, *RRM2* gene-specific nested primer. **b**, Agarose gel of 5′-RLM-RACE PCR amplification products from patient samples (A_{post}, B_{post}, $C2_{pre}$ and $C2_{post}$) and the *in vitro* positive control (cell culture). M, molecular mass ladder. **c**, The *RRM2* mRNA sequence and siRNA antisense strand are illustrated to show where the cleavage occurs with an RNAi mechanism. The sequence chromatographs obtained from an *in vitro* cell culture experiment with HT-144 melanoma cells and the patient $C2_{post}$ sample are illustrated.

administered siRNA. Moreover, these data demonstrate the first example of dose-dependent accumulation of targeted nanoparticles in human tumours. The reduction of the RRM2 mRNA and protein by the RRM2-specific siRNA is observed, and the results from 5′-RLM-RACE analyses show that the delivered siRNA engages the RNAi machinery. These data demonstrate that RNAi can occur in a human from a systemically delivered siRNA, and that siRNA can be used as a gene-specific therapeutic.

METHODS SUMMARY

Detection of targeted nanoparticles in biopsy samples. Snap-frozen patient biopsy samples were embedded in Tissue-Tek O.C.T. compound (Sakura) for the generation of 6-μm-thick cryosections. After immersion in PBS at 37 °C for 1 h to remove any surface O.C.T., and subsequent fixation with acetone at −20 °C for 20 min to permeabilize the cell membrane, sections received staining of PEGylated, AD-modified gold nanoparticles (Au-PEG-AD; see Supplementary Information for a description of their preparation) in the dark for 2 h. Brief rinses with PBS were used to remove any non-specifically bound Au-PEG-AD before mounting with ProLong Gold antifade reagent and staining with 4′,6-diamidino-2-phenylindole (DAPI; Invitrogen). A Zeiss LSM 510 confocal scanning microscope was used to collect the images (DAPI-excitation: 370 nm, emission: 440 nm; Au-PEG-AD-excitation: 488 nm, emission: 507 nm).

5′-RLM-RACE. 5′-RLM-RACE was performed according to the Invitrogen GeneRacer manual with modifications. Two-to-eight micrograms of total RNA was ligated directly to 250 ng GeneRacer RNA adaptor using T4 RNA ligase. After phenol extraction and ethanol precipitation, the purified ligation products were reverse-transcribed using SuperScriptIII (Invitrogen) and an *RRM2* gene-specific reverse-transcription primer (5′-CTCTCTCCTCCGATGGTTTG-3′). 5′-RLM-RACE PCR was performed using the GeneRacer 5′ and an *RRM2* gene-specific reverse primer (5′-GGCCAGGCATCAGTCCTCGTTTCTTG-3′). PCR was performed using a Bio-Rad MJ Mini personal thermocycler using PCR conditions of 95 °C for 3 min (1 cycle), 95 °C for 30 s, 60 °C for 30 s, 72 °C for 1 min (40 cycles), 72 °C for 10 min (1 cycle). A second round of nested PCR was then performed using the GeneRacer 5′ nested primer and an *RRM2* gene-specific nested primer (5′-GGCCCAGTCTGCCTTCTTCTTGAC-3′). PCR products were run on a 2% agarose gel and stained with 1 μg μl^{-1} ethidium bromide. PCR products were excised from the gel and sequenced directly to confirm RACE band identities.

Full Methods and any associated references are available in the online version of the paper at www.nature.com/nature.

Received 23 September 2009; accepted 1 March 2010.
Published online 21 March 2010.

1. Bumcrot, D., Manoharan, M., Koteliansky, V. & Sah, D. W. Y. RNAi therapeutics: a potential new class of pharmaceutical drugs. *Nature Chem. Biol.* **2,** 711–719 (2006).
2. Castanotto, D. & Rossi, J. J. The promises and pitfalls of RNA-interference-based therapeutics. *Nature* **457,** 426–433 (2009).
3. Fire, A. *et al.* Potent and specific genetic interference by double-stranded RNA in *Caenorhabditis elegans. Nature* **391,** 806–811 (1998).
4. Elbashir, S. M. *et al.* Duplexes of 21-nucleotide RNAs mediate RNA interference in cultured mammalian cells. *Nature* **411,** 494–498 (2001).
5. McCaffrey, A. P. *et al.* RNA interference in adult mice. *Nature* **418,** 38–39 (2002).
6. Lewis, D. L., Hagstrom, J. E., Loomis, A. G., Wolff, J. A. & Herweijer, H. Efficient delivery of siRNA for inhibition of gene expression in postnatal mice. *Nature Genet.* **32,** 107–108 (2002).
7. Song, E. *et al.* RNA interference targeting Fas protects mice from fulminant hepatitis. *Nature Med.* **9,** 347–351 (2003).
8. Soutschek, J. *et al.* Therapeutic silencing of an endogenous gene by systemic administration of modified siRNAs. *Nature* **432,** 173–178 (2004).
9. DeVincenzo, J. *et al.* Evaluation of the safety, tolerability and pharmacokinetics of ALN-RSV01, a novel RNAi antiviral therapeutic directed against respiratory syncytial virus (RSV). *Antiviral Res.* **77,** 225–231 (2008).
10. Leachman, S. A. *et al.* First-in-human mutation-targeted siRNA phase Ib trial of an inherited skin disorder. *Mol. Ther.* **18,** 442–446 (2010).
11. Alvarez, R. *et al.* RNA interference-mediated silencing of the respiratory syncytial virus nucleocapsid defines a potent anti-viral strategy. *Antimicrob. Agents Chemother.* **53,** 3952–3962 (2009).
12. Kleinman, M. E. *et al.* Sequence- and target-independent angiogenesis suppression by siRNA via TLR3. *Nature* **452,** 591–597 (2008).
13. Davis, M. E. The first targeted delivery of siRNA in humans via a self-assembling, cyclodextrin polymer-based nanoparticle: from concept to clinic. *Mol. Pharm.* **6,** 659–668 (2009).
14. Heidel, J. D. *et al.* Potent siRNA inhibitors of ribonucleotide reductase subunit RRM2 reduce cell proliferation *in vitro* and *in vivo. Clin. Cancer Res.* **13,** 2207–2215 (2007).
15. Gatter, K. C., Brown, G., Trowbridge, I. S., Wollston, R. E. & Mason, D. Y. Transferrin receptors in human tissues: their distribution and possible clinical relevance. *J. Clin. Pathol.* **36,** 539–545 (1983).
16. Cerqueira, N. M. F. S. A., Pereira, S., Fernandes, P. A. & Ramos, M. J. Overview of ribonucleotide reductase inhibitors: an appealing target in anti-tumor therapy. *Curr. Med. Chem.* **12,** 1283–1294 (2005).
17. Heidel, J. D. *et al.* Administration in non-human primates of escalating intravenous doses of targeted nanoparticles containing ribonucleotide reductase subunit M2 siRNA. *Proc. Natl Acad. Sci. USA* **104,** 5715–5721 (2007).
18. Koldehoff, M., Steckel, N. K., Beelen, D. W. & Elmaagacli, A. H. Therapeutic application of small interfering RNA directed against *bcr-abl* transcripts to a patient with imatinib-resistant chronic myeloid leukaemia. *Clin. Exp. Med.* **7,** 47–55 (2007).
19. Bartlett, D. W., Su, H., Hildebrandt, I. J., Weber, W. A. & Davis, M. E. Impact of tumor-specific targeting on the biodistribution and efficacy of siRNA nanoparticles measured by multimodality *in vivo* imaging. *Proc. Natl Acad. Sci. USA* **104,** 15549–15554 (2007).
20. Schluep, T. *et al.* Pharmacokinetics and tumor dynamics of the nanoparticle IT-101 from PET imaging and tumor histological measurements. *Proc. Natl Acad. Sci. USA* **106,** 11394–11399 (2009).
21. Riehl, R., Schartl, M. & Kollinger, G. Comparative studies on the ultrastructure of malignant melanoma in fish and human by freeze-etching and transmission electron microscropy. *J. Cancer Res. Clin. Oncol.* **107,** 21–31 (1984).
22. Juhasz, A., Vassilakos, A., Chew, H. K., Gandara, D. & Yen, Y. Analysis of ribonucleotide reductase M2 mRNA levels in patient samples after GTI-2040 antisense drug treatment. *Oncol. Rep.* **15,** 1299–1304 (2006).
23. Bartlett, D. W. & Davis, M. E. Impact of tumor-specific targeting and dosing schedule on tumor growth inhibition after intravenous administration of siRNA-containing nanoparticles. *Biotechnol. Bioeng.* **99,** 975–985 (2008).
24. McClarty, G. A., Chan, A. K., Engstrom, Y., Wright, J. A. & Thelander, L. Elevated expression of M1 and M2 components and drug-induced posttranscriptional modulation of ribonucleotide reductase in a hydroxyurea-resistant mouse cell line. *Biochemistry* **26,** 8004–8011 (1987).
25. Bartlett, D. W. & Davis, M. E. Insights into the kinetics of siRNA-mediated gene silencing from live-cell and live-animal bioluminescent imaging. *Nucleic Acids Res.* **34,** 322–333 (2006).

Supplementary Information is linked to the online version of the paper at www.nature.com/nature.

Acknowledgements We thank H. Sazegar, E. Seja, A. Villanueva and the G-CRC nursing staff at University of California, Los Angeles (UCLA), and L. Kalinoski, J. Peterkin, S. Rele, Y. Liang and J. Y. C. Liu for their assistance in conducting the clinical trial. We thank J. S. Economou for performing the tumour biopsies, and B. Chmielowski and Z. Wainberg for patient referrals. Histotechnology support at the UCLA Biomarker Innovations Laboratory was provided by C. Savina and J. Reiss. We also thank J. Rossi for discussions on RACE analyses. This work was supported in part by the National Cancer Institute Grant CA U54 119347 and the Daljit S. & Elaine Sarkaria Biomarker Laboratory Fund.

Author Contributions M.E.D., J.E.Z., A.R. and J.D.H. planned the experiments, J.E.Z., D.S., C.H.J.C., C.A.A., Y.Y., A.T. and A.R. conducted the experiments, M.E.D., J.E.Z., J.D.H., D.S., C.H.J.C. and A.R. analysed the data, and M.E.D., J.E.Z. and A.R. wrote the paper.

Author Information Reprints and permissions information is available at www.nature.com/reprints. The authors declare competing financial interests: details accompany the full-text HTML version of the paper at www.nature.com/nature. Correspondence and requests for materials should be addressed to M.E.D. (mdavis@cheme.caltech.edu).

METHODS

Detection of targeted nanoparticles in biopsy samples. Snap-frozen patient biopsy samples were embedded in Tissue-Tek O.C.T. compound (Sakura) to generate 6-μm-thick cryosections. After immersion in PBS at 37 °C for 1 h to remove any surface O.C.T., and in acetone at −20 °C for 20 min to permeabilize the cell membrane, sections received staining of PEGylated, adamantane-modified gold nanoparticles (Au-PEG-AD; see Supplementary Information for their preparation) in the dark for 2 h. Brief rinses with PBS were used to remove any non-specifically bound Au-PEG-AD before mounting with ProLong Gold antifade reagent and staining with DAPI (Invitrogen). A Zeiss LSM 510 confocal scanning microscope (with a Plan-Neofluar ×40/0.75 objective and up to 2× digital zoom) was used to collect the images (DAPI-excitation: 740 nm (two-photon laser), emission filter: 390–490 nm; Au-PEG-AD-excitation: 488 nm (argon laser), emission filter: band-pass (BP) 500–550 nm infrared radiation (IR)). The measured resolution at which images were acquired is 512 × 512 pixels, and the image bit-depth is 8-bit. The Zeiss LSM Image Browser Software allows the extraction of images.

RNA extraction. Patient samples preserved in RNALater (Ambion) were suspended in TRIzol reagent (Invitrogen) and homogenized in a FastPrep-24 Tissue Homogenizer (MP Biomedicals). Total RNA was purified from the aqueous phase of TRIzol extract using the PureLink RNA Mini Kit (Invitrogen) following manufacturer recommendations. RNA was extracted from archived patient samples using RecoverAll total nucleic acid isolation kit (Ambion) following manufacturer instructions.

5′-RLM-RACE. 5′-RLM-RACE was performed according to the Invitrogen GeneRacer manual with modifications. Two-to-eight micrograms of total RNA was ligated directly to 250 ng GeneRacer RNA adaptor (5′-CGACUGGA GCACGAGGACACUGACAUGGACUGAAGGAGUAGAAA-3′) using T4 RNA ligase (5 units) for 1 h at 37 °C. After phenol extraction and ethanol precipitation, the purified ligation products were reverse-transcribed using SuperScriptIII (Invitrogen) and an *RRM2* gene-specific reverse-transcription primer (5′-CT CTCTCCTCCGATGGTTTG-3′) at 55 °C for 45 min followed by inactivation at 70 °C. 5′-RLM-RACE-PCR was performed using the GeneRacer 5′ primer (5′-CGACTGGAGCACGAGGACACTGA-3′) and an *RRM2* gene-specific reverse primer (5′-GGCCAGGCATCAGTCCTCGTTTCTTG-3′). PCR was performed using a Bio-Rad MJ Mini personal thermocycler using PCR conditions of 95 °C for 3 min (1 cycle), 95 °C for 30 s, 60 °C for 30 s, 72 °C for 1 min (40 cycles), 72 °C for 10 min (1 cycle). A second round of nested PCR was then performed using the GeneRacer 5′ nested primer (5′-GGACACTGACATGGACTGAAGG AGTA-3′) and an *RRM2* gene-specific nested primer (5′-GGCCCAGTCTGCCT TCTTCTTGAC-3′). PCR products were run on a 2% agarose gel and stained with 1 μg μl^{-1} ethidium bromide. PCR products were excised from the gel and sequenced directly to confirm RACE band identities. For the cell culture RACE experiments, 500,000 HT-144 melanoma cells were transfected with 20 nM *RRM2* siRNA using Lipofectamine RNAiMax (Invitrogen). RNA was extracted for the RLM-RACE as described earlier, 48 h after transfection.

qRT–PCR. Patient RNA samples were reversed-transcribed using SuperScriptIII reverse transcriptase. White blood cell (WBC) cDNA (0.4–200 ng) was used as a PCR template for standard curves of *RRM2* and *TBP*. Two microlitres of prepared sample or standard cDNA was used for triplicate Taqman real-time PCR as described elsewhere[25]. Concentrations of *RRM2* and *TBP* in the samples were calculated from the WBC cDNA standard curve, and *RRM2* levels were normalized to *TBP* levels within the same sample.

Western blots. Total protein was recovered from the phenol/chloroform phase of TRIzol extraction (see description of the RNA extraction earlier). Samples were diluted to equivalent protein concentration and denatured by the addition of β-mercaptoethanol-containing Laemmli sample buffer. The primary antibodies were goat polyclonal anti-RRM2 antibody (Santa Cruz Biotechnology), and mouse polyclonal anti-actin antibody (BD Biosciences). The secondary antibodies were horseradish-peroxidase-conjugated donkey anti-goat antibody, and rabbit anti-mouse antibody (Santa Cruz Biotechnology). Development was done using SuperSignal West Dura Extended Duration Substrate (Thermo-Fisher). Blot images were captured using a Molecular Imager VersaDoc 3000 system (Bio-Rad). Band quantification was performed using Image-Quant TL software (GE/Amersham Biosciences).

Tissues and immunohistochemical assay. Formalin-fixed, paraffin-embedded human tissue samples from patient-matched pre- and post-treatment cases were obtained under UCLA Institutional Review Board (IRB) approval. IHC assays were performed using a Dako Autostainer Plus (Dako) with fresh sections of pre- and post-treatment cases stained at the same time. Tissue sections 4-μm thick were deparaffinized in xylene and rehydrated in graded alcohols. The sections were then placed in a pressure cooker (17.5 PSI, 122 °C; Biocare Decloaking Chamber, Biocare Medical) in 0.01 M sodium citrate buffer, pH 6.0, or 0.1 M Tris-HCl buffer, pH 9.0, for 10 min for heat-antigen retrieval of RRM2 and TFR antigens, respectively. Endogenous peroxidase was quenched with 3% hydrogen peroxide at room temperature. Primary goat anti-human R2 polyclonal antibody (sc-10846; Santa Cruz Biotechnology), was applied for 30 min at room temperature at a final concentration of 1.0 μg ml^{-1} (1:200). Mouse anti-human TFR monoclonal IgG1 antibody (clone H68.4, 13-6800; Invitrogen) was applied for 30 min at room temperature at a final concentration of 0.5 μg ml^{-1} (1:1,000). Antigen detection was accomplished using the Vectastain ABC Elite Goat HRP kit (Vector Labs) or the Dako Envision goat anti-mouse IgG secondary antibody with attached HRP-labelled dextran polymer (K4001; Dako), for RRM2 and TFR, respectively. All tissues were either amelanotic or only lightly melanized, therefore bleaching was not performed and Nova Red (Vector Labs) was used as the chromagen to easily discern staining from any endogenous pigment. The sections were then counterstained with Meyer's haematoxylin, followed by dehydration in graded alcohols, xylene and the addition of a coverslip. Human tonsil and colon cancer served as positive assay controls. Negative controls consisted of duplicate tissue sections stained with either non-immune pooled goat IgG (I-5000, Vector Labs) or monoclonal mouse IgG1 (02-6100; Invitrogen), applied at identical final concentrations as used for RRM2 and TFR primary antibodies, respectively. For each sample, ten random tumour regions were scored for maximal expression and mean expression.

LETTERS

Long non-coding RNA *HOTAIR* reprograms chromatin state to promote cancer metastasis

Rajnish A. Gupta[1], Nilay Shah[4], Kevin C. Wang[1], Jeewon Kim[2], Hugo M. Horlings[6], David J. Wong[1], Miao-Chih Tsai[1], Tiffany Hung[1], Pedram Argani[5], John L. Rinn[7], Yulei Wang[8], Pius Brzoska[8], Benjamin Kong[8], Rui Li[3], Robert B. West[3], Marc J. van de Vijver[6], Saraswati Sukumar[4] & Howard Y. Chang[1]

Large intervening non-coding RNAs (lincRNAs) are pervasively transcribed in the genome[1–3] yet their potential involvement in human disease is not well understood[4,5]. Recent studies of dosage compensation, imprinting, and homeotic gene expression suggest that individual lincRNAs can function as the interface between DNA and specific chromatin remodelling activities[6–8]. Here we show that lincRNAs in the *HOX* loci become systematically dysregulated during breast cancer progression. The lincRNA termed *HOTAIR* is increased in expression in primary breast tumours and metastases, and *HOTAIR* expression level in primary tumours is a powerful predictor of eventual metastasis and death. Enforced expression of *HOTAIR* in epithelial cancer cells induced genome-wide re-targeting of Polycomb repressive complex 2 (PRC2) to an occupancy pattern more resembling embryonic fibroblasts, leading to altered histone H3 lysine 27 methylation, gene expression, and increased cancer invasiveness and metastasis in a manner dependent on PRC2. Conversely, loss of *HOTAIR* can inhibit cancer invasiveness, particularly in cells that possess excessive PRC2 activity. These findings indicate that lincRNAs have active roles in modulating the cancer epigenome and may be important targets for cancer diagnosis and therapy.

We hybridized RNA derived from normal human breast epithelia, primary breast carcinomas, and distant metastases to ultra-dense *HOX* tiling arrays[7] (Fig. 1a, b). We found that 233 transcribed regions in the *HOX* loci, comprising 170 non-coding RNAs (ncRNAs) and 63 *HOX* exons, were differentially expressed (Fig. 1a). Unsupervised hierarchical clustering showed systematic variation in the expression of *HOX* lincRNAs among normal breast epithelia, primary tumour, and metastases. *HOXA5*, a known breast tumour suppressor[9], along with dozens of *HOX* lincRNAs, are expressed in normal breast but with reduced expression in all cancer samples (Supplementary Fig. 1). A set of *HOX* lincRNAs and messenger RNAs, including the known oncogene *HOXB7* (ref. 10), is frequently expressed in primary tumours but not in metastases (Supplementary Fig. 1). A distinct set of *HOX* lincRNAs is sometimes overexpressed in primary tumours, and very frequently overexpressed in metastases (Fig. 1b). Notably, one such metastasis-associated lincRNA is *HOTAIR* (Fig. 1b), which has a unique association with patient prognosis (Supplementary Figs 1, 2 and Supplementary Table 1). *HOTAIR* is a lincRNA in the mammalian *HOXC* locus that binds to and targets the PRC2 complex to the *HOXD* locus, located on a different chromosome[7]. PRC2 is a histone H3 lysine 27 (H3K27) methylase involved in developmental gene silencing and cancer progression[11,12]. We proposed that altered *HOTAIR* expression may be involved in human cancer by promoting genomic relocalization of the Polycomb complex and H3K27 trimethylation.

Quantitative PCR showed that *HOTAIR* is overexpressed from hundreds to nearly two-thousand-fold in breast cancer metastases, and the *HOTAIR* expression level is sometimes high but heterogeneous among primary tumours (Fig. 1c). We next measured the *HOTAIR* level in an independent panel of 132 primary breast tumours (stage I and II) with extensive clinical follow-up[13]. Indeed, nearly one-third of primary breast tumours overexpress *HOTAIR* by more than 125-fold compared to normal breast epithelia, the minimum level of *HOTAIR* overexpression observed in bona fide metastases (Fig. 1d), and a high *HOTAIR* level is a significant predictor of subsequent metastasis and death ($P = 0.0004$ and $P = 0.005$ for metastasis and death, respectively, Fig. 1e, f). Multivariate analysis showed that prognostic stratification of metastasis and death by *HOTAIR* is independent of known clinical risk factors such as tumour size, stage and hormone receptor status (Supplementary Table 2).

We next examined the effects of manipulating *HOTAIR* level in several breast cancer cell lines. *HOTAIR* levels in cell lines are significantly lower than those seen in primary or metastatic breast tumours (Supplementary Figs 3 and 4). Retroviral transduction allowed stable overexpression of *HOTAIR* of several-hundred-fold compared to vector-transduced cells, which are comparable to levels observed in patients (Supplementary Fig. 4). *HOTAIR* overexpression promoted colony growth in soft agar (Supplementary Fig. 5). In addition, enforced expression of *HOTAIR* in four different breast cancer cell lines increased cancer cell invasion through Matrigel, a basement-membrane like extracellular matrix, (Fig. 2a). Conversely, depletion of *HOTAIR* by small interfering RNAs (siRNAs) in MCF7, a cell line that expresses endogenous *HOTAIR*, decreased its matrix invasiveness (Fig. 2b and Supplementary Fig. 6). To probe the effects of *HOTAIR* on cancer cell dynamics *in vivo*, we labelled control and *HOTAIR*-expressing cells with firefly luciferase, enabling *in vivo* bioluminescence imaging. When MDA-MB-231 cells expressing vector or *HOTAIR* were orthotopically grafted into mammary fat pads, serial imaging showed that *HOTAIR* expression modestly increased the rate of primary tumour growth (Fig. 2c, left). Notably, in the same animals, we observed significantly increased foci of luciferase signal in the lung fields of mice bearing $HOTAIR^+$ primary tumours (Fig. 2c, right), which suggests that *HOTAIR* promotes lung metastasis.

To quantify further metastatic potential *in vivo*, we performed tail vein xenografts and compared the rates of lung colonization. Vector expression in the non-metastatic cell line SK-BR3 never showed lung colonization after tail vein xenograft (0 out of 15 mice), but *HOTAIR*

[1]Howard Hughes Medical Institute and Program in Epithelial Biology, [2]Stanford Cancer Center and Transgenic Mouse Research Center, [3]Department of Pathology, Stanford University School of Medicine, Stanford, California 94305, USA. [4]Sidney Kimmel Comprehensive Cancer Center, [5]Department of Pathology, Johns Hopkins University School of Medicine, Baltimore, Maryland 21231, USA. [6]Department of Pathology, Academic Medical Center, Meibergdreef 9, 1105AZ, Amsterdam, The Netherlands. [7]The Broad Institute of Harvard and Massachusetts Institute of Technology, Cambridge, Massachusetts 02142, USA. [8]Applied Biosystems, Foster City, California 94404, USA.

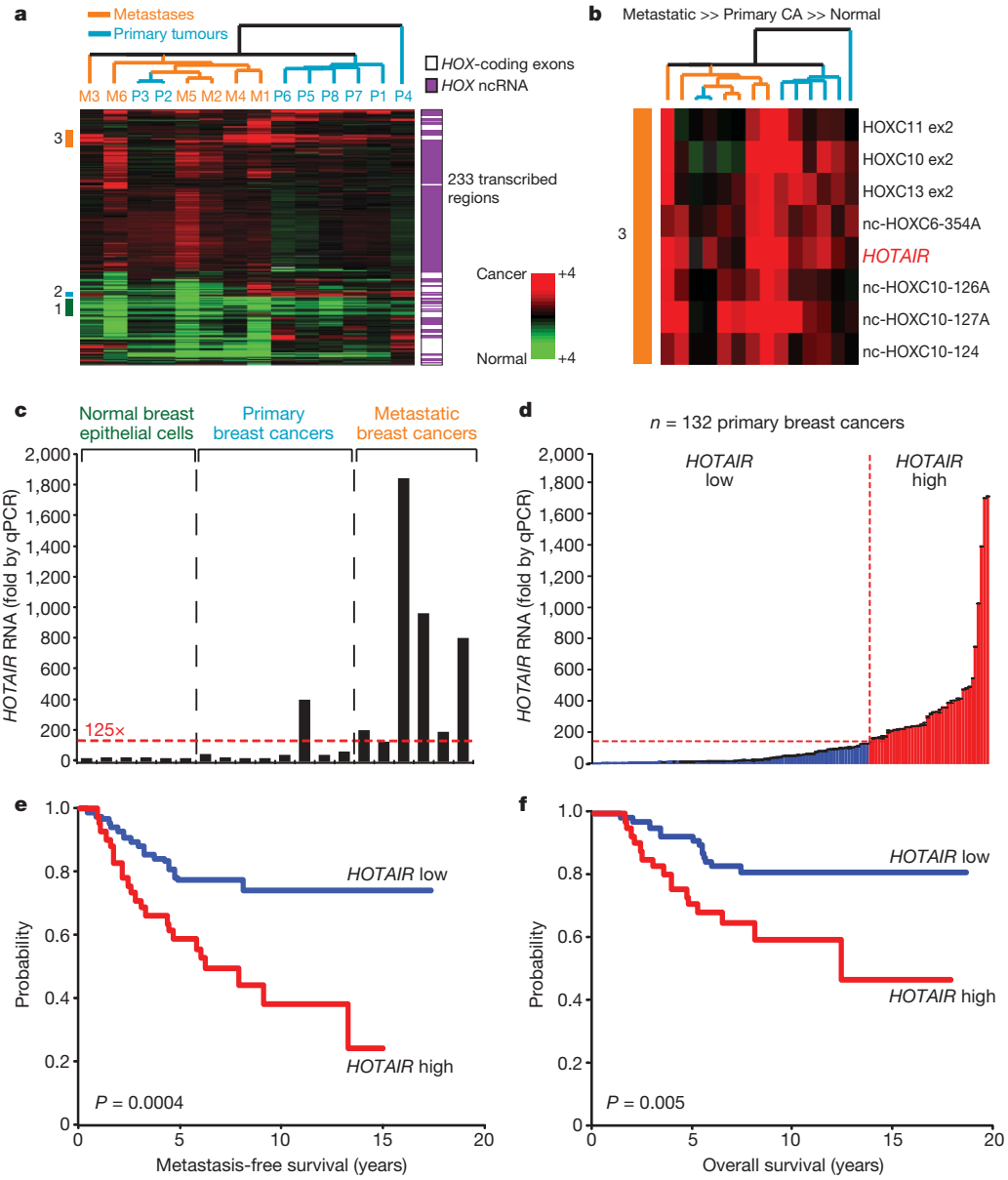

Figure 1 | *HOX* lincRNAs are systematically dysregulated in breast carcinoma and have prognostic value for metastasis and survival. **a**, Heat map representing unsupervised hierarchical clustering of expression values of a panel of primary and metastatic breast cancers relative to normal breast epithelial cells (pooled from five breast organoids). An ultra-high-density *HOX* tiling array[7] was interrogated with either normal breast organoid RNA (Cy3 channel) or RNA derived from primary or metastatic breast tumours (Cy5 channel). Each column represents the indicated clinical sample. Each row indicates a transcribed region, either a *HOX*-coding exon or *HOX* ncRNA. Expression values are depicted as the ratio relative to pooled normal and represented as a red–green colour scale. **b**, Higher resolution of subset 3 identifying transcripts that show higher relative expression in metastatic as compared to primary tumours and normal epithelia. *HOTAIR* is one such transcript ($P = 0.03$, Student's *t*-test). **c**, qRT–PCR validation of the expression tiling array results measuring *HOTAIR* abundance in a panel of normal breast epithelial-enriched organoids, primary breast tumours, and metastatic breast tumours. Metastatic tumours had a minimum of 125-fold higher levels of *HOTAIR* than normal breast epithelia. Error bars represent s.d. ($n = 3$). **d**, qRT–PCR analysis of *HOTAIR* in 132 primary breast tumours (stage I or II). Approximately one-third of primary breast tumours had >125-fold overexpression of *HOTAIR* compared to normal tissue (*HOTAIR* high, indicated in red), whereas roughly two-thirds of tumours did not (*HOTAIR* low, indicated in blue). Error bars represent s.d. ($n = 3$). **e**, **f**, Kaplan–Meier curves for metastasis-free survival (**e**) or overall survival (**f**) of the same 132 primary breast tumours measured in **d**.

expression allowed SK-BR3 cells to colonize the lung in 80% of animals (12 out of 15 mice, Fig. 2c). SK-BR3 cells apparently lack further genetic elements required to persist in the lung, because *HOTAIR*-transduced SK-BR3 cells in the lung disappeared after approximately 1 week. In contrast, *HOTAIR* expression in MDA-MB-231 cells resulted in approximately eight- to ten- fold more cells to engraft the lung after tail vein xenograft (Fig. 2d). These differences persisted until the end of the experiment, resulting in tenfold more lung metastases as verified by histology ($P = 0.00005$, Fig. 2e). The tumours retained *HOTAIR* expression for the length of the experiment (Supplementary Fig. 7).

We next tested whether *HOTAIR* overexpression affected the pattern of PRC2 occupancy. We mapped PRC2 occupancy genome-wide by chromatin immunoprecipitation followed by hybridization to tiling microarrays interrogating all human promoters (ChIP-chip, Fig. 3). Compared to vector-expressing cells, *HOTAIR* overexpression induced localization of H3K27me3 and PRC2 subunits SUZ12 and EZH2 on 854 new genes while concomitantly losing PRC2 occupancy and H3K27me3 on 37 genes (Fig. 3a). A significant fraction of these 854 genes also showed consequent changes in gene expression after *HOTAIR* overexpression (39% observed versus 7% expected by chance alone, $P = 2.5 \times 10^{-209}$, hypergeometric distribution). Most

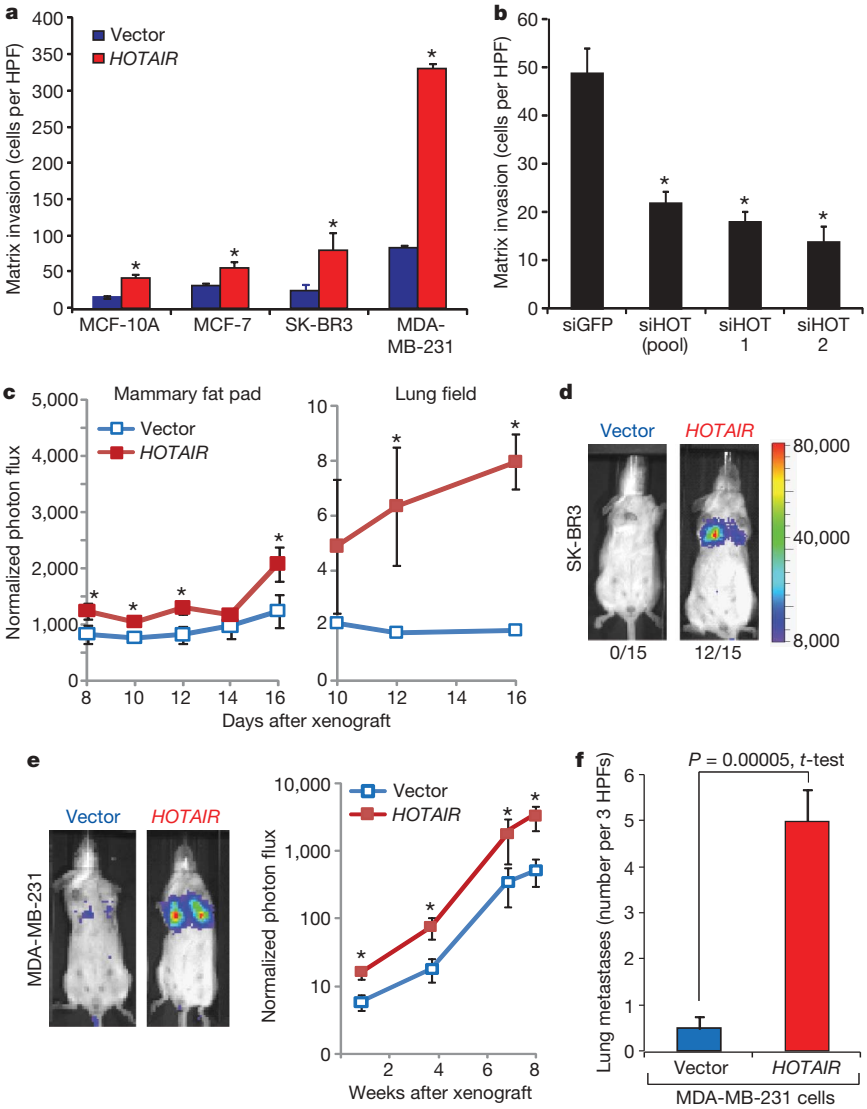

Figure 2 | *HOTAIR* promotes invasion of breast carcinoma cells. **a**, Relative fold increase in matrix invasion in four breast carcinoma cell lines after enforced *HOTAIR* expression. Mean ± s.d. are shown ($n = 3$). HPF, high power field. **b**, Matrix invasion in the MCF-7 breast carcinoma cell line transfected with individual or pooled siRNAs targeting *HOTAIR* (error bars = s.d., $n = 3$). siGFP denotes siRNA targeting green fluorescent protein (GFP) as a control. **c**, *HOTAIR* expression in MDA-MB-231 cells enhances orthotopic growth in mammary fat pads and metastasis to lung ($n = 5$ per arm; error bars are s.e.m.). **d**, *HOTAIR* promotes transient lung colonization of SK-BR3 after tail vein xenograft ($n = 15$ per arm). **e**, *HOTAIR* promotes lung colonization of MDA-MB-231 cells after tail vein xenograft. **f**, Histological analysis of the number of lung metastasis in vector- or *HOTAIR*-expressing MDA-MB-231 cells 8–9 weeks after tail vein xenograft ($n = 18$ per arm, error bars are s.e.m.). Similar results were obtained using luciferase-marked cells. *$P < 0.05$ between control cells and cells manipulated for *HOTAIR*.

PRC2 occupancy sites on promoters genome-wide showed little change (data not shown), and *HOTAIR* overexpression did not change the levels of PRC2 subunits (Fig. 4a, lane 1 versus lane 4). Several genes with *HOTAIR*-induced PRC2 occupancy are implicated in inhibiting breast cancer progression, including transcription factors *HOXD10* (ref. 14) and *PGR* encoding progesterone receptor (a classic favourable prognostic factor); cell adhesion molecules of the protocadherin (*PCDH*) gene family[15] and *JAM2* (ref. 16); and *EPHA1* (refs 17, 18), encoding an ephrin receptor involved in tumour angiogenesis. Gene Ontology[19] analysis suggested that most of the 854 genes are involved in pathways related to cell–cell signalling and development (Supplementary Fig. 8). *HOTAIR*-induced PRC2 occupancy tended to spread over promoters, and to a lesser extent, gene bodies (Fig. 3b). *HOTAIR* may also induce PRC2 localization to other intergenic regions not present on our tiling arrays. ChIP followed by quantitative PCR confirmed that *HOTAIR* substantially increased PRC2 occupancy and H3K27me3 of all target genes examined (Supplementary Fig. 9). Notably, like *HOTAIR* itself, the 854 *HOTAIR*–PRC2 target genes are coordinately downregulated in aggressive breast tumours that tend to cause death ($P < 0.0003$, Supplementary Fig. 10).

We next compared the 854 genes with *HOTAIR*-induced PRC2 occupancy in MDA-MB-231 cells with a compendium of published PRC2 occupancy profiles in diverse cell types (Fig. 3c). PRC2 occupancy patterns from different cancer, fibroblastic and embryonic stem cell lines were annotated from existing databases (Supplementary Table 3). Using a pattern-matching algorithm[20], we found that the *HOTAIR*-induced PRC2 occupancy pattern in breast cancer cells most closely resembled the endogenous PRC2 occupancy pattern in embryonic and neonatal fibroblasts, especially fibroblasts derived from posterior and distal anatomic sites where endogenous *HOTAIR* is expressed[7] ($P < 10^{-50}$ for each comparison, false discovery rate (FDR) $\ll 0.05$, Fig. 3c). These 854 genes are also significantly enriched for genes in primary fibroblasts that are bound by PRC2 in a *HOTAIR*-dependent manner (32% overlap observed versus 9.9% expected by chance alone, $P = 8.5 \times 10^{-93}$, hypergeometric distribution, M.-C.T., unpublished data). These results indicate that increased *HOTAIR* expression in breast cancer cells seems to reprogram the Polycomb

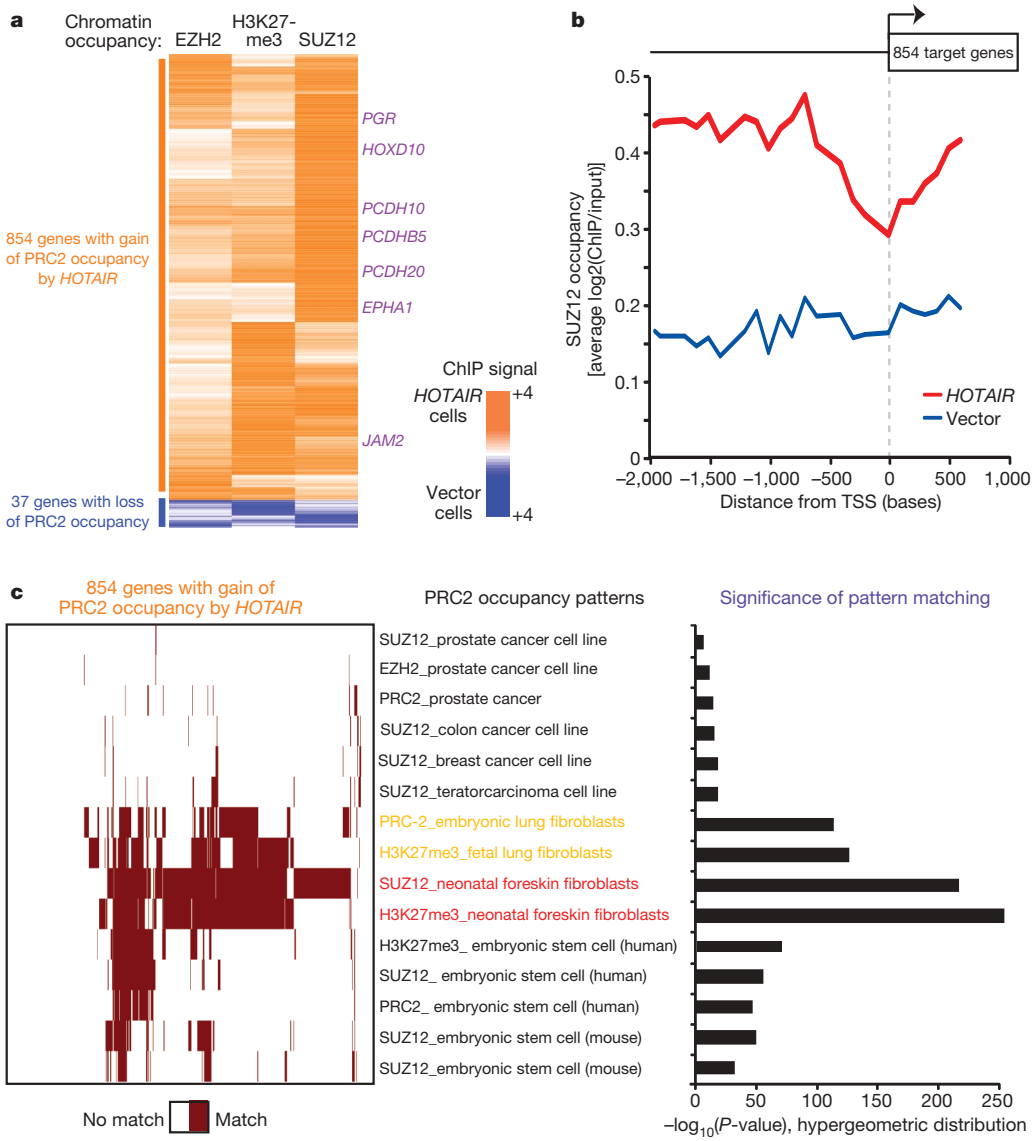

Figure 3 | *HOTAIR* promotes selective re-targeting of PRC2 and H3K27me3 genome-wide. a, Heat map representing genes with a significant relative change in chromatin occupancy of EZH2, SUZ12 and H3K27 after *HOTAIR* expression. MDA-MB-231 vector or *HOTAIR* cells were subjected to ChIP using anti-EZH2, -H3K27me3 and -SUZ12 antibodies followed by interrogation on a genome-wide promoter array. Values are depicted as the relative ratio of *HOTAIR* to vector cells and represented as an orange–blue scale. **b**, Average SUZ12 occupancy of >800 PRC2 target genes in *HOTAIR* or vector-expressing cells across the length of gene promoter and gene body. All target genes are aligned by their transcriptional start sites (TSS). **c**, Module map[20] of the 854 genes with a gain in PRC2 occupancy after *HOTAR* overexpression. Left, heat map of genes (column) showing a gain in PRC2 occupancy after *HOTAR* expression in breast carcinoma cells (see **a**) compared with PRC2 occupancy patterns from the indicated cell or tissue type (rows). Binary scale is brown (match) or white (no match). Right, quantification of significance of pattern matching between gene sets.

binding profile of a breast epithelial cell to that of an embryonic fibroblast.

Finally, we addressed whether the ability of *HOTAIR* to induce breast cancer invasiveness required an intact PRC2 complex. We transduced vector- or *HOTAIR*-expressing MDA-MB-231 cells with short hairpin RNAs (shRNAs) targeting PRC2 subunits EZH2 or SUZ12. Immunoblot analyses confirmed efficient depletion of the targeted proteins (Fig. 4a). Depletion of either SUZ12 or EZH2 had little effect on the invasiveness of control cells, but completely reversed the ability of *HOTAIR* to promote matrix invasion (Fig. 4b). Depletion of EZH2 also inhibited *HOTAIR*-driven lung colonization after tail vein xenograft by approximately 50% ($P < 0.05$). These results indicate that PRC2 is specifically required for *HOTAIR* to promote cellular invasiveness. Global gene expression analysis showed hundreds of genes that were induced or repressed as a consequence of *HOTAIR* overexpression (Fig. 4c, left). Importantly, concomitant depletion of PRC2 in large part reversed the global gene expression pattern to that of cells not overexpressing *HOTAIR* (Fig. 4c, right). Quantitative PCR with reverse transcription (qRT–PCR) confirmed that *HOTAIR*-induced PRC2 target genes, such as *JAM2*, *PCDH10* and *PCDHB5*, were transcriptionally repressed after *HOTAIR* expression and de-repressed after concomitant PRC2 depletion (Fig. 4d). *HOTAIR*-induced genes were also reversed after PRC2 depletion (Fig. 4d). Of note, many of the genes induced by *HOTAIR* are known positive regulators of cancer metastasis, including *ABL2* (ref. 21), *SNAIL*[22], and laminins[23]. Conversely, overexpression of EZH2 in H16N2 breast cells is known to promote matrix invasion[12], but concomitant depletion of endogenous *HOTAIR* in large measure inhibited the ability of EZH2 to induce matrix invasion (Fig. 4e and Supplementary Fig. 6). Together, these results demonstrate a functional interdependency between *HOTAIR* and PRC2 in promoting cancer invasiveness.

In summary, the cancer transcriptome is more complex than previously believed. In addition to protein-coding genes and microRNAs,

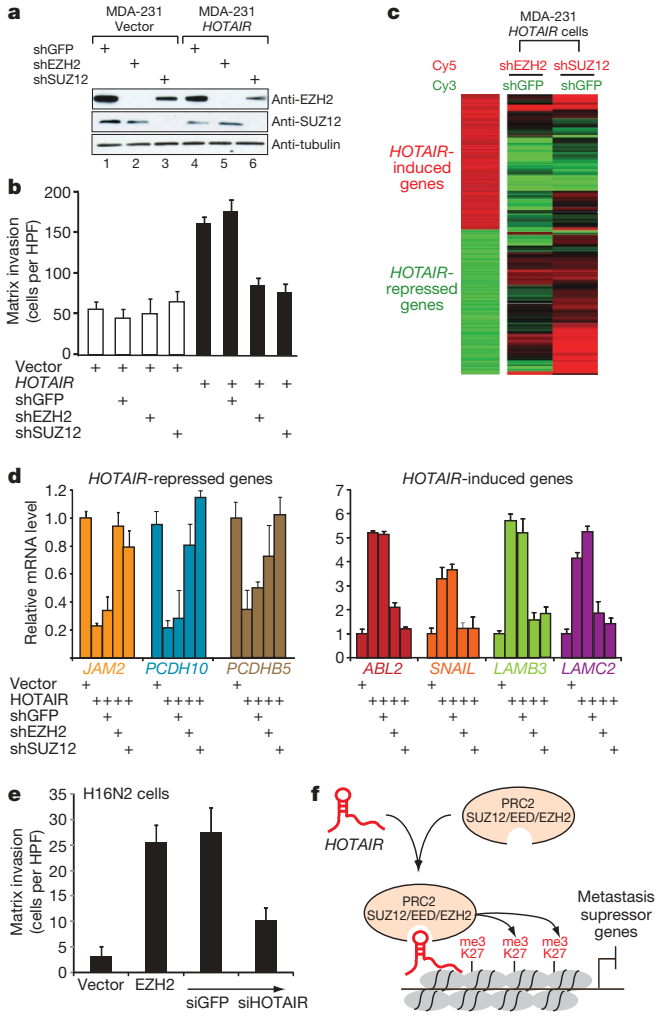

Figure 4 | *HOTAIR*-induced matrix invasion and global gene expression changes requires PRC2. a, Immunoblot of SUZ12 and EZH2 protein levels after transduction of MDA-MB-231 vector or *HOTAIR* cells with retrovirus expressing an shRNA targeting either GFP, EZH2 or SUZ12. **b**, Matrix invasion in vector or *HOTAIR* cells expressing the indicated shRNA. Mean ± s.d. are shown ($n = 3$). **c**, Left, heat map of genes with significant induction (red) or repression (green) after *HOTAIR* expression in the MDA-MB-231 cells. Right, the relative expression of the same gene list in MDA-MB-231 *HOTAIR* cells expressing shEZH2 or shSUZ12 (expressed as a ratio to *HOTAIR* cells expressing shGFP). **d**, qRT–PCR of a representative panel of genes in MDA-MB-231 vector or *HOTAIR* cells also expressing the indicated shRNA (error bars are s.d., $n = 3$). **e**, Matrix invasion in the immortalized H16N2 breast epithelial line expressing vector or EZH2 as well as EZH2-expressing cells transfected with siRNAs targeting GFP or *HOTAIR* (error bars = s.d., $n = 3$). **f**, Working model of the role of *HOTAIR* in breast cancer progression. Selection for increased *HOTAIR* expression in a subset of breast primary tumours leads to a genome-wide retargeting of the PRC2 and H3K27me3 patterns, resulting in gene expression changes that promote tumour metastasis.

dysregulated expression of lincRNAs is probably pervasive in human cancers and can drive cancer development and progression. Notably, the lincRNA *HOTAIR* regulates metastatic progression. *HOTAIR* recruits the PRC2 complex to specific target genes genome-wide, leading to H3K27 trimethylation and epigenetic silencing of metastasis suppressor genes (Fig. 4f). The concept of epigenomic reprogramming by lincRNAs may also be applicable to many other human disease states characterized by aberrant lincRNA expression and chromatin states. *HOTAIR* is normally involved in specifying the chromatin state associated with fibroblasts from anatomically posterior and distal sites. Within the context of cancer cells, ectopic expression of *HOTAIR* seems to re-impose that chromatin state, thereby enabling gene expression programs that are conducive to cell motility and matrix invasion.

The interdependence between *HOTAIR* and PRC2 has therapeutic implications. High levels of *HOTAIR* may identify tumours that are sensitive to small molecule inhibitors of PRC2 (ref. 24). Conversely, tumours that overexpress Polycomb proteins may be sensitive to therapeutic strategies that target endogenous *HOTAIR* or inhibit *HOTAIR*–PRC2 interactions. Understanding the precise molecular mechanisms by which *HOTAIR* regulates PRC2 will be a critical first step in exploring these potential new strategies in cancer therapy.

METHODS SUMMARY

Human material was obtained from Johns Hopkins Hospital and the Netherlands Cancer Institute. Expression of *HOX* transcripts was determined using ultra-high-density HOX tiling arrays[7] and qRT–PCR. Kaplan–Meier analyses of breast cancer patients were as described[13]. We used retroviral transduction to overexpress *HOTAIR* and luciferase, and used siRNA or shRNA to deplete the indicated transcripts. Matrix invasion was measured by the transwell Matrigel assay. We implanted cells in the mammary fat pad of severe combined immunodeficient (SCID) mice, and monitored primary tumour growth and lung metastasis by bioluminescence. Cells were injected into the tail vein of nude mice, and lungs were analysed at 9 weeks to quantify lung colonization *in vivo*. ChIP-chip was performed as described[7] using human whole genome promoter tiling arrays (Roche Nimblegen). Module map and Gene Ontology enrichment analyses were done using Genomica[20].

Full Methods and any associated references are available in the online version of the paper at www.nature.com/nature.

Received 6 August 2009; accepted 26 February 2010.

1. Amaral, P. P., Dinger, M. E., Mercer, T. R. & Mattick, J. S. The eukaryotic genome as an RNA machine. *Science* **319,** 1787–1789 (2008).
2. The FANTOM Consortium. The transcriptional landscape of the mammalian genome. *Science* **309,** 1559–1563 (2005).
3. Guttman, M. *et al.* Chromatin signature reveals over a thousand highly conserved large non-coding RNAs in mammals. *Nature* **458,** 223–227 (2009).
4. Calin, G. A. *et al.* Ultraconserved regions encoding ncRNAs are altered in human leukemias and carcinomas. *Cancer Cell* **12,** 215–229 (2007).
5. Yu, W. *et al.* Epigenetic silencing of tumour suppressor gene *p15* by its antisense RNA. *Nature* **451,** 202–206 (2008).
6. Ponting, C. P., Oliver, P. L. & Reik, W. Evolution and functions of long noncoding RNAs. *Cell* **136,** 629–641 (2009).
7. Rinn, J. L. *et al.* Functional demarcation of active and silent chromatin domains in human *HOX* loci by noncoding RNAs. *Cell* **129,** 1311–1323 (2007).
8. Khalil, A. M. *et al.* Many human large intergenic noncoding RNAs associate with chromatin-modifying complexes and affect gene expression. *Proc. Natl Acad. Sci. USA* **106,** 11667–11672 (2009).
9. Raman, V. *et al.* Compromised HOXA5 function can limit p53 expression in human breast tumours. *Nature* **405,** 974–978 (2000).
10. Wu, X. *et al.* HOXB7, a homeodomain protein, is overexpressed in breast cancer and confers epithelial-mesenchymal transition. *Cancer Res.* **66,** 9527–9534 (2006).
11. Sparmann, A. & van Lohuizen, M. Polycomb silencers control cell fate, development and cancer. *Natl. Rev.* **6,** 846–856 (2006).
12. Kleer, C. G. *et al.* EZH2 is a marker of aggressive breast cancer and promotes neoplastic transformation of breast epithelial cells. *Proc. Natl Acad. Sci. USA* **100,** 11606–11611 (2003).
13. van de Vijver, M. J. *et al.* A gene-expression signature as a predictor of survival in breast cancer. *N. Engl. J. Med.* **347,** 1999–2009 (2002).
14. Ma, L., Teruya-Feldstein, J. & Weinberg, R. A. Tumour invasion and metastasis initiated by microRNA-10b in breast cancer. *Nature* **449,** 682–688 (2007).
15. Novak, P. *et al.* Agglomerative epigenetic aberrations are a common event in human breast cancer. *Cancer Res.* **68,** 8616–8625 (2008).
16. Naik, M. U., Naik, T. U., Suckow, A. T., Duncan, M. K. & Naik, U. P. Attenuation of junctional adhesion molecule-A is a contributing factor for breast cancer cell invasion. *Cancer Res.* **68,** 2194–2203 (2008).
17. Fox, B. P. & Kandpal, R. P. Invasiveness of breast carcinoma cells and transcript profile: Eph receptors and ephrin ligands as molecular markers of potential diagnostic and prognostic application. *Biochem. Biophys. Res. Commun.* **318,** 882–892 (2004).
18. Herath, N. I., Doecke, J., Spanevello, M. D., Leggett, B. A. & Boyd, A. W. Epigenetic silencing of EphA1 expression in colorectal cancer is correlated with poor survival. *Br. J. Cancer* **100,** 1095–1102 (2009).
19. The Gene Ontology Consortium. Gene ontology: tool for the unification of biology. *Nature Genet.* **25,** 25–29 (2000).
20. Segal, E., Friedman, N., Koller, D. & Regev, A. A module map showing conditional activity of expression modules in cancer. *Nature Genet.* **36,** 1090–1098 (2004).

21. Srinivasan, D. & Plattner, R. Activation of Abl tyrosine kinases promotes invasion of aggressive breast cancer cells. *Cancer Res.* **66,** 5648–5655 (2006).
22. Olmeda, D. *et al.* SNAI1 is required for tumor growth and lymph node metastasis of human breast carcinoma MDA-MB-231 cells. *Cancer Res.* **67,** 11721–11731 (2007).
23. Marinkovich, M. P. Tumour microenvironment: laminin 332 in squamous-cell carcinoma. *Natl. Rev.* **7,** 370–380 (2007).
24. Tan, J. *et al.* Pharmacologic disruption of Polycomb-repressive complex 2-mediated gene repression selectively induces apoptosis in cancer cells. *Genes Dev.* **21,** 1050–1063 (2007).

Supplementary Information is linked to the online version of the paper at www.nature.com/nature.

Acknowledgements We thank Y. Chen-Tsai, M. Guttman, G. Sen, T. Ridky, P. Khavari, V. Band and Y. Kang for advice and reagents. Supported by National Institutes of Health (NIH), Emerald Foundation, and American Cancer Society (H.Y.C.), Dermatology Foundation (R.A.G., K.C.W. and D.J.W.), Susan Komen Foundation (M.-C.T.), NSF (T.H.), and Department of Defense BCRP (S.S.). H.Y.C. is an Early Career Scientist of the Howard Hughes Medical Institute.

Author Contributions R.A.G. measured lincRNAs in cancer samples and performed all gene transfer and knockdown experiments. R.A.G. and N.S. performed cell growth, invasion, and *in vivo* xenograft assays. R.A.G., K.C.W., M.-C.T. and T.H. performed ChIP-chip studies and analyses. R.A.G., J.L.R. and D.J.W. performed bioinformatic analyses. J.K. performed *in vivo* bioluminescence studies. H.M.H., P.A. and M.J.v.d.V. procured and analysed human tumour samples. Y.W., P.B. and B.K. designed lincRNA Taqman probes and analysed tumour RNAs by qRT–PCR. R.L. and R.B.W. performed *in situ* hybridization studies. R.A.G., N.S., S.S. and H.Y.C. designed the experiments and interpreted the results. R.A.G. and H.Y.C. wrote the paper.

Author Information Microarray data are deposited in Gene Expression Omnibus (GEO) under accession numbers GSE20435 and GSE20737. Reprints and permissions information is available at www.nature.com/reprints. The authors declare no competing financial interests. Correspondence and requests for materials should be addressed to H.Y.C. (howchang@stanford.edu).

METHODS

Reagents. The MDA-MB-231, SK-BR-3, MCF-10A, MCF-7, HCC1954, T47D and MDA-MB-453 cell lines were obtained from the American Type Culture Collection (ATCC). The H16N2 cell line was a gift from V. Band. pLZRS, pLZRS-luciferase and pSuper Retro-shGFP, -shSUZ12 and -shEZH2 (ref. 25) were obtained from P. Khavari. pLZRS-HOTAIR and pLZRS-EZH2-Flag were constructed by subcloning the full-length human *HOTAIR*[7] or Flag–EZH2–ER fusion protein (representing amino acids 1–751 of EZH2 fused with the murine oestrogen receptor (amino acids 281–599)) into pLZRS using the Gateway cloning system (Invitrogen).

Human materials. Normal breast organoid RNA was prepared as reported[26]. In brief, tissues from reduction mammoplasties performed at Johns Hopkins Hospital were mechanically macerated then digested overnight with hyaluronic acid and collagenase. The terminal ductal units are placed into suspension by this method; they were then isolated by serial filtration. Samples were treated with TRIzol and RNA extracted.

Fresh frozen primary breast tumour specimens were obtained from the Department of Pathology breast tumour bank; specimens were all from patients 45–55 years of age, with oestrogen receptor expression by immunohistochemistry as performed during routine tumour staging at diagnosis, for uniformity of samples.

Metastatic breast carcinoma samples were obtained from the Rapid Autopsy Program at Johns Hopkins Hospital[27]. All specimens were snap-frozen at time of autopsy and stored at −80 °C. Twenty 20-μm sections were obtained from metastasis to the liver (for uniformity of samples) and embedded in OCT. These slices were macerated by use of the BioMasher centrifugal sample preparation device (Cartagen), with 350 μl of lysis buffer from the Qiagen RNeasy Mini Extraction kit. RNA extraction was completed with the flow-through from the BioMasher, as per the commercial protocol.

***HOTAIR* expression and survival/metastasis analysis of primary breast tumours.** The database of 295 breast cancer patients from the Netherlands Cancer Institute with detailed clinical and gene expression data was used[13]. Clinical data are available at http://microarray-pubs.stanford.edu/wound_NKI, http://www.rii.com/publications, or http://microarrays.nki.nl. RNA from 132 primary breast tumours from the NKI 295 cohort was isolated along with RNA from normal breast organoid cultures ($n = 6$). *HOTAIR* and *GAPDH* were measured by qRT–PCR. *HOTAIR* values were normalized to *GAPDH* and expressed relative to pooled normal *HOTAIR* RNA levels. For both univariate and multivariate analysis, the expression of *HOTAIR* was treated as a binary variable divided into 'high' and 'low' *HOTAIR* expression. To determine the criteria for high *HOTAIR* expression, the minimum relative level of *HOTAIR* seen in six metastatic breast cancer samples (see Fig. 1c and accompanying methods) was determined (≥125 above normal). By this criteria, 44 primary breast tumours were categorized as high, and 88 were labelled as low, out of 132 tumours. For statistical analysis, overall survival was defined by death from any cause. Distant metastasis-free probability was defined by a distant metastasis as the first recurrence event. Kaplan–Meier survival curves were compared by the Cox–Mantel log-rank test in Winstat (R. Fitch software). Multivariate analysis by the Cox proportional hazard method was done using SPSS 15.0 (SPSS)

RNA expression analysis. qRT–PCR: total RNA from cells was extracted using TRIzol and the RNeasy mini kit (Qiagen). RNA levels (starting with 50–100 ng per reaction) for a specific gene (primer set sequences listed in Supplementary Table 4) were measured using the Brilliant SYBR Green II qRT–PCR kit (Strategene) according to manufacturer instructions. All samples were normalized to *GAPDH*.

HOX tiling array: RNA samples (primary or metastatic breast carcinoma in channel in Cy5 channel and normal breast organoid RNA representing a pool of six unique samples in Cy3 channel) were labelled and hybridized to a custom human *HOX* tiling array with 50-base-pair resolution (Roche Nimblegen) as described[7]. For each sample, robust multichip average (RMA) normalized intensity values for previously defined peaks encoding *HOX*-coding-gene exons (as defined in version HG17) and *HOX* lincRNAs (as defined previously[7]) were determined relative to normal. Unsupervised hierarchical clustering was performed by CLUSTER[28].

Microarray: total RNA from cells was extracted using TRIzol and the RNeasy mini kit (Qiagen) and hybridized to Stanford human oligonucleotide (HEEBO) arrays as described[29]. Data analysis was done using CLUSTER[28].

Gene transfer experiments. Retrovirus was generated using amphotrophic phoenix cells and used to infect target cells as described[30]. For LZRS vector, *HOTAIR*, EZH2–ER, and firefly luciferase, no further selection was done after infection. For pRetro-Super-shGFP, -shSUZ12 and -shEZH2, target cells were selected using puromycin (0.5 μg ml^{-1}). Many of the epigenetic changes due to *HOTAIR* expression were only seen after several cell passages; thus all experiments post-*HOTAIR* transduction were done after passage 10.

Non-radioactive *in situ* hybridization of paraffin sections. Digoxigenin (DIG)-labelled sense and antisense RNA probes were generated by PCR amplification of T7 promoter incorporated into the primers. *In vitro* transcription was performed with DIG RNA labelling kit and T7 polymerase according to the manufacturer's protocol (Roche Diagnostics). Sections (5-μm thick) were cut from the paraffin blocks, deparaffinized in xylene, and hydrated in graded concentrations of ethanol for 5 min each. Sections were incubated with 1% hydrogen peroxide, followed by digestion in 10 μg ml^{-1} proteinase K at 37 °C for 30 min. Sections were hybridized overnight at 55 °C with either sense or antisense riboprobes at 200 ng ml^{-1} dilution in mRNA hybridization buffer (Chemicon). The next day, sections were washed in 2×SSC and incubated with 1:35 dilution of RNase A cocktail (Ambion) in 2×SSC for 30 min at 37 °C. Next, sections were stringently washed twice in 2×SSC/50% formamide, followed by one wash in 0.08×SSC at 55 °C. Biotin-blocking reagents (Dako) were applied to the section to block the endogenous biotin. For signal amplification, a horseradish peroxidase (HRP)-conjugated sheep anti-DIG antibody (Roche) was used to catalyse the deposition of biotinyl-tyramide, followed by secondary streptavidin complex (GenPoint kit; Dako). The final signal was developed with DAB (GenPoint kit; Dako), and the tissues were counter-stained in haematoxylin for 30 s.

RNA interference. RNA interference for *HOTAIR* was done as described[7]. In brief, cells were transfected with 50 nM siRNAs targeting *HOTAIR* (siHOTAIR-1, 5′-GAACGGGAGUACAGAGAGAUU-3′; siHOTAIR-2, 5′-CCACAUGAACGC CCAGAGAUU-3′; siHOTAIR-3, 5′-UAACAAGACCAGAGAGCUGUU-3′) or siGFP (5′-CUACAACAGCCACAACGUCdTdT-3′) using Lipofectamine 2000 (Invitrogen) as per the manufacturer's direction. Total RNA was collected 72 h later for qRT–PCR analysis.

RNA interference of EZH2 and SUZ12 was done by infecting target cells with retrovirus expressing shEZH2, shSUZ12 and shGFP as described[25]. To confirm knockdown, protein lysates were resolved on 10% SDS–PAGE followed by immunoblot analysis as described[30] using anti-SUZ12 (Abcam), anti-EZH2 (Upstate) and anti-tubulin (Santa Cruz).

Matrigel invasion assay and cell proliferation assay. The matrigel invasion assay was done using the Biocoat Matrigel Invasion Chamber from Becton Dickson according to manufacturer protocol. In brief, 5×10^4 cells were plated in the upper chamber in serum-free media. The bottom chamber contained DMEM media with 10% FBS. After 24–48 h, the bottom of the chamber insert was fixed and stained with Diff-Quick stain. Cells on the stained membrane were counted under a dissecting microscope. Each membrane was divided into four quadrants and an average from all four quadrants was calculated. Each matrigel invasion assay was at least done in biological triplicates. For invasion assays in the H16N2 cell line using EZH2–ER, all experiments (both vector and with EZH2–ER) were done in the presence of 500 nM oestradiol.

For cell proliferation assays, 1×10^3 cells were plated in quadruplicate in 96-well plates and cell number was calculated using the MTT assay (Roche).

Soft agar colony formation assay. Soft agar assays were constructed in 6-well plates. The base layer of each well consisted of 2 ml with final concentrations of 1× media (RPMI (HCC1954), McCoy's Media (SKBR3), or DMEM (MDA-MB-231) plus 10% or 2% heat-inactivated FBS (Invitrogen)) and 0.6% low melting point agarose. Plates were chilled at 4 °C until solid. Upon this, a 1-ml growth agar layer was poured, consisting of 1×10^4 cells (infected with either LZRS-HOTAIR or LZRS vector as described earlier) suspended in 1× media and 0.3% low melting point agarose. Plates were again chilled at 4 °C until the growth layer congealed. A further 1 ml of 1× media without agarose was added on top of the growth layer on day 0 and again on day 14 of growth. Cells were allowed to grow at 37 °C for 1 month and total colonies were counted (>200 μm in diameter for MDA-MB-231; >50 μm in diameter for HCC1954 and SKBR3). Assays were repeated a total of three times. Results were statistically analysed by paired *t*-test using the PRISM Graphpad program.

Mammary fat pad xenografts. Six-week-old female SCID beige mice were purchased from Charles River laboratories, housed at the animal care facility at Stanford University Medical Center and kept under standard temperature, humidity and timed lighting conditions and provided mouse chow and water *ad libitum*. MDA-MB-231-Luc or MDA-MB-231-Luc tumour cells transduced with *HOTAIR* were injected directly into the mammary fat pad of the mice semi-orthotopically ($n = 10$ each) in 0.05 ml of sterile DMEM (2,500,000 cells per animal).

Mouse tail-vein assay. Female athymic nude mice were used. Two-million MDA-MB-231 HOTAIR-luciferase or vector-luciferase cells in 0.2 ml PBS were injected by the tail vein into individual mice (18 for each cell line). Mice were observed generally for signs of illness weekly for the length of the experiment. The lungs were excised and weighed fresh, then bisected. Half was fixed in formalin overnight then embedded in paraffin, from which sections were made and stained with haematoxylin and eosin by our pathology consultation service. These slides were examined for the presence of micrometastases, which were

counted in three low-power (×5) fields per specimen. The other half of the tumour was fast-frozen into OCT and stored at −80 °C. RNA was extracted by the TRIzol protocol from ten sections, 20-μm thick each, obtained from the frozen sections. RT–PCR confirmed expression of *HOTAIR* RNA in lungs bearing micrometastases of MDA-MB-231 HOTAIR cells at the end of the experiment.

Bioluminescence imaging. Mice received luciferin (300 mg kg^{-1}, 10 min before imaging) and were anaesthetized (3% isoflurane) and imaged in an IVIS spectrum imaging system (Xenogen, part of Caliper Life Sciences). Images were analysed with Living Image software (Xenogen, part of Caliper Life Sciences). Bioluminescent flux (photons s^{-1} sr^{-1} cm^{-2}) was determined for the primary tumours or lungs (upper abdomen region of interest).

ChIP-chip. ChIP-chip experiments were done as previously described[7]. Each experiment was done in biological triplicate. The following antibodies were used: anti-H3K27me3 (Abcam), anti-SUZ12 (Abcam) and anti-EZH2 (Upstate). Immunoprecipitated DNA was amplified using the Whole Genome Amplification kit (Sigma) based on the manufacturer's protocol. Amplified and labelled DNA was hybridized to the HG18 whole genome two array promoter set from Roche Nimblegen. Probe labelling, hybridization, and data extraction and analysis were performed using Roche Nimblegen protocols. The relative ratio of *HOTAIR* to vector was calculated for each promoter peak by extracting the normalized (over input) intensity values for promoter peaks showing peaks with an FDR score ≤ 0.2 in either vector or *HOTAIR* cells. These values were weighted to determine the significance of the relative ratio: using Cluster[28], only those promoters with a consistent relative ratio (*HOTAIR*/vector) ≥1.5-fold or ≤0.5-fold in two out of the three ChIP were selected and displayed in TreeView. Selected ChIP-chip results were confirmed by PCR using the Lightcycler 480 SYBR Green I kit (see Supplementary Table 5 for primer sequences).

TaqMan real-time PCR assays. A panel of 96 TaqMan real-time PCR HOX assays (Supplementary Table 6) was developed targeting 43 *HOX* lincRNAs and 39 HOX transcription factors across the four *HOX* loci. Two housekeeping genes (*ACTB* and *PPIA*) were also included in this panel in triplicates as endogenous controls for normalization between samples. The transcript specificity and genome specificity of all TaqMan assays were verified using a position-specific alignment matrix to predict potential cross-reactivity between designed assays and genome-wide non-target transcripts or genomic sequences. Using this HOX assay panel we profiled 88 total RNA samples from a cohort of five normal breast organoids, 78 primary breast tumours (from the NKI 295 cohort) and five metastatic breast tumours. cDNAs were generated from 30 ng total RNA using the High Capacity cDNA Reverse Transcription Kit (Life Technologies). The resulting cDNA was subjected to a 14-cycle PCR amplification followed by real-time PCR reaction using the manufacturer's TaqMan PreAmp Master Mix Kit Protocol (Life Technologies). Four replicates were run for each gene for each sample in a 384-well format plate on a 7900HT Fast Real-Time PCR System (Life Technologies). Between the two measured endogenous control genes (*PPIA* and *ACTB*), we chose *PPIA* for normalization across different samples based on the fact that this gene showed the most relatively constant expression in different breast carcinomas (data not shown).

Gene set analysis. For gene set enrichment analysis, gene sets from fifteen different H3K27, SUZ12 or EZH2 global occupancy lists from the indicated cell lineages were procured (see Supplementary Table 3 for references and platforms). Pattern matching between the 854-gene set with increased PRC2 occupancy (Supplementary Table 7) and these 15 gene sets were visualized using CLUSTER and TreeView. The significance of enrichment between these gene sets was calculated using module map analysis implemented in Genomica[20] (corrected for multiple hypotheses using FDR).

25. Sen, G. L., Webster, D. E., Barragan, D. I., Chang, H. Y. & Khavari, P. A. Control of differentiation in a self-renewing mammalian tissue by the histone demethylase JMJD3. *Genes Dev.* **22,** 1865–1870 (2008).
26. Bergstraesser, L. M. & Weitzman, S. A. Culture of normal and malignant primary human mammary epithelial cells in a physiological manner simulates *in vivo* growth patterns and allows discrimination of cell type. *Cancer Res.* **53,** 2644–2654 (1993).
27. Wu, J. M. *et al.* Heterogeneity of breast cancer metastases: comparison of therapeutic target expression and promoter methylation between primary tumors and their multifocal metastases. *Clin. Cancer Res.* **14,** 1938–1946 (2008).
28. Eisen, M. B., Spellman, P. T., Brown, P. O. & Botstein, D. Cluster analysis and display of genome-wide expression patterns. *Proc. Natl Acad. Sci. USA* **95,** 14863–14868 (1998).
29. Rinn, J. L., Bondre, C., Gladstone, H. B., Brown, P. O. & Chang, H. Y. Anatomic demarcation by positional variation in fibroblast gene expression programs. *PLoS Genet.* **2,** e119 (2006).
30. Adler, A. S. *et al.* Genetic regulators of large-scale transcriptional signatures in cancer. *Nature Genet.* **38,** 421–430 (2006).

LETTERS

Fructose 1,6-bisphosphate aldolase/phosphatase may be an ancestral gluconeogenic enzyme

Rafael F. Say[1] & Georg Fuchs[1]

Most archaeal groups and deeply branching bacterial lineages harbour thermophilic organisms with a chemolithoautotrophic metabolism. They live at high temperatures in volcanic habitats at the expense of inorganic substances, often under anoxic conditions[1]. These autotrophic organisms use diverse carbon dioxide fixation mechanisms generating acetyl-coenzyme A, from which gluconeogenesis must start[2–4]. Here we show that virtually all archaeal groups as well as the deeply branching bacterial lineages contain a bifunctional fructose 1,6-bisphosphate (FBP) aldolase/phosphatase with both FBP aldolase and FBP phosphatase activity. This enzyme is missing in most other Bacteria and in Eukaryota, and is heat-stabile even in mesophilic marine Crenarchaeota. Its bifunctionality ensures that heat-labile triosephosphates are quickly removed and trapped in stabile fructose 6-phosphate, rendering gluconeogenesis unidirectional. We propose that this highly conserved, heat-stabile and bifunctional FBP aldolase/phosphatase represents the pacemaking ancestral gluconeogenic enzyme, and that in evolution gluconeogenesis preceded glycolysis[5].

The theory of a chemoautotrophic origin of life by transition-metal-catalysed, autocatalytic carbon fixation assumes that chemoevolution took place in a hot volcanic flow setting[6,7]. It has become evident that in the phylogenetic tree of life the Archaea and deeply branching lineages of the Bacteria harbour thermophiles that thrive in volcanic environments on volcanic gases and inorganic substrates under anoxic or microaerobic conditions[1] (Fig. 1). From carbon dioxide (CO_2) or carbon monoxide (CO) they synthesize activated acetic acid, acetyl-coenzyme A (acetyl-CoA), as biosynthetic starting material. Their energy metabolism often makes use of hydrogen or CO as electron donors, and CO_2 or sulphur compounds serve as electron acceptors in anaerobic respiration. Therefore, these chemolithoautotrophic organisms may serve as models for the study of primordial metabolism requiring the synthesis of organic building blocks from inorganic carbon. In none of these microorganisms does the Calvin–Benson–Bassham cycle seem to operate in CO_2 fixation. Instead, other autotrophic pathways are functioning that have in common the formation of acetyl-CoA from inorganic carbon[2–4].

If so, the biosynthesis of sugars requires gluconeogenesis to start from acetyl-CoA as a precursor. Pyruvate and phosphoenolpyruvate (PEP) formation from acetyl-CoA and CO_2 may differ[2–4]. In contrast, gluconeogenesis starting from PEP seems to be uniform. All enzyme activities and genes of a trunk Embden–Meyerhof–Parnas gluconeogenic pathway, which are necessary for the formation of FBP from PEP, are assumed to be present in Archaea. This is in contrast to the great diversity of glycolytic pathways and enzymes present in Archaea[8]. However, it has been generally difficult or impossible to detect FBP aldolase activity[9]. In many cases this enzyme activity could only be measured in the direction of FBP formation, whereas detection of the reverse reaction, FBP cleavage, has failed[9,10]. This discrepancy is puzzling as the FBP aldolase reaction is freely reversible. Furthermore, tracer studies with several autotrophic Archaea revealed a labelling pattern of hexoses that was consistent with the classical gluconeogenic route involving FBP aldolase[10,11].

None of the archaeal genomes sequenced so far contains a classical FBP aldolase of class I (Schiff base intermediate, mainly found in Eukaryota) or class II (metal based catalysis, mainly in Bacteria and Fungi) (Supplementary Table 1). However, one small group harbours the gene encoding a different archaeal class IA aldolase[12,13]; this enzyme has a common evolutionary origin with class I and II aldolases[14]. Its function as FBP aldolase has been shown experimentally only in three cases generally by measuring the glycolytic direction. The other aldolase genes are only distantly related to this FBP aldolase and may have a different function (for example, in the archaeal aromatic biosynthesis pathway[15]; Supplementary Table 1). The majority of archaeal genomes sequenced so far lack any proven FBP aldolase gene, whereas generally the gene encoding an archaeal type V FBP phosphatase is present[16] (Supplementary Table 1). This phosphatase also catalyses the sought-after FBP aldolase reaction, as the following experiments show.

We searched for FBP aldolase plus FBP phosphatase activity in extracts from autotrophically grown cells of the thermophilic Archaea *Ignicoccus hospitalis*, *Metallosphaera sedula* and *Thermoproteus neutrophilus*, the central carbon metabolism of which has been studied recently[2–4,10]. The assay, at 65–85 °C, is based on the measurement of phosphate release, when triosephosphates were incubated with cell extracts. However, it was difficult to measure FBP aldolase activity owing to the heat instability of triosephosphates producing toxic methylglyoxal and forming phosphate, which interfered with the assay. The half-life of triosephosphates at 80 °C, pH 7, was confirmed to be 4 min[12]. Furthermore, we could not detect the reverse reaction; that is, FBP cleavage.

However, FBP aldolase and phosphatase activities were readily detected using a discontinuous spectrophotometric assay for fructose 6-phosphate formation (for assay see Supplementary Information). The specific FBP aldolase activities were 0.02 μmol min^{-1} (per mg of protein; 85 °C) in *I. hospitalis*, 0.006 μmol min^{-1} (per mg of protein; 75 °C) in *M. sedula*, and 0.02 μmol min^{-1} (per mg of protein; 85 °C) in *T. neutrophilus*. The specific FBP phosphatase activities were 1.5-fold as high. To convert efficiently the aldol reaction product FBP into fructose 6-phosphate, we added purified recombinant archaeal type V FBP phosphatase from *I. hospitalis* (Igni_0363) as auxiliary enzyme to the assay to pull forward the reaction. Only FBP phosphatase activity was observed when the intermediate FBP was supplied as substrate. Surprisingly, addition of triosephosphates resulted in a burst of FBP aldolase activity, even when cell extract was omitted. The archaeal type V FBP phosphatase has been studied in detail[16,17] and its crystal structure was solved[18]; however, the main physiological function of the enzyme seems to have gone unnoticed. We meticulously purified the enzyme so that it showed no contaminating protein

[1]Mikrobiologie, Fakultät Biologie, Universität Freiburg, Schänzlestraße 1, D-79104 Freiburg, Germany.

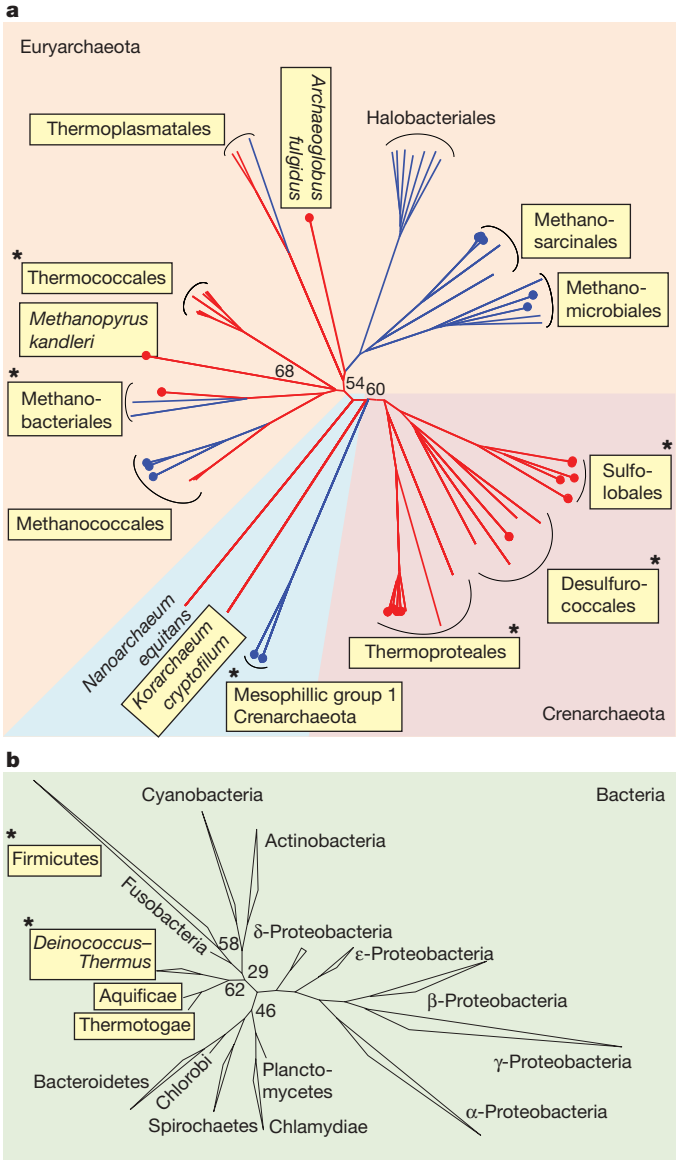

Figure 1 | Phylogenetic unrooted trees of Archaea and Bacteria. Boxes indicate phyla containing FBP aldolase/phosphatase. Asterisks indicate phyla from which enzymes were studied. Only bootstrap values <70% are indicated. **a**, Archaebacterial tree based on analyses of 64 conserved proteins (59 genomes). Red lines represent (hyper)thermophilic Archaea (>65 °C); blue lines mesophilic Archaea. Autotrophic lineages are marked with a dot. **b**, Eubacterial tree based on concatenated 37 ribosomal proteins (120 genomes[30]). Note that the systematic positions of the Thermotogae, Aquificae, Chloroflexi (not shown on the tree), the *Deinococcus–Thermus* lineage and in some respects also the deeply branching, thermophilic, acetogenic Clostridia/Firmicutes[23] are considered as early branching[22].

(Supplementary Fig. 1 and Supplementary Table 2), but it still catalysed both aldolase and phosphatase reactions, demonstrating bifunctionality. The kinetic constants at 48 °C for *I. hospitalis* FBP aldolase activity were maximal velocity (v_{max}) of 0.54 μmol min^{-1} (per mg of protein) and Michaelis constant (K_m) of 0.23 mM for triosephosphates. The FBP phosphatase activity (v_{max} of 0.88 μmol min^{-1} (per mg of protein); K_m of 0.02 mM for FBP) was nearly twice as high as the aldolase activity, as observed in cell extract (for optimal pH see Supplementary Fig. 2).

As further proof of bifunctionality, recombinant putative FBP phosphatases were overproduced and partly purified from five other Archaea covering different lineages (Fig. 2). We also expressed the synthetic FBP phosphatase gene of *Cenarchaeum symbiosum*[19], a member of the marine group I Crenarchaeota (Fig. 2); similar genes allocated to this marine group occur in high numbers in the GOS databases. All six recombinant archaeal enzymes exhibited both FBP aldolase and phosphatase activities. This enzyme, now referred to as FBP aldolase/phosphatase, was previously considered as a potential determinant of hyperthermophily, besides reverse gyrase, a type I DNA topoisomerase able to stabilize DNA at high temperature by introducing positive supercoils[20]. Notably, even the *Cenarchaeum* enzyme, adapted to ocean temperature, was heat-stabile at 70 °C, with a half-life of 20 min at 82 °C, and the *Ignicoccus* enzyme even survived boiling for 1 h (Supplementary Fig. 3). The catalytic properties of the *Cenarchaeum* enzyme were analysed at 40 °C and are shown in Fig. 3. AMP, ADP or glucose (2 mM), known allosteric regulators of FBP phosphatases, had no effect. The lower activation energy of the *Cenarchaeum* enzyme compared to the *Ignicoccus* enzyme (Supplementary Fig. 4) indicates that these enzymes are adapted to the respective cold or hot optimal temperature for growth. The specific activity of the enzyme in cell extract is generally low, reflecting the minor need for carbohydrates in Archaea. Even in *Escherichia coli*, with its high content of sugars in lipopolysaccharides, the biosynthetic fluxes leading away from hexosephosphates add up to only ~13% of all biosynthetic fluxes.

A data base search of sequenced genomes revealed that almost all Archaea contain the corresponding FBP aldolase/phosphatase gene (*e*-values <10^{-75}), except for halophilic and a very few methanogenic Archaea that harbour, in most cases, the genes for other types of FBP aldolases and phosphatases (Supplementary Table 1). In most Archaea that do not grow on sugars the FBP aldolase/phosphatase gene is the only candidate gene for both FBP aldolase and FBP phosphatase. A look at the regulation of the FBP aldolase/phosphatase gene corroborates our expectation. *Thermococcus kodakarensis* forms this enzyme solely under gluconeogenic, but not under glycolytic, conditions[16,17] (using the Embden–Meyerhof–Parnas pathway)[8]. A deletion mutant could grow under glycolytic, but not under gluconeogenic, conditions. Yet, complementation of this mutant by a different monofunctional FBP phosphatase did not restore growth under gluconeogenic conditions[17]. This is consistent with the notion that the deleted enzyme has, in addition, FBP aldolase activity. In contrast, *Sulfolobus solfataricus* uses a branched Entner–Doudoroff pathway for glycolysis[8], in which FBP is not an intermediate, and therefore may tolerate constitutive expression of FBP aldolase/phosphatase[21].

A gene highly similar to the archaeal FBP aldolase/phosphatase gene (*e*-values <10^{-80}) is also present in members of the deeply branching bacterial phyla[22] (Fig. 2). They include genera of Aquificae (*Aquifex*, *Hydrogenobaculum*, *Hydrogenivirga*), Thermotogae (*Petrotoga*), Chloroflexi (*Roseiflexus*, *Dehalococcoides*), the *Deinococcus–Thermus* group (*Thermus*), as well as the mostly homoacetogenic, thermophilic Clostridia/Firmicutes (*Carboxydibrachium*, *Thermoanaerobacter*, *Moorella*, *Pelotomaculum*, *Carboxydothermus*, *Natranaerobius*) that also exhibit traits of a deeply branching phylum[23,24] (for phylogenetic positions of the phyla see Fig. 1b). As a proof of concept, we overproduced the enzymes from *Thermus thermophilus* and *Moorella thermoacetica* and showed that they were an FBP aldolase/phosphatase, like the archaeal enzyme. There are only rare exceptions to the rule that this bifunctional enzyme is restricted to the Archaea and deeply branching, mostly thermophilic and autotrophic Bacteria (*e*-value <10^{-60}). Probably all those bacteria have to perform a unidirectional gluconeogenesis from C_2 or C_3 compounds under some conditions, which may have favoured the acquisition of the gene by lateral transfer (for example, from mesophilic group 1 Crenarchaeota). Examples are the pathogenic *Coxiella burnetii* (γ-Proteobacteria), the denitrifying *Nitrococcus mobilis* (γ-Proteobacteria) and the symbiotic *Bradyrhizobium japonicum* (α-Proteobacteria) (Fig. 2). Syntrophs like *Syntrophus aciditrophicus* (δ-Proteobacteria) depend on a close spatial contact with other Bacteria or (methanogenic) Archaea, which favours not only interspecies hydrogen transfer but also lateral gene transfer. *Saccharopolyspora erythraea* (Actinobacteria) contains many

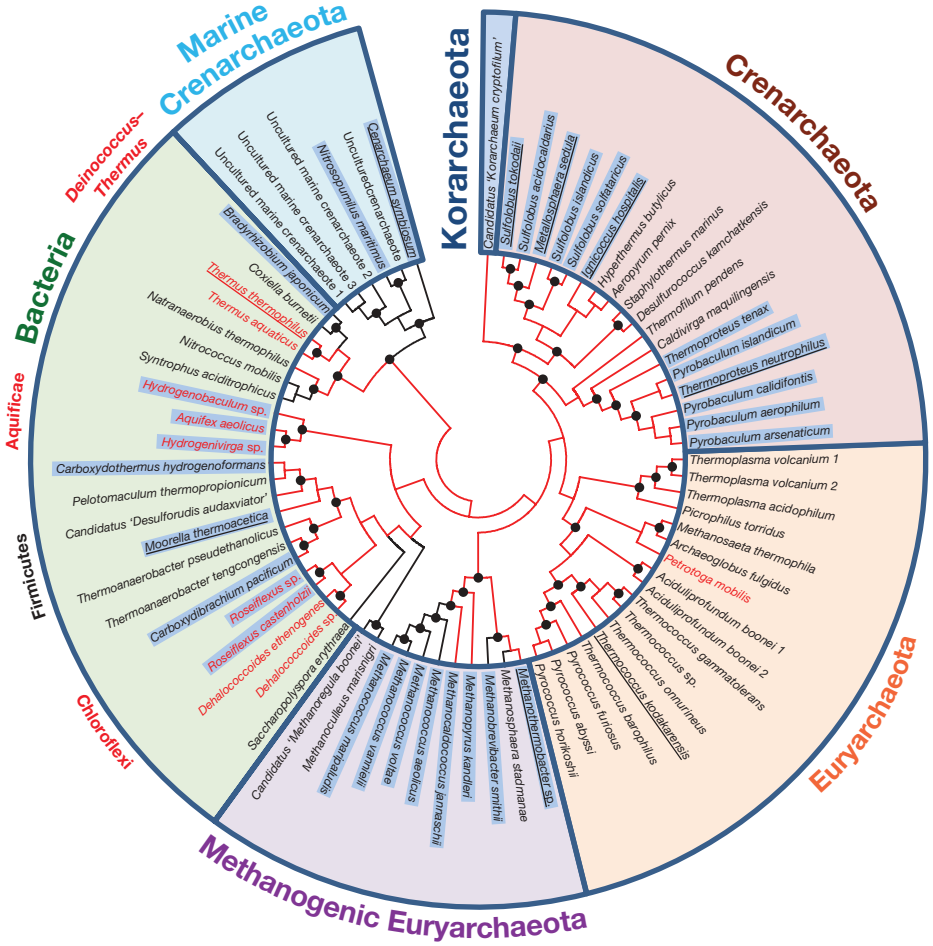

Figure 2 | Phylogenetic tree of FBP aldolases/phosphatases (compare with the ribosomal proteins trees in Fig. 1). Species in red are members of early-branching lineages of the Bacteria; the Clostridia cluster is shown in black characters. Species for which their enzymes were overproduced and studied here are underlined. The tree was constructed using the neighbour-joining algorithm. When maximum-parsimony or maximum-likelihood algorithms were used, the same groups were obtained. Bootstrap values higher than 75% are marked with dots. (Hyper)thermophiles are marked by red lineages; autotrophs by blue boxes.

integrative and conjugative elements[25], which may have facilitated the acquisition of the FBP aldolase/phosphatase gene.

The phylogenetic tree of the enzyme (Fig. 2) largely corresponds to the phylogenetic archaeal (Fig. 1a) and bacterial (Fig. 1b) ribosomal proteins trees. Note that the phylogenetic position of Nanoarchaeota, Korarchaeota and 'marine group I' Crenarchaeota is currently under discussion. Both ribosomal proteins and enzyme trees clearly separate 'marine Crenarchaeota' from Crenarchaeota, which were suggested recently to form a new archaeal phylum[26]. The apparent association of members of Methanomicrobiales (*Methanoculleus marisnigri* and *Candidatus* '*Methanoregula boonei*') with Bacteria in Fig. 2 is probably not significant. The absence of the gene in the heterotrophic Halobacteriales and in several Methanosarcinales and Methanomicrobiales (Euryarchaeota) is interpreted as loss of the gene in these derived phyla. Loss of function is expected for *Nanoarchaeum equitans*, which has lost the genes for all biosynthetic pathways[27]. The presence of the gene in some but not all major bacterial phyla can reflect either loss (in the late-branching phyla) or gain (in the early-branching lineages) since they diverged from a common ancestor. It is impossible to conclude this case here with certainty because of the low bootstrap values in the deep branches. Yet, the marked coincidence of the presence of the highly conserved gene in the deeply branching (mostly autotrophic and thermophilic) bacterial lineages as well as the distinct lineages in the phylogenetic enzyme tree support loss in the late-branching lineages rather than gain in the early bacterial lineages. Why of all phyla should these deep branches have acquired the gene? The data may, however, be interpreted differently, as indicating that the gene is archaeal specific and that very early it was transferred twice laterally from Archaea to Bacteria, followed by independent vertical transfer. Such an ambiguous situation is similar to the chimaeric nature of Thermotogales[28]. Whereas ribosomal protein genes strongly place Thermotogales as a sister group to Aquificales, the majority of genes with sufficient phylogenetic signal show affinities to Archaea and Clostridia/Firmicutes. Many of the bacterial species harbouring the gene (Fig. 2) are members of the deeply branching Clostridia/Firmicutes[23]. The huge impact of lateral gene transfer, often unrecognized, on prokaryote genome evolution has been impressively documented[29].

What makes FBP aldolase/phosphatase a peculiar aldolase? The enzyme contains four Mg^{2+} ions required to bind the phosphate residue (C1-phosphate in FBP and C3-phosphate in dihydroxyacetone phosphate (DHAP))[18] and is consequently inactivated by EDTA (80%; a typical feature of class II enzymes). The crystal structure of the *Sulfolobus tokodaii* enzyme[18] shows that substrate binding requires the interaction of two subunits (Fig. 4a). A conserved lysine (Lys 133) and tyrosine (Tyr 348) approximate to the C2 and C4 hydroxyl groups of FBP may be essential for catalysis (Fig. 4b and Supplementary Fig. 5). Indeed, the inactivation of the enzyme by borohydride in the presence of its substrates FBP (95%) or triosephosphates (80%) indicates that a lysine residue forms a Schiff base with DHAP (a characteristic feature of class I enzymes).

Unexpectedly, Lys 232 (rather than Lys 133), which is located in a conserved stretch of five amino acids (GKDDP; Supplementary Fig. 5), carried DHAP after borohydride treatment (*S. tokodaii* Lys 232,

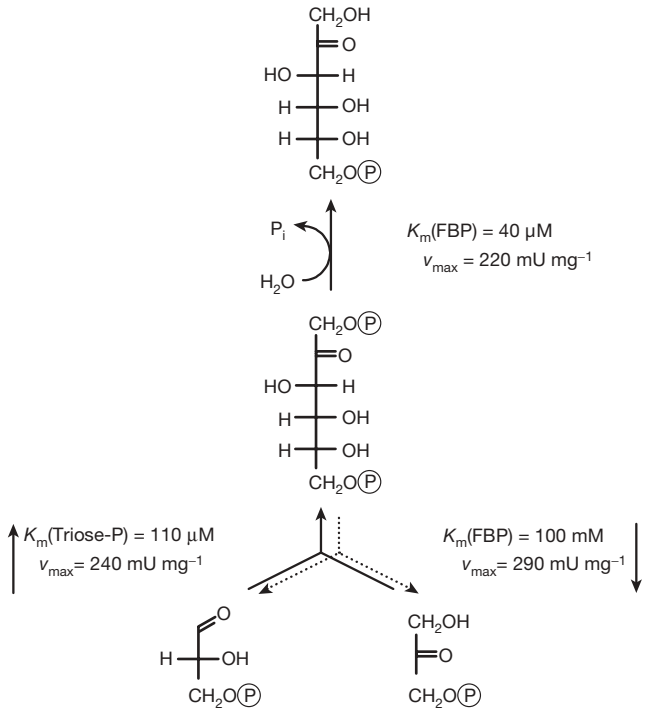

Figure 3 | Reactions of the bifunctional FBP aldolase/phosphatase. The kinetic constants of the partial reactions are shown for the *Cenarchaeum symbiosum* enzyme.

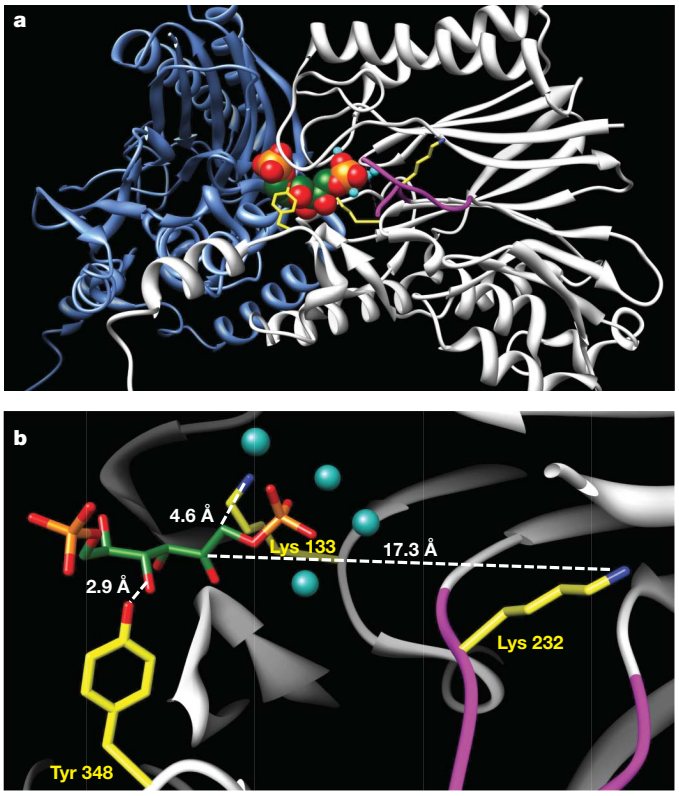

Figure 4 | Active centre of FBP aldolase/phosphatase[18]. **a**, Interaction of subunits for substrate binding. **b**, Active centre. Highly conserved lysine and tyrosine residues assumed to be essential for catalysis are highlighted in yellow. Note that the distant Lys 232 reacts with DHAP, forming a Schiff base (Supplementary Fig. 5). This obviously requires a conformational change of the enzyme. The C1 phosphate group is surrounded by four Mg^{2+} cations (blue spheres), promoting the subsequent phosphatase reaction. C, green; O, red; P, orange; N, dark blue; flexible loop, magenta.

Lys 133 and Tyr 348 correspond to *C. symbiosum* Lys 227, Lys 129 and Tyr 342). This lysine residue is far away from C2 of FBP in the crystal structure (Fig. 4b). However, the final structural model did not include the region between amino acids 226 and 228, as there was no observable electron density[18]. Lys 232 therefore might be located in a highly flexible loop (residues 220–233 between β9 and β10) and we postulate that the enzyme undergoes a structural change in the course of the catalytic cycle. Substitution in the *C. symbiosum* protein of Lys 232 by Arg and Tyr 348 by Phe (in the *S. tokodaii* nomenclature) gave interesting results. The Lys232Arg mutant protein had lost FBP aldolase activity, whereas the FBP phosphatase activity was unimpaired and even threefold enhanced. In contrast, the Tyr348Phe mutant showed unaltered FBP aldolase activity, but had lost FBP phosphatase activity (<5%). Thus, the bifunctional enzyme can be converted by only two mutations into a pure FBP aldolase or FBP phosphatase. Owing to the Schiff base intermediate the new aldolase is more of a class I enzyme, albeit with no resemblance to any known aldolase. Mg^{2+} may assist in binding and is essential for hydrolysing off phosphate. The crystal structure of the enzyme shows FBP bound in the open-keto form at the active site[18], possibly a consequence of the preceding aldol reaction, whereas other FBP phosphatases use the closed-ring form.

There are several benefits of this newly discovered FBP aldolase/phosphatase. First, it guarantees a unidirectional gluconeogenic pathway, under conditions where the carbon flux does not need to be turned to sugar degradation. Second, the combination of FBP aldolase/phosphatase with modified Entner–Doudoroff pathways, in which FBP is not an intermediate, opens a great metabolic flexibility. It allows an instantaneous adaptation to different growth substrates that require either glycolysis or gluconeogenesis, without the burden of transcriptional regulation. Third, its bifunctionality and high substrate affinity ensure that heat-labile triosephosphates are quickly removed and trapped in stabile fructose 6-phosphate. Fourth, the enzyme may be useful for metabolic engineering to direct at will the carbon flux to carbohydrate biosynthesis, avoiding the allosteric control of classical FBP phosphatase.

The distribution pattern of the enzyme, its phylogenetic tree and the unidirectional catalysis lend further support to the theory of a chemolithoautotrophic origin of life[6,7]. The data suggest that the Embden–Meyerhof–Parnas pathway evolved in the direction of gluconeogenesis[5] and the aldolase/phosphatase represents the ancestral gluconeogenic enzyme. Early organisms probably contained few carbohydrates (compared to the cellulose-containing plants, the primary producers of modern biology), making sugars rare primordial organic growth substrates. The great diversity of glycolytic pathways in heterotrophic Archaea[8] may be the result of late and, sometimes, convergent adaptation to sugar metabolism, when large quantities of sugar-containing cyanobacterial and finally plant cell walls could serve as growth substrates. This change in global sugar supply may have caused the loss of the ancestral unidirectional enzyme in heterotrophic Bacteria and Eukaryota.

METHODS SUMMARY

Recombinant FBP aldolase/phosphatase from *I. hospitalis* (Igni_0363) was heterologously expressed in *E. coli* and purified by heat precipitation, gel filtration and MonoQ-Sepharose chromatography. The gene for His_6-tagged FBP aldolase/phosphatase from *C. symbiosum* (GeneID 6370744) was synthesized by Mr Gene GmbH, heterologously expressed in *E. coli* and purified by Ni^{2+}-affinity chromatography.

Enzymatic activities of FBP aldolase/phosphatase were measured by coupled, continuous, photometric assays, following the reduction of $NAD(P)^+$ or the oxidation of NAD(P)H. For temperatures above 50 °C a similar but discontinuous assay was used.

Phylogenetic trees were constructed on the data set of a CLUSTAL W sequence alignment, using neighbour-joining as well as maximum-parsimony and maximum-likelihood algorithms.

Site-directed mutagenesis used homologous primers for reverse PCR that contained the desired mutation near the middle of the nucleotide sequence.

FBP aldolase/phosphatase of *C. symbiosum* was treated with borohydride in the presence of DHAP and purified by SDS–PAGE, followed by in-gel digestion with trypsin, peptide extraction, high-performance liquid chromatography (HPLC) separation and mass spectrometric detection.

Full Methods and any associated references are available in the online version of the paper at www.nature.com/nature.

Received 14 September 2009; accepted 5 February 2010.
Published online 28 March 2010.

1. Stetter, K. O. Hyperthermophiles in the history of life. *Phil. Trans. R. Soc. Lond. B* **361,** 1837–1843 (2006).
2. Berg, I. A. *et al.* Autotrophic carbon fixation in Archaea. *Nature Rev. Microbiol.* (in the press).
3. Huber, H. *et al.* A dicarboxylate/4-hydroxybutyrate autotrophic carbon assimilation cycle in the hyperthermophilic Archaeum *Ignicoccus hospitalis*. *Proc. Natl Acad. Sci. USA* **105,** 7851–7856 (2008).
4. Berg, I. A., Kockelkorn, D., Buckel, W. & Fuchs, G. A 3-hydroxypropionate/4-hydroxybutyrate autotrophic carbon dioxide assimilation pathway in Archaea. *Science* **318,** 1782–1786 (2007).
5. Ronimus, R. S. & Morgan, H. W. Distribution and phylogenies of enzymes of the Embden-Meyerhof-Parnas pathway from archaea and hyperthermophilic bacteria support a gluconeogenic origin of metabolism. *Archaea* **1,** 199–221 (2003).
6. Wächtershäuser, G. On the chemistry and evolution of the pioneer organism. *Chem. Biodivers.* **4,** 584–602 (2007).
7. Martin, W., Baross, J., Kelley, D. & Russell, M. J. Hydrothermal vents and the origin of life. *Nature Rev. Microbiol.* **6,** 805–814 (2008).
8. Siebers, B. & Schönheit, P. Unusual pathways and enzymes of central carbohydrate metabolism in Archaea. *Curr. Opin. Microbiol.* **8,** 695–705 (2005).
9. Fuchs, G., Winter, H., Steiner, I. & Stupperich, E. Enzymes of gluconeogenesis in the autotroph *Methanobacterium thermoautotrophicum*. *Arch. Microbiol.* **136,** 160–162 (1983).
10. Jahn, U., Huber, H., Eisenreich, W., Hügler, M. & Fuchs, G. Insights into the autotrophic CO_2 fixation pathway of the archaeon *Ignicoccus hospitalis*: comprehensive analysis of the central carbon metabolism. *J. Bacteriol.* **189,** 4108–4119 (2007).
11. Schäfer, S., Barkowski, C. & Fuchs, G. Carbon assimilation by the autotrophic thermophilic archaebacterium *Thermoproteus neutrophilus*. *Arch. Microbiol.* **146,** 301–308 (1986).
12. Imanaka, H., Fukui, T., Atomi, H. & Imanaka, T. Gene cloning and characterization of fructose-1,6-bisphosphate aldolase from the hyperthermophilic archaeon *Thermococcus kodakaraensis* KOD1. *J. Biosci. Bioeng.* **94,** 237–243 (2002).
13. Lorentzen, E., Siebers, B., Hensel, R. & Pohl, E. Structure, function and evolution of the Archaeal class I fructose-1,6-bisphosphate aldolase. *Biochem. Soc. Trans.* **32,** 259–263 (2004).
14. Andreeva, A. *et al.* Data growth and its impact on the SCOP database: new developments. *Nucleic Acids Res.* **36,** D419–D425 (2008).
15. Grochowski, L. L. & White, R. H. Promiscuous anaerobes: new and unconventional metabolism in methanogenic archaea. *Ann. NY Acad. Sci.* **1125,** 190–214 (2008).
16. Rashid, N. *et al.* A novel candidate for the true fructose-1,6-bisphosphatase in archaea. *J. Biol. Chem.* **277,** 30649–30655 (2002).
17. Sato, T. *et al.* Genetic evidence identifying the true gluconeogenic fructose-1,6-bisphosphatase in *Thermococcus kodakaraensis* and other hyperthermophiles. *J. Bacteriol.* **186,** 5799–5807 (2004).
18. Nishimasu, H., Fushinobu, S., Shoun, H. & Wakagi, T. The first crystal structure of the novel class of fructose-1,6-bisphosphatase present in thermophilic archaea. *Structure* **12,** 949–959 (2004).
19. Hallam, S. J. *et al.* Genomic analysis of the uncultivated marine crenarchaeote *Cenarchaeum symbiosum*. *Proc. Natl Acad. Sci. USA* **103,** 18296–18301 (2006).
20. Makarova, K. S., Wolf, Y. I. & Koonin, E. V. Potential genomic determinants of hyperthermophily. *Trends Genet.* **19,** 172–176 (2003).
21. Chong, P. K., Burja, A. M., Radianingtyas, H., Fazeli, A. & Wright, P. C. Proteome analysis of *Sulfolobus solfataricus* P2 propanol metabolism. *J. Proteome Res.* **6,** 1430–1439 (2007).
22. Ludwig, W. & Klenk, H.-P. In *The Archaea and the Deeply Branching and Phototrophic Bacteria* (eds Boone, D. R. & Garrity, G. M.). Bergey's Manual of Systematic Bacteriology, 2nd edn, Vol. One, 49–65 (Springer, 2001).
23. Pierce, E. *et al.* The complete genome sequence of *Moorella thermoacetica* (f. *Clostridium thermoaceticum*). *Environ. Microbiol.* **10,** 2550–2573 (2008).
24. Ferry, J. G. & House, C. H. The stepwise evolution of early life driven by energy conservation. *Mol. Biol. Evol.* **23,** 1286–1292 (2006).
25. te Poele, E. M., Bolhuis, H. & Dijkhuizen, L. Actinomycete integrative and conjugative elements. *Antonie Van Leeuwenhoek* **94,** 127–143 (2008).
26. Brochier-Armanet, C., Boussau, B., Gribaldo, S. & Forterre, P. Mesophilic Crenarchaeota: proposal for a third archaeal phylum, the Thaumarchaeota. *Nature Rev. Microbiol.* **6,** 245–252 (2008).
27. Waters, E. *et al.* The genome of *Nanoarchaeum equitans*: insights into early archaeal evolution and derived parasitism. *Proc. Natl Acad. Sci. USA* **100,** 12984–12988 (2003).
28. Zhaxybayeva, O. *et al.* On the chimeric nature, thermophilic origin, and phylogenetic placement of the Thermotogales. *Proc. Natl Acad. Sci. USA* **106,** 5865–5870 (2009).
29. Dagan, T., Artzy-Randrup, Y. & Martin, W. Modular networks and cumulative impact of lateral gene transfer in prokaryote genome evolution. *Proc. Natl Acad. Sci. USA* **105,** 10039–10044 (2008).
30. Teeling, H. & Glöckner, F. O. RibAlign: a software tool and database for eubacterial phylogeny based on concatenated ribosomal protein subunits. *BMC Bioinform.* **7,** 1–6 (2006).

Supplementary Information is linked to the online version of the paper at www.nature.com/nature.

Acknowledgements We thank R. Thauer, S. Ragsdale, H. Atomi and H. Huber for the supply of strains; F. Drepper for help with bioinformatic approaches; W. Haehnel and B. Knapp for MS analysis; N. Gad'on and C. Ebenau-Jehle for growing cells and maintaining the laboratory running; the DOE Joint Genome Institute for early release of archaeal genomic sequence data; and the Deutsche Forschungsgemeinschaft and Evonik-Degussa for financial support. We also thank M. Ziemski and I. Berg for help with data base analysis as the basis of Fig. 1a, and H. Teeling and F. O. Glöckner for providing Fig. 1b.

Author Contributions R.F.S. performed the experiments; R.F.S. and G.F. designed the work and wrote the paper.

Author Information Reprints and permissions information is available at www.nature.com/reprints. The authors declare no competing financial interests. Correspondence and requests for materials should be addressed to G.F. (georg.fuchs@biologie.uni-freiburg.de).

METHODS

Strains and growth conditions. *Ignicoccus hospitalis* strain KIN4/I^T (DSMZ 18386^T) was obtained from the culture collection of the Lehrstuhl für Mikrobiologie, University of Regensburg, Germany. Cells were grown autotrophically in [1/2] SME (synthetic sea water) medium without organic substrates using elemental sulphur as an electron acceptor under a gas phase of H_2/CO_2 (80%/20%, v/v) at 90 °C and pH 5.5[31]. *Thermoproteus neutrophilus* (DSMZ 2338^T) was grown anaerobically and autotrophically on a defined mineral medium with elemental sulphur under gassing with a mixture of 80% H_2 and 20% CO_2 (v/v) at 85 °C and pH 6.8[32]. *Metallosphaera sedula* (DSMZ 5348^T) was grown autotrophically at 75 °C on a chemically defined medium (pH 2.0) under gassing with a mixture of 19% CO_2, 3% O_2 and 78% H_2[33]. Cells of *Methanothermobacter marburgensis*, *Moorella thermoacetica*, *Thermococcus kodakarensis* and *Ignicoccus hospitalis* were supplied by R. Thauer, S. Ragsdale, H. Atomi and H. Huber, respectively. *Thermus thermophilus* HB27 (DSMZ 7093) was grown aerobically at 75 °C and 180 r.p.m. on 200 ml of LB medium. *Sulfolobus tokodaii* (DSMZ 16993^T) was grown aerobically on a defined medium (pH 3.0) with 1 g l^{-1} yeast extract, 1 g l^{-1} glucose and 1 g l^{-1} casamino acids at 75 °C.

Production of FBP aldolase/phosphatase from different organisms in *E. coli*. Chromosomal DNA was extracted using an illustra bacteria genomicPrep Mini Spin Kit (GE Healthcare). The genes encoding FBP aldolase/phosphatase (Supplementary Table 3) were amplified by PCR with Pfu polymerase (Gennaxon) using the primers, annealing temperatures and elongation times summarized in Supplementary Table 3. PCR conditions were as follow: 33 cycles of 1 min denaturation at 94 °C, 1 min primer annealing, and elongation at 72 °C as indicated. The PCR products were isolated and cloned into the expression vector pT7-7[34]. Purification of PCR products and plasmids was performed with Quiagen kids according to the manufacturer's specifications. Competent *E. coli* Rosetta 2 (DE3) cells (Novagen) were transformed with the corresponding plasmid and grown at 37 °C in a 10-l fermenter or 1 l flasks with self-inducing media[35] containing 100 μg ampicillin per ml and 34 μg chloramphenicol per ml. After 5–6 h of growth, the temperature was lowered to 20 °C, and the culture was grown overnight. Cells were harvested by centrifugation and stored in liquid nitrogen until use.

Production of FBP aldolase/phosphatase from *Cenarchaeum symbiosum* in *E. coli*. The gene encoding FBP aldolase/phosphatase of *C. symbiosum* (GeneID: 6370744) was synthesized by Mr Gene GmbH (D-93059 Regensburg). Owing to false identification of the start codon the annotated gene was 387 bp longer than the corresponding genes from all other organisms. Therefore, a shorter version of the gene with the assumed right start codon was synthesized introducing a NdeI site (underlined). In front of the stop codon, sequences encoding a His_6-tag (italic) and a HindIII restriction site (underlined) were integrated. The sequence was optimized for the expression in *E. coli* by Mr Gene GmbH: CATAT
G CGTATCACCGTTAGCGCCATTAAAGCCGATGTTGGGGGAATTGGAGG
TCACACACTGCCTAGTAGCGGACTGCTGGATGCTGTTCGTCGTAAAGT
TTCGTCAAGCTCTCTGCTGATTGATCACTATATTGGCTATTGTGGGGAT
GATGTTCACATTGTCATGACTCATACACGTGGCACCGATAATAGCGAT
ATCCATAAACTGGCGTGGGACGCCTTCATGGAAGGAACTCGTGTTGCC
AAAGAAGAGGGCCTGTATGGTGCTGGTCAAGACCTGCTGCGCGATTCA
TTTTCCGGGAACGTTAAAGGGATGGGTCCTGGAGTGGCAGAACTGGAA
TTCGAAGAACGTGCTAATGAGGCCTTCACCGTGTTTGCTGCCGATAAA
ACCGAACCTGGAGCCTTCAACTATCCTTTCTATCGTATGTTTGTCGACT
CTCTGAGCAATACTGGTCTGATCGTGAATAAAAGCCTGGCGGAAGGTG
TTGTTATTAACATTATGGACGTGTCCAAAGCTCGTACAGCTCGTCTGGT
ACTGTGGGAGGATAAACCAACCATCGAAGCAGCACTGATGTATCCTGG
CCGTTTTGTTGTGAGCAGCGTGGAAACCCGTGATGGAGAACCGATTGC
CTCTGCTAGTACAGATCGCCTGCATAACATTGCCGGCACCTATGTTGG
GAAAGATGACCCGATTTGTCTGGTCCGTACACAGAAACGTTTTCCAGC
GACGGAAGAAGCTGGTTCTTGCTTCAATAACCCACACTATGTGGCGGG
TAATACTCGTGGTTCACACCACATGCCGCTGATGCCTGTCCGTCTGAA
TTCTCCGGCCTCTATCAACTTCTGTATCCCGATCGTGGAAGCACTGGTT
TTTAGCATGCACGAAGGGCGCCTGACTGGACCTTTTGATGGCTTCTCT
ACGCCTGATTGGGACGATGTCCGCCGTACTGCTACTCGCCGTGCTCAT
GCCATGCGTCGTCAGGGATTCGTTCATCCGGCTACCCTGGTGCCTGAT
GAGCTGGAGTATGCCGAAGGTTATCGTTCTCGTATGGACGTGCTGGAT
AGCAAAATGGTTCCGCTGAAAGATTCAGGTCCTGCCGGTACAGGACGT
GCTTATGAAGATCCGGATCTGGAG*CATCACCACCATCATCAC*TGAT*AAG*
CTT.

The synthesized gene was cloned in the expression vector pT7-7 resulting in the plasmid FBP_C.symb-X-pT7-7; heterologous expression of the gene was performed as described above.

Purification of recombinant FBP aldolase/phosphatase from *I. hospitalis*. The results of the following purification steps are summarized in Supplementary Table 2. (1) Preparation of cell extract. Frozen *E. coli* cells (6 g wet mass) were suspended in 7 ml buffer AP (20 mM Tris-HCl pH 7.8, 20 mM $MgCl_2$, 20 mM dithioerythritol (DTE)) containing 0.1 mg DNase I per ml and passed twice through a French pressure cell at 137 MPa. The cell lysate was centrifuged at 100,000*g* for 1 h (4 °C), and the supernatant was used for the following purification steps.

(2) Heat precipitation. Cell extract was incubated for 20 min at 80 °C, cooled on ice for 15 min and centrifuged at 17,000*g* for 30 min (4 °C). The supernatant (5 ml) was directly applied to a gel filtration column.

(3) Gel filtration. Portions of the supernatant after heat precipitation (2.5 ml) were applied onto a Superdex 200 HR 26/60 gel filtration column (Pharmacia) equilibrated with 20 mM Tris-HCl pH 7.8 containing 20 mM $MgCl_2$ and 100 mM KCl. The flow rate was 2 ml min^{-1}. Activity was eluted after a volume of 94 ml in a volume of 36 ml. Active fractions were pooled and stored at −20 °C with 20% of glycerol and 5 mM DTE.

(4) MonoQ-Sepharose chromatography. The enzyme solution from the gel filtration step (45 ml) was applied to a MonoQ HR 5/5 anion exchange column (Amersham Bioscience) equilibrated with 20 mM Tris-HCl pH 7.8 containing 20 mM $MgCl_2$ and 3 mM DTE. The flow rate was 0.5 ml min^{-1}. The salt concentration was increased stepwise (50 mM steps) from 0 mM to 500 mM KCl. Activity was eluted at 200–250 mM KCl in a volume of 16 ml. Active fractions were pooled and stored at −20 °C until use.

Purification of recombinant FBP aldolase/phosphatase from *C. symbiosum*. (1) Preparation of cell extract (see above). (2) Affinity chromatography. Cell extract from 5.5 g wet mass (8 ml) was applied onto a 1-ml Ni^{2+}-chelating Sepharose affinity column (GE Healthcare) equilibrated with buffer A (20 mM Tris-HCl pH 7.8, 50 mM $MgCl_2$ and 200 mM KCl) at a flow rate of 1 ml min^{-1}. The column was washed with buffer A containing 50 mM imidazole, and the recombinant FBP aldolase/phosphatase was eluted with buffer A containing 500 mM imidazole. Active fractions (4.5 ml) were pooled and stored at −20 °C with 40% of glycerol and 10 mM DTE.

FBP aldolase/phosphatase enzyme assays. Continuous assays. FBP aldolase and FBP phosphatase activities were both determined at 48 °C using a coupled spectrophotometric assay, in which the reduction of $NAD(P)^+$ or oxidation of NAD(P)H was followed at 365 nm ($\varepsilon_{365\,nm}$ NAD(P)H = 3,400 M^{-1} cm^{-1}). One enzyme unit (U) corresponds to 1 μmol substrate converted per minute. The pH of the buffers was adjusted at 20 °C, and the actual values for higher temperatures were calculated[36].

(1) FBP phosphatase assay. The FBP-dependent fructose 6-phosphate formation was measured by coupling the reaction with exogenous phosphoglucose isomerase and glucose 6-phosphate dehydrogenase, and NADPH formation was followed. The assay mixture (0.5 ml) contained 100 mM Tris-HCl pH 7.8, 20 mM $MgCl_2$, 20 mM DTE, 0.5 mM $NADP^+$ and 1 U each of phosphoglucose isomerase and glucose 6-phosphate dehydrogenase from baker's yeast (Sigma-Aldrich), respectively. The reaction was started either by the addition of 5 mM FBP or (partially) purified enzyme (2–200 μg of protein). The pH optimum of the *I. hospitalis* enzyme was determined using a mixture of *N*-2-acetamido-2-hydroxyethanesulphonic acid (ACES), tris(hydroxymethyl)aminomethane (Tris), and ethanolamine buffers[37]; the pH was adjusted at room temperature. To test the stability of the enzyme at elevated temperatures, it was incubated at 67, 82 and 97 °C in a water bath, and samples were taken at intervals, rapidly cooled on ice and subsequently used in the photometric assay described above.

(2) FBP aldolase assay (anabolic direction). The triosephosphate-dependent fructose 6-phosphate formation was measured by coupling the reaction with exogenous triosephosphate isomerase, phosphoglucose isomerase and glucose 6-phosphate dehydrogenase from baker's yeast (Sigma-Aldrich), and NADPH formation was followed. The assay mixture (0.5 ml) containing 100 mM Tricine-KOH pH 8.0, 20 mM $MgCl_2$, 20 mM DTE, 0.5 mM $NADP^+$, 4 U of triosephosphate isomerase, 1 U of phosphoglucose isomerase and 1 U of glucose 6-phosphate dehydrogenase was pre-incubated for 4 min. After addition of glyceraldehyde 3-phosphate (8 mM), the assay mixture was incubated for another minute to approach the equilibrium between glyceraldehyde 3-phosphate and DHAP. The reaction was started by addition of (partially) purified enzyme (2–200 μg of protein). The pH optimum was determined as described above.

(3) FBP aldolase assay (catabolic direction). The FBP-dependent formation of triosephosphates was measured by coupling the reaction with triosephosphate isomerase from baker's yeast and glycerolphosphate dehydrogenase from rabbit (Sigma-Aldrich). The assay mixture (0.5 ml) contained 100 mM Tricine-KOH pH 8.0, 20 mM $MgCl_2$, 20 mM DTE, 0.55 mM NADH, 20 U of triosephosphate isomerase, and 2 U of glycerolphosphate dehydrogenase. The reaction was started by the addition of FBP (5 mM) or purified enzyme (20–100 μg of protein).

Discontinuous assay. The FBP aldolase/phosphatase activities at temperatures higher than 48 °C were determined in a discontinuous assay. The reaction mixture (0.4 ml) containing 100 mM Tris-HCl pH 8.2, 20 mM $MgCl_2$, 20 mM DTE and

enzyme solution was pre-incubated at the chosen temperature for 2 min, and the reaction was started by addition of either 5 mM FBP or 4 mM triosephosphates for phosphatase or aldolase measurement, respectively. The triosephosphate mixture used in the aldolase assay contained glyceraldehyde 3-phosphate and DHAP and was obtained by incubation of 8 mM glyceraldehyde 3-phosphate with 20 U of triosephosphate isomerase per ml in 100 mM morpholinoethanesulfonic acid (MES)-KOH pH 6.0 for 10 min at room temperature. The amounts of fructose 6-phosphate formed in the reaction after 1–8 min of incubation were determined by transferring the sample (0.1 ml) into an assay mixture (0.4 ml; 22 °C) containing 100 mM Tris-HCl pH 7.8, 2 mM $MgCl_2$, 0.5 mM $NADP^+$, 1 U of phosphoglucose isomerase, and 1 U of glucose 6-phosphate dehydrogenase, and the increase in absorption at 365 nm was monitored. As a control, assays lacking FBP aldolase/phosphatase or substrates were performed.

EDTA and borohydride treatment of the FBP aldolase/phosphatase from *C. symbiosum*. To classify the FBP aldolase/phosphatase to either class I (Schiff base intermediate) or class II (metal-based catalysis) aldolases, the enzyme from *C. symbiosum* was incubated with the specific inhibitors for each class[38].

(1) Active site labelling. Borohydride inhibits class I aldolases by reducing the Schiff base between the epsilon-NH_2 group of the active site lysine and the carbonyl group of the substrate FBP or DHAP. The effect of borohydride on aldolase activity was tested in the presence of triosephosphates (anabolic direction) or FBP (catabolic direction) as substrates. When inhibition of anabolic FBP aldolase reaction was tested, the enzyme (0.17 mg of protein) was incubated at 20 °C in 0.1 ml of 200 mM MES-KOH pH 6.0 in the presence or absence of 10 mM triosephosphates (obtained as described above). After 30 min of incubation, 100 mM $NaBH_4$ (1 M stock solution in 10 mM NaOH) was added. The mixture was incubated for an additional 30 min on ice, and FBP aldolase activity was measured using the continuous anabolic assay described above. The inhibition of catabolic FBP aldolase reaction was studied by incubating the enzyme (0.34 mg of protein) at room temperature in 0.2 ml of 200 mM MES-KOH pH 6.0 in the presence or absence of 20 mM FBP. Again, the samples were incubated for 30 min at room temperature, and $NaBH_4$ (100 mM) was added. After another 30 min of incubation on ice, activity was measured in the continuous catabolic assay as described above.

(2) EDTA inhibition. The effect of EDTA on the FBP aldolase activity was tested with the continuous catabolic assay described above but the reaction mixture contained only 5 mM $MgCl_2$ instead of 20 mM. Addition of 10 mM EDTA (pH 8.0) to the reaction resulted in 80% inhibition and activity was completely restored by addition of 20 mM $MgCl_2$.

Determination of subunits and native molecular masses. Cell extracts of *I. hospitalis*, *T. neutrophilus*, *M. sedula* and *M. marburgensis* were prepared as described for *E. coli* extracts described above. Protein fractions were analysed by SDS–12.5% polyacrylamide gel electrophoresis[39] and proteins were visualized by Coomassie brilliant blue R-250 staining. The native molecular mass of the enzyme was estimated using a 24 ml Superdex 200 HR 10/30 (Amersham Bioscience) gel filtration column calibrated with vitamin B12 (1.35 kDa), RNase A (13.7 kDa), ovalbumin (43 kDa), bovine serum albumin (69 and 138 kDa), aldolase (158 kDa), ferritin (440 kDa) and blue dextran 2000 (2,000 kDa).

Active site lysine identification by HPLC-electrospray mass spectrometry. The FBP aldolase/phosphatase of *C. symbiosum* was treated with borohydride as described above. As DHAP is the triosephosphate that forms the Schiff base with the active site lysine, DHAP alone instead of a mixture of triosephosphates was used as substrate. Fractions incubated with or without substrate were treated with borohydride and purified by SDS–PAGE. In-gel digestion with trypsin, peptide extraction, HPLC separation and mass spectrometric detection was performed as described[40]. The sequences of the peptides were determined by MS–MS spectrometry. The native *Cenarchaeum* enzyme yielded three fragments 217L-227K (observed mass 1,171.6351, calculated mass 1,171.6350), 217L-235R (one trypsin-missed cleavage; observed mass 2,140.1093, calculated mass 2,140.1099) and 205D-235R (observed mass 3,339.6546, calculated mass 3,339.6517; two trypsin-missed cleavages), with Lys 227 being the only lysine residue in these fragments. Lys 227 of the *Cenarchaeum* enzyme corresponds to Lys 232 of the *Sulfolobus tokodaii* enzyme (see Supplementary Fig. 5). The enzyme treated with borohydride in the presence of DHAP yielded the same fragments and in addition the modified fragments 217L-235R (observed mass 2,294.1135, calculated mass with one molecule of DHAP bound as reduced Schiff base 2,294.1130) and 205D-235R (observed mass 3,493.6561, calculated mass 3,493.6548). The indicated masses are the monoisotopic relative masses of the peptides. Note that trypsin does not cleave after modified lysine residues. No other lysine residue in the whole protein was found to be modified by DHAP. The corresponding modification in a fragment representing Lys 133 (in the *S. tokodaii* enzyme; corresponding to Lys 129 in the *Cenarchaeum* enzyme) was not observed despite sequence coverage of 95%.

Computational analysis. The BLASTP searches were performed in June 2009 via the NCBI BLAST server (http://blast.ncbi.nlm.nih.gov/Blast.cgi)[41] with BAC10571 from *Thermococcus kodakarensis* KOD1[42] as a query in the database of non-redundant protein sequences. The sequences with an expectation value smaller than 1×10^{-60} were aligned using CLUSTAL W[43] implemented within MEGA4.0.2 software[44].

The phylogenetic trees were reconstructed using neighbour-joining algorithm[44,45] as well as maximum-parsimony[46] and maximum-likelihood algorithms[47]. The archaebacterial tree was based on the analyses of a concatamer of 9 subunits of RNA polymerase, 3 transcription factors (NusA, NusG, TFE), and 53 ribosomal proteins from 59 currently finished archaeal genomes. The eubacterial tree was based on concatenated 37 ribosomal protein subunits from 120 bacterial species.

The search in the environmental data base was performed in October 2008 via the NCBI BLAST server with BLASTP algorithm using the same query as above but in the environmental samples database. Open reading frames having expectation values smaller than 10^{-10} were aligned and used for further phylogenetic analysis as described above.

To study the distribution of several putative aldolases and FBP phosphatases among completely sequenced archaeal genomes (Supplementary Table 1), the standard BLASTP search was automated using the NCBI BLAST software (http://blast.ncbi.nlm.nih.gov/Blast.cgi?CMD=Web&PAGE_TYPE=BlastDocs&DOC_TYPE=Download). Therefore, a database with all completely sequenced chromosomes of Archaea and Bacteria was compiled in March 2009 taking the sequences from the NCBI Genome website (http://www.ncbi.nlm.nih.gov/sites/entrez). The following proteins were used as queries: FBP aldolase class I (Q07159)[48]; FBP aldolase class II (AAF22441)[49–51]; FBP aldolase class IA (BAC21177)[42]; 2-amino-3,7-dideoxy-D-threo-hept-6-ulosonic acid (ADH) synthase (NP_247374)[52]; 3-deoxy-D-arabino-heptulosonate 7-phosphate synthase (1ZCO_A)[53]; FBP phosphatase class I (NP_418653)[54]; FBP phosphatase class II (P0A9C9)[55]; FBP phosphatase class III (Q45597)[56]; FBP phosphatase class IV (NP_247073)[57]; FBP phosphatase class V (BAC10571)[42]. A cutoff value of 1×10^{-45} was used in the table. Only for the FBP phosphatases of class I from the halophilic and methanogenic Euryarchaeota a cutoff value of 1×10^{-28} was used considering the reported presence of an FBP phosphatase in halophilic archaea[58]. The values for *C. symbiosum* were obtained by manual BLAST searches, because its genome is not available on the NCBI Genome website.

The software package USFC Chimera 1.4 (http://www.cgl.ucsf.edu/chimera/) was used to visualize the active site of the FBP aldolase/phosphatase of *Sulfolobus tokodaii* (1UMG). The software package GraphPad Prism 4.0.2 (http://www.graphpad.com/Prism/organize.htm) was used to calculate the K_m and v_{max} values of the enzymes. All *in silico* cloning steps were performed with the program Clone Manager 7.11 (Scientific & Educational Software).

Site-directed mutagenesis. The mutations were introduced into the expression vector pT7-7 carrying the *Cenarchaeum* gene (for nucleotide sequence see above) by reverse PCR using homologous primers carrying the mutation in the middle of the nucleotide sequence. Primers for Lys232Arg (in the *S. tokodaii* nomenclature) were CACCTATGTTGGGAGGGATGACCCGATTTG and CAAATC GGGTCATCCCTCCCAACATAGGTG. Primers for Tyr348Phe were GATGAG CTGGAGTTTGCCGAAGGTTATC and GATAACCTTCGGCAAACTCCAGC TCATC. The exchanged codons are underlined. PCR conditions were as follows: 25 cycles of 20 s denaturation at 98 °C, 20 s primer annealing at 60 °C (Tyr 348 mutant) or 58 °C (Lys 232 mutant), and 110 s elongation at 72 °C using Phusion DNA polymerase (BioLabs New England). The linear PCR products were incubated at 37 °C with 20 U of DpnI for 3 h to digest the methylated template plasmid. After amplification of the plasmid in *E. coli* DH5α, the mutated plasmids from four clones for each mutant were sequenced.

Materials. All Materials were obtained from the sources described previously[59].

31. Huber, H. *et al. Ignicoccus* gen. nov., a novel genus of hyperthermophilic, chemolithoautotrophic Archaea, represented by two new species, *Ignicoccus islandicus* sp. nov. and *Ignicoccus pacificus* sp. nov. *Int. J. Syst. Evol. Microbiol.* **50,** 2093–2100 (2000).
32. Ramos-Vera, W. H., Berg, I. A. & Fuchs, G. Autotrophic carbon dioxide assimilation in Thermoproteales revisited. *J. Bacteriol.* **191,** 4286–4297 (2009).
33. Teufel, R., Kung, J. W., Kockelkorn, D., Alber, B. E. & Fuchs, G. 3-Hydroxypropionyl-coenzyme A dehydratase and acryloyl-coenzyme A reductase, enzymes of the autotrophic 3-hydroxypropionate/4-hydroxybutyrate cycle in Sulfolobales. *J. Bacteriol.* **191,** 4572–4581 (2009).
34. Tabor, S. & Richardson, C. C. A bacteriophage T7 RNA polymerase/promoter system for controlled exclusive expression of specific genes. *Proc. Natl Acad. Sci. USA* **82,** 1074–1078 (1985).
35. Studier, F. W. Protein production by auto-induction in high density shaking cultures. *Protein Expr. Purif.* **41,** 207–234 (2005).

36. Dawson, R. M. C., Elliott, D. C., Elliott, W. H. & Jones, K. M. *Data for Biochemical Research* 3rd edn (Oxford Univ. Press, 1986).
37. Ellis, K. J. & Morrison, J. F. Buffers of constant ionic strength for studying pH-dependent processes. *Methods Enzymol.* **87,** 405–426 (1982).
38. Scamuffa, M. D. & Caprioli, R. M. Comparison of the mechanisms of two distinct aldolases from *Escherichia coli* grown on gluconeogenic substrates. *Biochim. Biophys. Acta* **614,** 583–590 (1980).
39. Laemmli, U. K. Cleavage of structural proteins during the assembly of the head of bacteriophage T4. *Nature* **227,** 680–685 (1970).
40. Schopfer, P., Heyno, E., Drepper, F. & Krieger-Liszkay, A. Naphthoquinone-dependent generation of superoxide radicals by quinone reductase isolated from the plasma membrane of soybean. *Plant Physiol.* **147,** 864–878 (2008).
41. Gish, W. & States, D. J. Identification of protein coding regions by database similarity search. *Nature Genet.* **3,** 266–272 (1993).
42. Rashid, N. *et al.* A novel candidate for the true fructose-1,6-bisphosphatase in archaea. *J. Biol. Chem.* **277,** 30649–30655 (2002).
43. Larkin, M. A. *et al.* Clustal W and Clustal X version 2.0. *Bioinformatics* **23,** 2947–2948 (2007).
44. Tamura, K., Dudley, J., Nei, M. & Kumar, S. MEGA4: Molecular Evolutionary Genetics Analysis (MEGA) software version 4.0. *Mol. Biol. Evol.* **24,** 1596–1599 (2007).
45. Gascuel, O. & Steel, M. Neighbor-joining revealed. *Mol. Biol. Evol.* **23,** 1997–2000 (2006).
46. Fitch, M. W. Toward defining the course of evolution: Minimum change for a specific tree topology. *Syst. Zool.* **20,** 406–416 (1971).
47. Felsenstein, J. Evolutionary trees from DNA sequences: a maximum likelihood approach. *J. Mol. Evol.* **17,** 368–376 (1981).
48. Witke, C. & Götz, F. Cloning, sequencing, and characterization of the gene encoding the class I fructose-1,6-bisphosphate aldolase of *Staphylococcus carnosus. J. Bacteriol.* **175,** 7495–7499 (1993).
49. De Montigny, C. & Sygusch, J. Functional characterization of an extreme thermophilic class II fructose-1,6-bisphosphate aldolase. *Eur. J. Biochem.* **241,** 243–248 (1996).
50. Sauvé, V. & Sygusch, J. Crystallization and preliminary X-ray analysis of native and selenomethionine fructose-1,6-bisphosphate aldolase from *Thermus aquaticus. Acta Crystallogr. D* **57,** 310–313 (2001).
51. Sauve, V. & Sygusch, J. Molecular cloning, expression, purification, and characterization of fructose-1,6-bisphosphate aldolase from *Thermus aquaticus. Protein Expr. Purif.* **21,** 293–302 (2001).
52. White, R. H. L. Aspartate semialdehyde and a 6-deoxy-5-ketohexose 1-phosphate are the precursors to the aromatic amino acids in *Methanocaldococcus jannaschii. Biochemistry* **43,** 7618–7627 (2004).
53. Schofield, L. R., Patchett, M. L. & Parker, E. J. Expression, purification, and characterization of 3-deoxy-D-arabino-heptulosonate 7-phosphate synthase from *Pyrococcus furiosus. Protein Expr. Purif.* **34,** 17–27 (2004).
54. Babul, J. & Guixe, V. Fructose bisphosphatase from *Escherichia coli*. Purification and characterization. *Arch. Biochem. Biophys.* **225,** 944–949 (1983).
55. Donahue, J. L., Bownas, J. L., Niehaus, W. G. & Larson, T. J. Purification and characterization of glpX-encoded fructose 1, 6-bisphosphatase, a new enzyme of the glycerol 3-phosphate regulon of *Escherichia coli. J. Bacteriol.* **182,** 5624–5627 (2000).
56. Fujita, Y. & Freese, E. Purification and properties of fructose-1,6-bisphosphatase of *Bacillus subtilis. J. Biol. Chem.* **254,** 5340–5349 (1979).
57. Stec, B., Yang, H., Johnson, K. A., Chen, L. & Roberts, M. F. MJ0109 is an enzyme that is both an inositol monophosphatase and the 'missing' archaeal fructose-1,6-bisphosphatase. *Nature Struct. Biol.* **7,** 1046–1050 (2000).
58. Falb, M. *et al.* Metabolism of halophilic archaea. *Extremophiles* **12,** 177–196 (2008).
59. Erb, T. J., Retey, J., Fuchs, G. & Alber, B. E. Ethylmalonyl-CoA mutase from *Rhodobacter sphaeroides* defines a new subclade of coenzyme B12-dependent acyl-CoA mutases. *J. Biol. Chem.* **283,** 32283–32293 (2008).

Vol 464|15 April 2010|doi:10.1038/nature08924

LETTERS

CpG islands influence chromatin structure via the CpG-binding protein Cfp1

John P. Thomson[1]*, Peter J. Skene[1]*, Jim Selfridge[1], Thomas Clouaire[1], Jacky Guy[1], Shaun Webb[1], Alastair R. W. Kerr[1], Aimée Deaton[1], Rob Andrews[2], Keith D. James[2], Daniel J. Turner[2], Robert Illingworth[1] & Adrian Bird[1]

CpG islands (CGIs) are prominent in the mammalian genome owing to their GC-rich base composition and high density of CpG dinucleotides[1,2]. Most human gene promoters are embedded within CGIs that lack DNA methylation and coincide with sites of histone H3 lysine 4 trimethylation (H3K4me3), irrespective of transcriptional activity[3,4]. In spite of these intriguing correlations, the functional significance of non-methylated CGI sequences with respect to chromatin structure and transcription is unknown. By performing a search for proteins that are common to all CGIs, here we show high enrichment for Cfp1, which selectively binds to non-methylated CpGs *in vitro*[5,6]. Chromatin immunoprecipitation of a mono-allelically methylated CGI confirmed that Cfp1 specifically associates with non-methylated CpG sites *in vivo*. High throughput sequencing of Cfp1-bound chromatin identified a notable concordance with non-methylated CGIs and sites of H3K4me3 in the mouse brain. Levels of H3K4me3 at CGIs were markedly reduced in Cfp1-depleted cells, consistent with the finding that Cfp1 associates with the H3K4 methyltransferase Setd1 (refs 7, 8). To test whether non-methylated CpG-dense sequences are sufficient to establish domains of H3K4me3, we analysed artificial CpG clusters that were integrated into the mouse genome. Despite the absence of promoters, the insertions recruited Cfp1 and created new peaks of H3K4me3. The data indicate that a primary function of non-methylated CGIs is to genetically influence the local chromatin modification state by interaction with Cfp1 and perhaps other CpG-binding proteins.

To characterize the chromatin modifications typical of CGIs, we used the methyl-CpG-sensitive restriction endonuclease HinPI (cleavage site GCGC) to release small chromatin fragments from purified brain nuclei, as described previously[9]. As sites for this enzyme in bulk chromatin are rare and generally uncleavable owing to DNA methylation, the released fraction predominantly contains non-methylated CGIs. Confirming this, further digestion of the deproteinized DNA with HpaII (cleavage site CCGG) specifically collapsed the nucleosomal ladder generated by HinPI, but had little effect on DNA released from bulk chromatin with MseI (cleavage site TTAA; Supplementary Fig. 1)[9]. Western blotting confirmed that non-methylated CGI chromatin is enriched for histone modifications associated with actively transcribed genes (acetylated histone H3, H3K4me3 and H3K4me2) compared with bulk chromatin (Fig. 1a). In contrast, CGI chromatin was depleted for marks not found at active promoters: H3K36me3, H3K9me3, H3K27me3 and H4K20me3 (Fig. 1a). Agreement between these results and genome-wide studies of chromatin modifications[3,4,10,11] indicated that this fraction could be used to identify proteins that preferentially localize to non-methylated CGIs. We first tested CXXC finger protein 1 (Cfp1), which binds to non-methylated CpG dinucleotides *in vitro* by a CXXC zinc finger domain[6,12]. The data showed that Cfp1 is enriched within the CGI fraction of the genome (Fig. 1a). Similarly, Kdm2a, an H3K36 demethylase that also contains a CXXC domain[13], was enriched in the CGI fraction.

Focusing on Cfp1, we tested its *in vivo* binding specificity by chromatin immunoprecipitation (ChIP) at an endogenous CGI that is present in both methylated and non-methylated states. The *Xist* CGI is mono-allelically methylated in female cells, but fully methylated in males, which only have one X chromosome[14]. ChIP analysis of mouse brain tissue identified a peak of Cfp1 binding over the *Xist* CGI in females, but no peak was present in males, suggesting that Cfp1 exclusively binds to the non-methylated allele (Fig. 1b). To test this more stringently, we used bisulphite sequencing across the *Xist* locus to determine the methylation status of the immunoprecipitated chromatin recovered from females. As expected, input DNA comprised equal numbers of methylated and non-methylated DNA clones. DNA immunoprecipitated by the Cfp1 antibody was almost exclusively non-methylated (96%), however, whereas DNA immunoprecipitated with an antibody against the methyl-CpG-binding protein MeCP2 (refs 15–17) was predominantly methylated (88%; Fig. 1c). We conclude that Cfp1 selectively binds to non-methylated CpGs *in vivo*.

To test whether Cfp1 is concentrated at non-methylated CpGs within CGIs, we analysed the genome-wide distribution of Cfp1 using high-throughput DNA sequencing of immunoprecipitated DNA (ChIP-Seq). Prominent peaks of Cfp1 binding co-localized with non-methylated CGIs (Fig. 2a), 81% of which were Cfp1-associated. Cfp1 has been identified as part of the Setd1 H3K4 methyltransferase complex[8] and ChIP-Seq with H3K4me3 antibodies showed that 93% of Cfp1-bound CGIs also possess this histone modification (Fig. 2b and Supplementary Table 1). Consistent with the possibility that Cfp1 binding is responsible for recruiting the Setd1 complex to these sites, Cfp1-negative non-methylated CGIs (19% of the total) also lack H3K4me3 (Fig. 2b). Despite being rich in non-methylated CpGs, these CGIs are somehow refractory to Cfp1 binding. One potential explanation came from alignment with the published[18] distribution of the polycomb-associated mark H3K27me3 (ref. 19) in mouse brain. More than half (58%) of Cfp1-negative and H3K4me3-negative CGIs contained the H3K27 modification (Fig. 2a, b and Supplementary Fig. 2). In these cases H3K27me3 and polycomb binding may render a CpG island refractory to Cfp1 binding and to H3K4 methylation.

To assess the importance of Cfp1 for the recruitment of H3K4me3, we used stably expressed short hairpin RNAs (shRNAs) directed

[1]Wellcome Trust Centre for Cell Biology, Michael Swann Building, University of Edinburgh, Mayfield Road, Edinburgh EH9 3JR, UK. [2]Wellcome Trust Sanger Institute, Wellcome Trust Genome Campus, Hinxton, Cambridge CB10 1SA, UK.
*These authors contributed equally to this work.

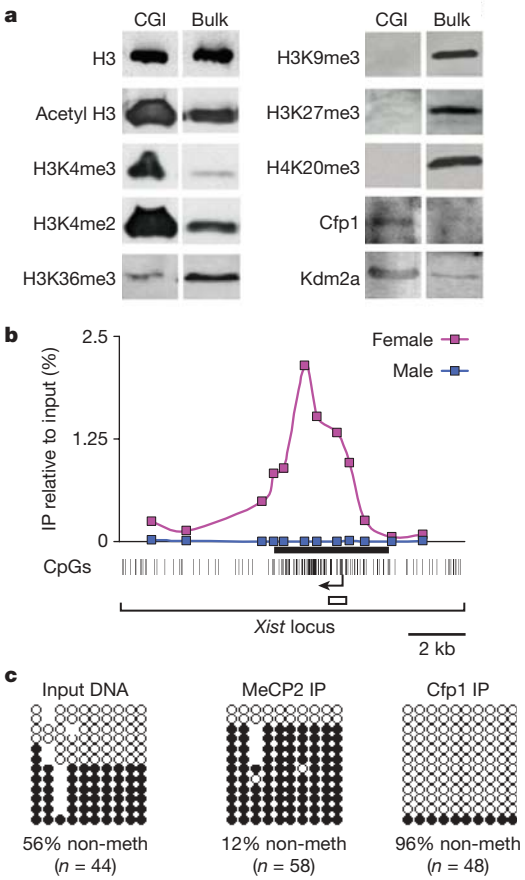

Figure 1 | Cfp1 is enriched in non-methylated CpG island chromatin. **a**, Western blot analysis of non-methylated CGI and bulk chromatin released from purified nuclei using antibodies against selected histone modifications and CpG-binding proteins (normalized to histone H3 levels). An antibody against histone H3 served as a loading control. Modifications associated with transcriptional activity, including H3 acetylated on amino acids K9 and K14, H3K4me3 and H3K4me2 were enriched in CGI chromatin, whereas the elongation and silencing marks H3K36me3, H3K9me3, H3K27me3 and H4K20me3 were depleted. The CXXC domain proteins Cfp1 and Kdm2a also showed enrichment within the CGI fraction. **b**, Cfp1 ChIP assayed by qPCR across the X-linked mouse *Xist* locus. Vertical strokes beneath the plot represent CpGs within the locus and the black bar above demarcates the CGI. The open box below the CpG map shows the region amplified for bisulphite analysis. IP, immunoprecipitation. **c**, Bisulphite analysis of input chromatin (female brain) and chromatin immunoprecipitated with Cfp1 antibodies and control MeCP2 antibodies. Twelve representative clones are shown from the total number sequenced (number in brackets). Solid and open circles represent methylated and non-methylated CpGs, respectively. Uncharacterized CpGs are represented as gaps.

against *Cfp1* to reduce its level in NIH3T3 cells. Single shRNAs reduced Cfp1 (Supplementary Fig. 3), but a combination of three gave a greater effect (Fig. 3a). Depleted cells showed altered morphology (Fig. 3b) and retarded growth (Fig. 3c). ChIP analysis revealed a loss of Cfp1 binding compared with vector-only transfected cells accompanied by a precipitous drop in levels of H3K4me3 across CGIs at the brain-derived neurotrophic factor (*Bdnf*), β-actin (*Actb*), *c-Myc* and *Dlx5/6* genes (Fig. 3d). The same results were obtained with clones expressing each of two independent shRNA sequences, ruling out off-target effects of shRNA expression (Supplementary Fig. 3). As a further control, H3K27me3 profiles at the same loci were unaffected by depletion of Cfp1 (Fig. 3d and Supplementary Fig. 3b). The loss of H3K4me3 at six randomly selected CGI promoters in Cfp1-depleted cells argues that this modification is dependent on the presence of Cfp1.

Although Cfp1 binds non-methylated CpGs and seems to be required for H3K4 methylation at CGIs, it is possible that this reflects indirect recruitment of Setd1 by RNA polymerase II, which is present at active CGI promoters. Alignment of ChIP-Seq profiles for Cfp1, H3K4me3 and the unphosphorylated form of RNA polymerase II indeed showed co-localization of all three signals at 86% of all Cfp1-bound CGIs (Supplementary Table 1 and Supplementary Fig. 4). In a small proportion (7%) of cases, however, RNA polymerase II was undetectable, despite the presence of robust peaks of H3K4me3 and Cfp1 (Supplementary Fig. 4). This raised the possibility that RNA polymerase II may not be required and that Cfp1 binding is sufficient to direct H3K4 trimethylation. To test this hypothesis, we used embryonic stem (ES) cell lines in which artificial promoterless CpG-rich DNA sequences had been introduced into the genome at sites that normally lack H3K4me3. The DNA insert in ES line TβC44 (ref. 20) comprises a 720-base-pair (bp) enhanced green fluorescent protein (eGFP) coding sequence containing 60 CpGs[21] adjacent to a 600-bp puromycin-resistance gene with 93 CpGs (Fig. 4a). The inserted sequence has the typical CpG density of a CGI, but lacks a promoter. Bisulphite analysis showed that integrated sequence is non-methylated (Fig. 4a). In the targeted cells, prominent domains of Cfp1 and H3K4me3 coincided with the inserted CpG-rich DNA (Fig. 4b). Interestingly, the peaks of H3K4me3 and Cfp1 tracked CpG density as expected if H3K4me3 is determined by this DNA dinucleotide sequence (Fig. 4b, broken line). No peak of RNA polymerase was detected. An independent ES cell line carrying an eGFP insertion on the X chromosome[22] (Fig. 4c) also created a peak of H3K4me3 and Cfp1 (Fig. 4d). In this case, bisulphite sequencing showed that approximately a quarter of the integrated sequences were hypomethylated and the remainder were densely methylated (Fig. 4e, input panel). ChIP-bisulphite analysis demonstrated that Cfp1 and H3K4me3 antibodies significantly enriched the hypomethylated sequences (Fig. 4e). We conclude that clusters of non-methylated CpG are sufficient to recruit Cfp1 and create a peak of H3K4me3 modification, even in the absence of a promoter.

The density of non-methylated CpG is ~50-fold higher in CGIs than in bulk genomic DNA, as CpG in the latter is deficient (20% of expected[23]) and mostly methylated (~70%). It is unclear whether this high CpG density arises as a passive consequence of events at promoters and has no functional significance, or whether it has been selected over evolutionary time because it facilitates transcription (or other DNA-related processes). Our results favour selection, as they indicate that CpG density per se can directly influence histone modification status by the recruitment of the Cfp1 protein and its associated Setd1 histone H3K4 methyltransferase complex. The ability of an exogenous promoter-less CpG-rich insertion to create *de novo* an H3K4me3 focus provides strong support for this notion. An attractive biological rationale for this phenomenon may be simplification of the large mammalian genome by the creation of 'beacons' of H3K4me3 that highlight CGI promoters within the genomic landscape[1].

Whether CpG clustering is sufficient to create stable non-methylated CGIs is uncertain. There is evidence that H3K4me3 is incompatible with *de novo* methylation as components of the DNA methyltransferase complex (Dnmt3L) are repelled by this modification[24]. In theory, therefore, Cfp1-bound CGIs should be intrinsically stable in the non-methylated state. Previous studies suggest, however, that transcription also has a role. Maintenance of non-methylated CGIs through the waves of *de novo* methylation in the early embryo depends on promoter function, as point mutations that prevent transcription factor binding without significantly reducing CpG density destroy the immunity of a CpG island to DNA methylation[25,26]. It follows that H3K4 methylation due to CpG clustering may not be sufficient to reliably perpetuate the non-methylated state. Indeed, more than half of cells carrying the promoter-less eGFP insertion at the *Mecp2* locus had acquired dense methylation in ES cells despite the presence of a CpG cluster.

Our data suggest that chromatin modification need not arise secondarily as a result of, for example, transcriptional status, but can be determined genetically due to the sequence characteristics of

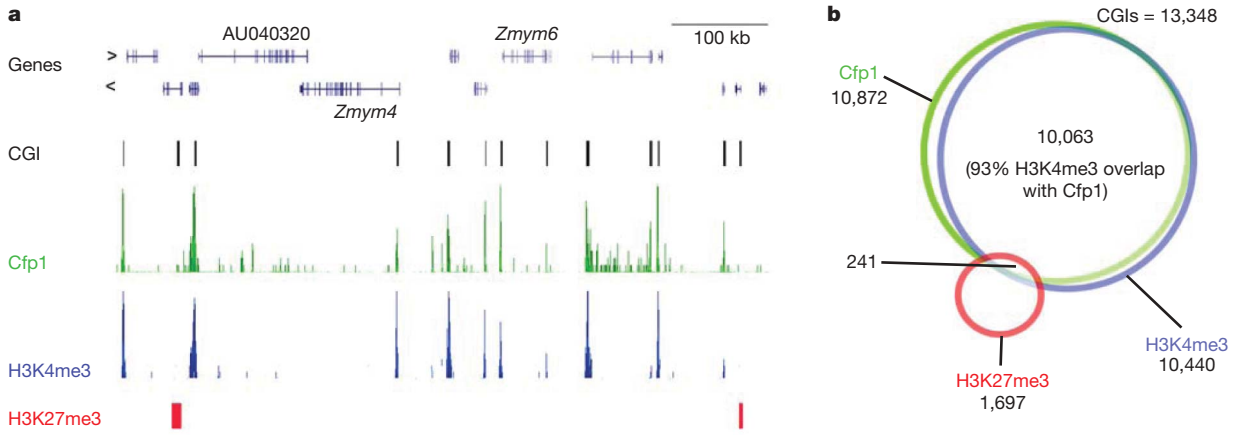

Figure 2 | Genome-wide ChIP sequencing shows a tight association between Cfp1 and H3K4me3 at CGIs. **a**, Typical Cfp1 ChIP-Seq profiles from whole mouse brain. For comparison, we also carried out H3K4me3 ChIP-Seq. The data were aligned with non-methylated CGIs mapped in mouse brain using a CXXC affinity column[29]. The panel shows a typical region of the genome from chromosome 4 (nucleotides 126,333,759–127,054,849) demonstrating the coincidence of Cfp1 and H3K4me3 peaks with CGIs. A subset of genes is labelled (RefSeq). Two CGIs that lack H3K4me3 and Cfp1 coincide with sites of H3K27me3 binding (red rectangles; data of ref. 30 for mouse brain). **b**, Venn diagram showing strong overlap between H3K4me3 and Cfp1 peaks in mouse brain chromatin, but minimal overlap with H3K27me3.

the underlying DNA. In particular CpG, by virtue of its widely varying local densities and alternative modification states, has the properties of a signalling module that locally influences genome function. As shown here, DNA methylation-free CpG clusters can recruit Cfp1 and probably other CXXC domain proteins. Densely methylated CGIs, on the other hand, attract methyl-CpG-binding proteins, which in turn recruit enzymes that can reinforce repressive histone modifications[17,27,28]. Future studies of proteins that read and interpret CpG signals promise to shed further light on both genetic and epigenetic determinants of chromosome function.

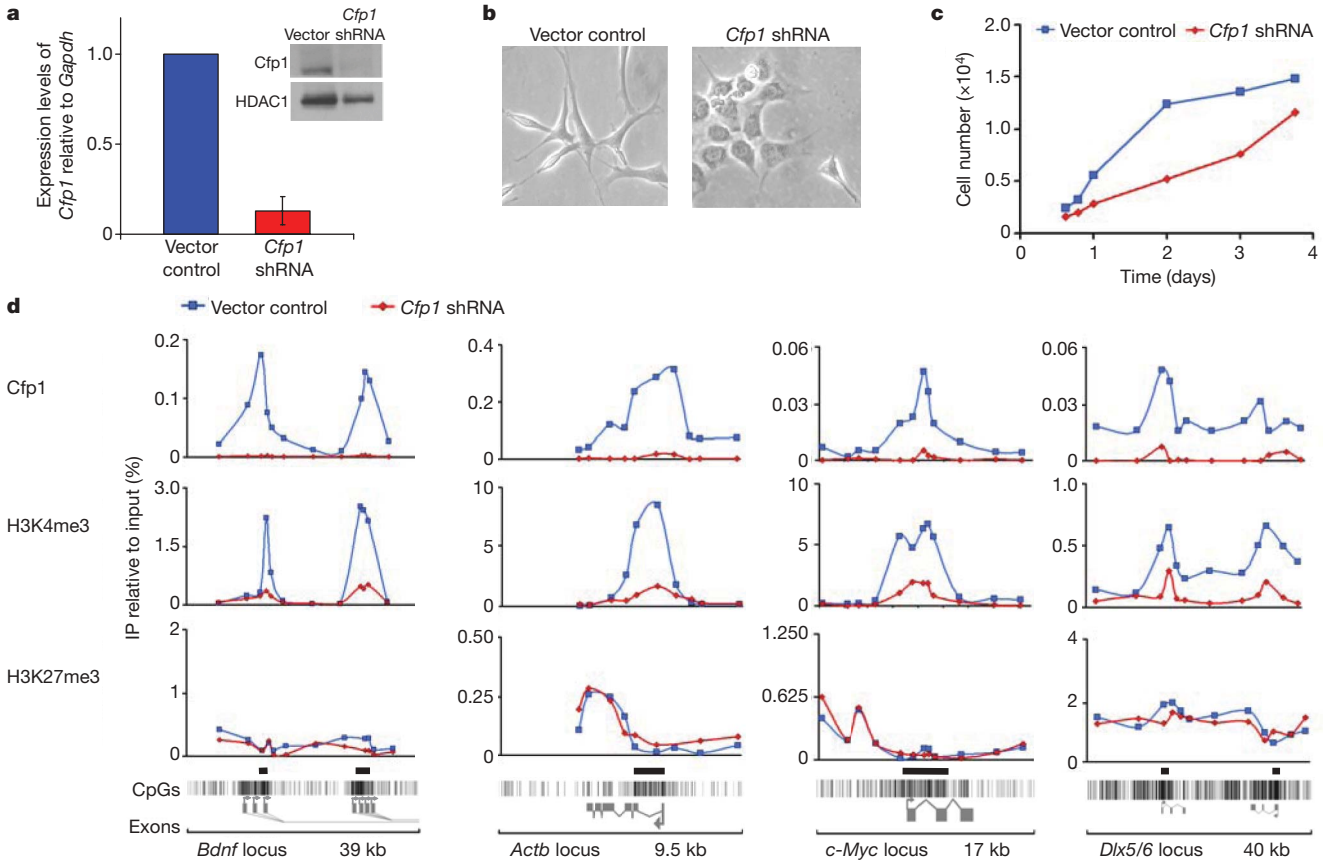

Figure 3 | Depletion of Cfp1 results in reduced H3K4 trimethylation levels at CpG islands. **a**, Expression of three short hairpin RNAs in NIH3T3 fibroblasts reduced *Cfp1* messenger RNA levels to 15% compared with vector-only transfected control cells. Expression of *Cfp1* relative to *Gapdh* in control cells is set to 1. The inset shows reduction of Cfp1 by western blotting. Error bars indicate s.d. ($n = 3$) **b**, **c**, Gross morphology (**b**) and growth rate (**c**) of Cfp1-depleted versus vector-only transformant cells. Cells were plated at low density and monitored at the times shown using a haemocytometer. Original magnification, ×200. **d**, ChIP qPCR using Cfp1, H3K4me3 and H3K27me3 antibodies at selected loci in vector-only control and Cfp1-depleted NIH3T3 cells. The results were replicated with an independent clone expressing the same shRNA combination (data not shown) and with each of two individual shRNA constructs (see Supplementary Fig. 3).

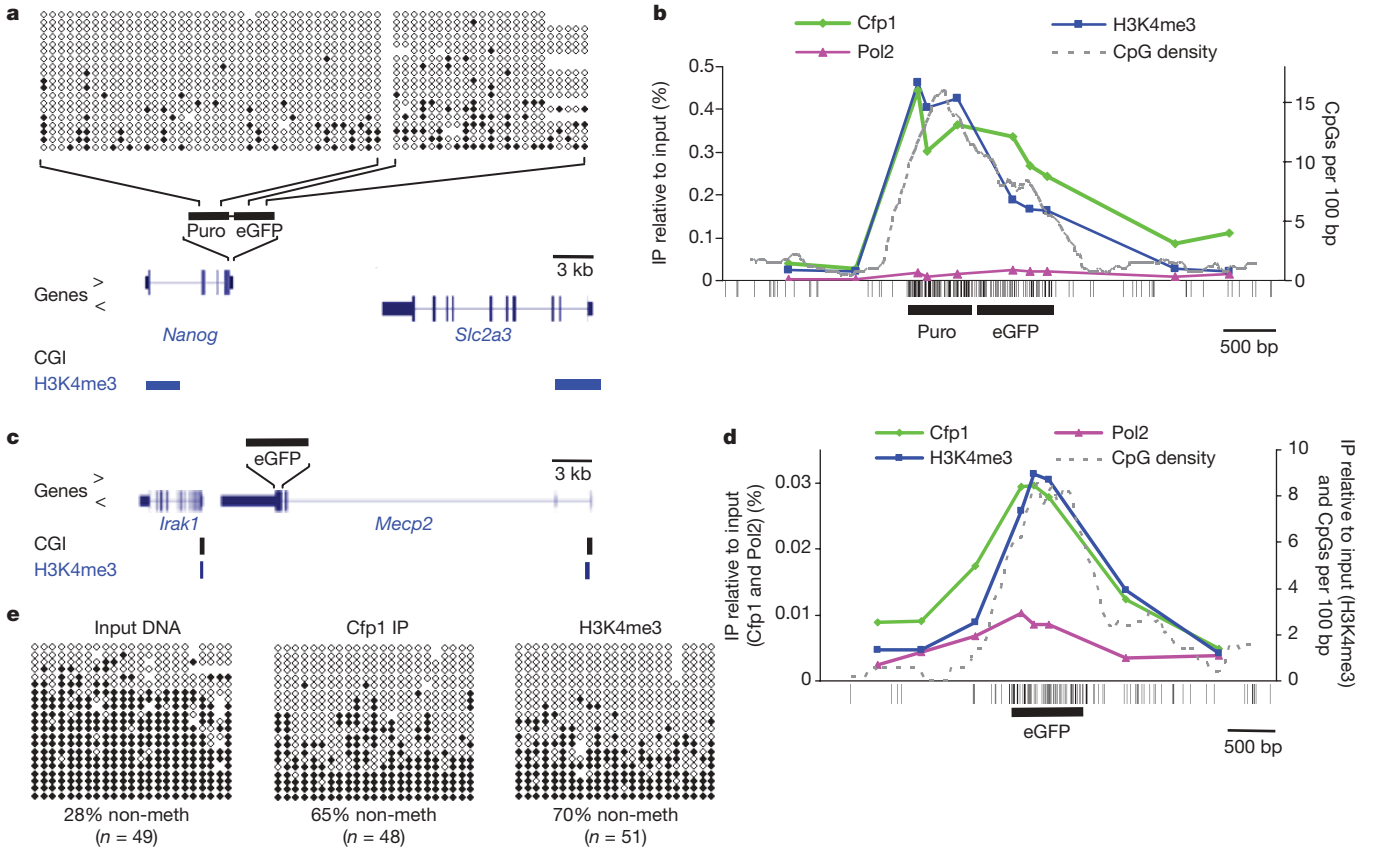

Figure 4 | Artificial promoterless CpG-rich sequences recruit Cfp1 and generate new H3K4me3 peaks in mouse ES cells. a, The TCβ44 ES cell line carries adjacent promoterless eGFP and bacterial puromycin-resistance sequences (black bars) inserted together within the 3′ untranslated region of the *Nanog* gene[20]. The positions of CGIs and H3K4me3 peaks[4] at this locus in wild-type ES cells are shown below the map. DNA methylation within the insertion was determined by bisulphite sequencing of 306-bp (eGFP) and 275-bp (Puro) segments of the inserted sequence. **b**, ChIP qPCR across the region containing the insertion using antibodies against Cfp1, RNA polymerase II (Pol2) and H3K4me3. The dotted line plots CpG density in a 500-bp window with a 100-bp step size. Vertical strokes below the graph mark CpG sites within and surrounding the insertion. **c**, A second ES cell line carried an eGFP coding sequence (black bar) inserted into the 3′ untranslated region of the X-linked *Mecp2* gene. CGIs and H3K4me3 peaks[4] at this locus in wild-type ES cells are shown below. **d**, ChIP qPCR across the region containing the insertion (black bar) using antibodies against Cfp1, RNA polymerase II and H3K4me3. **e**, Bisulphite sequence analysis determined the methylation status of input and DNA immunoprecipitated by the Cfp1 and H3K4me3 antibodies. The percentage of non-methylated CpGs is shown below each panel. H3K4me3 ChIP data in **b** and **d** used different commercial antibodies with differing affinities (see Supplementary Table 2).

METHODS SUMMARY

Mouse brain nuclei were incubated with restriction enzymes and then pelleted to liberate small fragments of CGI chromatin that were then analysed by western blotting. ChIP was performed on mature mouse brain with antibodies against various chromatin proteins. Immunoprecipitated DNA was used for: (1) quantitative PCR (qPCR) analysis of specific loci; (2) bisulphite analysis to determine DNA methylation patterns; and (3) ligation of linkers and Solexa sequencing to identify sites of binding. To knockdown Cfp1, mouse NIH3T3 cells were transfected using shRNA targeting *Cfp1* or vector alone as a control, and stable clones were selected by puromycin resistance. RNA and protein samples were prepared to verify the knockdown of Cfp1. For Fig. 3, three shRNA were used in combination, but comparable results were obtained with two individual shRNAs (Supplementary Fig. 3). ChIP with antibodies against Cfp1, H3K4me3 and H3K27me3 determined the effect of Cfp1 knockdown at four loci using qPCR. The eGFP insert was targeted to the *Mecp2* locus by homologous recombination of a construct containing a PGK-Neo cassette flanked by *loxP* sites. Cre-mediated recombination was used to delete the selectable marker before bisulphite and ChIP analysis.

Full Methods and any associated references are available in the online version of the paper at www.nature.com/nature.

Received 2 October 2009; accepted 15 February 2010.

1. Bird, A. P. CpG-rich islands and the function of DNA methylation. *Nature* **321,** 209–213 (1986).
2. Suzuki, M. M. & Bird, A. DNA methylation landscapes: provocative insights from epigenomics. *Nature Rev. Genet.* **9,** 465–476 (2008).
3. Guenther, M. G., Levine, S. S., Boyer, L. A., Jaenisch, R. & Young, R. A. A chromatin landmark and transcription initiation at most promoters in human cells. *Cell* **130,** 77–88 (2007).
4. Bernstein, B. E. *et al.* A bivalent chromatin structure marks key developmental genes in embryonic stem cells. *Cell* **125,** 315–326 (2006).
5. Lee, J. H. & Skalnik, D. G. CpG-binding protein is a nuclear matrix- and euchromatin-associated protein localized to nuclear speckles containing human trithorax. Identification of nuclear matrix targeting signals. *J. Biol. Chem.* **277,** 42259–42267 (2002).
6. Shin Voo, K., Carlone, D. L., Jacobsen, B. M., Flodin, A. & Skalnik, D. G. Cloning of a mammalian transcriptional activator that binds unmethylated CpG motifs and shares a CXXC domain with DNA methyltransferase, human trithorax, and methyl-CpG binding domain protein 1. *Mol. Cell. Biol.* **20,** 2108–2121 (2000).
7. Lee, J. H. & Skalnik, D. G. CpG-binding protein (CXXC finger protein 1) is a component of the mammalian Set1 histone H3-Lys4 methyltransferase complex, the analogue of the yeast Set1/COMPASS complex. *J. Biol. Chem.* **280,** 41725–41731 (2005).
8. Lee, J. H., Tate, C. M., You, J. S. & Skalnik, D. G. Identification and characterization of the human Set1B histone H3-Lys4 methyltransferase complex. *J. Biol. Chem.* **282,** 13419–13428 (2007).
9. Tazi, J. & Bird, A. Alternative chromatin structure at CpG islands. *Cell* **60,** 909–920 (1990).
10. Mikkelsen, T. S. *et al.* Genome-wide maps of chromatin state in pluripotent and lineage-committed cells. *Nature* **448,** 553–560 (2007).
11. Barski, A. *et al.* High-resolution profiling of histone methylations in the human genome. *Cell* **129,** 823–837 (2007).
12. Lee, J. H., Voo, K. S. & Skalnik, D. G. Identification and characterization of the DNA binding domain of CpG-binding protein. *J. Biol. Chem.* **276,** 44669–44676 (2001).
13. Tsukada, Y. *et al.* Histone demethylation by a family of JmjC domain-containing proteins. *Nature* **439,** 811–816 (2006).
14. McDonald, L. E., Paterson, C. A. & Kay, G. F. Bisulfite genomic sequencing-derived methylation profile of the *Xist* gene throughout early mouse development. *Genomics* **54,** 379–386 (1998).

15. Lewis, J. D. *et al.* Purification, sequence and cellular localisation of a novel chromosomal protein that binds to methylated DNA. *Cell* **69,** 905–914 (1992).
16. Nan, X., Tate, P., Li, E. & Bird, A. DNA methylation specifies chromosomal localization of MeCP2. *Mol. Cell. Biol.* **16,** 414–421 (1996).
17. Skene, P. J. *et al.* Neuronal MeCP2 is expressed at near histone-octamer levels and globally alters the chromatin state. *Mol. Cell* **37,** 457–468 (2010).
18. Mikkelsen, T. S. *et al.* Dissecting direct reprogramming through integrative genomic analysis. *Nature* **454,** 49–55 (2008).
19. Schwartz, Y. B. & Pirrotta, V. Polycomb complexes and epigenetic states. *Curr. Opin. Cell Biol.* **20,** 266–273 (2008).
20. Chambers, I. *et al.* Nanog safeguards pluripotency and mediates germline development. *Nature* **450,** 1230–1234 (2007).
21. Yang, T. T., Cheng, L. & Kain, S. R. Optimized codon usage and chromophore mutations provide enhanced sensitivity with the green fluorescent protein. *Nucleic Acids Res.* **24,** 4592–4593 (1996).
22. Guy, J., Gan, J., Selfridge, J., Cobb, S. & Bird, A. Reversal of neurological defects in a mouse model of Rett syndrome. *Science* **315,** 1143–1147 (2007).
23. Waterston, R. H. *et al.* Initial sequencing and comparative analysis of the mouse genome. *Nature* **420,** 520–562 (2002).
24. Ooi, S. K. *et al.* DNMT3L connects unmethylated lysine 4 of histone H3 to *de novo* methylation of DNA. *Nature* **448,** 714–717 (2007).
25. Brandeis, M. *et al.* Sp1 elements protect a CpG island from *de novo* methylation. *Nature* **371,** 435–438 (1994).
26. Macleod, D., Charlton, J., Mullins, J. & Bird, A. P. Sp1 sites in the mouse *aprt* gene promoter are required to prevent methylation of the CpG island. *Genes Dev.* **8,** 2282–2292 (1994).
27. Lorincz, M. C., Dickerson, D. R., Schmitt, M. & Groudine, M. Intragenic DNA methylation alters chromatin structure and elongation efficiency in mammalian cells. *Nature Struct. Mol. Biol.* **11,** 1068–1075 (2004).
28. Lorincz, M. C., Schubeler, D. & Groudine, M. Methylation-mediated proviral silencing is associated with MeCP2 recruitment and localized histone H3 deacetylation. *Mol. Cell. Biol.* **21,** 7913–7922 (2001).
29. Illingworth, R. *et al.* A novel CpG island set identifies tissue-specific methylation at developmental gene loci. *PLoS Biol.* **6,** e22 (2008).
30. Meissner, A. *et al.* Genome-scale DNA methylation maps of pluripotent and differentiated cells. *Nature* **454,** 766–770 (2008).

Supplementary Information is linked to the online version of the paper at www.nature.com/nature.

Acknowledgements We are grateful to D. Skalnik for the gift of a Cfp1 antibody, I. Chambers for the TβC44 ES cell line, R. Klose for discussions, E. Sheridan for testing the DNA sequencing protocol, and K. Auger and J. Parkhill for coordinating the DNA sequencing. We also thank R. Ekiert and J. Connelly for comments on the manuscript. This work was funded by a Cancer Research UK studentship to J.P.T. and by grants from the Wellcome Trust, the Medical Research Council and the European Union 'Epigenome' Network of Excellence.

Author Contributions J.P.T. and P.J.S. performed the ChIP, knockdown and bisulphite analysis. T.C. did preliminary ChIP analysis. J.S. and J.G. generated the MeCP2-eGFP cell line. J.S. performed bisulphite analysis of the TβC44 ES cell line. R.I. prepared samples for sequencing. K.D.J., D.J.T. and R.A. performed the sequencing and mapping. S.W., A.R.W.K., A.D. and R.I. performed the bioinformatic analysis. J.P.T., P.J.S., T.C., R.I. and A.B. wrote the manuscript.

Author Information High throughput sequencing data has been deposited in the Gene Expression Omnibus (GEO) under the accession number GSE18578. Reprints and permissions information is available at www.nature.com/reprints. The authors declare no competing financial interests. Correspondence and requests for materials should be addressed to A.B. (a.bird@ed.ac.uk).

METHODS

Release of CGI chromatin. Nuclei were prepared from brains of 4-week-old mice as previously described[31]. Nuclear preparations were digested with a two-fold excess of HinP1 or Mse1 in a buffer containing 50 mM Tris-HCl, pH 8, 100 mM NaCl, 5 mM $MgCl_2$, 0.1 mM EGTA and 1 mM β-mercaptoethanol. The released chromatin was retained in the supernatant after centrifugation at 3,800*g* for 5 min and the proteins were precipitated using trichloroacetic acid before western blot analysis.

Antibodies. Antibodies used are listed in Supplementary Table 2.

Chromatin immunoprecipitation and bisulphite sequencing. ChIP on brain tissue was performed as described[17] using antibodies as shown in Supplementary Table 2. Most ChIP-qPCR profiles were replicated using independent Cfp1 antibodies. Illumina linkers were ligated in-house and Solexa sequencing was carried out using Illumina 2G Solexa sequencers using two replicate lanes per biological sample. ChIP-Seq was analysed using custom bioinformatic tools generated in-house (see Supplementary Table 3 for the parameters used). ChIP using formaldehyde crosslinked NIH3T3 cells was performed as previously described[32]. Bisulphite sequencing was performed as described[29]. Real-time PCR was carried out using Quantace Sensimix Plus using a Biorad iCycler according to the manufacturer's instructions (primer sequences are available on request).

Generation of stable Cfp1-knockdown cells. NIH3T3 cells were transfected using lipofectamine reagent (Invitrogen) with three independent pSuper vectors containing short hairpin constructs directed against *Cfp1* (Oligoengine) or vector alone. Target sequences were as follows: target 986, 5′-GAAGGUGAA GCACGUGAAG-3′; target 1250, 5′-CAGCCAACCGAAUCUAUGA-3′; and target 1920, 5′-CUUCACCAAACGAUCCAAC-3′. Stable clones were selected for puromycin resistance. A combination of the three shRNAs reduced Cfp1 more robustly and was therefore used for the data in Fig. 3. Individual shRNAs gave comparable results by western and ChIP (see Supplementary Fig. 3). RNA was extracted using Tri reagent (Sigma) and was complementary DNA was prepared using reverse transcriptase (Promega). Expression levels were determined using real-time PCR analysis (primer sequences available on request).

ES cell lines. ES cell line TβC44 was generated by homologous recombination as described[20]. A *Mecp2-eGFP* knock-in targeting vector was constructed by sequential cloning of 5′ (5.3 kb) and 3′ (1.9 kb) regions of *Mecp2* homology into peGFP-N1 (Clontech). A PGK-Neo cassette flanked by *loxP* sites was added to enable selection of transfected cells. Gene targeting was carried out in the ES cell line E14 TG2a to generate an insertion into the *Mecp2* gene transcription unit at the junction between the open reading frame and the 3′ untranslated region. This construct was initially designed to create a MeCP2-eGFP fusion protein after transcription and translation. Cells were grown on gelatinized dishes in the presence of recombinant human LIF in Glasgow MEM (Invitrogen) supplemented with 10% FBS (Globepharm), 1× MEM non-essential amino acids, sodium pyruvate (1 mM) and β-mercaptoethanol (50 μM; all Invitrogen). ES cells (5×10^7 cells) were transfected with linearized targeting vector (250 μg DNA in 0.8 ml HEPES buffered saline) by electroporation (800 V, 3 μF, BioRad Gene Pulser) and plated at 5×10^6 cells per dish. Correctly targeted clones were first identified by PCR specific for homologous recombination. The integrity of the targeted locus was confirmed by Southern blot analyses. A single positive clone was transiently transfected with pCAGGS-CRE[33] for the Cre-mediated deletion of the selectable marker and a recombinant clone was then used for this study.

31. Klose, R. J. & Bird, A. P. MeCP2 behaves as an elongated monomer that does not stably associate with the Sin3a chromatin remodeling complex. *J. Biol. Chem.* **279,** 46490–46496 (2004).
32. Schmiedeberg, L., Skene, P., Deaton, A. & Bird, A. A temporal threshold for formaldehyde crosslinking and fixation. *PLoS ONE* **4,** e4636 (2009).
33. Araki, K., Araki, M. & Yamamura, K. Targeted integration of DNA using mutant lox sites in embryonic stem cells. *Nucleic Acids Res.* **25,** 868–872 (1997).

Q&A

Evolutionary geneticist **Harmit Malik** of the Fred Hutchinson Cancer Research Center in Seattle, Washington, has won the 2010 Vilcek Prize for Creative Promise in Biomedical Science for his work on the coevolution of humans and diseases.

How would you describe your early academic years?

I grew up in a family of businesspeople and engineers in India, but I was not that inspired by my early pursuits in chemical engineering at the Indian Institute of Technology in Mumbai. When I turned 18, I began to really think about what I wanted. I started reading author and evolutionary biologist Richard Dawkins and got interested in molecular biology. My chemical-engineering adviser steered me to K. Krishnamurthy Rao, a professor at the institute's new department of biosciences and bioengineering. He changed the course of my career, teaching me during informal afternoon meetings because a timing conflict prevented me from sitting in on his class. Despite my not having done any formal coursework, those meetings helped me to write strong letters of application to graduate programmes in India and abroad.

Why study 'selfish' genes?

In cell biology, the many components of cells seem to work in concert to help the cell survive. But that's not necessarily how it happens. To me, it was really eye-opening to realize that collaboration might be the exception rather than the rule — that a cell is not surviving because of the collaboration, but in spite of it. That seemed a radical concept worthy of study.

What work did the 'creative promise' award recognize?

My colleague Mike Emerman, a molecular virologist at the Fred Hutchinson Cancer Research Center, found that we had a mutual interest in host–virus interactions. We decided to study 'fossilized' viruses — viral remnants in our genomes. In a fresh approach, we looked for genetic evidence of the evolutionary pressures that these viruses had placed on host genes as a way of inferring what palaeoviruses were capable of. We gained insight into how these genes, which are so important in present-day infections, became battle-hardened by repeated conflicts. We published a series of papers demonstrating how past conflicts shape current interactions.

How does it feel to receive an award for creative promise?

I'd be lying if I said it wasn't a little intimidating. I'm humbled and surprised and quite honoured to have this prize — particularly because it is meant to reward those who take novel approaches. My group really tries to ask questions outside our comfort zone. It is awesome to be recognized and rewarded for that.

How might this award open career doors for you?

The award does provide an endorsement of my abilities. We're often trying to collaborate with scientists in different fields in order to explore a new technique or idea. But there is always an initial pushback, or hesitation, as the potential collaborator tries to confirm that we have something substantial to offer. This type of award may establish some credibility for us with potential collaborators. The biggest thing holding people back in science is the constant worry about sustaining a productive lab, and that often leads to hesitancy in developing new interests.

Have you had a career-defining moment?

I was still unclear on how the field would view our work when the first postdoc from my lab started exploring the job market. It was daunting. But when she started getting awards and fantastic job interviews, I was quite relieved. I remember thinking: 'We're training people who will do well. We're not destroying someone's career.'

What is the best advice you've ever been given?

I was once advised to carefully consider potential colleagues and the departmental environment before accepting a new position. You'll eventually consume all the start-up money you get, but your colleagues will be the same. Your success hinges on that scientific atmosphere.

What scientific atmosphere do you try to create in your lab?

The premise of my lab is that everybody works on a different project — which works as long as people talk to and challenge each other. I encourage my students to be very creative in their efforts to push paradigms beyond what we know. To do that, I encourage them to take risks. In exchange, I provide the safety net to make sure it won't hurt their careers. ■

Interview by Virginia Gewin

IN BRIEF

US overseas applicants up

International graduate applications to US institutes rose for the fifth consecutive year in 2010, says the Council of Graduate Schools (CGS) in Washington DC. Its 6 April report, based on 437,000 applications, showed a 7% rise. Those from China rose by 19%, in a fifth year of double-digit increases. Applications fell by 2% from India and were unchanged for South Korea, after plunging by 12% and 9% last year. Applications in life sciences — including medical and nursing school — climbed by 3% after no change in 2009. "Last year may have been a bit of a blip," says Nathan Bell, CGS director of research and policy analysis. Those in physical and Earth sciences soared by 10%.

Science funding boost

The UK government is aiming to recruit researchers in science, technology, engineering and maths (STEM) with a set of new initiatives. Launching later this year, the Newton Scholarships will provide 100 UK and international postgraduates with £25,000 (US$38,052) to take to the research institution of their choice. And a £270-million Modernisation Fund aims to help UK universities provide 20,000 more places for STEM undergraduates by August. In addition, a £40-million International Space Innovation Centre in Harwell is being set up to serve as a central hub for Britain's £6.5-billion space sector. The centre is expected to create 700 jobs over the next five years.

Industry job cuts plunge

The US pharmaceutical and biotechnology industries shed just 308 jobs in March 2010, compared with the 17,700 jobs lost in the sector in February 2010 and also in March 2009, according to a report by global outplacement firm Challenger, Gray and Christmas of Chicago, Illinois. In the first quarter of 2010, these industries cut 26,165 jobs, just over half of the 48,665 that were slashed in the same period last year, the report found. A total of 61,109 jobs were lost in the sector in 2009. James Pedderson, the company's public-relations director, says that the large number of cuts in February and in 2009 resulted largely from mergers. "Companies have pulled back on downsizing and are starting to stabilize now," he says. But he warns that hiring is not yet on an upswing.

A SYSTEMS APPROACH

Applying systems biology to cancer research has become a growth area for computationally minded scientists. **Kelly Rae Chi** tallies the possibilities.

SPL

Research associate Katie Hoadley works in a genetics wet lab, but she hasn't picked up a pipette for three years. On this particular morning, at the University of North Carolina at Chapel Hill, she scrolls through lines of computer code to identify patients who responded well to a breast-cancer treatment in a published clinical trial. Using algorithms based on gene-expression data from human breast-tumour cell lines, she is looking for molecular signatures that might help to predict which breast-cancer patients will be most amenable to the treatment.

An experimentalist by training, Hoadley has benefited from the increasing demand worldwide for cancer systems biologists, especially those who can handle computation. Instead of collecting data on animals or cells and funnelling them through basic statistical formulae, Hoadley has learned to merge and analyse data from others' experiments.

The rise of systems biology could not have come soon enough for cancer: recent findings point to daunting heterogeneity within individuals, and even within tumours over time. This genetic complexity plays a part in many tumours' tendency to resist treatment, and rummaging through that complexity is exactly what systems biologists do. For young cancer researchers searching for a niche, it's clearly an area with promise.

Pinpointing the start of the systems-biology approach to cancer is difficult. Researchers have been examining cellular systems for therapeutic leads for some time. But the Human Genome Project and technological improvements have brought a new level of complexity to the approach. Rather than focusing on one molecular pathway, this integrative approach blends many contexts, including DNA, RNA, proteins, signalling networks, cells, organs, whole organisms and even environmental factors.

This varied data mix requires scientists to build complex mathematical models of cancer, which in turn drive new research questions. Once they have been validated in cells, animals or human tissues, those results inform new or better models. The ultimate goal is to create a more comprehensive understanding of cancer and to forecast outcomes and therapeutic efficacy in the clinic. The increasing volumes of data reaped from comprehensive scans of molecular markers offer a fertile career ground for those willing and able to acquire computational know-how. In Hoadley's case, for example, doing so required on-the-job learning to code in the programming languages R and Perl.

> **"It is important that we are all in the same room talking to each other."**

Technical feat

Technological advances have enabled researchers to measure molecular processes such as DNA methylation, copy-number variants or single-base mutations in a single experiment. And they can use a variety of approaches, including next-generation sequencing platforms, mass spectrometry, high-end imaging and analysis tools. "This sounds terrific, except for the fact that the data analysis and visualization are very difficult," says David Botstein, director of the Lewis-Sigler Institute for Integrative Genomics at Princeton University in New Jersey. The approaches require a level of mathematical sophistication that many biologists do not have, he adds. Biologists now often receive such training in graduate school, as part of postdoctoral positions, or they at least learn how to communicate and work closely with computational experts. Industry and academia need researchers who can manipulate and interpret reams of data, turning the information, for example, into markers of disease progression or therapeutic efficacy.

Because training in systems or integrative biology is so new, and programmes are still emerging, many established cancer systems biologists began with either theoretical or experimental backgrounds, but not both. Many graduate-level programmes provide a good grounding in systems biology, but

students may have to make a concerted effort to steer their training towards cancer applications. For example, there are no specific curricula in cancer systems biology in Germany, says Ralf Herwig, group leader of bioinformatics at the Max Planck Institute for Molecular Genetics in Berlin. In the next five years, he predicts, more systems-biology curricula will appear at universities, and he expects that cancer-biology applications will appear in places affiliated with clinics, such as the Charité University Hospital in Berlin.

Irrespective of location, the key is often on-the-job training. Those with a foundation in biology or clinical oncology may glean statistical and computational skills from other projects. This is still a reasonable strategy, although the field is beginning to recognize the need for more interdisciplinary training, says Hoadley's supervisor Chuck Perou.

Hoadley and Perou both began as bench scientists and learnt computational skills by working with accomplished collaborators. As a postdoc, Perou listened to statisticians talk about specific methods during lab meetings. Afterwards, he would study those methods on his own.

Those interested in experimental aspects of systems biology should be comfortable with commonly used tools in data analysis and mathematical modelling, notes Steven Altschuler, a pharmacologist at the University of Texas Southwestern Medical Center's Green Comprehensive Center for Computational and Systems Biology in Dallas. They should take classes in cell and molecular biology and discuss their thoughts and questions with people in those fields. "If they come from engineering, physics or math, we always ask, 'Have you sat in on a biology class?'," he says.

Close contact

To encourage interaction, Perou arranges his lab space so that at least one computational student or postdoc works in each room of the wet lab. "There's this constant interplay between statisticians, biologists and computer scientists," Perou says. Two papers have come from algorithms generated through these interactions. "It is important that we are all in the same room talking to each other," he adds.

In an effort to improve systems-biology training at the postdoctoral level, the US National Cancer Institute in Bethesda, Maryland, earlier this year awarded Sage Bionetworks, a non-profit medical-research organization based in Seattle, Washington, a US$6.7-million grant to help train more systems and network biologists. The programme will pair clinical biologists with physicists or mathematicians, preferably those who have already completed a postdoc in their area of expertise. The pairs will then work together on a project for two years. Sage Bionetworks president and chief executive Stephen Friend says that the programme will generate more systems and network biologists for both academia and industry.

Training in cancer systems biology will change as the tools advance. Massive efforts such as the Cancer Genome Atlas, a project funded by the US government and started in 2005 to uncover genetic mutations responsible for cancer, have led to better analysis tools. And some speculate that these tools will become more user-friendly with time. "As that happens, it will become easier for people who aren't deeply trained in computational biology to ask computational questions," says Joe Gray, director of the life-sciences division at the Lawrence Berkeley National Laboratory in California. "But you are still going to have to understand how the algorithms work, and the nuances of how the data are analysed."

"Your background matters less than the research questions you want to answer."

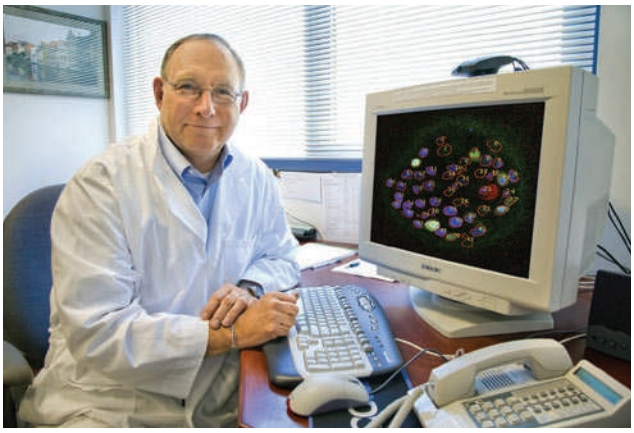

R. KALTSCHMIDT, BERKELEY LAB PUBLIC AFFAIRS

Even though technology is becoming more user-friendly, Joe Gray thinks applicants will need to understand the basic principles of computation.

But Peter Sorger, director of the Massachusetts Institute of Technology's Cell Decision Process Center in Boston, says he doesn't see the challenges of modelling cancer going away any time soon. "I don't think that one person can do it all," he says. The field will demand an even greater shift in academic structure and culture towards interdisciplinary training, according to Sorger. That means that all individuals on a team should have at least a working knowledge of both modelling and experimentation. Then trainees will gain a grounding for future collaborations in academia and industry, he adds.

Academic job opportunities abound, particularly in the United States, Britain, Germany and Switzerland, and at postdoctoral and group-leader levels. These include jobs in traditional university departments and in specialized research centres such as the Institute of Systems Biology in Seattle or the European Bioinformatics Institute in Cambridge, UK. In addition, the Cancer Genome Atlas and other efforts to sequence thousands of individual tumours are upping the demand for bioinformaticians. "That's really one of the limiting things for them — finding competent people to analyse all these data," says Botstein, who adds that the same is true for industry. According to Botstein, this means that interested scientists should be learning computation in any way possible.

In many places, however, the field remains nascent, says Duncan Odom, leader of the cancer-genomics group at Cancer Research UK's Cambridge Research Institute. Odom emigrated to Britain after completing a postdoc at the Whitehead Institute for Biomedical Research in Cambridge, Massachusetts. He says that systems biology is a strong theme at Cancer Research UK, but that the organization does not have a set programme, something that Odom is pushing to change.

Historically, industry has viewed cancer systems biology, particularly large-scale proteome and genome analysis, as requiring a large investment with few immediate returns. In the past year or so, however, this perspective has changed as firms start to realize that relatively small-scale but systematic experiments can help them to prioritize potential drug targets and uncover drug mechanisms. If this initial promise pans out, pharma and biotech will probably expand their hiring efforts, Sorger says. In Europe, that means big companies, and in the United States, it ranges from small to big firms. Some, such as Pfizer, Genentech and Microsoft Research, are already starting to hire, particularly postdocs. "I think we're in transition," Friend says, noting that several companies have invested in projects to model networks of genes, proteins and other molecules.

Altschuler says that he and his co-lab head Lani Wu are looking for researchers with training in cancer biology, imaging and cell signalling who can examine the responses of cancer cells to drugs. "The people we hire who have strong mathematical backgrounds also have a strong interest in applying their skills to cancer biology," he says. But with the field constantly changing, graduate education is not the only qualification. In the case of cancer systems biology, Wu says, "your background matters less than the research questions you want to answer". ■

Kelly Rae Chi is a freelance journalist based in Cary, North Carolina.

The frozen hive of her mind

A familiar face.

Deborah Walker

JACEY

My sister came to my mother's funeral. She stood at the gates, watching my uncles carrying the coffin from the flower-lined hearse. A pale ghost, standing apart from the rest of the mourners. Rose looked exactly as I remembered her. I had not seen her for 12 years, but she had not aged. I touched my hand to my hair, streaked through with grey.

Terminal cancer does that, slowly pulling its victim towards its breast and swiping its vicious claws at the grieving family, bleeding the life of out them. I had sent word to Rose when my mother was first diagnosed.

She was late, too late.

When she tried to enter the church, Reverend Joyce stepped in front of her. He stood with his arms crossed at the threshold of the church. "Your kind will not enter here," he said.

Dad came to reason with him, and there was a scene. Reverend Joyce had always seemed such a tolerant man. It surprised me to see him spluttering with righteous hatred. Cold-lifers spark the most astonishing feelings of passion.

After the service, I had a quiet word with Rose and asked her not to attend the grave. I didn't want Dad upset, anymore than he had to be.

"I'll go straight to the Green Man," she said.

She remembered, then. My mother had enjoyed a drink and the Green Man had been her local for almost 30 years.

"You should have stayed away," I said to Rose. I'd picked her out a plate of food from the buffet. We sat outside the pub in the biting November wind. We were in a mildewed corner of the patio, hidden from the rest of the mourners inside the pub.

"She was my mother, Elise." Her speech was slow, as if she had to sort through multiple options before selecting the correct response. I didn't tell her that Mother hadn't mentioned her name for more than ten years.

My sister's face was pale. I knew that her blood surged with cryoprotectants: anti-nucleating proteins, polyols and glucose derivatives that allowed her body to maintain the state of unnatural coldness that facilitated communication with the others of her lattice.

Our cousins, Alan and Sam, came outside lighting cigarettes. When they saw Rose, they stared. Sam looked away. Alan spat on the floor and muttered, "You cold bitch."

My voice was tight: "This is my mother's funeral."

Alan gave Rose one last look, nodded, and he and Sam both went back indoors.

Some people say that the cold-lifers are dead. That the spirit leaves the body when the heart stops beating. The programme had laser-cooled Rose to a point approaching absolute zero. I imagined her laid out on a stainless-steel slab with the 11 other volunteers, Bose–Einstein condensates forming throughout her body. Subatomic particles at extremely low temperatures act strangely. The condensates in Rose's body reached out and became entangled, linking Rose to the nascent lattice mind.

"Where are the others?" I asked.

"Most of us are in the observatory listening to the whispers from the Bowtie Nebula."

I nodded. The Bowtie Nebula was 5,000 light-years from Earth. It was the coldest natural place in the Universe. Bose–Einstein condensates form in its heart. Cold-lifers can communicate with entangled particles, regardless of distance. Distance was meaningless to cold-lifers, I wondered if time was also meaningless to my sister.

"Are you cold, Rose?" I asked. I rubbed her fingers, trying to push a little warmth into them. "You feel cold."

I wanted to ask whether she was happy, but I couldn't find the words.

Taken to the point of extreme and slowly revived, the cold-lifers changed; their blood sang with odd substances; their cells reached out and grew in strange patterns.

I hoped that she would live long enough for the lattice minds to gain acceptance. As part of the hive mind, Rose was smarter than scientists on the programme could measure. The government could appreciate, though, the technological advances that the cold-lifers were bringing. We were, the government repeatedly told us, standing on the cusp of incredible change. Would the cold-lifers be accepted once the material advantages they generated filtered through to the real world? Would their strangeness be overlooked?

Today I laid my mother to rest. My sister was ten years older than me, but she would certainly outlive me. Perhaps this was at the heart of the hatred that the cold-lifers engendered. It was the hatred for those who might never die.

"It was good to see you, Elise." I had the impression that the words were merely rote. There was no emotion, no humanity behind them. I could see why they were hated.

She stood up and walked away. I thought that part of my sister still existed, in that strange frozen hive of her mind. She had looked outward, and felt pity. She had wanted to share this moment of loss with her drone-sister, who would not outlive the coming of the cold winter. ■

After a 20-year period of procrastination, Deborah Walker has started to write short stories, poetry and tweets. Find her science fiction in *M-BRANE SF*, *Warrior Wisewoman II* and *DayBreak Magazine*.

Join the discussion of Futures in *Nature* at go.nature.com/QMAm2a